

Z. FICEK

**QUANTUM INTERFERENCE
AND COHERENCE**

Dedicated to our wives

Agnieszka Lichańska and Gisela Ilse

in appreciation of their help, patience and understanding

**ZBIGNIEW FICEK
STUART SWAIN**

QUANTUM INTERFERENCE AND COHERENCE

Theory and Experiments

Preface

The field that encompasses the term “quantum interference” combines a number of separate concepts, and has a variety of manifestations in different areas of physics. In the sense considered here, quantum interference is concerned with coherence and correlation phenomena in radiation fields and between their sources. It is intimately connected with the phenomenon of non-separability (or entanglement) in quantum mechanics. On account of this, it is obvious that quantum interference may be regarded as a component of quantum information theory, which investigates the ability of the electromagnetic field to transfer information between correlated (entangled) systems. Since it is important to transfer information with the minimum of corruption, the theory of quantum interference is naturally related to the theory of quantum fluctuations and decoherence.

Since the early days of quantum mechanics, interference has been described as the real quantum mystery. Feynman, in his famous introduction to the lectures on the single particle superposition principle, referred in the following way to the phenomenon of interference: “it has in it the heart of quantum mechanics”, and it is really ‘the only mystery’ of quantum mechanics. With the development of experimental techniques, it has been possible to carry out many of the early *Gedanken* experiments that played an important role in developing our understanding of the fundamentals of quantum interference and entanglement. Despite its long history, quantum interference still challenges our understanding, and continues to excite our imagination.

Quantum interference arises in some form or other in almost all the phenomena of quantum mechanics and its applications. Obviously, we have to be very selective in the topics we discuss here, and many important aspects are dealt with only briefly, or not at all. In writing the book our intention has been to concentrate on a systematic and consistent exposition of coherence and quantum interference phenomena in optical fields and atomic systems and to discuss the details of the most recent theoretical and experimental work in the field. We begin in Chap. 1 by discussing the basic principles of classical and quantum interference and summarizing some quite elementary concepts and definitions that are frequently used in the analysis of interference phenomena. The most important first- and second-order coherence effects are discussed including the welcher-weg problem, two-photon

nonclassical interference, interferometric interaction-free measurements, and quantum lithography. We also discuss important experiments that confirm these basic interference predictions.

The mathematical formalism of quantum interference in atomic systems is developed in Chap. 2 for multi-level and multi-atom systems in free space and cavity environments. For our purposes, the master equation of an atomic system is derived in the Born–Markov and rotating-wave approximations. The relation of the source field operators to the atomic dipole operators and retardation effects are then discussed. In this way the correlation functions of the electric field and their relationship to the atomic dipole operators are developed as a basic formulation. The concept of superposition states is then introduced in Chap. 3 and applied to three-level systems in Vee and Lambda configurations. The concept of multi-atom entangled states is also introduced so that one can see the relation between quantum interference effects in multi-level and multi-atom systems. A full description of the quantum beats phenomenon and its relation to quantum interference phenomena is also included.

Chapter 4 discusses quantum interference effects induced by spontaneous emission and the experimental evidence of spontaneously induced quantum interference effects in a molecular multi-level system. This chapter includes a discussion of decoherence free subspaces and the role of decoherence in the formation of entanglement. A section on the effect of cavity and photonic bandgap materials on spontaneous emission from an atomic system is included here because these are examples of other practical systems to control and suppress spontaneous emission.

The subject of coherence effects in multi-level systems is treated in Chap. 5. The theory of two major quantum interference effects – coherent population trapping and electromagnetically induced transparency in simple three-level systems – are explored and described in terms of the density matrix elements of these systems. These processes depend on the creation of coherent superpositions of atomic states with accompanying loss of absorption. The chapter includes a general treatment of the spatial propagation of electromagnetic fields in optically dense media, and the absorption properties of coherently prepared atomic systems. This chapter also discusses applications of coherently prepared systems in the enhancement of optical nonlinearities in electromagnetically induced transparency.

Material on the implementation of quantum interference is included in Chap. 6. This chapter also discusses the phase control of quantum interference and extremely large values (superbunching) of the second-order correlation functions. Methods for producing quantum interference effects in three-level systems with perpendicular transition dipole moments is considered to show how one can get around the well-known difficulty of finding atomic or molecular systems with parallel transition dipole moments. This chapter concludes

with a fairly detailed description of Fano profiles, laser-induced continuum structures and population trapping in photonic bandgap materials.

In Chap. 7 the theory of subluminal and superluminal propagation of a weak electromagnetic field in coherently prepared media is formulated and accompanied with many examples of the experimental observation of slow and fast light, and the storage of photons. The concept of polaritons is then introduced in terms of atomic and field operators.

The subject of quantum interference in a superposition of field states is considered in Chap. 8. The phase space formalism is described and quantum interference effects in phase space for several field states are discussed. Examples of the experimental reconstruction of Wigner functions and of the production of single-photon states are also included.

The final chapter discusses quantum interference effects with cold atoms. This includes the subjects of diffraction of cold atoms, interference of two Bose–Einstein condensates, collapses and revivals of an atomic interference pattern and interference experiments in coherent atom optics.

Since this book is based to a large extent on the combined work of many earlier contributors to the field of quantum interference, it is impossible to acknowledge our debts on an individual basis. We should, however, like to express our thanks to Peng Zhou who, during his stay at The Queen’s University of Belfast, carried out some of the work on control of decoherence and field induced quantum interference presented in Chaps. 4 and 6. We are greatly appreciative of the help and suggestions received from many colleagues, including Ryszard Tanaś, Helen Freedhoff, Peter Drummond, Bryan Dalton, Shi-Yao Zhu, Christoph Keitel, Josip Seke, Gerhard Adam, Andrey Soldatov, Joerg Evers, Terry Rudolph and Uzma Akram. We are also grateful to Alexander Akulshin, Immanuel Bloch, Dmitry Budker, Milena D’Angelo, Juergen Eschner, Edward Fry, Christian Hettich, Alexander Lvovsky, Steven Rolston, and Lorenz Windholz for sending us originals of the reproduced figures of their experimental results.

Brisbane, Belfast,
March 2004

Zbigniew Ficek
Stuart Swain

Contents

| | | |
|----------|---|-----------|
| 1 | Classical and Quantum Interference and Coherence | 1 |
| 1.1 | Classical Interference and Optical Interferometers | 2 |
| 1.1.1 | Young's Double Slit Interferometer | 2 |
| 1.1.2 | First-Order Coherence | 4 |
| 1.1.3 | Welcher Weg Problem | 7 |
| 1.1.4 | Experimental Tests of the Welcher Weg Problem | 11 |
| 1.1.5 | Second-Order Coherence | 15 |
| 1.1.6 | Hanbury-Brown and Twiss Interferometer | 17 |
| 1.1.7 | Mach–Zehnder Interferometer | 19 |
| 1.2 | Principles of Quantum Interference | 20 |
| 1.2.1 | Two-Photon Nonclassical Interference | 21 |
| 1.2.2 | The Hong–Ou–Mandel Interferometer | 25 |
| 1.3 | Quantum Erasure | 28 |
| 1.4 | Quantum Nonlocality | 30 |
| 1.5 | Interferometric Interaction-Free Measurements | 32 |
| 1.5.1 | Negative-Result Measurements | 33 |
| 1.5.2 | Schemes of Interaction-Free Measurements | 34 |
| 1.6 | Quantum Interferometric Lithography | 38 |
| 1.7 | Three-Photon Interference | 42 |
| 1.7.1 | Three-Photon Classical Interference | 43 |
| 1.7.2 | Three-Photon Nonclassical Interference | 44 |
| 2 | Quantum Interference in Atomic Systems: Mathematical Formalism | 47 |
| 2.1 | Master Equation of a Multi-Dipole System | 48 |
| 2.1.1 | Master Equation of a Single Multi-Level Atom | 48 |
| 2.1.2 | Master Equation of a Multi-Atom System | 67 |
| 2.2 | Correlation Functions of Atomic Operators | 74 |
| 2.2.1 | Correlation Functions for a Multi-Level Atom | 74 |
| 2.2.2 | Correlation Functions for a Multi-Atom System | 80 |
| 2.2.3 | Spectral Expressions | 82 |

| | | |
|----------|--|-----|
| 3 | Superposition States and Modification of Spontaneous Emission Rates | 85 |
| 3.1 | Superposition States in a Multi-Level System | 85 |
| 3.1.1 | Superpositions Induced by Spontaneous Emission | 87 |
| 3.2 | Multi-Atom Superposition (Entangled) States | 91 |
| 3.2.1 | Entanglement | 91 |
| 3.2.2 | Two Interacting Atoms | 93 |
| 3.2.3 | Entangled States of Two Identical Atoms | 94 |
| 3.2.4 | Entangled States of Two Nonidentical Atoms | 96 |
| 3.3 | Experimental Evidence of the Collective Damping and Frequency Shift | 104 |
| 3.4 | General Criteria for Interference in Two-Atom Systems | 110 |
| 3.4.1 | Interference Pattern with Two Atoms | 111 |
| 3.4.2 | Experimental Observation of the Interference Pattern in a Two-Atom System | 113 |
| 3.5 | Quantum Beats | 115 |
| 3.5.1 | Theory of Quantum Beats in Multi-Level Systems | 116 |
| 3.5.2 | Quantum Beats in the Radiation Intensity from a Multi-Level Atom | 120 |
| 3.5.3 | Quantum Beats in the Radiation Intensity from Two Nonidentical Atoms | 126 |
| 3.5.4 | Experimental Observation of Quantum Beats in a Type I System | 129 |
| 3.5.5 | Quantum Beats in the Intensity–Intensity Correlations | 131 |
| 3.6 | Interference Pattern with a Dark Center | 135 |
| 4 | Quantum Interference as a Control of Decoherence | 139 |
| 4.1 | Modified Spontaneous Emission | 139 |
| 4.1.1 | Effect of Environment on Spontaneous Emission | 140 |
| 4.1.2 | Modification by a Moderate Q Cavity | 142 |
| 4.1.3 | Modification by Photonic Crystals | 145 |
| 4.2 | Quantum Interference in Vee Systems | 146 |
| 4.2.1 | Population Trapping and Dark States | 148 |
| 4.2.2 | Probing Quantum Interference in a Vee System | 150 |
| 4.3 | Spectral Control of Spontaneous Emission | 156 |
| 4.4 | Experimental Evidence of Quantum Interference | 162 |
| 4.4.1 | Energy Levels of the Molecular System | 162 |
| 4.4.2 | Master Equation of the System | 163 |
| 4.4.3 | Two-Photon Excitation | 164 |
| 4.4.4 | One- and Two-Photon Excitations | 166 |
| 4.5 | Decoherence Free Subspaces | 169 |
| 4.5.1 | A Simple Example of a Decoherence Free Subspace | 169 |
| 4.5.2 | Experimental Verification of Decoherence Free Subspaces | 171 |

| | | |
|----------|--|------------|
| 4.5.3 | Tests on the Master Equation for a Decoherence Free Subspace | 173 |
| 5 | Coherence Effects in Multi-Level Systems | 179 |
| 5.1 | Three-Level Systems | 179 |
| 5.1.1 | The Basic Equations for Coherent Population Trapping | 181 |
| 5.1.2 | The Solutions Under Two-Photon Resonance | 182 |
| 5.1.3 | The General Equations of Motion for the Density Matrix | 183 |
| 5.1.4 | Steady-State Solutions | 188 |
| 5.1.5 | Observation of Coherent Population Trapping | 190 |
| 5.1.6 | Velocity-Selective Coherent Population Trapping | 192 |
| 5.2 | Electromagnetically Induced Transparency in the Lambda System | 196 |
| 5.2.1 | Realization of EIT | 200 |
| 5.3 | Lasing Without Inversion | 201 |
| 5.3.1 | A Model for LWI | 203 |
| 5.3.2 | Observation of LWI | 205 |
| 5.4 | Spatial Propagation of EM Fields in Optical Media | 207 |
| 5.5 | Absorptive and Dispersive Properties of Optically Dense Media | 210 |
| 5.5.1 | Absorptive and Dispersive Properties of Two-Level Atoms | 213 |
| 5.5.2 | Dressed-Atom Model of a Driven Two-Level Atom | 220 |
| 5.5.3 | Absorption and Dispersion with Multichromatic Driving Fields | 223 |
| 5.5.4 | Collisional Dephasing and Coherent Population Oscillations | 226 |
| 5.6 | Applications of EIT in Nonlinear Optics | 229 |
| 5.6.1 | Enhancement of Nonlinear Susceptibilities | 230 |
| 5.6.2 | Observation of Enhancement of Nonlinear Susceptibilities | 234 |
| 5.6.3 | Enhancement of Refractive Index | 236 |
| 6 | Field Induced Quantum Interference | 237 |
| 6.1 | Resonance Fluorescence in Driven Vee Systems | 238 |
| 6.2 | Phase Control of Quantum Interference | 244 |
| 6.2.1 | Phase Control of Population Distribution | 245 |
| 6.2.2 | Phase Control of the Fluorescence Spectrum | 247 |
| 6.2.3 | Experimental Evidence of Phase Control of Quantum Interference | 248 |
| 6.3 | Superbunching | 251 |
| 6.3.1 | Distinguishable Photons | 253 |
| 6.3.2 | Indistinguishable Photons | 254 |

| | | |
|----------|---|------------|
| 6.3.3 | Physical Interpretation | 256 |
| 6.4 | Implementation of Quantum Interference | 258 |
| 6.4.1 | External Field Mixing | 258 |
| 6.4.2 | Two-Level Atom in a Polychromatic Field | 260 |
| 6.4.3 | dc Field Simulation of Quantum Interference | 262 |
| 6.4.4 | Pre-selected Cavity Polarization Method | 267 |
| 6.4.5 | Anisotropic Vacuum Approach | 270 |
| 6.5 | Fano Profiles | 271 |
| 6.6 | Laser-Induced Continuum Structure | 275 |
| 6.6.1 | Weak-Field Treatment | 275 |
| 6.6.2 | Observation of Laser-Induced Structures | 277 |
| 6.7 | Nonperturbative Treatment of Laser-Induced Continuum Structure | 279 |
| 6.8 | Quantum Interference in Photonic Bandgap Structures | 282 |
| 6.8.1 | The Two-Level Atom | 285 |
| 6.8.2 | The Three-Level Atom | 288 |
| 7 | Slow and Fast Light and Storage of Photons | 293 |
| 7.1 | Refractive Index and Group Velocity | 294 |
| 7.1.1 | Light Guiding Light | 297 |
| 7.1.2 | Group Velocity Reduction in a Driven Lambda-Type Atom | 301 |
| 7.1.3 | Group Velocity Reduction in a System with Decay-Induced Coherences | 305 |
| 7.1.4 | Phase Control of Group Velocity | 309 |
| 7.2 | Experimental Observations of Slow Propagation of Light | 313 |
| 7.3 | Experimental Observation of Negative Group Velocities | 322 |
| 7.4 | Bright- and Dark-State Polaritons | 326 |
| 7.4.1 | Collective Atomic Trapping States | 330 |
| 7.4.2 | Experimental Realization of Light Storage in Atomic Media | 332 |
| 8 | Quantum Interference in Phase Space | 337 |
| 8.1 | Phase Space in Classical and Quantum Mechanics | 337 |
| 8.2 | The Quasi-probability Distributions | 339 |
| 8.3 | Wigner Functions for Some Common Fields | 343 |
| 8.3.1 | Fock States | 343 |
| 8.3.2 | Coherent States | 344 |
| 8.3.3 | Chaotic Field | 345 |
| 8.3.4 | Squeezed Coherent States | 345 |
| 8.4 | Expansion in Fock States | 346 |
| 8.5 | Superpositions of Fock States | 348 |
| 8.6 | Experimental Considerations | 352 |
| 8.6.1 | Reconstruction of Wigner Functions | 352 |
| 8.6.2 | Production of Single-Photon States | 353 |

| | | |
|----------|--|------------|
| 8.7 | Photon Number Distribution | 354 |
| 8.8 | Superpositions of Coherent States | 356 |
| 8.8.1 | Superposition of N Coherent States | 356 |
| 8.8.2 | Two Coherent State Superpositions | 357 |
| 8.9 | Photon Number Distribution of Displaced Number States ... | 361 |
| 8.10 | Photon Number Distribution of a Highly Squeezed State | 362 |
| 8.11 | Quantum Interference in Phase Space | 366 |
| 8.11.1 | The WKB Method | 366 |
| 8.12 | Area of Overlap Formalism | 368 |
| 8.12.1 | Photon Number Distribution of Coherent States | 371 |
| 8.12.2 | Photon Number Distribution of Squeezed State | 373 |
| 9 | Quantum Interference in Atom Optics | 377 |
| 9.1 | Interference and Diffraction of Cold Atoms | 378 |
| 9.2 | Interference of Two Bose–Einstein Condensates | 386 |
| 9.2.1 | Relative Phase Between Two Condensates | 387 |
| 9.2.2 | Relative Phase in Josephson Junctions | 389 |
| 9.3 | Interference Between Colliding Condensates | 392 |
| 9.4 | Collapses and Revivals of an Atomic Interference Pattern | 393 |
| 9.5 | Interference Experiments in Coherent Atom Optics | 395 |
| 9.5.1 | Experimental Evidence of Relative Phase Between Two Condensates | 395 |
| 9.5.2 | Atomic Interferometers | 397 |
| 9.5.3 | Collapses and Revivals of a Bose–Einstein Condensate | 401 |
| 9.6 | Higher Order Coherence in a BEC | 402 |
| | References | 405 |
| | Index | 413 |

1 Classical and Quantum Interference and Coherence

Interference is the simplest phenomenon that reveals the wave nature of radiation and the correlations between radiation fields. The concept of optical interference is illustrated with Michelson's and Young's experiments, in which a beam of light is divided into two beams that, after travelling separately a distance long compared to the optical wavelength, are recombined at an observation point. If there is a small path difference between the beams, interference fringes are found at the observation (recombination) point. The observation of the fringes is a manifestation of temporal coherence (Michelson interferometer) or spatial coherence (Young interferometer) between the two light beams. Interference experiments played a central role in the early discussions of the dual nature of light, and the appearance of an interference pattern was recognized as a demonstration that light is wave-like [1]. The interpretation of interference experiments changed with the birth of quantum mechanics, when corpuscular properties of light showed up in many experiments. In addition, interference was predicted and observed between independent light beams [2]. This type of interference results from higher order correlations between radiation fields, and apparently contradicts the well-known remark of Dirac that "each photon interferes only with itself. Interference between different photons never occurs". We may interpret the detection of a photon as a measurement that forces the photon into a superposition state. The interference pattern observed in the Young's double slit experiment results from a superposition of the probability amplitudes for the photon to take either of the two possible pathways. After the interaction of the photon with the slits, the system of the two slits and a photon is a *single* quantum system. The resulting interference is a clear example of non-separability or entanglement in quantum mechanics [3]. Although interference is usually associated with light, interference has also been observed with many kinds of material particles, such as electrons, neutrons and atoms [4].

This introductory chapter concerns the basic theoretical concepts of classical and quantum interference, and elementary interference experiments with optical fields. We introduce concepts and definitions that are important for later discussion and present some essential mathematical approaches. The experiments discussed are those that demonstrate the basic physical ideas concerning first- and second-order interference and coherence. The nature of

interference is so fundamental that it connects with many different aspects of atomic physics, classical and quantum optics, such as atom-field interactions, the theory of measurement, entanglement and collective interactions.

1.1 Classical Interference and Optical Interferometers

Optical interference is generally regarded as a classical wave phenomenon. Despite this, classical and quantum theories of optical interference readily explain the presence of an interference pattern, but there are interference effects that distinguish the quantum nature of light from the wave nature. In particular, there are second-order interference effects involving the joint detection of two fields where correlations are measured by two photodetectors and the quantum nature of light becomes apparent when the number of photons is small. In this section, we present elementary concepts and descriptions of the classical theory of optical interference, and illustrate the role of optical coherence.

We characterize a light field by its electric field. In many classical calculations, a Fourier series or integral is used to express the electric field $\mathbf{E}(\mathbf{R}, t)$ as the sum of two complex terms

$$\mathbf{E}(\mathbf{R}, t) = \mathbf{E}(\mathbf{R}, t) + \mathbf{E}^*(\mathbf{R}, t) . \quad (1.1)$$

The first term, $\mathbf{E}(\mathbf{R}, t)$ is called the *positive frequency part*, and contains all terms which vary as $\exp(i\omega t)$, for $\omega > 0$. In future, we shall work almost exclusively with the positive frequency part, and we shall specify the electric simply by its positive frequency part $\mathbf{E}(\mathbf{R}, t)$.

1.1.1 Young's Double Slit Interferometer

The first step in our study of optical interference and coherence is Young's double slit experiment, which is the prototype for demonstrations of optical interference and for all quantitative measurements of so-called first-order coherence. The presence of interference fringes in the experiment may be regarded as a manifestation of first-order coherence. Young's double slit experiment has been central to our understanding of many important aspects of classical and quantum mechanics [1]. The essential feature of any optical interference experiment is that the light beams from several sources are allowed to come together and mix with each other, and the resulting light intensity is measured by photodetectors located at various points. We characterize interference by the dependence of the resulting light intensities on the optical path difference or phase shifts.

A schematic diagram of an interference experiment of the Young type is shown in Fig. 1.1. Two monochromatic light beams of amplitudes $\mathbf{E}_1(\mathbf{r}_1, t_1)$ and $\mathbf{E}_2(\mathbf{r}_2, t_2)$ produced at two narrow slits S_1 and S_2 , separated by the

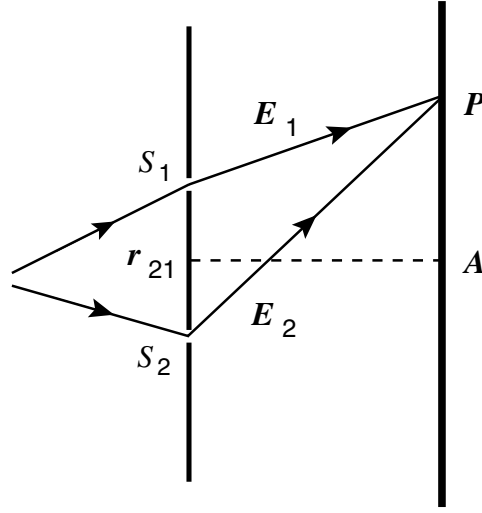


Fig. 1.1. Schematic diagram of Young's double slit experiment. Two monochromatic light beams emerging from the slits S_1 and S_2 interfere to form on the observing screen an interference pattern, symmetrical about the point A

vector $\mathbf{r}_{21} \equiv \mathbf{r}_2 - \mathbf{r}_1$, incident on the screen at a point P . The resultant amplitude of the field detected at the point P is a linear superposition of the two fields

$$\mathbf{E}(\mathbf{R}, t) = \mathbf{E}_1(\mathbf{R}, t) + \mathbf{E}_2(\mathbf{R}, t) , \quad (1.2)$$

where $\mathbf{E}_i(\mathbf{R}, t)$ is the electric field produced by the i th slit and evaluated at the position \mathbf{R} of the observation point P . We can relate the field $\mathbf{E}_i(\mathbf{R}, t)$ to the field $\mathbf{E}_i(\mathbf{r}_i, t - t_i)$ emerging from the position of the i th slit:

$$\mathbf{E}_i(\mathbf{R}, t) = \frac{s_i}{R_i} \mathbf{E}_i(\mathbf{r}_i, t - t_i) , \quad i = 1, 2 , \quad (1.3)$$

where $R_i = |\mathbf{R} - \mathbf{r}_i|$ is the displacement of the i th slit from the field point P at \mathbf{R} , $t_i = R_i/c$ is the time taken for the field to travel from the i th slit to the point P , and s_i is a constant which depends on the geometry and the size of the i th slit.

The fact that the resultant amplitude at a given point is obtained by adding the amplitudes of the light beams produced by the slits gives rise to the possibility of constructive or destructive interference. There are, however, certain fundamental conditions that must be satisfied to obtain the phenomenon of interference, and we discuss these conditions in the following section.

In Young's experiment, a single photodetector is used to measure the probability $P_1(\mathbf{R}, t)$ of detecting a photon at time t within a short time interval Δt as a function of the position \mathbf{R} of the detector. Assuming that the photodetector responds to the *total* electric field at \mathbf{R} , the mean probability is given by

$$P_1(\mathbf{R}, t) = \sigma \langle I(\mathbf{R}, t) \rangle \Delta t, \quad (1.4)$$

where σ is the efficiency of the detector, $I(\mathbf{R}, t)$ is the instantaneous total intensity at \mathbf{R} :

$$I(\mathbf{R}, t) = \mathbf{E}^*(\mathbf{R}, t) \cdot \mathbf{E}(\mathbf{R}, t), \quad (1.5)$$

and the angular brackets denote an ensemble average over different realizations of the field.

Substituting (1.2) and (1.3) into (1.5), we obtain

$$\begin{aligned} I(\mathbf{R}, t) = & |u_1|^2 I_1(\mathbf{r}_1, t - t_1) + |u_2|^2 I_2(\mathbf{r}_2, t - t_2) \\ & + 2\text{Re} [u_1^* u_2 \mathbf{E}_1^*(\mathbf{r}_1, t - t_1) \cdot \mathbf{E}_2(\mathbf{r}_2, t - t_2)] , \end{aligned} \quad (1.6)$$

where

$$I_i(\mathbf{r}_i, t - t_i) = \mathbf{E}_i^*(\mathbf{r}_i, t - t_i) \cdot \mathbf{E}_i(\mathbf{r}_i, t - t_i) \quad (1.7)$$

is the intensity of the field emerging from the i th slit in the absence of the other, and $u_i = s_i/R_i$.

Hence, the average intensity at the point \mathbf{R} on the screen at time t may be written as

$$\begin{aligned} \langle I(\mathbf{R}, t) \rangle = & |u_1|^2 \langle I_1(\mathbf{r}_1, t - t_1) \rangle + |u_2|^2 \langle I_2(\mathbf{r}_2, t - t_2) \rangle \\ & + 2\text{Re} \{ u_1^* u_2 \langle \mathbf{E}_1^*(\mathbf{r}_1, t - t_1) \cdot \mathbf{E}_2(\mathbf{r}_2, t - t_2) \rangle \} , \end{aligned} \quad (1.8)$$

where the brackets denote an ensemble average over different realizations of the field.

1.1.2 First-Order Coherence

It is convenient to introduce the first-order field correlation functions by the relation

$$G_{12}^{(1)}(\mathbf{r}_1, \tau_1; \mathbf{r}_2, \tau_2) = \langle \mathbf{E}_1^*(\mathbf{r}_1, \tau_1) \cdot \mathbf{E}_2(\mathbf{r}_2, \tau_2) \rangle . \quad (1.9)$$

It gives the correlation between the field amplitudes \mathbf{E}_1 and \mathbf{E}_2 emanating from the two slits. The normalized form is given by

$$\begin{aligned} g_{12}^{(1)}(\mathbf{r}_1, \tau_1; \mathbf{r}_2, \tau_2) &= \frac{G_{12}^{(1)}(\mathbf{r}_1, \tau_1; \mathbf{r}_2, \tau_2)}{\sqrt{G_{12}^{(1)}(\mathbf{r}_1, \tau_1; \mathbf{r}_1, \tau_1) G_{12}^{(1)}(\mathbf{r}_2, \tau_2; \mathbf{r}_2, \tau_2)}} \\ &= \frac{\langle \mathbf{E}_1^*(\mathbf{r}_1, \tau_1) \cdot \mathbf{E}_2(\mathbf{r}_2, \tau_2) \rangle}{\sqrt{\langle I_1(\mathbf{r}_1, \tau_1) \rangle \langle I_2(\mathbf{r}_2, \tau_2) \rangle}} . \end{aligned} \quad (1.10)$$

With this notation (1.6) may be written as

$$\begin{aligned} \langle I(\mathbf{R}, t) \rangle &= |u_1|^2 G_{12}^{(1)}(\mathbf{r}_1, t - t_1; \mathbf{r}_1, t - t_1) + |u_2|^2 G_{12}^{(1)}(\mathbf{r}_2, t - t_2; \mathbf{r}_2, t - t_2) \\ &\quad + 2\text{Re} \left\{ u_1^* u_2 G_{12}^{(1)}(\mathbf{r}_1, t - t_1; \mathbf{r}_2, t - t_2) \right\} . \end{aligned} \quad (1.11)$$

The normalized first-order correlation function determines the correlations between the field amplitudes relative to the magnitudes of the uncorrelated amplitudes, and satisfies the condition $0 \leq |g^{(1)}| \leq 1$. The normalized correlation function (1.10) is often called the *degree of coherence*, and $g^{(1)} = 0$ for a field that is the sum of two independent (completely uncorrelated) fields, whereas $g^{(1)} = 1$ for perfectly correlated fields. The intermediate values of the correlation function ($0 < |g^{(1)}| < 1$) characterize a partial correlation (coherence) between the fields.

Before proceeding, we note that the definition of the correlation function given in (1.10) is appropriate to the case where the detector at the viewing point P of the Young's fringes experiment responds to the *total* electric field at that point. However, one could have the situation where the detector responds only to a particular polarization of the positive frequency part of the electric field at P . In this case, the detector responds to the component of the electric field in the polarization direction, $E_d(\mathbf{R}, t) = \bar{\mathbf{e}}_d \cdot \mathbf{E}(\mathbf{R}, t)$, where $\bar{\mathbf{e}}_d$ is the unit vector that defines the polarization detected. Instead of (1.4), the appropriate observable is then

$$P_{1,d}(\mathbf{R}, t) = \sigma \langle I_d(\mathbf{R}, t) \rangle \Delta t , \quad (1.12)$$

where

$$I_d(\mathbf{R}, t) = E_d^*(\mathbf{R}, t) \cdot E_d(\mathbf{R}, t) , \quad (1.13)$$

is the fraction of the intensity carried by the field component $E_d(\mathbf{R}, t)$. This prompts us to introduce the more general definition of the correlation function

$$G_{\alpha\beta}^{(1)}(\mathbf{r}_1, \tau_1; \mathbf{r}_2, \tau_2) = \langle E_\alpha^*(\mathbf{r}_1, \tau_1) E_\beta(\mathbf{r}_2, \tau_2) \rangle , \quad (1.14)$$

where E_α and E_β are specified components of the positive frequency part of the electric field. The normalized correlation function is defined analogously to (1.10) as

$$\begin{aligned} g_{\alpha\beta}^{(1)}(\mathbf{r}_1, \tau_1; \mathbf{r}_2, \tau_2) &= \frac{G_{\alpha\beta}^{(1)}(\mathbf{r}_1, \tau_1; \mathbf{r}_2, \tau_2)}{\sqrt{G_{\alpha\beta}^{(1)}(\mathbf{r}_1, \tau_1; \mathbf{r}_1, \tau_1) G_{\alpha\beta}^{(1)}(\mathbf{r}_2, \tau_2; \mathbf{r}_2, \tau_2)}} \\ &= \frac{\langle \mathbf{E}_1^*(\mathbf{r}_1, \tau_1) \cdot \mathbf{E}_2(\mathbf{r}_2, \tau_2) \rangle}{\sqrt{\langle I_d(\mathbf{r}_1, \tau_1) \rangle \langle I_d(\mathbf{r}_2, \tau_2) \rangle}} . \end{aligned} \quad (1.15)$$

The definitions (1.14) and (1.15) are the ones usually employed in discussions of first-order coherence [5]. Here, to be definite, we continue to work with the definitions (1.9) and (1.10).

Usually in experiments the detection time of the fields is much longer than a characteristic time of the system, e.g. the time required for the field to travel from a slit to the detector. In this case, the transient properties of the fields are not important, and we can replace the field amplitudes by their stationary values. For a stationary field the first-order correlation function is independent of translations of the time origin – that is, the correlation function depends only on the time difference $\tau = t_2 - t_1$. For this type of field, the ensemble average can be replaced by the time average

$$\langle \dots \rangle = \lim_{T \rightarrow \infty} \frac{1}{T} \int_0^T \dots dt, \quad (1.16)$$

where T is the detection time of the field. Then, the first-order correlation function for a stationary field can be written as

$$g_{12}^{(1)}(\mathbf{r}_1, \mathbf{r}_2, \tau) = \lim_{T \rightarrow \infty} \frac{1}{T} \int_0^T dt \mathbf{E}_1^*(\mathbf{r}_1, t) \cdot \mathbf{E}_2(\mathbf{r}_2, t + \tau). \quad (1.17)$$

To simplify our discussion, we assume that u_1 and u_2 have the same phase. Then, (1.8) shows that the average intensity detected at the point P depends only on the real part of the first-order correlation function. To explore this dependence, we can write the normalized first-order correlation function as

$$g_{12}^{(1)}(\mathbf{r}_1, t - t_1; \mathbf{r}_2, t - t_2) = |g_{12}^{(1)}(\mathbf{r}_1, t - t_1; \mathbf{r}_2, t - t_2)| \times \exp[i\alpha(\mathbf{r}_1, t - t_1; \mathbf{r}_2, t - t_2)], \quad (1.18)$$

where

$$\alpha(\mathbf{r}_1, t - t_1; \mathbf{r}_2, t - t_2) = \arg \left[g_{12}^{(1)}(\mathbf{r}_1, t - t_1; \mathbf{r}_2, t - t_2) \right]. \quad (1.19)$$

Substituting (1.2) and (1.10) into (1.8), we obtain the following expression for the average intensity

$$\begin{aligned} \langle I(\mathbf{R}, t) \rangle &= |u_1|^2 \langle I_1(\mathbf{r}_1, t - t_1) \rangle + |u_2|^2 \langle I_2(\mathbf{r}_2, t - t_2) \rangle \\ &\quad + 2|u_1||u_2| \sqrt{\langle I_1(\mathbf{r}_1, t - t_1) \rangle \langle I_2(\mathbf{r}_2, t - t_2) \rangle} \\ &\quad \times |g_{12}^{(1)}(\mathbf{r}_1, t - t_1; \mathbf{r}_2, t - t_2)| \\ &\quad \times \cos[\alpha(\mathbf{r}_1, t - t_1; \mathbf{r}_2, t - t_2)]. \end{aligned} \quad (1.20)$$

The average intensity $\langle I(\mathbf{R}, t) \rangle$ depends on $|g_{12}^{(1)}|$ and the position of the observation point P through the cosine term. In many cases, the $|g_{12}^{(1)}|$ factor in (1.18) will be very slowly-varying compared to the phase α . For the remainder of this section, we assume $|g_{12}^{(1)}|$ to be constant. Moving along the screen, the cosine term will change rapidly with position. Hence, the average intensity will vary sinusoidally with the position of P on the observing screen, giving an *interference pattern* symmetrical about the point A . In the case of

identical slits ($u_1 = u_2 = u$) and perfectly correlated fields ($|g_{12}^{(1)}| = 1$), the observed intensity can exhibit alternate minima $(\sqrt{I_1} - \sqrt{I_2})^2$ and maxima $(\sqrt{I_1} + \sqrt{I_2})^2$. The maxima correspond to constructive interference, and the minima correspond to the opposite case of destructive interference. Thus, for equal intensities of the two fields ($I_1 = I_2 = I_0$), the total average intensity can vary at the point P from $\langle I \rangle_{\min} = 0$ to $\langle I \rangle_{\max} = 4\langle I_0 \rangle$, giving maximal variation in the interference pattern. For two independent fields, $|g_{12}^{(1)}| = 0$, and then the resulting intensity at P is just the sum of the intensities of the two fields, and does not vary with the position of P .

The usual measure of the depth of modulation (fringe contrast) of interference fringes is the *visibility* of the interference pattern, defined as

$$C = \frac{\langle I(\mathbf{R}, t) \rangle_{\max} - \langle I(\mathbf{R}, t) \rangle_{\min}}{\langle I(\mathbf{R}, t) \rangle_{\max} + \langle I(\mathbf{R}, t) \rangle_{\min}}, \quad (1.21)$$

where $\langle I(\mathbf{R}, t) \rangle_{\max}$ and $\langle I(\mathbf{R}, t) \rangle_{\min}$ represent the intensity maxima and minima at the point P .

Since

$$\langle I(\mathbf{R}, t) \rangle_{\max} = |u|^2 \left(\langle I_1 \rangle + \langle I_2 \rangle + 2\sqrt{\langle I_1 \rangle \langle I_2 \rangle} |g_{12}^{(1)}| \right), \quad (1.22)$$

and

$$\langle I(\mathbf{R}, t) \rangle_{\min} = |u|^2 \left(\langle I_1 \rangle + \langle I_2 \rangle - 2\sqrt{\langle I_1 \rangle \langle I_2 \rangle} |g_{12}^{(1)}| \right), \quad (1.23)$$

we readily find for the visibility of the resulting interference pattern

$$C = \frac{2\sqrt{\langle I_1 \rangle \langle I_2 \rangle}}{(\langle I_1 \rangle + \langle I_2 \rangle)} |g_{12}^{(1)}|. \quad (1.24)$$

Thus, the coherence $|g_{12}^{(1)}|$ and the relative intensities of the fields determine the visibility of the interference fringes. In the special case of equal intensities of the two fields ($\langle I_1 \rangle = \langle I_2 \rangle$), the visibility (1.24) reduces to $C = |g_{12}^{(1)}|$, i.e. the visibility equals the degree of coherence. For perfectly correlated fields $|g_{12}^{(1)}| = 1$, and then $C = 1$, while $C = 0$ for uncorrelated fields. When the intensities of the superimposed fields are different ($I_1 \neq I_2$), the visibility of the interference fringes is always smaller than unity even for perfectly correlated fields, and reduces to zero for either $I_1 \gg I_2$ or $I_1 \ll I_2$.

1.1.3 Welcher Weg Problem

Interference is the physical manifestation of the intrinsic indistinguishability of the sources or of the radiation paths. According to (1.24), the visibility reduces to zero for either $I_1 \gg I_2$ or $I_1 \ll I_2$, in which case the path followed by the field is well established. The dependence of the visibility on the relative

intensities of the superimposed fields is related to the problem of extracting which way information has been transferred through the slits into the point P . This problem is often referred to by the German phrase “welcher weg” (which-way). This example shows that the observation of an interference pattern and the acquisition of which-way information are mutually exclusive.

We introduce an inequality which relates, at the point P , the fringe visibility C displayed and the degree of which-way information D as [6]

$$D^2 + C^2 \leq 1 . \quad (1.25)$$

It is apparent that the extreme conditions of perfect fringe visibility ($C = 1$) and complete which-way information ($D = 1$) are mutually exclusive. The inequality (1.25) is therefore a kind of uncertainty relationship, in the sense that high fringe visibility must be accompanied by low which-way information, and vice-versa. In fact, the relation (1.25) is an example of Bohr’s principle of *complementarity*, that interference and which-way information are mutually exclusive concepts [7]. For example, if the fields emanating from the slits s_1 and s_2 are of very different intensities, one can obtain which-way information by locating an intensity detector at the point P . This rules out any first-order interference, which is always a manifestation of the intrinsic indistinguishability of two possible paths of the detected field. If the intensities of the fields are very different, the detector can register with almost perfect accuracy the path taken, giving $D \simeq 1$, and thus from (1.25) $C \simeq 0$, resulting in the disappearance of the interference fringes. This is also clearly seen from (1.24), since if either $I_1 \gg I_2$ or $I_1 \ll I_2$, the visibility $C \approx 0$ even for $|g_{12}^{(1)}| = 1$. On the other hand, interference fringes can occur when the fields have equal intensities, as the detector cannot then distinguish from which slit the field arriving at the point P emanated. Then the which-way information is zero, ($D = 0$), and perfect fringe visibility ($C = 1$) is possible.

In a similar way, the frequencies and phases of the detected fields can be used to determine which-way information. The information about the frequencies and phases of the detected fields is provided by the argument (phase) of $g_{12}^{(1)}$. Moreover, the phase of $g_{12}^{(1)}$ determines the positions of the fringes in the interference pattern. If the observation point P lies in the far field zone of the radiation emitted by the slits, the fields at the observation point can be approximated by plane waves, for which we can write

$$\begin{aligned} \mathbf{E}(\mathbf{R}_i, t - t_i) &\approx \mathbf{E}(\mathbf{R}_i, t) \exp[-i(\omega_i t_i + \phi_i)] \\ &= \mathbf{E}(\mathbf{R}_i, t) \exp[-i(\omega_i R_i/c + \phi_i)] , \quad i = 1, 2 , \end{aligned} \quad (1.26)$$

where ω_i is the angular frequency of the i th field and ϕ_i is its initial phase which, in general, can depend on time. We can express the frequencies in terms of the average frequency $\omega_0 = (\omega_1 + \omega_2)/2$ and the difference frequency $\Delta = \omega_2 - \omega_1$ of the two fields as

$$\omega_1 = \omega_0 - \frac{1}{2}\Delta , \quad \omega_2 = \omega_0 + \frac{1}{2}\Delta . \quad (1.27)$$

Since the observation point lies in far field zone of the radiation emitted by the slits, i.e. the separation between the slits is very small compared to the distance to the point P , we can write approximately

$$R_i = |\mathbf{R} - \mathbf{r}_i| \approx R - \bar{\mathbf{R}} \cdot \mathbf{r}_i, \quad (1.28)$$

where $\bar{\mathbf{R}} = \mathbf{R}/R$ is the unit vector in the direction \mathbf{R} . Hence, substituting (1.26) with (1.27) and (1.28) into (1.10), we obtain

$$\begin{aligned} g_{12}^{(1)}(\mathbf{R}_1, t_1; \mathbf{R}_2, t_2) &= |g_{12}^{(1)}(\mathbf{R}_1, t; \mathbf{R}_2, t)| \exp(-ik_0 \bar{\mathbf{R}} \cdot \mathbf{r}_{21}) \\ &\times \exp \left[i \left(k_0 \tilde{R} \frac{\Delta}{\omega_0} + \delta\phi \right) \right], \end{aligned} \quad (1.29)$$

where $\mathbf{r}_{ij} = \mathbf{r}_i - \mathbf{r}_j$ so that $\mathbf{r}_{21} = \mathbf{r}_2 - \mathbf{r}_1$ is the separation of the slits, $\tilde{R} = R + \bar{\mathbf{R}} \cdot (\mathbf{r}_1 + \mathbf{r}_2)/2$, $\delta\phi = \phi_2 - \phi_1$, $k_0 = \omega_0/c = 2\pi/\lambda_0$, and λ_0 represents the mean wavelength of the fields. Let us analyze the physical meaning of the exponents appearing on the right-hand side of (1.29). We assume $|g_{12}^{(1)}(\mathbf{R}_1, t; \mathbf{R}_2, t)|$ to be slowly-varying, as is usually the case. The first exponent depends on the separation between the slits and the position \mathbf{R} of the point P . For small separations the exponent slowly changes with the position \mathbf{R} and leads to minima and maxima in the interference pattern. The minima appear whenever

$$k_0 \bar{\mathbf{R}} \cdot \mathbf{r}_{21} = (2n + 1)\pi, \quad n = 0, \pm 1, \pm 2, \dots \quad (1.30)$$

The second exponent, appearing in (1.29), depends on the sum of the position of the slits, the ratio Δ/ω_0 and the difference $\delta\phi$ between the initial phases of the fields. This term introduces limits on the visibility of the interference pattern and can affect the pattern only if the frequencies and the initial phases of the fields are different. Even for equal and well stabilized phases, but significantly different frequencies of the fields such that $\Delta/\omega_0 \approx 1$, the exponent oscillates rapidly with \mathbf{R} leading to the disappearance of the interference pattern. Thus, in order to observe an interference pattern it is important to have two fields of well stabilized phases and equal or nearly equal frequencies. Otherwise, no interference pattern can be observed even if the fields are perfectly correlated.

Similar to the dependence of the interference pattern on the relative intensities of the fields, the dependence of the interference pattern on the frequencies and phases of the fields is also related to the problem of extracting which way information has been transferred to the observation point P . For perfectly correlated fields with equal frequencies ($\Delta = 0$) and equal initial phases $\phi_1 = \phi_2$, the total intensity at the point P is

$$\langle I(\mathbf{R}) \rangle = 2\langle I_0 \rangle [1 + \cos(k_0 \bar{\mathbf{R}} \cdot \mathbf{r}_{21})], \quad (1.31)$$

giving maximum possible interference pattern with the maximum visibility of 100%. When $\Delta \neq 0$ and/or $\phi_1 \neq \phi_2$, the total intensity at the point P is given by

$$\begin{aligned} \langle I(\mathbf{R}) \rangle = 2\langle I_0 \rangle \left\{ 1 + \cos(k_0 \bar{\mathbf{R}} \cdot \mathbf{r}_{21}) \cos\left(k_0 \tilde{R} \frac{\Delta}{\omega_0} + \delta\phi\right) \right. \\ \left. + \sin(k_0 \bar{\mathbf{R}} \cdot \mathbf{r}_{21}) \sin\left(k_0 \tilde{R} \frac{\Delta}{\omega_0} + \delta\phi\right) \right\}. \end{aligned} \quad (1.32)$$

In this case the intensity exhibits additional cosine and sine modulations, and at the minima the intensity is different from zero indicating that the maximum depth of modulation of 100% is not possible for two fields of different frequencies and/or initial phases. Thus, in order to obtain well-defined fringes, it is essential that the two fields originate from the same source. This follows from the incoherent nature of independent wave fields, since the phase difference $\delta\phi$ of the fields from two independent sources is arbitrary, and its fluctuations average the interference terms to zero.

Moreover, for large differences between the frequencies of the fields ($\Delta/\omega_0 \gg 1$), the $\cos[k_0 \tilde{R}(\Delta/\omega_0) + \delta\phi]$ and $\sin[k_0 \tilde{R}(\Delta/\omega_0) + \delta\phi]$ terms oscillate rapidly with \mathbf{R} and average to zero, washing out the interference pattern. Which-way information may be obtained by using a detector located at P that could distinguish the frequency or phase of the two fields. Clearly, this determines which way the detected field came to the point P . Maximum possible which-way information results in no interference pattern, and vice versa, no which-way information results in maximum visibility of the interference pattern.

The welcher weg problem has created many discussions on the validity of the principle of complementarity. Einstein proposed modifying the Young's double slit experiment by using freely-moving slits. A light beam, or a particle, arriving at point P must have changed momentum when passing through the slits. Since the paths of the light beams travelling from the slits to the point P are different, the change of the momentum at each slit must be different. Einstein's proposal was simply to observe the motion of the slits after the light beam traversed them. Depending on how rapidly they were moving, one could deduce through which slit the light beam had passed, and simultaneously, one could observe an interference pattern. If this were possible, it would be a direct contradiction of the principle of complementarity. However, Bohr proved that this proposal was deceptive in the sense that the position of the recoiling slits is subject to some uncertainty provided by the uncertainty principle. As a result, if the slits are moveable, a random phase is imparted to the light beams, and hence the interference pattern disappears.

Feynman in his proposal for a welcher weg experiment suggested replacing the slits in the usual Young's experiment by electrons [8]. Because electrons are charged particles, they can interact with the incoming electromagnetic field. Feynman suggested putting a light source symmetrically between the slits. If the light beam is scattered by an electron, the direction of the scattered beam will precisely determine from which electron the beam has been scattered. In this experiment, the momentum of the electrons and their positions are both important parameters. In order to determine which electron

had scattered the light beam and at the same moment observe interference, the momentum and the position of the electron would have to be measured to accuracies greater than allowed by the uncertainty principle.

1.1.4 Experimental Tests of the Welcher Weg Problem

The variation of the interference pattern with welcher weg information has been observed by Wang, Zou and Mandel [9] in a series of optical interference experiments in which, by varying the transmissivity of a filter, they were able to continuously vary the amount of path information available. Figure 1.2 il-

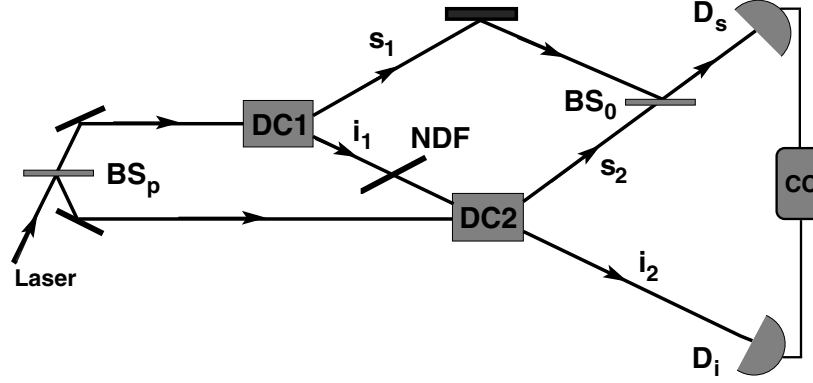


Fig. 1.2. Schematic diagram of the experimental setup of Wang, Zou and Mandel [9] to measure one-photon interference relative to the which-way information

lustrates the experimental setup to measure one-photon interference relative to the which-way information available. The experiment involved two downconverters DC1 and DC2, both optically pumped by the mutually coherent uv light beams from a common argon-ion laser of wavelength 351.1 nm. As a result, downconversion occurred at DC1 with the simultaneous emission of a signal s_1 and an idler i_1 photons at wavelengths near 700 nm, and at DC2 with the simultaneous emission of s_2 and i_2 photons. The downconverters were aligned such that i_1 and i_2 were collinear and overlapping. With this arrangement, a photon detected in the i_2 beam could have come from DC1 or DC2. At the same time the s_1 and s_2 signal beams were mixed at the 50 : 50 beam splitter BS_0 , where they interfered, and the resulting intensity (counting rate) $R_s = \sigma_s \langle I_s(t) \rangle$ was measured by the photodetector D_s of efficiency σ_s as a function of the displacement of the beam splitter BS_0 . Two separate sets of measurements were made for two extreme values of the transmissivity of the filter inserted between DC1 and DC2. For perfect transmissivity, which was obtained simply by removing the neutral density filter (NDF), an interference pattern was observed. However, for zero transmissivity where i_1 was blocked from reaching DC2, all interference disappeared. In Fig. 1.3 the

experimental results are shown for the two extreme values of the transmissivity. In curve A, there was no filter present, and then a perfect interference

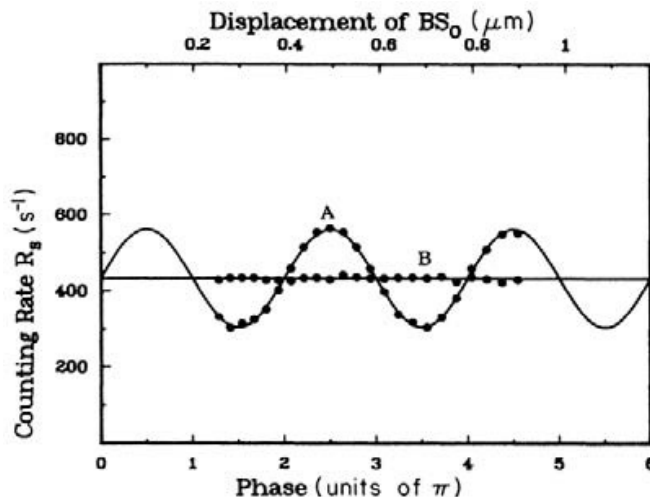


Fig. 1.3. The observed interference pattern as a function of the beamsplitter BS_0 displacement with no (curve A) and full (curve B) which-way information available. The solid lines indicate the predictions of theory, and the black circles are experimental measurements. From L.J. Wang, X.Y. Zou, L. Mandel: *Phys. Rev. A* **44**, 4614 (1991). Copyright (1991) by the American Physical Society

pattern was observed. Conversely, in curve B the beam i_1 was blocked, and then no interference pattern was observed. Finally, in Fig. 1.4, we illustrate their experimental results for the fringe contrast versus the transmissivity (path information). We see a linear dependence of the fringe contrast on the path information, which confirms the relation (1.25).

The experimental results manifest the principle of complementarity and can be explained as follows. In the absence of the filter, the detection of a photon by the photodetector D_i does not disturb the interference experiment involving the s_1 and s_2 beams as one cannot predict whether the photon detected by D_i came from i_1 or i_2 . In this case the signal beams are completely indistinguishable, and a perfect interference pattern is observed. However, when the filter is present, the beam i_1 is blocked and then D_i provides information about the source of the signal photon detected by D_s . For example, if the detection of a signal photon by D_s is accompanied by the simultaneous detection of an idler photon by D_i this indicates that the signal photon must have come from DC2. On the other hand, in the absence of the filter, detection of a signal photon by D_s which is not accompanied by the simultaneous detection of an idler photon by D_i indicates that the detected signal photon cannot have come from DC2 and must have originated in DC1. Thus, with the help of the auxiliary detector D_i , the experiment could identify the source of each detected signal photon whenever i_1 was blocked, and this dis-

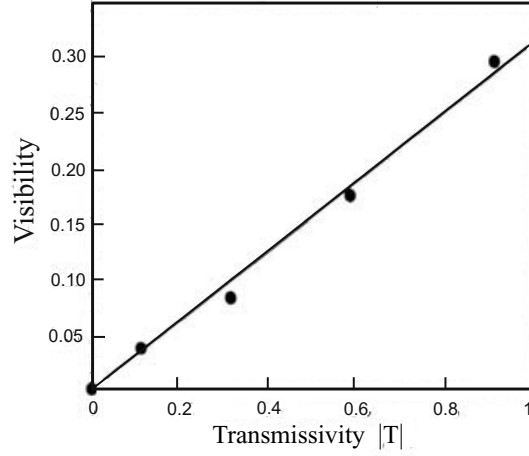


Fig. 1.4. Visibility versus the transmissivity (which-way information) observed in the Wang, Zou and Mandel experiment [9]. The solid line is the theory and the black circles are the experimental data. From L.J. Wang, X.Y. Zou, L. Mandel: Phys. Rev. A **44**, 4614 (1991). Copyright (1991) by the American Physical Society

tinguishability wipes out all interference between s_1 and s_2 . The situation is intermediate when the transmissivity is neither close to unity nor zero.

A further demonstration of the principle of complementarity was reported by Eichmann et al. [10] in a modified version of the Young's double slit experiment. In their experiment they observed interference effects in the light scattered from two trapped ions, which played a role similar to the two slits in Young's interferometer. The experimental arrangement is shown in Fig. 1.5. Two closely spaced $^{198}\text{Hg}^+$ ions were confined in a linear Paul trap. The ions

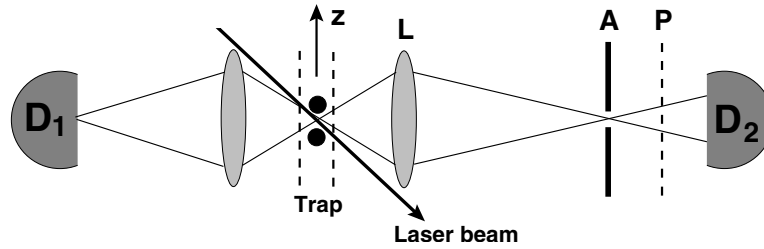


Fig. 1.5. Schematic diagram of the Eichmann et al. [10] experiment used to test the principle of complementarity in the light scattered from two trapped ions

were driven by a coherent laser field tuned below the resonance frequency of the $^2\text{S}_{1/2} - ^2\text{P}_{1/2}$ atomic transition, and directed through the center of the trap at an angle $\theta = 62^\circ$ with respect to the trap axis z . The scattered field was observed with two photodetectors D_1 and D_2 . The detector D_1 served

as a monitor of the number of ions to ensure that exactly two ions had been trapped. The detector D_2 was set up to measure the intensity of the scattered field (collected by the lens L, aperture A, and an optional polarizer P) as a function of the scattered angle.

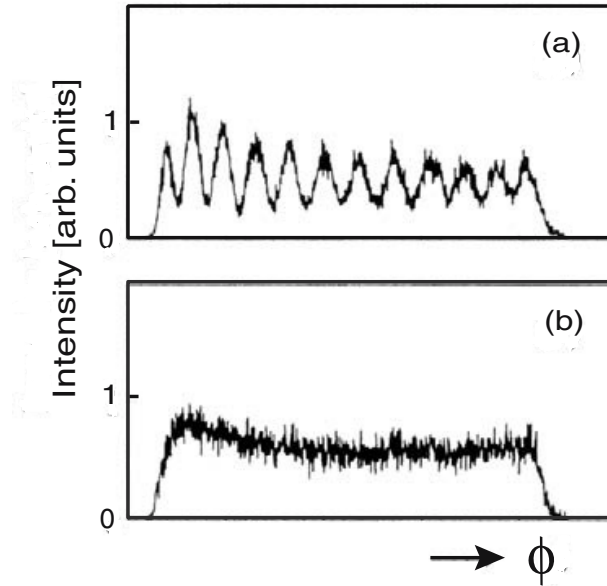


Fig. 1.6. Results of the Eichmann et al. experiment. The graphs represent the scattered intensities as a function of the position of the detector D_2 for two different polarizations: Trace (a) is the intensity of the π polarized scattered field, and trace (b) is the intensity of the σ polarized field. From U. Eichmann, J.C. Bergquist, J.J. Bollinger, J.M. Gilligan, W.M. Itano, D.J. Wineland: *Phys. Rev. Lett.* **70**, 2359 (1993). Copyright (1993) by the American Physical Society

The which-way information was obtained by measuring the polarization of the scattered field. The atomic transition, driven by the laser field, consists of ground state $^2S_{1/2}$ and excited state $^2P_{1/2}$, which are twofold degenerate with respect to the magnetic quantum number m . The effect of this level configuration is that the scattered field can have either π (linear) or σ (circular) polarization. With a linearly polarized and low intensity driving field, such that only one photon can be scattered by the ions, the π polarized scattered field indicates that the final state of the ion which scattered the photon is the same as the initial state. In this case, no information is provided as to which ion scattered the photon, and an interference pattern is expected to be observed in the scattered field. On the other hand, observation of a σ polarized scattered field indicates that the final state of one of the ions differs from the initial state. This information allows one to distinguish which ion scattered the photon, and hence to determine which way the photon travelled. Consequently, there is no interference pattern in the scattered field. Figure 1.6 shows the experimental results for the scattered intensity as a function of the

position of the detector D_2 for two different polarizations. As expected, the interference pattern was observed for the case of the π polarized scattered field [Fig. 1.6(a)] and no interference pattern was observed for the σ polarized scattered field [Fig. 1.6(b)].

The above experiments clearly demonstrated that interference and which-way information are mutually exclusive. When which-way information is present, no interference pattern is observed, and vice versa: a lack of which-way information results in the appearance of the interference pattern [11].

1.1.5 Second-Order Coherence

The analysis of interference phenomenon can be extended to higher-order correlation functions, and we illustrate here some properties of the second-order correlation function. The higher-order correlation functions involve intensities of the measured fields and carry information about the fluctuations of the fields. They describe higher-order coherence and interference phenomena observable with the help of a number of photodetectors whose photocurrents are correlated.

Usually an experimental measurement of the second-order correlation function involves two separate photodetectors. We define the second-order correlation function

$$G^{(2)}(\mathbf{R}_1, t_1; \mathbf{R}_2, t_2) = \langle \mathbf{E}^*(\mathbf{R}_1, t_1) \mathbf{E}^*(\mathbf{R}_2, t_2) \times \mathbf{E}(\mathbf{R}_2, t_2) \mathbf{E}(\mathbf{R}_1, t_1) \rangle, \quad (1.33)$$

which relates to the measurement of the field $\mathbf{E}(\mathbf{R}, t)$ at two separate space-time points \mathbf{R}_1, t_1 and \mathbf{R}_2, t_2 . The correlation function $G^{(2)}(\mathbf{R}_1, t_1; \mathbf{R}_2, t_2)$ is termed the *second-order* correlation function because it depends on the second power of the intensity, and it measures second-order interference. In this expression, we have neglected considerations of the vector nature of the fields, and of the tensor nature of the correlation function since they are not important in our subsequent discussions, and to include them explicitly would greatly complicate the expressions. Strictly, we should replace each field in (1.33) by a particular component, $\mathbf{E} \rightarrow E_\alpha$, and we should add a subscript to $G^{(2)}$ specifying the particular components used, $G^{(2)} \rightarrow G_{\alpha, \beta, \gamma, \delta}^{(2)}$.

It is often convenient to introduce the normalized second-order correlation function

$$g^{(2)}(\mathbf{R}_1, t_1; \mathbf{R}_2, t_2) = \frac{G^{(2)}(\mathbf{R}_1, t_1; \mathbf{R}_2, t_2)}{G^{(1)}(\mathbf{R}_1, t_1) G^{(1)}(\mathbf{R}_2, t_2)}, \quad (1.34)$$

where $G^{(1)}(\mathbf{R}_i, t_i) \equiv G^{(1)}(\mathbf{R}_i, t_i; \mathbf{R}_i, t_i)$. The normalized second-order correlation function allows us to determine correlations between the two detected fields relative to the intensity of the independent (uncorrelated) fields.

Let us now suppose that the light field falling on our detectors is the sum of the light fields coming from two distinct sources. When two light beams

of intensities $I_1(\mathbf{R}_1, t_1)$ and $I_2(\mathbf{R}_2, t_2)$ fall on two photodetectors located at \mathbf{R}_1 and \mathbf{R}_2 , respectively, the joint probability of photoelectric detections at both detectors within the time intervals t_1 to Δt_1 and t_2 to Δt_2 is given by

$$P_{12}(\mathbf{R}_1, t_1; \mathbf{R}_2, t_2) = \sigma_1 \sigma_2 G^{(2)}(\mathbf{R}_1, t_1; \mathbf{R}_2, t_2) \Delta t_1 \Delta t_2, \quad (1.35)$$

where σ_1, σ_2 are the quantum efficiencies of the photodetectors.

As in our discussion of first-order coherence, we may relate the fields at the detectors to the fields emanating from the sources. Let $\mathbf{R}_{ij} = \mathbf{R}_i - \mathbf{r}_j$ be the position vector of the j th source relative to the field point at \mathbf{R}_i . Then, using the plane-wave approximation, we may write

$$\begin{aligned} \mathbf{E}(\mathbf{R}_i, t) &= \sum_{j=1}^2 \mathbf{E}_j(\mathbf{R}_{ij}, t - t_j) \\ &= \sum_{j=1}^2 \mathbf{E}_j(\mathbf{R}_{ij}, t) \exp(-ik_j R_i - \phi_j) \exp(ik_j \bar{\mathbf{R}}_i \cdot \mathbf{r}_j) . \end{aligned} \quad (1.36)$$

For simplicity, we here assume these two fields to have the same frequency. Analogously to (1.33) we can define the second-order correlation function (1.33) for the two fields at the slits as

$$\begin{aligned} G_{12}^{(2)}(\mathbf{R}_1, t_1; \mathbf{R}_2, t_2) &= \sum_{i,j,k,l=1}^2 \langle \mathbf{E}_i^*(t_1) \mathbf{E}_k^*(t_2) \mathbf{E}_l(t_2) \mathbf{E}_j(t_1) \rangle \\ &\quad \times \exp[ik(\bar{\mathbf{R}}_1 \cdot \mathbf{r}_{ij} + \bar{\mathbf{R}}_2 \cdot \mathbf{r}_{kl})] \\ &\quad \times \exp[i(\phi_i + \phi_k - \phi_l - \phi_j)] , \end{aligned} \quad (1.37)$$

where k is the wave-vector of the measured fields. There are sixteen terms contributing to the right-hand side of (1.37), each accompanied by a phase factor which depends on the relative phase of the fields.

First of all, it will be useful to establish certain facts about the possible values of the second-order correlation function. We note from (1.37) that the second-order correlation function has completely different coherence properties to the first-order correlation function. An interference pattern can be observed in the second-order correlation function, but in contrast to the first-order correlation function, the interference appears between two points located at \mathbf{R}_1 and \mathbf{R}_2 . Moreover, an interference pattern can be observed even if the fields are produced by two independent sources for which the phase difference $\phi_2 - \phi_1$ between the two detected fields is completely random [2]. In this case the second-order correlation function (1.37) is given by

$$\begin{aligned} G_{12}^{(2)}(\mathbf{R}_1, t_1; \mathbf{R}_2, t_2) &= \langle I_1^2(t_1) \rangle + \langle I_2^2(t_2) \rangle + 2\langle I_1(t_1) I_2(t_2) \rangle \\ &\quad + 2\langle I_1(t_1) I_2(t_2) \rangle \cos(k\mathbf{r}_{21} \cdot \Delta \bar{\mathbf{R}}) , \end{aligned} \quad (1.38)$$

where $\Delta \bar{\mathbf{R}} = \bar{\mathbf{R}}_1 - \bar{\mathbf{R}}_2$.

Clearly, the second-order correlation function contains an interference term. The interference pattern depends on the separation $\Delta\bar{\mathbf{R}}$ between the two detectors, not on the position of the detectors separately. Thus, an interference pattern can be observed in the second-order correlations even for two completely independent fields.

As with the first-order correlations, the sharpness of the interference fringes depends on the relative intensities of the fields. For stationary fields of equal intensities, $I_1 = I_2 = I_0$, the correlation function (1.38) reduces to

$$G_{12}^{(2)}(\mathbf{R}_1, t; \mathbf{R}_2, t) = 4\langle I_0^2 \rangle \left\{ 1 + \frac{1}{2} \cos [k\mathbf{r}_{21} \cdot (\bar{\mathbf{R}}_1 - \bar{\mathbf{R}}_2)] \right\}. \quad (1.39)$$

In analogy to the visibility in the first-order correlation function, we can define the visibility of the interference pattern of the intensity correlations as

$$C^{(2)} = \frac{G_{12,\max}^{(2)} - G_{12,\min}^{(2)}}{G_{12,\max}^{(2)} + G_{12,\min}^{(2)}}, \quad (1.40)$$

and using (1.38), we find that the visibility of the interference fringes is given by

$$C^{(2)} = \frac{2\langle I_1 I_2 \rangle}{\langle I_1^2 \rangle + \langle I_2^2 \rangle + 2\langle I_1 I_2 \rangle} = \frac{2\langle I_1 I_2 \rangle}{\langle (I_1 + I_2)^2 \rangle}. \quad (1.41)$$

Since $\langle I_1^2 \rangle + \langle I_2^2 \rangle \geq 2\langle I_1 I_2 \rangle$, it follows that $C^{(2)} \leq 1/2$. Thus, two independent fields of random and uncorrelated phases can produce an interference pattern in the intensity correlation with a maximum visibility of 50%.

1.1.6 Hanbury-Brown and Twiss Interferometer

The first experimental demonstration that the two-photon correlations exist in optical fields was given by Hanbury-Brown and Twiss [12], who measured the second-order correlation function of a thermal field. In the experiment, the 435.8 nm light beam from an emission line of a mercury arc was isolated by a system of filters and sent to a half-silvered mirror. The light beam was kept at very low intensity such that, at given time, practically only a single photon was falling on the mirror. The two output beams were registered by two photodetectors connected to a coincidence counter. At the front of each photodetector was a narrowband 435.8 nm interference filter. The filters ensured that only photons of the correct wavelength entered the photodetector tubes. To be precise, a photon that somehow “split” at the mirror, such that half of its energy went one way and half the other, would have a wavelength outside the bandwidth of the filters and would not be registered.

In the experiment, they measured the normalized second-order correlation function, which in terms of the intensities of the output beams can be written as

$$g^{(2)}(\tau) \equiv g_{12}^{(2)}(\mathbf{R}_1, t; \mathbf{R}_2, t + \tau) = \frac{\langle I_1(t) I_2(t + \tau) \rangle}{\langle I_1(t) \rangle \langle I_2(t + \tau) \rangle}, \quad (1.42)$$

where τ is the delay time of the detectors.

The results of the Hanbury-Brown and Twiss (HBT) experiment were astonishing. Assuming photons to be indivisible, they expected no coincidence for $\tau = 0$, that is, $g^{(2)}(0) = 0$. However, they observed precisely the opposite result. Their measured value of $g^{(2)}(0)$ turned out to be $g^{(2)}(0) = 2$, showing that photons seemed to travel through space grouped together, even with light beams of very low intensity. This phenomenon is known as *photon bunching*.

How can we interpret their result? We shall use a semiclassical model to understand the HBT results. In this model, the light beam is described in purely classical terms, but the detectors are treated quantum-mechanically. The detectors produce discrete particles (photoelectrons) whose statistics is monitored by analyzing the output of the coincidence counter. Since the probability of a photodetection is proportional to the intensity of the detected field, the average number of photo-counts n is given by

$$\langle n \rangle = \sigma \langle I \rangle, \quad (1.43)$$

where, as before, σ is the efficiency of the detector and I is the intensity of the detected light.

We can also calculate the variance of the number of counts, which for independent photoemissions, is given by

$$\langle (\Delta n)^2 \rangle = \langle n \rangle + \sigma^2 \langle (\Delta I)^2 \rangle, \quad (1.44)$$

where $\langle (\Delta I)^2 \rangle$ is the variance of the intensity of the detected field.

Hence, we find that the normalized second-order correlation function of the photo-counts can be written as

$$g^{(2)}(0) = 1 + \frac{\langle (\Delta n)^2 \rangle - \langle n \rangle}{\langle n \rangle^2} = 1 + \frac{\langle (\Delta I)^2 \rangle}{\langle I \rangle^2}. \quad (1.45)$$

Since in the HBT experiment, the mercury arc produced a thermal (Gaussian) field whose variance $\langle (\Delta I)^2 \rangle = \langle I \rangle^2$, the correlation function simplifies to

$$g^{(2)}(0) = 2. \quad (1.46)$$

Clearly, the experiment provided no evidence for the particle (photon) nature of light, but the experiment provided the stimulus for a systematic treatment of optical coherence and launched an entirely new discipline, the explicit study of the quantum nature of light [13].

With the invention of single atom sources of light, the HBT experiment was repeated by Dagenais, Kimble and Mandel [14], see also [15], who replaced the thermal field from the mercury arc by the resonance fluorescence

from the sodium atoms of a very dilute atomic beam. In their experiment, sodium atoms were driven by a tunable dye laser stabilized in intensity to a few per cent and in frequency to about 1 MHz. The laser was tuned to the $3^2S_{1/2}(F = 2) \rightarrow 3^2P_{3/2}(F = 3)$ transition. The atoms were initially prepared in the $3^2S_{1/2}(F = 2, m_F = 2)$ state by an optical pumping technique. This initial preparation ensured that the atoms behaved as a pure two-level quantum system. The experiment demonstrated *photon antibunching* – that is, the correlation function satisfied $g^{(2)}(\tau) > g^{(2)}(0)$, and *photon anticorrelation*, $g^{(2)}(0) < 1$. Each of these properties indicates that photons produced by single atoms have the tendency to travel well-separated. Their experiment provided evidence that light is composed of particles. Photon antibunching has also been observed in similar experiments involving trapped atoms [16] and a cavity quantum electrodynamics (QED) system [17].

Physically, the vanishing of $g^{(2)}(\tau)$ at $\tau = 0$ for a single two-level atom implies that immediately after emitting a photon, the atom is unable to emit another. A short time is required to re-excite the atom so that a photon may be emitted again. This process results in an even temporal spacing of the photon train.

1.1.7 Mach–Zehnder Interferometer

One of the most important devices making use of interference phenomena is the Mach–Zehnder interferometer, shown schematically in Fig. 1.7. The interferometer consists of two beamsplitters, the input beamsplitter B_1 and the output beamsplitter B_2 , and two totally reflecting mirrors, M_1 and M_2 . There can be a single or two separate beams a and b incident on the input beamsplitter and a single or two detectors D_1 and D_2 employed to measure the output from the beamsplitter B_2 . In the interferometer, the incident

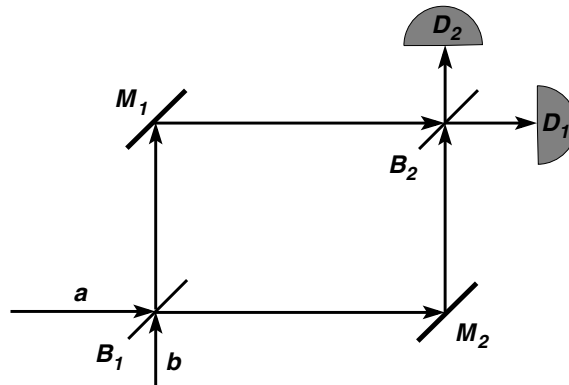


Fig. 1.7. Schematic diagram of the Mach–Zehnder interferometer

light beam is split by the beamsplitter B_1 into two beams travelling along separate paths at right angles to each other. The mirrors M_1 and M_2 reflect

both beams towards the output beamsplitter B_2 where they overlap, and the superposition of these two beams is measured by the detectors D_1 and D_2 . As four mirrors are involved, the number of degrees of freedom of the system is large. This allows the detectors to be localized in any desired plane, but also it makes the adjustment of the interferometer complex and difficult. However, the mirrors in the interferometer can be separated widely from each other. This fact makes possible many applications, for example, we can allow the beams to pass through different materials and thus determine their optical properties. The measurement of the correlations between two beams, and the detection of an object without interacting with it, are other important applications of the Mach–Zehnder interferometer. Some of these applications will be discussed in the following sections.

1.2 Principles of Quantum Interference

In the classical theory of optical interference and coherence, discussed in the previous sections, the electric field is represented as the sum of its positive and negative frequency parts, which we represent as the complex vectorial amplitudes $\mathbf{E}(\mathbf{r}, t)$ and $\mathbf{E}^*(\mathbf{r}, t)$, respectively. In the quantum theory of interference, the classical electric field, whose magnitude is a c-number, is replaced by the electric field operator $\hat{\mathbf{E}}(\mathbf{r}, t)$. This Hermitian operator is usually expressed by the sum of two non-Hermitian operators as

$$\hat{\mathbf{E}}(\mathbf{r}, t) = \hat{\mathbf{E}}^{(+)}(\mathbf{r}, t) + \hat{\mathbf{E}}^{(-)}(\mathbf{r}, t) , \quad (1.47)$$

where $\hat{\mathbf{E}}^{(+)}$ and $\hat{\mathbf{E}}^{(-)}$ are the positive and negative frequency components, respectively. The situation is analogous to (1.1).

In free space and in the transverse mode decomposition, the positive and negative frequency components of the electromagnetic field can be expressed in terms of plane waves as

$$\begin{aligned} \hat{\mathbf{E}}^{(+)}(\mathbf{r}, t) &= \left(\hat{\mathbf{E}}^{(-)}(\mathbf{r}, t) \right)^\dagger \\ &= i \sum_{\mathbf{k}s} \left(\frac{\hbar \omega_{\mathbf{k}s}}{2\varepsilon_0 \mathcal{V}} \right)^{\frac{1}{2}} \bar{\mathbf{e}}_{\mathbf{k}s} \hat{a}_{\mathbf{k}s} \exp[i(\mathbf{k} \cdot \mathbf{r} - \omega_{\mathbf{k}s}t)] , \end{aligned} \quad (1.48)$$

where \mathcal{V} is the volume occupied by the field, ε_0 is the permittivity of free space, $\hat{a}_{\mathbf{k}s}$ is the annihilation operator for the \mathbf{k} th mode of the field, $\bar{\mathbf{e}}_{\mathbf{k}s}$ is the unit polarization vector, and $\omega_{\mathbf{k}s}$ is the angular frequency of the mode. The annihilation and creation operators $\hat{a}_{\mathbf{k}s}$ and $\hat{a}_{\mathbf{k}s}^\dagger$ obey the usual Bose commutation rules

$$[\hat{a}_{\mathbf{k}s}, \hat{a}_{\mathbf{k}'s'}^\dagger] = \left[\hat{a}_{\mathbf{k}s}^\dagger, \hat{a}_{\mathbf{k}'s'}^\dagger \right] = 0 , \quad [\hat{a}_{\mathbf{k}s}, \hat{a}_{\mathbf{k}'s'}^\dagger] = \delta^3(\mathbf{k} - \mathbf{k}') \delta_{ss'} , \quad (1.49)$$

where $\delta^3(\mathbf{k} - \mathbf{k}')$ is the three dimensional Dirac delta function.

1.2.1 Two-Photon Nonclassical Interference

What principally distinguishes quantum interference from classical interference is the properties of the higher order correlation functions, in particular, those of the second-order correlation function, which can differ greatly. Here, we discuss separately spatial and temporal interference effects in the second-order correlations, which distinguish quantum (nonclassical) interference from the classical form.

Spatial Nonclassical Interference

In the case of the quantum description of the field, the first- and second-order correlation functions are defined in terms of the normally ordered field operators $\hat{\mathbf{E}}^{(+)}$ and $\hat{\mathbf{E}}^{(-)}$ as

$$\begin{aligned} G^{(1)}(\mathbf{R}_1, t_1; \mathbf{R}_2, t_2) &= \langle \hat{\mathbf{E}}^{(-)}(\mathbf{R}_1, t_1) \cdot \hat{\mathbf{E}}^{(+)}(\mathbf{R}_2, t_2) \rangle, \\ G^{(2)}(\mathbf{R}_1, t_1; \mathbf{R}_2, t_2) &= \langle \hat{\mathbf{E}}^{(-)}(\mathbf{R}_1, t_1) \hat{\mathbf{E}}^{(-)}(\mathbf{R}_2, t_2) \\ &\quad \times \hat{\mathbf{E}}^{(+)}(\mathbf{R}_2, t_2) \hat{\mathbf{E}}^{(+)}(\mathbf{R}_1, t_1) \rangle. \end{aligned} \quad (1.50)$$

The normal ordering of the field operators means that all field creation operators $\hat{\mathbf{E}}^{(-)}$ stand to the left of all annihilation operators $\hat{\mathbf{E}}^{(+)}$.

If we introduce the density operator ϱ for the field, we can rewrite the correlation functions as

$$\begin{aligned} G^{(1)}(\mathbf{R}_1, t_1; \mathbf{R}_2, t_2) &= \text{Tr} \left[\varrho \hat{\mathbf{E}}^{(-)}(\mathbf{R}_1, t_1) \cdot \hat{\mathbf{E}}^{(+)}(\mathbf{R}_2, t_2) \right], \\ G^{(2)}(\mathbf{R}_1, t_1; \mathbf{R}_2, t_2) &= \text{Tr} \left\{ \varrho \hat{\mathbf{E}}^{(-)}(\mathbf{R}_1, t_1) \hat{\mathbf{E}}^{(-)}(\mathbf{R}_2, t_2) \right. \\ &\quad \left. \times \hat{\mathbf{E}}^{(+)}(\mathbf{R}_2, t_2) \hat{\mathbf{E}}^{(+)}(\mathbf{R}_1, t_1) \right\}, \end{aligned} \quad (1.51)$$

where the trace is taken over the states of the field.

The correlation functions (1.50) described by the field operators are similar to the correlation functions (1.9) and (1.33) of the classical field. A closer look at the definitions of the correlation functions (1.9), (1.33), and (1.51) could suggest that the only difference between the classical and quantum correlation functions is the classical amplitudes $\mathbf{E}^*(\mathbf{R}, t)$ and $\mathbf{E}(\mathbf{R}, t)$ are replaced by the field operators $\hat{\mathbf{E}}^{(-)}(\mathbf{R}, t)$ and $\hat{\mathbf{E}}^{(+)}(\mathbf{R}, t)$, respectively, and by the substitution $\langle \dots \rangle \rightarrow \text{Tr} \{ \varrho \dots \}$. Of course, the correspondence between the classical and quantum correlation functions is not unique since the operators $\hat{\mathbf{E}}^{(-)}(\mathbf{R}, t)$ and $\hat{\mathbf{E}}^{(+)}(\mathbf{R}, t)$ do not commute. In addition, this correspondence is true only as long as first-order correlation functions are considered, where interference effects do not distinguish between quantum

and classical theories of the electromagnetic field. However, there are significant differences between the classical and quantum descriptions of the field in the properties of the second-order correlation function [18].

As an example, consider the simple case of two single-mode fields of equal frequencies and polarizations. In this case the positive and negative frequency parts of the total field operator in the interference region can be written as

$$\begin{aligned}\hat{\mathbf{E}}^{(+)}(\mathbf{r}, t) &= i \left(\frac{\hbar\omega}{2\varepsilon_0\mathcal{V}} \right)^{\frac{1}{2}} \bar{\mathbf{e}} (\hat{a}_1 + \hat{a}_2) e^{i(\mathbf{k}\cdot\mathbf{r}-\omega t)} , \\ \hat{\mathbf{E}}^{(-)}(\mathbf{r}, t) &= -i \left(\frac{\hbar\omega}{2\varepsilon_0\mathcal{V}} \right)^{\frac{1}{2}} \bar{\mathbf{e}}^* (\hat{a}_1^\dagger + \hat{a}_2^\dagger) e^{-i(\mathbf{k}\cdot\mathbf{r}-\omega t)} ,\end{aligned}\quad (1.52)$$

where ω is the frequency of the fields, \hat{a}_i and \hat{a}_i^\dagger are the usual annihilation and creation operators of the i th mode, and $\bar{\mathbf{e}}$ is the unit polarization vector of the field mode.

Suppose that there are initially n photons in the field 1 and m photons in the field 2. The state vector of the total field $|\psi\rangle = |n\rangle|m\rangle$ is a product of the Fock states $|\psi_1\rangle = |n\rangle$ and $|\psi_2\rangle = |m\rangle$ of the corresponding modes. Using (1.52), we find that the field intensity correlation functions appearing in (1.38) become

$$\begin{aligned}\langle I_1^2 \rangle &= \left(\frac{\hbar\omega}{2\varepsilon_0\mathcal{V}} \right)^2 n(n-1) , \\ \langle I_2^2 \rangle &= \left(\frac{\hbar\omega}{2\varepsilon_0\mathcal{V}} \right)^2 m(m-1) , \\ \langle I_1 I_2 \rangle &= \left(\frac{\hbar\omega}{2\varepsilon_0\mathcal{V}} \right)^2 nm ,\end{aligned}\quad (1.53)$$

and then the two-photon correlation function takes the form

$$\begin{aligned}G^{(2)}(\mathbf{R}_1, t; \mathbf{R}_2, t) &= \left(\frac{\hbar\omega}{2\varepsilon_0\mathcal{V}} \right)^2 \left[n(n-1) + m(m-1) \right. \\ &\quad \left. + 2nm \{1 + \cos[k\mathbf{r}_{21} \cdot (\bar{\mathbf{R}}_1 - \bar{\mathbf{R}}_2)]\} \right] .\end{aligned}\quad (1.54)$$

It is interesting to note that the first two terms on the right-hand side of (1.54) vanish when there is exactly one photon in each field, i.e. when $n = 1$ and $m = 1$. In this limit the correlation function (1.54) reduces to

$$G^{(2)}(\mathbf{R}_1, t; \mathbf{R}_2, t) = 2 \left(\frac{\hbar\omega}{2\varepsilon_0\mathcal{V}} \right)^2 \{1 + \cos[k\mathbf{r}_{21} \cdot (\bar{\mathbf{R}}_1 - \bar{\mathbf{R}}_2)]\} .\quad (1.55)$$

Thus, a perfect interference pattern with visibility $C^{(2)} = 1$ can be observed in the second-order correlation function of two quantum fields each containing only one photon, which is of course impossible for a classical field of

nonzero mean. Needless to say, this phenomenon is nonclassical and cannot be observed with classical fields [19]. As we have shown, the classical theory predicts only a visibility of $C^{(2)} = 1/2$. For $n, m \gg 1$, the first two terms on the right-hand side of (1.54) are both different from zero, and can be approximated by m^2 and n^2 . Hence, in this limit, the quantum correlation function (1.54) reduces to that of the classical field.

The appearance of a perfect interference pattern with two fields each containing only a single photon can be explained in terms of the relationship between interference and indistinguishability. In the process of detection of photons from two fields by two detectors there are two indistinguishable two-photon pathways. One of the pathways corresponds to the situation that the photon from the field 1 is registered by the detector located at \mathbf{R}_1 , and the photon from the field 2 is registered by the detector located at \mathbf{R}_2 . The other pathway corresponds to the situation that the photon from the field 1 is registered by the detector at \mathbf{R}_2 , and the photon from the field 2 is registered by the detector at \mathbf{R}_1 . Because these two pathways are indistinguishable, a perfect interference pattern is observed.

With the above prediction of two-photon interference, the question arises as to whether this result contradicts the well-known remark of Dirac that “each photon interferes only with itself. Interference between different photons never occurs”. In general, two-photon interference with independent light beams is in agreement with the Dirac remark since any detection (localization) of a photon in space-time automatically rules out the possibility of knowing its momentum, as a consequence of the uncertainty principle. Therefore, one cannot say from which beam the detected photon came. Since each photon is considered as being partly in both beams, it interferes only with itself.

Experimental Evidence of Spatial Nonclassical Interference

Evidence of spatial nonclassical correlations has been observed in some remarkable experiments by Ou and Mandel [20]. In these experiments, pairs of frequency-degenerate signal and idler photons were produced in the process of spontaneous parametric down-conversion.

Parametric down conversion is a nonlinear process used to produce light fields possessing strong quantum features, such as reduced quantum fluctuations and entangled photon pairs, which are manifested by the simultaneous or nearly simultaneous production of pairs of photons in momentum-conserving, phase matched modes. The entangled photon pairs are especially useful in the studies of two-photon quantum interference, where they can demonstrate a variety of nonclassical features.

The photon pairs were produced in a LiIO_3 crystal pumped by 351 nm light from an argon-ion laser. Thus, the photon pairs were of wavelength 720 nm, and were selected using an interference filter. The experimental setup is sketched in Fig. 1.8. The signal and idler photons were directed

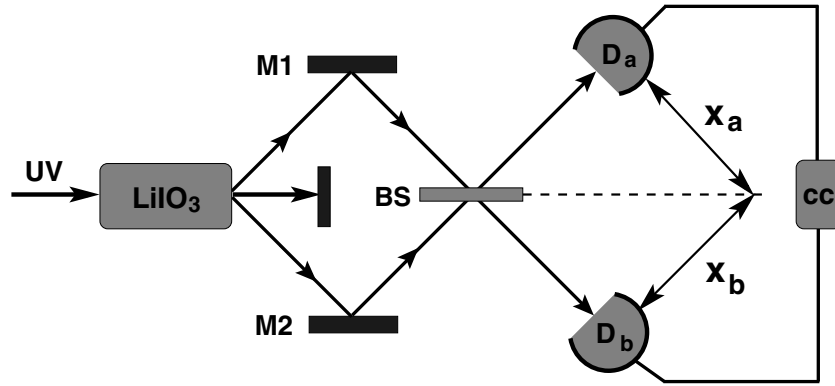


Fig. 1.8. Schematic diagram of the Ou and Mandel experiment to demonstrate the spatial nonclassical two-photon interference

to a 50 : 50 beam splitter BS from opposite sides by mirrors M1 and M2. The beam splitter outputs were measured by two photodetectors D_a and D_b , and next the resulting photocurrents, after amplification and pulse sharpening, were analyzed by the coincidence counter CC. In an experimental run, the photodetector D_b was fixed and the coincidence rates (interference patterns) were recorded as the detector D_a was moved transversely to the incident beam.

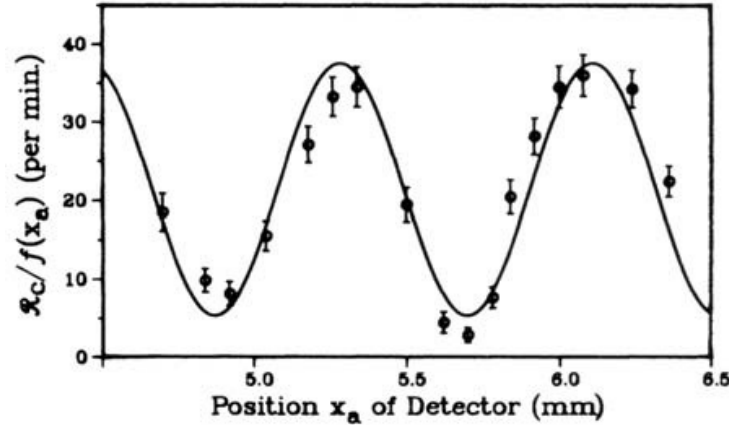


Fig. 1.9. Results of the Ou and Mandel experiment demonstrating the spatial nonclassical two-photon interference. The solid line is the theoretical prediction. From Y. Ou, L. Mandel: Phys. Rev. Lett. **62**, 2941 (1989). Copyright (1989) by the American Physical Society

Figure 1.9 shows recordings of the coincidence counting rate as a function of the position R_a of the detector D_a . The solid line indicates the prediction of the theory outlined previously, see (1.55), and its shape is determined mainly by the interference factor

$$1 + \cos [k\mathbf{r}_{21} \cdot (\bar{\mathbf{x}}_a - \bar{\mathbf{x}}_b)] , \quad (1.56)$$

which governs the spatial properties of the second-order correlation function. The good agreement between the theory and experiment indicates that photons can indeed exhibit two-photon correlations even if they are produced by two independent sources.

1.2.2 The Hong–Ou–Mandel Interferometer

In the preceding section, we have shown that spatial correlations between two photons can lead to nonclassical interference effects in the two-photon correlations. Here, we consider temporal correlations between photons produced by the same source. As a detector of the time correlations of photons, we consider the simple situation of two-photon interference at a beam splitter, shown in Fig. 1.10.

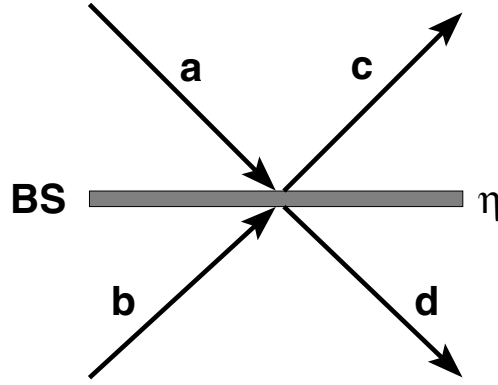


Fig. 1.10. Schematic diagram of two-photon interference at a beam-splitter of reflectivity η . Two beams a and b are incident on the beam-splitter BS and produce output beams c and d

The photons in the modes a and b are incident on a beam splitter of reflectivity η and produce output modes c and d . The amplitudes of the output modes are related to the amplitudes of the input modes by

$$\begin{aligned}\hat{c} &= i\sqrt{\eta} \hat{a} + \sqrt{1-\eta} \hat{b} , \\ \hat{d} &= i\sqrt{\eta} \hat{b} + \sqrt{1-\eta} \hat{a} ,\end{aligned}\tag{1.57}$$

where the factor “ i ” indicates a $\pi/2$ phase shift between the reflected and transmitted fields.

The joint (coincidence) probability that a photon is detected in the arm c at time t and another one in the arm d at time $t + \tau$ is proportional to the second-order correlation function

$$P_{cd}(\tau) = \langle \Psi | \hat{E}_c^{(-)}(t) \hat{E}_d^{(-)}(t + \tau) \hat{E}_d^{(+)}(t + \tau) \hat{E}_c^{(+)}(t) | \Psi \rangle , \tag{1.58}$$

where $|\Psi\rangle$ is the state of the input fields.

For an arbitrary state of the input fields, and in the limit of a long time, the coincidence probability takes the form

$$P_{cd}(\tau) = |E_0|^4 \left\{ \eta(1 - \eta) \langle \hat{a}^\dagger \hat{a}^\dagger(\tau) \hat{a}(\tau) \hat{a} \rangle + \eta(1 - \eta) \langle \hat{b}^\dagger \hat{b}^\dagger(\tau) \hat{b}(\tau) \hat{b} \rangle \right. \\ \left. + \eta^2 \langle \hat{a}^\dagger \hat{b}^\dagger(\tau) \hat{b}(\tau) \hat{a} \rangle + (1 - \eta)^2 \langle \hat{b}^\dagger \hat{a}^\dagger(\tau) \hat{a}(\tau) \hat{b} \rangle \right. \\ \left. - \eta(1 - \eta) \langle \hat{a}^\dagger \hat{b}^\dagger(\tau) \hat{a}(\tau) \hat{b} \rangle - \eta(1 - \eta) \langle \hat{b}^\dagger \hat{a}^\dagger(\tau) \hat{b}(\tau) \hat{a} \rangle \right\} . \quad (1.59)$$

The first two terms on the right-hand of (1.59) describe correlations between reflected and transmitted photons of the same input beam. It is easy to see that these correlations vanish if there is only one photon in each of the input beams. The third and fourth terms describe correlations between the amplitudes of the reflected-reflected and transmitted-transmitted photons. The last two terms arise from interference between the amplitudes of the reflected-transmitted and transmitted-reflected photons of the two beams mixed at the beam splitter, and are the real quantum interference contributions to the coincidence probability. If the state of the input fields is $|\Psi\rangle = |1\rangle_a |1\rangle_b$ – that is, each of the input fields contains only one photon, and if $\tau = 0$, the coincidence probability takes the form

$$P_{cd}(0) = (1 - 2\eta)^2 . \quad (1.60)$$

Thus, if the beam-splitter is either fully reflecting ($\eta = 1$) or fully transmissive ($\eta = 0$), there is unit probability that a coincidence will be detected. In other words, there is a photon in each of the output ports. This agrees with our intuition: if the beam-splitter is fully reflective (transmissive), the photon in the mode a will be reflected (transmitted) into mode c (d), and vice versa for the photon in the mode b .

An interesting quantum interference effect arises when a 50 : 50 ($\eta = 1/2$) beamsplitter is used. In this case, the probability of detecting a coincidence goes to zero, indicating that both photons are always found together in either c or d . Therefore, no coincidence counts between detectors located in the arms c and d are registered. This effect results from quantum interference, since the two paths are indistinguishable, as the detected photons have the same frequency and can come from either of the two input modes. This effect is known in the literature as the Hong–Ou–Mandel (HOM) dip, for reasons we explain below.

Consider the experiment by Hong, Ou and Mandel [21], in which they measured time separations between two photons by interference at a beam splitter. The experimental setup is illustrated in Fig. 1.11. Two photons of the same frequency are produced by a degenerate parametric down-conversion process (DPO) and fall on the beamsplitter BS from opposite sides. In order to introduce a time delay between the photons, the beamsplitter was translated slightly in the vertical direction. This shortened the path for one photon relative to the other, or equivalently, introduced the time delay between pho-

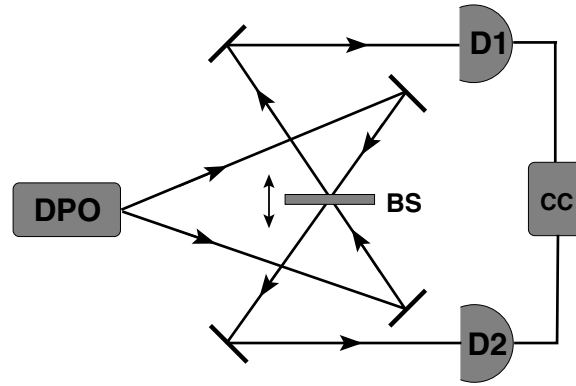


Fig. 1.11. The experimental setup of Hong, Ou and Mandel to measure two-photon coincidence for different delay times

tons in the two beams. The coincidences were detected by two photodetectors D1 and D2 and multiplied at the coincidence counter CC.

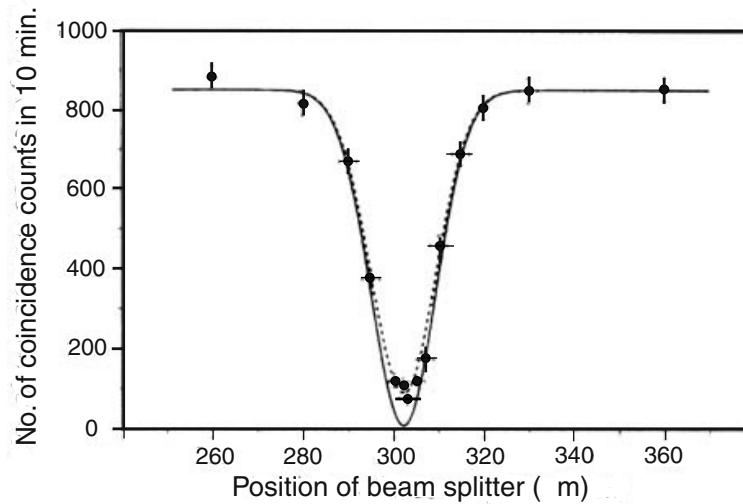


Fig. 1.12. Experimental results of Hong, Ou and Mandel showing the two-photon coincidence rate as a function of beamsplitter displacement. The solid line is theoretical. From C.K. Hong, Z.Y. Ou, L. Mandel: Phys. Rev. Lett. **59**, 2044 (1987). Copyright (1987) by the American Physical Society

Figure 1.12 shows the experimental results for the number of observed photon coincidences as a function of the displacement of the beamsplitter. The solid line indicates the theoretical prediction, outlined below, which agrees excellently with the measurements. For a certain position of the beamsplitter, the two-photon coincidence rate reduces to zero by virtue of the destructive interference of the two-photon probability amplitudes. In this two-photon interference experiment a time resolution between two photons on a femtosecond scale was achieved, which is a million times shorter than the time resolution of the photon detectors and the associated electronics.

The appearance of the HOM dip can be explained as follows. In parametric down-conversion, the photons are randomly produced with the cross correlations between the field amplitudes given by a Gaussian distribution in time

$$\langle \hat{a}^\dagger \hat{b}^\dagger \hat{a} \hat{b} \rangle = \langle \hat{a}^\dagger \hat{b} \rangle \langle \hat{b}^\dagger \hat{a} \rangle = \exp \left[-(\Delta\omega\tau)^2 \right] , \quad (1.61)$$

where $\Delta\omega$ is the bandwidth of the downconverted beam.

Hence, for a 50 : 50 beamsplitter

$$P_{cd}(\tau) = \frac{1}{2} |E_0|^4 \left[1 - \exp(-\Delta\omega^2 \tau^2) \right] , \quad (1.62)$$

which shows that the quantum coincidence probability can be reduced to zero, i.e. the theoretical quantum coincidence probability clearly exhibits the HOM dip – that is, the coincidence probability vanishes for $\tau = 0$ and approaches the classical limit of $P_{cd}(\tau) = 1/2$ as $\tau \rightarrow \infty$.

For a classical field, the coincidence probability (1.59) reduces to

$$P_{cd}(\tau) = \frac{1}{2} I^2 \left[1 - \frac{1}{2} \exp(-\Delta\omega^2 \tau^2) \right] , \quad (1.63)$$

where $I = |E_0|^2$ is the intensity of the input fields (assumed to be equal for both fields). Thus, for classical fields the coincidence probability is always different from zero, and normalized to I^2 , can be reduced only to 1/4.

1.3 Quantum Erasure

The concept of the quantum eraser was introduced by Scully and Drühl [22], and concerns the relationship between coherence and the indistinguishability of different photon paths in an interference experiment. According to the theoretical analysis of Sect. 1.1.3 and the experimental results of Sect. 1.1.4, interference effects disappear whenever it is possible to identify the path of the photons. However, the loss of interference need not be irreversible if the which-way detector is itself a part of the system. If the path information could be erased by a suitable measurement, the interference should reappear.

Consider two fields $\hat{\mathbf{E}}_1(\mathbf{R}, t)$ and $\hat{\mathbf{E}}_2(\mathbf{R}, t)$ produced by two sources (slits or atoms) and travelling along two separate paths. The fields are registered by a detector located a distance \mathbf{R} from the sources. If the detector is calibrated to register only one photon at a given time t , the result of a single detection is the first-order correlation function

$$\begin{aligned} G_{12}^{(1)}(\mathbf{R}, t; \mathbf{R}, t) &= \langle \hat{\mathbf{E}}_1^{(-)}(\mathbf{R}, t) \cdot \hat{\mathbf{E}}_1^{(+)}(\mathbf{R}, t) \rangle + \langle \hat{\mathbf{E}}_2^{(-)}(\mathbf{R}, t) \cdot \hat{\mathbf{E}}_2^{(+)}(\mathbf{R}, t) \rangle \\ &\quad + 2\text{Re} \left\{ \langle \hat{\mathbf{E}}_1^{(-)}(\mathbf{R}, t) \cdot \hat{\mathbf{E}}_2^{(+)}(\mathbf{R}, t) \rangle \right\} , \end{aligned} \quad (1.64)$$

where $\hat{\mathbf{E}}_i^{(+)}(\mathbf{R}, t)$ is the positive frequency part of the i th field ($i = 1, 2$).

Let the state of the system (the two fields plus the detector) just after the detection be given by

$$|\Psi\rangle = |n-1\rangle_1 |m\rangle_2 |d_1\rangle + |n\rangle_1 |m-1\rangle_2 |d_2\rangle, \quad (1.65)$$

where $|n\rangle_1, |m\rangle_2$ are the photon states of the fields, and $|d_1\rangle, |d_2\rangle$ are the states of the detector after absorbing (detecting) a photon from either field $\hat{\mathbf{E}}_1(\mathbf{R}, t)$ or $\hat{\mathbf{E}}_2(\mathbf{R}, t)$.

Using the plane-wave representation of the fields (1.48), we find that in the state (1.65) the “interference” term in the correlation function (1.64) takes the form

$$2\text{Re} \left\{ \langle \hat{\mathbf{E}}_1^{(-)}(\mathbf{R}, t) \cdot \hat{\mathbf{E}}_2^{(+)}(\mathbf{R}, t) \rangle \right\} = 2 \left(\frac{\hbar\omega}{2\varepsilon_0\mathcal{V}} \right) \sqrt{nm} \langle d_2 | d_1 \rangle. \quad (1.66)$$

The interference term depends on the scalar product of the two states in which the detector is left as a result of the absorption of a photon from the superposed fields. If the states are orthogonal, i.e. $\langle d_2 | d_1 \rangle = 0$, the interference term vanishes indicating that the two paths are distinguishable. In other words, the interference is lost if we know by which route the registered photon came to the detector.

Suppose now that in an interval of time τ after the first detection, the detector registers another photon, and we calculate the joint probability of detecting two photons. The joint probability is proportional to the second-order correlation function, which for the two fields considered here, can be written as

$$\begin{aligned} G^{(2)}(\mathbf{R}, t; \mathbf{R}, t + \tau) &= \sum_{i,j,k,l=1}^2 \left\langle \hat{\mathbf{E}}_i^{(-)}(\mathbf{R}, t) \hat{\mathbf{E}}_k^{(-)}(\mathbf{R}, t + \tau) \right. \\ &\quad \left. \times \hat{\mathbf{E}}_l^{(+)}(\mathbf{R}, t + \tau) \hat{\mathbf{E}}_j^{(+)}(\mathbf{R}, t) \right\rangle. \end{aligned} \quad (1.67)$$

There are sixteen terms contributing to the right-hand side of (1.67), from which four terms contribute to the “interference” term in the correlation function. Consider one of the interference terms, and calculate the expectation value in the state (1.65). We find

$$\begin{aligned} &\langle \hat{\mathbf{E}}_1^{(-)}(\mathbf{R}, t) \hat{\mathbf{E}}_2^{(-)}(\mathbf{R}, t + \tau) \hat{\mathbf{E}}_2^{(+)}(\mathbf{R}, t + \tau) \hat{\mathbf{E}}_1^{(+)}(\mathbf{R}, t) \rangle \\ &= \left(\frac{\hbar\omega}{2\varepsilon_0\mathcal{V}} \right)^2 nm \langle d_1 | d_1 \rangle. \end{aligned} \quad (1.68)$$

Since $\langle d_1 | d_1 \rangle = 1$, the joint detection of two photons can exhibit interference effects between the superposed fields. It means that the second detection is an eraser, called the *quantum eraser*, of the which-way information. We can

understand this effect by recalling that a detector cannot distinguish between two identical photons, and then no which-way information is available.

There is a practical use of quantum erasure in quantum computing and quantum cryptography. The basic information unit, the qubit, requires an entangled state, such as (1.65), which can be manipulated in a controllable way. In practice, it is difficult to keep the system in a superposition state. Therefore, by applying quantum erasure, this problem can be solved and the entangled state can be maintained as desired. In Sect. 3.5.5, we will analyze the possibility of realizing quantum erasure in entangled two-atom systems and single multi-level atoms.

In fact, the quantum eraser concept, although not described in the language used by Scully and Drühl, has been observed in the experiment discussed in Sect. 1.1.4. In the experiment, the neutral density filter (NDF) was introduced to block the path i_1 . With the filter present, it was possible to tell from a measurement made with an auxiliary detector D_i whether the photon registred by D_s came from DC1 or DC2. The interference effect was not observed. However, in the absence of the filter, it was impossible in principle to tell whether the photon detected by D_s came from DC1 or DC2, and the interference effect was observed. The alignment of i_1 and i_2 therefore served as the “quantum eraser” in the experiment. In the language of Scully and Drühl, the removal of the NDF, mixing of i_1 and i_2 and subsequent detection by D_i ‘erases’ the path information, restoring the interference.

1.4 Quantum Nonlocality

Classical intuition tells us that a measurement on one system cannot have any effect on a distant system with which there is no direct interaction. We call this property “locality”. However, it follows from (1.55) that the quantum second-order correlation function vanishes when

$$k\mathbf{r}_{21} \cdot (\bar{\mathbf{R}}_1 - \bar{\mathbf{R}}_2) = (2l + 1) \pi, \quad l = 0, \pm 1, \pm 2, \dots \quad (1.69)$$

In other words, two photons can never be detected at two points separated by an odd number of $\lambda/2r_{12}$, despite the fact that one photon can be detected anywhere. As we have shown before, this is a nonclassical interference effect since two independent classical sources can produce the maximum realizable visibility of 50%, so that the second-order correlation function of two classical fields can never vanish.

The vanishing of $G^{(2)}(\mathbf{R}_1, t; \mathbf{R}_2, t)$ for two photons at widely separated points \mathbf{R}_1 and \mathbf{R}_2 is an example of quantum-mechanical nonlocality, in that the outcome of a detection measurement at \mathbf{R}_1 appears to be influenced by where we have chosen to locate the \mathbf{R}_2 detector. At certain positions \mathbf{R}_2 we can never detect a photon at \mathbf{R}_1 when there is a photon detected at \mathbf{R}_2 , whereas at other position \mathbf{R}_2 it is possible. The photon correlation argument

shows clearly that quantum theory does not in general describe an objective physical reality independent of observation.

Einstein–Podolsky–Rosen (EPR) took the view that local realism must be valid [23]. If we measure a particular physical quantity, then that physical quantity must correspond to an element of physical reality. They adopted the following definition of physical reality: “If without any way disturbing a system, we can predict the value of a physical quantity, then there exists an element of physical reality corresponding to this physical quantity”. Following this definition and using the unusual properties of correlated quantum systems, such as the vanishing $G^{(2)}(\mathbf{R}_1, t; \mathbf{R}_2, t)$ function, they argued that quantum mechanics must be incomplete. One would have to assume the existence of extra “hidden variables”, or parameters, that are not part of quantum theory, in order to describe the localized subsystems consistently with the quantum predictions. The argument is perhaps best viewed as a demonstration of the inconsistency between quantum mechanics as we know it (that is without “completion”) and local realism.

Consider a simple example of a quantum system composed of two particles a and b . Each particle has spin $\pm 1/2$, and their wave-function is the singlet state

$$|\Psi\rangle = \frac{1}{2} (|a+, \bar{\mathbf{n}}\rangle |b-, \bar{\mathbf{n}}\rangle - |a-, \bar{\mathbf{n}}\rangle |b+, \bar{\mathbf{n}}\rangle) , \quad (1.70)$$

where $|a\pm, \bar{\mathbf{n}}\rangle$ is a single-particle state with particle a having spin up (+) or down (−) along an arbitrary direction of the unit vector $\bar{\mathbf{n}}$. The state $|\Psi\rangle$ is an example of an entangled state of a system composed of two subsystems, since their combined wave-function cannot be written as a product of the eigenfunctions of the individual subsystems.

According to the EPR definition of physical reality, the spin of particle b in any direction can be predicted with certainty from a measurement of the spin of particle a in that direction. For example, if one measures the z component of the spin of particle a using a Stern–Gerlach apparatus, and finds that particle a has spin up, then the particle b has spin down. Thus, the spin of particle b can be predicted with certainty by making measurements *only* on particle a , i.e. without disturbing particle b . This means, that either there must be an instantaneous signal between the two particles (non-locality), or the value of the z component of the spin for each particle must effectively be determined before the measurement (incompleteness of the wave-function $|\Psi\rangle$).

Let us now change the experiment so that instead of measuring the spin of particle a in the z direction, we chose to measure it in the x direction. Then, we can infer from this measurement the spin of particle b in the x direction, and conclude that the spin components of the particle in both the z and x directions must be elements of physical reality. However, according to quantum mechanics the z and x components cannot be simultaneously measured with complete precision, as the associated spin operators S_z and S_x do

not commute, $[S_z, S_x] = 2iS_y$. Hence, according to EPR, quantum mechanics does not account for these elements of physical reality and therefore it cannot be considered as a complete description of physical reality.

Many resolutions of the EPR paradox have been suggested. It is sufficient to emphasize that there is no paradox within the framework of quantum mechanics, since the EPR argument does not involve simultaneous measurements or predictions of both the x and y components of particle b . Quantum mechanics involves the possibility of measuring either but not both components, and since it is possible to predict either with certainty, it can be concluded that both are elements of physical reality.

A different quantum-mechanical approach to refuting the EPR argument involves the so-called reduction of the state vector [24]. If we measure particle a to have spin up in the \bar{n} direction, then this measurement reduces the state vector (1.70) to $|\psi\rangle = |a+, \bar{n}\rangle|b-, \bar{n}\rangle$. Therefore, measurement plays a projective role rather than merely ascertaining what is already there.

1.5 Interferometric Interaction-Free Measurements

In the preceding section, we have discussed the direct measurement scheme in which a detected field is directly absorbed by photodetectors. In the direct detection process, the field is destroyed, as the detector absorbs all the field interacting with it. From the point of view of quantum physics, the measurement instantly changes the state vector of the field, in such a way that the state collapses to the appropriate eigenstate of the measured field. For example, if prior to the measurement the state vector of the field is $|\alpha\rangle + |\beta\rangle$, at the measurement the state vector collapses to $|\alpha\rangle$ if the value α is obtained, or to $|\beta\rangle$ if β is obtained.

Apart from the collapse of the wave-function, the measurement disturbs the system, so that it is impossible to predict future values of certain variables. This is a major difference between quantum and classical physics, in that in quantum physics the measurement disturbs the system to an extent that cannot be made arbitrary small. This fact is clear from the Heisenberg uncertainty relation that an observation of the position of a particle to within an accuracy Δx disturbs the momentum of the particle with an uncertainty Δp such that $\Delta x \Delta p \geq \hbar/2$. Thus if the measurement of the position is precise, a subsequent measurement of the momentum will possess infinite error: the momentum has no physical reality. We may call this a “disturbance interpretation” of quantum theory, in that the physical act of detection disturbs the state of the observed system uncontrollably, so that we cannot have complete knowledge of the system, and we cannot therefore predict its future development.

In the coming subsections, we shall discuss the particular interferometric experiments called “negative-result experiments” and “interaction-free measurements” which will help us to clarify these problems.

1.5.1 Negative-Result Measurements

In interferometric negative-result experiments, the result is obtained not through the occurrence of a physical event as for a normal measurement, but by the absence of such an event.

Theoretically, we can describe these experiments as follows. Suppose that we wish to measure an observable A that is associated with an operator \hat{A} . We assume for simplicity that the operator \hat{A} has two eigenfunctions $|\Psi_1\rangle$ and $|\Psi_2\rangle$, with corresponding eigenvalues A_1 and A_2 . If the initial wave-function is $|\Psi_1\rangle$, the measurement of A will yield the concrete physical result A_1 , but the result will definitely *not* be A_1 if the initial wave-function is $|\Psi_2\rangle$. Suppose now we choose for the initial state a linear superposition $c_1|\Psi_1\rangle + c_2|\Psi_2\rangle$ with both c_1 and c_2 nonzero. Measurement of A may yield either A_1 , or not- A_1 with probabilities $|c_1|^2$ and $|c_2|^2$, respectively. If the result was not- A_1 – that is, A_1 was not observed – we conclude that the measured eigenvalue of \hat{A} was A_2 , and the initial wave-function collapsed to $|\Psi_2\rangle$.

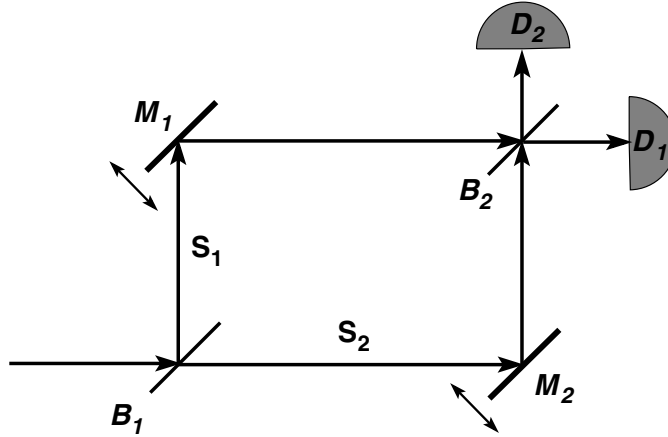


Fig. 1.13. Scheme to demonstrate negative-result measurement. The mirrors M_1 and M_2 can be fixed or can move (recoil) under the impact of a photon

To illustrate these ideas, we consider an experiment, shown in Fig. 1.13, which was proposed by Epstein [25] and involves a Mach–Zehnder interferometer. In the interferometer a beam of light, so weak that only one photon is generally present in the system in the time taken to perform the experiment, is split by the 50/50 beam splitter B_1 into two beams which travel in the arms S_1 and S_2 . The mirrors M_1 and M_2 may be fixed or can move (recoil) under the impact of a photon, but the mirrors do not absorb (destroy) the photon. In general, we may describe the state of the photon inside the system by the wave function

$$|\Psi\rangle = c_1|S_1\rangle + c_2|S_2\rangle, \quad (1.71)$$

where $|S_j\rangle$ corresponds to the photon following path S_j , $j = 1, 2$.

If both mirrors are fixed, the state of the photon inside the system is given by (1.71) with $c_1 = c_2 = 2^{-1/2}$. The two beams are coherent – that is, they will produce interference fringes when combined. By considering the phase change of $\pi/2$ on each reflection, it is easy to see that all photons will be detected at D_1 , and none at D_2 . In this case, we observe photons only by direct detection.

Next, suppose both mirrors are free to recoil. Then we can determine the path, S_1 or S_2 , taken by a photon by observing which mirror, M_1 or M_2 , recoiled. We have which-path information, and the beams are now incoherent. 50% of the photon counts will register at D_1 , and 50% at D_2 .

Now let the mirror M_2 be fixed, and assume that a photon enters the system.¹ If M_1 recoils, the photon follows path S_1 , whereas if it does not recoil, the photon must have followed path S_2 . It follows that we can determine the path followed by the photon equally well by having only one moveable mirror as two. Again, there is an equal probability of the photon being detected at D_1 or D_2 .

Thus, with M_2 fixed, in the 50% of cases that M_1 does not recoil, we can determine the path taken by the photon seemingly without any interaction between the complete measuring setup (detectors) and the photon. In this event, the state of the photon has also collapsed to $|S_2\rangle$, corresponding to it taking the path S_2 , without any apparent interaction.

1.5.2 Schemes of Interaction-Free Measurements

The fact that by means of interference it is possible to obtain information about an object without touching it makes this technique of special value in those cases where contact would seriously perturb or destroy the object being investigated.

In this section we discuss an interesting effect, referred to as interaction-free measurement, which is based mostly on the same type of physical situation as the negative-result measurement. However, the arrangement is carefully constructed to make it natural to claim that one is able to detect the presence of an object without interacting with it at all. This type of measurement is not possible under classical theory, but using the concepts of quantum theory the claim can be justified. The method makes particular use of the fact that light consists of photons, and where a beam of light has a choice of paths, we will talk of an individual photon taking one path or another. Such an idea would be totally inappropriate under a classical model of light. We consider two schemes of interaction-free measurement, one proposed by Elitzur and Vaidman [26], and the other proposed by Kwiat et al. [27].

The first scheme used a single Mach–Zehnder interferometer, in a similar way as in the Epstein proposal. The difference is that the present scheme

¹ By inserting another moveable mirror in the beam before B_1 we can determine whether a photon has entered the system.

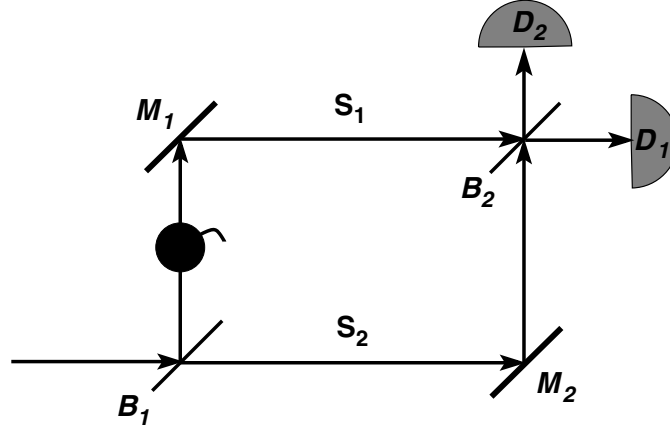


Fig. 1.14. The scheme of Elitzur and Vaidman [26] to demonstrate interaction-free measurement. The mirrors M_1 and M_2 are fixed, but there is an object in the arm S_1

assumes that the mirrors are fixed and there is an object in the arm S_1 , as shown in Fig. 1.14. We suppose the system to be set up in such a way that, without the object in the arm S_1 , all the photons passing through the system will be detected by D_1 , and none by D_2 . However, if there is an object in the arm S_1 , photons will reach the second beam splitter travelling only through the arm S_2 , and then the probabilities of detecting the photons at D_1 and D_2 are both equal to $1/2$. Thus, in this arrangement, the detector D_2 detects photons only if the blocking object is in one of the arms.

We may explain this results in the following way. We know from classical optics that a reflection changes the phase of the wave by $\pi/2$. In quantum theory, this translates to the property that a reflection multiplies the state-vector by “ i ”. Let us indicate the state of a photon moving to the right by $|1\rangle$, and that of a photon moving upwards by $|2\rangle$. At the beam splitter B_1 , the state $|1\rangle$ will change to

$$|1\rangle \rightarrow \frac{1}{\sqrt{2}} (|1\rangle + i|2\rangle) . \quad (1.72)$$

At the mirrors M_1 and M_2 , the states will change into

$$|1\rangle \rightarrow i|2\rangle , \quad |2\rangle \rightarrow i|1\rangle . \quad (1.73)$$

Thus, if the object is absent, the evolution of the initial state $|1\rangle$ will be as follows

$$\begin{aligned} |1\rangle &\rightarrow \frac{1}{\sqrt{2}} (|1\rangle + i|2\rangle) \rightarrow \frac{1}{\sqrt{2}} (i|2\rangle - |1\rangle) \\ &\rightarrow \frac{1}{2} (i|2\rangle - |1\rangle) - \frac{1}{2} (|1\rangle + i|2\rangle) = -|1\rangle . \end{aligned} \quad (1.74)$$

Hence, if the object is absent, the photon leaves B_2 moving towards the right and is detected by the detector D_1 .

On the other hand, if the object is present, the evolution of the initial state $|1\rangle$ is as follows

$$\begin{aligned} |1\rangle &\rightarrow \frac{1}{\sqrt{2}} (|1\rangle + i|2\rangle) \rightarrow \frac{1}{\sqrt{2}} (i|2\rangle + i|s\rangle) \\ &\rightarrow \frac{1}{2} (i|2\rangle - |1\rangle) + \frac{i}{\sqrt{2}} |s\rangle, \end{aligned} \quad (1.75)$$

where $|s\rangle$ is the state of a photon scattered by the object. We assume that a photon in state $|s\rangle$ is not detectable by D_1 or D_2 .

Equation (1.75) shows that the detectors D_1 and D_2 will each click with probability $1/4$, and there is probability $1/2$ that there is no detection.

In summary, if the detector D_1 clicks, no information is obtained about the object: this could happen whether the object is present in the arm S_1 or not. If there is no click in both D_1 and D_2 , we have discovered that the object is present, but our measurement has not been interaction-free as the photon has been scattered or absorbed by the object. However, if the detector D_2 clicks, we deduce that the object is present in the system, but the photon has not interacted with it since it travelled along the S_2 arm. Thus, we have a method of detecting the object without interacting with it. However, the method has at most a 50% efficiency.

In the second, more efficient scheme, proposed by Kwiat et al. [27], instead of a single Mach–Zehnder interferometer, a series of n such interferometers is used, the amplitude reflectivity r of each beam splitter being equal to $\cos(\pi/2n)$, and the amplitude transmissivity $t = \sin(\pi/2n)$. The scheme is illustrated in Fig. 1.15. As we show, this arrangement has the property that a photon entering at the lower part of the interferometer and passing through all n interferometers will be transferred into the upper part of the interferometer. Thus, if there is no object in one of the interferometers, each photon is certain to exit via the “up” port of the last beam splitter. If, however, the object is present, there will be a nonzero probability that the photon will leave through the “down” port of the last beam splitter.

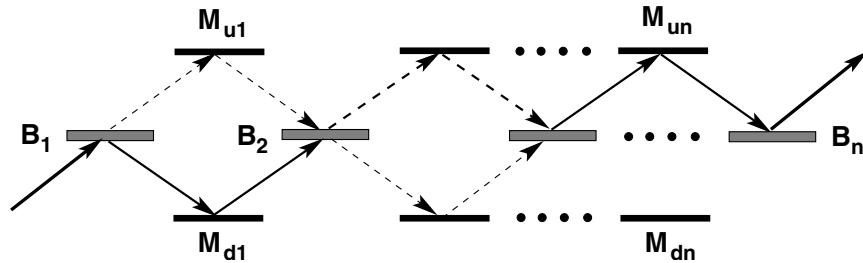


Fig. 1.15. The scheme of Kwiat et al. [27] to demonstrate interaction-free measurement. Thickness of the arrows indicates the intensities of the reflected and transmitted beams

We may explain this experiment as follows. Consider the state of the photon after leaving the second beam splitter, i.e. the first interferometer. There are two contributions to the state of the photon. The first one is from the pass $B_{r1} \rightarrow M_{d1} \rightarrow B_{r2}$ and the second one is from the pass $B_{t1} \rightarrow M_{u1} \rightarrow B_{t2}$, where B_{ri} and B_{ti} mean reflection and transmission at the i th beam splitter, respectively. The first beam has been reflected twice at beam splitters B_1 and B_2 and once at the mirror M_{d1} , three reflections giving a phase factor i^3 , and the amplitude

$$\alpha_1 = -i \cos^2 \left(\frac{\pi}{2n} \right) . \quad (1.76)$$

The second beam has been transmitted twice at the beam splitters and reflected once at the mirror M_{u1} , giving the total transmission coefficient multiplied by the factor i as

$$\alpha_2 = i \sin^2 \left(\frac{\pi}{2n} \right) . \quad (1.77)$$

Thus, after passing the first interferometer (two beam splitters), the intensity of the light going downwards is given by

$$I_2 = |\alpha_1 + \alpha_2|^2 = \cos^2 \left(\frac{\pi}{n} \right) . \quad (1.78)$$

Hence, after passing m beam splitters, the intensity downwards will be

$$I_m = \cos^2 \left(\frac{m\pi}{2n} \right) . \quad (1.79)$$

If the photon passes $m = n$ beam splitters, the intensity exiting the whole system at the “down” port is equal to zero.

However, if there is an object in one of the arms of the interferometer, the intensity I_n will be different from zero, as in this case $m < n$. Then, a detector located in the “down” port after the last beam splitter will click. Following our previous analysis, if there is an object in the upper arm of the first interferometer, the amplitude α_2 is suppressed and then the intensity of the light going downwards at the end of the first interferometer is given by

$$\tilde{I}_2 = |\alpha_1|^2 = \cos^4 \left(\frac{\pi}{2n} \right) . \quad (1.80)$$

Hence, if there are objects in the upper half of each interferometer, after passing m beam splitters, the intensity downwards will be

$$\tilde{I}_m = \cos^{2m} \left(\frac{\pi}{2n} \right) . \quad (1.81)$$

Thus, for $m = n$ we find that the probability of the photon leaving the system via the lower port is equal to $\cos^{2n}(\pi/2n)$, which becomes very close to unity when n is large.

The detection of a photon leaving the interferometers through the lower port is equivalent to the observation that there is an object inside the interferometer. This is interaction-free detection as the photon was not scattered or absorbed by the object. Furthermore, the probability of obtaining this interaction-free measurement is greater than the Elitzur and Vaidman maximum of $1/2$, and tends to unity for large n . The probability of the photon *not* leaving by the lower port is equal to $1 - \cos^{2n}(\pi/2n)$, and corresponds to the probability that the photon was scattered by the object. Naturally, this also corresponds to an observation that there is the object inside the interferometer, but in this case is not, of course, interaction-free.

1.6 Quantum Interferometric Lithography

Optical lithography is a technology for writing features of very small size onto substrates using coherent optical fields. However, the resolution is limited by the Rayleigh diffraction criterion, which states that the minimal resolvable feature size occurs at a spacing corresponding to the distance between an intensity maximum and an adjacent intensity minimum. The Rayleigh diffraction limit is $\Delta x_{\min} = \lambda/2$, where Δx_{\min} is the fringe separation and λ is the optical wavelength. This is the best resolution that can be achieved with classical fields. Hence, it has become necessary to use optical fields of very short wavelengths to fabricate smaller objects. With current technology, it is possible to write 180–200 nm size objects using KrF excimer laser light at 248 nm, and new technological approaches consider even shorter wavelengths, in the vacuum ultraviolet or even in the soft-x-ray regime, in order to write objects of 100 nm size or below.

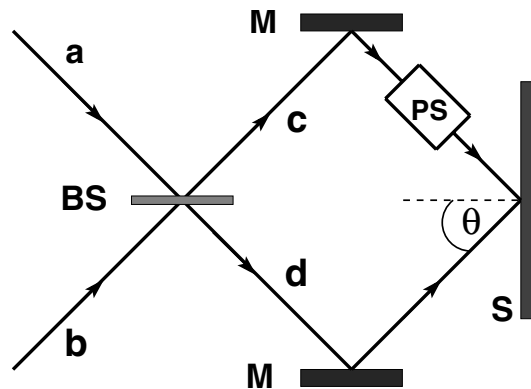


Fig. 1.16. Schematic diagram of an interferometric lithography experiment

A modification of optical lithography, called *classical interferometric lithography*, involves two coherent plane waves of laser radiation intersecting at an angle 2θ , as shown in Fig. 1.16. A phase shifter PS located in one of

the two arms introduces a phase difference between the two coherent optical paths producing an interference pattern on the screen S (lithographic plate), with the resolution given by the diffraction formula

$$\Delta x = \frac{\lambda}{2 \sin \theta} . \quad (1.82)$$

Then, in the grazing incidence limit of $\theta \rightarrow \pi/2$, the minimum resolution is $\Delta x_{\min} = \lambda/2$.

Consider now a quantum description of interference lithography [28, 29] in which we use the photon picture of the incident fields mixed at the beam splitter BS. The photons are reflected by the mirrors M onto the screen. We introduce a phase shifter placed in the upper arm which produces a phase shift $\phi = ks$, where $k = 2\pi/\lambda$ and s is the difference between the two optical paths. The input fields, ports a and b , are represented by the annihilation operators \hat{a} and \hat{b} , respectively, and obey the usual commutation relations

$$[\hat{a}, \hat{a}^\dagger] = [\hat{b}, \hat{b}^\dagger] = 1 , \quad [\hat{a}, \hat{b}] = 0 . \quad (1.83)$$

The output fields c and d are represented by two operators \hat{c} and \hat{d} which are linear combinations of the reflected and transmitted input-field operators as

$$\begin{aligned} \hat{c} &= \frac{1}{\sqrt{2}} (\hat{a} + \hat{b}) e^{i\phi} , \\ \hat{d} &= \frac{1}{\sqrt{2}} (\hat{a} - \hat{b}) , \end{aligned} \quad (1.84)$$

where $\exp(i\phi)$ represents the phase difference between the fields impinging on the screen S .

Hence, the annihilation operator of the total field detected at the screen S is given by

$$\hat{u} = \hat{c} + \hat{d} = \frac{1}{\sqrt{2}} (1 + e^{i\phi}) \hat{a} + \frac{1}{\sqrt{2}} (1 - e^{i\phi}) \hat{b} . \quad (1.85)$$

The n -photon absorption rate, corresponding to the deposition rate of n photons on the screen, is proportional to the n -order correlation function of the total field operators as

$$A_n = \frac{1}{n!} \langle (\hat{u}^\dagger)^n (\hat{u})^n \rangle , \quad (1.86)$$

where $\hat{u} = \hat{c} + \hat{d}$.

Consider first the one-photon absorption rate with an input state $|\Psi_1\rangle = |1\rangle_a |0\rangle_b$. It is easy to show that in this state the one-photon absorption rate is given by

$$A_1 = \langle \Psi_1 | \hat{u}^\dagger \hat{u} | \Psi_1 \rangle = 1 - \sin \phi , \quad (1.87)$$

which represents an interference pattern as a function of ϕ . The Rayleigh criterion demands $\phi_{\min} = \pi$ for the minimal distance between a maximum and an adjacent minimum of the interference pattern, from which we find the minimum fringe spacing $x_{\min} = \lambda/2$ (for $\theta \simeq \pi/2$). This is the usual classical result, called the single photon diffraction limit.

We will now consider the two-photon absorption rate with an input state $|\Psi_{2c}\rangle = |2\rangle_a|0\rangle_b$. This state is an example of a so-called two-photon classical state. It gets this name because it is possible to distinguish through which channel the incident photons arrive. We then find

$$\begin{aligned} A_{2c} &= \frac{1}{2!} \langle \Psi_{2c} | \hat{u}^\dagger \hat{u}^\dagger \hat{u} \hat{u} | \Psi_{2c} \rangle \\ &= (1 - \sin \phi)^2 = \frac{3}{2} - 2 \sin \phi - \frac{1}{2} \cos 2\phi . \end{aligned} \quad (1.88)$$

The classical two-photon absorption rate (1.88) has a term $\cos 2\phi$ that oscillates in space with twice the frequency as the one-photon absorption rate. This dependence leads to narrower interference fringes than that for the one-photon absorption rate.

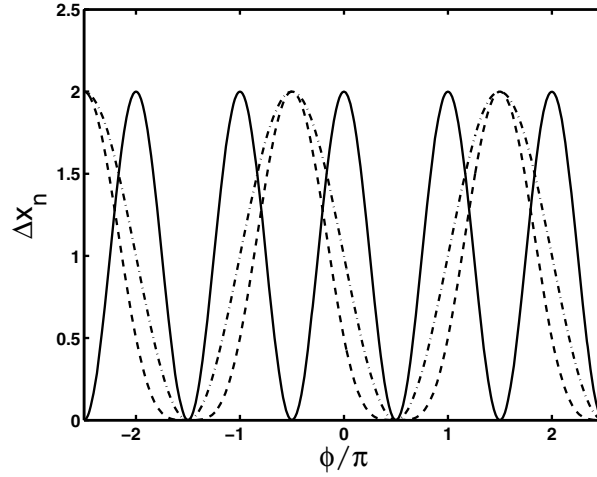


Fig. 1.17. The absorption rates A_n as a function of the phase shift ϕ for uncorrelated one-photon excitation (*dashed-dotted line*), uncorrelated two-photon excitation (*dashed line*), and quantum (entangled) two-photon excitation (*solid line*)

The two-photon absorption rate can exhibit even narrower features with the fringe spacing reduced by a factor of two if the input state is of the form $|\Psi_{2q}\rangle = |1\rangle_a|1\rangle_b$. The state $|\Psi_{2q}\rangle$ is an example of a ‘quantum’ state – so-called because there it possesses a photon in each channel, so that when a photon is detected, one cannot say from which channel it originated. With the input state $|\Psi_{2q}\rangle$, the two-photon absorption rate takes the form

$$\Delta x_{2q} = \frac{1}{2!} \langle \Psi_{2q} | \hat{u}^\dagger \hat{u}^\dagger \hat{u} \hat{u} | \Psi_{2q} \rangle = 1 + \cos 2\phi . \quad (1.89)$$

Comparing (1.89) with (1.88), we see that in the case of the input quantum field, the slowly oscillating term $\sin \phi$ has been eliminated, and we are left with only the $\cos 2\phi$ term, giving the minimum resolution $x_{\min} = \lambda/4$. In Fig. 1.17, we plot the absorption rates as a function of the phase shift ϕ . It is evident that the classical two-photon excitation pattern has the same period but is narrower than the one-photon excitation pattern, and the quantum two-photon excitation pattern has a period half that of the corresponding classical interference pattern. This unusual property of the interference pattern is a consequence of the division of the two photons between the two channels in the input state $|\Psi_{2q}\rangle$.

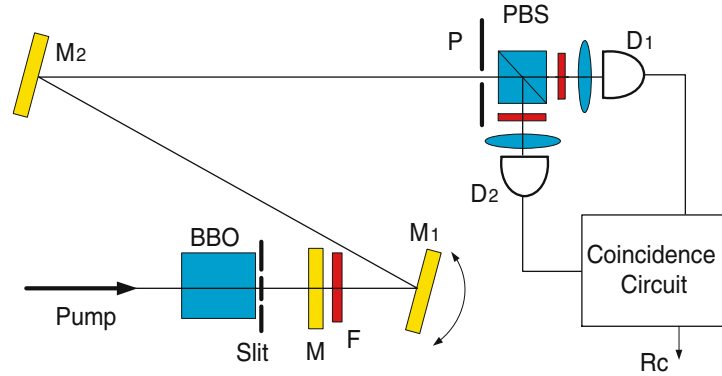


Fig. 1.18. Schematic diagram of the D'Angelo et al. [30] experiment to observe the spatial two-photon interference pattern. From M. D'Angelo, M.V. Chekhova, Y. Shih: Phys. Rev. Lett. **87**, 013602 (2001). Copyright (2001) by the American Physical Society

A spatial interference pattern with the modulation period reduced by a factor of two has been observed experimentally by D'Angelo, Chekhova and Shih [30]. The experimental arrangement is shown in Fig. 1.18. An argon ion laser was used to pump a nonlinear BBO (BaB_2O_4) crystal to produce orthogonally polarized pairs of signal and idler photons. Each pair was generated collinearly, with degenerate frequencies, $\omega_s = \omega_i = \omega_p/2$, where ω_j ($j = s, i, p$) are the frequencies of the signal, idler and pump fields, respectively. The pump field was separated from the signal-idler pair by a mirror M. The signal-idler beam passed through a double slit and then was reflected by two mirrors M_1 and M_2 onto a polarizing beam splitter PBS. The orthogonally-polarized signal and idler photons were separated by the PBS and next detected by two detectors D_1 and D_2 . The output photocurrent was sent to a coincidence counter.

Figure 1.19 shows the observed interference pattern of the two-photon coincidences produced by rotating the mirror M_1 . The upper trace, Fig. 1.19(a), shows the measured two-photon coincidences with the quantum field. The lower trace, Fig. 1.19(b), shows the interference pattern with classical light in the same experimental setup. On each graph, the solid line represents the

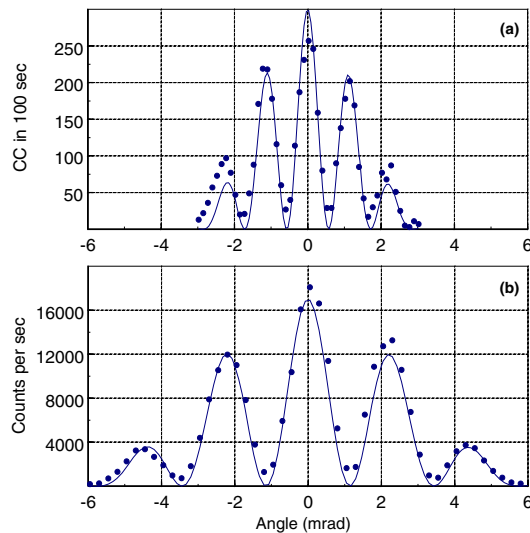


Fig. 1.19. Measured (a) interference pattern of the quantum two-photon coincidences and (b) interference pattern for classical light as a function of the rotation angle of mirror M_1 . From M. D’Angelo, M.V. Chekhova, Y. Shih: *Phys. Rev. Lett.* **87**, 013602 (2001). Copyright (2001) by the American Physical Society

prediction of the theory, and the good agreement indicates that the quantum two-photon interference pattern has a spatial modulation faster than the classical case by a factor of two. The experiment has demonstrated that the classical resolution limit of $\lambda/2$ can be overcome and shows that one could write features smaller than the single photon diffraction limit.

The resolution can even be improved beyond the $\lambda/4$ limit with n photon correlated quantum fields. In recent difficult and pioneering experiments based on linear optics, the Steinberg’s group at University of Toronto has demonstrated improved resolution to the limit of $\lambda/6$ with a quantum three-photon correlated field [31], and the Zeilinger’s group at Vienna University has demonstrated improved resolution to the limit of $\lambda/8$ with a quantum four-photon correlated field [32].

This research on super resolution interferometry demonstrates that our understanding of quantum interference and coherence has truly developed to a high degree. It is now possible to observe interference fringes with a periodicity beyond the classical limit using correlated quantum fields. The developments are of fundamental interest, and they hold promise for advances in optical interferometry and in applications such as quantum metrology and gravitational wave studies.

1.7 Three-Photon Interference

The analysis of spatial correlations between two output fields in the Young type experiment can be extended to higher-order correlation functions. An

interesting question is the extent to which the higher-order correlation functions can distinguish between classical and quantum fields. As an example, we will consider the third-order correlation function in the superposition of two output fields in the Young type experiment. We will assume that the frequencies and polarizations of the fields are equal but their phases are random and uncorrelated.

1.7.1 Three-Photon Classical Interference

The third-order correlation function corresponding to the superposition of two classical fields detected at three different points and at three different times is defined as

$$\begin{aligned}
 G_{123}^{(3)}(\mathbf{R}_1, t_1; \mathbf{R}_2, t_2; \mathbf{R}_3, t_3) \\
 = \sum_{i,j,k,l,p,q=1}^2 \langle \mathbf{E}_i^*(t_1) \mathbf{E}_k^*(t_2) \mathbf{E}_p^*(t_3) \mathbf{E}_q(t_3) \mathbf{E}_l(t_2) \mathbf{E}_j(t_1) \rangle \\
 \times \exp[ik(\mathbf{r}_{ij} \cdot \bar{\mathbf{R}}_1 + \mathbf{r}_{kl} \cdot \bar{\mathbf{R}}_2 + \mathbf{r}_{pq} \cdot \bar{\mathbf{R}}_3)] \\
 \times \exp[i(\phi_i + \phi_k + \phi_p - \phi_l - \phi_j - \phi_q)] , \quad (1.90)
 \end{aligned}$$

where $\mathbf{E}_r(t)$ and ϕ_r are, respectively, the amplitude and the phase of the r th field registered by a detector located at the point \mathbf{R}_k ($k = 1, 2, 3$).

Let us illustrate some of the properties of the equal-time third-order correlation function. In terms of the intensities of the incident fields, and after averaging over the random phase difference between the fields, the equal-time third-order correlation function takes the form

$$\begin{aligned}
 G_{123}^{(3)}(\mathbf{R}_1, t; \mathbf{R}_2, t; \mathbf{R}_3, t) &= \langle (I_1(t) + I_2(t))^3 \rangle \\
 &+ 2(\langle I_1^2(t) I_2(t) \rangle + \langle I_1(t) I_2^2(t) \rangle) \{ \cos[k\mathbf{r}_{21} \cdot (\bar{\mathbf{R}}_1 - \bar{\mathbf{R}}_2)] \\
 &+ \cos[k\mathbf{r}_{21} \cdot (\bar{\mathbf{R}}_1 - \bar{\mathbf{R}}_3)] + \cos[k\mathbf{r}_{21} \cdot (\bar{\mathbf{R}}_2 - \bar{\mathbf{R}}_3)] \} . \quad (1.91)
 \end{aligned}$$

Suppose that the detectors located at the points \mathbf{R}_i ($i = 1, 2, 3$) are placed equidistantly on a straight line

$$\bar{\mathbf{R}}_1 - \bar{\mathbf{R}}_2 = \hat{\mathbf{R}}_2 - \bar{\mathbf{R}}_3 \equiv \Delta \bar{\mathbf{R}} , \quad \bar{\mathbf{R}}_1 - \bar{\mathbf{R}}_3 = 2\Delta \bar{\mathbf{R}} . \quad (1.92)$$

In this case, the correlation function (1.91) simplifies to [33]

$$\begin{aligned}
 G_{123}^{(3)}(\mathbf{R}_1, t; \mathbf{R}_2, t; \mathbf{R}_3, t) &= \langle (I_1 + I_2)(I_1^2 + I_2^2) \rangle \\
 &\times \left\{ 1 + \mathcal{R} \cos(k\mathbf{r}_{21} \cdot \Delta \bar{\mathbf{R}}) \left[1 + \cos(k\mathbf{r}_{21} \cdot \Delta \hat{\mathbf{R}}) \right] \right\} , \quad (1.93)
 \end{aligned}$$

where $I_i \equiv I_i(t)$, and

$$\mathcal{R} = \frac{4\langle I_1 I_2 (I_1 + I_2) \rangle}{\langle (I_1 + I_2)(I_1^2 + I_2^2) \rangle} . \quad (1.94)$$

It follows from (1.93) that the third-order correlation function attains its maximal value for $\cos(k\mathbf{r}_{21} \cdot \Delta\bar{\mathbf{R}}) = 1$, or equivalently, when

$$k\mathbf{r}_{21} \cdot \Delta\bar{\mathbf{R}} = 2n\pi, \quad n = 0, \pm 1, \pm 2, \dots \quad (1.95)$$

On the other hand, the third-order correlation function attains its minimal value for $\cos(k\mathbf{r}_{21} \cdot \Delta\bar{\mathbf{R}}) = -1/2$, or equivalently, when

$$k\mathbf{r}_{21} \cdot \Delta\bar{\mathbf{R}} = 2\left(n + \frac{1}{3}\right)\pi \quad \text{or} \quad k\mathbf{r}_{21} \cdot \Delta\bar{\mathbf{R}} = 2\left(n + \frac{2}{3}\right)\pi, \\ n = 0, \pm 1, \pm 2, \dots \quad (1.96)$$

By analogy with the visibility of the interference pattern of the first and second order correlation functions, we can define the visibility in the third-order correlations as

$$C^{(3)} = \frac{G_{123,\max}^{(3)} - G_{123,\min}^{(3)}}{G_{123,\max}^{(3)} + G_{123,\min}^{(3)}}, \quad (1.97)$$

and find from (1.93) that the visibility of the third-order correlations is given by

$$C^{(3)} = \frac{\frac{9}{8}\mathcal{R}}{1 + \frac{7}{8}\mathcal{R}}. \quad (1.98)$$

The visibility (1.98) attains its maximum possible value of $C^{(3)} = 0.82$ when the intensities of the interfering fields are equal, $I_1 = I_2$ ($\mathcal{R} = 2$). As with the first and second-order correlations, the visibility of the third-order correlations decreases for $I_1 \neq I_2$. For example, for $I_1 = 2I_2$, $\mathcal{R} = 8/5$ and then the visibility reduces to $C^{(3)} = 0.75$.

1.7.2 Three-Photon Nonclassical Interference

We now turn to the quantum treatment of third-order interference. The quantum-mechanical analog of the classical third-order correlation function (1.90) is the normally ordered correlation function of the field operators $\hat{\mathbf{E}}^{(+)}$ and $\hat{\mathbf{E}}^{(-)}$ defined as

$$G_{123}^{(3)}(\mathbf{R}_1, t_1; \mathbf{R}_2, t_2; \mathbf{R}_3, t_3) \\ = \langle \hat{\mathbf{E}}^{(-)}(\mathbf{R}_1, t_1) \hat{\mathbf{E}}^{(-)}(\mathbf{R}_2, t_2) \hat{\mathbf{E}}^{(-)}(\mathbf{R}_3, t_3) \\ \times \hat{\mathbf{E}}^{(+)}(\mathbf{R}_3, t_3) \hat{\mathbf{E}}^{(+)}(\mathbf{R}_2, t_2) \hat{\mathbf{E}}^{(+)}(\mathbf{R}_1, t_1) \rangle, \quad (1.99)$$

where the positive and negative frequency parts of the total field are given in (1.52).

We now examine the third-order correlation function for fixed numbers of photons in the two interfering fields. If there are n photons in the mode 1 and m photons in the mode 2, the third order correlation function takes the form

$$\begin{aligned}
 G_{123}^{(3)}(\mathbf{R}_1, \mathbf{R}_2, \mathbf{R}_3) &\equiv G_{123}^{(3)}(\mathbf{R}_1, t; \mathbf{R}_2, t; \mathbf{R}_3, t) \\
 &= E_0^3 [n(n-1)(n-2) + m(m-1)(m-2) \\
 &\quad + 2nm(n+m-2) \left\{ \frac{3}{2} + \cos[k\mathbf{r}_{21} \cdot (\bar{\mathbf{R}}_1 - \bar{\mathbf{R}}_2)] \right. \\
 &\quad \left. + \cos[k\mathbf{r}_{21} \cdot (\bar{\mathbf{R}}_1 - \bar{\mathbf{R}}_3)] \right. \\
 &\quad \left. + \cos[k\mathbf{r}_{21} \cdot (\bar{\mathbf{R}}_2 - \bar{\mathbf{R}}_3)] \right\}] . \tag{1.100}
 \end{aligned}$$

It is to be noted that the quantum third-order correlation function depends crucially on the photon (particle-like) nature of the fields. The first two terms on the right-hand side of (1.100) correspond to the simultaneous detection of three photons from each of the two modes. The last term corresponds to the simultaneous detection of two photons from either of the two fields and one photon from the other field.

If the three detectors are placed equidistantly on a straight line, the correlation function (1.100) reduces to

$$\begin{aligned}
 G_{123}^{(3)}(\mathbf{R}_1, \mathbf{R}_2, \mathbf{R}_3) &= E_0^3 (n+m-2) \{ n(n-1) \\
 &\quad + m(m-1) + 4nm \cos(k\mathbf{r}_{21} \cdot \Delta\bar{\mathbf{R}}) \\
 &\quad \times [1 + \cos(k\mathbf{r}_{21} \cdot \Delta\bar{\mathbf{R}})] \} . \tag{1.101}
 \end{aligned}$$

The correlation function (1.101) vanishes when the number of photons is smaller than three, i.e. when $n+m < 3$. This simply reflects the fact that the detectors cannot simultaneously register three photons from fields containing in total less than three photons. For $n, m \gg 1$, we can approximate $E_0(n+m-2)$ by $E_0(n+m) = I_1 + I_2$, $E_0^2 n(n-1)$ by $E_0^2 n^2 = I_1^2$, and $E_0^2 m(m-1)$ by $E_0^2 m^2 = I_2^2$, and then the quantum correlation function (1.101) reduces to (1.93) for classical fields. It is quite clear that the difference between the correlation functions is due to the difference between n^3 and $n(n-1)(n-2)$, as well as between m^3 and $m(m-1)(m-2)$, which is connected with the fact that the detectors can absorb photons as individual quanta only.

The difference between the classical and quantum correlation functions is reflected in the visibility, which for the third-order quantum correlations is given by

$$C^{(3)} = \frac{9nm}{2(n+m)(n+m-1) + 3nm} , \tag{1.102}$$

with $n+m > 2$.

When $n = m$, the visibility (1.102) reduces to

$$C^{(3)} = \frac{9n}{11n - 4} , \quad (1.103)$$

that is always greater than $9/11$, the maximal value of $C^{(3)}$ for the classical fields. This is again a nonclassical interference effect, as the quantum third-order correlation function evidently violates the classical limit of the visibility. For $n \rightarrow \infty$, the visibility (1.103) reduces to that of the classical fields. The

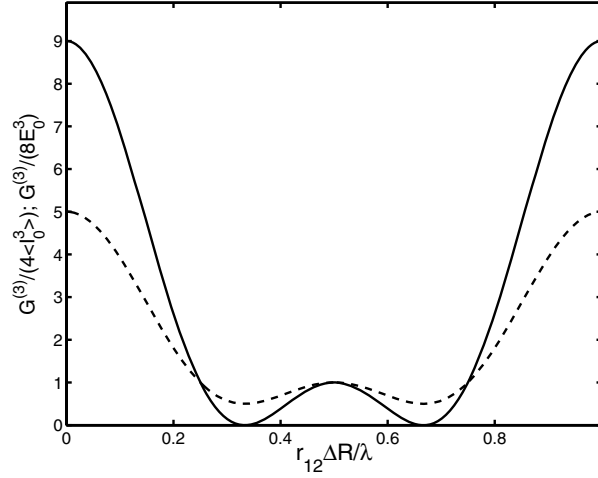


Fig. 1.20. The normalized third-order correlation functions plotted versus the separation between the detectors for two quantum fields (*solid line*) with the number of photons $n = m = 2$, and two classical fields (*dashed line*) with the intensities $I_1 = I_2 = I_0$

most striking feature of the quantum third-order correlations is that the visibility (1.103) attains its maximum possible value of $C^{(3)} = 1$ only if there are two photons in each of the two fields ($n = m = 2$). In this case, the third-order correlation function (1.101) takes a simple form [33]

$$G_{123}^{(3)}(\mathbf{R}_1, \mathbf{R}_2, \mathbf{R}_3) = 8E_0^3 [1 + 2 \cos(k\mathbf{r}_{21} \cdot \Delta\bar{\mathbf{R}})]^2 . \quad (1.104)$$

The correlation function (1.104) vanishes when $\cos(k\mathbf{r}_{21} \cdot \Delta\bar{\mathbf{R}}) = -1/2$. This is in contrast with the classical correlation function, which can never be reduced to zero. This is shown in Fig. 1.20, where we plot the normalized classical (1.93) and quantum (1.104) third-order correlation functions versus the relative position of the detectors given in terms of $r_{21} = |\mathbf{r}_{21}|$, normalized to the wavelength λ .

To summarize, the classical limit for visibility increases with increasing order of the correlation functions. In particular, for the third-order correlation function the classical limit of the visibility is $C^{(3)} = 0.82$. This feature makes the classical limit more difficult to violate than that of $C^{(3)} = 0.5$ for the second-order correlation function.

2 Quantum Interference in Atomic Systems: Mathematical Formalism

In the preceding chapter we have shown that the correlation functions of the quantized field can be calculated if we know the initial pure state of the field or, in the more general case of an initial mixed state, the density operator of the field. As we shall see in this chapter, the phenomenon of quantum interference can be described not only for light beams but also for electromagnetic (EM) fields spontaneously emitted from atoms, molecules, or even for the EM field emitted from single multi-level systems. In this case the correlation functions of the EM field can be related to the correlation functions of the internal variables of the systems, such as the atomic dipole moments.

There are a number of theoretical approaches that can be used to calculate correlation functions of the atomic variables. One such method is to use a standard formalism to derive the master equation, from which the correlation functions may be obtained. In this method, the dynamics are studied in terms of the reduced density operator ϱ_A of a “small” system, such as an atom, that is interacting with a much larger system, referred to as the reservoir. There are many possible realizations of reservoirs. The typical reservoir to which atomic systems are coupled is the quantized three-dimensional multimode electromagnetic (EM) field. The reservoir can be modelled as a vacuum field whose modes are in ordinary vacuum states, or in thermal states, or even in squeezed vacuum states. The master equation technique can be used to study a wide variety of problems involving the interaction of an atomic system with the radiation field. The major advantage of the master equation is that it allows us to consider the evolution of the combined system, the atom plus the EM field, entirely in terms of average values of atomic operators. We can derive equations of motion for the expectation value of an arbitrary combination of atomic operators, and solve these equations for time-dependent averages or the steady-state.

The aim of this chapter is to provide the most convenient expressions for the later applications to specific radiative systems. We shall describe how the correlation functions of the EM field can be related to the correlation functions of the atomic variables, such as transition dipole moments. We will present a derivation of the master equation for the density operator of a system composed of $M + 1$ energy levels in an arbitrary configuration and

connected by electric dipole transition moments. The atomic transitions can be driven by coherent fields, and can be simultaneously coupled to the quantized three-dimensional reservoir field whose modes are assumed to be in a thermal state. Dipole moments corresponding to different transitions are assumed to oscillate with different frequencies. A knowledge of the density operator will allow us to calculate the correlation functions of the dipole operators that contain information about correlations and coherences between different atomic transitions or different atoms.

2.1 Master Equation of a Multi-Dipole System

Much of our subsequent development is concerned with the time evolution of a multi-dipole system interacting with the three-dimensional dissipative EM field (the reservoir). We will therefore specify the system in terms of the density operator and give a detailed derivation of the master equation describing the time evolution of the system. An example of a multi-dipole system is an $(M + 1)$ -level atom with an arbitrary configuration of the energy levels, or a set of M two-level atoms with different transition dipole moments, interacting with a vacuum field [34].

There are many techniques for deriving the master equation of a system coupled to a reservoir. However, most are limited to the case of a single two-level atom or a single-mode harmonic oscillator interacting with a multi-mode reservoir. For the purposes of quantum interference, we need the master equations of a multi-level atom and a multi-atom system interacting with the three-dimensional multimode EM field. The derivation of the master equation presented here has similarities with the previous treatments of Louisell [35], Lehmberg [36] and Agarwal [37], except that we extend the technique to more complicated systems of M dipole moments interacting with a multimode thermal vacuum field. We also include the effects of optical cavities. The formalism developed here can be directly applied to the case of atoms interacting with colored (frequency dependent) reservoirs such as optical cavities [38] or photonic band-gap materials [39], and can be easily extended, with only minor modifications, to the case of electric quadrupole transitions in atoms or molecules [40]. Some of these applications are discussed in Chaps. 4 and 5.

2.1.1 Master Equation of a Single Multi-Level Atom

Let us start with the Hamiltonian of the combined system, a multi-level atom plus the three-dimensional multimode EM field, which in the electric dipole approximation is composed of three terms

$$H = H_A + H_F + H_{AF} , \quad (2.1)$$

where

$$H_A = \sum_{m=0}^M E_m |m\rangle\langle m| \quad (2.2)$$

is the Hamiltonian of the atom, with the energy eigenstates $|0\rangle, |1\rangle, \dots, |M\rangle$ and corresponding energies $E_0 = \hbar\omega_0, E_1 = \hbar\omega_1, \dots, E_M = \hbar\omega_M$, with $E_0 < E_1 < \dots < E_M$. The energy levels can be degenerate or nondegenerate.

The second term in (2.1) is the Hamiltonian of the three-dimensional EM field

$$H_F = \sum_{\mathbf{k}s} \hbar\omega_{\mathbf{k}s} \left(\hat{a}_{\mathbf{k}s}^\dagger \hat{a}_{\mathbf{k}s} + \frac{1}{2} \right) , \quad (2.3)$$

where $\hat{a}_{\mathbf{k}s}$ and $\hat{a}_{\mathbf{k}s}^\dagger$ are the annihilation and creation operators of the field mode \mathbf{k}, s , which has wave vector \mathbf{k} , frequency $\omega_{\mathbf{k}s}$ and index of polarization s .

The final term in (2.1) is the interaction Hamiltonian between the atom and the three-dimensional EM field. The interaction depends upon the total electric dipole operator $\hat{\boldsymbol{\mu}}$ of the atom, which can be written as the sum of an upward (raising) component $\hat{\boldsymbol{\mu}}^+$ and a downward (lowering) component $\hat{\boldsymbol{\mu}}^-$ as

$$\hat{\boldsymbol{\mu}} = \hat{\boldsymbol{\mu}}^+ + \hat{\boldsymbol{\mu}}^- . \quad (2.4)$$

With the energy-levels configuration $E_0 < E_1 < \dots < E_M$, the total electric dipole moment of the atom can be written in the representation of the atomic energy levels as

$$\hat{\boldsymbol{\mu}} = \sum_{m=0}^M \sum_{n>m}^{M-1} (\boldsymbol{\mu}_{nm} A_{nm} + \boldsymbol{\mu}_{mn} A_{mn}) , \quad (2.5)$$

where $\boldsymbol{\mu}_{nm} = \boldsymbol{\mu}_{mn}^* = \langle n | \boldsymbol{\mu} | m \rangle$ is the dipole matrix element and $A_{nm} = |n\rangle\langle m|$ is the atomic transition dipole operator between the atomic energy levels $|n\rangle$ and $|m\rangle$. Here, the subscripts n and m enumerate the atomic energy levels.

The atomic dipole operators satisfy the usual commutation relations

$$[A_{mn}, A_{pq}] = A_{mq}\delta_{np} - A_{pn}\delta_{qm} , \quad (2.6)$$

and the closure property

$$\sum_{m=0}^M |m\rangle\langle m| = \sum_{m=0}^M A_{mm} = 1 . \quad (2.7)$$

With the representation (2.5) and assuming that the EM field couples to all of the atomic dipole moments, the interaction Hamiltonian H_{AF} in the electric-dipole approximation takes the form

$$H_{AF} = -\hat{\boldsymbol{\mu}} \cdot \hat{\mathbf{E}}(\mathbf{r}) = -i\hbar \sum_{\mathbf{k}s}^M \sum_{m=0}^{M-1} \sum_{n>m}^{M-1} [\boldsymbol{\mu}_{nm} \cdot \mathbf{u}_{\mathbf{k}s}(\mathbf{r}) A_{nm} \hat{a}_{\mathbf{k}s} + \boldsymbol{\mu}_{nm}^* \cdot \mathbf{u}_{\mathbf{k}s}(\mathbf{r}) A_{mn} \hat{a}_{\mathbf{k}s} - \text{H.c.}] , \quad (2.8)$$

where

$$\mathbf{u}_{\mathbf{k}s}(\mathbf{r}) = \left(\frac{\omega_{\mathbf{k}s}}{2\varepsilon_0 \hbar \mathcal{V}} \right)^{\frac{1}{2}} \bar{\mathbf{e}}_{\mathbf{k}s} e^{i\mathbf{k} \cdot \mathbf{r}} , \quad (2.9)$$

describes the mode function of the three-dimensional multi-mode field in free space, \mathcal{V} is the normalization volume, and $\bar{\mathbf{e}}_{\mathbf{k}s}$ is the unit polarization vector of the field. The mode function is evaluated at the position \mathbf{r} of the atom, and from now on we will take the atom to be stationary: the position \mathbf{r} is independent of time.

The time evolution of the atomic dipole moments interacting with the three-dimensional multi-mode field can be described in terms of the density operator ϱ_{AF} characterizing the statistical state of the combined system of the atom and the field. The density operator of the combined system satisfies the Liouville–von Neumann equation

$$\frac{\partial}{\partial t} \varrho_{AF} = \frac{1}{i\hbar} [H, \varrho_{AF}] . \quad (2.10)$$

While this equation is straightforward, it is often simpler to work in the interaction picture in which the density operator evolves in time according to the atom–field interaction.

Transforming the density operator into the interaction picture with

$$\varrho_{AF}^I(t) = e^{iH_0 t/\hbar} \varrho_{AF} e^{-iH_0 t/\hbar} , \quad (2.11)$$

we find that the transformed density operator satisfies the equation of motion

$$\frac{\partial}{\partial t} \varrho_{AF}^I(t) = \frac{1}{i\hbar} [V(t), \varrho_{AF}^I(t)] , \quad (2.12)$$

where

$$H_0 = \sum_{m=0}^M E_m |m\rangle \langle m| + \sum_{\mathbf{k}s} \hbar \omega_{\mathbf{k}s} \left(\hat{a}_{\mathbf{k}s}^\dagger \hat{a}_{\mathbf{k}s} + \frac{1}{2} \right) \quad (2.13)$$

is the Hamiltonian of the non-interacting atom and the EM field,

$$\begin{aligned} V(t) &= e^{iH_0 t/\hbar} H_{AF} e^{-iH_0 t/\hbar} \\ &= -i\hbar \sum_{\mathbf{k}s}^M \sum_{m=0}^{M-1} \sum_{n>m}^{M-1} \left\{ \boldsymbol{\mu}_{nm} \cdot \mathbf{u}_{\mathbf{k}s}(\mathbf{r}) A_{nm} \hat{a}_{\mathbf{k}s} e^{-i(\omega_{\mathbf{k}s} - \omega_{nm})t} \right. \\ &\quad \left. + \boldsymbol{\mu}_{nm}^* \cdot \mathbf{u}_{\mathbf{k}s}(\mathbf{r}) A_{mn} \hat{a}_{\mathbf{k}s} e^{-i(\omega_{\mathbf{k}s} + \omega_{nm})t} - \text{H.c.} \right\} \end{aligned} \quad (2.14)$$

is the interaction Hamiltonian H_{AF} in the interaction picture, and $\omega_{nm} = (E_n - E_m) / \hbar$ is the transition frequency between the two atomic energy levels $|n\rangle$ and $|m\rangle$, with $n > m$.

In practice, many of the A_{mn} will correspond to dipole forbidden transitions, i.e. transitions for which $\boldsymbol{\mu}_{nm} = 0$. These will play no role in the evolution of the system, and may be omitted from our description. Hence we may employ an alternative, single subscript notation that is also frequently used

$$\omega_i \equiv \omega_{nm} , \quad S_i^+ \equiv A_{nm} , \quad S_i^- \equiv A_{mn} , \quad (2.15)$$

where the subscript “ i ” represents a unique enumeration of all the dipole allowed transitions in the system. For example, if we have a three level system with only the transitions $|0\rangle \rightarrow |1\rangle$ and $|1\rangle \rightarrow |2\rangle$ allowed, the only operators of interest are A_{10} and A_{21} , and their Hermitean conjugates. Instead we could use the operators $S_1^+ = A_{10}$ and $S_2^+ = A_{21}$, and their Hermitean conjugates. Using the alternative notation, the interaction Hamiltonian (2.14) reads

$$\begin{aligned} V(t) = -i\hbar \sum_{\mathbf{k}s} \sum_i \left\{ \boldsymbol{\mu}_i \cdot \mathbf{u}_{\mathbf{k}s}(\mathbf{r}) S_i^+ \hat{a}_{\mathbf{k}s} e^{-i(\omega_{\mathbf{k}s} - \omega_i)t} \right. \\ \left. + \boldsymbol{\mu}_i^* \cdot \mathbf{u}_{\mathbf{k}s}(\mathbf{r}) S_i^- \hat{a}_{\mathbf{k}s} e^{-i(\omega_{\mathbf{k}s} + \omega_i)t} - \text{H.c.} \right\} . \end{aligned} \quad (2.16)$$

The natural procedure is to solve the equation of motion (2.12), a simple first-order differential equation, by for example, the iteration method. For the initial time $t = 0$, direct integration of (2.12) leads to the following first-order solution in $V(t)$:

$$\varrho_{AF}^I(t) = \varrho_{AF}^I(0) + \frac{1}{i\hbar} \int_0^t dt' [V(t'), \varrho_{AF}^I(t')] . \quad (2.17)$$

Substituting (2.17) back into the right side of (2.12), we obtain the integro-differential equation

$$\begin{aligned} \frac{\partial}{\partial t} \varrho_{AF}^I(t) = \frac{1}{i\hbar} [V(t), \varrho_{AF}^I(0)] \\ - \frac{1}{\hbar^2} \int_0^t dt' [V(t), [V(t'), \varrho_{AF}^I(t')]] . \end{aligned} \quad (2.18)$$

We can continue the procedure to obtain an infinite series of integral terms, which can be regarded as an exact explicit solution for $\varrho_{AF}^I(t)$. The usual practice however is to introduce approximations into the exact second order equation (2.18). By tracing (2.18) over the field states, and noting that

$$\text{Tr}_F \varrho_{AF}^I(t) \equiv \varrho_A^I(t) \quad (2.19)$$

is the reduced density operator of the atom, i.e. it is a function of the atomic variables only, we find that the master equation for the reduced atomic density operator is

$$\begin{aligned} \frac{\partial}{\partial t} \varrho_A^I(t) &= \frac{1}{i\hbar} \text{Tr}_F \{ [V(t), \varrho_{AF}^I(0)] \} \\ &\quad - \frac{1}{\hbar^2} \int_0^t dt' \text{Tr}_F \{ [V(t), [V(t'), \varrho_{AF}^I(t')]] \} . \end{aligned} \quad (2.20)$$

This equation holds for an arbitrary initial state of the combined system. We choose an initial state of the system that has no correlations between the atom and the field, which may thus be written as the tensor product

$$\varrho_{AF}^I(0) = \varrho_A^I(0) \otimes \varrho_F(0) , \quad (2.21)$$

where $\varrho_F(0)$ is the density operator of the field.

The master equation (2.20), which has been derived without any approximations, is still a complicated equation, and at this stage some approximations are desirable in order to simplify the calculation.

The interaction between an atom and the three-dimensional field is typically very weak, and then there is no back reaction of the atom on the field. Thus, we can make our first approximation, the *weak coupling* or *Born approximation*, in which we assume that the effect of the atomic system on the field is very small, so that the state of the field, appearing as a large reservoir to the atom, does not change in time. Therefore, we can write the time dependent density operator $\varrho_{AF}^I(t')$, appearing under the integral in (2.20), as

$$\varrho_{AF}^I(t') = \varrho_A^I(t') \otimes \varrho_F(0) . \quad (2.22)$$

Thus, under the Born approximation and after changing the time variable to $t' = t - \tau$, the master equation (2.20) takes the form

$$\begin{aligned} \frac{\partial}{\partial t} \varrho^I(t) &= \frac{1}{i\hbar} \text{Tr}_F \{ [V(t), \varrho^I(0) \varrho_F] \} \\ &\quad - \frac{1}{\hbar^2} \int_0^t d\tau \text{Tr}_F \{ [V(t), [V(t-\tau), \varrho^I(t-\tau) \varrho_F]] \} , \end{aligned} \quad (2.23)$$

where, for simplicity, we have introduced a shorter notation $\varrho_F(0) \equiv \varrho_F$ and $\varrho_A^I \equiv \varrho^I$.

Consider the trace over the field modes of the double commutator in the second term of (2.23), which can be written as

$$\begin{aligned} &\frac{1}{\hbar^2} \text{Tr}_F \{ [V(t), [V(t-\tau), \varrho^I(t-\tau) \varrho_F]] \} \\ &= \frac{1}{\hbar^2} \text{Tr}_F \{ V(t) V(t-\tau) \varrho^I(t-\tau) \varrho_F \} \\ &\quad + \frac{1}{\hbar^2} \text{Tr}_F \{ \varrho^I(t-\tau) \varrho_F V(t-\tau) V(t) \} \\ &\quad - \frac{1}{\hbar^2} \text{Tr}_F \{ V(t) \varrho^I(t-\tau) \varrho_F V(t-\tau) \} \\ &\quad - \frac{1}{\hbar^2} \text{Tr}_F \{ V(t-\tau) \varrho^I(t-\tau) \varrho_F V(t) \} . \end{aligned} \quad (2.24)$$

To calculate the first term on the right-hand side of (2.24), we substitute the explicit form (2.16) for the interaction Hamiltonian $V(t)$, and obtain

$$\begin{aligned}
& \frac{1}{\hbar^2} \text{Tr}_F \{ V(t) V(t-\tau) \varrho^I(t-\tau) \varrho_F(0) \} \\
&= - \sum_{\mathbf{k}s} \sum_{\mathbf{k}'s'} \left[\hat{D}_i(t) \hat{D}_j(t-\tau) \text{Tr}_F \{ \varrho_F \hat{a}_{\mathbf{k}s}(t) \hat{a}_{\mathbf{k}'s'}(t-\tau) \} \right. \\
&\quad - \hat{D}_i(t) \hat{D}_j^\dagger(t-\tau) \text{Tr}_F \left\{ \varrho_F \hat{a}_{\mathbf{k}s}(t) \hat{a}_{\mathbf{k}'s'}^\dagger(t-\tau) \right\} \\
&\quad - \hat{D}_i^\dagger(t) \hat{D}_j(t-\tau) \text{Tr}_F \left\{ \varrho_F \hat{a}_{\mathbf{k}s}^\dagger(t) \hat{a}_{\mathbf{k}'s'}(t-\tau) \right\} \\
&\quad \left. + \hat{D}_i^\dagger(t) \hat{D}_j^\dagger(t-\tau) \text{Tr}_F \left\{ \varrho_F \hat{a}_{\mathbf{k}s}^\dagger(t) \hat{a}_{\mathbf{k}'s'}^\dagger(t-\tau) \right\} \right] \varrho^I(t-\tau) , \quad (2.25)
\end{aligned}$$

where

$$\hat{D}_i(t) = \sum_i [\boldsymbol{\mu}_i \cdot \mathbf{u}_{\mathbf{k}s}(\mathbf{r}) S_i^+ e^{i\omega_i t} + \boldsymbol{\mu}_i^* \cdot \mathbf{u}_{\mathbf{k}s}(\mathbf{r}) S_i^- e^{-i\omega_i t}] , \quad (2.26)$$

and

$$\hat{a}_{\mathbf{k}s}(t) = \hat{a}_{\mathbf{k}s} \exp(-i\omega_{\mathbf{k}s}t) . \quad (2.27)$$

It is seen from (2.25) that the evolution of the reduced density operator depends on the second order correlation functions of the field operators. In order to evaluate these, we assume that the modes of the three-dimensional EM field are in a finite temperature thermal (black-body) state. In this case, the field correlation functions are given by

$$\begin{aligned}
& \text{Tr}_F \{ \varrho_F \hat{a}_{\mathbf{k}s}(t) \} = \text{Tr}_F \left\{ \varrho_F \hat{a}_{\mathbf{k}s}^\dagger(t) \right\} = 0 , \\
& \text{Tr}_F \left\{ \varrho_F \hat{a}_{\mathbf{k}s}(t) \hat{a}_{\mathbf{k}'s'}^\dagger(t-\tau) \right\} = [N(\omega_{\mathbf{k}s}) + 1] \exp[-i(\omega_{\mathbf{k}s} - \omega_{\mathbf{k}'s'})t] \\
&\quad \times \exp(-i\omega_{\mathbf{k}'s'}\tau) \delta^3(\mathbf{k} - \mathbf{k}') \delta_{ss'} , \\
& \text{Tr}_F \left\{ \varrho_F \hat{a}_{\mathbf{k}s}^\dagger(t) \hat{a}_{\mathbf{k}'s'}(t-\tau) \right\} = N(\omega_{\mathbf{k}s}) \exp[i(\omega_{\mathbf{k}s} - \omega_{\mathbf{k}'s'})t] \\
&\quad \times \exp(i\omega_{\mathbf{k}'s'}\tau) \delta^3(\mathbf{k} - \mathbf{k}') \delta_{ss'} , \\
& \text{Tr}_F \left\{ \varrho_F \hat{a}_{\mathbf{k}s}^\dagger(t) \hat{a}_{\mathbf{k}'s'}^\dagger(t-\tau) \right\} = \text{Tr}_F \{ \varrho_F \hat{a}_{\mathbf{k}s}(t) \hat{a}_{\mathbf{k}'s'}(t-\tau) \} = 0 , \quad (2.28)
\end{aligned}$$

where $N(\omega_{\mathbf{k}s}) = \text{Tr}_F \left\{ \varrho_F \hat{a}_{\mathbf{k}s}^\dagger \hat{a}_{\mathbf{k}s} \right\}$ is the number of photons in the mode $\mathbf{k}s$ of frequency $\omega_{\mathbf{k}s}$, and $\delta^3(\mathbf{k} - \mathbf{k}')$ is the three dimensional Dirac delta function.

With the aid of the correlation functions (2.28), we find that of the four terms in (2.25), two vanish, and then the first term on the right-hand side of (2.24) simplifies to

$$\begin{aligned} \frac{1}{\hbar^2} \text{Tr}_F \{ V(t) V(t-\tau) \varrho^I(t-\tau) \varrho_F \} &= \sum_{\mathbf{k}s} \left\{ \hat{D}_i(t) \hat{D}_j^\dagger(t-\tau) e^{-i\omega_{\mathbf{k}s}\tau} \right. \\ &\quad \left. + \hat{D}_i^\dagger(t) \hat{D}_j(t-\tau) e^{i\omega_{\mathbf{k}s}\tau} \right\} \varrho^I(t-\tau) . \end{aligned} \quad (2.29)$$

Proceeding in a similar manner, we calculate the remaining three terms in (2.24), and also find that with the correlation functions (2.28) the first term on the right hand side of (2.23) vanishes.

With the above results for the double commutator, we now evaluate the sum over the field modes $\mathbf{k}s$, that appears in (2.29). First, we consider all modes of the three-dimensional EM field available for the interaction with the atomic transitions, and go over to the free space continuum limit $\mathcal{V} \rightarrow \infty$. This allows us to replace the sums over the wave vectors \mathbf{k} by frequency and angular integrals

$$\sum_{\mathbf{k}s} \longrightarrow \frac{\mathcal{V}}{(2\pi c)^3} \sum_{s=1}^2 \int_0^\infty d\omega_{\mathbf{k}s} \omega_{\mathbf{k}s}^2 \int_{\Omega_k} d\Omega_k , \quad (2.30)$$

where $\Omega_k = (\theta_k, \phi_k)$ is the solid angle over which the modes of the EM field available for the interaction with the atom are distributed.

The above expression applies for an atom in free space. For different environments, such as an optical cavity, an optical waveguide, or a photonic bandgap material, the density of modes of the vacuum field into which the radiating system can emit will be different.

Next, we substitute (2.26) into (2.29) and make our second approximation, the *Rotating-Wave Approximation* (RWA) [41], in which we ignore all terms oscillating at time t at the higher frequencies, $2\omega_i$ and $\omega_i + \omega_j$ (the so-called counter rotating terms). Thus, with the field correlation functions (2.28) and under the RWA approximation, the master equation (2.23) simplifies to

$$\begin{aligned} \frac{\partial}{\partial t} \varrho^I(t) &= \sum_{i,j} \left\{ [S_j^- X_{ij}(t), S_i^+] + [S_j^-, X_{ji}^\dagger(t) S_i^+] \right. \\ &\quad \left. + [S_j^+ Y_{ij}(t), S_i^-] + [S_j^+, Y_{ji}^\dagger(t) S_i^-] \right\} , \end{aligned} \quad (2.31)$$

where the summation is over the atomic dipole transitions, and the time dependent operators are of the form

$$\begin{aligned} X_{ij}(t) &= \frac{\mathcal{V}}{(2\pi c)^3} \int_0^\infty d\omega_{\mathbf{k}s} \omega_{\mathbf{k}s}^2 e^{i(\omega_i - \omega_j)t} \int_{\Omega_k} d\Omega_k \mathcal{F}_{ij}^{(-)}(\mathbf{k}s, t) , \\ Y_{ij}(t) &= \frac{\mathcal{V}}{(2\pi c)^3} \int_0^\infty d\omega_{\mathbf{k}s} \omega_{\mathbf{k}s}^2 e^{-i(\omega_i - \omega_j)t} \int_{\Omega_k} d\Omega_k \mathcal{F}_{ij}^{(+)}(\mathbf{k}s, t) , \end{aligned} \quad (2.32)$$

with the operators $\hat{\mathcal{F}}_{ij}^{(\pm)}(\mathbf{k}s, t)$ involving an integral over the retarded time τ and the retarded density operator

$$\begin{aligned}
\mathcal{F}_{ij}^{(\pm)}(\mathbf{k}s, t) &= \int_0^t d\tau \varrho^I(t - \tau) e^{-i(\omega_{\mathbf{k}s} \pm \omega_j)\tau} \\
&\times \sum_{s=1}^2 [N(\omega_{\mathbf{k}s}) + 1] [\boldsymbol{\mu}_i \cdot \mathbf{u}_{\mathbf{k}s}(\mathbf{r})] [\boldsymbol{\mu}_j^* \cdot \mathbf{u}_{\mathbf{k}s}^*(\mathbf{r})] \\
&+ \int_0^t d\tau \varrho^I(t - \tau) e^{i(\omega_{\mathbf{k}s} \mp \omega_j)\tau} \\
&\times \sum_{s=1}^2 N(\omega_{\mathbf{k}s}) [\boldsymbol{\mu}_i^* \cdot \mathbf{u}_{\mathbf{k}s}(\mathbf{r})] [\boldsymbol{\mu}_j \cdot \mathbf{u}_{\mathbf{k}s}^*(\mathbf{r})] . \quad (2.33)
\end{aligned}$$

The master equation (2.31) is still in the form of an integro-differential equation, and is non-Markovian since the left side $\partial \varrho^I(t) / \partial t$ is related to the density operator on the right side at earlier times $(t - \tau)$. Here, we can make our third approximation, *the Markov approximation*, in which we replace $\varrho^I(t - \tau)$ by $\varrho^I(t)$ in (2.33), and extend the integral to infinity. In the Markov approximation the integral over the time delay τ contains functions which decay to zero over a short correlation time τ_c . This correlation time is of the order of the time scale of the radiative processes in the atom, and the short correlation time approximation is formally equivalent to assuming that the bandwidth of the electromagnetic field is much larger than the atomic linewidths. In a typical atom, the density operator changes on a time scale corresponding to the spontaneous emission rate, $t_s \sim 10^{-8}$ s, and if ω_0 is an optical frequency, the exponents oscillate on the time scale $t_o \sim 10^{-15}$ s, which is much shorter than the atomic time-scale. Thus, the Markov approximation is justified for atoms interacting with the ordinary vacuum field. For a thermal field, it requires the bandwidth of the thermal field to be much larger than the atomic linewidths.

Under the Markov approximation, we can evaluate the integral over τ , appearing in (2.33) to obtain

$$\lim_{t \rightarrow \infty} \int_0^t d\tau \varrho^I(t - \tau) e^{ix\tau} \approx \varrho^I(t) \left[\pi \delta(x) + i \frac{\mathcal{P}}{x} \right] , \quad (2.34)$$

where \mathcal{P} indicates the principal value of the integral. Moreover, for thermal field bandwidths much larger than the atomic linewidths, we can approximate the $N(\omega_{\mathbf{k}s})$ by replacing them by their values evaluated at the average frequency ω_0 of the atomic transitions, i.e. we take $N(\omega_{\mathbf{k}s}) = N(\omega_0) \equiv N$.

Thus, under the Born–Markov and RWA approximations, the field mode functions (2.33) take the form

$$\begin{aligned}
\mathcal{F}_{ij}^{(\pm)}(\mathbf{k}s, t) &= (N+1) \sum_{s=1}^2 [\boldsymbol{\mu}_i \cdot \mathbf{u}_{\mathbf{k}s}(\mathbf{r})] [\boldsymbol{\mu}_j^* \cdot \mathbf{u}_{\mathbf{k}s}^*(\mathbf{r})] \\
&\quad \times \left[\pi \delta(\omega_{\mathbf{k}s} \pm \omega_j) - \mathcal{P} \frac{i}{\omega_{\mathbf{k}s} \pm \omega_j} \right] \varrho^I(t) \\
&\quad + N \sum_{s=1}^2 [\boldsymbol{\mu}_i^* \cdot \mathbf{u}_{\mathbf{k}s}(\mathbf{r})] [\boldsymbol{\mu}_j \cdot \mathbf{u}_{\mathbf{k}s}^*(\mathbf{r})] \\
&\quad \times \left[\pi \delta(\omega_{\mathbf{k}s} \mp \omega_j) + \mathcal{P} \frac{i}{\omega_{\mathbf{k}s} \mp \omega_j} \right] \varrho^I(t) . \quad (2.35)
\end{aligned}$$

We now proceed to evaluate the polarization sums in (2.35), which will allow us to evaluate the integrals over $d\Omega_k$ in (2.32). The integral over $d\Omega_k$ contains integrals over the spherical polar coordinates θ_k and ϕ_k . Hence, we will express the wave vector \mathbf{k} , the unit polarization vector $\bar{\mathbf{e}}_{\mathbf{k}s}$ and the atomic transition dipole moments $\boldsymbol{\mu}_i$ and $\boldsymbol{\mu}_j$ in terms of the components of the spherical coordinates. The angle θ_k is formed by the z axis of the Cartesian coordinates and \mathbf{k} direction, so we can write

$$\mathbf{k} = |\mathbf{k}| [\sin \theta_k \cos \phi_k, \sin \theta_k \sin \phi_k, \cos \theta_k] . \quad (2.36)$$

In this representation, the unit polarization vectors $\bar{\mathbf{e}}_{\mathbf{k}1}$ and $\bar{\mathbf{e}}_{\mathbf{k}2}$ may be chosen as

$$\begin{aligned}
\bar{\mathbf{e}}_{\mathbf{k}1} &= [-\cos \theta_k \cos \phi_k, -\cos \theta_k \sin \phi_k, \sin \theta_k] , \\
\bar{\mathbf{e}}_{\mathbf{k}2} &= [\sin \phi_k, -\cos \phi_k, 0] , \quad (2.37)
\end{aligned}$$

and for $\Delta m = 0$ transitions in the atom, the orientation of the atomic dipole moments can be taken in the xy plane

$$\begin{aligned}
\boldsymbol{\mu}_i &= |\boldsymbol{\mu}_i| [\cos \theta_i, \sin \theta_i, 0] , \\
\boldsymbol{\mu}_j &= |\boldsymbol{\mu}_j| [\cos \theta_j, \sin \theta_j, 0] . \quad (2.38)
\end{aligned}$$

With this choice of the polarization vectors and the orientation of the dipole moments, the summation over s in (2.35) leads to

$$\begin{aligned}
\sum_{s=1}^2 [\boldsymbol{\mu}_i \cdot \mathbf{u}_{\mathbf{k}s}(\mathbf{r})] [\boldsymbol{\mu}_j^* \cdot \mathbf{u}_{\mathbf{k}s}^*(\mathbf{r})] &= \sum_{s=1}^2 [\boldsymbol{\mu}_i^* \cdot \mathbf{u}_{\mathbf{k}s}(\mathbf{r})] [\boldsymbol{\mu}_j \cdot \mathbf{u}_{\mathbf{k}s}^*(\mathbf{r})] \\
&= \frac{\omega_{\mathbf{k}s} |\boldsymbol{\mu}_i| |\boldsymbol{\mu}_j|}{2\varepsilon_0 \hbar \mathcal{V}} \left\{ \cos \theta_i \cos \theta_j (\cos^2 \theta_k \cos^2 \phi_k + \sin^2 \phi_k) \right. \\
&\quad + \sin \theta_i \sin \theta_j (\cos^2 \theta_k \sin^2 \phi_k + \cos^2 \phi_k) \\
&\quad \left. - \sin(\theta_i + \theta_j) \sin^2 \theta_k \cos \phi_k \sin \phi_k \right\} . \quad (2.39)
\end{aligned}$$

The final step is to evaluate the angular integrals over the spherical angles θ_k and ϕ_k that appear in (2.32). Since the integrals over the azimuthal angle ϕ_k are

$$\begin{aligned} \int_0^{2\pi} d\phi_k \sin \phi_k \cos \phi_k &= 0 , \\ \int_0^{2\pi} d\phi_k \sin^2 \phi_k &= \int_0^{2\pi} d\phi_k \cos^2 \phi_k = \pi , \end{aligned} \quad (2.40)$$

and the integral over the polar angle θ_k is

$$\pi \int_0^\pi d\theta_k \sin \theta_k (\cos^2 \theta_k + 1) = \frac{8}{3} \pi , \quad (2.41)$$

we arrive at

$$\begin{aligned} X_{ij}(t) &= \varrho^I(t) e^{i(\omega_i - \omega_j)t} \left\{ \frac{1}{2} (1 + N) \gamma_{ij} + i \left[N \Lambda_{ij}^{(+)} - (1 + N) \Lambda_{ij}^{(-)} \right] \right\} , \\ Y_{ij}(t) &= \varrho^I(t) e^{-i(\omega_i - \omega_j)t} \left\{ \frac{1}{2} N \gamma_{ij} + i \left[N \Lambda_{ij}^{(-)} - (1 + N) \Lambda_{ij}^{(+)} \right] \right\} , \end{aligned} \quad (2.42)$$

where

$$\gamma_i \equiv \gamma_{ii} = \frac{\omega_i^3 \mu_i^2}{3\pi \varepsilon_0 \hbar c^3} , \quad (2.43)$$

and

$$\Lambda_{ij}^{(\pm)} = \frac{\sqrt{\gamma_i \gamma_j} \cos(\theta_i - \theta_j)}{2\pi \omega_0^3} \mathcal{P} \int_0^\infty d\omega_{\mathbf{k}s} \frac{\omega_{\mathbf{k}s}^3}{\omega_{\mathbf{k}s} \pm \omega_j} . \quad (2.44)$$

In the derivation of (2.44) we have replaced the transition frequencies ω_i and ω_j by the average frequency $\omega_0 = (1/M) \sum_{i=1}^M \omega_i$, in a way consistent with the RWA that is already made here, as in this case the spread of the frequencies satisfies $(\omega_i - \omega_j) \ll \omega_0$.

The parameters $\Lambda_{ij}^{(\pm)}$ that appear in (2.42) will contribute to the shifts of the atomic levels, whereas the parameter γ_i , equal to the Einstein A coefficient, is the spontaneous emission rate of the i th atomic dipole transition. This parameter determines the full width at half of maximum of a given atomic transition. The parameters γ_{ij} for $i \neq j$ describe the cross-damping between a pair of atomic transitions. They arise from decay-induced coherence (quantum interference) between atomic transitions, and are given by

$$\gamma_{ij} = \gamma_{ji} = \sqrt{\gamma_i \gamma_j} \cos(\theta_i - \theta_j) \quad (i \neq j) . \quad (2.45)$$

The cross-damping term (2.45) depends on the mutual orientation of the atomic transition dipole moments, which is represented here by the cosine of the relative angle between the two dipole moment vectors. If the dipole moments are parallel, $\cos(\theta_i - \theta_j) = 1$, and then the cross-damping term is maximal with $\gamma_{ij} = \sqrt{\gamma_i \gamma_j}$, whilst $\gamma_{ij} = 0$ if the dipole moments are perpendicular ($\cos(\theta_i - \theta_j) = 0$), and the quantum interference term vanishes.

Thus, decay-induced quantum interference between two transitions in a single multi-level atom may occur only if the dipole moments of the transitions involved are non-orthogonal, i.e. when

$$\boldsymbol{\mu}_i \cdot \boldsymbol{\mu}_j \neq 0 . \quad (2.46)$$

To carry out the polarization sums in (2.35) we have used a linear representation for the unit polarization vectors $\bar{\mathbf{e}}_{\mathbf{k}s}$ and $\Delta m = 0$ atomic transitions. It is not difficult to show that with a circular representation for the unit polarization vectors, i.e.

$$\begin{aligned} \bar{\mathbf{e}}_{\mathbf{k}+} &= \frac{1}{\sqrt{2}} (\bar{\mathbf{e}}_{\mathbf{k}1} + i\bar{\mathbf{e}}_{\mathbf{k}2}) , \\ \bar{\mathbf{e}}_{\mathbf{k}-} &= \frac{1}{\sqrt{2}} (\bar{\mathbf{e}}_{\mathbf{k}1} - i\bar{\mathbf{e}}_{\mathbf{k}2}) , \end{aligned} \quad (2.47)$$

where $\bar{\mathbf{e}}_{\mathbf{k}+}$ and $\bar{\mathbf{e}}_{\mathbf{k}-}$ are complex spherical unit vectors, and with dipole moments for $\Delta m = \pm 1$ transitions

$$\begin{aligned} \boldsymbol{\mu}_i &= |\boldsymbol{\mu}_i| [\cos \theta_i , i \sin \theta_i , 0] , \\ \boldsymbol{\mu}_j &= |\boldsymbol{\mu}_j| [\cos \theta_j , -i \sin \theta_j , 0] , \end{aligned} \quad (2.48)$$

the calculations of the sums in (2.39) leads to the same spontaneous emission rates and frequency shifts as given in (2.43)–(2.44).

With the parameters (2.43)–(2.44), the general master equation (2.31) of a multi-level atom in an arbitrary configuration of the energy levels takes the following form

$$\begin{aligned} \frac{\partial \varrho^I}{\partial t} &= -\frac{1}{2} \sum_{i,j=1}^M (1+N) \gamma_{ij} (\varrho^I S_i^+ S_j^- + S_i^+ S_j^- \varrho^I - 2S_j^- \varrho^I S_i^+) e^{i(\omega_i - \omega_j)t} \\ &\quad -\frac{1}{2} \sum_{i,j=1}^M N \gamma_{ij} (\varrho^I S_i^- S_j^+ + S_i^- S_j^+ \varrho^I - 2S_j^+ \varrho^I S_i^-) e^{-i(\omega_i - \omega_j)t} \\ &\quad -i \sum_{i,j=1}^M \delta_{ij}^{(+)} [S_i^+ S_j^-, \varrho^I] e^{i(\omega_i - \omega_j)t} \\ &\quad -i \sum_{i,j=1}^M \delta_{ij}^{(-)} [S_i^- S_j^+, \varrho^I] e^{-i(\omega_i - \omega_j)t} , \end{aligned} \quad (2.49)$$

where

$$\delta_{ij}^{(\pm)} = (N+1) \Lambda_{ij}^{(\mp)} - N \Lambda_{ij}^{(\pm)} . \quad (2.50)$$

Equation (2.49) is the final form of the master equation that gives us an elegant description of the physics involved in the dynamics of multi-level atoms.

The coefficients γ_{ii} are the spontaneous emission damping rates, whereas the γ_{ij} for $i \neq j$ are the cross-damping rates that arise from the coupling between the atomic transitions. The coefficients γ_{ij} contribute to the atomic dynamics only if the dipole moments of the transitions are not perpendicular: then the spontaneous emission from one transition influences the spontaneous emission from the other. Moreover, their contribution is also limited by the fact that they appear in time dependent terms that oscillate at the frequency $\omega_i - \omega_j$. For a large difference between the atomic transition frequencies such terms are rapidly oscillating and their contributions to the atomic dynamics can be neglected. However, when $\omega_i - \omega_j$ is small, as can occur with degenerate or nearly degenerate transition frequencies, such terms must be included in the atomic dynamics.

The parameters

$$\begin{aligned} \delta_{ii}^{(\pm)} = & N \frac{\gamma_i}{2\pi\omega_0^3} \mathcal{P} \int_0^\infty d\omega_{\mathbf{k}s} \omega_{\mathbf{k}s}^3 \left[\frac{1}{\omega_{\mathbf{k}s} \mp \omega_i} - \frac{1}{\omega_{\mathbf{k}s} \pm \omega_i} \right] \\ & + \frac{\gamma_i}{2\pi\omega_0^3} \mathcal{P} \int_0^\infty d\omega_{\mathbf{k}s} \frac{\omega_{\mathbf{k}s}^3}{\omega_{\mathbf{k}s} \mp \omega_i} , \end{aligned} \quad (2.51)$$

are the amplitudes of diagonal terms ($S_i^+ S_i^- = |i\rangle\langle i|$) in the master equation and therefore represent a frequency shift of the atomic levels, since they appear in (2.49) as the coefficients of a term $[|i\rangle\langle i|, \varrho^I]$. They correspond to a renormalization of the energies in the original system Hamiltonian (2.2). Such terms are familiar in atomic spectroscopy as the intensity dependent Stark shift. For $N = 0$, the Stark shift reduces to the ordinary Lamb shift [42, 43]. It is well-known that to obtain a complete calculation of the Lamb shift, it is necessary to extend the calculations to higher-order terms in the multi-level Hamiltonian including electron mass renormalization [44]. If these are included the standard nonrelativistic vacuum Lamb shift result is obtained. Even then, an appropriate cutoff of the frequency at $\omega_{\mathbf{k}s} = \omega_{\max} \sim c/r_0$ needs to be added at an atomic dimension r_0 , in order for the present approximation to be valid and to obtain an approximate analytical formula for the Lamb shift. In fact, it is only in the case of a fully relativistic Hamiltonian that the Lamb shift can be made finite, and even then, only after quantum electrodynamic renormalization, which involves the removal of infinities.

The parameters

$$\begin{aligned} \delta_{ij}^{(\pm)} = & N \frac{\sqrt{\gamma_i \gamma_j} \cos(\theta_i - \theta_j)}{2\pi\omega_0^3} \mathcal{P} \int_0^\infty d\omega_{\mathbf{k}s} \omega_{\mathbf{k}s}^3 \left[\frac{1}{\omega_{\mathbf{k}s} \mp \omega_j} - \frac{1}{\omega_{\mathbf{k}s} \pm \omega_j} \right] \\ & + \frac{\sqrt{\gamma_i \gamma_j} \cos(\theta_i - \theta_j)}{2\pi\omega_0^3} \mathcal{P} \int_0^\infty d\omega_{\mathbf{k}s} \frac{\omega_{\mathbf{k}s}^3}{\omega_{\mathbf{k}s} \mp \omega_j} , \quad i \neq j , \end{aligned} \quad (2.52)$$

result from the coherent coupling between two atomic transitions. As with the cross-damping rates γ_{ij} , these parameters are different from zero only if the dipole moments of the two transitions are not perpendicular. In addition,

these terms appear in the master equation as off-diagonal terms and therefore lead not to a shift of the atomic levels but rather to a dynamical coupling between atomic transitions.

We note here that the presence of the coherent terms $\delta_{ij}^{(\pm)}$ ($i \neq j$) in the master equation (2.49) depends also on the configuration of the atomic levels. These terms will contribute to the atomic dynamics only for those configurations for which the $S_i^+ S_j^-$ and $S_i^- S_j^+$ combinations of the atomic operators are nonzero. For example, for a three-level atom in the cascade configuration with three energy levels, the ground level $|0\rangle$, intermediate level $|1\rangle$, and upper level $|2\rangle$, connected by transition dipole moments μ_{01} and μ_{12} , we may take $S_1^+ = |1\rangle\langle 0|$ and $S_2^+ = |2\rangle\langle 1|$. Then the combinations of the atomic operators $S_1^+ S_2^-$ and $S_2^+ S_1^-$ are zero. This is not the case for Lambda and Vee configurations, where the combinations of the atomic operators of the two allowed dipole transitions can be different from zero. We will study this problem in more detail in Sects. 3.1 and 3.5.1.

Multi-Level Atom in the Cavity Environment

The master equation (2.49) describes the dynamics of a multi-level atom interacting with the three-dimensional thermal field in free space. In practice it is more likely that the interaction would take place inside frequency dependent reservoirs such as electromagnetic cavities, photonic bandgap materials or deposited quantum dots. If optical cavities are used, the atom-field interaction is modified since inside the cavity the atom interacts strongly only with the privileged cavity modes, which occupy only a small solid angle about the cavity axis. In other words, the cavity “tailors” the vacuum modes surrounding the atom to those orthogonal to the mirrors, which modifies the structure of modes available to the atom for spontaneous emission, thus changing the spontaneous emission rates.

Suppose we have a plane mirror Fabry–Perot cavity, shown in Fig. 2.1, with two mirrors that lie parallel to the xy plane. The first is a perfectly reflecting mirror located at $z = 0$, and the second a partially transmitting lossless mirror located at $z = L$, with L a distance we assume to be of the order of the atomic transition wavelength λ_i . The partially transmitting mirror has a real reflectivity R and transmissivity $i(1 - R^2)^{1/2}$, the same for both directions. We assume that the mirrors are very large, so that end effects can be ignored. The coherent driving fields may be admitted through the open sides of the cavity. Our treatment is based on the quantum theory of spontaneous emission from the microscopic Fabry–Perot cavity, developed by DeMartini et al. [45].

Let \mathbf{k} denote an incident wave mode propagating in the $-z$ direction, and \mathbf{k}' denote a reflected wave mode propagating in the $+z$ direction, as shown in Fig. 2.1. After multiple reflections at the mirrors and transmissions through the partially transmitting mirror, the mode function of the field inside the cavity can be written as the sum of incident and reflected waves as

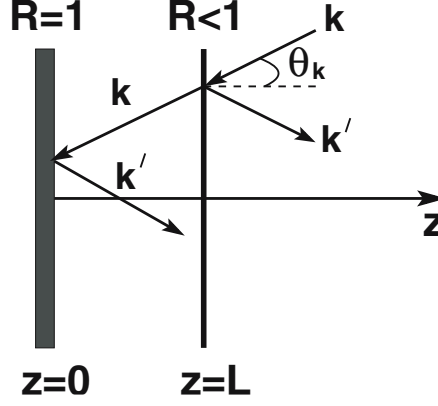


Fig. 2.1. Geometry of the microscopic plane mirror Fabry–Perot cavity. The left mirror is perfectly reflecting, \mathbf{k} is an incident wave mode and \mathbf{k}' is a reflected wave mode

$$\mathbf{u}_{\mathbf{k}s}(\mathbf{r}) = \left(\frac{\omega_{\mathbf{k}s}}{2\varepsilon_0 \hbar \mathcal{V}} \right)^{\frac{1}{2}} Y(\theta_k, L) \left(\bar{\mathbf{e}}_{\mathbf{k}s} e^{i\mathbf{k} \cdot \mathbf{r}} + \bar{\mathbf{e}}_{\mathbf{k}'s} e^{i\mathbf{k}' \cdot \mathbf{r}} \right), \quad (2.53)$$

where $Y(\theta_k, L)$ is the cavity transfer function

$$Y(\theta_k, L) = \frac{i(1 - R^2)^{1/2}}{1 - R \exp(-2ikL \cos \theta_k)}, \quad (2.54)$$

with θ_k the angle between the \mathbf{k} vector and the z -axis (cavity axis). We have assumed that the reflectivity R is the same for both polarizations.

The mode function (2.53) for the cavity field is modified compared to that for the field in free space (2.9) by the presence of the mirrors. This is manifested by the function $Y(\theta_k, L)$. The effect of $Y(\theta_k, L)$ on the mode function inside the cavity is most clearly exhibited by considering

$$|Y(\theta_k, L)|^2 = \frac{(1 - R^2)}{(1 - R)^2 + 4R \sin^2(kL \cos \theta_k)}, \quad (2.55)$$

which is identified as the Airy function of the cavity [1]. If R is close to one, then the Airy function displays a series of sharp peaks for angles of incidence such that $\sin(kL \cos \theta_k) = 0$. If $L = \lambda/2$, where λ is the resonance wavelength, the Airy function will exhibit a sharp peak centered at $\cos \theta_k = 1$. This means that the atom can be coupled only to those modes which are contained in a small solid angle around the cavity axis.

The polarization unit vectors $\bar{\mathbf{e}}_{\mathbf{k}s}$ and $\bar{\mathbf{e}}_{\mathbf{k}'s}$ can be written as a sum of components parallel and perpendicular to the xy plane as

$$\begin{aligned} \bar{\mathbf{e}}_{\mathbf{k}s} &= \bar{\mathbf{e}}_{\mathbf{k}s}^{\perp} + \bar{\mathbf{e}}_{\mathbf{k}s}^{\parallel}, \\ \bar{\mathbf{e}}_{\mathbf{k}'s} &= \bar{\mathbf{e}}_{\mathbf{k}s}^{\perp} - \bar{\mathbf{e}}_{\mathbf{k}s}^{\parallel}, \end{aligned} \quad (2.56)$$

and a similar decomposition can be made for the wave vectors \mathbf{k} and \mathbf{k}'

$$\begin{aligned}\mathbf{k} &= \mathbf{k}^\perp + \mathbf{k}^\parallel, \\ \mathbf{k}' &= -\mathbf{k}^\perp + \mathbf{k}^\parallel.\end{aligned}\quad (2.57)$$

To study the behavior of a multi-level atom interacting with the multi-mode EM field inside the Fabry–Perot cavity, we derive the master equation for the reduced density operator of the system. Because of a small mirror spacing, the process of spontaneous emission inside the cavity can be regarded as irreversible, and we may employ the familiar Born–Markov approximations to derive the master equation. The influence of the microcavity on the interaction of the atom with the vacuum field is illustrated most clearly if one assumes that the dipole moments of the atom are parallel to each other and oriented in directions parallel or perpendicular to the cavity mirrors. In this case, the polarization sums in (2.35) and integrals over $d\Omega_k$ in (2.32) with the cavity field mode function (2.53) lead to a master equation which is formally equivalent to (2.49), the master equation for the atom in free space, but with “cavity renormalized” parameters. The modified electromagnetic vacuum field inside the cavity changes the spontaneous emission rates from those corresponding to the normal vacuum, γ_{ij} , into

$$\gamma_{ij}^\parallel = \frac{3}{2}\gamma_{ij}\frac{(1+R)}{(1-R)}\left[\int_0^1 du (1+u^2) \frac{\sin^2(k_0 r_z u)}{1+F\sin^2(k_0 Lu)}\right], \quad (2.58)$$

and

$$\gamma_{ij}^\perp = \frac{3}{2}\gamma_{ij}\frac{(1+R)}{(1-R)}\left[\int_0^1 du (1-u^2) \frac{\cos^2(k_0 r_z u)}{1+F\sin^2(k_0 Lu)}\right], \quad (2.59)$$

where $u = \cos\theta_k$, $F = 4R/(1-R)^2$, r_z is the z -coordinate of the atomic position inside the cavity, γ_{ij}^\parallel is the spontaneous emission rate for the dipole moments parallel to the mirrors, and γ_{ij}^\perp is the spontaneous emission rate for the dipole moments oriented in the direction perpendicular to the mirrors. In the derivation of (2.58) we have assumed with no loss of generality that the dipole moments are parallel to the x -axis. This is not an essential feature, since the cavity is isotropic in the xy plane.

Similarly, the frequency shifts change from their free space values $\Lambda_{ij}^{(\pm)}$ into

$$\begin{aligned}\Lambda_{ij}^{(\pm)\parallel} &= \frac{\gamma_{ij}}{2\pi\omega_0^3}\frac{(1+R)}{(1-R)}\mathcal{P}\int_0^\infty d\omega_{\mathbf{k}s} \frac{\omega_{\mathbf{k}s}^3}{\omega_{\mathbf{k}s} \pm \omega_j} \\ &\times \left[\int_0^1 du (1+u^2) \frac{\sin^2(\omega_{\mathbf{k}s} r_z u/c)}{1+F\sin^2(\omega_{\mathbf{k}s} Lu/c)}\right].\end{aligned}\quad (2.60)$$

and

$$\Lambda_{ij}^{(\pm)\perp} = \frac{\gamma_{ij}}{2\pi\omega_0^3} \frac{(1+R)}{(1-R)} \mathcal{P} \int_0^\infty d\omega_{\mathbf{k}s} \frac{\omega_{\mathbf{k}s}^3}{\omega_{\mathbf{k}s} \pm \omega_j} \times \left[\int_0^1 du (1-u^2) \frac{\cos^2(\omega_{\mathbf{k}s} r_z u/c)}{1 + F \sin^2(\omega_{\mathbf{k}s} L u/c)} \right]. \quad (2.61)$$

These results demonstrate that there is no essential distinction between the master equations of the multi-level atom in free space and inside the microcavity. The only difference is that the spontaneous emission rates and frequency shifts are now dependent on the cavity parameters. In particular, in the so-called good cavity limit of $R \rightarrow 1$ with $r_z = L/2$ and $L = \lambda_0/2$, the spontaneous emission rate γ_{ij}^{\parallel} approaches $1.5\gamma_{ij}$, which is in agreement with the spontaneous emission rate of a two-level atom in a cavity, predicted by Milonni and Knight [46] and observed experimentally by Kleppner [47]. This result shows that the spontaneous emission rate is three times greater than the free space rate, when the atom is midway between perfect plane parallel mirrors separated by half a wavelength. We shall approach this problem in another way in Sect. 4.1.

Multi-Level Atom Driven by Coherent Fields

In the derivation of the master equation (2.49) we have assumed that the multi-level atom interacts only with the vacuum modes of the quantized electromagnetic field, with no interaction or coupling to external coherent fields. This master equation has limited applications to only incoherent thermal driving fields, and therefore we shall extend the derivation to include external coherent fields. These fields are assumed to be tuned near the atomic resonances, in the sense that the detunings are small compared to the atomic transition frequencies.

To derive the master equation of a multi-level atom interacting with external coherent fields, we start from the equation of motion (2.23) for the reduced density operator. With the interaction Hamiltonian (2.14), and after making the rotating wave approximation in which we ignore the rapidly oscillating terms, the first term on the right-hand side of (2.23) becomes

$$\begin{aligned} & \frac{1}{i\hbar} \text{Tr}_F \{ [V(t), \varrho^I(0) \varrho_F(0)] \} \\ &= - \sum_{\mathbf{k}s} \sum_i \text{Tr}_F \left\{ \left[\boldsymbol{\mu}_i \cdot \mathbf{u}_{\mathbf{k}s}(\mathbf{r}) S_i^+ \hat{a}_{\mathbf{k}s} e^{-i(\omega_{\mathbf{k}s} - \omega_i)t} \right. \right. \\ & \quad \left. \left. - \boldsymbol{\mu}_i^* \cdot \mathbf{u}_{\mathbf{k}s}^*(\mathbf{r}) S_i^- \hat{a}_{\mathbf{k}s}^\dagger e^{i(\omega_{\mathbf{k}s} - \omega_i)t}, \varrho^I(0) \varrho_F(0) \right] \right\}. \end{aligned} \quad (2.62)$$

This term yields zero on taking the trace over the radiation field if no external coherent fields are applied to the system. However, let us assume that W

coherent fields, described by coherent states $|\alpha_l\rangle$, $l = 1, \dots, W$, and corresponding frequencies ω_{Ll} , are applied. The coherent state $|\alpha_l\rangle$ is the eigenstate of \hat{a}_l with eigenvalue α_l . Then, the trace over the field states leads to

$$\begin{aligned}\mathrm{Tr}_F \{ \hat{a}_{\mathbf{k}s} \varrho_F(0) \} &= \sum_{l=1}^W \langle \alpha_l | \hat{a}_l | \alpha_l \rangle , \\ \mathrm{Tr}_F \{ \hat{a}_{\mathbf{k}s}^\dagger \varrho_F(0) \} &= \sum_{l=1}^W \langle \alpha_l | \hat{a}_l^\dagger | \alpha_l \rangle .\end{aligned}\quad (2.63)$$

With the help of (2.9), we then obtain

$$\frac{1}{i\hbar} \mathrm{Tr}_F \{ [V(t), \varrho^I(0) \varrho_F(0)] \} = \frac{1}{i\hbar} [H_L(t), \varrho^I] , \quad (2.64)$$

where

$$H_L(t) = -\frac{1}{2} i\hbar \sum_{l=1}^W \sum_i \left[\Omega_i^{(l)} S_i^+ e^{-i(\omega_{Ll} - \omega_i)t} - \text{H.c.} \right] \quad (2.65)$$

is the Hamiltonian of the external coherent fields of frequencies ω_{Ll} , and

$$\Omega_i^{(l)} = 2\boldsymbol{\mu}_i \cdot \boldsymbol{\mathcal{E}}_l / \hbar \quad (2.66)$$

is the Rabi frequency of the l th coherent field of amplitude

$$\boldsymbol{\mathcal{E}}_l = \left(\frac{\hbar\omega_l}{2\varepsilon_0\mathcal{V}} \right)^{\frac{1}{2}} \bar{\mathbf{e}}_l \alpha_l e^{i\mathbf{k}_l \cdot \mathbf{r}} , \quad (2.67)$$

and wave vector \mathbf{k}_l .

The Rabi frequency is a measure of the strength of the interaction between an atomic dipole moment and an external coherent field. For example, if a multi-level atom is driven by a single laser field ($W = 1$) and the dipole moments of the atom are not parallel, the Rabi frequencies Ω_i and Ω_j of two arbitrary dipole moments are related by

$$\Omega_j = \Omega_i \frac{|\boldsymbol{\mu}_j| \cos \theta_i}{|\boldsymbol{\mu}_i| \cos \theta_j} , \quad (2.68)$$

where θ_i is the angle between the atomic dipole moment $\boldsymbol{\mu}_i$ and the polarization vector of the laser field.

Including the contribution of the external coherent fields, term (2.65), the master equation of a multi-level atom coupled to the reservoir of a three-dimensional multi-mode EM field can be written as

$$\begin{aligned}
\frac{\partial \varrho^I}{\partial t} = & -\frac{1}{2} \sum_{i,j=1}^M (1+N) \gamma_{ij} (\varrho^I S_i^+ S_j^- + S_i^+ S_j^- \varrho^I - 2S_j^- \varrho^I S_i^+) e^{i(\omega_i - \omega_j)t} \\
& -\frac{1}{2} \sum_{i,j=1}^M N \gamma_{ij} (\varrho^I S_i^- S_j^+ + S_i^- S_j^+ \varrho^I - 2S_j^+ \varrho^I S_i^-) e^{-i(\omega_i - \omega_j)t} \\
& + \frac{1}{i\hbar} [H_L(t), \varrho^I] - i \sum_{i,j=1}^M \delta_{ij}^{(+)} [S_i^+ S_j^-, \varrho^I] e^{i(\omega_i - \omega_j)t} \\
& - i \sum_{i,j=1}^M \delta_{ij}^{(-)} [S_i^- S_j^+, \varrho^I] e^{-i(\omega_i - \omega_j)t}, \tag{2.69}
\end{aligned}$$

where $H_L(t)$ is given in (2.65).

Equation (2.69) is the master equation of the atomic density operator in the interaction picture. One can see that the coefficients of the master equation depend explicitly on time. Of course, we can follow the traditional method and transform the master equation into the Schrödinger picture. However, even in this case some of the coefficients in the master equation still depend explicitly on time. In particular, in the Schrödinger picture the coefficients of the Hamiltonian H_L are multiplied by factors such as $\exp(\pm i\omega_{Li}t)$. We can simplify the time dependence of the coefficients in (2.69) by making a transformation

$$\varrho = e^{-iH't/\hbar} \varrho^I e^{iH't/\hbar}, \tag{2.70}$$

where

$$H' = \hbar \sum_i (\omega_i - \omega_{Li}) |i\rangle \langle i|. \tag{2.71}$$

With the transformation (2.70), the master equation (2.69) takes the form

$$\begin{aligned}
\frac{\partial \varrho}{\partial t} = & -\frac{i}{\hbar} [H_T, \varrho] \\
& -\frac{1}{2} \sum_{i,j=1}^M (1+N) \gamma_{ij} (\varrho S_i^+ S_j^- + S_i^+ S_j^- \varrho - 2S_j^- \varrho S_i^+) e^{-i(\omega_{Li} - \omega_{Lj})t} \\
& -\frac{1}{2} \sum_{i,j=1}^M N \gamma_{ij} (\varrho S_i^- S_j^+ + S_i^- S_j^+ \varrho - 2S_j^+ \varrho S_i^-) e^{i(\omega_{Li} - \omega_{Lj})t}, \tag{2.72}
\end{aligned}$$

where

$$\begin{aligned}
H_T = & \hbar \sum_i (\omega_i - \omega_{Li}) |i\rangle \langle i| + \hbar \sum_{i,j=1}^M \delta_{ij}^{(+)} S_i^+ S_j^- e^{-i(\omega_{Li} - \omega_{Lj})t} \\
& + \hbar \sum_{i,j=1}^M \delta_{ij}^{(-)} S_i^- S_j^+ e^{i(\omega_{Li} - \omega_{Lj})t} - i \frac{\hbar}{2} \sum_i (\Omega_i S_i^+ - \text{H.c.}) \quad . \quad (2.73)
\end{aligned}$$

It is seen from (2.72) and (2.73) that the coefficients of the master equation depend explicitly on time only when $\omega_{Li} \neq \omega_{Lj}$, i.e. when the atom is driven by laser fields of different frequencies. The coefficients become time independent only for the case of a single driving field or when the driving fields have the same frequency. The situation of a master equation with time independent coefficients is also obtained when the atomic transitions are independent, so that the terms $\delta_{ij}^{(\pm)}$ and γ_{ij} arising from spontaneously induced quantum interference are equal to zero.

The Markovian master equation (2.69) or (2.72) can also be written in the standard Lindblad form. It is easy to transform the master equation (2.69) into

$$\begin{aligned}
\frac{\partial \varrho^I}{\partial t} = & \frac{1}{i\hbar} [H_L(t), \varrho^I] - i \sum_{i,j=1}^M \delta_{ij}^{(+)} [S_i^+ S_j^-, \varrho^I] e^{i(\omega_i - \omega_j)t} \\
& - i \sum_{i,j=1}^M \delta_{ij}^{(-)} [S_i^- S_j^+, \varrho^I] e^{-i(\omega_i - \omega_j)t} \\
& - \frac{1}{2} \sum_{i,j=1}^M (1 + N) \gamma_{ij} ([\varrho^I S_i^+, S_j^-] + [S_i^+, S_j^- \varrho^I]) e^{i(\omega_i - \omega_j)t} \\
& - \frac{1}{2} \sum_{i,j=1}^M N \gamma_{ij} ([\varrho^I S_i^-, S_j^+] + [S_i^-, S_j^+ \varrho^I]) e^{-i(\omega_i - \omega_j)t} \quad , \quad (2.74)
\end{aligned}$$

which is the standard Lindblad form [48]. Writing the master equation in Lindblad form is convenient for the introduction of quantum trajectory methods. These methods are not used in the present book, but can be used to give a stochastic interpretation of the system dynamics and to relate these to various measurement processes.

In the following chapters, we will illustrate applications of the master equation (2.74) to a wide variety of cases ranging from a two-level atom to multi-level atoms in arbitrary configurations of the energy levels, interacting with the vacuum field and driven by coherent laser fields. Particular attention will be paid to the quantum interference effects resulting from the presence of the cross-damping term γ_{ij} ($i \neq j$) and vacuum induced coherent couplings $\delta_{ij}^{(\pm)}$ ($i \neq j$). The diagonal parameters $\delta_{ii}^{(\pm)}$ will be absorbed into atomic transition frequencies.

2.1.2 Master Equation of a Multi-Atom System

Using the same procedure as for the derivation of the master equation of a multi-level system, we can derive the master equation for the density operator of a multi-atom system. The only difference between these two systems is that non-overlapping atoms can occupy different positions \mathbf{r}_i , which introduces position dependent phase factors into the atomic dipole moments. Consider a system of M non-overlapping atoms coupled to the three-dimensional multi-mode vacuum field. Each atom is modelled as a two-level system, with excited state $|1\rangle_i$, ground state $|0\rangle_i$ of energies $E_0^{(i)}$ and $E_1^{(i)}$ such that $E_1^{(i)} - E_0^{(i)} = \hbar\omega_i$, where ω_i is the transition frequency. The energy levels are connected by an electric dipole transition with the dipole moment $\boldsymbol{\mu}_i \equiv \boldsymbol{\mu}_{10}^{(i)}$. We assume that the atoms are located at different points $\mathbf{r}_1, \dots, \mathbf{r}_M$, have different transition frequencies $\omega_1 \neq \omega_2 \neq \dots \neq \omega_M$, and different transition dipole moments $\boldsymbol{\mu}_1 \neq \boldsymbol{\mu}_2 \neq \dots \neq \boldsymbol{\mu}_M$.

The total atomic dipole moment operator of the system of M two-level atoms can be written in the form

$$\hat{\boldsymbol{\mu}} = \sum_{i=1}^M \left(\boldsymbol{\mu}_{10}^{(i)} A_{10}^{(i)} + \boldsymbol{\mu}_{01}^{(i)} A_{01}^{(i)} \right), \quad (2.75)$$

where $A_{10}^{(i)}$ and $A_{01}^{(i)}$ are the raising and lowering operators respectively of the i th atom, and $\boldsymbol{\mu}_{10}^{(i)}$ are the matrix elements of the transition dipole moments. Here, the superscript (i) enumerates the atoms, and the subscripts “0” and “1” indicate the atomic energy levels $|0\rangle_i$, and $|1\rangle_i$, respectively. Since all atoms are composed of only two energy states, we can drop the subscripts and simplify the notation of the atomic dipole moments and the dipole operators. Henceforth, we will use the compact notation

$$\boldsymbol{\mu}_i \equiv \boldsymbol{\mu}_{10}^{(i)}, \quad S_i^+ \equiv A_{10}^{(i)}, \quad S_i^- \equiv A_{01}^{(i)}. \quad (2.76)$$

In the electric dipole approximation, the total Hamiltonian of the combined system, the atoms plus the EM field, is given by

$$\begin{aligned} H = & \sum_{i=1}^M \hbar\omega_i S_i^z + \sum_{\mathbf{k}s} \hbar\omega_{\mathbf{k}s} \left(\hat{a}_{\mathbf{k}s}^\dagger \hat{a}_{\mathbf{k}s} + \frac{1}{2} \right) \\ & - i\hbar \sum_{\mathbf{k}s} \sum_{i=1}^M \left[\boldsymbol{\mu}_i \cdot \mathbf{u}_{\mathbf{k}s}(\mathbf{r}_i) (S_i^+ + S_i^-) \hat{a}_{\mathbf{k}s} - \text{H.c.} \right], \end{aligned} \quad (2.77)$$

where $S_i^z = (|1\rangle_{ii}\langle 1| - |0\rangle_{ii}\langle 0|)/2$ is the energy operator of the i th atom, $\hat{a}_{\mathbf{k}s}$ and $\hat{a}_{\mathbf{k}s}^\dagger$ are the annihilation and creation operators of the field mode $\mathbf{k}s$, and

$$\mathbf{u}_{\mathbf{k}s}(\mathbf{r}_i) = \left(\frac{\omega_{\mathbf{k}s}}{2\varepsilon_0 \hbar \mathcal{V}} \right)^{\frac{1}{2}} \bar{\mathbf{e}}_{\mathbf{k}s} e^{i\mathbf{k} \cdot \mathbf{r}_i}, \quad (2.78)$$

is the mode function of the three-dimensional vacuum field, evaluated at the position \mathbf{r}_i of the i th atom.

The atomic dipole operators satisfy the well-known commutation relations for the spin- $\frac{1}{2}$ operators

$$[S_i^+, S_j^-] = 2S_i^z \delta_{ij} , \quad [S_i^z, S_j^\pm] = \pm S_i^\pm \delta_{ij} , \quad [S_i^+, S_j^-]_+ = \delta_{ij} , \quad (2.79)$$

with $(S_i^\pm)^2 \equiv 0$.

As in our previous treatment of a multi-level atom, we study the time evolution of the density operator of the combined system of two-level non-overlapping atoms plus the three-dimensional multimode vacuum field. The derivation of the master equation for the reduced density operator of the atomic system is formally unchanged from the previous formalism up to the expression

$$\begin{aligned} \frac{\partial}{\partial t} \varrho(t) = & \sum_{i,j=1}^M \left\{ [S_j^- X_{ij}(t), S_i^+] + [S_j^-, X_{ji}^\dagger(t) S_i^+] \right. \\ & \left. + [S_j^+ Y_{ij}(t), S_i^-] + [S_j^+, Y_{ji}^\dagger(t) S_i^-] \right\} , \end{aligned} \quad (2.80)$$

where the time dependent operators are

$$\begin{aligned} X_{ij}(t) &= \frac{\mathcal{V}}{(2\pi c)^3} \int_0^\infty d\omega_{\mathbf{k}s} \omega_{\mathbf{k}s}^2 e^{i(\omega_i - \omega_j)t} \int_{\Omega_k} d\Omega_k \mathcal{K}_{ij}^{(-)}(\mathbf{k}s, t) , \\ Y_{ij}(t) &= \frac{\mathcal{V}}{(2\pi c)^3} \int_0^\infty d\omega_{\mathbf{k}s} \omega_{\mathbf{k}s}^2 e^{-i(\omega_i - \omega_j)t} \int_{\Omega_k} d\Omega_k \mathcal{K}_{ij}^{(+)}(\mathbf{k}s, t) , \end{aligned} \quad (2.81)$$

with the sum over the polarization involving mode functions dependent on the positions of the atoms

$$\begin{aligned} \mathcal{K}_{ij}^{(\pm)}(\mathbf{k}s, t) &= (N+1) \sum_{s=1}^2 [\boldsymbol{\mu}_i \cdot \mathbf{u}_{\mathbf{k}s}(\mathbf{r}_i)] [\boldsymbol{\mu}_j^* \cdot \mathbf{u}_{\mathbf{k}s}^*(\mathbf{r}_j)] \\ &\quad \times \left[\pi \delta(\omega_{\mathbf{k}s} \pm \omega_j) - \mathcal{P} \frac{i}{\omega_{\mathbf{k}s} \pm \omega_j} \right] \varrho^I(t) \\ &\quad + N \sum_{s=1}^2 [\boldsymbol{\mu}_i^* \cdot \mathbf{u}_{\mathbf{k}s}(\mathbf{r}_i)] [\boldsymbol{\mu}_j \cdot \mathbf{u}_{\mathbf{k}s}^*(\mathbf{r}_j)] \\ &\quad \times \left[\pi \delta(\omega_{\mathbf{k}s} \mp \omega_j) + \mathcal{P} \frac{i}{\omega_{\mathbf{k}s} \mp \omega_j} \right] \varrho^I(t) . \end{aligned} \quad (2.82)$$

Expression (2.80) has been derived under the Born–Markov and RWA approximations, and we have explicitly included in (2.82) the dependence of the mode functions $\mathbf{u}_{\mathbf{k}s}(\mathbf{r}_i)$ on the positions of the atoms.

Three integrals remain to be performed, over ϕ_k , θ_k and $\omega_{\mathbf{k}s}$, and the summation over the polarizations s . To carry out the polarization sums in (2.82),

we introduce Cartesian coordinates such that the direction of the z axis coincides with the direction of the interatomic vector $\mathbf{r}_{ij} = \mathbf{r}_i - \mathbf{r}_j$, and assume that the dipole moments of the atoms are parallel and polarized in the xz plane as

$$\begin{aligned}\boldsymbol{\mu}_i &= |\boldsymbol{\mu}_i| [\sin \alpha, 0, \cos \alpha] , \\ \boldsymbol{\mu}_j &= |\boldsymbol{\mu}_j| [\sin \alpha, 0, \cos \alpha] ,\end{aligned}\quad (2.83)$$

where α is the angle between the dipole moments and \mathbf{r}_{ij} .

Using the spherical representation we can choose the direction of the propagation vector \mathbf{k} to form the angle θ_k with \mathbf{r}_{ij} , so we can write

$$\mathbf{k} = |\mathbf{k}| [\sin \theta_k \cos \phi_k, \sin \theta_k \sin \phi_k, \cos \theta_k] , \quad (2.84)$$

where θ_k and ϕ_k are the spherical angles. Accordingly, the unit polarization vectors $\bar{\mathbf{e}}_{\mathbf{k}1}$ and $\bar{\mathbf{e}}_{\mathbf{k}2}$ may be chosen as

$$\begin{aligned}\bar{\mathbf{e}}_{\mathbf{k}1} &= [-\cos \theta_k \cos \phi_k, -\cos \theta_k \sin \phi_k, \sin \theta_k] , \\ \bar{\mathbf{e}}_{\mathbf{k}2} &= [\sin \phi_k, -\cos \phi_k, 0] ,\end{aligned}\quad (2.85)$$

and then we find that the polarization sums are

$$\begin{aligned}&\sum_{s=1}^2 [\boldsymbol{\mu}_i \cdot \mathbf{u}_{\mathbf{k}s}(\mathbf{r}_i)] [\boldsymbol{\mu}_j^* \cdot \mathbf{u}_{\mathbf{k}s}^*(\mathbf{r}_j)] = \sum_{s=1}^2 [\boldsymbol{\mu}_i^* \cdot \mathbf{u}_{\mathbf{k}s}(\mathbf{r}_i)] [\boldsymbol{\mu}_j \cdot \mathbf{u}_{\mathbf{k}s}^*(\mathbf{r}_j)] \\ &= \frac{\omega_{\mathbf{k}s} |\boldsymbol{\mu}_i| |\boldsymbol{\mu}_j|}{2\varepsilon_0 \hbar \mathcal{V}} \left\{ \sin^2 \alpha (\cos^2 \theta_k \cos^2 \phi_k + \sin^2 \phi_k) \right. \\ &\quad \left. + \cos^2 \alpha \sin^2 \theta_k - \frac{1}{4} \sin 2\alpha \sin 2\theta_k \cos \phi_k \right\} e^{ikr_{ij} \cos \theta_k} ,\end{aligned}\quad (2.86)$$

where $k = |\mathbf{k}|$ and $r_{ij} = |\mathbf{r}_{ij}|$ is the distance between the atoms. The polarization sums depend on the distance between two atoms. As a consequence, they contain contributions involving the dipole moments of two atoms, not just the usual single-atom terms.

Substituting (2.86) into (2.82), we find that the angular integrals over $d\Omega_k$ that appear in (2.81) yield

$$\begin{aligned}&\int_{\Omega_k} d\Omega_k \sum_{s=1}^2 [\boldsymbol{\mu}_i \cdot \mathbf{u}_{\mathbf{k}s}(\mathbf{r}_i)] [\boldsymbol{\mu}_j^* \cdot \mathbf{u}_{\mathbf{k}s}^*(\mathbf{r}_j)] \\ &= \int_{\Omega_k} d\Omega_k \sum_{s=1}^2 [\boldsymbol{\mu}_i^* \cdot \mathbf{u}_{\mathbf{k}s}(\mathbf{r}_i)] [\boldsymbol{\mu}_j \cdot \mathbf{u}_{\mathbf{k}s}^*(\mathbf{r}_j)] \\ &= \frac{2\pi\omega_{\mathbf{k}s} |\boldsymbol{\mu}_i| |\boldsymbol{\mu}_j|}{\varepsilon_0 \hbar \mathcal{V}} \left\{ \left[1 - (\bar{\boldsymbol{\mu}} \cdot \bar{\mathbf{r}}_{ij})^2 \right] \frac{\sin(kr_{ij})}{kr_{ij}} \right. \\ &\quad \left. + \left[1 - 3(\bar{\boldsymbol{\mu}} \cdot \bar{\mathbf{r}}_{ij})^2 \right] \left[\frac{\cos(kr_{ij})}{(kr_{ij})^2} - \frac{\sin(kr_{ij})}{(kr_{ij})^3} \right] \right\} ,\end{aligned}\quad (2.87)$$

where $\bar{\boldsymbol{\mu}} = \bar{\boldsymbol{\mu}}_i = \bar{\boldsymbol{\mu}}_j$ and $\bar{\mathbf{r}}_{ij}$ are unit vectors along the atomic transition dipole moments and the vector \mathbf{r}_{ij} , respectively.

Hence, substituting (2.82) with (2.87) into (2.81), and noting that the delta function $\delta(\omega_{\mathbf{k}s} + \omega_j)$ will yield zero in the subsequent integration over $\omega_{\mathbf{k}s}$, we obtain

$$\begin{aligned} X_{ij}(t) &= \left[(1+N) \left(\frac{1}{2} \gamma_{ij} - i \Lambda_{ij}^{(-)} \right) + i N \Lambda_{ij}^{(+)} \right] \varrho^I(t) e^{-i(\omega_i - \omega_j)t}, \\ Y_{ij}(t) &= \left[N \left(\frac{1}{2} \gamma_{ij} + i \Lambda_{ij}^{(-)} \right) - i (1+N) \Lambda_{ij}^{(+)} \right] \varrho^I(t) e^{i(\omega_i - \omega_j)t}, \end{aligned} \quad (2.88)$$

where the diagonal term

$$\gamma_{ii} \equiv \gamma_i = \frac{\omega_i^3 \mu_i^2}{3\pi \varepsilon_0 \hbar c^3} \quad (2.89)$$

is the spontaneous emission rate of the i th atom, while the off-diagonal terms

$$\gamma_{ij} = \gamma_{ji} = \sqrt{\gamma_i \gamma_j} F(k_0 r_{ij}) \quad (i \neq j), \quad (2.90)$$

with

$$\begin{aligned} F(k_0 r_{ij}) &= \frac{3}{2} \left\{ \left[1 - (\bar{\boldsymbol{\mu}} \cdot \bar{\mathbf{r}}_{ij})^2 \right] \frac{\sin(k_0 r_{ij})}{k_0 r_{ij}} \right. \\ &\quad \left. + \left[1 - 3(\bar{\boldsymbol{\mu}} \cdot \bar{\mathbf{r}}_{ij})^2 \right] \left[\frac{\cos(k_0 r_{ij})}{(k_0 r_{ij})^2} - \frac{\sin(k_0 r_{ij})}{(k_0 r_{ij})^3} \right] \right\}, \end{aligned} \quad (2.91)$$

are collective spontaneous emission rates arising from the coupling between the atoms through the vacuum field. In the expression (2.91), $k_0 = \omega_0/c$, where $\omega_0 = (\omega_i + \omega_j)/2$, and we have assumed that the differences between atomic transition frequencies are small compared to the average atomic frequency, $(\omega_i - \omega_j) \ll \omega_0$.

The remaining parameters $\Lambda_{ij}^{(\pm)}$ that appear in (2.88) will contribute to the shifts of the atomic levels, and are given by

$$\Lambda_{ij}^{(\pm)} = \frac{\sqrt{\gamma_i \gamma_j}}{2\pi \omega_0^3} \mathcal{P} \int_0^\infty d\omega_{\mathbf{k}s} \frac{\omega_{\mathbf{k}s}^3 F(\omega_{\mathbf{k}s} r_{ij}/c)}{\omega_{\mathbf{k}s} \pm \omega_j}, \quad (2.92)$$

where $F(\omega_{\mathbf{k}s} r_{ij}/c)$ is given in (2.91) with k_0 replaced by $\omega_{\mathbf{k}s}/c$.

With the explicit form of the operators (2.88), the master equation of the system of non-identical atoms interacting with a broadband thermal vacuum field reads

$$\begin{aligned}
\frac{\partial \varrho^I}{\partial t} = & -\frac{1}{2} \sum_{i,j=1}^M \gamma_{ij} (1+N) (\varrho^I S_i^+ S_j^- + S_i^+ S_j^- \varrho^I - 2S_j^- \varrho^I S_i^+) e^{i(\omega_i - \omega_j)t} \\
& -\frac{1}{2} \sum_{i,j=1}^M \gamma_{ij} N (\varrho^I S_i^- S_j^+ + S_i^- S_j^+ \varrho^I - 2S_j^+ \varrho^I S_i^-) e^{-i(\omega_i - \omega_j)t} \\
& -i \sum_{i=1}^M \delta_i [S_i^z, \varrho^I] - i \sum_{i \neq j}^M \Lambda_{ij} [S_i^+ S_j^-, \varrho^I] e^{i(\omega_i - \omega_j)t} , \tag{2.93}
\end{aligned}$$

where the diagonal terms

$$\delta_i = (2N + 1) \left(\Omega_{ii}^{(+)} - \Omega_{ii}^{(-)} \right) \tag{2.94}$$

represent a part of the intensity dependent Lamb shift of the atomic levels, while the off-diagonal terms

$$\Lambda_{ij} = - \left(\Lambda_{ij}^{(+)} + \Lambda_{ij}^{(-)} \right) , \quad (i \neq j) \tag{2.95}$$

represent the vacuum induced coherent (dipole–dipole) interaction between the atoms.

Recall that the parameter Λ_{ij} is independent of the intensity N of the thermal field and therefore plays the role of a coherent vacuum induced coupling between the atoms. Thus, the collective interactions between the atoms give rise not only to modified dissipative spontaneous emission but also lead to a coherent coupling between the atoms. Physically, as one deduces from (2.93), the parameter γ_{ij} is the real part, and Λ_{ij} the imaginary part of the interaction between atoms i and j mediated by the vacuum field.

Using contour integration, we find the explicit form of Λ_{ij} to be [36, 37]

$$\begin{aligned}
\Lambda_{ij} = & \frac{3}{4} \sqrt{\gamma_i \gamma_j} \left\{ - \left[1 - (\bar{\boldsymbol{\mu}} \cdot \bar{\mathbf{r}}_{ij})^2 \right] \frac{\cos(k_0 r_{ij})}{k_0 r_{ij}} \right. \\
& \left. + \left[1 - 3(\bar{\boldsymbol{\mu}} \cdot \bar{\mathbf{r}}_{ij})^2 \right] \left[\frac{\sin(k_0 r_{ij})}{(k_0 r_{ij})^2} + \frac{\cos(k_0 r_{ij})}{(k_0 r_{ij})^3} \right] \right\} . \tag{2.96}
\end{aligned}$$

The collective parameters γ_{ij} and Λ_{ij} , which both depend on the interatomic separation, determine the collective properties of the multiatom system. In Fig. 2.2, we plot γ_{ij} and Λ_{ij} as a function of the interatomic separation relative to the resonant wavelength λ_0 . For large separations ($r_{ij} \gg \lambda_0$) the parameters are very small ($\gamma_{ij} = \Lambda_{ij} \approx 0$), and become important for $r_{ij} < \lambda_0/2$. For atomic separations much smaller than the resonant wavelength (the small sample model), the parameters attain their maximal values

$$\gamma_{ij} = \sqrt{\gamma_i \gamma_j} , \tag{2.97}$$

and

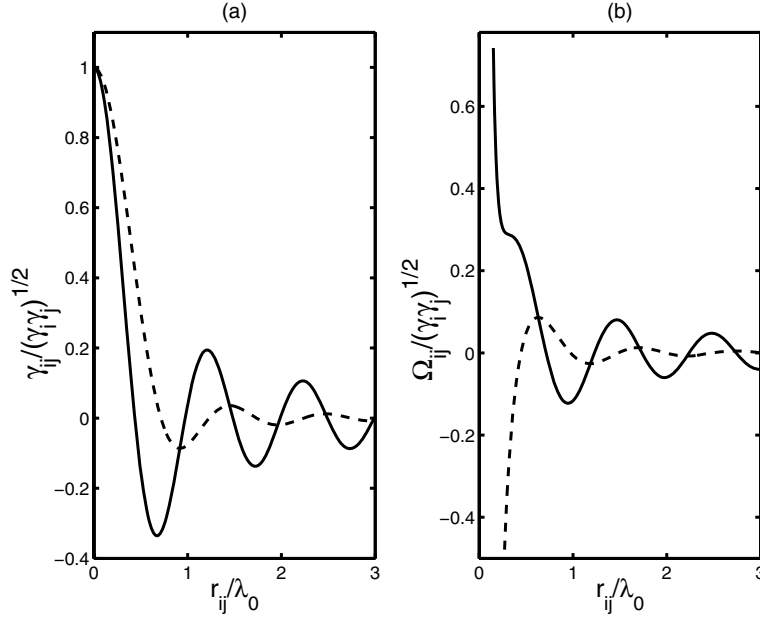


Fig. 2.2. (a) Collective damping $\gamma_{ij}/\sqrt{\gamma_i\gamma_j}$ and (b) the dipole–dipole interaction $\Lambda_{ij}/\sqrt{\gamma_i\gamma_j}$ as a function of the interatomic separation r_{ij}/λ_0 for two different orientations of the atomic dipole moments with respect to the interatomic axis: $\bar{\mu} \perp \bar{r}_{ij}$ (solid line) and $\bar{\mu} \parallel \bar{r}_{ij}$ (dashed line)

$$\Lambda_{ij} \approx \frac{3\sqrt{\gamma_i\gamma_j}}{4(k_0 r_{ij})^3} \left[1 - 3(\bar{\mu} \cdot \bar{r}_{ij})^2 \right]. \quad (2.98)$$

In this small sample model Λ_{ij} reduces to the quasistatic dipole–dipole interaction potential.

Equation (2.93) is the final form of the master equation that provides an elegant description of the physics involved in the dynamics of interacting atoms. The collective parameters γ_{ij} and Λ_{ij} , which arise from the mutual interaction between the atoms, significantly modify the master equation of a two-atom system. The physical consequences of the presence of the collective parameters are as follows: the parameter γ_{ij} introduces a coupling between the atoms through the vacuum field so that the spontaneous emission from one atom influences the spontaneous emission from the other, and the dipole–dipole interaction term Λ_{ij} introduces a coherent coupling between the atoms. Owing to the dipole–dipole interaction, the population is coherently transferred back and forth from one atom to the other. Here, the dipole–dipole interaction parameter Λ_{ij} plays a role similar to that of the Rabi frequency in the atom–field interaction.

The master equation (2.93) has been derived assuming that the atoms interact only with the multimode vacuum field, with no interaction with external coherent fields. Proceeding in a manner identical to Sect. 2.1.1, we easily find that in the presence of a coherent driving field the master equation (2.93), after transforming back to the Schrödinger picture, takes the form

$$\begin{aligned}
\frac{\partial \varrho}{\partial t} = & -\frac{i}{\hbar} [H_s, \varrho] \\
& -\frac{1}{2} \sum_{i,j=1}^M \gamma_{ij} (1+N) (\varrho S_i^+ S_j^- + S_i^+ S_j^- \varrho - 2S_j^- \varrho S_i^+) \\
& -\frac{1}{2} \sum_{i,j=1}^M \gamma_{ij} N (\varrho S_i^- S_j^+ + S_i^- S_j^+ \varrho - 2S_j^+ \varrho S_i^-) , \quad (2.99)
\end{aligned}$$

where

$$H_s = \hbar \sum_{i=1}^M (\omega_i + \delta_i) S_i^z + \hbar \sum_{i \neq j}^M \Lambda_{ij} S_i^+ S_j^- + H_L , \quad (2.100)$$

and

$$H_L = -\frac{1}{2} i \hbar \sum_{i=1}^M \left[\Omega(\mathbf{r}_i) S_i^+ e^{i(\omega_L t + \phi_L)} - \text{H.c.} \right] , \quad (2.101)$$

is the interaction Hamiltonian of the atoms with a classical coherent laser field of Rabi frequency $\Omega(\mathbf{r}_i)$, angular frequency ω_L and phase ϕ_L .

Note that the Rabi frequencies of the driving field are evaluated at the positions of the atoms and are defined as

$$\Omega(\mathbf{r}_i) \equiv \Omega_i = 2\boldsymbol{\mu}_i \cdot \boldsymbol{\mathcal{E}}_L e^{i\mathbf{k}_L \cdot \mathbf{r}_i} / \hbar , \quad (2.102)$$

where $\boldsymbol{\mathcal{E}}_L$ is the amplitude, given by (2.67), and \mathbf{k}_L is the wave vector of the driving field, respectively. The Rabi frequencies depend on the positions of the atoms and can be different for the atoms located at different points. For example, if the dipole moments of the atoms are parallel, the Rabi frequencies Ω_i and Ω_j of two arbitrary atoms separated by a distance r_{ij} are related by

$$\Omega_j = \Omega_i \frac{|\boldsymbol{\mu}_j|}{|\boldsymbol{\mu}_i|} e^{i\mathbf{k}_L \cdot \mathbf{r}_{ij}} . \quad (2.103)$$

Thus, for two identical atoms, $|\boldsymbol{\mu}_i| = |\boldsymbol{\mu}_j|$, and then the Rabi frequencies differ by the position dependent phase factor $\exp(i\mathbf{k}_L \cdot \mathbf{r}_{ij})$. However, the phase factor also depends on the orientation of the interatomic axis with respect to the direction of propagation of the driving field, and therefore $\exp(i\mathbf{k}_L \cdot \mathbf{r}_{ij})$ can be equal to one, even for large interatomic separations r_{ij} . This happens when the direction of propagation of the driving field is perpendicular to the interatomic axis, $\mathbf{k}_L \cdot \mathbf{r}_{ij} = 0$. For directions different from perpendicular, $\mathbf{k}_L \cdot \mathbf{r}_{ij} \neq 0$, the atoms are in nonequivalent positions in the driving field, with different Rabi frequencies ($\Omega_i \neq \Omega_j$). For a very special geometrical configuration in which the atoms are confined to a volume with linear dimensions much smaller than the laser wavelength, the phase factor $\exp(i\mathbf{k}_L \cdot \mathbf{r}_{ij}) \approx 1$,

and then the Rabi frequencies are equal and independent of the atomic positions. This specific configuration of the atoms is known as the small sample model or the Dicke model [49, 50]. The disadvantage of the Dicke model is that it does not correspond to experimentally realized spatially extended atomic systems such as atomic beams, trapped atoms or deposited quantum dots.

In the following chapters, we will illustrate the application of the master equation (2.99) to the dynamics of two identical and two nonidentical atoms interacting with the ordinary vacuum. The effects of an applied laser field, and the role of quantum interference in the atomic dynamics, will also be investigated.

2.2 Correlation Functions of Atomic Operators

Where atoms or molecules act as a source of the EM field, the correlation functions of the emitted field can be given in terms of the correlation functions of the atomic variables, such as the atomic dipole operators, and hence related to atomic populations and coherences. Throughout this section, we present a derivation of the relation between the normally ordered correlation functions of the amplitudes of the quantized EM field and the correlation functions of the atomic dipole operators.

2.2.1 Correlation Functions for a Multi-Level Atom

The combined system of the quantum EM field and a multi-level atom can be described by the multi-polar Hamiltonian, and the interaction between the field and the atom is given to a good approximation by the electric-dipole interaction Hamiltonian. The total electric field operator $\hat{\mathbf{E}}(\mathbf{R}, t)$ evaluated at the position \mathbf{R} of a detector can be expressed as the sum of the positive $\hat{\mathbf{E}}^{(+)}(\mathbf{R}, t)$ and negative $\hat{\mathbf{E}}^{(-)}(\mathbf{R}, t)$ frequency components. The positive frequency component of the EM field registered by the detector is given by

$$\hat{\mathbf{E}}^{(+)}(\mathbf{R}, t_R) = \mathrm{i} \sum_{\mathbf{k}s} \left(\frac{\hbar \omega_{\mathbf{k}s}}{2\epsilon_0 \mathcal{V}} \right)^{\frac{1}{2}} \bar{\mathbf{e}}_{\mathbf{k}s} \hat{a}_{\mathbf{k}s}(t_R) e^{\mathrm{i}\mathbf{k} \cdot \mathbf{R}}, \quad (2.104)$$

where \mathcal{V} is the volume occupied by the field, $\bar{\mathbf{e}}_{\mathbf{k}s}$ is the unit polarization vector of the field amplitude, $\hat{a}_{\mathbf{k}s}$ is the annihilation operator for the \mathbf{k} th mode with polarization s and frequency $\omega_{\mathbf{k}s}$, and $t_R - R/c = t$ is the retarded time that the field registered at the detector at time t_R . It depends on the evolution of the source field at early times t .

The starting point for relating the normally ordered correlation functions of the EM field operators to the correlation functions of the atomic dipole moments is the Heisenberg equation of motion for the annihilation operators $\hat{a}_{\mathbf{k}s}$:

$$\frac{d}{dt} \hat{a}_{\mathbf{k}s}(t) = \frac{1}{i\hbar} [\hat{a}_{\mathbf{k}s}(t), H] , \quad (2.105)$$

which, after applying the Hamiltonian (2.1) and introducing the compact notation (2.15), takes the form

$$\begin{aligned} \frac{d}{dt} \hat{a}_{\mathbf{k}s}(t) = & -i\omega_{\mathbf{k}s} \hat{a}_{\mathbf{k}s}(t) \\ & + \sum_i [\boldsymbol{\mu}_i \cdot \mathbf{u}_{\mathbf{k}s}^*(\mathbf{r}) S_i^-(t) + \boldsymbol{\mu}_i^* \cdot \mathbf{u}_{\mathbf{k}s}(\mathbf{r}) S_i^+(t)] , \end{aligned} \quad (2.106)$$

where we have used the operator commutation relations (1.44).

Equation (2.106) is a simple inhomogeneous first-order differential equation whose solution can be written in integral form as

$$\begin{aligned} \hat{a}_{\mathbf{k}s}(t) = & \hat{a}_0(t) + \sum_i \int_0^t dt' [\boldsymbol{\mu}_i \cdot \mathbf{u}_{\mathbf{k}s}^*(\mathbf{r}) S_i^-(t') \\ & + \boldsymbol{\mu}_i^* \cdot \mathbf{u}_{\mathbf{k}s}(\mathbf{r}) S_i^+(t')] e^{-i\omega_{\mathbf{k}s}(t-t')} . \end{aligned} \quad (2.107)$$

The first term in (2.107) represents the evolution of $\hat{a}_{\mathbf{k}s}$ due to the unperturbed field Hamiltonian H_F , and $\hat{a}_0(t) = \hat{a}_{\mathbf{k}s} \exp(-i\omega_{\mathbf{k}s}t)$ is the solution of the homogeneous or free-field equation of motion that characterizes the field without the atom. The second term in (2.107), called the “source term”, is proportional to the transition electric dipole moments of the atom and describes the radiation field created by all the dipole moments as they radiate from the initial time $t' = 0$ to time $t' = t$. The integral appearing in (2.107) cannot be calculated exactly since we do not know the explicit time dependence of the atomic operators. However, as far as atoms are concerned, spontaneous radiative decay is a very slow process, requiring on average many millions of cycles of dipole oscillations before it is completed. Thus, we can apply to a good approximation the so-called *harmonic decomposition*, in which we write the time-dependent dipole operators as

$$\begin{aligned} S_i^-(t') & \approx S_i^-(t) e^{-i\omega_0(t'-t)} , \\ S_i^+(t') & \approx S_i^+(t) e^{i\omega_0(t'-t)} . \end{aligned} \quad (2.108)$$

The harmonic decomposition is formally equivalent to the Markov approximation that the system variables $S_i^\pm(t)$ change slowly in time compared to the free dipole oscillations characteristic of the exponent $\exp(\pm i\omega_0 t)$.

With the harmonic approximation (2.108), the integral appearing in (2.107) can be easily evaluated. Replacing the atomic operators $S_i^\pm(t')$ by the harmonic decompositions (2.108) and removing the slowly varying atomic operators outside the integral, as they are evaluated at time t , we arrive at the following integral equation

$$\begin{aligned}\hat{a}_{\mathbf{k}s}(t) = \hat{a}_0(t) + \sum_i [\boldsymbol{\mu}_i \cdot \mathbf{u}_{\mathbf{k}s}^*(\mathbf{r}) S_i^-(t) J_-(t) \\ + \boldsymbol{\mu}_i^* \cdot \mathbf{u}_{\mathbf{k}s}(\mathbf{r}) S_i^+(t) J_+(t)] ,\end{aligned}\quad (2.109)$$

where

$$J_{\pm}(t) = \int_0^t dt' e^{i(\omega_{\mathbf{k}s} \pm \omega_0)(t'-t)} . \quad (2.110)$$

Substituting the solution for $\hat{a}_{\mathbf{k}s}(t)$ into the expression for $\hat{\mathbf{E}}^{(+)}(\mathbf{R}, t_R)$ and replacing the sum over the field modes $\mathbf{k}s$ by the frequency and angular integrals, we can write the positive frequency component of the field as

$$\hat{\mathbf{E}}^{(+)}(\mathbf{R}, t_R) = \hat{\mathbf{E}}_0^{(+)}(\mathbf{R}, t_R) + \hat{\mathbf{E}}_S^{(+)}(\mathbf{R}, t_R) , \quad (2.111)$$

where

$$\hat{\mathbf{E}}_0^{(+)}(\mathbf{R}, t_R) = i \sum_{\mathbf{k}s} \left(\frac{\hbar \omega_{\mathbf{k}s}}{2\varepsilon_0 \mathcal{V}} \right)^{\frac{1}{2}} \bar{\mathbf{e}}_{\mathbf{k}s} \hat{a}_{\mathbf{k}s}(t_R) e^{i\mathbf{k} \cdot \mathbf{R}} \quad (2.112)$$

is the positive frequency part of the free field, and

$$\begin{aligned}\hat{\mathbf{E}}_S^{(+)}(\mathbf{R}, t_R) = \frac{i}{16\pi^3 \varepsilon_0 c^3} \sum_i \int_0^\infty d\omega_{\mathbf{k}s} \omega_{\mathbf{k}s}^3 \int d\Omega_k e^{i\mathbf{k} \cdot (\mathbf{R}-\mathbf{r})} \\ \times \sum_{s=1}^2 [\bar{\mathbf{e}}_{\mathbf{k}s} (\boldsymbol{\mu}_i \cdot \bar{\mathbf{e}}_{\mathbf{k}s}^*) S_i^-(t_R) J_-(t) \\ + \bar{\mathbf{e}}_{\mathbf{k}s} (\boldsymbol{\mu}_i^* \cdot \bar{\mathbf{e}}_{\mathbf{k}s}^*) S_i^+(t_R) J_+(t)]\end{aligned}\quad (2.113)$$

is the positive frequency component of the source field, the field emitted by the atom.

The sums over the polarization s involving the orthogonal unit polarization vectors $\bar{\mathbf{e}}_{\mathbf{k}s}$, are easily evaluated as

$$\begin{aligned}\sum_{s=1}^2 \bar{\mathbf{e}}_{\mathbf{k}s} (\boldsymbol{\mu}_i \cdot \bar{\mathbf{e}}_{\mathbf{k}s}^*) &= \boldsymbol{\mu}_i - \bar{\mathbf{k}} (\bar{\mathbf{k}} \cdot \boldsymbol{\mu}_i) , \\ \sum_{s=1}^2 \bar{\mathbf{e}}_{\mathbf{k}s} (\boldsymbol{\mu}_i^* \cdot \bar{\mathbf{e}}_{\mathbf{k}s}^*) &= \boldsymbol{\mu}_i^* - \bar{\mathbf{k}} (\bar{\mathbf{k}} \cdot \boldsymbol{\mu}_i^*) ,\end{aligned}\quad (2.114)$$

where $\bar{\mathbf{k}}$ is the unit vector in the direction of \mathbf{k} , and we have used the well known orthogonality properties of the unit polarization vectors

$$\bar{\mathbf{e}}_{\mathbf{k}1} \times \bar{\mathbf{e}}_{\mathbf{k}2} = \bar{\mathbf{k}} , \quad \bar{\mathbf{e}}_{\mathbf{k}1} \times \bar{\mathbf{k}} = -\bar{\mathbf{e}}_{\mathbf{k}2} . \quad (2.115)$$

The integral over the solid angle Ω_k of the available EM modes remains to be evaluated. It can be simplified if we notice that the only important

contribution to the detected field comes from those directions around $\mathbf{k} = \pm(\mathbf{R} - \mathbf{r})$ where the phase $\mathbf{k} \cdot (\mathbf{R} - \mathbf{r})$ is stationary. Hence, we can replace $\bar{\mathbf{k}}$ in (2.114) by $\bar{\mathbf{R}}_A$, where $\bar{\mathbf{R}}_A$ is the unit vector in the direction $\mathbf{R}_A = \mathbf{R} - \mathbf{r}$, and remove the factors $\boldsymbol{\mu}_i - \bar{\mathbf{R}}_A (\bar{\mathbf{R}}_A \cdot \boldsymbol{\mu}_i)$ and $\boldsymbol{\mu}_i^* - \bar{\mathbf{R}}_A (\bar{\mathbf{R}}_A \cdot \boldsymbol{\mu}_i^*)$ from the integral over $d\Omega_k$. Then, the integral over $d\Omega_k$ is easily evaluated. After transforming to spherical coordinates, the angular integrations yield the result

$$\begin{aligned} \int d\Omega_k e^{i\mathbf{k} \cdot \mathbf{R}_A} &= \int_0^\pi \int_0^{2\pi} d\theta_k d\phi_k \sin \theta_k e^{ikR_A \cos \theta_k} \\ &= -i \frac{2\pi c}{\omega_{\mathbf{k}s} R_A} \left(e^{i\omega_{\mathbf{k}s} R_A / c} - e^{-i\omega_{\mathbf{k}s} R_A / c} \right), \end{aligned} \quad (2.116)$$

and then the positive frequency component (2.113) becomes

$$\begin{aligned} \hat{\mathbf{E}}_S^{(+)}(\mathbf{R}, t_R) &= \frac{1}{8\pi^2 \varepsilon_0 c^2} \sum_i \int_0^\infty d\omega_{\mathbf{k}s} \omega_{\mathbf{k}s}^2 \left(e^{i\omega_{\mathbf{k}s} R_A / c} - e^{-i\omega_{\mathbf{k}s} R_A / c} \right) \\ &\quad \times \left\{ \left[\boldsymbol{\mu}_i - \bar{\mathbf{R}}_A (\bar{\mathbf{R}}_A \cdot \boldsymbol{\mu}_i) \right] S_i^-(t_R) J_-(t) \right. \\ &\quad \left. + \left[\boldsymbol{\mu}_i^* - \bar{\mathbf{R}}_A (\bar{\mathbf{R}}_A \cdot \boldsymbol{\mu}_i^*) \right] S_i^+(t_R) J_+(t) \right\}. \end{aligned} \quad (2.117)$$

Since

$$\begin{aligned} S_i^-(t_R) &\approx S_i^-(t) e^{-ik_0 R}, \\ S_i^+(t_R) &\approx S_i^+(t) e^{ik_0 R}, \end{aligned} \quad (2.118)$$

where as usual $k_0 = \omega_0/c$, we find that there are two exponential terms $\exp[\pm i(\omega_{\mathbf{k}s} - \omega_0) R_A / c]$ and $\exp[\pm i(\omega_{\mathbf{k}s} + \omega_0) R_A / c]$ which contribute to the field in (2.117). Since the largest contributions come from frequencies $\omega_{\mathbf{k}s}$ close to the average atomic frequency ω_0 , the terms $\exp[\pm i(\omega_{\mathbf{k}s} + \omega_0) R_A / c]$ oscillate rapidly and therefore make a negligible contribution to the field. The only significant contribution to the field will come from the terms oscillating at $\omega_{\mathbf{k}s} - \omega_0$. Hence, we obtain the following expression for the positive frequency component

$$\hat{\mathbf{E}}_S^{(+)}(\mathbf{R}, t_R) = \frac{1}{8\pi^2 \varepsilon_0 c^2} \sum_i \int_0^\infty d\omega_{\mathbf{k}s} \omega_{\mathbf{k}s}^2 [L_i^-(t) - L_i^+(t)], \quad (2.119)$$

where

$$\begin{aligned} L_i^+(t) &= \left[\boldsymbol{\mu}_i^* - \bar{\mathbf{R}}_A (\bar{\mathbf{R}}_A \cdot \boldsymbol{\mu}_i^*) \right] S_i^+(t) J_+(t) e^{-i(\omega_{\mathbf{k}s} R_A - \omega_0 R) / c}, \\ L_i^-(t) &= \left[\boldsymbol{\mu}_i - \bar{\mathbf{R}}_A (\bar{\mathbf{R}}_A \cdot \boldsymbol{\mu}_i) \right] S_i^-(t) J_-(t) e^{i(\omega_{\mathbf{k}s} R_A - \omega_0 R) / c}. \end{aligned} \quad (2.120)$$

Performing the t' integration in $J_\pm(t)$, we find

$$\begin{aligned}
L_i^+(t) &= [\boldsymbol{\mu}_i^* - \bar{\mathbf{R}}_A (\bar{\mathbf{R}}_A \cdot \boldsymbol{\mu}_i^*)] S_i^+(t) \\
&\quad \times \left\{ \frac{e^{i(\omega_{\mathbf{k}s} + \omega_0)R/c} - e^{-i(\omega_{\mathbf{k}s} + \omega_0)t}}{i(\omega_{\mathbf{k}s} + \omega_0)} \right\} e^{-i(\omega_{\mathbf{k}s} R_A - \omega_0 R)/c} , \\
L_i^-(t) &= [\boldsymbol{\mu}_i - \bar{\mathbf{R}}_A (\bar{\mathbf{R}}_A \cdot \boldsymbol{\mu}_i)] S_i^-(t) \\
&\quad \times \left\{ \frac{e^{i(\omega_{\mathbf{k}s} - \omega_0)R/c} - e^{-i(\omega_{\mathbf{k}s} - \omega_0)t}}{i(\omega_{\mathbf{k}s} - \omega_0)} \right\} e^{i(\omega_{\mathbf{k}s} R_A - \omega_0 R)/c} . \quad (2.121)
\end{aligned}$$

The term $L_i^-(t)$ is only large near $\omega_{\mathbf{k}s} = \omega_0$, whereas $L_i^+(t)$ is only large near $\omega_{\mathbf{k}s} = -\omega_0$, which is outside the integral range $(0, \infty)$ for the values of $\omega_{\mathbf{k}s}$. On the other hand, the $L_i^-(t)$ term gives significant contributions near $\omega_{\mathbf{k}s} = \omega_0$, which is inside the range. Thus, the $L_i^+(t)$ contribution can be ignored. With $L_i^-(t)$ only being significant for $\omega_{\mathbf{k}s}$ near ω_0 , we can then approximate the term in large curly brackets in (2.121) by $2\pi\delta(\omega_{\mathbf{k}s} - \omega_0)$, and obtain

$$\hat{\mathbf{E}}_S^{(+)}(\mathbf{R}, t_R) = \vartheta \sum_{i=1}^M \frac{[\boldsymbol{\mu}_i - \bar{\mathbf{R}}_A (\bar{\mathbf{R}}_A \cdot \boldsymbol{\mu}_i)]}{R_A} S_i^-(t) e^{ik_0(R_A - R)} , \quad (2.122)$$

where $\vartheta = \omega_0^2 / (4\pi\epsilon_0 c^2)$.

Finally, by adding the free-field term (2.112) and using the vectorial property

$$[\boldsymbol{\mu}_i - \bar{\mathbf{R}}_A (\bar{\mathbf{R}}_A \cdot \boldsymbol{\mu}_i)] = -[\bar{\mathbf{R}}_A \times (\bar{\mathbf{R}}_A \times \boldsymbol{\mu}_i)] , \quad (2.123)$$

we obtain the positive frequency component of the total radiation field at the detector as

$$\begin{aligned}
\hat{\mathbf{E}}^{(+)}(\mathbf{R}, t_R) &= \hat{\mathbf{E}}_0^{(+)}(\mathbf{R}, t_R) \\
&\quad - \vartheta \sum_{i=1}^M \frac{\bar{\mathbf{R}}_A \times (\bar{\mathbf{R}}_A \times \boldsymbol{\mu}_i)}{R_A} S_i^-(t) e^{ik_0(R_A - R)} . \quad (2.124)
\end{aligned}$$

For the source field the summation is over different atomic dipole transitions whose dipole operators $S_i^-(t)$ are evaluated at the retarded time $t = t_R - R/c$. The free field term has the same time dependence that would apply if there were no source atom present. The expression (2.124) is valid for all space-time points (\mathbf{R}, t) . In the usual case where we detect the field at a large distance from the source atom, i.e. when $R \gg \lambda_0$, where λ_0 is the average wavelength of the radiation emitted by the atom, we can use the Taylor expansion and write

$$R_A - R \approx -\bar{\mathbf{R}} \cdot \mathbf{r} . \quad (2.125)$$

Then the field component $\hat{\mathbf{E}}^{(+)}(\mathbf{R}, t_R)$ becomes

$$\hat{\mathbf{E}}^{(+)}(\mathbf{R}, t_R) = \hat{\mathbf{E}}_0^{(+)}(\mathbf{R}, t_R) - \vartheta \sum_{i=1}^M \frac{\bar{\mathbf{R}}_A \times (\bar{\mathbf{R}}_A \times \boldsymbol{\mu}_i)}{R_A} S_i^-(t) e^{-ik_0 \bar{\mathbf{R}} \cdot \mathbf{r}} . \quad (2.126)$$

We now consider how to translate the relation between the radiation field and the atomic dipole moments into the correlation functions of the radiation field. The first and second-order correlation functions for the total radiation field can be considered in terms of the correlation functions of the free-field and the source field by substituting (2.126) for $\hat{\mathbf{E}}^{(\pm)}(\mathbf{R}, t_R)$ into the expressions for the correlation functions (1.45). For example, the first-order correlation function of the total field takes the form

$$\begin{aligned} G^{(1)}(\mathbf{R}, t) &= \langle \hat{\mathbf{E}}^{(-)}(\mathbf{R}, t) \cdot \hat{\mathbf{E}}^{(+)}(\mathbf{R}, t) \rangle = \langle \hat{\mathbf{E}}_0^{(-)}(\mathbf{R}, t) \cdot \hat{\mathbf{E}}_0^{(+)}(\mathbf{R}, t) \rangle \\ &+ \langle \hat{\mathbf{E}}_0^{(-)}(\mathbf{R}, t) \cdot \hat{\mathbf{E}}_S^{(+)}(\mathbf{R}, t) \rangle + \langle \hat{\mathbf{E}}_S^{(-)}(\mathbf{R}, t) \cdot \hat{\mathbf{E}}_0^{(+)}(\mathbf{R}, t) \rangle \\ &+ \langle \hat{\mathbf{E}}_S^{(-)}(\mathbf{R}, t) \cdot \hat{\mathbf{E}}_S^{(+)}(\mathbf{R}, t) \rangle . \end{aligned} \quad (2.127)$$

Thus, the first-order correlation function equals the sum of the normally ordered correlation function for the free field and for the source field together with possible interference terms involving both the free field and the source field. The following question then arises: under what conditions can the first order correlation function for the total field be equated to the normally ordered correlation function for the source atom field? In practice the atomic systems are driven by fields and we can choose the position \mathbf{R} of a photodetector such that it lies outside the driving field. Then the amplitudes of the driving fields are zero at the photodetector and ultimately this enables us to eliminate the free field and interference terms.

Alternatively, we may assume that the free field is in the multimode vacuum state for which

$$\hat{\mathbf{E}}_0^{(+)}(\mathbf{R}, t) |\{0\}\rangle = 0 , \quad \langle \{0\} | \hat{\mathbf{E}}_0^{(-)}(\mathbf{R}, t) = 0 , \quad (2.128)$$

and then all correlation functions vanish except the correlation function for the source atom field in (2.127).

If we assume that initially the field is in the vacuum state, then the free-field part $\hat{\mathbf{E}}_0^{(+)}(\mathbf{R}, t)$ does not contribute to the expectation values of the normally ordered field operators, and we obtain the following expressions for the first- and second-order correlation functions

$$G^{(1)}(\mathbf{R}, t) = v(\mathbf{R}) \sum_{i,j} \sqrt{\gamma_i \gamma_j} \langle S_i^+(t) S_j^-(t) \rangle , \quad (2.129)$$

and

$$\begin{aligned} G^{(2)}(\mathbf{R}_1, t_1; \mathbf{R}_2, t_2) &= v(\mathbf{R}_1) v(\mathbf{R}_2) \sum_{i,j} \sum_{k,l} \sqrt{\gamma_i \gamma_j} \sqrt{\gamma_k \gamma_l} \\ &\times \langle S_i^+(t_1) S_k^+(t_2) S_l^-(t_2) S_j^-(t_1) \rangle , \end{aligned} \quad (2.130)$$

where

$$v(\mathbf{R}) = \frac{3\hbar\omega_0}{16\pi\epsilon_0 c R_A^2} [\cos\theta_{ij} - \cos\psi_i \cos\psi_j] \quad (2.131)$$

is a geometrical factor, with θ_{ij} the angle between the dipole moments $\boldsymbol{\mu}_i$ and $\boldsymbol{\mu}_j$, and ψ_n ($n = i, j$) is the angle between the observation direction \mathbf{R}_A and the atomic dipole moment $\boldsymbol{\mu}_n$. For parallel dipole moments, $\theta_{ij} = 0$, $\psi_i = \psi_j = \psi$, and then the factor $v(\mathbf{R})$ reduces to

$$v(\mathbf{R}) = \frac{3\hbar\omega_0}{16\pi\epsilon_0 c R_A^2} \sin^2 \psi, \quad (2.132)$$

which is recognized as the radiation pattern of a linear dipole moment. It shows that the maximum of the radiation emitted by a dipole moment is in the direction perpendicular to the atomic dipole moments $\boldsymbol{\mu}$.

The cross-damping rate is sensitive to the mutual polarization of the dipole moments of the two systems, which we represent by the angle θ_{ij} . If the dipole moments are parallel, $\theta_{ij} = 0^\circ$, and the cross-damping rate is maximal, whilst $\gamma_{ij} = 0$ if the dipole moments are perpendicular ($\theta_{ij} = 90^\circ$).

It is evident from (2.129) and (2.130) that the atomic dipole correlation functions with $i \neq j$ represent coherence terms resulting from the correlations between different atomic transitions. The second order correlation function depends on various two-time dipole correlation functions of the form $\langle S_i^+(t_1) S_j^+(t_2) S_j^-(t_2) S_i^-(t_1) \rangle$. The functions are proportional to the probabilities of detecting two photons emitted from the same ($i = j$) or different ($i \neq j$) bare systems. For example, the correlation function $\langle S_i^+(t_1) S_j^+(t_2) S_j^-(t_2) S_i^-(t_1) \rangle$ for $i \neq j$ is proportional to the probability of detecting a photon at time t_2 emitted from the j th transition if a photon emitted from the i th transition was detected at time t_1 .

The second-order correlation function (2.130) also depends on the dipole correlation functions of the form $\langle S_i^+(t_1) S_j^+(t_2) S_i^-(t_2) S_j^-(t_1) \rangle$, which result from correlations of photons emitted from a superposition of the atomic transitions. We study this phenomenon in Chap. 3.5.5, where we analyze the second-order correlation functions for the radiation field emitted from three-level atoms.

2.2.2 Correlation Functions for a Multi-Atom System

The formalism developed here for the relation between the radiation field and the atomic dipole moments can be generalized to the case of multi-atom two-level systems. For a system of M two-level atoms the positive frequency component of the electric field can be derived using the same procedure as we have used before in the derivation of (2.126), and is given by the expression

$$\hat{\mathbf{E}}^{(+)}(\mathbf{R}, t_R) = \hat{\mathbf{E}}_0^{(+)}(\mathbf{R}, t_R) - \vartheta \sum_{i=1}^M \frac{\bar{\mathbf{R}} \times (\bar{\mathbf{R}} \times \boldsymbol{\mu}_i)}{R} S_i^-(t) e^{-ik_0 \bar{\mathbf{R}} \cdot \mathbf{r}_i}, \quad (2.133)$$

where the summation is taken over the atoms, and R is the distance from the center of the atomic system to the detector. On comparing (2.133) with (2.126), we see that the positive frequency component of the field emitted by the system of M atoms can be obtained directly from (2.126) simply by replacing the summation over the atomic levels by the summation over the atoms, and changing $\mathbf{r} \rightarrow \mathbf{r}_i$.

If we assume that initially the field is in the vacuum state, then the free-field part $\mathbf{E}_0^{(+)}(\mathbf{R}, t_R)$ does not contribute to the expectation values of the normally ordered operators. Hence, substituting (2.133) into (1.45), we obtain

$$G^{(1)}(\mathbf{R}, t) = v(\mathbf{R}) \sum_{i,j=1}^M \sqrt{\gamma_i \gamma_j} \langle S_i^+(t) S_j^-(t) \rangle \times \exp(ik \bar{\mathbf{R}} \cdot \mathbf{r}_{ij}), \quad (2.134)$$

and

$$G^{(2)}(\mathbf{R}_1, t_1; \mathbf{R}_2, t_2) = v(\mathbf{R}_1) v(\mathbf{R}_2) \sum_{i,j,k,l=1}^M \sqrt{\gamma_i \gamma_j \gamma_k \gamma_l} \times \langle S_i^+(t_1) S_k^+(t_2) S_l^-(t_2) S_j^-(t_1) \rangle \times \exp[ik(\bar{\mathbf{R}}_1 \cdot \mathbf{r}_{ij} + \bar{\mathbf{R}}_2 \cdot \mathbf{r}_{kl})], \quad (2.135)$$

where γ_i is the spontaneous emission rate of the i th atom, and $v(\mathbf{R})$ is a geometrical factor given in (2.132). The correlation functions (2.134) and (2.135) describe correlations between photons emitted in particular directions relative to the interatomic axis and can be used to calculate the angular distribution of the radiation emitted from the atoms and the spatial correlations between photons emitted in different directions.

On integrating (2.134) and (2.135) over all solid angles $d\Omega_{\bar{\mathbf{R}}}$, we obtain the correlation functions of the total radiation emitted by the atoms as

$$G^{(1)}(\mathbf{R}, t) = w(\mathbf{R}) \sum_{i,j=1}^M \gamma_{ij} \langle S_i^+(t) S_j^-(t) \rangle, \quad (2.136)$$

$$G^{(2)}(\mathbf{R}_1, t_1; \mathbf{R}_2, t_2) = w(\mathbf{R}_1) w(\mathbf{R}_2) \sum_{i,j,k,l=1}^M \gamma_{ij} \gamma_{kl} \times \langle S_i^+(t_1) S_k^+(t_2) S_l^-(t_2) S_j^-(t_1) \rangle, \quad (2.137)$$

where γ_{ij} for $i \neq j$ is the collective damping rate given in (2.90), and

$$w(R) = \frac{3\hbar\omega_0}{4\pi\epsilon_0 c R^2} , \quad (2.138)$$

is a geometrical factor.

The correlation functions (2.136) and (2.137) are very similar in form to the ones found previously for a multi-level atom. In particular, the first-order correlation functions (2.129) and (2.136) differ only in that the geometrical factor $v(\mathbf{R})$ has been replaced by the factor $w(\mathbf{R})$, and the cross-damping rate has been replaced by the collective damping rate. Thus the collective damping rate, that arises from the interaction between the atoms, plays a similar role to the cross-damping rate that arises from the interaction between two dipole moments in a multi-level atom. These two damping rates, if nonzero, give rise to vacuum induced quantum interference between dipole transitions.

2.2.3 Spectral Expressions

The first- and second-order correlation functions are the quantities of most direct physical interest, and are used to analyze various spectroscopic and statistical properties of the field emitted by an atomic system. The physically measurable quantities such as radiation intensity, fluorescence spectra, absorption spectra and photon statistics are directly related to the field correlation functions. The fluorescence spectrum, for example, gives information on the first-order correlation function of the radiation field and measures the number of photons emitted by the system into vacuum field modes as a function of the spectral frequency of these modes. The absorption spectrum, on the other hand, measures the relative number of photons absorbed by the system from a weak probe field as a function of the probe field frequency.

The fluorescence spectrum is given by the real part of the Fourier transform of the two-time first-order correlation function $\langle \hat{E}^{(-)}(\mathbf{R}, t) \hat{E}^{(+)}(\mathbf{R}, t + \tau) \rangle$ for the positive and negative frequency components of the electric field operator at the position of the detector. Since the electric field operators are related to the dipole operators for the system, we can write the steady-state fluorescence spectrum in terms of expectation values of appropriate atomic dipole operators as

$$S(\omega) = \text{Re} \int_0^\infty d\tau \lim_{t \rightarrow \infty} \sum_{ij} \gamma_{ij} \langle S_i^+(t) S_j^-(t + \tau) \rangle e^{i\omega\tau} . \quad (2.139)$$

The correlation functions of the dipole operators are calculated from the master equation of the system. In the case of $\tau > 0$, the two-time correlation functions can be calculated applying the quantum regression theorem [51]. According to the quantum regression theorem, for $\tau > 0$, the two-time correlation function $\langle S_i^+(t) S_j^-(t + \tau) \rangle$ satisfies the same equation of motion as the one-time average $\langle S_j^-(t) \rangle$. On the other hand, the one-time average $\langle S_j^-(t) \rangle$

of the atomic dipole operator corresponding to a transition $|m\rangle \rightarrow |n\rangle$, satisfies the same equation of motion as the density matrix element $\varrho_{nm}(t)$, which is found from the master equation of the system.

The fluorescence spectrum can be decomposed into a *coherent* component, associated with replacing the correlation function $\langle \hat{E}^{(-)}(\mathbf{R}, t) \hat{E}^{(+)}(\mathbf{R}, t + \tau) \rangle$ by $\langle \hat{E}^{(-)}(\mathbf{R}, t) \rangle \langle \hat{E}^{(+)}(\mathbf{R}, t + \tau) \rangle$, and an *incoherent* component. The incoherent component of the spectrum $S_I(\omega)$ is then obtained by subtracting the coherent component from the fluorescence spectrum

$$S_I(\omega) = \text{Re} \int_0^\infty d\tau \lim_{t \rightarrow \infty} \sum_{ij} \gamma_{ij} [\langle S_i^+(t) S_j^-(t + \tau) \rangle - \langle S_i^+(t) \rangle \langle S_j^-(t + \tau) \rangle] e^{i\omega\tau} . \quad (2.140)$$

The absorption spectrum of a weak probe field monitoring the system is given by the real part of the Fourier transform of the two-time commutator

$$A(\omega_p) = \text{Re} \int_0^\infty d\tau \lim_{t \rightarrow \infty} \sum_{ij} \gamma_{ij} \langle [S_i^-(t), S_j^+(t + \tau)] \rangle e^{i\omega_p\tau} , \quad (2.141)$$

where ω_p is the frequency of the probe field. The term $\langle S_i^-(t) S_j^+(t + \tau) \rangle$ is associated with the absorption, and the term $\langle S_j^+(t + \tau) S_i^-(t) \rangle$ with stimulated emission of the probe field. The net absorption is equal to the difference between the absorption and stimulated emission by the system.

We can also calculate the refractive index of the probe field, which is proportional to the imaginary part of the two-time commutator, and is given by

$$D(\omega_p) = \text{Im} \int_0^\infty d\tau \lim_{t \rightarrow \infty} \sum_{ij} \gamma_{ij} \langle [S_i^-(t), S_j^+(t + \tau)] \rangle e^{i\omega_p\tau} . \quad (2.142)$$

The structure and population distribution of the energy levels of the system can also be studied by monitoring the system with a weak probe field coupled to an auxiliary level. It is assumed that the auxiliary level $|c\rangle$ is connected to an atomic level with nonzero dipole moment and the probe field transfers the population from the atomic level to the initially unpopulated level $|c\rangle$. The absorption spectrum is called the Autler–Townes spectrum and is defined as

$$A_T(\omega_p) = \text{Re} \int_0^\infty d\tau \lim_{t \rightarrow \infty} \sum_{ij} \gamma_{cij} \times \langle [W_i^-(t), W_j^+(t + \tau)] \rangle e^{i\omega_p\tau} , \quad (2.143)$$

where $W_i^+ = (W_i^-)^\dagger = |c\rangle\langle i|$ is the dipole operator of the $|c\rangle \rightarrow |i\rangle$ transition and $|i\rangle$ is the i th atomic level. The parameter γ_{cii} with $i = j$ is the spontaneous emission rate of the $|c\rangle \rightarrow |i\rangle$ transition, and γ_{cij} for $i \neq j$ is the cross-damping rate between $|c\rangle \rightarrow |i\rangle$ and $|c\rangle \rightarrow |j\rangle$ transitions.

Alternatively, we can include the auxiliary level and the probe field in the atomic dynamics, and then the Autler–Townes spectrum is obtained by monitoring the population of the level $|c\rangle$ as a function of the probe field frequency.

The *intensity* of emitted light and the *total absorption rate* are given in terms of the one-time first-order correlation functions, which can be calculated directly from the master equation of the system, or can be obtained from (2.139) and (2.141) by integrating over the spectral frequencies. The time-dependent intensity and the absorption rate are given by

$$I(t) = \sum_{ij} \gamma_{ij} \langle S_i^+(t) S_j^-(t) \rangle , \quad (2.144)$$

$$A(t) = \sum_{ij} \gamma_{ij} \langle [S_i^-(t), S_j^+(t)] \rangle , \quad (2.145)$$

and the steady-state values are obtained by taking $t \rightarrow \infty$. The absorption rate involves the one-time commutator, which, if different from zero, is given in terms of the diagonal (population) operators. The average value of the population operators is equal to the diagonal density matrix elements of the system.

The analysis of the field correlation functions can be extended to the second-order correlation functions, which provide further information about photon statistics and nonclassical properties of the radiation field. The one-time ($\tau = 0$) second-order correlation function, for example, gives information about the photon statistics of the radiated field, whereas the two-time ($\tau \neq 0$) second-order correlation function describes photon bunching and the nonclassical photon antibunching effects.

3 Superposition States and Modification of Spontaneous Emission Rates

In this chapter we use the formalism developed in the last chapter to consider how quantum interference can modify spontaneous emission rates, and we illustrate its role in atomic dynamics. Simple examples of spontaneous emission from initially excited atomic systems will be analyzed in the context of which-way information, quantum beats and quantum erasure. We will analyze the coherence properties of light emitted by different kinds of source systems, and will study second-order correlation processes in which two or more photons are simultaneously emitted.

3.1 Superposition States in a Multi-Level System

To illuminate the basic ideas of quantum interference and in order to link the concept of quantum interference with the existence of correlations (coherences) between atomic dipole transitions, we will first study the master equation in terms of superposition states of different atomic transitions or different two-level atoms. This method will also allow us to explore the physical significance of the multi-level and collective parameters γ_{ij} , δ_{ij} , and Λ_{ij} ($i \neq j$), and to gain insight into the underlying dynamics of the systems. To make our discussion more transparent, we concentrate on quantum interference effects in multi-level systems composed of only two dipole transitions, and ignore all the remaining nonparticipating atomic transitions. Examples of such systems are three-level atoms or two two-level atoms [52]. In addition, we assume that the atomic transitions are damped by the ordinary vacuum field, $N = 0$.

There are a number of theoretical approaches that can be used to calculate quantum interference effects in atomic systems. The traditional method to analyze the dynamics of atoms interacting with external fields is to derive equations of motion for the probability amplitudes or density matrix elements in the bare atomic basis and to solve them by direct integration, or by a transformation to easily solvable algebraic equations [35, 36, 37, 50].

There is an important and interesting way of rewriting the master equation (2.75) in terms of superposition operators that, in many respects, is more useful than the master equation we have derived. This form of the master equation is obtained by transforming the system operators into an appropriate basis of superposition states. The new basis forms a complete set of states

and thus allows for a full description of the physics, and enables one to identify quantum interference effects directly in the master equation of a system composed of two dipole transitions. For the simple example of a system composed of two atomic dipole transitions, we introduce linear superpositions of the dipole operators, defined as

$$\begin{aligned} S_s^+ &= uS_1^+ + vS_2^+ , & S_s^- &= u^*S_1^- + v^*S_2^- , \\ S_a^+ &= vS_1^+ - uS_2^+ , & S_a^- &= v^*S_1^- - u^*S_2^- , \end{aligned} \quad (3.1)$$

where u and v are the transformation coefficients which are in general complex numbers. The coefficients form a complete and orthonormal set

$$|u|^2 + |v|^2 = 1 , \quad (3.2)$$

which ensure that the transition to the superposition operators is an unitary transformation.

If the superpositions are induced by spontaneous emission, the coefficients can be chosen as

$$u = \sqrt{\frac{\gamma_1}{\gamma_1 + \gamma_2}} , \quad v = \sqrt{\frac{\gamma_2}{\gamma_1 + \gamma_2}} , \quad (3.3)$$

where γ_1 and γ_2 are the spontaneous decay rates of the two dipole transitions. The parameters u and v given in terms of the decay rates reflect the superposition states induced by spontaneous emission, due to the two atomic transitions being coupled to each other through the vacuum field.

Alternatively, in the presence of external fields driving the atomic transitions, the superposition states can be defined in terms of the Rabi frequencies of the driving fields as

$$u = \frac{\Omega_1}{\sqrt{|\Omega_1|^2 + |\Omega_2|^2}} , \quad v = \frac{\Omega_2}{\sqrt{|\Omega_1|^2 + |\Omega_2|^2}} , \quad (3.4)$$

where Ω_1 and Ω_2 are the Rabi frequencies of the laser fields driving the atomic transitions.

The operators S_s^+ and S_a^+ represent respectively symmetric and anti-symmetric superpositions of the dipole moments of the two bare systems. In particular, for a three-level Vee-type atom with ground level $|0\rangle$ and two upper levels $|1\rangle$ and $|2\rangle$, the superposition operators are of the form

$$S_s^+ = (S_s^-)^\dagger = |s\rangle\langle 0| , \quad S_a^+ = (S_a^-)^\dagger = |a\rangle\langle 0| , \quad (3.5)$$

and correspond to dipole transitions between the symmetric and antisymmetric superposition states

$$\begin{aligned} |s\rangle &= u|1\rangle + v|2\rangle , \\ |a\rangle &= v|1\rangle - u|2\rangle , \end{aligned} \quad (3.6)$$

and the ground state $|0\rangle$. In this case, the parameters γ_1, γ_2 in (3.3) are the spontaneous emission rates of the $|1\rangle \rightarrow |0\rangle$ and $|2\rangle \rightarrow |0\rangle$ transitions respectively.

Similarly, for a three-level Lambda-type atom with the lower levels $|0\rangle, |1\rangle$, and upper level $|2\rangle$, the superposition operators take the form

$$S_s^+ = (S_s^-)^\dagger = |2\rangle\langle s|, \quad S_a^+ = (S_a^-)^\dagger = |2\rangle\langle a|, \quad (3.7)$$

where the superposition states are linear combinations of the lower atomic states

$$\begin{aligned} |s\rangle &= u|1\rangle + v|0\rangle, \\ |a\rangle &= v|1\rangle - u|0\rangle, \end{aligned} \quad (3.8)$$

and now γ_1, γ_2 are the spontaneous emission rates of the $|2\rangle \rightarrow |0\rangle$ and $|2\rangle \rightarrow |1\rangle$ transitions respectively.

Applying the transformation (3.1) to a Vee-type atom, and assuming that the superposition states are induced by spontaneous emission, the dissipative part of the master equation (2.69) takes the form

$$\begin{aligned} \mathcal{L}_d \varrho &= -\gamma_{ss} (S_s^+ S_s^- \varrho + \varrho S_s^+ S_s^- - 2S_s^- \varrho S_s^+) \\ &\quad -\gamma_{aa} (S_a^+ S_a^- \varrho + \varrho S_a^+ S_a^- - 2S_a^- \varrho S_a^+) \\ &\quad -\gamma_{sa} (S_s^+ S_a^- \varrho + \varrho S_s^+ S_a^- - 2S_a^- \varrho S_s^+) \\ &\quad -\gamma_{as} (S_a^+ S_s^- \varrho + \varrho S_a^+ S_s^- - 2S_s^- \varrho S_a^+) , \end{aligned} \quad (3.9)$$

where the damping coefficients are

$$\begin{aligned} \gamma_{ss} &= |u|^2 \gamma_1 + |v|^2 \gamma_2 + (uv^* + u^*v) \gamma_{12}, \\ \gamma_{aa} &= |v|^2 \gamma_1 + |u|^2 \gamma_2 - (uv^* + u^*v) \gamma_{12}, \\ \gamma_{as} &= uv^* \gamma_1 - u^*v \gamma_2 - (|u|^2 - |v|^2) \gamma_{12}, \\ \gamma_{sa} &= u^*v \gamma_1 - uv^* \gamma_2 - (|u|^2 - |v|^2) \gamma_{12}. \end{aligned} \quad (3.10)$$

The first two terms in (3.9) are the spontaneous emission terms of the symmetric and antisymmetric transitions, and the parameters γ_{ss} and γ_{aa} are the spontaneous emission rates of the transitions, respectively. The last two terms are due to coherence between the superposition states and the parameters γ_{as} and γ_{sa} describe cross-damping rates between the superpositions.

The dissipative part of the master equation is quite generally independent of the configuration of the atomic levels.

3.1.1 Superpositions Induced by Spontaneous Emission

Although the two forms (2.69) and (3.9) of the master equation look similar, the advantage of the transformed form (3.9) over (2.69) is obtained when the

superpositions are induced by spontaneous emission. In this case, the coefficients u and v are given by (3.3), and then the damping coefficients (3.10) simplify to

$$\begin{aligned}\gamma_{ss} &= \frac{1}{2} \frac{(\gamma_1^2 + \gamma_2^2 + 2\gamma_{12}\sqrt{\gamma_1\gamma_2})}{\gamma_1 + \gamma_2}, \\ \gamma_{aa} &= \frac{(\sqrt{\gamma_1\gamma_2} - \gamma_{12})\sqrt{\gamma_1\gamma_2}}{\gamma_1 + \gamma_2}, \\ \gamma_{sa} = \gamma_{as} &= \frac{1}{2} \frac{(\gamma_1 - \gamma_2)(\sqrt{\gamma_1\gamma_2} - \gamma_{12})}{\gamma_1 + \gamma_2}.\end{aligned}\quad (3.11)$$

In general, all the damping coefficients are different from zero, but the cross-damping rates vanish when the damping rates of the original systems are equal ($\gamma_1 = \gamma_2 = \gamma$). In this case $\gamma_{sa} = \gamma_{as} = 0$, and then the transitions out of or into the symmetric and antisymmetric superposition states decay independently with the decay rates $(\gamma + \gamma_{12})/2$ and $(\gamma - \gamma_{12})/2$, respectively. In other words, for $\gamma_1 = \gamma_2$ the transformation (3.1) diagonalizes the dissipative part of the master equation. Furthermore, if $\gamma_{12} = \sqrt{\gamma_1\gamma_2}$, which corresponds to the case of parallel dipole moments of the two atomic transitions, the damping parameters $\gamma_{aa} = \gamma_{sa} = \gamma_{as} = 0$ regardless of the ratio between γ_1 and γ_2 . In this case, the antisymmetric superposition state does not decay. This implies that spontaneous emission can be controlled and even suppressed by appropriately engineering the cross-damping rate γ_{12} arising from the dissipative interaction between two atomic transitions.

The basic feature induced by the cross-damping rate γ_{ij} ($i \neq j$) on the atomic dynamics is the existence of an antisymmetric superposition state whose decay rate may be greatly reduced or even completely suppressed. The modification of the spontaneous emission rates is an example of quantum interference between two atomic transitions in that the spontaneous emission from one of the transitions modifies the spontaneous emission from the other.

The preceding discussion focused on the dissipative part of the master equation, and explored the physical significance of the cross-damping term γ_{ij} . Consider now the coherent part determined by the Hamiltonian H_T , given in (2.73), which contains the contribution from the vacuum induced coherent couplings $\delta_{ij}^{(\pm)}$. In terms of the superposition operators S_s^\pm and S_a^\pm , the Hamiltonian (2.73) takes the form

$$\begin{aligned}H_T &= -\hbar \{ [\Delta_L + (|u|^2 - |v|^2) \Delta] S_s^+ S_s^- + [\Delta_L - (|u|^2 - |v|^2) \Delta] S_a^+ S_a^- \\ &\quad + \Delta_L (uv^* - u^*v) (S_s^+ S_a^- - S_a^+ S_s^-) \\ &\quad + \Delta (uv^* + u^*v) (S_s^+ S_a^- + S_a^+ S_s^-) \} \\ &\quad + \hbar \delta_{12}^{(+)} [(uv^* + u^*v) (S_s^+ S_s^- - S_a^+ S_a^-) \\ &\quad - (|u|^2 - |v|^2) (S_s^+ S_a^- + S_a^+ S_s^-)] \\ &\quad - \frac{i\hbar}{\sqrt{2}} \{ (u\Omega_1 + v\Omega_2) S_s^+ + (v\Omega_1 - u\Omega_2) S_a^+ - \text{H.c.} \},\end{aligned}\quad (3.12)$$

where $\Delta_L = \omega_L - (\omega_1 + \omega_2)/2$ is the detuning of the laser frequency from the average of the atomic transition frequencies, and $\Delta = (\omega_2 - \omega_1)$ is the frequency splitting of the upper energy levels.

The first term in (3.12) arises from the Hamiltonian H_A and shows that the energies of the symmetric and antisymmetric superpositions, as given by the coefficients of the $S_s^+ S_s^-$ and $S_a^+ S_a^-$ terms, depend on the spontaneous emission rates γ_i and the splitting Δ between the atomic transition frequencies. (The terms in Δ_L represent an *equal* shift of the $|s\rangle$ and $|a\rangle$ levels.) In addition, the splitting Δ introduces a direct coupling between the superposition states, which is characterized by the terms involving the cross products $S_s^+ S_a^-$ and $S_a^+ S_s^-$. If the atomic transitions are degenerate, $\Delta = 0$, and the spontaneous emission rates are equal ($\gamma_1 = \gamma_2$) so that $u = v$, then the superposition states have the same energy and there is no contribution to the direct coherent evolution from the Hamiltonian H_A .

The second term in (3.12), proportional to the vacuum induced coupling $\delta_{12}^{(+)}$, has two effects on the dynamics of the symmetric and antisymmetric superpositions. The first is a shift of the energies and the second is a direct coupling between the superpositions. It is seen from (3.12) that the contribution of $\delta_{12}^{(+)}$ to the coherent coupling between the superpositions vanishes for $\gamma_1 = \gamma_2$ ($u = v$) and then the effect of $\delta_{12}^{(+)}$ is only a shift of the energies from their unperturbed values. Note that the parameter $\delta_{12}^{(+)}$ shifts the energies in opposite directions.

The remaining term in (3.12) represents the interaction of the superpositions with the driving laser field. We see that the transition involving the symmetric superposition couples to the laser field with an enhanced Rabi frequency proportional to $u\Omega_1 + v\Omega_2$, whereas the Rabi frequency of the transition involving the antisymmetric superposition is reduced and vanishes for $v\Omega_1 = u\Omega_2$.

We may rewrite the Hamiltonian (3.12) in a physically transparent form which shows explicitly the physical significance of the vacuum induced coupling $\delta_{12}^{(+)}$

$$H_T = -\hbar \{ (\Delta_L + \Delta') S_s^+ S_s^- + (\Delta_L - \Delta') S_a^+ S_a^- + \Delta_c S_s^+ S_a^- + \Delta_c^* S_a^+ S_s^- \} \\ - \frac{i\hbar}{\sqrt{2}} \{ (u\Omega_1 + v\Omega_2) S_s^+ + (v\Omega_1 - u\Omega_2) S_a^+ - \text{H.c.} \} , \quad (3.13)$$

where Δ' and Δ_c are given by

$$\Delta' = \frac{1}{2} (|u|^2 - |v|^2) \Delta - (uv^* + u^*v) \delta_{12}^{(+)} , \\ \Delta_c = (|u|^2 - |v|^2) \delta_{12}^{(+)} + \frac{1}{2} (uv^* + u^*v) \Delta + (uv^* - u^*v) \Delta_L . \quad (3.14)$$

The parameters Δ' and Δ_c allow us to gain physical insight into how the vacuum induced coupling $\delta_{12}^{(+)}$ and the frequency difference Δ can modify the

dynamics of the Vee-type atom. The parameter Δ' appears as a shift of the energies of the superposition states, whereas Δ_c determines the magnitude of the coherent coupling between the superposition states. Regarding the vacuum induced coupling $\delta_{12}^{(+)}$, its effect on the atomic dynamics depends on whether $\gamma_1 = \gamma_2$ or $\gamma_1 \neq \gamma_2$. For $\gamma_1 = \gamma_2$ the parameters (3.14) reduce to

$$\Delta' = -\delta_{12}^{(+)} , \quad \Delta_c = \frac{1}{2}\Delta , \quad (3.15)$$

whereas for $\gamma_1 \neq \gamma_2$, the parameters become

$$\begin{aligned} \Delta' &= \frac{1}{2} \frac{\gamma_1 - \gamma_2}{\gamma_1 + \gamma_2} \Delta - \frac{2\sqrt{\gamma_1\gamma_2}}{\gamma_1 + \gamma_2} \delta_{12}^{(+)} , \\ \Delta_c &= \frac{\gamma_1 - \gamma_2}{\gamma_1 + \gamma_2} \delta_{12}^{(+)} + \frac{\sqrt{\gamma_1\gamma_2}}{\gamma_1 + \gamma_2} \Delta . \end{aligned} \quad (3.16)$$

Thus, for $\gamma_1 = \gamma_2$ the vacuum induced coupling appears only as a shift of the superposition states. However, for $\gamma_1 \neq \gamma_2$, the parameter $\delta_{12}^{(+)}$ affects both the shift and the coupling of the superposition states. The vacuum coupling $\delta_{12}^{(+)}$ can have a constructive as well as destructive effect on the parameters Δ' and Δ_c . For example, if the atomic transitions are degenerate, $\Delta = 0$, then the parameters Δ' and Δ_c are nonzero only if the vacuum coupling is included. On the other hand, for nondegenerate atomic transitions, $\Delta \neq 0$, the vacuum coupling can have a destructive effect on Δ' and Δ_c , in that the parameters can vanish. The shift Δ' vanishes when

$$\Delta = \frac{4\sqrt{\gamma_1\gamma_2}}{\gamma_1 - \gamma_2} \delta_{12}^{(+)} , \quad (3.17)$$

whereas the coherent coupling Δ_c vanishes for

$$\Delta = -2 \frac{\gamma_1 - \gamma_2}{\sqrt{\gamma_1\gamma_2}} \delta_{12}^{(+)} . \quad (3.18)$$

Obviously, with the condition (3.18) and $\gamma_{12} = \sqrt{\gamma_1\gamma_2}$, the antisymmetric state completely decouples from the remaining states and therefore becomes a non-interacting (dark) state. In this case, the dynamics of the three-level atom reduces to that characteristic of a two-level atom.

Thus, the condition $\gamma_{12} = \sqrt{\gamma_1\gamma_2}$ for suppression of spontaneous emission from the antisymmetric state is valid for degenerate as well as nondegenerate transitions, whereas the coherent coupling between the superposition states appears only for nondegenerate transitions with different transition frequencies.

Following our procedure, we can also analyze the dynamics of a Lambda-type atom in the basis of the superposition states. Hence, consider a three-level Lambda-type atom composed of a single upper level $|2\rangle$ of energy $E_2 = 0$, and two ground levels $|1\rangle$ and $|0\rangle$ of energies $E_1 = -\hbar\omega_1$ and $E_2 = -\hbar\omega_2$,

respectively. The upper level is connected to the ground levels via transition dipole moments μ_{21} and μ_{20} , and the transition between the lower levels is forbidden in the electric dipole approximation. Applying the transformation (3.1) to the master equation (2.69), we obtain the master equation with the dissipative part of the same form as (3.9), but with the Hamiltonian H_T of the form

$$H_T = -\hbar \{ (\Delta_L + \Delta') S_s^- S_s^+ + (\Delta_L - \Delta') S_a^- S_a^+ + \Delta_c S_s^- S_a^+ + \Delta_c^* S_a^- S_s^+ \} \\ - i\hbar \{ (u\Omega_1 + v\Omega_2) S_s^+ + (v\Omega_1 - u\Omega_2) S_a^+ - \text{H.c.} \} . \quad (3.19)$$

Comparing (3.19) with the Hamiltonian (3.13) for the Vee-type atom, one notices that the master equations of the two systems are of the same type. The only difference is that the ordering of the superposition operators in (3.19) is the reverse of that for the Vee system. Thus, we expect that the dynamics of a three-level Lambda-type atom are similar to the dynamics of a three-level Vee-type atom.

In the following chapters, we illustrate various spectroscopic effects in three-level atoms paying particular attention to effects arising from the presence of interference terms in the master equations.

3.2 Multi-Atom Superposition (Entangled) States

The quantum phenomenon of *entanglement* is the one that is most at odds with classical mechanics. The term was introduced by Schrödinger in his discussions of the foundations of quantum mechanics [3]. Entanglement is a property of two or more systems that has no analogue in the classical theory. It is also a topic of great current interest, because it provides the basis for many new applications, ranging from quantum information processing, cryptography and quantum computation to atomic and molecular spectroscopy. Information encoded in entangled states may be transmitted with absolute safety against eavesdropping, processed in massively parallel ways by a quantum computer, or used for quantum teleportation, the reproduction of an object at a different place in space and time. These practical implementations all stem from the realization that we may control and manipulate quantum systems at the level of single atoms and photons to store and transfer information in a controlled way and with high fidelity.

In this section, we consider multiatom superposition states, which are also entangled states, as a basis for representing the density operator.

3.2.1 Entanglement

Consider a quantum system that is composed of two subsystems A and B (which need not interact). We first suppose that the composite system is in a pure state: that is, it can be represented by a single wave function. If

the wave function of the composite system can be written as the product of a wave function for system A with a wave function for system B , the state of the composite system is said to be *separable*; if the wave function cannot be written in this form, the state of the composite system is said to be *nonseparable*, or more commonly, *entangled*. As a simple example we may consider two subsystems such that each consist of two states – for example, two-level atoms. Another example of a suitable subsystem is that of a photon in which the two states are the horizontal (H) and vertical (V) states of its polarization. Taking the the latter case to be definite, examples of separable and entangled states are:

$$|H_A\rangle|H_B\rangle - \text{separable} , \quad (3.20a)$$

$$|H_A\rangle|V_B\rangle - \text{separable} , \quad (3.20b)$$

$$(|H_A\rangle|H_B\rangle \pm |V_A\rangle|V_B\rangle)/\sqrt{2} - \text{entangled} , \quad (3.20c)$$

$$(|H_A\rangle|V_B\rangle \pm |V_A\rangle|H_B\rangle)/\sqrt{2} - \text{entangled} . \quad (3.20d)$$

States having the structure of the last four states, (3.20c) and (3.20d), are called Bell states, and are examples of maximally entangled states.

For a composite system which must be described by a density matrix, rather than a pure state, the system is said to be separable if the composite density matrix can be written in the form

$$\varrho_{AB} = \sum_k p_k \varrho_k^A \varrho_k^B , \quad (3.21)$$

otherwise the system is said to be entangled. The p_k are constants, and ϱ_k^A and ϱ_k^B are the reduced density matrices for subsystem ‘A’ and subsystem ‘B’ respectively.

Entangled states of a multi-partite system have the astonishing property that the results of a measurement on one subsystem cannot be specified independently of the results of measurements on the other subsystems, even when the subsystems are noninteracting, and may be very far from one another: in other words, for entangled states, the subsystems can no longer be considered as independent.

When we study decoherence, we are looking at a composite system consisting of the ‘system of interest’ (usually just called the ‘system’) and a ‘reservoir’ with which the system interacts. The properties of the reservoir are usually of no interest, or cannot be measured in practice. It is the entangling of the degrees of freedom of the system with the unobserved (or unobservable) degrees of freedom of the reservoir that leads to decoherence. (We include in our use of the term decoherence dissipative processes, such as spontaneous emission, in which energy is lost from the system to the reservoir.)

We shall illustrate entanglement creation in a simple system of two two-level atoms and explore its relation to quantum interference [50]. The procedure can be easily extended into multi-atom systems or multi-level atoms.

A single two-level atom is an example of the simplest quantum bit of information, or *qubit*, the basic building block in quantum information processing.

3.2.2 Two Interacting Atoms

The modification of spontaneous emission by collective damping and in particular the presence of the dipole–dipole interaction between atoms suggests that the bare atomic states are no longer eigenstates of the atomic system. We illustrate this on a system of two atoms, identical as well as nonidentical, and present a general formalism for the diagonalization of the atomic Hamiltonian with respect to the dipole–dipole interaction.

In the absence of the dipole–dipole interaction and the driving laser field, the space of the two-atom system is spanned by four product states

$$|0\rangle_1|0\rangle_2, \quad |1\rangle_1|0\rangle_2, \quad |0\rangle_1|1\rangle_2, \quad |1\rangle_1|1\rangle_2, \quad (3.22)$$

with corresponding energies

$$E_{00} = -\hbar\omega_0, \quad E_{10} = -\frac{1}{2}\hbar\Delta, \quad E_{01} = \frac{1}{2}\hbar\Delta, \quad E_{11} = \hbar\omega_0, \quad (3.23)$$

where, as usual, $\omega_0 = (\omega_1 + \omega_2)/2$ and $\Delta = (\omega_2 - \omega_1)$.

The product states $|1\rangle_1|0\rangle_2$ and $|0\rangle_1|1\rangle_2$ form a pair of nearly degenerate states with the energy splitting $2\hbar\Delta$. When we include the dipole–dipole interaction between the atoms, the product states combine into two linear superpositions (entangled states), with their energies shifted from the unperturbed values $\pm\hbar\Delta/2$ by the dipole–dipole interaction energy. To see this, we begin with the Hamiltonian of the two atoms including the dipole–dipole interaction

$$H_{aa} = \sum_{i=1}^2 \hbar\omega_i S_i^z + \hbar \sum_{i \neq j} \Lambda_{ij} S_i^+ S_j^- . \quad (3.24)$$

In the basis of the product states (3.22), the Hamiltonian (3.24) can be written in matrix form as

$$H_{aa} = \hbar \begin{pmatrix} -\omega_0 & 0 & 0 & 0 \\ 0 & -\frac{1}{2}\Delta & \Lambda_{12} & 0 \\ 0 & \Lambda_{12} & \frac{1}{2}\Delta & 0 \\ 0 & 0 & 0 & \omega_0 \end{pmatrix} . \quad (3.25)$$

Evidently, in the presence of the dipole–dipole interaction between the atoms the matrix (3.25) is not diagonal, which indicates that the product states (3.22) are not the eigenstates of the interacting atoms. We will diagonalize the matrix (3.25) separately for the case of identical ($\Delta = 0$) and nonidentical ($\Delta \neq 0$) atoms to find eigenstates of the interacting system of atoms and their energies.

3.2.3 Entangled States of Two Identical Atoms

Consider first a system of two identical atoms ($\Delta = 0$). In order to determine the energies and corresponding eigenstates of the system, we diagonalize the matrix (3.25). The resulting eigenstates of the system, first introduced by Dicke, are the so-called collective states or “molecular eigenstates” [49]

$$\begin{aligned} |g\rangle &= |0\rangle_1 |0\rangle_2 , \\ |s\rangle &= \frac{1}{\sqrt{2}} (|1\rangle_1 |0\rangle_2 + |0\rangle_1 |1\rangle_2) , \\ |a\rangle &= \frac{1}{\sqrt{2}} (|1\rangle_1 |0\rangle_2 - |0\rangle_1 |1\rangle_2) , \\ |e\rangle &= |1\rangle_1 |1\rangle_2 , \end{aligned} \quad (3.26)$$

with corresponding nondegenerate eigenvalues (energies)

$$E_g = -\hbar\omega_0, \quad E_s = \hbar\Lambda_{12}, \quad E_a = -\hbar\Lambda_{12}, \quad E_e = \hbar\omega_0 . \quad (3.27)$$

The eigenstates (3.26) form a complete set of states. The ground state $|g\rangle$ and the upper state $|e\rangle$ are not affected by the dipole–dipole interaction, whereas the states $|s\rangle$ and $|a\rangle$ are shifted from their unperturbed energies by the amount $\pm\Lambda_{12}$, the dipole–dipole energy. The most important property of the collective states $|s\rangle$ and $|a\rangle$ is that they are maximally entangled states of the two-atom system. The states are linear superpositions of the product states that cannot be separated into product states of the individual atoms.

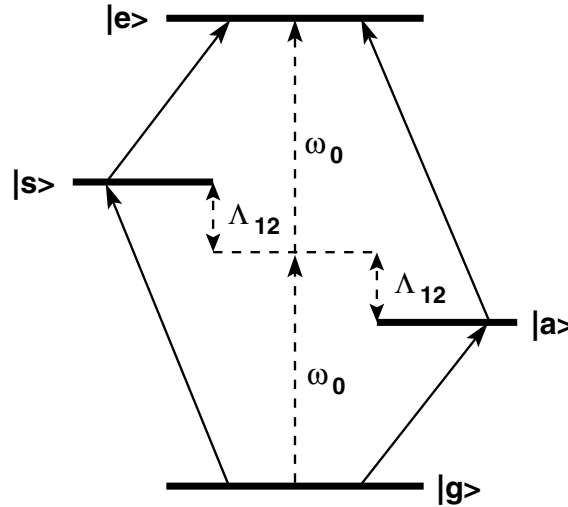


Fig. 3.1. Collective states of two identical atoms. The energies of the symmetric and antisymmetric states are shifted by the dipole–dipole interaction Λ_{12} . The solid arrows indicate one-photon transitions, and the dashed arrows indicate a two-photon transition

We show the collective states of two identical atoms in Fig. 3.1. It is seen that in the collective states representation, the two-atom system behaves as a single four-level system, with the ground state $|g\rangle$, the upper state $|e\rangle$, and two intermediate states: the symmetric state $|s\rangle$ and the antisymmetric state $|a\rangle$. The energies of the intermediate states depend on the dipole–dipole interaction and suffer a large shift when the interatomic separation is small. There are two transition channels $|e\rangle \rightarrow |s\rangle \rightarrow |g\rangle$ and $|e\rangle \rightarrow |a\rangle \rightarrow |g\rangle$, each with two cascaded, nondegenerate transitions. For two identical atoms, these two channels are uncorrelated, but the transitions in these channels are damped with significantly different rates. To illustrate these features, we transform the master equation (2.99) into the basis of the collective states (3.26). We define collective operators $A_{ij} = |i\rangle\langle j|$, where $i, j = e, a, s, g$, that represent the energies ($i = j$) of the collective states and coherences ($i \neq j$). Using (3.26), we find that the collective operators are related to the atomic operators S_i^\pm through the following identities

$$\begin{aligned} S_1^+ &= \frac{1}{\sqrt{2}} (A_{es} - A_{ea} + A_{sg} + A_{ag}) , \\ S_2^+ &= \frac{1}{\sqrt{2}} (A_{es} + A_{ea} + A_{sg} - A_{ag}) . \end{aligned} \quad (3.28)$$

Substituting the transformation identities into (2.99), we find that in the basis of the collective states the master equation of the system can be written as

$$\frac{\partial}{\partial t} \varrho = -\frac{i}{\hbar} [H_{as}, \varrho] + \left(\frac{\partial}{\partial t} \varrho \right)_s + \left(\frac{\partial}{\partial t} \varrho \right)_a , \quad (3.29)$$

where

$$\begin{aligned} H_{as} &= \hbar [\omega_0 (A_{ee} - A_{gg}) + \Lambda_{12} (A_{ss} - A_{aa})] \\ &\quad - \frac{\hbar}{2\sqrt{2}} (\Omega_1 + \Omega_2) \left[(A_{es} + A_{sg}) e^{i(\omega_L t + \phi_L)} + \text{H.c.} \right] \\ &\quad - \frac{\hbar}{2\sqrt{2}} (\Omega_2 - \Omega_1) \left[(A_{ea} - A_{ag}) e^{i(\omega_L t + \phi_L)} + \text{H.c.} \right] , \end{aligned} \quad (3.30)$$

is the Hamiltonian of the interacting atoms and the driving laser field,

$$\begin{aligned} \left(\frac{\partial}{\partial t} \varrho \right)_s &= -\frac{1}{2} (\gamma + \gamma_{12}) [(A_{ee} + A_{ss}) \varrho + \varrho (A_{ee} + A_{ss}) \\ &\quad - 2(A_{se} + A_{gs}) \varrho (A_{es} + A_{sg})] , \end{aligned} \quad (3.31)$$

describes dissipation through the cascade $|e\rangle \rightarrow |s\rangle \rightarrow |g\rangle$ channel involving the symmetric state $|s\rangle$, and

$$\begin{aligned} \left(\frac{\partial}{\partial t} \varrho \right)_a &= -\frac{1}{2} (\gamma - \gamma_{12}) [(A_{ee} + A_{aa}) \varrho + \varrho (A_{ee} + A_{aa}) \\ &\quad - 2(A_{ae} - A_{ga}) \varrho (A_{ea} - A_{ag})] , \end{aligned} \quad (3.32)$$

describes dissipation through the cascade $|e\rangle \rightarrow |a\rangle \rightarrow |g\rangle$ channel involving the antisymmetric state $|a\rangle$.

We will call the two cascade channels $|e\rangle \rightarrow |s\rangle \rightarrow |g\rangle$ and $|e\rangle \rightarrow |a\rangle \rightarrow |g\rangle$ symmetric and antisymmetric transitions, respectively. The first term in H_{as} is the energy of the collective states, whereas the second and third terms are the interactions of the laser field with the symmetric and antisymmetric transitions, respectively. The symmetric state couples to $|g\rangle$ and $|e\rangle$ with an enhanced Rabi frequency $(\Omega_1 + \Omega_2)/\sqrt{2}$, whereas the antisymmetric state couples to $|g\rangle$ and $|e\rangle$ with a reduced Rabi frequency $(\Omega_2 - \Omega_1)/\sqrt{2}$. The most important property arising from the master equation (3.29) is that the symmetric and antisymmetric channels are *uncorrelated* and decay with different rates; the symmetric transitions decay with an enhanced (superradiant) rate $(\gamma + \gamma_{12})$, while the antisymmetric transitions decay with a reduced (subradiant) rate $(\gamma - \gamma_{12})$. For $\gamma_{12} = \gamma$, which according to (2.91) appears when the interatomic separation is much smaller than the resonant wavelength, the antisymmetric transition decouples from the driving field and does not decay. In this case, the antisymmetric state is completely decoupled from the remaining states and the system decays only through the symmetric channel. Hence, for $\gamma_{12} = \gamma$ the system reduces to a three-level cascade system, referred to as the small-sample model or two-atom Dicke model [49, 50]. The model assumes that the atoms are close enough for us to ignore any effects resulting from different spatial positions of the atoms. In other words, the phase factors $\exp(i\mathbf{k} \cdot \mathbf{r}_i)$ are assumed to have the same value for all the atoms, and are set equal to one. This assumption may prove difficult to realize experimentally as present atom trapping and cooling techniques can trap two atoms at distances of the order of a resonant wavelength. At these distances the collective damping parameter γ_{12} differs significantly from γ (see Fig. 2.2), and we cannot ignore the transitions to and from the antisymmetric state. We can, however, employ the Dicke model to spatially extended atomic systems. This could be achieved assuming that the observation time of the atomic dynamics is shorter than γ^{-1} . The antisymmetric state $|a\rangle$ decays on a time scale $\sim (\gamma - \gamma_{12})^{-1}$, which for $\gamma_{12} \approx \gamma$ is much longer than γ^{-1} . On the other hand, the symmetric state decays on a time scale $\sim (\gamma + \gamma_{12})^{-1}$, which is shorter than γ^{-1} . Clearly, if we consider short observation times, the antisymmetric state does not participate in the dynamics and the system can be considered as evolving only between the Dicke states.

Although the symmetric and antisymmetric transitions of the collective system are uncorrelated, the dynamics of the four-level system may be significantly different from the three-level Dicke model.

3.2.4 Entangled States of Two Nonidentical Atoms

The dipole–dipole interaction between two identical atoms leads to the maximally entangled symmetric and antisymmetric states that decay independently with different damping rates. Furthermore, in the case of small sepa-

rations between the atoms, the antisymmetric state decouples from the external coherent field and the environment, and consequently becomes optically inactive. The decoupling of the antisymmetric state from the coherent field protects the state from external perturbations. This is not, however, an useful property from the point of view of quantum state manipulation and quantum computation where it is required to prepare entangled states that are decoupled from the external environment, but should be simultaneously accessible by coherent processes. This requirement can be achieved if the atoms are not identical, and we discuss here some consequences of the fact that the atoms could have different transition frequencies or different spontaneous emission rates. To make our discussion more transparent, we concentrate on two specific cases: (1) $\Delta \neq 0$ and $\gamma_1 = \gamma_2$, and (2) $\Delta = 0$ and $\gamma_1 \neq \gamma_2$.

The Case $\Delta \neq 0$ and $\gamma_1 = \gamma_2$

When the atoms are nonidentical with different transition frequencies, the states (3.26) are no longer eigenstates of the Hamiltonian (3.24). The diagonalization of the matrix (3.25) with $\Delta \neq 0$ leads to the following eigenstates of the interacting nonidentical atoms

$$\begin{aligned} |g\rangle &= |0\rangle_1 |0\rangle_2 , \\ |s'\rangle &= \beta |1\rangle_1 |0\rangle_2 + \alpha |0\rangle_1 |1\rangle_2 , \\ |a'\rangle &= \alpha |1\rangle_1 |0\rangle_2 - \beta |0\rangle_1 |1\rangle_2 , \\ |e\rangle &= |1\rangle_1 |1\rangle_2 , \end{aligned} \quad (3.33)$$

with corresponding energies

$$E_g = -\hbar\omega_0 , \quad E_{a'} = -\hbar w , \quad E_{s'} = \hbar w , \quad E_e = \hbar\omega_0 , \quad (3.34)$$

where

$$\alpha = \sqrt{\frac{d^2}{d^2 + \Lambda_{12}^2}} , \quad \beta = \sqrt{\frac{\Lambda_{12}^2}{d^2 + \Lambda_{12}^2}} , \quad w = \sqrt{\Lambda_{12}^2 + \frac{1}{4}\Delta^2} , \quad (3.35)$$

and

$$d = \frac{1}{2}\Delta + \sqrt{\Lambda_{12}^2 + \frac{1}{4}\Delta^2} . \quad (3.36)$$

The energy level structure of the collective system of two nonidentical atoms is similar to that of the identical atoms, with the ground state $|g\rangle$, the upper state $|e\rangle$, and two intermediate states $|s'\rangle$ and $|a'\rangle$. The effect of the frequency difference Δ on the collective atomic states is to increase the splitting between the intermediate levels, which now is equal to $w = (\Lambda_{12}^2 + \Delta^2/4)^{1/2}$. However, the most dramatic effect of the detuning Δ is on the degree of

entanglement of the intermediate states $|s'\rangle$ and $|a'\rangle$, in that for the case of nonidentical atoms the states are no longer maximally entangled states. For $\Delta = 0$ the states $|s'\rangle$ and $|a'\rangle$ reduce to the maximally entangled states $|s\rangle$ and $|a\rangle$, whereas for $\Delta \gg \Lambda_{12}$ the entangled states reduce to the product states $|1\rangle_1|0\rangle_2$ and $-|0\rangle_1|1\rangle_2$, respectively. The less than maximally entangled states (3.33) can be represented in terms of the maximally entangled states (3.26) as

$$\begin{aligned} |s'\rangle &= \frac{1}{\sqrt{2}} [(\beta + \alpha) |s\rangle + (\beta - \alpha) |a\rangle] , \\ |a'\rangle &= \frac{1}{\sqrt{2}} [(\beta + \alpha) |a\rangle - (\beta - \alpha) |s\rangle] . \end{aligned} \quad (3.37)$$

Using the same procedure as for the case of identical atoms, we rewrite the master equation (2.99) in terms of the collective operators $A_{ij} = |i\rangle\langle j|$, where now the collective states $|i\rangle$ are given in (3.33). First, we find that in the case of nonidentical atoms the atomic dipole operators can be written in terms of the linear combinations of the collective operators as

$$\begin{aligned} S_1^+ &= \alpha A_{es'} - \beta A_{ea'} + \beta A_{s'g} + \alpha A_{a'g} , \\ S_2^+ &= \beta A_{es'} + \alpha A_{ea'} + \alpha A_{s'g} - \beta A_{a'g} . \end{aligned} \quad (3.38)$$

Hence, in terms of the collective operators A_{ij} , the master equation takes the form

$$\frac{\partial}{\partial t} \varrho = -\frac{i}{\hbar} [H_{s'}, \varrho] + \mathcal{L} \varrho , \quad (3.39)$$

where

$$\begin{aligned} H_{s'} &= \hbar [\omega_0 (A_{ee} - A_{gg}) + w (A_{s's'} - A_{a'a'})] \\ &\quad - \frac{\hbar}{2} \left\{ [(\alpha\Omega_1 + \beta\Omega_2) A_{es'} + (\beta\Omega_1 + \alpha\Omega_2) A_{s'g}] e^{i(\omega_L t + \phi_L)} \right. \\ &\quad + [(\alpha\Omega_2 - \beta\Omega_1) A_{ea'} \\ &\quad \left. - (\beta\Omega_2 - \alpha\Omega_1) A_{a'g}] e^{i(\omega_L t + \phi_L)} + \text{H.c.} \right\} \end{aligned} \quad (3.40)$$

is the Hamiltonian of the system in the collective states basis, and the Liouville operator $\mathcal{L} \varrho$ describes the dissipative part of the evolution. The dissipative part is composed of three terms

$$\mathcal{L} \varrho = \left(\frac{\partial}{\partial t} \varrho \right)_s + \left(\frac{\partial}{\partial t} \varrho \right)_a + \left(\frac{\partial}{\partial t} \varrho \right)_I , \quad (3.41)$$

where

$$\begin{aligned} \left(\frac{\partial}{\partial t} \varrho \right)_s &= -\gamma_{s'} \{ (A_{ee} + A_{s's'}) \varrho + \varrho (A_{ee} + A_{s's'}) \\ &\quad - 2(A_{s'e} \varrho A_{es'} + A_{gs'} \varrho A_{s'g}) \} \\ &\quad - (\alpha\beta\gamma + \gamma_{12}) (A_{s'e} \varrho A_{s'g} + A_{gs'} \varrho A_{es'}) , \end{aligned} \quad (3.42)$$

$$\begin{aligned} \left(\frac{\partial}{\partial t} \varrho \right)_a &= -\gamma_{a'} \{ (A_{ee} + A_{a'a'}) \varrho + \varrho (A_{ee} + A_{a'a'}) \\ &\quad - 2(A_{a'e} \varrho A_{ea'} + A_{ga'} \varrho A_{a'g}) \} \\ &\quad - (\alpha\beta\gamma - \gamma_{12}) (A_{a'e} \varrho A_{a'g} + A_{ga'} \varrho A_{ea'}) , \end{aligned} \quad (3.43)$$

and

$$\begin{aligned} \left(\frac{\partial}{\partial t} \varrho \right)_I &= -\gamma_{a's'} \{ (A_{a's'} + A_{s'a'}) \varrho + \varrho (A_{a's'} + A_{s'a'}) \\ &\quad - 2(A_{ga'} \varrho A_{s'g} + A_{gs'} \varrho A_{a'g} + A_{s'e} \varrho A_{ea'} + A_{a'e} \varrho A_{es'}) \} \\ &\quad + (\alpha^2 - \beta^2) \gamma \{ A_{a'e} \varrho A_{s'g} + A_{gs'} \varrho A_{ea'} \\ &\quad + A_{s'e} \varrho A_{a'g} + A_{ga'} \varrho A_{es'} \} , \end{aligned} \quad (3.44)$$

with the damping coefficients

$$\begin{aligned} \gamma_{s'} &= \frac{1}{2} (\gamma + 2\alpha\beta\gamma_{12}) , & \gamma_{a'} &= \frac{1}{2} (\gamma - 2\alpha\beta\gamma_{12}) , \\ \gamma_{a's'} &= \frac{1}{2} (\alpha^2 - \beta^2) \gamma_{12} . \end{aligned} \quad (3.45)$$

The dissipative part of this master equation, unlike the case of identical atoms, contains an interference term between the symmetric and antisymmetric transitions. The terms (3.42) and (3.43) describes spontaneous transitions in the symmetric and antisymmetric channels, respectively. The coefficients $\gamma_{s'}$ and $\gamma_{a'}$ are the spontaneous emission rates of the transitions. The interference term (3.44) results from spontaneously induced coherences between the symmetric and antisymmetric transitions. This term appears only in systems of atoms with different transition frequencies ($\Delta \neq 0$), and reflects the fact that, as the system decays from the state $|s'\rangle$, it drives the antisymmetric state, and vice versa. Thus, in contrast to the case of identical atoms, the symmetric and antisymmetric transitions are no longer independent and are correlated due to the presence of the detuning Δ . Moreover, for nonidentical atoms the damping rate of the antisymmetric state cannot be reduced to zero. In the case of interatomic separations much smaller than the optical wavelength (the small sample model), the damping rate reduces to

$$\gamma_{a'} = \frac{1}{2} \gamma (\alpha - \beta)^2 , \quad (3.46)$$

which is different from zero, unless $\Delta = 0$.

Figure 3.2 shows the damping rate $\gamma_{a'}$ as a function of Δ for different interatomic separations. The damping rate attains a minimum at $\Delta = 0$, which

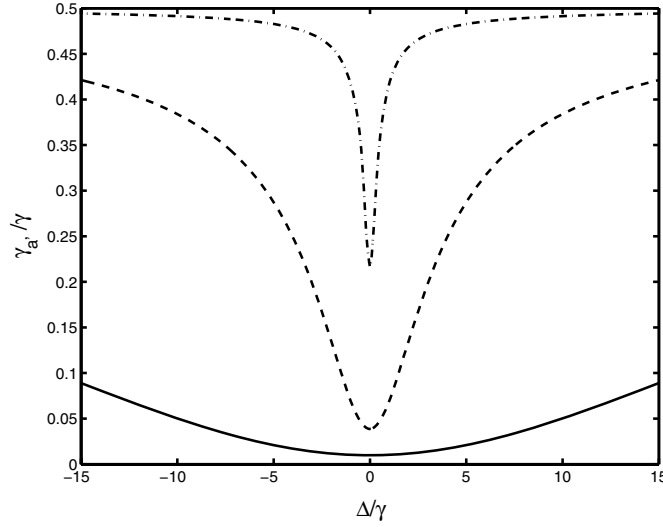


Fig. 3.2. The spontaneous emission damping rate $\gamma_{a'}$ as a function of Δ for $\boldsymbol{\mu} \perp \bar{\mathbf{r}}_{12}$, and different interatomic separations: $r_{21}/\lambda_0 = 0.05$ (solid line), $r_{21}/\lambda_0 = 0.1$ (dashed line), $r_{21}/\lambda_0 = 0.25$ (dashed-dotted line)

is close to zero for very small interatomic separations. For larger separations, the damping rate is reduced only in a very narrow range of Δ . However, for small interatomic separations there is a significant range of Δ for which the spontaneous emission rate in the antisymmetric channels $\gamma_{a'} \ll \gamma$.

The Case $\Delta = 0$ and $\gamma_1 \neq \gamma_2$

The Hamiltonian (3.24) for two atoms with equal transition frequencies ($\Delta = 0$) is diagonal in the basis of the collective states of two identical atoms. This suggests that the dynamics of two nonidentical atoms with equal transition frequencies but different transition rates can be completely described in terms of the collective states of two identical atoms. However, for $\gamma_1 \neq \gamma_2$, the dissipative part of the master equation of the system is not diagonal in the basis of the collective states (3.26), and can be written as

$$\begin{aligned} \mathcal{L}\varrho = & -\frac{1}{2}(\gamma_1 + \gamma_2 + 2\gamma_{12}) (S_s^+ S_s^- \varrho + \varrho S_s^+ S_s^- - 2S_s^- \varrho S_s^+) \\ & -\frac{1}{2}(\gamma_1 + \gamma_2 - 2\gamma_{12}) (S_a^+ S_a^- \varrho + \varrho S_a^+ S_a^- - 2S_a^- \varrho S_a^+) \\ & -\frac{1}{2}(\gamma_1 - \gamma_2) (S_s^+ S_a^- \varrho + \varrho S_s^+ S_a^- - 2S_a^- \varrho S_s^+) \\ & -\frac{1}{2}(\gamma_1 - \gamma_2) (S_a^+ S_s^- \varrho + \varrho S_a^+ S_s^- - 2S_s^- \varrho S_a^+) , \end{aligned} \quad (3.47)$$

where $S_s^\pm = (S_1^\pm + S_2^\pm)/\sqrt{2}$ and $S_a^\pm = (S_1^\pm - S_2^\pm)/\sqrt{2}$ are the symmetric and antisymmetric combinations of the atomic operators, respectively. There are four terms in the dissipative part of the master equation. The first

two terms describe dissipation through the symmetric and antisymmetric channels, and the remaining two terms are due to coherences between those two channels. The damping rate of the transitions involving the antisymmetric state is nonzero, even for small interatomic separations, where $\gamma_{12} = (\gamma_1 \gamma_2)^{1/2}$.

We can simplify the dissipative part (3.47) by introducing new basis states, which allow us to obtain a simple physical interpretation of the different processes involved in the dynamics of two nonidentical atoms. This can be done by choosing the following collective basis states

$$\begin{aligned} |g\rangle &= |0\rangle_1 |0\rangle_2 , \\ |+\rangle &= \frac{1}{\sqrt{\gamma_1 + \gamma_2}} (\sqrt{\gamma_1} |1\rangle_1 |0\rangle_2 + \sqrt{\gamma_2} |0\rangle_1 |1\rangle_2) , \\ |-\rangle &= \frac{1}{\sqrt{\gamma_1 + \gamma_2}} (\sqrt{\gamma_2} |1\rangle_1 |0\rangle_2 - \sqrt{\gamma_1} |0\rangle_1 |1\rangle_2) , \\ |e\rangle &= |1\rangle_1 |1\rangle_2 . \end{aligned} \quad (3.48)$$

The collective states (3.48) differ from those for identical atoms in that the states $|+\rangle$ and $|-\rangle$ are non-maximally entangled states. For $\gamma_1 = \gamma_2$, the states coincide with the maximally entangled states of two identical atoms, whereas for either $\gamma_1 \gg \gamma_2$ or $\gamma_1 \ll \gamma_2$, the entangled states reduce to the product states $|1\rangle_i |0\rangle_j$ ($i \neq j$). In the general case of $\gamma_1 \neq \gamma_2$, the states $|+\rangle$ and $|-\rangle$ can be represented by linear superpositions of the maximally entangled states (3.26) as

$$\begin{aligned} |+\rangle &= \frac{1}{\sqrt{2(\gamma_1 + \gamma_2)}} [(\sqrt{\gamma_1} + \sqrt{\gamma_2}) |s\rangle + (\sqrt{\gamma_1} - \sqrt{\gamma_2}) |a\rangle] , \\ |-\rangle &= \frac{1}{\sqrt{2(\gamma_1 + \gamma_2)}} [(\sqrt{\gamma_1} + \sqrt{\gamma_2}) |a\rangle - (\sqrt{\gamma_1} - \sqrt{\gamma_2}) |s\rangle] , \end{aligned} \quad (3.49)$$

which clearly shows that in the case of identical atoms ($\gamma_1 = \gamma_2$), the states $|+\rangle$ and $|-\rangle$ reduce to the maximally entangled states $|s\rangle$ and $|a\rangle$, respectively.

We can also introduce superposition operators

$$\begin{aligned} S_+^\pm &= \frac{1}{\sqrt{\gamma_1 + \gamma_2}} (\sqrt{\gamma_1} S_1^\pm + \sqrt{\gamma_2} S_2^\pm) , \\ S_-^\pm &= \frac{1}{\sqrt{\gamma_1 + \gamma_2}} (\sqrt{\gamma_2} S_1^\pm - \sqrt{\gamma_1} S_2^\pm) , \end{aligned} \quad (3.50)$$

which in the basis of the collective states (3.48) take the following form

$$\begin{aligned}
S_+^+ &= (S_+^-)^\dagger = |+\rangle\langle g| \\
&\quad + \frac{1}{\sqrt{\gamma_1 + \gamma_2}} [2\sqrt{\gamma_1\gamma_2}|e\rangle\langle +| - (\gamma_1 - \gamma_2)|e\rangle\langle -|] , \\
S_-^+ &= (S_-^-)^\dagger = |-\rangle\langle g| \\
&\quad + \frac{-1}{\sqrt{\gamma_1 + \gamma_2}} [2\sqrt{\gamma_1\gamma_2}|e\rangle\langle -| + (\gamma_1 - \gamma_2)|e\rangle\langle +|] . \tag{3.51}
\end{aligned}$$

Before proceeding further, it is worth pointing out the physical significance of the various terms in (3.51) to gain insight into the underlying dynamics of the two nonidentical atoms. We see that as in the case of identical atoms, there are two excitation channels: the symmetric channel $|g\rangle \rightarrow |+\rangle \rightarrow |e\rangle$ and the antisymmetric channel $|g\rangle \rightarrow |-\rangle \rightarrow |e\rangle$. The channels are correlated in such a way that unequal damping rates correlate transitions only from the upper state to the intermediate states, while the transitions from the intermediate states to the ground state are independent of each other.

Next, we write the dissipative part of the master equation in terms of the superposition operators (3.38). From the master equation (2.99), or transforming the dissipative part (3.47) into the representation in terms of the superposition operators (3.51), we obtain

$$\begin{aligned}
\mathcal{L}\varrho &= -\gamma_{++} (S_+^+ S_+^- \varrho + \varrho S_+^+ S_+^- - 2S_+^- \varrho S_+^+) \\
&\quad -\gamma_{--} (S_-^+ S_-^- \varrho + \varrho S_-^+ S_-^- - 2S_-^- \varrho S_-^+) \\
&\quad -\gamma_{+-} (S_+^+ S_-^- \varrho + \varrho S_+^+ S_-^- - 2S_-^- \varrho S_+^+) \\
&\quad -\gamma_{-+} (S_-^+ S_+^- \varrho + \varrho S_-^+ S_+^- - 2S_+^- \varrho S_-^+) , \tag{3.52}
\end{aligned}$$

where the damping coefficients are

$$\begin{aligned}
\gamma_{++} &= \frac{1}{2} (\gamma_1 + \gamma_2) + \frac{\sqrt{\gamma_1\gamma_2} (\gamma_{12} - \sqrt{\gamma_1\gamma_2})}{\gamma_1 + \gamma_2} , \\
\gamma_{--} &= \frac{(\sqrt{\gamma_1\gamma_2} - \gamma_{12}) \sqrt{\gamma_1\gamma_2}}{\gamma_1 + \gamma_2} , \\
\gamma_{+-} &= \gamma_{-+} = \frac{1}{2} \frac{(\gamma_1 - \gamma_2) (\sqrt{\gamma_1\gamma_2} - \gamma_{12})}{\gamma_1 + \gamma_2} . \tag{3.53}
\end{aligned}$$

The damping rates γ_{--} , γ_{-+} and γ_{+-} are of importance only for systems of atoms separated by intermediate or large distances relative to the resonance wavelength, where $\gamma_{12} < \sqrt{\gamma_1\gamma_2}$. For small atomic separations, $\gamma_{12} = \sqrt{\gamma_1\gamma_2}$, and then the spontaneous emission rates γ_{--} , γ_{-+} and γ_{+-} vanish regardless of the ratio between γ_1 and γ_2 . In this case, the antisymmetric state $|-\rangle$ does not decay and also decouples from the symmetric state $|+\rangle$. Thus, for nonidentical atoms the state $|-\rangle$ behaves similarly to the antisymmetric state $|a\rangle$ characteristic of two identical atoms.

The above analysis show that in the small sample model, the transitions $|+\rangle \rightarrow |g\rangle$ and $|-\rangle \rightarrow |g\rangle$ are not correlated by spontaneous transitions.

However, the transitions can be correlated by coherent processes contained in the system Hamiltonian (2.100). These processes can coherently couple the symmetric entangled state $|+\rangle$ to the nondecaying antisymmetric state $|-\rangle$. To check this, we write the Hamiltonian (2.100) in terms of the S_+^\pm and S_-^\pm operators as

$$\begin{aligned} H_s = & -\hbar\Delta_L (S_+^+ S_+^- + S_-^+ S_-^-) \\ & + \hbar \frac{\Lambda_{12}}{\gamma_1 + \gamma_2} [2\sqrt{\gamma_1\gamma_2} (S_+^+ S_+^- - S_-^+ S_-^-) + (\gamma_1 - \gamma_2) (S_+^+ S_-^- + S_-^+ S_+^-)] \\ & - \frac{\hbar}{2} (\Omega_+ S_+^+ + \Omega_- S_-^+ + \text{H.c.}) , \end{aligned} \quad (3.54)$$

where

$$\begin{aligned} \Omega_+ &= \frac{1}{\sqrt{\gamma_1 + \gamma_2}} (\sqrt{\gamma_1}\Omega_1 + \sqrt{\gamma_2}\Omega_2) , \\ \Omega_- &= \frac{1}{\sqrt{\gamma_1 + \gamma_2}} (\sqrt{\gamma_2}\Omega_1 - \sqrt{\gamma_1}\Omega_2) , \end{aligned} \quad (3.55)$$

are the Rabi frequencies of the symmetric and antisymmetric transitions, respectively, and $\Delta_L = \omega_L - \omega_0$ is the detuning of the laser field from the atomic transition frequency.

The first term in (3.54) arises from the atomic Hamiltonian and shows that in the absence of the interatomic interactions the symmetric and antisymmetric states have the same energy. The second term in (3.54), proportional to the dipole–dipole interaction between the atoms, has two effects on the dynamics of the symmetric and antisymmetric entangled states. The first is a shift of the energies and the second is the coherent interaction between the entangled states. It is seen from (3.54) that the dipole–dipole interaction shifts the energies in the opposite directions. The third term in (3.54) represents the interaction of the superpositions with the driving laser field. We see that the symmetric transitions couple to the laser field with an enhanced Rabi frequency Ω_+ , whereas the antisymmetric transitions are coupled with the reduced Rabi frequency Ω_- .

It is convenient to reparametrize the Hamiltonian (3.54) in order to explore the presence of the coherent coupling between the symmetric and antisymmetric states

$$\begin{aligned} H_s = & -\hbar [(\Delta_L - \Delta') S_+^+ S_+^- + (\Delta_L + \Delta') S_-^+ S_-^-] \\ & - \hbar\Delta_c (S_+^+ S_-^- + S_-^+ S_+^-) - \frac{1}{2}\hbar (\Omega_+ S_+^+ + \Omega_- S_-^+ + \text{H.c.}) , \end{aligned} \quad (3.56)$$

where the parameters Δ' and Δ_c are given by

$$\Delta' = \frac{2\sqrt{\gamma_1\gamma_2}}{\gamma_1 + \gamma_2} \Lambda_{12} , \quad \Delta_c = \frac{\gamma_1 - \gamma_2}{\gamma_1 + \gamma_2} \Lambda_{12} . \quad (3.57)$$

The parameters Δ' and Δ_c allow us to gain physical insight into how the dipole–dipole interaction Λ_{12} and the unequal damping rates $\gamma_1 \neq \gamma_2$ can modify the dynamics of the two-atom system. The parameter Δ' represents a shift of the energies of the entangled states due to the dipole–dipole interaction between the atoms. The shift depends on Λ_{12} and the ratio γ_2/γ_1 . For $\gamma_2 = \gamma_1$ the shift is maximal and equal to Λ_{12} , and decreases with increasing or decreasing γ_2/γ_1 . The parameter Δ_c determines the coherent coupling between the entangled states, and is nonzero *only* for nonidentical atoms. In contrast to the frequency shift, the coherent coupling increases with increasing or decreasing γ_2/γ_1 .

We conclude that spontaneous emission from the antisymmetric state can be suppressed for both identical and nonidentical atoms, whereas the coherent interaction between the entangled states appears only for nonidentical atoms with different spontaneous damping rates. Thus, in two atom systems one may create an entangled antisymmetric state, which could be decoupled from the external environment and, at the same time, the state could exhibit a strong coherent coupling with the remaining states. This coupling can be used as a coherent channel for decoherence free transfer of entanglement to the antisymmetric state, where it can stay unchanged for a long time.

The treatment presented in this section can be extended with only a minor modification to a number of other schemes of two-atom systems. For example, it can be applied to the case of two atoms that experience different intensities and phases of the driving field.

3.3 Experimental Evidence of the Collective Damping and Frequency Shift

The prediction of collective damping resulting from the interaction between two atoms separated by a small distance r_{21} has been realized in very elegant experiments performed in the late sixties by Drexhage [53]. The principle of the experiments was to observe the effect of a reflecting surface, a so called half-cavity, on the spontaneous emission rate of a radiating atom or molecule. It was the first step in the study of controlled collective effects in atomic and molecular spectroscopy. Typically, an experimental observation of the collective modification of the spontaneous emission rate, such as superradiance and subradiance, requires a large number of atoms confined to a very small region, of the order of the resonant wavelength of the atomic transitions. The experiments of Drexhage were the first which demonstrated a modification of the spontaneous damping rate of a single two-level atom kept at a fixed distance r from a metallic mirror. This system is formally equivalent to two identical atoms separated by the constant distance $r_{21} = 2r$, where the role of the second atom is played by the mirror image, located at a distance r behind the mirror, of the physical atom. In the experiments, they studied the fluorescence from a thin layer of optically excited organic-dye molecules that

were separated from a metallic mirror by a dielectric layer of known thickness. The sample was composed of a glass plate with a gold coating covered with a certain number of CdC₂₀ spacer layers on top of which a monomolecular layer of the dye (europium) molecules was deposited. In order to avoid the refraction at the layer-air interface, the sample was placed at the center of a cylindrical cell filled with a liquid whose refractive index matches the index of the layer system. The sample was excited with ultraviolet light from a high-pressure mercury arc, which was chopped by a rotating disc into pulses with a sharp cutoff. The fluorescence field emitted by the sample was detected by a photomultiplier tube and the fluorescence intensity recorded by a sampling technique. These experiments showed variations in both the spontaneous emission rate and the angular distribution of the fluorescence due to the spatial variation and anisotropy of the vacuum field.

The experimental results were compared to the theoretical formulae for the spontaneous emission rate of an atom radiating in front of a mirror. The theoretical formulae for the modified spontaneous emission rate of an atom whose transition dipole moment is parallel or perpendicular to the perfectly reflecting mirror plane can be found from (2.58) and (2.59) by removing the partly reflecting mirror. This is realized by taking the limits $R \rightarrow 0$ and $L \rightarrow \infty$ while maintaining a fixed distance r_z from the atom to the perfectly reflecting mirror. In this limit, with the dipole moments oriented parallel to the perfectly reflecting mirror plane, the spontaneous emission rate (2.58) reduces to

$$\gamma_{ij}^{\parallel} = \frac{3}{2}\gamma_{ij} \int_0^1 du (1 + u^2) \sin^2(k_0 r_z u) , \quad (3.58)$$

whereas for dipole moments oriented perpendicular to the mirror plane, (2.59) reduces to

$$\gamma_{ij}^{\perp} = 3\gamma_{ij} \int_0^1 du (1 - u^2) \cos^2(k_0 r_z u) . \quad (3.59)$$

The integrals that appear in (3.58) and (3.59) can be evaluated analytically, and we find that the expression for γ_{ij}^{\parallel} and γ_{ij}^{\perp} take the form

$$\gamma_{ij}^{\parallel} = \gamma_{ij} \left\{ 1 - \frac{3}{2} \left[\frac{\cos(2k_0 r_z)}{(2k_0 r_z)^2} + \frac{\sin(2k_0 r_z)}{(2k_0 r_z)} \left(1 - \frac{1}{(2k_0 r_z)^2} \right) \right] \right\} , \quad (3.60)$$

and

$$\gamma_{ij}^{\perp} = \gamma_{ij} \left[1 - 3 \frac{\cos(2k_0 r_z)}{(2k_0 r_z)^2} + 3 \frac{\sin(2k_0 r_z)}{(2k_0 r_z)^3} \right] . \quad (3.61)$$

Thus, even in the presence of a single mirror, the spontaneous emission rate of the atom is altered from its free space value. For very small distances from the mirror, where $2k_0r_z \ll 1$, the spontaneous emission rate γ_{ij}^{\parallel} is suppressed ($\gamma_{ij}^{\parallel} \approx 0$), whereas γ_{ij}^{\perp} is enhanced ($\gamma_{ij}^{\perp} \approx 2\gamma_{ij}$). As the distance from the mirror becomes large compared to the radiation wavelength ($2k_0r_z \gg 1$), the spontaneous emission rates both tend to the free-space value γ_{ij} . The vanishing of the spontaneous emission rate from a parallel dipole is due to cancellation between the physical dipole and its inverted image. Similarly, the doubling of the spontaneous emission rate from a dipole normal to the mirror is due to constructive interference of the radiation fields when the image dipole is included. The results (3.60) and (3.61) have been obtained from the three-dimensional and fully quantum treatment of the interaction, and are in perfect agreement with the fully classical treatment of Drexhage [53] and Morawitz [54].

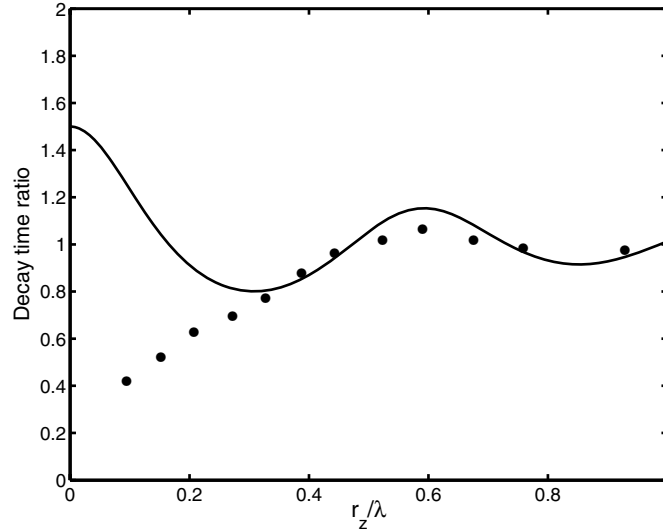


Fig. 3.3. Measured spontaneous decay time (*solid circles*) of the europium complex as a function of the distance from a gold mirror. The solid line indicates the theoretical average spontaneous decay time $\tau/\tau_{\text{free}} = \gamma_{ij}/\gamma_{ij}^a$, where τ_{free} is the decay time in the absence of the mirror

Since in the experiments the radiating dipole moments had isotropic spatial distributions, the combined expressions (3.60) and (3.61) give the average spontaneous emission rate

$$\gamma_{ij}^a = \frac{1}{3}\gamma_{ij}^{\perp} + \frac{2}{3}\gamma_{ij}^{\parallel} . \quad (3.62)$$

Figure 3.3 shows the experimental data (solid circles) together with the theoretical predictions for the average spontaneous decay time $\tau = 1/\gamma_{ij}^a$. For large distances of the atom from the mirror, the experimental results agree

with the theoretical predictions, but they disagree for small distances. As explained by Drexhage, the deviations occurring at small distances were caused by energy transfer to the metallic mirror plate, the probability of which is very large at small distances. This process is absent for dielectric mirrors. The experiments showed clearly that the rate of spontaneous emission near a mirror is a function of the distance from the mirror.

The dependence of the spontaneous emission rate on the distance from the mirror can be explained in terms of quantum interference between reflected and unreflected beams of the emitted light. The amplitude of the field detected by a detector located in the far field zone from the system is a superposition of the reflected and unreflected fields, and the superposition of the fields depends on the path difference between those two fields.

The modern technology of radio-frequency ion traps has made it possible to observe superradiant and subradiant spontaneous emission rates with two laser-cooled trapped ions. The interest in experimental testing of multi-atom effects using two trapped ions began with the work of Eichmann et al. [10]. In the experiment, discussed in the context of complementarity in Sect. 1.1.4, they also demonstrated interference fringes in the radiation scattered by two trapped ions in analogy to the interference fringes in Young's double slit experiment. However, they did not observe collective effects between the ions due to large ion-ion separations, $r_{21} > 15\lambda_0$, where λ_0 is the resonant wavelength of the radiation. At these separations, the collective parameters $\gamma_{ij} \approx \Lambda_{ij} \approx 0$.

The modifications of the spontaneous emission rate due to the collective interaction between atoms were first observed by DeVoe and Brewer [55]. In their experiment, two barium Ba^+ ions were confined in a spherical Paul trap and kept for a long time at constant distances of the order of the resonant wavelength, $r_{21} \geq 2\lambda_0$. Because of the small separation between the ions, they were able to observe a modification of the spontaneous emission rate of the two-ion system due to the presence of the collective interaction between the ions. To achieve such small separations between the ions, they developed microscopic, strongly confining ion traps of "planar" geometry (80 μm radius), which are strong enough to bring the ions to separations within 1 μm , or equivalently in terms of the resonant wavelength, to separations $\sim 2\lambda_0$.

The principal elements of the experimental setup are shown in Fig. 3.4. The central element is the planar ion trap producing a quadrupole field from flat electrodes with concentric circular apertures. Two identical ions (a two-ion crystal) were trapped at a nominal ion-ion spacing of $r_{21} = 1470$ nm when driven with an 500 V peak field at 93.5 MHz. The ions were laser cooled using two frequency stabilized cw dye lasers. In their experiment, the trapped ions were essentially motionless and lay at a known and controllable distance from one another, permitting the measurement of the collective damping rate γ_{12} as a function of the ion-ion separation r_{21} . The ion-ion distance was varied by changing the dc voltage on the trap. The spontaneous emission

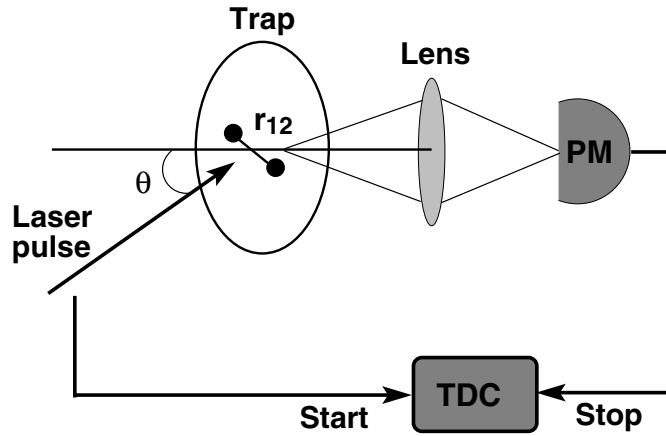


Fig. 3.4. Experimental setup of DeVoe and Brewer [55] to observe the variation of the collective damping rate with the distance between two trapped ions

rate was measured by a transient technique in which the ions were excited by a short pulse and the time of arrival of the fluorescence photons to the detector PM was recorded on a time-to-digital converter (TDC). The short pulses were generated by two nonlinear electro-optic modulators.

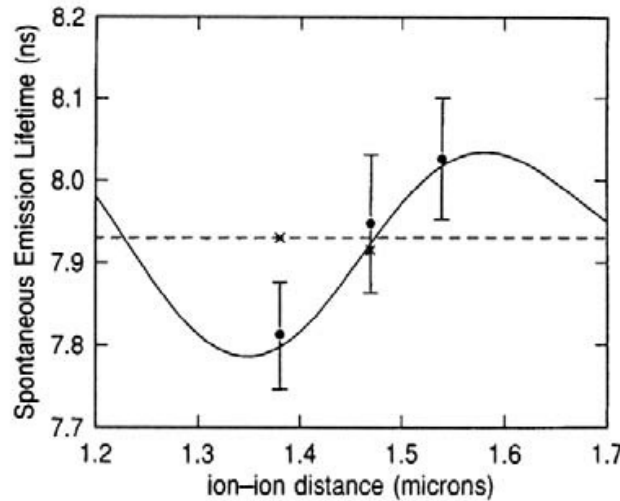


Fig. 3.5. Experimental results of DeVoe and Brewer showing the observed spontaneous emission lifetimes of the two-ion system at three different separations between the ions with the dipole moments perpendicular to the ion-ion axis. The solid line is the theoretical prediction and the dashed line indicates the lifetime of a single ion, measured in the same apparatus. The crosses are the measured lifetimes for the dipole moments of the ions parallel to the ion-ion axis. From R.G. DeVoe, R.G. Brewer: Phys. Rev. Lett. **76**, 2049 (1996). Copyright (1996) by the American Physical Society

Figure 3.5 shows the experimental results and the corresponding theoretical prediction of the spontaneous emission lifetime $\tau_{\text{sp}} = 1/\gamma_{12}$ as a function of the ion–ion separation r_{21} . The experimentally observed lifetime was obtained for three different separations adjusted by varying the dc voltage on the trap. The variation of τ_{sp} from enhanced (superradiant) to reduced (sub-radiant) values relative to the lifetime of independent atoms was observed when the separation was decreased from 1540 nm to 1380 nm. The experimental results clearly indicated the dependence of the spontaneous emission rate on the ion–ion separation, and were in excellent agreement with the theoretical predictions.

The first experimental evidence of the collective dipole–dipole interaction between two molecules has been observed in a difficult and pioneering experiment by Hettich et al. [56]. In practice, it is difficult to bring two atoms or molecules close enough to observe the effect of the dipole–dipole interaction on the atomic dynamics. As evident from Fig. 3.1, the dipole–dipole interaction is significant only for interatomic separations $r_{21} < \lambda_0$. In addition, two trapped ions cannot be kept for long at such small separations due to the repulsive ion–ion interaction. Therefore, it has been suggested to perform such experiments on molecules located in a solid matrix, where it is relatively easy to deposit molecules at very small separations, but it still could be difficult to locate such molecules for experiments. However, by performing cryogenic laser spectroscopy under a scanning probe electrode that induces a local electric field, the experimental team resolved a pair of nonidentical molecules separated by a distance much smaller than the resonant wavelength. At such small separations, the main interaction between the molecules is the collective dipole–dipole interaction Λ_{ij} . In the experiment, fluorescence excitation spectroscopy was performed at $T \approx 1.4$ K to detect single terylene molecules embedded in an organic para-terphenyl crystal with a thickness of about 250 nm. By monitoring the fluorescence from the molecular pair as a function of the detuning of a driving laser whose frequency was scanned through the inhomogeneous absorption band of terylene, the team observed a new peak in the fluorescence intensity spectrum arising from the two-photon excitation of the molecules [57].

The experimental results are shown in Fig. 3.6. The observed excitation spectrum was composed of three lines; two sideband lines located at the transition frequencies of the individual molecules, and a central line located at the average transition frequency of the molecules. The sideband lines arise from absorption of the excitation field at frequencies equal to the molecular transition frequencies, whereas the central line arises from the simultaneous two-photon excitation of the molecules. The central line results from the presence of the dipole–dipole interaction between the molecules, which shifts the energy levels of the combined molecular system. The shift suppresses the probability of one-photon absorption, so that the two-photon transition becomes the dominant radiative channel, which is manifested by an enhanced

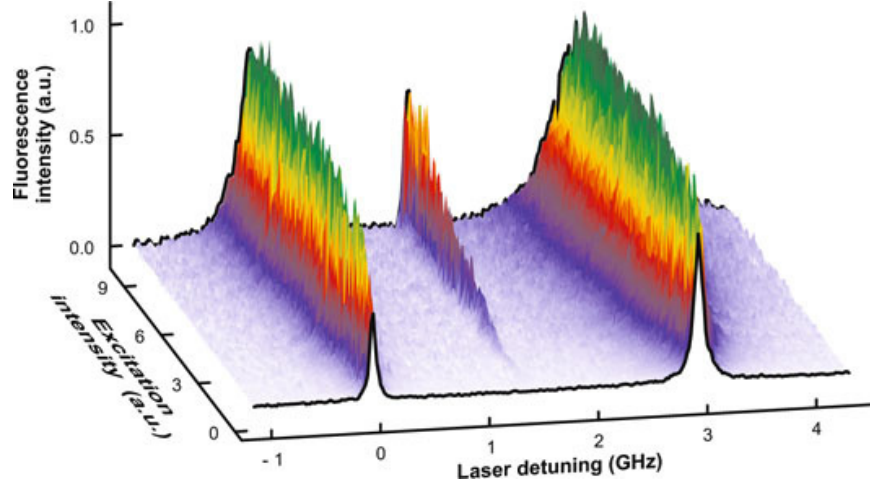


Fig. 3.6. First experimental evidence of the dipole–dipole interaction potential between two molecules observed in the excitation spectrum. From C. Hettich, C. Schmitt, J. Zitzmann, S. Kühn, I. Gerhardt, V. Sandoghdar: *Science* **298**, 385 (2002). Copyright (2002) AAAS

simultaneous two-photon absorption by the two molecules. This two-photon process, predicted theoretically but not observed in earlier optical studies, can only arise in a strongly interacting pair of atoms or molecules. The experimentally observed changes in the excitation spectrum confirm that for nonidentical atoms the two-photon transitions become important and manifest the presence of the dipole–dipole interaction between the atoms.

3.4 General Criteria for Interference in Two-Atom Systems

Here, we derive general criteria for first- and second-order interference in the fluorescence field emitted from two identical two-level atoms. Using these criteria, we can easily predict conditions for quantum interference in the two-atom system. In this approach, we apply the collective states of a two-atom system, and write the atomic correlation functions in terms of the density matrix elements of the collective system as

$$\begin{aligned}
 \langle S_1^+ S_1^- \rangle + \langle S_2^+ S_2^- \rangle &= \varrho_{ss} + \varrho_{aa} + 2\varrho_{ee} , \\
 \langle S_1^+ S_2^- \rangle &= \frac{1}{2} (\varrho_{ss} - \varrho_{aa} + \varrho_{as} - \varrho_{sa}) , \\
 \langle S_1^+ S_2^+ S_1^- S_2^- \rangle &= \varrho_{ee} ,
 \end{aligned} \tag{3.63}$$

where ϱ_{ii} ($i = a, s, e$) are the populations of the collective states and $\varrho_{sa}, \varrho_{as}$ are the coherences between the symmetric and antisymmetric states.

From the relations (2.135) and (3.63), we find that in terms of the density matrix elements the first-order correlation function can be written as

$$\begin{aligned}
G^{(1)}(\mathbf{R}, t) = & \gamma v(\mathbf{R}) \{ 2\varrho_{ee}(t) + \varrho_{ss}(t) + \varrho_{aa}(t) \\
& + [\varrho_{ss}(t) - \varrho_{aa}(t)] \cos(k\bar{\mathbf{R}} \cdot \mathbf{r}_{21}) \\
& + i[\varrho_{sa}(t) - \varrho_{as}(t)] \sin(k\bar{\mathbf{R}} \cdot \mathbf{r}_{21}) \} , \quad (3.64)
\end{aligned}$$

and the second-order correlation function (2.136) takes the form

$$\begin{aligned}
G^{(2)}(\mathbf{R}_1, t; \mathbf{R}_2, t) = & 4\gamma^2 v(\mathbf{R}_1) v(\mathbf{R}_2) \\
& \times \varrho_{ee}(t) \{ 1 + \cos[k(\bar{\mathbf{R}}_1 - \bar{\mathbf{R}}_2) \cdot \mathbf{r}_{21}] \} . \quad (3.65)
\end{aligned}$$

It is seen from (3.64) that the first-order correlation function can exhibit an interference pattern only if $\varrho_{ss} \neq \varrho_{aa}$ and/or $\text{Im}(\varrho_{sa}) \neq 0$. This happens when the matrix elements $\langle e_1 | \otimes \langle g_2 | \varrho | e_2 \rangle \otimes | g_1 \rangle$ and $\langle g_1 | \otimes \langle e_2 | \varrho | g_2 \rangle \otimes | e_1 \rangle$ are nonzero, i.e. when there are nonzero coherences between the atoms. Note that the second-order correlation function is independent of the populations of the entangled states $\varrho_{ss}, \varrho_{aa}$ and the coherences, and exhibits an interference pattern when $\varrho_{ee}(t) \neq 0$.

3.4.1 Interference Pattern with Two Atoms

We now examine some specific processes in which one could create unequal populations of the $|s\rangle$ and $|a\rangle$ states. Consider first the simple process of spontaneous emission from two identical atoms, with initially only one atom excited. In this case, $\varrho_{ee}(0) = 0$ and $\varrho_{ss}(0) = \varrho_{aa}(0) = \varrho_{sa}(0) = \varrho_{as}(0) = 1/2$. In order to find the time evolution of the first-order correlation function, we will use the master equation (2.99) and find the time evolution of the relevant density matrix elements. From the master equation (2.99) with $\Omega_1 = \Omega_2 = 0$, we find that $\varrho_{sa}(t) = \varrho_{as}(t) = 0$ for all t , and the time evolution of the populations $\varrho_{ss}(t)$ and $\varrho_{aa}(t)$ is given by

$$\begin{aligned}
\varrho_{ss}(t) &= \varrho_{ss}(0) \exp[-(\gamma + \gamma_{12})t] , \\
\varrho_{aa}(t) &= \varrho_{aa}(0) \exp[-(\gamma - \gamma_{12})t] . \quad (3.66)
\end{aligned}$$

Since the populations decay with different rates, the symmetric state decays with an enhanced rate $\gamma + \gamma_{12}$, whereas the antisymmetric state decays with a reduced rate $\gamma - \gamma_{12}$, and the population $\varrho_{aa}(t)$ is larger than $\varrho_{ss}(t)$ for all $t > 0$. Hence, an interference pattern can be observed in the first-order correlation function for $t > 0$. Note that this effect arises from the presence of the interatomic interactions ($\gamma_{12} \neq 0$). Thus, for two independent atoms the populations decay with the same rate resulting in the disappearance of the interference pattern.

When the atoms are driven by a coherent laser field, an interference pattern can be observed even for large distances between the atoms [58]. To show this, consider two identical atoms driven by a laser field propagating in the direction perpendicular to the interatomic axis ($\mathbf{k}_L \perp \mathbf{r}_{21}$). In this case,

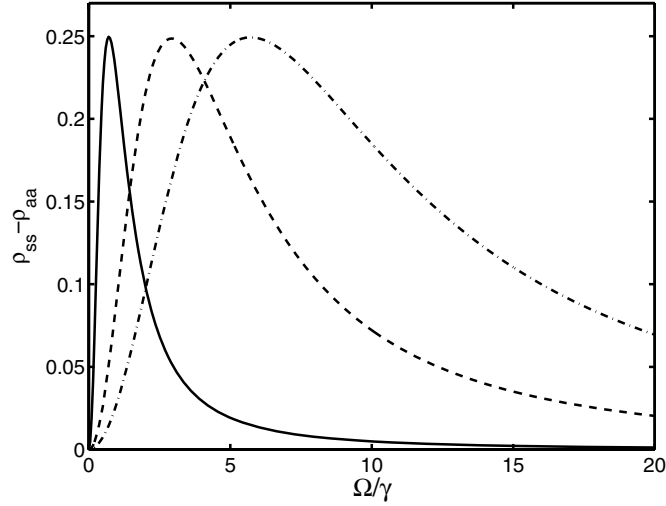


Fig. 3.7. The steady-state population difference $\rho_{ss} - \rho_{aa}$ as a function of the Rabi frequency Ω for $r_{21} = 5\lambda_0$ and different Δ_L : $\Delta_L = 0$ (solid line), $\Delta_L = 2\gamma$ (dashed line), and $\Delta_L = 4\gamma$ (dashed-dotted line)

the master equation (2.99) leads to the following steady-state values of the relevant density matrix elements

$$\begin{aligned}\varrho_{ee} &= \varrho_{aa} = \frac{\Omega^4}{\mathcal{W}}, \\ \varrho_{ss} &= \frac{\Omega^4 + 2\Omega^2(\gamma^2 + 4\Delta_L^2)}{\mathcal{W}}, \\ \varrho_{as} &= \varrho_{sa} = 0,\end{aligned}\tag{3.67}$$

where

$$\mathcal{W} = 4\Omega^4 + (\gamma^2 + 4\Delta_L^2) \left[4\Omega^2 + (\gamma + \gamma_{12})^2 + 4(\Delta_L - \Lambda_{12})^2 \right]. \tag{3.68}$$

It is evident from (3.67) that $\varrho_{ss} > \varrho_{aa}$ even in the absence of the interatomic interaction: ($\gamma_{12} = \Lambda_{12} = 0$). Hence, the first-order correlation function can exhibit an interference pattern, even for large distances between the atoms. In this case the interference pattern results from the coherent synchronization of the oscillations of the atomic dipole moments by the constant coherent phase of the driving laser field. In contrast, the second-order correlation function can exhibit an interference pattern for an arbitrary excitation process. The only requirement is to produce a nonzero population in the state $|e\rangle$.

Figure 3.7 shows the steady-state population difference $\varrho_{ss} - \varrho_{aa}$ as a function of the Rabi frequency for a large interatomic separation $r_{21} = 5\lambda_0$ and different detunings Δ_L . The population difference is large for weak driving fields, and reduces to zero for $\Omega \gg \gamma$. This indicates that no interference pattern is observed when the atoms are driven by a strong laser field. For

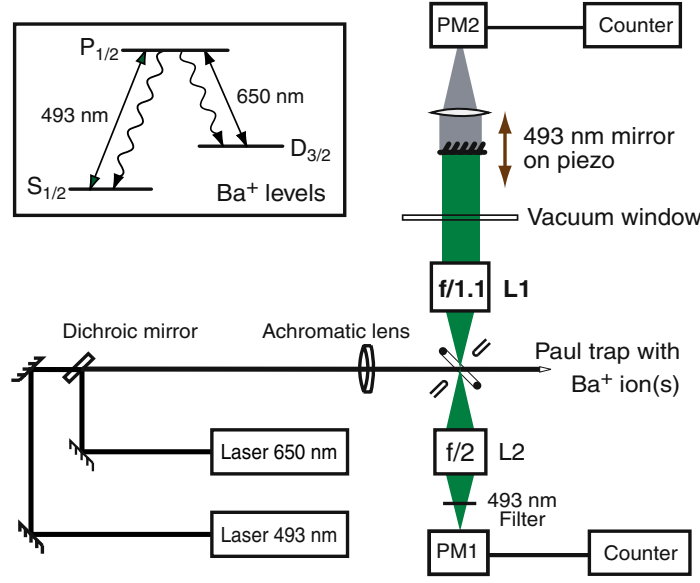


Fig. 3.8. Schematic diagram of the Eschner et al. experiment to observe the interference pattern in the fluorescence field emitted from a barium ion trapped at a fixed distance from the mirror. The insert shows the relevant energy levels of the ion. From J. Eschner, Ch. Raab, F. Schmidt-Kaler, R. Blatt: *Nature* **413**, 495 (2001), with permission

moderate Rabi frequencies, $\Omega \approx \gamma$, the interference pattern may be improved by detuning the laser field from the atomic resonance. This is easy to understand. For a weak driving field, the fluorescence field is predominantly composed of an elastic component and therefore the atoms behave as point sources of coherent light producing an interference pattern. Under strong excitation the fluorescence field is mostly composed of the incoherent part and consequently there is no interference pattern. Kochan et al. [59] have shown that the interference pattern of the strongly driven atoms can also be improved by placing the atoms inside an optical cavity. The coupling of the atoms to the cavity mode induces atomic correlations which improve the fringe visibility.

3.4.2 Experimental Observation of the Interference Pattern in a Two-Atom System

The interference pattern in the first-order correlation function was studied experimentally by Eschner et al. [60]. They observed interference fringes in the fluorescence intensity from a barium Ba^+ ion trapped at a fixed distance from a mirror. As we have shown in Sect. 3.3, this system is formally equivalent to a system of two atoms (or ions) separated by $2r_z$, where r_z is the distance of the atom (ion) from the mirror. The apparatus and partial level scheme of the Ba^+ ion are shown in Fig. 3.8. In the experiment, a single barium ion was confined in a Paul trap and cooled by narrow band lasers

at 493 nm and 650 nm tuned to the $^2S_{1/2} \rightarrow ^2P_{1/2}$ and $^2D_{3/2} \rightarrow ^2P_{1/2}$ transitions, respectively. A macroscopic lens L1 was employed to achieve small distances of the ion from the mirror and to enhance the effect of the mirror in the neighborhood of the ion. The mirror was located 25 cm away from the ion and reflected only the 493 nm part of the fluorescence field. The 650 nm part was completely transmitted through the mirror and recorded by the photomultiplier PM2. The lens L1 was located 12 mm from the ion such that it created an image of the mirror at the position of the ion, effectively changing the ion-mirror distance. The reflected field together with the field emitted by the ion were collected by the second lens L2 and detected by a photomultiplier PM1. In order to trace out the dependence of the fluorescence intensity on the distance of the ion from the mirror, the position of the mirror was varied.

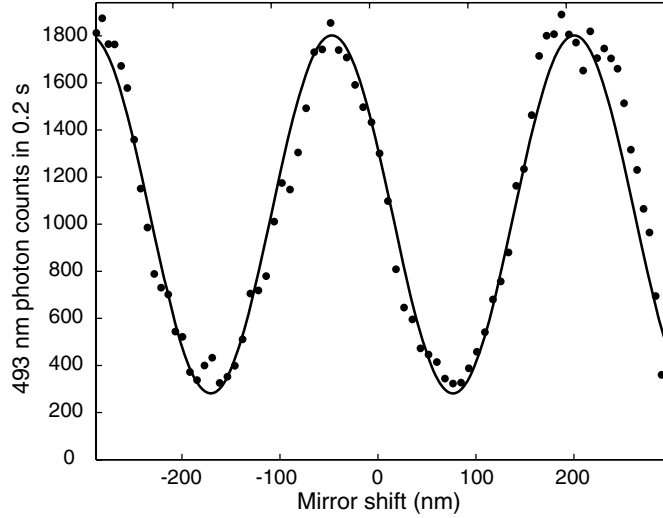


Fig. 3.9. Experimentally observed interference pattern as a function of the mirror shift. The solid line is the prediction of the theory. From J. Eschner, Ch. Raab, F. Schmidt-Kaler, R. Blatt: *Nature* **413**, 495 (2001), with permission

Figure 3.9 shows the experimental results for the intensity of the 493 nm fluorescence field detected by the PM2 as a function of the mirror shift. The solid line indicates the prediction of the theory and its shape is determined by the $\cos(2kr_z)$ function. The theoretically predicted interference fringes are clearly in agreement with measurement. In addition, it was observed that the visibility of the interference pattern (the magnitude of the oscillations) was significantly reduced when the Rabi frequency of the laser field driving the 493 nm transition was increased from a value below saturation to threefold saturation. This experimental observation confirms the theoretical prediction, shown in Fig. 3.7, that the visibility of the interference fringes decreases with increased Rabi frequency of the driving field.

In a modified version of the experiment, Eschner et al. [60] trapped two ions and adjusted the mirror such that the mirror image of each ion was superimposed with the real image of the other ion. This system is formally equivalent to a four-atom system, but the adjustment of the images allowed them to measure direct coherence between the trapped ions maintained by the mirror. Indeed, the experimental team observed interference fringes with the same period of oscillation as that for the single ion. The experimental results are shown in Fig. 3.10. Evidently, the fluorescence intensity from two trapped

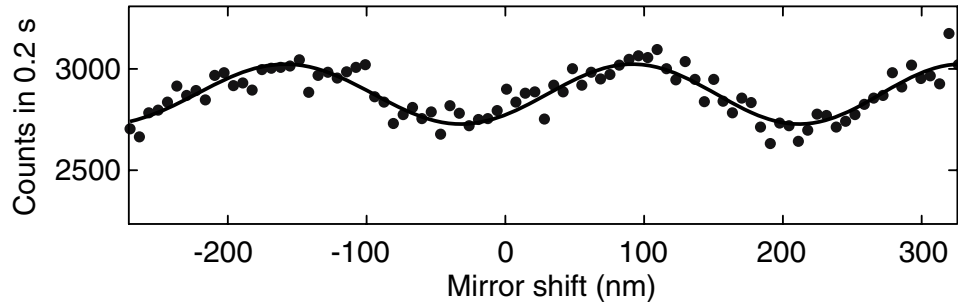


Fig. 3.10. Experimentally observed interference pattern with two trapped ions. From J. Eschner, Ch. Raab, F. Schmidt-Kaler, R. Blatt: *Nature* **413**, 495 (2001), with permission

ions exhibits interference fringes. However, the amplitude of the oscillations is reduced compared to that of a single ion. It was explained that the reduction of the amplitude of the oscillations was mainly due to thermal motion and the repulsive interaction of the ions in the Paul trap.

In summary, the experiment clearly demonstrated that light scattered by a driven ion and its mirror image, that is, light scattered by two coherently driven atoms, is coherent and can therefore exhibit an interference pattern. The experimental observation agrees perfectly with the above theoretical analysis involving the simplified system of two identical two-level atoms. A complete theoretical analysis of the experimental system involving a three-level Lambda-type atom, was presented by Dorner and Zoller [61] and Beige et al. [62], who arrived at the same conclusions as the above predictions based on properties of two two-level atoms.

3.5 Quantum Beats

To investigate further the role of quantum interference in the dynamics of multi-level and multi-atom systems, we consider the phenomenon of quantum beats, the most familiar of oscillatory phenomena. One could state that whenever two sources of quasimonochromatic radiation have slightly different center frequencies, there is the possibility of observing in their combined (superposed) field a periodic modulation of intensity with modulation frequency

given by the difference of the two source frequencies. Though this condition is a necessary one for quantum beats, it is not in general sufficient, since the phenomenon of quantum beats requires a coherence between the radiating sources. The required coherence between two completely independent sources can be induced by external coherent fields, for example when two, initially independent, atomic states are coupled by a short coherent pulse, which introduces a fixed phase relation between the initial atomic excitations. The coherences can be induced even when the initial atomic excitations have no special phase relations. In this case the coherences can develop spontaneously during the radiation process because photons emitted spontaneously by each source of radiation can be absorbed by the other source, forcing the source to oscillate at the frequency of the absorbed radiation. The oscillations induced in each source are partially coherent with their own spontaneous oscillations and can thus lead to quantum beats with well-defined phases.

The quantum beats just described are observed in the average radiation intensity at different space-time points and involve the first-order correlation functions of the superposed fields. However, there remain a number of quantum beat phenomena associated with the superposition of radiation fields which are observable even with completely independent radiation sources. These phenomena are observed in the intensity–intensity correlations and involve the second-order correlation functions of the combined fields.

The subject of quantum beats has provided an important method to study atomic spectra and various quantum mechanical interactions that lead to different types of splittings and shifts of the atomic energy levels [63]. Therefore, we will introduce the theory of quantum beats in multilevel atomic systems and next discuss them in detail in simple specific models, such as three-level atoms and two nonidentical two-level atoms. Our interest will be centered principally on quantum beats in spontaneous emission from an initially prepared excited state and from incoherently driven atomic systems. For this reason, we shall apply the master equations (2.75) and (2.99) to calculate the time-dependent first and second-order correlation function of the atomic dipole operators.

3.5.1 Theory of Quantum Beats in Multi-Level Systems

To describe the quantum beats that can occur in spontaneous emission we require two radiating systems of slightly different frequencies. When these systems are coupled to the electromagnetic vacuum field, they radiate spontaneously and their radiation field decays exponentially. At the same time they exert a strong dynamical influence on one another through their coupling to the electromagnetic modes of the radiation field. This influence can be felt, as we shall show, either through the spontaneously induced superpositions of the energy states of the systems or through the beating of their amplitudes.

The interest in quantum beats in radiation from multilevel systems lies in their direct connection with quantum interference between the amplitudes of different atomic transitions. As with the Young's double slit interferometer, the uncertainty in nondegenerate atomic transitions leads to interference between the amplitudes of the two atomic transitions, whose oscillations are analogous to quantum beats. Another intrinsic feature of quantum beats in the radiation from a multi-level system is that they provide information about the internal structure of the system, such as the splittings and shifts of the energy levels. The frequency of quantum beats oscillations is equal to the frequency difference between the two atomic transitions and their experimental observation provides a direct method to study the internal energy structure of an atom. Therefore, we will illustrate how the interference terms in the master equation of a three-level atom and two nonidentical atoms result in quantum beats in the time and spatial evolutions of the intensity and the second-order correlation functions of the radiated field.

Quantum beats that result from quantum interference between two atomic transitions can only occur if the atom is left in a final state devoid of information as to which transition the atom made. Otherwise, at some time, conceivably much later, one could probe the populations of the atomic energy levels to determine along which path the transition occurred. The discussion of quantum beats in atomic systems has centered around two types of atoms: one in which the transitions occur between each of two or more closely spaced upper levels and a single ground level (type I), and another in which the transitions occur between a common upper level and each of two or more closely spaced lower levels (type II). An example of type I and type II atoms is shown in Fig. 3.11.

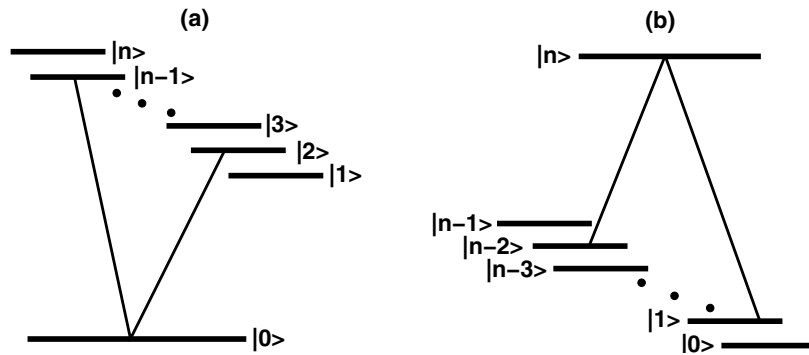


Fig. 3.11. Energy-level structure of (a) type I and (b) type II atoms

A qualitative difference in the theoretical prediction of beats in spontaneous emission from the two types of atoms was first noted by Breit [64]. If the upper levels of a type I atom are initially prepared in a linear superposition, quantum beats in the intensity of the emitted field are predicted. This is easily understood, since both transitions lead to the same final state,

a detector monitoring the population of the ground state cannot determine along which transition path the atom decayed. On the other hand, no beats are predicted from excitation and decay of type II atoms. Again, this is easily understood: the possible transition paths in type II atoms are distinguishable by a subsequent experiment designed to measure the populations of the lower atomic levels. The result of the experiment would then tell us by which transition the atom decayed. The difference between these two types of atoms has been the subject of many experiments.

To illustrate the difference in more detail, consider first a type I atom, a three-level Vee-type atom with two upper levels $|1\rangle$ and $|2\rangle$, and the ground level $|0\rangle$. The transitions $|1\rangle \rightarrow |0\rangle$ and $|2\rangle \rightarrow |0\rangle$ are dipole allowed and occur with frequencies ω_1 and ω_2 , respectively, while the transition $|1\rangle \rightarrow |2\rangle$ is forbidden in the electric dipole approximation. This does not exclude the possibility of exchanging the population between the upper states through other processes not involving the atomic dipole moments. The atom initially excited, e.g. by a short laser pulse, into one of the upper levels or into a linear superposition of the levels will quickly decay into its ground level emitting a photon of a frequency ω_1 or ω_2 . We may then detect the photon by measuring the intensity of the radiation field falling on a detector located at a point \mathbf{R} . The radiation intensity registered by the detector is given by (2.144), and for the Vee-type atom takes the form

$$I(t) = \gamma_1 \langle S_1^+(t) S_1^-(t) \rangle + \gamma_2 \langle S_2^+(t) S_2^-(t) \rangle + 2\gamma_{12} \text{Re} \{ \langle S_1^+(t) S_2^-(t) \rangle \} . \quad (3.69)$$

Since $S_i^\pm \approx S_i^\pm \exp(\mp i\omega_i t)$ ($i = 1, 2$), and $S_1^+ S_2^- = |1\rangle\langle 2| = A_{12}$, the radiation intensity can be written as

$$I(t) = \gamma_1 \langle S_1^+ S_1^- \rangle + \gamma_2 \langle S_2^+ S_2^- \rangle + 2\gamma_{12} \text{Re} \{ \langle A_{12} \rangle \} \cos(\Delta t) = I_1 + I_2 + 2\gamma_{12} \text{Re} \{ \langle A_{12} \rangle \} \cos(\Delta t) , \quad (3.70)$$

where $\Delta = \omega_2 - \omega_1$ is the frequency difference between the upper atomic levels, and $I_i = \gamma_i \langle S_i^+ S_i^- \rangle$ is the intensity of the field emitted on the i th transition.

The radiation intensity (3.70) clearly shows oscillations (quantum beats) at the frequency difference Δ , and there are no quantum beats if there is no quantum interference ($\gamma_{12} = 0$) between the transitions. In the later case, the radiation intensity is just the sum of the radiation intensities of the individual $|1\rangle \rightarrow |0\rangle$ and $|2\rangle \rightarrow |0\rangle$ transitions. Note the analogy of (3.70) with the two-slit interference intensity (1.6). We see similar mathematical structures: one term describing a field intensity from one slit, a second describing a field intensity from the other, and finally an interference term involving their product. Therefore, quantum beats are due to the interference between amplitudes describing the two decay paths.

The intensity can be written in terms of the density matrix elements of the system, and from (3.70), we find that in the case $\gamma_1 = \gamma_2 = \gamma$ and perfect

interference, $\gamma_{12} = \gamma$, the intensity is simply proportional to the population of the symmetric state $|s\rangle$, as

$$I(t) = \gamma \varrho_{ss}(t) . \quad (3.71)$$

To see how the interference terms depend on the configuration of the atomic levels, we now consider a type II atom. For example, a three-level Lambda-type atom with the upper level $|2\rangle$ and two lower levels $|0\rangle$ and $|1\rangle$ with the dipole allowed transitions $|2\rangle \rightarrow |1\rangle$ and $|2\rangle \rightarrow |0\rangle$. An identical procedure to the above leads to a quantum interference term of the form

$$2\gamma_{12} \text{Re} \{ \langle S_1^+ S_2^- \rangle \} \cos(\Delta t) . \quad (3.72)$$

Since $S_1^+ S_2^- = |2\rangle\langle 0|2\rangle\langle 1|$ and the atomic states are orthogonal, $\langle 0|2\rangle = 0$, the interference term vanishes. Therefore, there are no quantum beats in this system, and this conclusion holds regardless of whether the measurement of the final state of the system is actually carried out. In this case the intensity is given by

$$I(t) = \gamma_1 \langle S_1^+ S_1^- \rangle + \gamma_2 \langle S_2^+ S_2^- \rangle , \quad (3.73)$$

which is the sum of the intensities of the two atomic transitions, or in terms of the density matrix elements

$$I(t) = (\gamma_1 + \gamma_2) \varrho_{22}(t) , \quad (3.74)$$

showing that the intensity is simply proportional to the population of the upper level. This was to be expected as the initially excited atom decays to one of its ground states and then residual information exists after the emission process as to which transition the atom made, $|2\rangle \rightarrow |1\rangle$ or $|2\rangle \rightarrow |0\rangle$. Mathematically, the residual information left in the system after the decay results from the orthogonality of the two possible final states of the atom.

In the type II atom considered above, the residual information was in the atomic ground levels. Of course, this does not imply that it is impossible to observe quantum beats in a type II atom. In Sect. 3.5.2, we will show that quantum beats can be observed in the radiation intensity from a type II atom continuously driven by an incoherent field. In this case, the incoherent field drives the atom into a linear superposition of the atomic levels, and a detector cannot distinguish which way the atom decays to the lower levels. In addition, we will show that quantum beats can be observed in different processes involving higher-order correlation functions such as the intensity–intensity correlations. This type of quantum beats can be observed even if the first-order correlations disappear. We will investigate this type of quantum beats in more detail in Sect. 3.5.5.

3.5.2 Quantum Beats in the Radiation Intensity from a Multi-Level Atom

We investigate in detail the phenomenon of quantum beats in examples of the radiation emitted from a type I system (Vee-type atom), and from a type II system (Lambda-type atom). In both examples, we will consider the time evolution of the radiation intensity for two different sets of initial conditions at $t = 0$. In the first example, the atom is assumed to be prepared in one of its excited levels or in a linear superposition of the levels. In the second example, the atom is assumed to be prepared in one of the lower levels, or in a superposition of the levels. However, we will assume that the Lambda-type atom is continuously driven by an incoherent field.

Quantum Beats in the Decay of a Type I System

The radiation field emitted by an atom results from spontaneous emission from initially excited atomic levels. Consider the process of spontaneous emission from a Vee-type atom composed of two excited states $|1\rangle$, $|2\rangle$ and the ground state $|0\rangle$. For simplicity, we assume that spontaneous emission occurs from the excited states to the ground state with the same decay rates $\gamma_1 = \gamma_2 = \gamma$, and the spontaneous transitions between the excited states are forbidden in the electric dipole approximation.

We start from the master equation (2.69), which in the absence of the driving field ($\Omega_1 = \Omega_2 = 0$), leads to the following equations of motion for the density matrix elements

$$\begin{aligned}\dot{\varrho}_{11} &= -\gamma\varrho_{11} - \frac{1}{2}\gamma_{12}(\varrho_{12} + \varrho_{21}) , \\ \dot{\varrho}_{22} &= -\gamma\varrho_{22} - \frac{1}{2}\gamma_{12}(\varrho_{12} + \varrho_{21}) , \\ \dot{\varrho}_{12} &= -(\gamma + i\Delta)\varrho_{12} - \frac{1}{2}\gamma_{12}(\varrho_{11} + \varrho_{22}) , \\ \dot{\varrho}_{21} &= -(\gamma - i\Delta)\varrho_{21} - \frac{1}{2}\gamma_{12}(\varrho_{11} + \varrho_{22}) ,\end{aligned}\tag{3.75}$$

where, for simplicity, we have ignored the small coherent coupling terms $\delta_{12}^{(\pm)}$.

The time evolution of the density matrix elements depends on the frequency splitting Δ , which introduces oscillations in the coherence between the upper levels. This time evolution also depends on the cross-damping γ_{12} which results from the quantum interference (coherences) between the two atomic transitions.

We solve the set of coupled equations (3.75) for maximal quantum interference $\gamma_{12} = \gamma$ and the initial condition that at time $t = 0$ a short laser pulse is applied to the system to produce the desired population of the upper levels. By proper state preparation, any set of initial conditions can be achieved

and the general solution for the total intensity of the radiation field of such a system can be written as [65]

$$\begin{aligned} I(t) &= \gamma [\varrho_{11}(t) + \varrho_{22}(t) + 2\text{Re}\varrho_{12}(t)] \\ &= \frac{\gamma}{2\delta^2} \left[-2A_0\Delta e^{-\gamma t} + B_0(\gamma - \delta)e^{-(\gamma - \delta)t} \right. \\ &\quad \left. + D_0(\gamma + \delta)e^{-(\gamma + \delta)t} \right], \end{aligned} \quad (3.76)$$

where

$$\begin{aligned} A_0 &= \{\Delta [\varrho_{11}(0) + \varrho_{22}(0)] + i\gamma [\varrho_{12}(0) - \varrho_{21}(0)]\}, \\ B_0 &= \{\gamma [\varrho_{11}(0) + \varrho_{22}(0)] - (\delta + i\Delta) \varrho_{21}(0) - (\delta - i\Delta) \varrho_{12}(0)\}, \\ D_0 &= \{\gamma [\varrho_{11}(0) + \varrho_{22}(0)] + (\delta - i\Delta) \varrho_{21}(0) + (\delta + i\Delta) \varrho_{12}(0)\}, \end{aligned} \quad (3.77)$$

with $\delta = \sqrt{\gamma^2 - \Delta^2}$. Depending on the splitting Δ , the parameter δ can be a real or a complex number. A threshold at which the parameter δ changes character is $\Delta = \gamma$. Below the threshold, $\Delta < \gamma$, the parameter δ is real and contributes to the damping rates of the system. In this case the intensity (3.76) exhibits pure exponential decay with three different decay rates, and no quantum beats are present. Above the threshold, $\Delta > \gamma$, and then the parameter δ is a purely imaginary complex number. In this case, the intensity shows quantum-beat oscillations superimposed on a smooth exponential decay. The frequency of the oscillations depends on the ratio γ/Δ and reduces to Δ for $\Delta \gg \gamma$. In the following, we concentrate on the case of $\Delta > \gamma$, so that quantum beats occur.

The nature of quantum beats is very dependent on the initial conditions. For example, if the atom is initially prepared in one of the excited states

$$\varrho_{11}(0) = 1, \quad \varrho_{22}(0) = \varrho_{12}(0) = \varrho_{21}(0) = 0, \quad (3.78)$$

or in a uniform incoherent mixture of the excited states

$$\varrho_{11} = \varrho_{22}(0) = \frac{1}{2}, \quad \varrho_{12}(0) = \varrho_{21}(0) = 0, \quad (3.79)$$

the radiation intensity (3.76) takes a simple form

$$I(t) = \frac{\gamma}{|\delta|^2} [\Delta^2 - \gamma^2 \cos(|\delta|t) - \gamma|\delta| \sin(|\delta|t)] e^{-\gamma t}, \quad (3.80)$$

where $|\delta| = \sqrt{\Delta^2 - \gamma^2}$.

The intensity shows a sinusoidal modulation (quantum beats) superimposed on the exponential decay of the initial population. Note that the amplitude of the modulation is proportional to $1/|\delta|$ and decreases with increasing Δ .

When the atom is initially prepared in the symmetric superposition state $|s\rangle = (|1\rangle + |2\rangle)/\sqrt{2}$, the intensity (3.76) reduces to

$$I(t) = \frac{2\gamma}{|\delta|^2} \left[|\delta| \cos\left(\frac{1}{2}|\delta|t\right) - \gamma \sin\left(\frac{1}{2}|\delta|t\right) \right]^2 e^{-\gamma t}, \quad (3.81)$$

and with the atom initially prepared in the antisymmetric superposition state $|a\rangle = (|1\rangle - |2\rangle)/\sqrt{2}$, the intensity (3.76) takes the form

$$I(t) = \gamma \left(\frac{\Delta}{|\delta|} \right)^2 [1 - \cos(|\delta|t)] e^{-\gamma t}. \quad (3.82)$$

The intensity here also displays quantum beats and even more interestingly, the amplitude of the modulation decreases slowly with increasing Δ and attains a constant value for $\Delta \gg \gamma$. In order to understand why the amplitude of the oscillations depends strongly on the initial conditions, it is helpful to recall the relationship between interference and coherence. When the atom starts from one of the excited levels or from an incoherent mixture of the excited levels, there is no coherence between the two atomic transitions, and then spontaneous transitions occur independently until the coherence builds up during the spontaneous emission. However, if the atom starts from a linear superposition of the excited levels, there is a nonzero initial coherence between the transitions, which is manifested in a large amplitude of the oscillations.

An additional interesting effect of quantum interference is that the radiation intensity can be completely quenched at some discrete times. For the initial antisymmetric state, the quenching occurs approximately at times $t_q = 2n\pi/|\delta|$, ($n = 0, 1, 2, \dots$), whereas for the initial symmetric state the quenching occurs at $t_q = (2n + 1)\pi/|\delta|$, ($n = 0, 1, 2, \dots$).

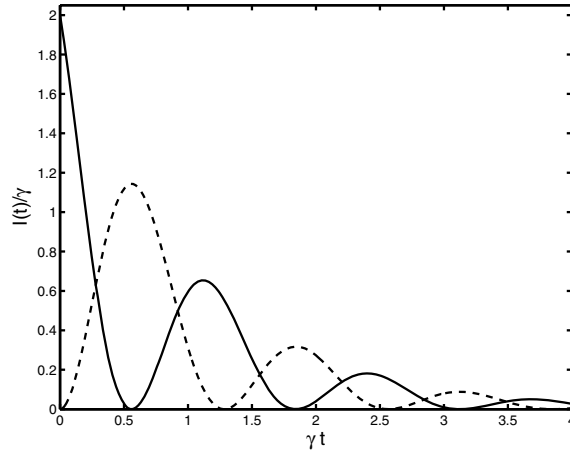


Fig. 3.12. Time evolution of the radiation intensity for $\Delta = 5\gamma$ and two different initial conditions: $\varrho_{ss}(0) = 1$ (solid line), $\varrho_{aa}(0) = 1$ (dashed line)

Figure 3.12 shows the time evolution of the radiation intensity for two different initial atomic states at $t = 0$. As predicted by (3.80)–(3.82), the intensity exhibits quantum beats, and intensity quenching occurs. Moreover,

the oscillations are shifted in phase: the maximum of the intensity for the initial state $|s\rangle$ corresponds to the quenching of the intensity for the initial state $|a\rangle$, and vice versa.

The transient behavior of the intensity and, in particular, the intensity quenching can be explained in terms of the superposition states induced by quantum interference. Following the procedure outlined in Sect. 3.1, we introduce superposition states $|s\rangle$ and $|a\rangle$ and find from (3.75) the following equations of motion for the populations of the superposition states

$$\begin{aligned}\dot{\varrho}_{ss} &= -\frac{1}{2}(\gamma + \gamma_{12})\varrho_{ss} - \frac{1}{2}i\Delta(\varrho_{sa} - \varrho_{as}) , \\ \dot{\varrho}_{aa} &= -\frac{1}{2}(\gamma - \gamma_{12})\varrho_{aa} + \frac{1}{2}i\Delta(\varrho_{sa} - \varrho_{as}) .\end{aligned}\quad (3.83)$$

A number of interesting conclusions follow from (3.83). As predicted by the general analysis of Sect. 3.1, the superposition states decay at different rates: the symmetric state decays with an enhanced rate $(\gamma + \gamma_{12})$, whereas the antisymmetric state decays at a reduced rate $(\gamma - \gamma_{12})$. For maximal quantum interference, $\gamma_{12} = \gamma$, and then the antisymmetric state does not decay at all. In this case the antisymmetric state can be regarded as a *dark state* in the sense that the state is decoupled from the environment. Secondly, we note from (3.83) that the state $|a\rangle$ is coupled to the state $|s\rangle$ through the splitting Δ , which plays here a role similar to the Rabi frequency of the coherent interaction between the symmetric and antisymmetric states. Consequently, an initial population in the state $|s\rangle$ can be coherently transferred to the non-radiative state $|a\rangle$, and then the intensity quenches at a time t_q corresponding to half of the Rabi cycle between $|s\rangle$ and $|a\rangle$. For $t > t_q$, the intensity reappears again and attains a maximum value at a time corresponding to the Rabi cycle of the $|a\rangle \rightarrow |s\rangle$ transition.

For the atom initially prepared in the antisymmetric state, the radiation intensity is zero for $t = 0$. This reflects the fact that the antisymmetric state does not decay. However, as time develops, the intensity builds up and attains the maximum at a time corresponding to half of the Rabi cycle between $|a\rangle$ and $|s\rangle$. The physical understanding of the delayed emission from the antisymmetric state can be achieved by considering the equations of motion (3.83) for the populations of the superposition states. The intensity builds up in time because the coherent coupling Δ transfers the population from $|a\rangle$ to $|s\rangle$, and in a time equal to half of the Rabi cycle of the $|a\rangle \rightarrow |s\rangle$ transition, all the population is in the symmetric state which rapidly decays to the ground state.

Quantum Beats in a Continuously Driven Type II System

In Sect. 3.5.1, we have shown that no quantum beats can be observed in a type II atom initially prepared in its upper level and spontaneously decaying

to one of its lower levels. We show here that quantum beats can be observed in the radiation intensity from a type II atom if the atom is continuously driven by an incoherent field [66].

To illustrate this, consider a Lambda-type atom with the upper level $|2\rangle$ and two lower energy levels $|0\rangle$ and $|1\rangle$. The atom is continuously driven by an incoherent thermal field of intensity N . As before, we assume that spontaneous emission occurs from the upper level to the lower levels with the same decay rates $\gamma_1 = \gamma_2 = \gamma$. We include the incoherent driving field to obtain a continuous emission of photons and to show that quantum beats can be observed even if the atom is driven by an incoherent field. Quantum beats in type II atoms can be attributed to the fact that atomic transitions are correlated through the coupling to the vacuum field ($\gamma_{12} \neq 0$) which, in turn, can be associated with the fact that the two excitation pathways $|0\rangle \rightarrow |2\rangle$ and $|1\rangle \rightarrow |2\rangle$ are not distinguishable when they are coupled through the cross-damping term γ_{12} . In this case, we use the master equation (2.69) and find the following equations of motion for the density matrix elements

$$\begin{aligned}\dot{\varrho}_{11} &= -N\gamma\varrho_{11} + (N+1)\gamma\varrho_{22} - \frac{1}{2}N\gamma_{12}(\varrho_{10} + \varrho_{01}) , \\ \dot{\varrho}_{22} &= N\gamma - (3N+2)\gamma\varrho_{22} + N\gamma_{12}(\varrho_{10} + \varrho_{01}) , \\ \dot{\varrho}_{10} &= -\frac{1}{2}N\gamma_{12} - \left(\frac{1}{2}N\gamma - i\Delta\right)\varrho_{10} + \frac{1}{2}\gamma_{12}(3N+2)\varrho_{22} , \\ \dot{\varrho}_{01} &= -\frac{1}{2}N\gamma_{12} - \left(\frac{1}{2}N\gamma + i\Delta\right)\varrho_{01} + \frac{1}{2}\gamma_{12}(3N+2)\varrho_{22} ,\end{aligned}\quad (3.84)$$

where, for simplicity, we have ignored the coherent coupling terms $\delta_{12}^{(\pm)}$.

We solve the set of equations of motion (3.84) for $\varrho_{22}(t)$ with two different initial conditions to see whether one can observe quantum beats in the radiation intensity from the type II atom where the interference term is zero. To keep the mathematical complications to a minimum, we solve the equations for perfect correlation between the atomic transitions, $\gamma_{12} = \gamma$, and large splittings $\Delta \gg \gamma$, which allow us to obtain simple analytical expressions for the time evolution of the density matrix elements.

The evolution of the population $\varrho_{22}(t)$ in time generally consists of oscillatory and non-oscillatory components. The degree of oscillatory behavior is a sensitive function of the initial atomic conditions. In order to study this dependence, we first consider the time evolution of the population with an initial condition in which the atom was in the state $|0\rangle$ at $t = 0$, i.e. $\varrho_{00}(0) = 1$. In this limit, the time evolution of the population of the upper level is given by

$$\begin{aligned}\varrho_{22}(t) &= \frac{N}{(3N+2)} \left[1 - \left(1 - \frac{N^2\gamma^2}{2\Delta^2} \right) e^{-(3N+2)\gamma t} \right] \\ &\quad + \left(\frac{N\gamma}{\Delta} \right)^2 e^{-\frac{1}{2}N\gamma t} \cos(\Delta t) .\end{aligned}\quad (3.85)$$

For the initial condition of $\varrho_{ss}(0) = 1$, we find from (3.84) that

$$\varrho_{22}(t) = \frac{N}{(3N+2)} \left[1 - e^{-(3N+2)\gamma t} \right] + \frac{N\gamma}{\Delta} e^{-\frac{1}{2}N\gamma t} \sin(\Delta t) . \quad (3.86)$$

From the above solutions and (3.74), it readily follows that the radiation intensity will exhibit quantum beats resulting from the oscillations of the population of the upper level. When the system starts from the ground state $|0\rangle$, the amplitude of the oscillations is rather small, proportional to $1/\Delta^2$, whereas if it starts from the superposition state $|s\rangle$, the amplitude of the oscillations is much larger and proportional to $1/\Delta$. Figure 3.13 shows the time evolution of the radiation intensity for $N = 1, \Delta = 5\gamma$ and two different initial states. We see that the amplitude of the oscillations depends strongly on the initial conditions, and with the initial superposition state $|s\rangle$, the amplitude of the oscillation is more pronounced than for the initial bare state $|0\rangle$.

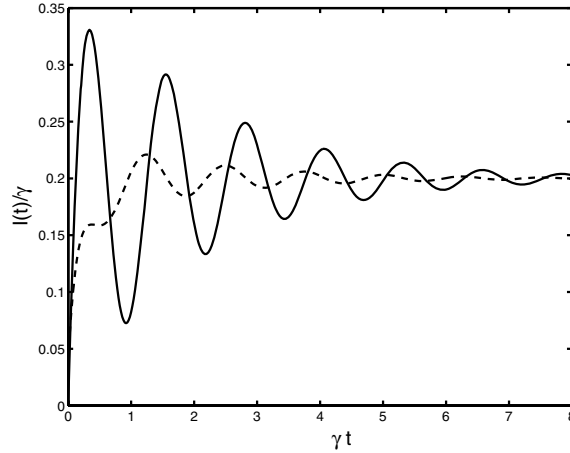


Fig. 3.13. Time evolution of the radiation intensity for $N = 1, \Delta = 5\gamma$, and different initial states: $\varrho_{ss}(0) = 1$ (solid line), $\varrho_{00}(0) = 1$ (dashed line)

Finally, we would like to explain in physical terms why the amplitude of the oscillations strongly depends on the initial conditions. Here it is instructive again to recall the relationship between interference and indistinguishability. There are two transition channels $|0\rangle \rightarrow |2\rangle$ and $|1\rangle \rightarrow |2\rangle$, and with the initial condition of $\varrho_{00}(t) = 1$, the amplitude of the $|0\rangle \rightarrow |2\rangle$ transition is much larger than the amplitude of the $|1\rangle \rightarrow |2\rangle$ transition. This partially destroys the indistinguishability of the two paths resulting in a reduced amplitude of the oscillations. On the other hand, with the initial state $|s\rangle$, both amplitudes contribute equally to the transition probability. With continuous driving of the atomic transitions, the emission time is random and unknown and there is no way to distinguish between the emission paths. This indistinguishability is manifested in an enhanced amplitude of the oscillations.

3.5.3 Quantum Beats in the Radiation Intensity from Two Nonidentical Atoms

The model for quantum beats that we wish to discuss here concerns two separate radiation sources such as two two-level atoms of different transition frequencies [67]. Unlike single-atom quantum beats, where a multi-level atom was initially prepared in a coherent superposition of its excited levels and beating was due to internal interference, here we deal with quantum interference in spontaneous emission from two different atoms. The atoms, as in the case of two isotopes, have slightly different resonance frequencies and/or spontaneous emission rates.

For two nonidentical atoms ($\Delta \neq 0$ and/or $\gamma_1 \neq \gamma_2$) and in the absence of the driving field ($\Omega_i = 0$), the master equation (2.99) leads to a closed set of five equations of motion for the density matrix elements. This set of equations can be written in matrix form as

$$\frac{d}{dt} \mathbf{X}(t) = A \mathbf{X}(t) , \quad (3.87)$$

where $\mathbf{X}(t)$ is a column vector with components

$$\begin{aligned} X_1 &= \langle S_1^+(t) S_1^-(t) \rangle , & X_2 &= \langle S_2^+(t) S_2^-(t) \rangle , \\ X_3 &= \langle S_1^+(t) S_2^-(t) \rangle , & X_4 &= \langle S_2^+(t) S_1^-(t) \rangle , \\ X_5 &= \langle S_1^+(t) S_2^+(t) S_1^-(t) S_2^-(t) \rangle , \end{aligned} \quad (3.88)$$

and A is the 5×5 matrix

$$A = \begin{pmatrix} -\gamma_1 & 0 & v & v^* & 0 \\ 0 & -\gamma_2 & v^* & v & 0 \\ v & v^* & -\zeta & 0 & 2\gamma_{12} \\ v^* & v & 0 & -\zeta^* & 2\gamma_{12} \\ 0 & 0 & 0 & 0 & -2\gamma_0 \end{pmatrix} , \quad (3.89)$$

with $v = -(\gamma_{12} + i\Lambda_{12})/2$, $\zeta = (\gamma_0 - i\Delta)$, and $\gamma_0 = (\gamma_1 + \gamma_2)/2$.

It is seen from (3.89) that the equation of motion for the population ρ_{ee} is decoupled from the remaining four equations. This allows for an exact solution of the set of equations (3.87). To simplify the mathematics, we consider separately the two special cases of $\Delta \neq 0, \gamma_1 = \gamma_2$ and $\Delta = 0, \gamma_1 \neq \gamma_2$, and calculate the time evolution of the total fluorescence intensity, defined in (2.144). We assume that initially ($t = 0$) atom “1” was in its excited state $|1\rangle_1$ and atom “2” was in its ground state $|0\rangle_2$.

The Case $\Delta \neq 0, \gamma_1 = \gamma_2 = \gamma$ and $\Lambda_{12} \gg \Delta$

In this case the atoms have the same spontaneous damping rates but different transition frequencies that, for simplicity, are taken much smaller than the

dipole-dipole interaction potential. In this limit, the approximate solution of (3.87) leads to the following total radiation intensity

$$I(t) = e^{-\gamma t} \left[\frac{\Delta \gamma_{12}}{4\Lambda_{12}} \cos(2wt) + \gamma \cosh(\gamma_{12}t) - \gamma_{12} \sinh(\gamma_{12}t) \right], \quad (3.90)$$

where $w = \sqrt{\Lambda_{12}^2 + \Delta^2}/4$.

From the above equation it is seen that the total radiation intensity exhibits sinusoidal modulation (beats) superimposed on an exponential decay with the rates $\gamma \pm \gamma_{12}$. The amplitude of the oscillations is proportional to Δ and vanishes for identical atoms. The damping rate $\gamma + \gamma_{12}$ describes the spontaneous decay from the state $|s'\rangle$ to the ground state $|g\rangle$, whereas $\gamma - \gamma_{12}$ is the decay rate of the $|a'\rangle \rightarrow |g\rangle$ transition. The frequency $2w$ of the oscillations is equal to the frequency difference between the $|s'\rangle$ and $|a'\rangle$ states. The oscillations reflect the spontaneously induced correlations between the $|s'\rangle \rightarrow |g\rangle$ and $|a'\rangle \rightarrow |g\rangle$ transitions. According to (3.45) the amplitude of the spontaneously induced correlations is equal to $\gamma_{a's'}$, which in the limit of $\Lambda_{12} \gg \Delta$ reduces to $\gamma_{a's'} = \Delta \gamma_{12}/(4\Lambda_{12})$. Hence, the amplitude of the oscillations appearing in (3.90) is exactly equal to the amplitude of the spontaneously induced correlations. Figure 3.14 shows the temporal dependence of the total radiation intensity for interatomic separation $r_{21} = \lambda/12$, $\gamma_1 = \gamma_2$, $\bar{\mu} \perp \bar{r}_{21}$, and different Δ . As predicted by (3.90), the intensity exhibits quantum beats whose amplitude increases with increasing Δ . Moreover, at short times, the intensity can become greater than its initial value $I(0)$. The enhancement of the intensity is known as a *superradiant* behavior and is absent in the case of two identical atoms. Thus, the spontaneously induced correlations between the $|s'\rangle \rightarrow |g\rangle$ and $|a'\rangle \rightarrow |g\rangle$ transitions can induce quantum beats and a superradiant effect in the intensity of the emitted field.

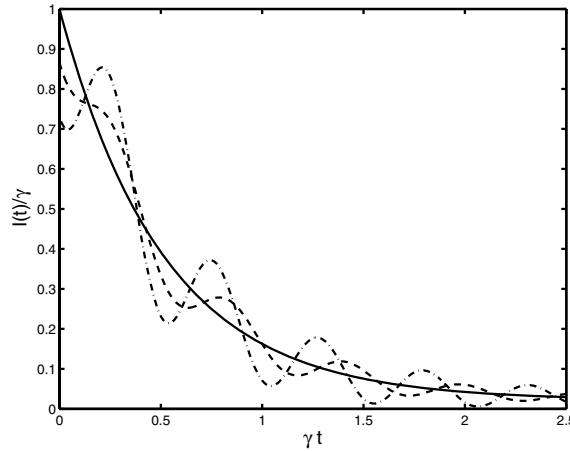


Fig. 3.14. Time evolution of the total radiation intensity for $r_{21} = \lambda/12$, $\gamma_1 = \gamma_2 = \gamma$, $\bar{\mu} \perp \bar{r}_{21}$, and different Δ : $\Delta = 0$ (solid line), $\Delta = -3\gamma$ (dashed line), $\Delta = -6\gamma$ (dashed-dotted line)

Superradiant effects are usually discussed for systems consisting of a large number of atoms, but here we obtain them in a system of only two atoms. Coffey and Friedberg [68] and Richter [69] have shown that the superradiant effect can be observed in some special cases of the atomic configuration of a three-atom system. Blank et al. [70] have shown that this effect, for atoms located in an equidistant linear chain, appears for at least six atoms. Recently, De Angelis et al. [71] have experimentally observed the superradiant effect in the radiation from two identical dipoles located inside a planar symmetrical microcavity.

The quantum beats predicted here for spontaneous emission from two nonidentical atoms are fully equivalent to the quantum beats predicted in Sect. 3.5.2 for a single three-level Vee-type atom with correlated spontaneous transitions. For the initial conditions used here that initially only one of the atoms was excited, the initial population distributes equally between the states $|s'\rangle$ and $|a'\rangle$. Since the transitions are correlated through the dissipative term $\gamma_{a's'}$, the system of two nonidentical atoms behaves as a Vee-type atom with spontaneously correlated transitions.

The Case of $\Delta = 0$, $\gamma_1 \neq \gamma_2$ and $\Lambda_{12} \gg \gamma_1, \gamma_2$

We now wish to show how quantum beats can be obtained in two nonidentical atoms that have equal frequencies but different damping rates. According to (3.52) and (3.56), the symmetric and antisymmetric transitions are correlated not only through the spontaneously induced coherences γ_{as} , but also through the coherent coupling Δ_c . One sees from (3.53) that for small interatomic separations $\gamma_{+-} \approx 0$. However, the coherent coupling parameter Δ_c , which is proportional to Λ_{12} , is very large, and we will show that the coherent coupling Δ_c can also lead to quantum beats and the superradiant effect. In the case of $\Delta = 0$, $\gamma_1 \neq \gamma_2$ and $\Lambda_{12} \gg \gamma_1, \gamma_2$, the approximate solution of (3.87) leads to the following expression for the total radiation intensity

$$I(t) = e^{-\frac{1}{2}(\gamma_1 + \gamma_2)t} \left\{ \frac{1}{2}(\gamma_1 - \gamma_2) \cos(2\Lambda_{12}t) + \frac{1}{2}(\gamma_1 + \gamma_2) \cosh(\gamma_{12}t) - \gamma_{12} \sinh(\gamma_{12}t) \right\}. \quad (3.91)$$

It is seen that the total radiation intensity displays quantum-beat oscillations at frequency $2\Lambda_{12}$ corresponding to the frequency splitting between the $|s'\rangle$ and $|a'\rangle$ states. The amplitude of the oscillations is equal to $(\gamma_1 - \gamma_2)/2$ that is proportional to the coherent coupling Δ_c . For $\gamma_1 = \gamma_2$ the coherent coupling parameter $\Delta_c = 0$ and no quantum beats occur. In this case the intensity exhibits pure exponential decay. This is shown in Fig. 3.15, where we plot the time evolution of $I(t)$ for interatomic separation $r_{21} = \lambda/12$, and different ratios γ_2/γ_1 . Similarly to the case of $\Delta \neq 0$ and $\gamma_1 = \gamma_2$, the intensity exhibits quantum beats and the superradiant effect. For $r_{21} = \lambda/12$ the collective

damping $\gamma_{12} \approx \sqrt{\gamma_1 \gamma_2}$, and then the parameter $\gamma_{as} \approx 0$, indicating that the quantum beats and the superradiant effect result from the coherent coupling between the $|s'\rangle$ and $|a'\rangle$ states.

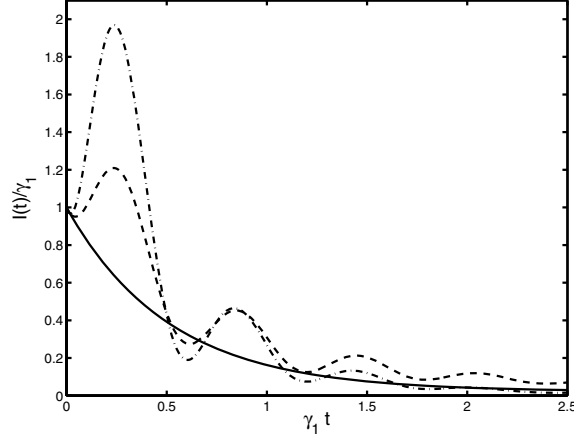


Fig. 3.15. Time evolution of the total radiation intensity for $r_{21} = \lambda/12$, $\Delta = 0$, $\bar{\mu} \perp \bar{r}_{21}$, and different γ_2/γ_1 : $\gamma_2/\gamma_1 = 1$ (solid line), $\gamma_2/\gamma_1 = 2$ (dashed line), $\gamma_2/\gamma_1 = 4$ (dashed-dotted line)

3.5.4 Experimental Observation of Quantum Beats in a Type I System

From the many experimental studies of quantum beats with an initially excited type I system, we draw on the experiment proposed by Walther's group [72]. The experiment involved a beam of barium atoms interacting with a weak magnetic field and excited by a short laser pulse. The magnetic field was applied perpendicularly to the direction of the atomic beam, and split the upper triply degenerate 1P_1 -level into three Zeeman sublevels, separated by the Larmor precession frequency ω_{LA} . These sublevels were excited by a short 1.5 ps pulse of broadband laser light with the middle frequency tuned to the barium resonance line $^1S_0 - ^1P_1$ and linearly polarized perpendicularly to the magnetic field direction. The pulse was broad enough to excite all the upper levels, but because of the selection rules governing the atomic transitions, the pulse excited only two of the Zeeman sublevels, those with magnetic quantum numbers $m = -1$ and $m = +1$, and produced linear superpositions of these levels. The superpositions reflect the presence of coherence between the upper atomic levels, crucial for the creation of quantum beats. The time dependence of the emitted fluorescence field was observed in the direction perpendicular to the atomic beam and the laser pulse directions. A polarizer with polarizing direction parallel to the direction of the atomic beam was placed in front of the photodetector to ensure that the detector was equally

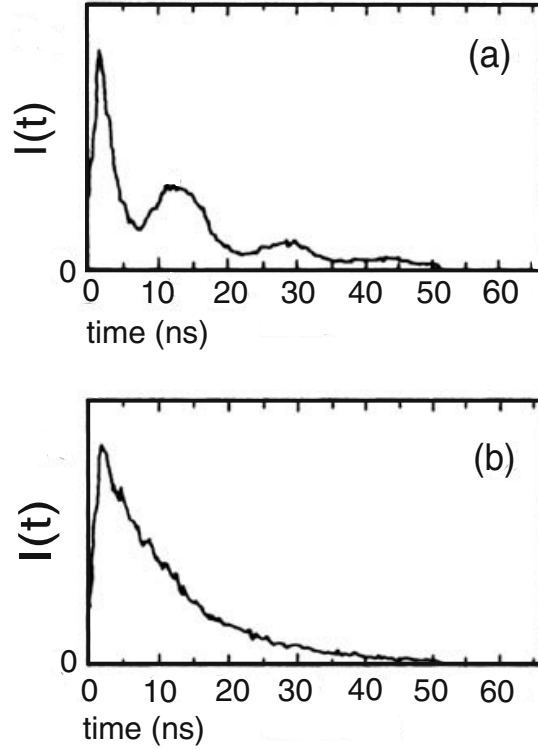


Fig. 3.16. Observation by Hellmuth et al. [72] of the time evolution of the fluorescence from pulse-excited barium atoms when (a) Pockels cell voltage was zero, and (b) a nonzero voltage was applied to the Pockels cell. From T. Hellmuth, H. Walther, A. Zajonc, W. Schleich: *Phys. Rev. A* **35**, 2532 (1987). Copyright (1987) by the American Physical Society

sensitive to both of the atomic decay channels $| - 1 \rangle \rightarrow | 0 \rangle$ and $| + 1 \rangle \rightarrow | 0 \rangle$. The results illustrating the time decay of the emitted fluorescence field are shown in Fig. 3.16(a). The observed signal exhibits a sinusoidal oscillation, with frequency $2\omega_{LA}$ corresponding to the splitting of the upper levels, superimposed on the exponential decay. Evidently, the quantum beats arise from the indistinguishability by the detector from which transition the detected photons came.

In a modified version of the experiment, the photodetector was made sensitive to the polarization of the incoming field. It was done by applying a Pockels cell which changed the circular polarization σ^- of the field emitted from the $| - 1 \rangle \rightarrow | 0 \rangle$ transition into a linearly polarized field with a polarization direction perpendicular to that of the filter, and was therefore blocked. This resulted in the detection of only the σ^+ polarized field emitted from the $| + 1 \rangle \rightarrow | 0 \rangle$ transition, and the disappearance of the quantum beats, as is shown in Fig. 3.16(b). The experimental results are another confirmation of the principle of complementarity, that quantum interference, which is here manifested by the presence of quantum beats, and which-way infor-

mation contained in the atom or in the emitted field, are mutually exclusive concepts.

3.5.5 Quantum Beats in the Intensity–Intensity Correlations

In the last few sections, we have examined many different schemes for producing quantum beats in the radiation intensity. We have also shown that no quantum beats can be observed in the radiation intensity from type II atoms initially prepared in their upper levels. An initially excited type II atom (e.g. a Lambda-type atom) decays to the lower energy levels and a measurement of the populations of these levels could determine along which transition pathway the atom decayed. However, quantum beats in this system can be observed by “erasing” the which-path information. Simply re-exciting the atom by sending in a second laser pulse to scramble the information will not be sufficient: in general, the information will only be transferred, for example, to the scattered second photon. Instead, if one detects two photons emitted by the system simultaneously excited by two short pulses and measures the second-order correlation function, all information can be erased as to along which transition pathway the photons were emitted, since detectors cannot distinguish between two photons registered in a very short interval of time. A similar situation appears in a system of two two-level atoms initially prepared in their upper levels.

Quantum Beats in an Initially Excited Type II System

Let us examine quantum beats in the intensity–intensity correlations of spontaneous emission from an initially excited type II atom. This problem was originally treated by Zajonc [73] and his results are quoted here. A slightly more complicated system is considered in this model, a four level atom composed of a single upper level and three lower levels, as shown in Fig. 3.17. An

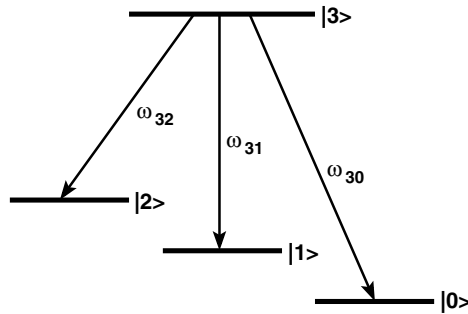


Fig. 3.17. Energy-level structure of a type II four-level system with a single upper level and three lower levels

example of such an atom is the energy level configuration of the barium resonance line $^1S_0 - ^1P_1$ with an upper singlet level $J = 0$, $m = 0$, and a triplet of lower levels composed of three degenerate Zeeman sublevels $m = 0, \pm 1$ of a $J = 1$ energy level. A magnetic field applied to the atom splits the lower sublevels into a triplet with the separation between the sublevels given by the Lamor precession frequency. The three atomic transitions are excited by two linearly polarized short laser pulses with wave vectors \mathbf{k}_1 and \mathbf{k}_3 propagating in opposite directions. We choose the polarizations of the pulses such that the pulse \mathbf{k}_1 is polarized parallel to the direction of the magnetic field, whereas the pulse \mathbf{k}_3 is polarized perpendicularly to the magnetic field direction. Because of the selection rules governing atomic transitions, the pulse \mathbf{k}_1 can excite only the $|1\rangle \rightarrow |3\rangle$ ($\Delta m = 0$) transition, whereas the pulse \mathbf{k}_3 can excite only the $|0\rangle \rightarrow |3\rangle$ and $|2\rangle \rightarrow |3\rangle$ transitions. The radiation field emitted by the atom is registered by two photodetectors arranged with linear polarizers orthogonal to one another such that one detector registers the radiation field emitted from the $|3\rangle \rightarrow |1\rangle$ transition, and the other registers the field emitted only from the $|3\rangle \rightarrow |2\rangle$ and $|3\rangle \rightarrow |0\rangle$ transitions. When we apply the two pulses, there are two distinguishable paths which the emitted photons can follow. In Fig. 3.18, we illustrate the two paths separately.

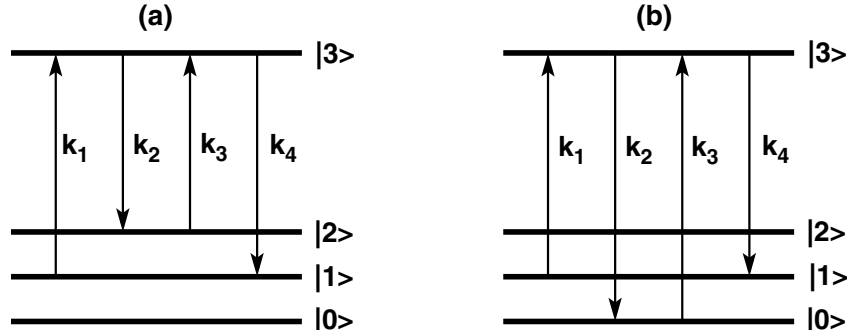


Fig. 3.18. The two distinguishable paths in the type II four-level system

The pulse \mathbf{k}_1 transfers the population from $|1\rangle$ to $|3\rangle$, which then can decay to any of the three lower levels. The decay from $|3\rangle$ to $|2\rangle$ distinguishes the path A, whereas the decay from $|3\rangle$ to $|0\rangle$ distinguishes the path B. The decay to $|1\rangle$ is uninteresting since the second pulse will not be able to transfer the population from $|1\rangle$ to $|3\rangle$ due to the dipole selection rules. The two decay paths are distinguishable in a one-photon detection, since one could probe the population of the lower levels to determine in which level the atom was before the second pulse was applied. However, this information can be erased by a simultaneous detection of two photons rather than a single photon because one cannot distinguish between two simultaneously detected photons. Important here is that one of the photodetectors, say D_1 can detect only the photon \mathbf{k}_4 , and the other photodetector, say D_2 is broad enough so that it

will be equally sensitive to the photon \mathbf{k}_2 emitted from either $|3\rangle \rightarrow |2\rangle$ or $|3\rangle \rightarrow |0\rangle$ transition, but will not be sensitive to the photon \mathbf{k}_4 .

The above considerations are supported by a simple calculation of the second-order correlation function of the fields registered by the two photodetectors. If the photodetectors are adjusted such that D_1 can register only the photon \mathbf{k}_4 , and D_2 can register only the photon \mathbf{k}_2 , the electric fields at the detectors are

$$\begin{aligned}\hat{\mathbf{E}}_1^{(\pm)}(\mathbf{R}_1, t_1) &= \hat{\mathbf{E}}_{31}^{(\pm)}(\mathbf{R}_1, t_1) , \\ \hat{\mathbf{E}}_2^{(\pm)}(\mathbf{R}_2, t_2) &= \frac{1}{\sqrt{2}} \left[\hat{\mathbf{E}}_{32}^{(\pm)}(\mathbf{R}_2, t_2) + \hat{\mathbf{E}}_{30}^{(\pm)}(\mathbf{R}_2, t_2) \right] .\end{aligned}\quad (3.92)$$

Let us introduce the state of the system describing the two paths just before detection

$$|\Psi(t)\rangle = C_1(t) |1, 1_{32}, 1_{31}\rangle + C_2(t) |1, 1_{30}, 1_{31}\rangle , \quad (3.93)$$

where C_1 and C_2 are complex amplitudes, $|1, 1_{ij}, 1_{ij}\rangle = |1\rangle \otimes |1_{ij}\rangle \otimes |1_{ij}\rangle$, and $|1_{ij}\rangle$ is the one-photon number state of the mode $|i\rangle \rightarrow |j\rangle$.

Hence, the second-order correlation function of the detected fields will contain cross-terms. For example, there will be a term

$$\begin{aligned}&\langle \Psi(t) | \hat{\mathbf{E}}_{32}^{(-)}(\mathbf{R}_2, t_2) \hat{\mathbf{E}}_{31}^{(-)}(\mathbf{R}_1, t_1) \hat{\mathbf{E}}_{31}^{(+)}(\mathbf{R}_1, t_1) \hat{\mathbf{E}}_{30}^{(+)}(\mathbf{R}_2, t_2) | \Psi(t) \rangle \\ &= \langle 1_{32}, 1_{31} | \hat{a}_{32}^\dagger \hat{a}_{31}^\dagger \hat{a}_{31} \hat{a}_{30} | 1_{30}, 1_{31} \rangle C_1^*(t) C_2(t) \\ &\quad \times \exp[i(\omega_{32}t_2 - \mathbf{k} \cdot \mathbf{R}_2)] \exp[-i(\omega_{30}t_2 - \mathbf{k} \cdot \mathbf{R}_2)] \\ &= C_1^*(t) C_2(t) \exp[i(\omega_{32} - \omega_{30})t_2] ,\end{aligned}\quad (3.94)$$

which oscillates with the frequency difference $(\omega_{32} - \omega_{30})$. Therefore, we expect quantum beats to appear in the time evolution of the second-order correlation function. This example is an analog of the Young's double slit experiment in which quantum interference effects appear subject to the erasure of which-way information in the atom or in the emitted field.

Quantum Beats with Initially Excited Two-Level Atoms

We have shown that first-order coherence is sensitive to the interatomic interactions and the excitation field. In contrast, the second-order correlation function can exhibit an interference pattern independent of the interatomic interactions and the excitation process. According to (3.65), to observe an interference pattern in the second-order correlation function, it is enough to produce a nonzero population in the state $|e\rangle$. This can be achieved by preparing both atoms in their upper levels. The interference results from the detection process in that a detector does not distinguish between two simultaneously detected photons. As an example, consider spontaneous emission

from two identical as well as nonidentical atoms with both initially atoms excited [74].

For two identical atoms, we easily find from (2.99), (3.65), and the quantum regression theorem, that the two-time second-order correlation function is given by

$$\begin{aligned} G^{(2)}(\mathbf{R}_1, t; \mathbf{R}_2, t + \tau) &= \frac{1}{2} \gamma^2 v(\mathbf{R}_1) v(\mathbf{R}_2) \exp[-\gamma(2t + \tau)] \\ &\times \{ (1 + \cos \Phi_1 \cos \Phi_2) \cosh(\gamma_{12} \tau) \\ &- (\cos \Phi_1 + \cos \Phi_2) \sinh(\gamma_{12} \tau) \\ &+ \sin \Phi_1 \sin \Phi_2 \cos(2\Lambda_{12} \tau) \} , \end{aligned} \quad (3.95)$$

where $\Phi_i = k \bar{\mathbf{R}}_i \cdot \mathbf{r}_{21}$ ($i = 1, 2$).

This equation shows that the two-time second-order correlation function exhibits a sinusoidal modulation in space and time. This modulation can be interpreted both in terms of interference fringes and quantum beats. The frequency of quantum beats is $2\Lambda_{12}$ and the amplitude of these beats depends on the direction of observation with respect to the interatomic axis. The quantum beats vanish for directions $\theta_1 = 90^\circ$ or $\theta_2 = 90^\circ$, where $\theta_1(\theta_2)$ is the angle between \mathbf{r}_{21} and $\bar{\mathbf{R}}_1(\bar{\mathbf{R}}_2)$, and the amplitude of the beats has its maximum for two photons detected in the direction $\theta_1 = \theta_2 = 0^\circ$. This directional effect is connected with the fact that the antisymmetric state $|a\rangle$ does not radiate in the direction perpendicular to the interatomic axis. For independent atoms, $\gamma_{12} = \Lambda_{12} = 0$, and then the correlation function (3.95) reduces to

$$\begin{aligned} G^{(2)}(\mathbf{R}_1, t; \mathbf{R}_2, t + \tau) &= \frac{1}{2} \gamma^2 v(\mathbf{R}_1) v(\mathbf{R}_2) \exp[-\gamma(2t + \tau)] \\ &\times \{ 1 + \cos[k(\bar{\mathbf{R}}_1 - \bar{\mathbf{R}}_2) \cdot \mathbf{r}_{21}] \} , \end{aligned} \quad (3.96)$$

which shows that the time modulation vanishes. This implies that quantum beats are absent in spontaneous emission from two independent atoms, but the spatial modulation is still present [74, 75].

Quantum interference is observed even though the photons arrive at the detectors at very different times. This effect can also be related to the principle of complementarity, in that the detectors cannot distinguish between two identical photons even if the photons are detected at significantly different times and places. Therefore, even though the different optical paths leading to each individual detector are completely distinguishable, they are completely indistinguishable in the coincidence detection, and we then see quantum interference between them.

The situation is different for two nonidentical atoms, which for $\omega_1 \neq \omega_2$ emit photons of different frequencies, or when $\gamma_1 \neq \gamma_2$, emit photons at different times. In this case, the two-time second-order correlation function exhibits quantum beats *even* if the atoms are independent. For $\gamma_{12} = 0$ and $\Lambda_{12} = 0$,

which corresponds to two independent atoms, the master equation (2.96) leads to the following correlation function

$$G^{(2)}(\mathbf{R}_1, t; \mathbf{R}_2, t + \tau) = \frac{1}{2} \gamma^2 v(\mathbf{R}_1) v(\mathbf{R}_2) \exp[-\gamma(2t + \tau)] \\ \times \left\{ \cosh \left[\frac{1}{2} (\gamma_2 - \gamma_1) \tau \right] + \cos [k(\bar{\mathbf{R}}_1 - \bar{\mathbf{R}}_2) \cdot \mathbf{r}_{21} - 2\Delta\tau] \right\}. \quad (3.97)$$

Thus, for independent nonidentical atoms, the correlation function shows a sinusoidal modulation both in space and time. However, the visibility contrast is reduced and the correlation function is always different from zero, unless $\tau = 0$. It is interesting to note that the modulation term in (3.97) is of the same form as that obtained by Mandel [76], who considered the second-order correlation function for two beams emitted by independent lasers.

3.6 Interference Pattern with a Dark Center

As we have seen in Sect. 1.1.3, the Young's interference experiment can be modified by replacing the slits by two atoms and still interference effects can be observed between coherent or incoherent fields scattered by the atoms. The advantage of using atoms instead of slits is that at a given time each atom cannot emit more than one photon. Therefore, the atoms can be regarded as sources of single photon fields and quantum interference effects at the level of single photons can be studied.

In Sect. 2.2.2, we have shown that the correlation functions of the radiation field emitted from single atoms can be related to the correlation functions of the atomic dipole moments. It means that interference effects can be studied in terms of the atomic correlation functions. Using the relation (2.135), we can write the visibility of the interference fringes produced by the field emitted from two atoms as

$$C = \frac{\langle S_1^+ S_2^- + S_2^+ S_1^- \rangle}{\langle S_1^+ S_1^- + S_2^+ S_2^- \rangle}. \quad (3.98)$$

As an application, consider a two-atom system driven by a coherent laser field propagating in the direction perpendicular to the interatomic axis. In this case, we can use the steady-state solutions (2.99) and obtain an analytical formula for the fringe visibility of the steady-state fluorescence field as

$$C = \frac{(\gamma^2 + 4\Delta_L^2)}{(\gamma^2 + 4\Delta_L^2) + 2\Omega^2}. \quad (3.99)$$

It is seen that in this specific case, the visibility is positive ($C > 0$) for all parameter values and is independent of the interatomic interactions.

Meyer and Yeoman [77] have shown that in contrast to coherent excitation, an incoherent field can produce an interference pattern with a dark

center, $C < 0$. To show how a two-atom system can produce this effect, we rewrite the visibility (3.98) in terms of the density matrix elements of the collective atomic system, and obtain

$$C = \frac{\varrho_{ss} - \varrho_{aa}}{\varrho_{ss} + \varrho_{aa} + 2\varrho_{ee}}. \quad (3.100)$$

This simple formula shows that the sign of C depends on the population difference between the symmetric and antisymmetric states. For $\varrho_{ss} > \varrho_{aa}$ the visibility C is positive, and then the interference pattern exhibits a maximum (bright center), whereas for $\varrho_{ss} < \varrho_{aa}$ the visibility C is negative and then there is a minimum (dark center). The optimum positive (negative) value is $C = 1$ ($C = -1$), and there is no interference pattern when $C = 0$. The latter happens when $\varrho_{ss} = \varrho_{aa}$.

One notices from (3.66) and (3.100) that spontaneous emission from two undriven atoms, with initially only one atom excited, can produce an interference pattern with a dark center [78]. This happens for $\gamma_{12} \neq 0$, i.e. when the symmetric and antisymmetric states decay with different rates.

An interference pattern with a dark center can also be obtained with two atoms driven by a coherent laser field [79]. This happens when the atoms experience different phases and/or intensities of the driving field. To show this, we solve numerically the master equation (2.96) for the steady-state density matrix elements of the driven system of two atoms. The visibility C is plotted

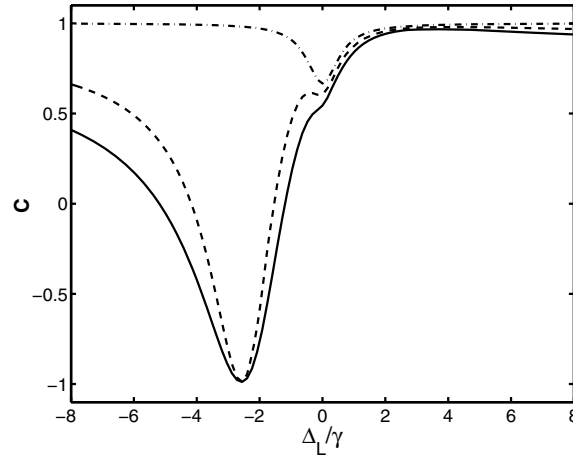


Fig. 3.19. The visibility C as a function of Δ_L for $r_{21} = 0.1\lambda$, $\bar{\mu} \perp \bar{r}_{12}$, $\Omega = 0.5\gamma$ and various angles θ_L ; $\theta_L = 0$ (solid line), $\theta_L = \pi/4$ (dashed line), $\theta_L = \pi/2$ (dashed-dotted line)

in Fig. 3.19 as a function of the detuning Δ_L for $r_{21} = 0.1\lambda$, $\Omega = 0.25\gamma$ and various angles θ_L between the interatomic axis and the direction of propagation of the laser field. The visibility C is positive for most values of Δ_L , except $\Delta_L \approx -\Lambda_{12}$. At this detuning the visibility factor C is negative and reaches

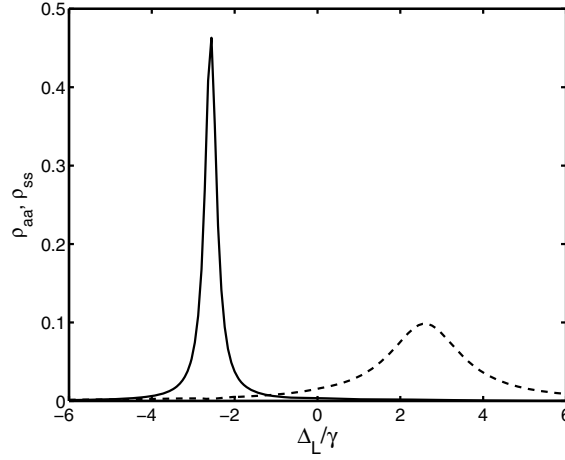


Fig. 3.20. Populations of the antisymmetric (*solid line*) and symmetric (*dashed line*) states as a function of Δ_L for $r_{21} = 0.1\lambda$, $\bar{\mu} \perp \bar{r}_{12}$, $\Omega = 0.5\gamma$ and $\theta_L = 0$

the optimum negative value $C = -1$, indicating that the system produces an interference pattern with a dark center. Figure 3.20 shows the populations of the symmetric and antisymmetric states for the same parameters as in Fig 3.19. It is evident from Fig. 3.20 that at $\Delta_L = -\Lambda_{12}$ the antisymmetric state is significantly populated, whereas the population of the symmetric state is close to zero. This population difference leads to negative values of C , as predicted by (3.100) and seen in Fig. 3.19. The experimental observation of an interference pattern with a dark center would be an interesting demonstration of the controlled excitation of a two-atom system with the entangled antisymmetric state.

The interference technique can be used as a way to detect entangled states of a two-atom system. This technique is particularly useful for detection of the symmetric or antisymmetric states. For example, when the system is prepared in the antisymmetric state or in a superposition of the antisymmetric and ground states, $\varrho_{ss} = \varrho_{ee} = 0$, and then the visibility has the optimum negative value $C = -1$. On the other hand, when the system is prepared in the symmetric state or in a linear superposition of the symmetric and ground states, the visibility has the maximum positive value $C = 1$. Thus, the visibility can provide information about the entangled states of a two-atom system.

4 Quantum Interference as a Control of Decoherence

In this chapter we consider how to modify and control spontaneous emission in simple atomic systems by means of quantum interference. Spontaneous emission occurs when an atom, prepared in an excited state, decays to a lower atomic level by emitting a photon, in the absence of any externally applied field. This process takes place by means of the vacuum interaction of quantum electrodynamics. (The word ‘vacuum’ emphasizes that the interaction is present even when there is no applied field.) In the applications of laser physics, this basic interaction often gives rise to undesirable noise. For example, it limits the precision to which the position of spectral lines can be measured in spectroscopy. In the fields of quantum communication and quantum computing, the fundamental operations are carried out on coherent superpositions of atomic states, and spontaneous emission results in this coherent superposition being gradually destroyed (a process known as “decoherence”) in a time of the order of the spontaneous lifetime (the time it takes the excited state to decay to $(1/e) \times$ its initial value by spontaneous emission). The control, and particularly the suppression of spontaneous emission, is therefore a matter of great importance in the context of quantum computation, teleportation, and quantum information processing. However, there are a few situations in which one would wish to *increase* the rate of spontaneous emission. For example, it may govern the rate of approach to equilibrium of nuclear magnetic spins, and one may wish this to be rapid. Thus much ingenuity has been expended in finding ways to manipulate spontaneous emission.

In the case of single atoms, there are several ways to achieve this end, including changing the atomic transition frequencies involved, or modifying the environment surrounding the atom, by such methods as placing the atom into an cavity, waveguide or photonic bandgap material. Spontaneous emission may also be changed by quantum interference effects, and that is our main concern here. Before discussing this method, for completeness, we briefly consider some alternative approaches.

4.1 Modified Spontaneous Emission

Radiative properties of atomic systems can be modified by changing the mode structure of the electromagnetic field to which the systems are coupled. If we

consider, for example, a two-level atom in its excited state $|1\rangle$, the rate of spontaneous emission from this level to the ground state $|0\rangle$ may be calculated by the “Golden Rule”¹ of perturbation theory

$$W_{10} = \frac{2\pi}{\hbar} |V_{10}|^2 \mathcal{D}_E(E_1 - E_0) , \quad (4.1)$$

where V_{10} is the interaction Hamiltonian between the atom and the vacuum electromagnetic field, and $\mathcal{D}_E(E)$ is the energy density of states, i.e. $\mathcal{D}_E(E)dE$ is the number of final states available in the energy range from E to $E + dE$. It is this factor that interests us here. We may therefore modify the emission rate W_{10} if we can change the density of states available to the atom for emission. This can be achieved by changing the environment in which the atom is situated. In the next few sections, we give some examples of different environments which can strongly modify spontaneous emission. Perhaps the simplest way, in principle, to modify the structure of the modes available for spontaneous emission is to place the emitting atom close to a mirror. This is discussed in the next sub-section. Then we consider placing the atom in a cavity, and finally we place it in a photonic bandgap structure.

4.1.1 Effect of Environment on Spontaneous Emission

The rate of spontaneous emission of an atom or molecule depends upon the nature of the emitter’s local environment – a fact that some people find surprising on first consideration, as there is a tendency to consider the spontaneous emission rate as a fundamental – and immutable – property of the emitting species. A simple example may illustrate the environmental dependence. Consider a two-level atom, with excited state $|1\rangle$ and ground state $|0\rangle$, placed a distance x from a perfectly reflecting plane mirror [54]. According to the method of images, described in texts on electromagnetism, to describe a charge in front of such a mirror we may replace the mirror by a charge of equal but *opposite* sign an equal distance the opposite side of the mirror plane. In our case, we may thus replace the mirror by a fictitious image atom, but with the dipole of the image rotated through π rad. with respect to the dipole of the atom. A photon with wave-vector \mathbf{k} and polarization s may be considered to be emitted either by the atom or by the image of the atom in the mirror. The processes are shown in Fig. 4.1. The photon carries no information as to whether it is emitted by the actual dipole or its mirror image, and so the initial wave-function of the composite system must be appropriately symmetrized. For simplicity, we consider the case where the atomic transition dipole is either parallel or perpendicular to the plane of the mirror. If the atom is initially in its excited state, the initial wave-function of the composite system is thus

¹ The use of the Golden Rule to calculate the spontaneous emission rate is discussed in more detail in Sect. 4.1.2. The spontaneous emission rate was calculated directly from the master equation in Sect. 2.1.1.

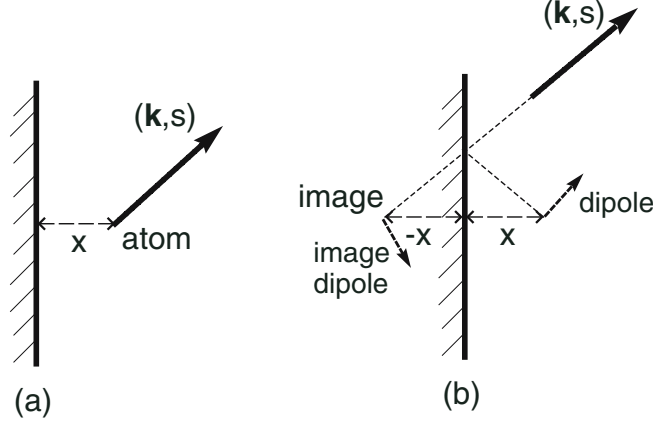


Fig. 4.1. (a) A photon considered as being emitted by the atom, or (b) its image

$$|\Psi_{\pm}\rangle = \frac{1}{\sqrt{2}} (|1\rangle_A |0\rangle_I \pm |0\rangle_A |1\rangle_I) , \quad (4.2)$$

where A indicates an atom state and I an image state. The ‘plus’ subscript in (4.2) indicates the wave function to be used when the atomic transition dipole is perpendicular to the plane of the mirror, as the dipole then has the same phase as its image. However, if the dipole is parallel to the plane of the mirror, the phase of the image is π out of phase with that of the atom, and then $|\Psi_{-}\rangle$ should be used. The state (4.2) corresponds to one in which one photon may be produced by spontaneous emission, which may be emitted by either the atom or its image.

The following important results may be deduced. As $x \rightarrow 0$, the entangled state (4.2) implies that for a perpendicular dipole, the spontaneous emission rate is doubled, whereas for a parallel dipole, it tends to zero. In the latter case, the atom does not radiate at all! This observation agrees perfectly with the exact calculations presented in Sect. 3.3.

The $x \rightarrow 0$ results may be considered as a special case of the situation treated by Dicke [49], who considered a system of M two-level atoms located within a volume of dimensions much less than a wavelength. He showed that cooperative initial states existed (of which (4.2) is a special case), some of which are *superradiant* (spontaneous emission rate equal to $M^2 \times$ the single isolated atom rate) and some of which are *subradiant* (spontaneous emission rate zero). We may regard Dicke’s work as an example of a situation in which an atom’s decay rate is affected by its environment. In this case, the environment is provided by the other $M - 1$ atoms. (Superradiant states are not possible in our system, because they would take the form $|1\rangle_A |1\rangle_I$, which does not describe our situation.) The atom–image theory of Morawitz [54] agrees well with experiment [80].

Stehle [81] has employed the image method to discuss the spontaneous emission of a two-level atom placed between two plane mirrors. This situation has been further developed by Milonni and Knight [46], and is in fact an

example of an atom in a bad cavity, considered in Sect. 3.3. However, it is instructive to treat the cavity environment in the different manner described in the next sub-section.

4.1.2 Modification by a Moderate Q Cavity

The suggestion that spontaneous emission could be enhanced by the use of a resonant circuit was first made in a short note as long ago as 1946 by Purcell [82] with the object of increasing the rate at which a nuclear magnetic resonance system approaches equilibrium. It was observed, together with inhibition of the spontaneous emission rate, by Kleppner in 1981 [47]. Further demonstrations using Rydberg atoms were reported shortly afterwards [83, 84].

The analysis of Sect. 2.2 showed that the spontaneous emission radiated from an atom in an excited state is due to the interaction of the atom with all the modes of the electromagnetic field that the environment of the atom supports. As we have seen in Sect. 4.1, an expression for γ , the spontaneous emission rate from the atomic level $|1\rangle$ to the level $|0\rangle$ whose energies are $E_1 = \hbar\omega_1$ and $E_0 = 0$ respectively, may be obtained from Fermi's Golden Rule, which gives

$$\gamma = \left(\frac{2\pi}{\hbar}\right)^2 \sum_{\lambda} |\langle 1, \{0\} | V_{10} | 0, \{1\}_{\lambda} \rangle|^2 \delta(\omega_1 - \omega_{\lambda}) , \quad (4.3)$$

where V_{10} is the interaction between the atom and the radiation field, which we here assume to be the dipole interaction. The matrix element is taken between states of the whole system: $|1, \{0\}\rangle$ is the state where the atom is in the excited state $|1\rangle$ and the electromagnetic field is in its vacuum state $|\{0\}\rangle$ with no photons present, whilst $|0, \{1\}_{\lambda}\rangle$ is the state where the atom is in the state $|0\rangle$ and the electromagnetic field is in the state in which just one photon is present, in the mode λ .

In many cases, the matrix element in (4.3) is a slowly varying function of $\omega_{\lambda} \equiv \omega_{(\mathbf{k},s)}$ and may be taken out of the summation as a constant, so that the expression (4.3) reduces to the form

$$\gamma = K_{10} \mathcal{D}(\omega_1) , \quad (4.4)$$

where K_{10} is a quantity which depends upon the atomic states $|1\rangle$ and $|0\rangle$ and $\mathcal{D}(\omega_1)$ is the density of electromagnetic field modes – the number of modes per unit volume of frequency space per unit volume of the space occupied by the electromagnetic field, evaluated at the frequency ω_1 . The latter is the important quantity for our present purposes, for it shows that the spontaneous emission rate depends upon the nature of the environment in which the atom is situated, as this affects the density of states. In free space, the photon density of states is given by the expression

$$\mathcal{D}_f(\omega) = \frac{\omega^2}{\pi^2 c^3} , \quad (4.5)$$

where a factor of two has been included to take account of the fact that there are two independent modes of polarization. (See Sect. 2.1.1 for a detailed derivation of the spontaneous emission rate in free space.) In such materials as photonic bandgaps, the slowly varying assumption which has been used to obtain (4.5), is *not* justified, as we discuss in Chap. 6.

The dependence of the spontaneous emission rate on the photon density of states suggests that spontaneous emission may be modified by changing the nature of the electromagnetic modes available to the atom for radiation. This can be done by suitably changing the environment. Suppose we place the atom in a cavity whose dimensions are of the order of the wavelength of the resonant transition. If the cavity is resonant with the atomic transition, there is essentially only one mode present, the cavity mode, distributed over the cavity width $\Delta\omega_c$, the frequency range supported by the cavity. The latter is equal to $\Delta\omega_c = \omega/Q$ where Q is the cavity Q factor. Taking the volume of the cavity to be of the order $\mathcal{V} \sim (\lambda/2)^3 = (\pi c/\omega)^3$, and assuming the cavity to be doubly degenerate, the density of states is essentially

$$\mathcal{D}_c(\omega) = 2 \times \frac{1}{\Delta\omega_c} \times \frac{1}{\mathcal{V}} = \frac{2}{\pi} \times Q \times \frac{\omega^2}{\pi^2 c^3} \sim Q \mathcal{D}_f(\omega) . \quad (4.6)$$

Thus the photon density of states in the resonant cavity is larger than the density of states in free space by a factor of the order of the cavity Q factor. Since Q can be very large (e.g. $Q \sim 10^5$), the spontaneous decay rate can be greatly increased.

Conversely, the spontaneous emission decay rate can be reduced if the cavity is detuned. If the atomic resonant frequency lies below the fundamental frequency of the cavity, spontaneous emission is greatly inhibited. For the case of an ideal cavity, no mode is then available into which the atom can emit a photon, and the spontaneous emission rate is zero.

This is all very well – in principle. The practical difficulty in achieving complete inhibition of spontaneous emission is that *all* the modes with which an atom can interact must be eliminated, and in general, this can only be achieved by using a completely enclosed, perfectly conducting cavity. The simplest kind of cavity is that consisting of two parallel conducting plates, but one would normally expect this to reduce the spontaneous emission rate by only a factor of two, because of the existence of transverse electromagnetic modes which are independent of the separation. An exception was reported in the experiments of Hulet et al. [84], who employed Rydberg atoms prepared in a “circular” state² using two parallel conducting plates with separation $d \simeq \lambda/2$. The reason that such a state is used is that it has only one decay

² This is a single-electron state with large principal quantum number n and magnetic quantum number $|m| = n - 1$.

channel. Using a result of Milonni and Knight [46], it was shown that the spontaneous emission rate was

$$\begin{aligned} \gamma &= 1.5\gamma_0 & \text{for } d > \lambda/2, \\ \gamma &= 0 & \text{for } d < \lambda/2, \end{aligned} \quad (4.7)$$

where γ_0 is the free space spontaneous emission rate. In the experiments of Hulet et al. [84], the inter-plate distance was set at $\lambda/2$ and then an electric field was used to change the value of the wavelength of the resonant transition so that $\lambda < 2d$ or $\lambda > 2d$. Excellent agreement with theory was obtained. Figure 4.2 shows their results for enhanced spontaneous emission.

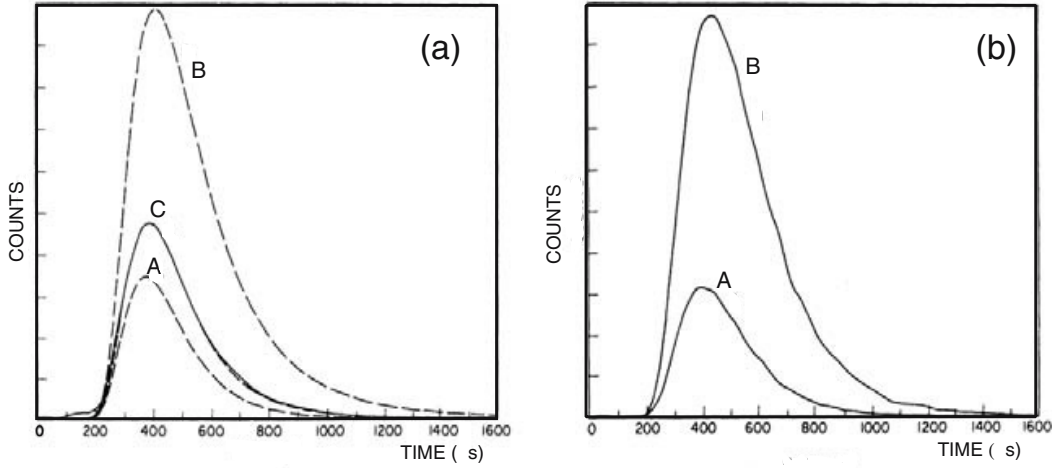


Fig. 4.2. Time of flight signals for various spontaneous decay rates. Mean time of flight $= 1.5/\gamma_0$, where γ_0 is the free-space radiative decay rate. In frame (a) are the calculated signals. Curve A is for an enhanced decay rate $\gamma = 3\gamma_0/2$. Curve B is for no radiative decay, and curve C is for free space, $\gamma = \gamma_0$. In the latter case, the measured signal is the solid line and the calculated is the dashed line (so close to the solid line as to be hardly visible). The frame (b) gives the measured data for inhibited spontaneous emission ($\lambda/2d > 1$, curve B) and enhanced spontaneous emission, ($\lambda/2d < 1$, curve A), taken simultaneously by modulation of the wavelength with an applied electric field. From R.J. Hulet, E.S. Hilfner, and D. Kleppner: Phys. Rev. Lett. **55**, 2137 (1985). Copyright (1985) by the American Physical Society

To investigate inhibited spontaneous emission they used the operating conditions $\lambda > 2d$, and found results consistent with the spontaneous emission rate $\gamma = (0 \pm 0.05)\gamma_0$. Thus the spontaneous emission rate was reduced by a factor of at least twenty.

It is obvious that inhibited/enhanced spontaneous emission becomes more difficult to observe as the wavelength of the resonant transition decreases – simply because it becomes more and more difficult to make a cavity with

dimensions of the order of the resonant wavelength. For this reason, the first observations were made on transitions in the microwave regime. However, in the late 1980s, these effects were observed in transitions in the optical region [85, 86].

4.1.3 Modification by Photonic Crystals

A photonic crystal, or a photonic bandgap material, is an artificially prepared, regularly structured material whose unit cell dimensions are comparable to the wavelength of light. If this structure has an appropriate symmetry, and is composed of material of sufficiently high refractive index, it can exhibit a complete photonic bandgap for light within a well-defined frequency range (say Δ_{pc}): that is, the photon density of states is zero for light frequencies within the range Δ_{pc} for all directions of propagation. A plot of the photon density of states for a highly idealized photon bandgap material is presented in Fig. 4.3. If an atom with a transition frequency falling within this forbidden

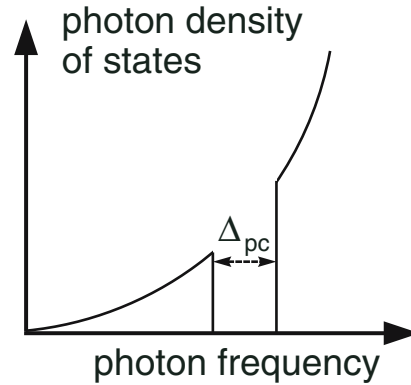


Fig. 4.3. The photon density of states for an ideal photonic crystal

range is placed inside the photonic crystal, its spontaneous emission is completely inhibited. Even if a complete gap does not exist, the photon density of states may be greatly modified from its free space form, and thus the spontaneous emission may be greatly modified. Photonic crystals are a subject of great current interest: one reason being that the bandgap in the photon energies is analogous to the electron energy gap in semiconductors. There is much fundamental physics to be understood as well as potentially exciting applications to be investigated. (We give just one sample application here. An antenna mounted on a conventional dielectric substrate emits much of its radiation into the substrate, rather than the intended direction. If the sub-

strate is replaced by a photon crystal with a gap at the radiation frequency, light is inhibited from entering the substrate, and losses are minimized.)³

We will consider quantum interference in photon bandgap materials later in Sect. 6.8.

4.2 Quantum Interference in Vee Systems

We begin our study of the control of spontaneous emission via quantum interference by considering a three-level Vee system as shown in Fig. 4.4. The

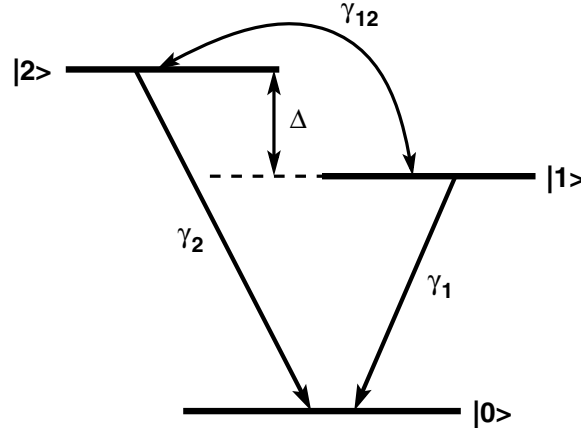


Fig. 4.4. The three-level Vee system with two dipole allowed spontaneous transitions of decay rates γ_1 and γ_2 . The frequency separation of the excited state doublet is Δ and the states are mutually coupled through the cross damping rate γ_{12}

ground state $|0\rangle$ is connected to the closely-spaced excited states $|1\rangle$ and $|2\rangle$ whose energies are $E_1 = \hbar\omega_1$ and $E_2 = \hbar\omega_2$ respectively, by nonzero dipole moments μ_{10} and μ_{20} . The frequency separation of the excited state doublet is $\Delta = \omega_2 - \omega_1$. Direct transitions between the excited levels are assumed to be forbidden in the electric dipole approximation, and are ignored here. The system interacts with the vacuum so that spontaneous decay may take place from the two excited levels to the ground state. The rate of the transition from $|i\rangle$ to the ground state is equal to the spontaneous transition rate γ_i .

If the system is such that the dipole moments for the two principal transitions are parallel or nearly so, then, in addition to this direct decay process, the interaction with the vacuum leads to an indirect coupling between the two excited states, as discussed in Sect. 2.1.1. This kind of coupling was noted by Landau as far back as 1927 [87]. Interest in such systems was renewed when Agarwal [37] showed that spontaneous emission could be controlled by means of the quantum interference displayed by such systems.

³ For further information on photon bandgap materials and references, see for example the Web site of Sajeev John: <http://www.physics.utoronto.ca/john>.

We follow the notation of Sect. 2.1.1 and denote the cross-damping rate γ_{ij} between the two atomic transitions as

$$\gamma_{12} = \gamma_{21} = \frac{\sqrt{\omega_1^3 \omega_2^3}}{3\pi\epsilon_0 \hbar c^3} \boldsymbol{\mu}_{10} \cdot \boldsymbol{\mu}_{20} . \quad (4.8)$$

We introduce the important parameter β , which is the cosine of the angle between the two dipole moments $\boldsymbol{\mu}_{10}$ and $\boldsymbol{\mu}_{20}$,

$$\beta = \frac{\boldsymbol{\mu}_{10} \cdot \boldsymbol{\mu}_{20}}{|\boldsymbol{\mu}_{10}| |\boldsymbol{\mu}_{20}|} , \quad (4.9)$$

so that

$$\gamma_{12} = \beta \sqrt{\gamma_1 \gamma_2} . \quad (4.10)$$

It is only when $\gamma_{12} \neq 0$ that quantum interference occurs: it results from vacuum induced coherences between the two atomic transitions: the spontaneous emission from one of the transitions modifies the spontaneous emission of the other transition. It is therefore essential that the dipole moments be non-perpendicular for the quantum interference effects to be evident. This can be difficult to arrange in practice. We return to this point in Chap. 6.

The dynamics of a multi-level system are governed by the master equation (2.72), which for the three-level undriven system in an ordinary vacuum ($N = 0$) and in the Schrödinger picture reads as

$$\dot{\varrho} = -\frac{i}{\hbar} [\varrho, H_0] + \mathcal{L}\varrho , \quad (4.11)$$

where

$$H_0 = \hbar (\omega_1 A_{11} + \omega_2 A_{22}) \quad (4.12)$$

with $A_{ij} \equiv |i\rangle\langle j|$ is the Hamiltonian of the atom, and the damping term (the term describing spontaneous decay), arising from the vacuum interaction, is

$$\begin{aligned} \mathcal{L}\varrho = & \frac{1}{2}\gamma_1 (2A_{01}\varrho A_{10} - A_{11}\varrho - \varrho A_{11}) \\ & + \frac{1}{2}\gamma_2 (2A_{02}\varrho A_{20} - A_{22}\varrho - \varrho A_{22}) \\ & + \frac{1}{2}\gamma_{12} (2A_{01}\varrho A_{20} - A_{21}\varrho - \varrho A_{21}) \\ & + \frac{1}{2}\gamma_{12} (2A_{02}\varrho A_{10} - A_{12}\varrho - \varrho A_{12}) . \end{aligned} \quad (4.13)$$

It is evident from the form of the Liouvillian \mathcal{L} that the spontaneous decay in this system is *off-diagonal* – that is, the equation of motion for the density matrix element ϱ_{ij} will contain damping terms that are proportional to ϱ_{kj} and/or ϱ_{ik} , in addition to the diagonal damping terms proportional

to ϱ_{ij} . This makes the physical interpretation of the density matrix equations difficult. If we transform to a new basis characterized by the following symmetric and antisymmetric superpositions of the excited levels, suggested by the analysis of Sect. 3.1:

$$|s\rangle = \frac{\sqrt{\gamma_1}|1\rangle + \sqrt{\gamma_2}|2\rangle}{\sqrt{\gamma_1 + \gamma_2}}, \quad (4.14a)$$

$$|a\rangle = \frac{\sqrt{\gamma_2}|1\rangle - \sqrt{\gamma_1}|2\rangle}{\sqrt{\gamma_1 + \gamma_2}}, \quad (4.14b)$$

the off-diagonal damping terms become proportional to $\gamma_1 - \gamma_2$, and vanish for $\gamma_1 = \gamma_2$.

Consider the effect of quantum interference on the intensity of the radiation field emitted from the Vee system. According to (2.5) and (2.144), the total intensity of radiation emitted by the atom is proportional to the expectation value of the square of the total atomic dipole moment

$$\hat{\mu} = \mu_{01}A_{01} + \mu_{02}A_{02}. \quad (4.15)$$

If the dipole moments are equal and parallel, $\mu_{01} = \mu_{02} = \mu$, and the decay rates are equal, $\gamma_1 = \gamma_2$, then

$$\hat{\mu} = \sqrt{2}\mu A_{0s}, \quad (4.16)$$

since $A_{01} + A_{02} = \sqrt{2}A_{0s}$. Hence

$$I = 2|\mu|^2 \langle A_{s0}A_{0s} \rangle = 2|\mu|^2 \varrho_{ss}, \quad (4.17)$$

where ϱ_{ss} is the population of the symmetric state $|s\rangle$.

Thus, if there is no population in the symmetric state $|s\rangle$, there is no atomic fluorescence. Moreover, if there is some population in the antisymmetric state, it will stay there for all times. This effect is known in the literature as *coherent population trapping*.

However, if the dipole moments are equal and perpendicular, then

$$\begin{aligned} I &= |\mu|^2 (\langle A_{11} \rangle + \langle A_{22} \rangle) = |\mu|^2 (\langle A_{ss} \rangle + \langle A_{aa} \rangle) \\ &= |\mu|^2 (\varrho_{11} + \varrho_{22}) = |\mu|^2 (\varrho_{ss} + \varrho_{aa}). \end{aligned} \quad (4.18)$$

Thus any population in any of the excited states, whether in the original atomic states or in the superposition states, will result in a nonzero atomic fluorescence.

4.2.1 Population Trapping and Dark States

In the literature, population trapping is often said to be a consequence of the cancellation of spontaneous emission. Here, we illustrate that cancellation of

spontaneous emission from an atomic state does not always lead to trapping of the population in that nondecaying state, by considering the process of spontaneous emission from a Vee-type atom. For simplicity, we assume that spontaneous emission occurs from the two excited states to the ground state with the same decay rate $\gamma_1 = \gamma_2 = \gamma$, and the transition between the excited states is forbidden in the electric dipole approximation. The allowed transitions are represented by the dipole operators $A_{01} = |0\rangle\langle 1|$ and $A_{02} = |0\rangle\langle 2|$. The master equation (4.11) leads to the following equations of motion for the density matrix elements

$$\begin{aligned}\dot{\varrho}_{11} &= -\gamma\varrho_{11} - \frac{1}{2}\gamma_{12}(\varrho_{12} + \varrho_{21}) , \\ \dot{\varrho}_{22} &= -\gamma\varrho_{22} - \frac{1}{2}\gamma_{12}(\varrho_{12} + \varrho_{21}) , \\ \dot{\varrho}_{00} &= \gamma(\varrho_{11} + \varrho_{22}) + \gamma_{12}(\varrho_{12} + \varrho_{21}) , \\ \dot{\varrho}_{12} &= -\left(\frac{1}{2}\gamma + i\Delta\right)\varrho_{12} - \frac{1}{2}\gamma_{12}(\varrho_{11} + \varrho_{22}) , \\ \dot{\varrho}_{21} &= -\left(\frac{1}{2}\gamma - i\Delta\right)\varrho_{21} - \frac{1}{2}\gamma_{12}(\varrho_{11} + \varrho_{22}) .\end{aligned}\quad (4.19)$$

In addition, the equations for ϱ_{01} and ϱ_{02} form a separate closed set:

$$\begin{aligned}\dot{\varrho}_{01} &= -\left(i\omega_1 + \frac{1}{2}\gamma\right)\varrho_{01} - \frac{1}{2}\gamma_{12}\varrho_{02} , \\ \dot{\varrho}_{02} &= -\left(i\omega_2 + \frac{1}{2}\gamma\right)\varrho_{02} - \frac{1}{2}\gamma_{12}\varrho_{01} .\end{aligned}\quad (4.20)$$

There are two different steady-state solutions of (4.19) depending on whether the transitions are degenerate ($\Delta = 0$) or nondegenerate ($\Delta \neq 0$). This fact is connected with the existence of a linear combination of the density matrix elements

$$\alpha(t) = \varrho_{11}(t) + \varrho_{22}(t) - \varrho_{12}(t) - \varrho_{21}(t) , \quad (4.21)$$

which, for $\Delta = 0$ and $\gamma_{12} = \gamma$ is a constant of motion.

In the case of $\Delta = 0$ and $\gamma_{12} = \gamma$, the steady-state solution of (4.19) is

$$\begin{aligned}\varrho_{11}(\infty) &= \varrho_{22}(\infty) = \frac{1}{4}\alpha(0) , \\ \varrho_{12}(\infty) &= \varrho_{21}(\infty) = -\frac{1}{4}\alpha(0) , \\ \varrho_{00}(\infty) &= \frac{1}{2}\alpha(0) .\end{aligned}\quad (4.22)$$

It is seen that the steady-state population distribution depends on the initial population. When $\alpha(0) \neq 0$, a part of the population can remain in the excited states.

On the other hand, for $\Delta \neq 0$ and/or $\gamma_{12} \neq \gamma$, the linear combination (4.21) is no longer a constant of the motion, and then the steady-state solution of (4.19) is

$$\begin{aligned}\varrho_{11}(\infty) &= \varrho_{22}(\infty) = \varrho_{12}(\infty) = \varrho_{21}(\infty) = 0, \\ \varrho_{00}(\infty) &= 1.\end{aligned}\tag{4.23}$$

In this case the population distribution does not depend on the initial state of the atom and in the steady-state the entire population is in the ground state.

The properties of this system can be understood by transforming to the linear superpositions (4.14), when from the master equation (4.11) we find the following equations of motion for the populations of these superposition states

$$\begin{aligned}\dot{\varrho}_{ss} &= -\frac{1}{2}(\gamma + \gamma_{12})\varrho_{ss} - \frac{1}{2}i\Delta(\varrho_{sa} - \varrho_{as}), \\ \dot{\varrho}_{aa} &= -\frac{1}{2}(\gamma - \gamma_{12})\varrho_{aa} + \frac{1}{2}i\Delta(\varrho_{sa} - \varrho_{as}).\end{aligned}\tag{4.24}$$

It is seen that the antisymmetric state decays at the reduced rate $(\gamma - \gamma_{12})$, and for $\gamma_{12} = \gamma$ the state does not decay at all. In this case the antisymmetric state can be regarded as a *dark state* in the sense that the state is decoupled from the environment, and produces no spontaneous emission. Secondly, we note from (4.24) that the population oscillates between the states with the amplitude Δ , which plays here a role similar to that of the Rabi frequency of a coherent interaction between the symmetric and antisymmetric states. Consequently, if $\Delta \neq 0$, an initial population in the state $|a\rangle$ can be coherently transferred to the state $|s\rangle$, which decays rapidly to the ground state. There is cancellation of spontaneous emission, but no population trapping. When $\Delta = 0$, the coherent interaction does not take place and then any initial population in $|a\rangle$ will stay in this state for all times. In this case we can say that the population is *trapped* in the state $|a\rangle$.

We conclude that cancellation of spontaneous emission does not necessarily lead to population trapping. The population can be trapped in a dark state only if the state is completely decoupled from any interactions.

4.2.2 Probing Quantum Interference in a Vee System

The quantum interference effects discussed in the previous section can be observed in the absorption spectrum of a weak, tunable probe beam monitoring a Vee-type atom. A variety of effects, including narrow resonances, transparency and gain without inversion, occur in this system [88]. Experiments involving probe absorption in undriven systems should be easier to perform than those involving resonance fluorescence from driven systems.

The two-time correlation functions for the atomic dipole operators, required to calculate the absorption spectrum (2.141) are found from the equations of motion of the reduced density matrix elements (4.19) and (4.20) and the quantum regression theorem [51]. In our simple situation, with a slight change of normalization, the absorption spectrum (2.141) reduces to

$$\begin{aligned} A(\omega_p) = \text{Re} \int_0^\infty d\tau \lim_{t \rightarrow \infty} \Big\{ & \gamma_1 \left\langle \left[\tilde{S}_1^-(t), \tilde{S}_1^+(t+\tau) \right] \right\rangle \\ & + \gamma_2 \left\langle \left[\tilde{S}_2^-(t), \tilde{S}_2^+(t+\tau) \right] \right\rangle + \gamma_{12} \left\langle \left[\tilde{S}_1^-(t), \tilde{S}_2^+(t+\tau) \right] \right\rangle \\ & + \gamma_{12} \left\langle \left[\tilde{S}_2^-(t), \tilde{S}_1^+(t+\tau) \right] \right\rangle \Big\} e^{i\omega\tau}, \end{aligned} \quad (4.25)$$

where $\tilde{S}_i^\pm(t) = S_i^\pm \exp(\mp i\omega_0 t)$ are the slowly varying parts of the atomic operators $S_i^+ = |i\rangle\langle 0|$, $S_i^- = |0\rangle\langle i|$, and $\omega_0 = (\omega_1 + \omega_2)/2$ is the mean atomic transition frequency. In this case, $\omega = \omega_p - \omega_0$, so that the spectrum is centered on ω_0 . The first two terms in (4.25) represent the incoherent contribution to the probe absorption spectrum, whilst the second two are the contributions due to quantum interference.

Since the quantum regression theorem is frequently used in the following pages, we present a statement of it here. It enables us to calculate correlation functions involving two time variables by solving the equations of motion for an operator involving only a single time variable. The theorem states that if $\tau \geq 0$, the correlation function $\langle A(t+\tau)B(t) \rangle$ obeys the same equations of motion as $\langle A(\tau) \rangle$, as obtained from the reduced density matrix equations, but with the initial density matrix replaced by $\varrho(0) \rightarrow B\varrho(t)$. Usually, we are interested in the steady state spectrum, when $\varrho(t)$ is given by $\bar{\varrho} = \lim_{t \rightarrow \infty} \varrho(t)$. Similarly, the correlation function $\langle A(t)B(t+\tau) \rangle$ obeys the same equations of motion as $\langle B(\tau) \rangle$, as obtained from the reduced density matrix equations, but with the initial density matrix replaced by $\varrho(0) \rightarrow \varrho(t)A$.

We indicate how to proceed by calculating the first term in (4.25), first introducing the Laplace transform by the definition

$$\tilde{\varrho}(z) = \int_0^\infty dz e^{-z\tau} \varrho(\tau). \quad (4.26)$$

We calculate the Laplace transform of (2.141), and then obtain the spectrum by changing the Laplace variable z to $-i\omega$. Applying the quantum regression equation to the first term of (4.25), we see that we need the equation of motion for $\langle S_1^+(\tau) \rangle = \varrho_{01}(\tau)$. This can be obtained from the set (4.20). Noting that the Laplace transform of $\dot{\varrho}(t)$ is $z\tilde{\varrho}(z) - \varrho(0)$, we easily find the solution of the Laplace transform of the set (4.20) to be

$$\tilde{\varrho}_{01}(z) = \frac{(z + i\omega_2 + \frac{1}{2}\gamma) \varrho_{01}(0) - \frac{1}{2}\gamma_{12}\varrho_{02}(0)}{(z + i\omega_1 + \frac{1}{2}\gamma)(z + i\omega_2 + \frac{1}{2}\gamma) - \frac{1}{4}\gamma_{12}^2}, \quad (4.27)$$

with a similar equation for $\bar{\varrho}_{02}(z)$, except that the subscripts ‘1’ and ‘2’ are interchanged. Note that $\gamma_{21} = \gamma_{12}$.

According to the quantum regression theorem, to evaluate the first term in the commutator of the first term of (4.25) we make the replacement $\varrho(0) \rightarrow \bar{\varrho}S_1^- = \bar{\varrho}|0\rangle\langle 1|$, where $\bar{\varrho} = \lim_{t \rightarrow \infty} \varrho(t)$ is the steady-state density matrix. Thus, we replace $\varrho_{01}(0)$ by $\bar{\varrho}_{00}$ and $\varrho_{02}(0)$ by 0 in (4.27). To evaluate the second term in the commutator of the first term in (4.25) we make the replacement $\varrho(0) \rightarrow S_1^- \bar{\varrho} = |0\rangle\langle 1|\bar{\varrho}$, necessitating the replacements $\varrho_{01}(0) \rightarrow \bar{\varrho}_{11}$ and $\varrho_{02}(0) \rightarrow \bar{\varrho}_{12}$ in (4.27). The remaining six terms in (4.25) are similarly evaluated.

By these means, we obtain the following expression for the absorption spectrum

$$A(\omega_p) = \text{Re} \left\{ \frac{(\Gamma/2 - i\gamma_1\omega_-)\bar{P}_{0,1} + (\Gamma/2 - i\gamma_2\omega_+)\bar{P}_{0,2}}{(\frac{1}{2}\gamma_1 - i\omega_+)(\frac{1}{2}\gamma_2 - i\omega_-) - \frac{1}{4}\gamma_{12}^2} + \frac{i\gamma_{12}(\omega_+\bar{\varrho}_{21} + \omega_-\bar{\varrho}_{12})}{(\frac{1}{2}\gamma_1 - i\omega_+)(\frac{1}{2}\gamma_2 - i\omega_-) - \frac{1}{4}\gamma_{12}^2} \right\}, \quad (4.28)$$

where $\omega_{\pm} = \omega_p - \omega_0 \pm \frac{1}{2}\Delta$, and

$$\Gamma = \gamma_1\gamma_2 - \gamma_{12}^2 = \gamma_1\gamma_2(1 - \beta^2) \quad (4.29)$$

measures the degree of quantum interference. Note, $\Gamma = 0$ for maximal quantum interference, and $\Gamma = 1$ for no quantum interference. The parameter $\bar{P}_{0,j} = \bar{\varrho}_{00} - \bar{\varrho}_{jj}$, ($j = 1, 2$), and

$$\bar{\varrho}_{21} = -\frac{\gamma_{12}(\bar{\varrho}_{11} + \bar{\varrho}_{22})}{\gamma_1 + \gamma_2 + 2i\Delta}, \quad \bar{\varrho}_{12} = \bar{\varrho}_{21}^*, \quad (4.30)$$

are the steady-state atomic coherences, induced by quantum interference.

Expression (4.28) is our basic result and clearly demonstrates that the absorption spectrum consists of three parts, the first two originating from the direct atomic transitions $|0\rangle \rightarrow |j\rangle$, ($j = 1, 2$) and proportional to the population difference $\bar{\varrho}_{00} - \bar{\varrho}_{jj}$ between the states $|0\rangle$ and $|j\rangle$, whilst the final one stems from quantum interference between the two absorption channels, and is proportional to γ_{12} , and the coherences $\bar{\varrho}_{21}$ and $\bar{\varrho}_{12}$. If $\gamma_{12} = 0$ – that is, there is no quantum interference – the probe absorption spectrum (4.28) reduces to the sum of two Lorentzians with linewidths γ_1 and γ_2 located at ω_1 and ω_2 respectively. Without population inversion, it is impossible to amplify the probe field. However, if quantum interference occurs, this conclusion is dramatically modified.

First we consider the degenerate case, with $\Delta = 0$. For no quantum interference, $\gamma_{12} = 0$, the absorption spectrum consists of a single, Lorentzian peak for $\gamma_1 = \gamma_2 = \gamma$. For $\alpha \equiv \sqrt{\gamma_1/\gamma_2} = 0.25$, the single peak is no longer

Lorentzian – a sharp peak of width γ_1 is symmetrically superimposed upon the broader peak of width γ_2 . The situation is illustrated in Fig. 4.5(a), where we plot the absorption spectrum as a function of $\nu = (\omega_p - \omega_0)/\gamma_2$.

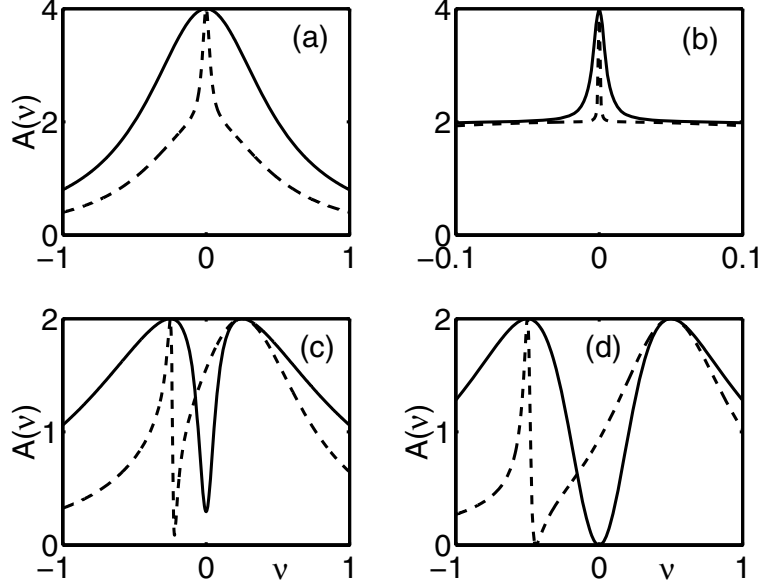


Fig. 4.5. The absorption spectrum $A(\nu)$ as a function of $\nu = (\omega_p - \omega_0)/\gamma_2$. In (a) and (b), we have $\Delta = 0$ (the degenerate case) with $\beta = 0$ (no quantum interference) in (a) and $\beta = 0.99$ in (b). Note the change of frequency scale in frame (b). In all the frames, the *solid line* is for $\alpha \equiv \sqrt{\gamma_1/\gamma_2} = 1$, and the *dotted line* for $\alpha = 0.25$. In (c), we have $\Delta = 0.5\gamma_2$, $\beta = 0.99$ and in (d) $\Delta = \gamma_2$, $\beta = 1$

With maximal quantum interference and equal decay rates, $\gamma_1 = \gamma_2 = \gamma = \gamma_{12}$, and thus $\Gamma = 0$. As we saw in Sect. 4.2.1, the steady-state solutions in this situation are surprisingly dependent on the particular initial states of the atom, due to quantum interference. We consider the following cases.

- (i) If the atom is initially in the antisymmetric state $|a\rangle = (|1\rangle - |2\rangle)/\sqrt{2}$, then the steady-state solutions are $\bar{\rho}_{00} = 0$, $\bar{\rho}_{11} = \bar{\rho}_{22} = 1/2$ and $\bar{\rho}_{21} = -1/2$.
- (ii) If the atom is initially in the symmetric state $|b\rangle = (|1\rangle + |2\rangle)/\sqrt{2}$, or in the ground state $|0\rangle$, then $\bar{\rho}_{00} = 1$, $\bar{\rho}_{11} = \bar{\rho}_{22} = 0$ and $\bar{\rho}_{21} = 0$.
- (iii) If the atom is initially in one of the excited doublet states $|1\rangle$, $|2\rangle$, then $\bar{\rho}_{00} = 1/2$, $\bar{\rho}_{11} = \bar{\rho}_{22} = 1/4$ and $\bar{\rho}_{21} = -1/4$.

The case (i) is the most interesting, because the absorption is zero for all frequencies of the probe beam: $A(\omega_p) = 0$, and the medium is transparent for the probe field. This effect is attributed to population trapping, and is also an example of population inversion without lasing: although there is a strong inversion between either of the excited doublet states and the ground state, there is no amplification of the probe beam. Again, this effect is due to quantum interference.

For the case (ii), the probe absorption spectrum is a single Lorentzian with linewidth 2γ , and for the case (iii), the probe absorption spectrum is also a Lorentzian with linewidth 2γ , but the maximum value is only half the value of case (ii). This is because half the population is trapped in the antisymmetric state $|a\rangle$, which is totally decoupled from the probe field.

We next consider imperfect quantum interference, $\Gamma \neq 0$, when $\bar{\varrho}_{00} = 1$ and $\bar{\varrho}_{11} = \bar{\varrho}_{22} = \bar{\varrho}_{21} = 0$, independent of the initial atomic states. Figure 4.5(b) shows the probe absorption spectrum for $\omega_{12} = 0$ and $\beta = 0.99$. A very narrow resonance occurs at the atomic frequency ω_0 when the dipole moments are very nearly parallel. The linewidth is dependent on the decay constants of the excited doublet. For example, the resonance for $\gamma_1 = 0.25\gamma_2$ (dashed curve) is narrower than the one for $\gamma_2 = \gamma_1$ (solid curve). However, when the dipole moments are perpendicular (frame (a), $\beta = 0$) or exactly parallel, $\beta = 1$, the narrow resonance does not occur. In the former case, the absorption spectrum is simply the sum of two Lorentzians with respective linewidths γ_1, γ_2 , whereas in the latter case, completely destructive interference occurs, resulting in a single broad Lorentzian.

In order to see the effects of quantum interference analytically, we assume β to be close to unity so that $\Gamma \ll \gamma_s^2$ where $\gamma_s = \gamma_1 + \gamma_2$. We may then approximate the spectrum (4.28) as:

$$A(\omega_p) \simeq \frac{1}{2} \left[\frac{\epsilon_0^2}{\left(\frac{1}{2}\epsilon_0\right)^2 + \delta_p^2} + \frac{\gamma_s^2}{\frac{1}{4}\gamma_s^2 + \delta_p^2} \right], \quad (4.31)$$

where $\delta_p = \omega_p - \omega_0$ and $\epsilon_0 = \Gamma/\gamma_s \ll \gamma_s$. It consists of the superposition of a broad Lorentzian with linewidth $(\gamma_1 + \gamma_2)$ and a narrow Lorentzian with linewidth ϵ_0 : the spectral profile shows a very sharp peak imposed on a broad one. Although it is clear from Fig. 4.5(a) that it is possible to obtain a narrow spectral line in the absence of quantum interference if one decay rate is much smaller than the other, the narrow resonance reported here is certainly a result of quantum interference. In principle, the resonance becomes arbitrarily narrow as the two dipole moments approach perfect alignment. For example, the width of the solid line in Fig. 4.5(c) is 1% of γ_1 . Expression (4.31) also clearly demonstrates that the quantum interference is destructive. If the dipole moments are exactly parallel, destructive interference is complete: no narrow line occurs, and the spectrum (4.31) is just a broad Lorentzian with linewidth $(\gamma_1 + \gamma_2)$.

For the nondegenerate case, $\Delta \neq 0$, we first assume $\gamma_1 = \gamma_2 = \gamma$. If $\Gamma = 0$, the spectrum is composed of two Lorentzians centered at the frequency ω_0 with linewidths

$$\sigma_{\pm} = \gamma^2 (1 - 2\varepsilon_1 \pm \sqrt{1 - 4\varepsilon_1}) / 2 \quad \text{with} \quad \varepsilon_1 = (\Delta/2\gamma)^2, \quad (4.32)$$

which depend on the doublet splitting. Interestingly, one Lorentzian has a negative weight, and at line centre $A(\omega_0) = 0$, indicating transparency of

the system. The effect of quantum interference on the absorption spectrum with the splitting $\Delta = 0.5\gamma_1$ is shown in Fig. 4.5(c). The spectrum is a broad structureless peak in the absence of interference, whilst if quantum interference is taken into account, there is a hole bored into the broad spectrum. The stronger the interference, the deeper the hole. For maximal quantum interference, perfect transparency occurs at the average atomic transition frequency ω_0 , as is seen from Fig. 4.5(d).

The width of the interference-induced hole is also dependent on the doublet splitting Δ . For $\varepsilon_1 \ll \gamma_s$, the absorption spectrum is approximately

$$A(\omega_p) \simeq 2 \left[\frac{\gamma^2}{\gamma^2 + \delta_p^2} - \frac{(\Delta^2/4\gamma)^2}{(\Delta^2/4\gamma)^2 + \delta_p^2} \right]. \quad (4.33)$$

The width of the hole represented by the Lorentzian with negative weight can be very narrow for $\Delta \ll \gamma$. For $\Delta = 0.1\gamma_2$, the hole linewidth is only 0.25% of γ_2 .

For the case of $\Delta \neq 0$, $\Gamma \neq 0$, $\gamma_1 \neq \gamma_2$, the absorption spectrum, shown by the dashed lines in Fig. 4.5 is asymmetric. A strongly dispersive profile occurs around the atomic transition frequency $\omega_2 = \omega_0 + \Delta/2$ for $\Gamma \neq 0$. Figure 4.5(d), where interference is maximal, also shows probe transparency at the frequency $\omega_p - \omega_0 \simeq 0.2\gamma_1$. Generally, transparency only occurs for maximal quantum interference, $\beta = 1$, and then at the frequency

$$\omega_T = \omega_0 + \frac{\Delta(\gamma_1 - \gamma_2)}{2(\gamma_1 + \gamma_2)}. \quad (4.34)$$

The formula (4.28) also permits a qualitative insight into gain without population inversion due to quantum interference in this simple system. With $\gamma_1 = \gamma_2 = \gamma$, the value of the probe absorption spectrum at the average atomic transition frequency ω_0 is

$$\begin{aligned} A(\omega_p = \omega_0) = 2\Gamma \frac{(\bar{\rho}_{00} - \bar{\rho}_{11}) + (\bar{\rho}_{00} - \bar{\rho}_{22})}{\Gamma + \omega_{12}^2} \\ - \frac{2\gamma_{12}^2 \Delta^2 (\bar{\rho}_{11} + \bar{\rho}_{22})}{\Gamma^2 + \Delta^2 (\gamma^2 + \Delta^2)}. \end{aligned} \quad (4.35)$$

The first two terms result from the usual absorption transitions $|0\rangle \rightarrow |1\rangle$ and $|0\rangle \rightarrow |2\rangle$, and describe amplification of the probe beam if population inversion could be achieved. Since they are also proportional to Γ , quantum interference reduces the magnitude of the usual contributions. For maximal interference, $\Gamma = 0$, these two terms disappear. However, the last term originates from quantum interference and is always negative – it promotes probe amplification. The interference contribution is nonzero only when there is some population in the doublet and it is nondegenerate. Assuming $\Delta \neq 0$, $\bar{\rho}_{11} = \bar{\rho}_{22} \neq 0$ and $\bar{\rho}_{00} - \bar{\rho}_{11} > 0$ (no population inversion), we find that $A(\omega_p = \omega_0) < 0$, and we have amplification of the probe beam due to quantum interference, when γ_{12} satisfies

$$\gamma_{12}^2 > \frac{\gamma^2 (\gamma^2 + \Delta^2)}{\gamma^2 + \eta \Delta^2}, \quad \text{with} \quad \eta = \frac{\bar{\varrho}_{00}}{\bar{\varrho}_{00} - \bar{\varrho}_{11}}. \quad (4.36)$$

It is worth emphasizing that for the closed Vee-type system with a nondegenerate excited doublet, the only steady-state solution is the ground state: $\bar{\varrho}_{00} = 1$. Thus no gain is possible because the contribution of quantum interference to the probe amplification is also proportional to the populations of the excited doublet, which are zero. However, if we extend our model to include a fourth atomic level $|f\rangle$, where the direct transition between $|0\rangle$ and $|f\rangle$ is forbidden, the situation is different. If the additional level is coupled to the excited doublet by a coherent field, the excited doublet states may be partially populated in the steady state. Furthermore, if the separation between $|f\rangle$ and the doublet $\{|1\rangle, |2\rangle\}$ is much greater than that between $|0\rangle$ and the doublet, the effect of the additional level $|f\rangle$ on atomic absorption under the levels $\{|0\rangle, |1\rangle, |2\rangle\}$ to be probed may be omitted, and our equation (4.28) for the absorption spectrum is thus still valid. Gain without population inversion, but due to quantum interference is possible.

4.3 Spectral Control of Spontaneous Emission

It is also possible to control the spectral distribution of spontaneous emission from atomic levels populated by a laser field coupled to an auxiliary level. To study this we consider the model shown in Fig. 4.6.

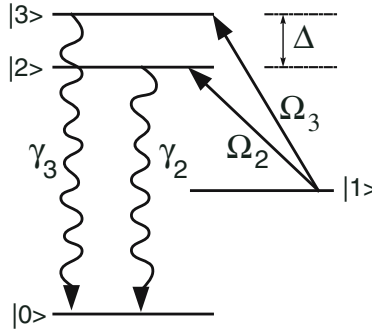


Fig. 4.6. The coupled four-level system. A single laser connects the level $|1\rangle$ to the two excited states $|2\rangle$ and $|3\rangle$ with Rabi frequencies Ω_2 and Ω_3 respectively. Spontaneous decay occurs only between levels $|2\rangle$ and $|3\rangle$ to level $|0\rangle$

The situation is similar to the Vee system considered previously, but now an additional, auxiliary level, $|1\rangle$, is added together with a single driving field that connects it to the excited doublet states $|2\rangle$ and $|3\rangle$ with corresponding Rabi frequencies Ω_2 and Ω_3 . Spontaneous emission may take place from the excited doublet to the ground state $|0\rangle$, with the possibility of quantum interference as before, but all other spontaneous transitions in the system are

assumed to have negligible rates. The Hamiltonian is

$$\begin{aligned} H'/\hbar = & \omega_1 A_{11} + \omega_2 A_{22} + \omega_3 A_{33} \\ & + \frac{i}{2} (\Omega_2 A_{21} + \Omega_3 A_{31} - \text{H.c.}) + H_{\text{vac}}/\hbar , \end{aligned} \quad (4.37)$$

where the Hamiltonian describing the interaction with the vacuum modes is given by

$$H_{\text{vac}}/\hbar = i \sum_k (g_{k2} \hat{a}_k A_{20} + g_{k3} \hat{a}_k A_{30} - \text{H.c.}) , \quad (4.38)$$

and g_{k1} and g_{k2} are coupling constants.

Following Zhu et al. [89], and Zhu and Scully [90], we treat this system by a different method to that used in Chap. 2. After transforming to the interaction picture, using the bare atomic Hamiltonian (the first three terms of (4.37)) as the unperturbed Hamiltonian, the transformed Hamiltonian becomes

$$\begin{aligned} H/\hbar = & \frac{i}{2} [\Omega_2 A_{21} \exp(-i\Delta_2 t) + \Omega_3 A_{31} \exp(-i\Delta_3 t) - \text{H.c.}] \\ & + i \sum_k [g_{k2} \hat{a}_k A_{20} \exp(i\delta_2 t) \\ & + g_{k3} \hat{a}_k A_{30} \exp(i\delta_3 t) - \text{H.c.}] , \end{aligned} \quad (4.39)$$

where

$$\Delta_j = \omega_{j,1} - \omega_L , \quad \delta_j = \omega_{j,0} - \omega_k . \quad (4.40)$$

In the above, $\omega_{m,n} \equiv \omega_m - \omega_n$ is the transition frequency between the states $|m\rangle$ and $|n\rangle$, ω_L is the frequency of the monochromatic driving field, and ω_k is the frequency of the k th mode of the vacuum field.

We expand the wave-function for the system as

$$|\psi(t)\rangle = \sum_{j=1}^3 C_j(t) |j\rangle |\{0\}\rangle + \sum_k C_k(t) |0\rangle |\{1\}_k\rangle , \quad (4.41)$$

where $|\{0\}\rangle$ denotes the state of the vacuum field in which no field mode is excited, and $|\{1\}_k\rangle$ is the state of the vacuum field in which the only excitation is a single photon in the mode k . Substituting into the Schrödinger equation

$$i \frac{d}{dt} |\psi\rangle = \frac{H}{\hbar} |\psi\rangle , \quad (4.42)$$

we obtain the equations of motion

$$\dot{C}_3 = \frac{1}{2}\Omega_3 \exp(i\Delta_3 t)C_1 + \sum_k g_{k1} \exp(i\delta_3 t)C_k , \quad (4.43a)$$

$$\dot{C}_2 = \frac{1}{2}\Omega_2 \exp(i\Delta_2 t)C_1 + \sum_k g_{k2} \exp(i\delta_2 t)C_k , \quad (4.43b)$$

$$\dot{C}_1 = -\frac{1}{2}\Omega_3^* \exp(-i\Delta_3 t)C_3 - \frac{1}{2}\Omega_2^* \exp(-i\Delta_2 t)C_2 , \quad (4.43c)$$

$$\dot{C}_k = -g_{k3} \exp(-i\delta_3 t)C_3 - g_{k2} \exp(-i\delta_2 t)C_2 . \quad (4.43d)$$

The final equation of the set (4.43) is formally integrated, and the result substituted into the other three equations. These equations then become:

$$\begin{aligned} \dot{C}_3 &= -\frac{1}{2}\gamma_3 C_3 - \frac{1}{2}\gamma_{23} C_2 \exp(i\omega_{3,2}t) + \frac{1}{2}\Omega_3 \exp(i\Delta_3 t)C_1 , \\ \dot{C}_2 &= -\frac{1}{2}\gamma_2 C_2 - \frac{1}{2}\gamma_{23} C_3 \exp(i\omega_{3,2}t) + \frac{1}{2}\Omega_2 \exp(i\Delta_2 t)C_1 , \\ \dot{C}_1 &= -\frac{1}{2}\Omega_3^* \exp(-i\Delta_3 t)C_3 - \frac{1}{2}\Omega_2^* \exp(-i\Delta_2 t)C_2 . \end{aligned} \quad (4.44)$$

Essentially, the Wigner–Weisskopf approximation has been used to treat the vacuum interaction, resulting in the introduction of the usual spontaneous emission rates γ_2 and γ_3 , including the quantum interference term $\gamma_{23} = \beta\sqrt{\gamma_2\gamma_3}$.

These differential equations can be solved straightforwardly using the Laplace transform method, which converts them to a closed set of algebraic equations. We use the following definition for the Laplace transform

$$\mathcal{L}[C(t)] \equiv \tilde{C}(z) \equiv \int_0^\infty dt C(t) \exp(-zt) , \quad (4.45)$$

together with the relation

$$\mathcal{L}(\dot{C}) = z\tilde{C}(z) - C(0) , \quad (4.46)$$

where $C(0)$ is the value of $C(t)$ at $t = 0$. The Laplace transform of the set of the equations of motion (4.44) is

$$\begin{aligned} \left(z + \frac{1}{2}\gamma_3\right) \tilde{C}_3(z) &= C_3(0) - \frac{1}{2}\gamma_{23}\tilde{C}_2(z - i\omega_{3,2}) + \frac{\Omega_3}{2}\tilde{C}_1(z - i\Delta_3) , \\ \left(z + \frac{1}{2}\gamma_2\right) \tilde{C}_2(z) &= C_2(0) - \frac{1}{2}\gamma_{23}\tilde{C}_3(z + i\omega_{3,2}) + \frac{\Omega_2}{2}\tilde{C}_1(z - i\Delta_2) , \\ z\tilde{C}_1(z) &= C_1(0) - \frac{\Omega_2}{2}\tilde{C}_2(z + \frac{i}{2}\Delta_2) + \frac{\Omega_3}{2}\tilde{C}_3(z + i\Delta_3) . \end{aligned} \quad (4.47)$$

The general solution of this set of equations may be written as

$$\begin{aligned}
D(z_3)C_3(z) &= C_3(0) \left[z_3(z_3 + i\Gamma_2) + \frac{1}{4}\Omega_2^2 \right] - C_2(0) \left(\frac{1}{2}\gamma_{23}z_3 + \frac{1}{4}\Omega_3\Omega_2^* \right) \\
&\quad + \frac{1}{2}C_1(0) \left[(z_3 + \Gamma_2)\Omega_3 - \frac{1}{2}\gamma_{23}\Omega_2 \right] \\
D(z_2)C_2(z) &= C_2(0) \left[z_2(z_2 + i\Gamma_3) + \frac{1}{4}\Omega_3^2 \right] - C_3(0) \left(\frac{1}{2}\gamma_{23}z_2 + \frac{1}{4}\Omega_2\Omega_3^* \right) \\
&\quad + C_1(0) \left[\frac{1}{2}(z_2 + \Gamma_3)\Omega_2 - \frac{1}{4}\gamma_{23}\Omega_3 \right] , \tag{4.48}
\end{aligned}$$

where

$$z_j = z - i\Delta_j , \quad \Gamma_j = i\Delta_j + \gamma_j/2 , \tag{4.49}$$

and

$$\begin{aligned}
D(z) &= z^3 + z^2(\Gamma_2 + \Gamma_3) + \frac{1}{4}z (|\Omega_2|^2 + |\Omega_3|^2 - \gamma_{23}^2 + 4\Gamma_2\Gamma_3) \\
&\quad + \frac{1}{4} \left[\Omega_2^2\Gamma_3 + |\Omega_3|^2\Gamma_2 + \frac{1}{2}\gamma_{23} (\Omega_2\Omega_3^* + \Omega_2^*\Omega_3) \right] . \tag{4.50}
\end{aligned}$$

The spectrum of spontaneous emission, $S(\omega_k)$ is proportional to the probability that, after a long period of time, a photon will be found in the mode k with frequency ω_k . This is proportional to $|\lim_{t \rightarrow \infty} C_k(t)|^2$:

$$S(\omega_k) = |\lim_{t \rightarrow \infty} C_k(t)|^2 = |\lim_{z \rightarrow 0} z\tilde{C}_k(z)|^2 , \tag{4.51}$$

where we have used a well-known Laplace identity. From the Laplace transform of (4.43d), we find

$$C_k(\infty) = -g_{k1}\tilde{C}_3(i\delta_1) - g_{k2}\tilde{C}_2(i\delta_2) . \tag{4.52}$$

However, we note that, since $z_3(z) = z - i\Delta_3$, we have

$$z_3(i\delta_3) = i\delta_3 - i\Delta_3 \equiv -i\delta , \tag{4.53}$$

where

$$\delta = -(\omega_3 - \omega_0 - \omega_k) + (\omega_3 - \omega_1 - \omega_L) = \omega_k - \omega_L - \omega_{1,0} , \tag{4.54}$$

and ω_L being the frequency of the driving field. We similarly find $z_2(i\delta_2) = -i\delta$. Assuming that $g_{kj} \propto \sqrt{\gamma_j}$, the spectrum is given by (4.48), (4.51) and (4.52) as

$$S(\delta) = |\sqrt{\gamma_3}C_3(z_3 = -i\delta) + \sqrt{\gamma_2}C_2(z_2 = -i\delta)|^2 . \tag{4.55}$$

There are a number of special cases that we can discuss. The simplest is to assume $\Omega_1 = \Omega_2 = 0$ – that is, there is no driving field. In this case, for

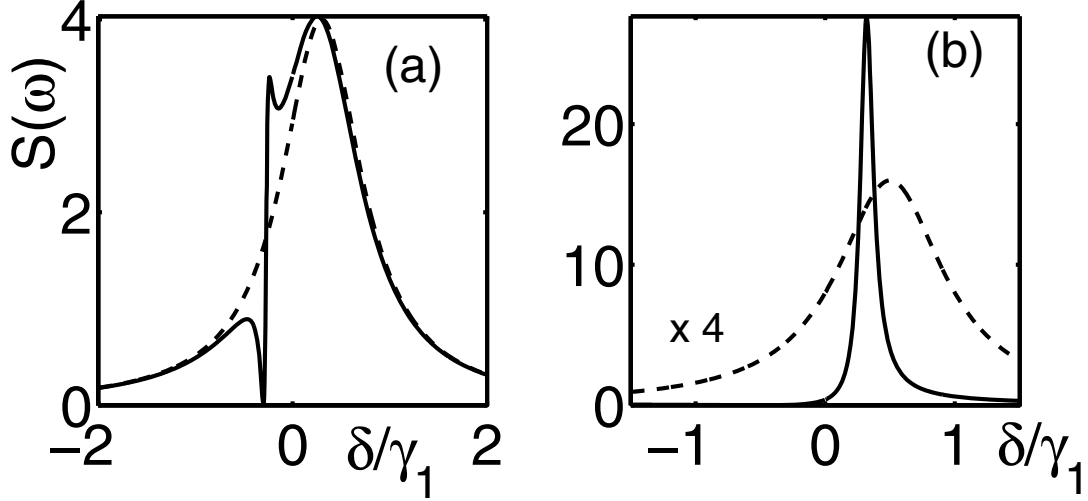


Fig. 4.7. The spontaneous emission spectrum in the absence of driving fields. The solid line is the plot for $\beta = 1$ and the dashed line is the corresponding spectrum in which $\beta = 0$. In (a), where $\gamma_1 = \gamma$, $\gamma_2 = 0.1\gamma$, $\Delta = 0.6\gamma$ and $\beta = 1$ (solid line), we demonstrate the dark line. In (b), where $\gamma_1 = \gamma$, $\gamma_2 = 4\gamma$ and $\Delta = \gamma$, we demonstrate line-narrowing. The $\beta = 0$ (dashed line) has been scaled by a factor of four to increase its visibility. It corresponds to a transition whose natural width is γ_1

complete quantum interference, a *dark line* is produced in the spontaneous emission spectrum of the effectively three-level atom (the level $|1\rangle$ may be disregarded). This is shown in Fig. 4.7(a). In all the figures of this section, we take $\gamma_1 = 1$: we also assume that the decay rates and the Rabi frequencies are connected by the same coupling constants, so that we assume that Ω_2 is given by $\Omega_2 = \sqrt{(\gamma_2/\gamma_1)}\Omega_1$. The dark line, which in this case has a dispersive profile, is clearly visible. Note that the intensity is actually zero at the centre of the dark line, if $\beta = 1$.

If $\gamma_2 > \gamma_1$, significant line narrowing can occur. This is shown in Fig. 4.7(b), where we take $\gamma_2 = 4\gamma_1$. The dashed line is the natural line-shape, unaffected by quantum interference.

Next we consider the situation where the driving field has a finite intensity. The interesting feature here, is that with an appropriate choice of parameters, quantum interference may lead to the disappearance of the central peak in the fluorescence spectrum. This is shown in Fig. 4.8, in which we assume that all the atomic population is initially in the state $|1\rangle$.

Finally, we briefly examine the situation in which the dipole transition moments from $|0\rangle$ (and from $|1\rangle$) to $|2\rangle$ and $|3\rangle$ are antiparallel ($\beta = -1$), rather than parallel ($\beta = 1$). This results in constructive, rather than destructive, interference. We illustrate this in Fig. 4.9. The various frames show how the relative heights of the central and sidepeaks vary appreciably with the orientations of the atomic dipole moments, as $\Omega_1 = \Omega_2$ is varied over a relatively small range. Notice that for $\beta = 1$, the spectrum is always doubly

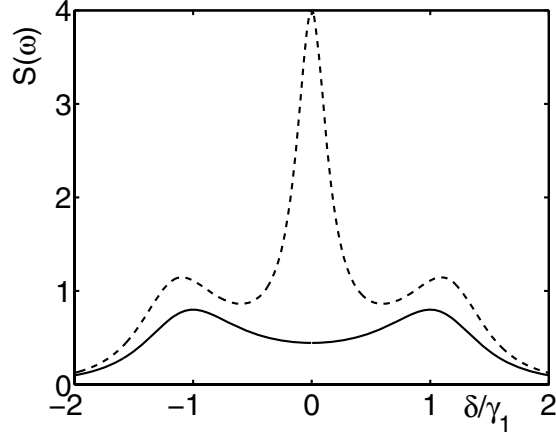


Fig. 4.8. The fluorescence spectrum for the four level system of Fig. 4.6 with $\gamma_1 = \gamma_2 = \gamma$, $\Omega_1 = 0.5\gamma$, $\Delta_1 = \gamma$, $\Delta_2 = \gamma$ and $\beta = 1$. The dashed line is the corresponding spectrum in which $\beta = 0$

peaked, and for $\beta = 0$ triply peaked, whereas for $\beta = -1$, the spectrum varies from triply peaked in Frame (a) to essentially doubly peaked in Frame (d).

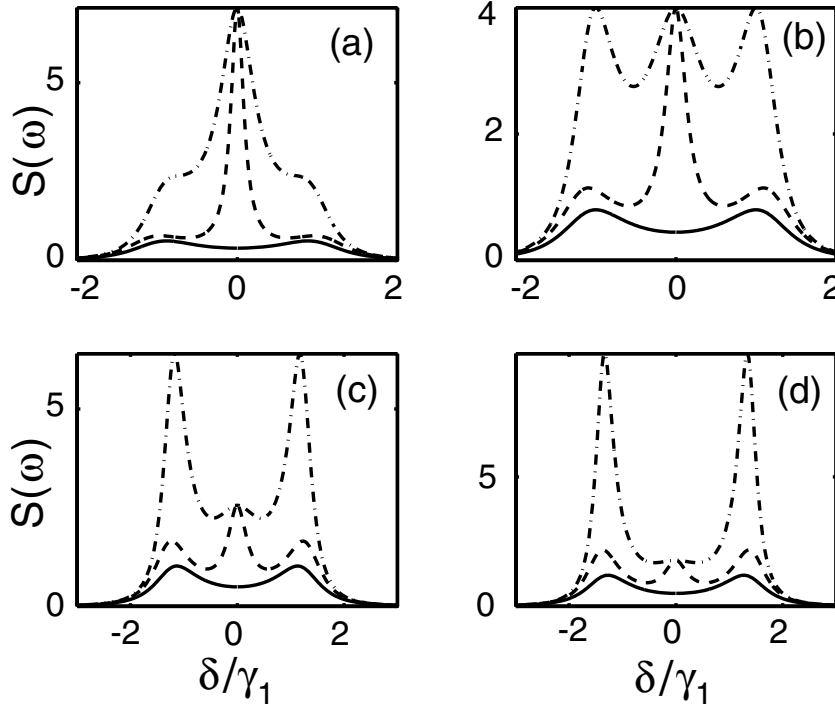


Fig. 4.9. The fluorescence spectrum for the four level system of Fig. 4.6 with $\gamma_3 = \gamma$, $\gamma_2 = \gamma$, $\Omega_3 = \Omega_2$, $\Delta_1 = \gamma$ and $\Delta_2 = -\gamma$. The *solid line* is for $\beta = 1$, the *dashed line* is the corresponding spectrum in which $\beta = 0$, and the *dot-dashed line*, showing constructive interference, is for $\beta = -1$. In (a) – (d), $\Omega_3 = 0.375\gamma$, 0.5γ , 0.625γ and 0.75γ , respectively

The reader may ask how one would establish in practice a system such as that shown in Fig. 4.6. This does not appear to be an easy matter. However, such a system was devised by Xia et al. [91] using sodium dimers. They conducted experiments on quantum interference that we analyze in detail in the next section.

4.4 Experimental Evidence of Quantum Interference

In 1996, Xia et al. [91] reported the first experimental demonstration of constructive and destructive interference effects in spontaneous emission. In the experiment they used sodium dimers, which can be modelled as five-level molecular systems with a single ground level, two intermediate and two upper levels, driven by a two-photon process from the ground level to the upper doublet. By monitoring the fluorescence from the upper levels they observed that the total fluorescent intensity, as a function of two-photon detuning, is composed of two peaks on transitions with parallel dipole moments and three peaks on transitions with antiparallel dipole moments. The observed variation of the number of peaks with the mutual polarization of the dipole moments gives compelling evidence for quantum interference in spontaneous emission. Wang et al. [92] have presented a theoretical model of the observed fluorescence intensity that explains the variation of the number of the observed peaks with the mutual polarization of the molecular dipole moments. The purpose of this section is to discuss the experimental scheme demonstrating quantum interference effects in the fluorescence intensity and to explore the theoretical approach of Wang et al. [92] that explains the observed intensity profile.

4.4.1 Energy Levels of the Molecular System

The energy-level scheme of the molecular system considered in the experiment is shown in Fig. 4.10. The five-level molecule consists of two upper levels $|3\rangle$ and $|4\rangle$, two intermediate levels $|1\rangle$ and $|2\rangle$, and a single ground level $|0\rangle$. The upper levels are separated by the frequency Δ , which is much smaller than the frequencies ω_{42} and ω_{32} of the $|4\rangle \rightarrow |2\rangle$ and $|3\rangle \rightarrow |2\rangle$ transitions and the frequencies ω_{41} and ω_{31} of the $|4\rangle \rightarrow |1\rangle$ and $|3\rangle \rightarrow |1\rangle$ transitions. As in the sodium dimers used in the experiment, we assume that the frequencies ω_{42} and ω_{32} correspond to the visible region, whereas the frequencies ω_{41} and ω_{31} correspond to the ultraviolet region and are significantly different from the remaining frequencies.

In the molecule, the one-photon transitions $|4\rangle, |3\rangle \rightarrow |2\rangle, |1\rangle \rightarrow |0\rangle$ are connected by electric dipole moments, whereas the transition $|4\rangle \rightarrow |3\rangle$ and the two-photon transitions $|4\rangle, |3\rangle \rightarrow |0\rangle$ are forbidden in the electric dipole approximation. The transition dipole moments μ_{42} and μ_{32} are parallel, whereas the transition dipole moments μ_{41} and μ_{31} are antiparallel.

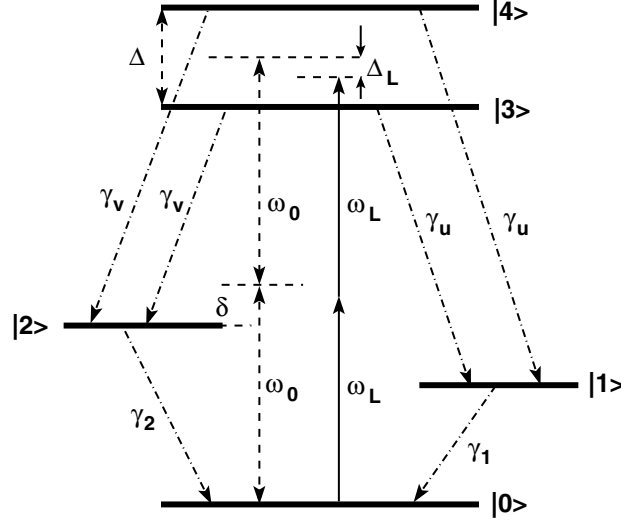


Fig. 4.10. Energy-level structure of the molecular system considered by Xia et al. [91]. The dashed-dotted arrows indicate possible one-photon spontaneous transitions

The system is driven by a single-mode tunable laser of amplitude \mathcal{E}_L and frequency ω_L coupled to the two-photon transitions $|0\rangle \rightarrow |3\rangle, |4\rangle$. The coupling strength of the laser field to the transitions is determined by the two-photon Rabi frequency

$$Q = \frac{1}{2} \sum_m \frac{\mu_{m0}\mu_{m3}\mathcal{E}_L^2}{\omega_L - \omega_{m0}} = \frac{1}{2} \sum_m \frac{\mu_{m0}\mu_{m4}\mathcal{E}_L^2}{\omega_L - \omega_{m0}}, \quad (4.56)$$

where $\mathcal{E}_L = |\mathcal{E}_L|$, and the sums are taken over intermediate virtual levels m .

4.4.2 Master Equation of the System

In the experiment, Xia et al. [91] observed the steady-state intensity of the fluorescence field emitted on the visible and ultraviolet molecular transitions. The intensity is proportional to the first-order correlation function $G^{(1)}(\mathbf{R}, t)$, which, according to (1.32), can be expressed in terms of the molecular dipole operators, or equivalently, in terms of matrix elements of the density operator of the molecular system. Using (2.145), we can write the intensities of the observed fluorescence fields on the visible (I_v) and ultraviolet (I_u) transitions as

$$\begin{aligned} I_v &= \gamma_v [\varrho_{33} + \varrho_{44} + 2\beta_v \text{Re}(\varrho_{34})], \\ I_u &= \gamma_u [\varrho_{33} + \varrho_{44} + 2\beta_u \text{Re}(\varrho_{34})], \end{aligned} \quad (4.57)$$

where γ_v is the spontaneous emission decay rate of the visible transitions, γ_u is the spontaneous emission decay rate of the ultraviolet transitions, ϱ_{33} and

ϱ_{44} are the steady-state populations of the upper levels $|3\rangle$ and $|4\rangle$, and ϱ_{34} is the steady-state coherence between them.

We find the density matrix elements from the master equation (2.67), which for this system reduces to

$$\frac{\partial}{\partial t}\varrho = -\frac{i}{\hbar}[H, \varrho] + \mathcal{L}\varrho, \quad (4.58)$$

where

$$\begin{aligned} H = & -\hbar\left(\Delta_L - \frac{1}{2}\Delta\right)A_{44} - \hbar\left(\Delta_L + \frac{1}{2}\Delta\right)A_{33} \\ & -\frac{\hbar}{2}(\Delta_L + 2\delta)A_{22} + \hbar[Q(A_{40} + A_{30}) + \text{H.c.}] , \end{aligned} \quad (4.59)$$

and

$$\begin{aligned} \mathcal{L} = & \frac{1}{2}\gamma_v(1 + \beta_v)\mathcal{D}[A_{24} + A_{23}] + \frac{1}{2}\gamma_v(1 - \beta_v)\mathcal{D}[A_{24} - A_{23}] \\ & + \frac{1}{2}\gamma_u(1 + \beta_u)\mathcal{D}[A_{14} + A_{13}] + \frac{1}{2}\gamma_u(1 - \beta_u)\mathcal{D}[A_{14} - A_{13}] \\ & + \gamma_2\mathcal{D}[A_{02}] + \gamma_1\mathcal{D}[A_{01}]. \end{aligned} \quad (4.60)$$

In (4.59) and (4.60), $\Delta_L = 2(\omega_L - \omega_0)$ is the two-photon detuning between the laser frequency ω_L and the mean frequency ω_0 of the upper levels relative to the ground level, $\delta = \omega_0 - \omega_2$ is the frequency difference between ω_0 and the frequency ω_2 of the $|2\rangle \rightarrow |0\rangle$ transition. The parameters γ_v and γ_u denote the spontaneous decay rates of the visible and ultraviolet transitions, respectively, γ_2 (γ_1) stands for the spontaneous decay from the intermediate level $|2\rangle$ ($|1\rangle$) to the ground level $|0\rangle$, and \mathcal{D} is a superoperator defined for arbitrary operators A and B as

$$\mathcal{D}[A]B \equiv ABA^\dagger - \frac{1}{2}(A^\dagger AB + BA^\dagger A). \quad (4.61)$$

4.4.3 Two-Photon Excitation

The master equation (4.58) leads to a closed system of twenty-five equations of motion for the density matrix elements. Since the laser field does not couple to the level $|1\rangle$, the system of equations splits into two independent subsystems: one of seventeen equations of motion directly coupled by the driving field and the other of eight equations of motion not coupled by the driving field. It is not difficult to show that the steady-state solutions for the eight density matrix elements are zero. Using the trace property, one of the remaining equations can be eliminated, and the system of equations reduces to sixteen coupled linear inhomogeneous equations.

Consider the weak-field limit where Q is much smaller than the spontaneous decay rates and assume, for simplicity, that the decay rates of the upper

levels on the visible and ultraviolet transitions are equal, $\gamma_v = \gamma_u = \gamma$. In this case, we can solve the system analytically, and we find that the steady-state populations and coherences appearing in (4.57) are

$$\varrho_{33} = \frac{Q^2}{(\Delta_L + \frac{1}{2}\Delta)^2 + \frac{1}{4}\gamma^2}, \quad (4.62)$$

$$\varrho_{44} = \frac{Q^2}{(\Delta_L - \frac{1}{2}\Delta)^2 + \frac{1}{4}\gamma^2}, \quad (4.63)$$

$$\text{Re}(\varrho_{34}) = \frac{Q^2 (\Delta_L^2 - \frac{1}{4}\Delta^2 + \frac{1}{4}\gamma^2)}{\left[(\Delta_L + \frac{1}{2}\Delta)^2 + \frac{1}{4}\gamma^2\right] \left[(\Delta_L - \frac{1}{2}\Delta)^2 + \frac{1}{4}\gamma^2\right]}. \quad (4.64)$$

It is seen that the populations and coherence exhibit resonances at $\Delta_L = \pm\Delta/2$, corresponding to the two-photon resonances of the laser field with the $|0\rangle \rightarrow |3\rangle$ and $|0\rangle \rightarrow |4\rangle$ transitions. Hence, the fluorescence intensity will exhibit two peaks located at $\Delta_L = \pm\Delta/2$.

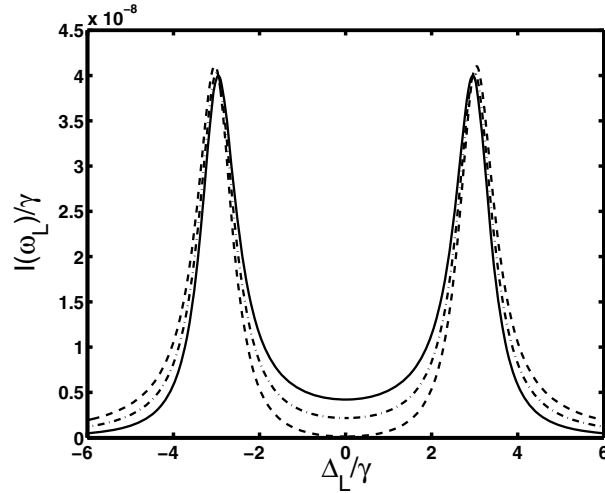


Fig. 4.11. The fluorescence intensity as a function of Δ_L for $Q = 10^{-4}\gamma$, $\delta = 0$, $\Delta = 6\gamma$ and $\gamma_u = \gamma_v = \gamma_1 = \gamma_2 = \gamma$. The *solid line* shows the intensity on the ultraviolet transition ($\beta_u = -1$), the *dashed line* shows the intensity on the visible transition ($\beta_v = 1$), and the *dashed-dotted line* is for the intensity for a transition with perpendicular dipole moments ($\beta = 0$)

Figure 4.11 shows the fluorescence intensity as a function of Δ_L for the visible and invisible transitions. It is evident that the intensity profile is composed of two peaks located at $\Delta_L = \pm\Delta/2$, and the amplitudes of the peaks are not sensitive to β . The intensity is sensitive to β only around $\Delta_L = 0$ and can be completely suppressed for $\beta_v = 1$ transitions. This is in agreement with the prediction by Agarwal [93] and Berman [94] that the two-photon excitation process involving the $|3\rangle$ and $|4\rangle$ levels can lead to cancellation of spontaneous emission at the two-photon resonance $\Delta_L = 0$.

In the experiment, however, a pronounced central peak at $\Delta_L = 0$ was observed, in addition to the sideband peaks located at $\Delta_L = \pm\Delta/2$, on the ultra-violet transitions with antiparallel dipole moments. According to (4.57), the theory does not predict the central peak for the $\beta_u = -1$ transitions. Thus, with two-photon excitation the fluorescence intensity exhibits two peaks regardless of the mutual orientation of the transition dipole moments. Wang et al. [92] have concluded that apart from the two-photon excitation process there must be some other processes involved in the dynamics of the system, and have suggested a two-step one-photon excitation in addition to the two-photon process.

4.4.4 One- and Two-Photon Excitations

Following the approach of Wang et al. [92], we suppose that the molecule is excited not only by the two-photon process but also by a two-step one-photon process involving the intermediate level $|2\rangle$. This channel of the excitation was possible in the experiment as the one-photon transitions in the molecule are in the visible region and their dipole moments are parallel [91]. Moreover, it is stated in the experimental paper [91] that the two-photon transition in sodium dimers was enhanced by a near-resonant intermediate level, indicating that the laser could also couple the ground state $|0\rangle$ to the upper states $|3\rangle, |4\rangle$ via cascaded one-photon transitions. Thus, the laser could also couple to the one-photon transitions $|0\rangle \rightarrow |2\rangle$ and $|2\rangle \rightarrow |3\rangle, |4\rangle$.

To illustrate the effect of the two-step one-photon coupling on the fluorescence intensity, we include into the Hamiltonian (4.59) the interaction of the laser field with the one-photon transitions, and obtain

$$\begin{aligned}
 H = & -\hbar \left(\Delta_L - \frac{1}{2}\Delta \right) A_{44} - \hbar \left(\Delta_L + \frac{1}{2}\Delta \right) A_{33} \\
 & - \frac{\hbar}{2} (\Delta_L + 2\delta) A_{22} + \hbar [Q (A_{40} + A_{30}) + \text{H.c.}] \\
 & + \frac{\hbar}{2} [\Omega_u (A_{42} + A_{32}) + \Omega_d A_{20} + \text{H.c.}] , \tag{4.65}
 \end{aligned}$$

where $\Omega_u = 2\boldsymbol{\mu}_{24} \cdot \boldsymbol{\mathcal{E}}_L/\hbar = 2\boldsymbol{\mu}_{23} \cdot \boldsymbol{\mathcal{E}}_L/\hbar$, and $\Omega_d = 2\boldsymbol{\mu}_{02} \cdot \boldsymbol{\mathcal{E}}_L/\hbar$ are the one-photon Rabi frequencies of the $|2\rangle \rightarrow |3\rangle, |4\rangle$ and $|0\rangle \rightarrow |2\rangle$ transitions, respectively.

Following the same procedure as in Sect. 4.4.3, we find that in the presence of the two-step one-photon excitation and in the weak-field limit ($\Omega_u, \Omega_d, Q \ll \gamma, \gamma_u, \gamma_d$), the steady-state solutions for the relevant populations and the coherence are

$$\begin{aligned}
\varrho_{44} &= \frac{4\Omega_u^2\Omega_d^2}{\left[(\Delta_L + 2\delta)^2 + \frac{1}{4}\gamma_2^2\right] \left[(\Delta_L - \frac{1}{2}\Delta)^2 + \frac{1}{4}\gamma^2\right]}, \\
\varrho_{33} &= \frac{4\Omega_u^2\Omega_d^2}{\left[(\Delta_L + 2\delta)^2 + \frac{1}{4}\gamma_2^2\right] \left[(\Delta_L + \frac{1}{2}\Delta)^2 + \frac{1}{4}\gamma^2\right]}, \\
\text{Re}(\varrho_{34}) &\simeq \frac{-16\Omega_u^2\Omega_d^2}{\Delta^2 \left[(\Delta_L + 2\delta)^2 + \frac{1}{4}\gamma_2^2\right]}. \tag{4.66}
\end{aligned}$$

The steady-state solution (4.66) shows that the populations of the upper levels as well as the coherences exhibit resonant behaviors not only on the two-photon resonances $\Delta_L = \pm\Delta/2$, but also on the one-photon resonance $\Delta_L = -2\delta$. The existence of the resonance at $\Delta_L = -2\delta$ illustrates the occurrence of the two-step one-photon excitation process. Hence, the fluorescence intensity will exhibit a peak at $\Delta_L = -2\delta$ of the linewidth γ_2 , and two sideband peaks located at $\Delta_L = \pm\Delta/2$ of the linewidth γ .

Substituting (4.66) into (4.57), we find that the fluorescence intensity for the ultraviolet and visible transitions can be written as

$$\begin{aligned}
I_{u/v} &= \frac{16\gamma\Omega_u^2\Omega_d^2}{\Delta^2} \left\{ \frac{2(1 - \beta_{u/v})}{(\Delta_L + 2\delta)^2 + \frac{1}{4}\gamma_2^2} \right. \\
&\quad \left. + \frac{1}{(\Delta_L - \frac{1}{2}\Delta)^2 + \frac{1}{4}\gamma^2} + \frac{1}{(\Delta_L + \frac{1}{2}\Delta)^2 + \frac{1}{4}\gamma^2} \right\}. \tag{4.67}
\end{aligned}$$

Thus, the fluorescence intensity is composed of three Lorentzians: the central peak located at $\Delta_L = -2\delta$ and two sidebands located at $\Delta_L = \pm\Delta/2$. Figure 4.12 shows the fluorescence intensity for a strong driving field obtained by numerical integration of the master equation (4.58) for three different values of the interference parameter β .

It is seen that the amplitude of the central peak strongly depends on the mutual polarization of the dipole moments. The peak is absent in the intensity I_v observed in the visible region with $\beta_v = 1$. For the fluorescence intensity I_u observed in the ultraviolet region with $\beta_u = -1$, the amplitude of the peak is enhanced. The strong dependence of the amplitude of the central peak on the mutual orientation of the molecular dipole moments is precisely the effect observed in the experiment. We emphasize again that the presence of the central peak in the fluorescent intensity results from the coupling of the driving laser to the one-photon transitions. This peak would be present even if there was no interference between the transitions (that is, even if the dipole moments were orthogonal with $\beta = 0$). The interference leads to an enhancement ($\beta_u = -1$) or cancellation ($\beta_v = 1$) of this central peak arising from cascaded one-photon excitations.

The intensity profile shown in Fig. 4.12 is symmetric about $\Delta_L = 0$. However, the experimentally observed fluorescent intensity was asymmetric

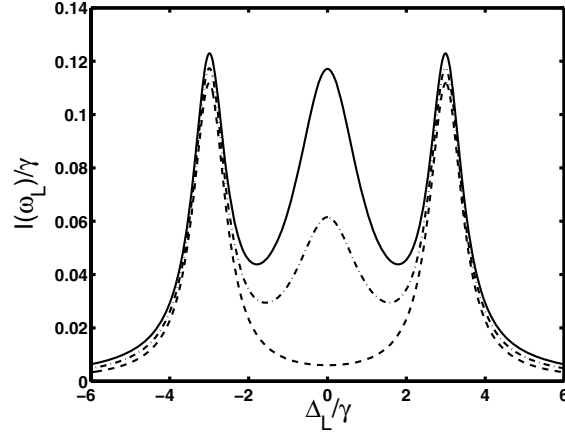


Fig. 4.12. The fluorescence intensity as a function of Δ_L for $\Omega_u = \Omega_d = 0.5\gamma$, $Q = 10^{-4}\gamma$, $\delta = 0$, $\Delta = 6\gamma$ and $\gamma_u = \gamma_v = \gamma_1 = \gamma_2 = \gamma$. The *solid line* shows the intensity on the ultraviolet transition ($\beta_u = -1$), the *dashed line* shows the intensity on the visible transition ($\beta_v = 1$), and the *dashed-dotted line* is for the intensity for a transition with perpendicular dipole moments ($\beta = 0$)

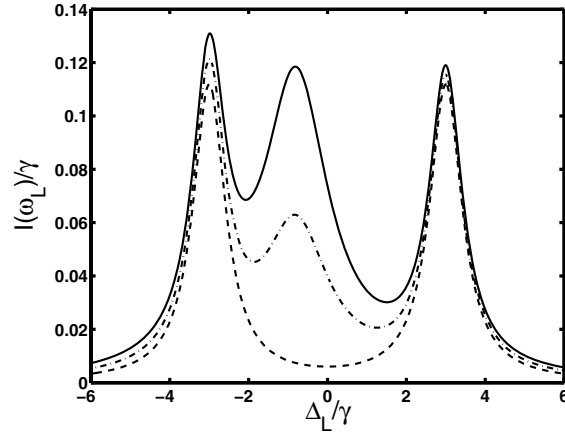


Fig. 4.13. The fluorescence intensity as a function of Δ_L for $\Omega_u = \Omega_d = 0.5\gamma$, $Q = 10^{-4}\gamma$, $\delta = 0.3\gamma$, $\Delta = 6\gamma$ and $\gamma_u = \gamma_v = \gamma_1 = \gamma_2 = \gamma$. The *solid line* shows the intensity on the ultraviolet transition ($\beta_u = -1$), the *dashed line* shows the intensity on the visible transition ($\beta_v = 1$), and the *dashed-dotted line* is for the intensity for a transition with perpendicular dipole moments ($\beta = 0$)

about $\Delta_L = 0$. There are a few factors that could contribute towards the observed asymmetry. For example, the decay rates from the two upper levels to the intermediate levels could be unequal. Another reason could be that the central peak is not exactly at $\Delta_L = 0$. The analytical solution (4.67) predicts the central peak to be at $\Delta_L = -2\delta$ and the condition of $\delta = 0$ implies that the energy of the level $|2\rangle$ is exactly half of the mean energy of the upper levels. There is no reason to expect this condition to be satisfied in the real molecule, and in fact it appears from the experimental results that δ

is positive. In Fig. 4.13 we plot the fluorescence intensity for a nonzero δ . In this case the intensity profile is asymmetric and the asymmetry increases with increasing δ .

The experiment of Xia et al. [91] provides a nice demonstration of the quantum interference effects in a multi-level system. However, Li et al. [95] repeated the two-photon experiment and did not observe the fluorescence signal reported by Xia et al. [91]. The major disagreement between these two experiments is found in the linewidths of the observed signals. However, a detailed comparison of these two experiments and theoretical calculations of the linewidths are rather difficult. In particular, the experimental conditions were not sufficiently well defined, which considerably complicates the interpretation of the observed signals and makes it difficult to resolve the disagreement between the experiments. Despite these disagreements, the theoretical model proposed by Wang et al. [92] correctly predicts the shape of the observed intensity profile and the variation of the number of peaks with the polarization of the dipole moments.

4.5 Decoherence Free Subspaces

Decoherence in physical systems is a consequence of the unavoidable coupling of the system to its environment, which results in an irreversible loss of information from the system. Clearly decoherence limits the efficiency of quantum information processing, and much activity has been devoted to ways of reducing or eliminating it. One manifestation of decoherence is the decay of the population of an atomic system due to spontaneous emission. However, we have seen in previous sections that systems can evolve into states that are decoherence-free – for example, the dark state of (4.14b). If we could find a set of states that had zero spontaneous decay rates, and were closed under the Hamiltonian evolution of the system, the set would be called a “decoherence-free subspace”, and it would obviously be of interest for applications such as quantum information processing. We wish to consider this concept in a little detail here, and to relate it to our previous work in this chapter. We refer the reader to an excellent review on decoherence-free subspaces by Lidar and Whaley [96].

4.5.1 A Simple Example of a Decoherence Free Subspace

First we consider a system with two states $|0\rangle$ and $|1\rangle$. We assume that a decohering process operates in this system that attaches a random phase to the second state only:

$$|0\rangle \rightarrow |0\rangle, \quad |1\rangle \rightarrow e^{i\phi}|1\rangle. \quad (4.68)$$

If the initial state of the system is $a|0\rangle + b|1\rangle$, where a and b are arbitrary, then after a single dephasing event the state of the system will be $a|0\rangle + be^{i\phi}|1\rangle$,

and the corresponding density matrix will be

$$\varrho(\phi) = |a|^2|0\rangle\langle 0| + |b|^2|1\rangle\langle 1| + ab^*e^{-i\phi}|0\rangle\langle 1| + a^*be^{i\phi}|1\rangle\langle 0|. \quad (4.69)$$

The random phase ϕ can take any value between $-\infty$ and $+\infty$. The simplest assumption is that it is distributed according to a gaussian distribution. Then the density matrix after a single dephasing event, averaged over all values of the phase, is given by

$$\bar{\varrho}_1 = \frac{1}{\sqrt{4\pi\sigma}} \int_{-\infty}^{\infty} d\phi \varrho(\phi) e^{-\phi^2/4\sigma}. \quad (4.70)$$

The integrals are easily evaluated: the density matrix becomes

$$\bar{\varrho}_1 = \begin{pmatrix} |a|^2 & ab^*e^{-\sigma} \\ a^*be^{-\sigma} & |b|^2 \end{pmatrix}. \quad (4.71)$$

The decay of the off-diagonal elements is a signature of decoherence. After many dephasing events, the off-diagonal elements decay to zero, leaving the density matrix diagonal:

$$\bar{\varrho}_\infty = \begin{pmatrix} |a|^2 & 0 \\ 0 & |b|^2 \end{pmatrix}. \quad (4.72)$$

Now we come to the idea of decoherence free subspace. Suppose we have two two-level systems, distinguished by the index j , and that the phase imposed on the state $|1\rangle$ is independent of j :

$$|0\rangle_j \rightarrow |0\rangle_j, \quad |1\rangle_j \rightarrow e^{i\phi}|1\rangle_j, \quad (j = 1, 2). \quad (4.73)$$

Under a single dephasing event, the four basis states are transformed to

$$\begin{aligned} |0\rangle_1|0\rangle_2 &\rightarrow |0\rangle_1|0\rangle_2, & |1\rangle_1|1\rangle_2 &\rightarrow e^{2i\phi}|1\rangle_1|1\rangle_2, \\ |0\rangle_1|1\rangle_2 &\rightarrow e^{i\phi}|0\rangle_1|1\rangle_2, & |1\rangle_1|0\rangle_2 &\rightarrow e^{i\phi}|1\rangle_1|0\rangle_2. \end{aligned} \quad (4.74)$$

The fact that both states in (4.74) transform with the same factor $\exp(i\phi)$ suggests that if we replace the set $\{|0\rangle_1|1\rangle_2, |1\rangle_1|0\rangle_2\}$ by the symmetrized (but un-normalized) set

$$\{|+\rangle = |0\rangle_1|1\rangle_2 + |1\rangle_1|0\rangle_2, |-\rangle = |0\rangle_1|1\rangle_2 - |1\rangle_1|0\rangle_2\}, \quad (4.75)$$

then the new states transform under multiplication by the same factor $\exp(i\phi)$:

$$\{|+\rangle, |-\rangle\} \rightarrow \{e^{i\phi}|+\rangle, e^{i\phi}|-\rangle\}. \quad (4.76)$$

This means that the density matrix elements in this subspace are unaffected by a dephasing event:

$$\langle j|\varrho|k\rangle \rightarrow (\langle j|e^{-i\phi}) \varrho (e^{i\phi}|k\rangle) = \langle j|\varrho|k\rangle, \quad (j, k = +, -), \quad (4.77)$$

and thus do not suffer decoherence. In other words, the set (4.75) forms a decoherence free subspace.

4.5.2 Experimental Verification of Decoherence Free Subspaces

An experimental demonstration of the existence of decoherence free subspaces was provided by Kwiat et al. [97], using a system rather similar to that described in the previous subsection. The two-level system employed was provided by the two independent polarization states of a photon: $|0\rangle$ being represented by a horizontal (H) polarization and $|1\rangle$ by a vertical (V) polarization. Pairs of correlated photons were produced by the process of spontaneous parametric down conversion in two thin, adjacent, nonlinear optical crystals of beta barium borate, cut for type 1 phase matching. An ultraviolet pump photon may be split inside the crystals into two correlated daughter photons emitted in different directions, energy being conserved in the process. An incident pump photon polarized at 45° has equal probability of down-converting in the first crystal to produce two H photons, or in the second crystal to produce two V photons. This leads to the maximally entangled state $(|HH\rangle + |VV\rangle)/\sqrt{2}$. The output state obtained can be varied by changing the experimental conditions – for example, by imposing a birefringent phase shift. By such means, one can produce photon pairs in any one of the four so-called Bell states

$$\begin{aligned} |\Phi^\pm\rangle &= (|HH\rangle \pm |VV\rangle)/\sqrt{2} , \\ |\Psi^\pm\rangle &= (|HV\rangle \pm |VH\rangle)/\sqrt{2} . \end{aligned} \quad (4.78)$$

We introduced the Bell states (4.78) in Sect. 3.2 as examples of maximally entangled states.

In the previous subsection, we discussed the effect of introducing a random phase to each of the single-photon basis states $\{|H\rangle, |V\rangle\}$. A more general situation is where the random phase shifts are introduced in the rotated basis states $\{|H\rangle \cos \theta + |V\rangle \sin \theta, -|H\rangle \sin \theta + |V\rangle \cos \theta\}$ for an arbitrary value of θ . The effect of such decoherence on each of the Bell states depends upon the basis to which the random phases are applied – that is, on the value of θ .

A measure of the effect of decoherence on a given state is provided by a quantity known as the *fidelity*, \mathcal{F} , which we now define. It is a quantity of general interest, as it is a measure of the change imposed upon a system by an arbitrary process, not necessarily decoherence. Consider a system which is prepared initially in a pure state $|\psi_{\text{in}}\rangle$, and then undergoes an interaction which changes the state, so that the system is finally described by a density matrix ϱ_{out} . In this case, the fidelity is defined to be

$$\mathcal{F}(\psi) = \langle \psi_{\text{in}} | \varrho_{\text{out}} | \psi_{\text{in}} \rangle . \quad (4.79)$$

In general, the initial state of the system is described by a density matrix

Table 4.1. A summary of the experimental results in terms of the fidelities. The $\mathcal{F}_{\text{out-pure}}$ column lists the fidelity of the final state with the target Bell state, the $\mathcal{F}_{\text{out-init}}$ column with the experimentally produced initial state, and the $\mathcal{F}_{\text{theory}}$ column the theoretically expected value. (The errors in this column reflect the fact that there is an experimental uncertainty of 0.5° in the value of θ .) The final column lists the fidelity of the final state with the theoretical prediction. From P.G. Kwiat, A.J. Berglund, J.B. Altepeter, A.G. White: Science **290**, 498 (2000). Copyright (2000) AAAS

| Bell state | $\mathcal{F}_{\text{out-pure}}$ | $\mathcal{F}_{\text{out-init}}$ | $\mathcal{F}_{\text{theory}}$ | $\mathcal{F}_{\text{out-init}}$ |
|-------------------|---------------------------------|---------------------------------|-------------------------------|---------------------------------|
| HH + VV | 0.51 ± 0.03 | 0.54 ± 0.04 | 0.5 | 1.00 ± 0.02 |
| HH - VV | 0.35 ± 0.02 | 0.34 ± 0.02 | 0.33 ± 0.01 | 0.98 ± 0.02 |
| HV + VH | 0.54 ± 0.02 | 0.53 ± 0.02 | 0.52 ± 0.02 | 0.99 ± 0.02 |
| HV - VH | 0.97 ± 0.04 | 1.00 ± 0.04 | 1 | 0.97 ± 0.04 |

ϱ_{in} rather than by a wavefunction, in which case the above definition is generalized to

$$\mathcal{F} = \left\{ \text{Tr} \left[(\sqrt{\varrho_{in}} \varrho_{out} \sqrt{\varrho_{in}})^{1/2} \right] \right\}^2. \quad (4.80)$$

For example, for $\theta = 0$, it can be shown that for the four Bell states, $\mathcal{F}(\Phi^\pm) = 0.5$, and $\mathcal{F}(\Psi^\pm) = 1$.

Of particular interest is the value $\theta = 17.6^\circ$, because this was a main focus of the experiments. Then it can be shown that $\mathcal{F}(\Phi^+) = 0.5$, $\mathcal{F}(\Phi^-) = 0.33$, $\mathcal{F}(\Psi^+) = 0.33$ and $\mathcal{F}(\Psi^-) = 1$. Thus the state $|\Psi^-\rangle$ suffers no decoherence losses if the random phases are introduced to the basis states with $\theta = 17.6^\circ$.

In the experiments, the quantum state of the two-photon contribution to the reduced density matrix with respect to polarization was determined tomographically. Decoherence was produced in this system by introducing a random phase into each arm by means of quartz plates. Detecting the photons introduces effectively a trace over the frequency degree of freedom, which plays the role of the environment, and the resulting reduced density matrix for the polarization becomes mixed.

Figure 4.14 shows the experimentally measured density matrices for the four Bell states. The left-hand panels represent the input states without decoherence and the right-hand panels the states after applying a specific collective decoherence. It can be seen that in case (d) the left- and right-hand density matrices appear identical.

The Table 4.1 compares the fidelity of the final state with the target state and the experimentally produced initial state.

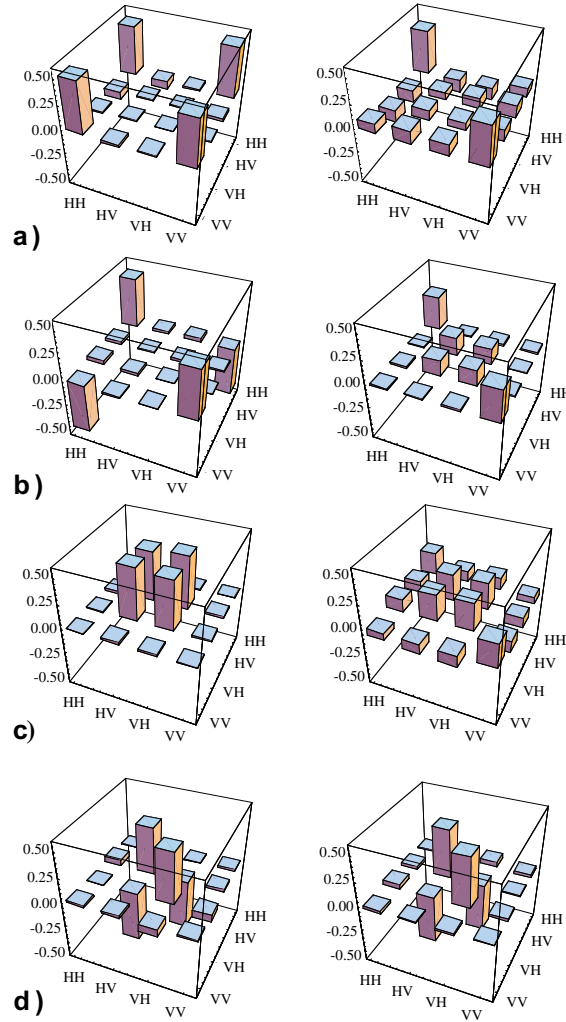


Fig. 4.14. The experimentally measured density matrices for the Bell states (a) $HH+VV$, (b) $HH-VV$, (c) $HV+VH$, and (d) $HV-VH$. The left panels represent the input states without decoherence; the right panels represent the resulting states after collective decoherence is applied in the 17° basis. Only the real parts are shown: the imaginary components, which theoretically are zero, were always less than a few percent. From P.G. Kwiat, A.J. Berglund, J.B. Altepeter, A.G. White: *Science* **290**, 498 (2000). Copyright (2000) AAAS

4.5.3 Tests on the Master Equation for a Decoherence Free Subspace

We have seen in Chap. 2 that if we start with the equation for the density matrix for a system interacting with a reservoir, and eliminate the degrees of freedom corresponding to the reservoir, we can obtain an equation for the reduced density matrix for the system alone (the “master equation”). Whilst the evolution of the composite ‘system plus reservoir’ is unitary, that of the reduced density matrix for the system alone is, in general, non-unitary. Lindblad has shown that if

1. the evolution of the master equation is Markovian,
2. the evolution is “completely positive”,⁴ and
3. the system and bath density matrices are initially decoupled,

then the master equation has the (Lindblad) form

$$\frac{d\rho(t)}{dt} = -\frac{i}{\hbar}[H_S, \rho(t)] + \mathcal{L}\rho(t) , \quad (4.81)$$

where $\rho(t)$ is the evolution of the reduced density matrix for the system alone, H_S is the effective system Hamiltonian, including possibly a unitary contribution from the reservoir (e.g. Lamb shifts), and

$$\mathcal{L}\rho(t) = \frac{1}{2} \sum_{i,j=1}^M \gamma_{ij} \left(2F_i \rho(t) F_j^\dagger - F_j^\dagger F_i \rho(t) - \rho(t) F_j^\dagger F_i \right) . \quad (4.82)$$

The term $\mathcal{L}\rho(t)$ contains all the terms responsible for decoherence, and represents a non-unitary evolution. The γ_{ij} are non-negative constants, and the F_i are system operators.

By inspection of the Lindblad form, it is easy to see the conditions for a subspace to be a decoherence free subspace. Let a subspace \mathbb{V} be spanned by the states

$$\{|\phi_\alpha\rangle\} , \quad \alpha = 1, \dots, n . \quad (4.83)$$

An arbitrary density matrix defined on this subspace is

$$\rho = \sum_{\alpha,\beta=1}^n \rho_{\alpha,\beta} |\phi_\alpha\rangle \langle \phi_\beta| , \quad (4.84)$$

and we define the operator subspace \mathcal{S} to be that subspace spanned by the basis operators

$$\{|\phi_\alpha\rangle \langle \phi_\beta|\} , \quad \alpha, \beta = 1, \dots, n . \quad (4.85)$$

Then clearly, if

$$H_S |\phi_\alpha\rangle \langle \phi_\beta| \in \mathcal{S} , \quad (4.86)$$

$$\mathcal{L} |\phi_\alpha\rangle \langle \phi_\beta| = 0 , \quad \alpha, \beta = 1, \dots, n , \quad (4.87)$$

then the subspace \mathbb{V} is a decoherence free subspace.

⁴ Basically this means that $\rho(t)$ satisfies the proper physical conditions of positivity for all t . For a technical definition and discussion, see M.A. Nielsen, I.L. Chang: *Quantum Computation and Quantum Information*, (Cambridge University Press Cambridge, 2000), Chap. 8.

Conditions (4.86) and (4.87) are the basic requirements for the set (4.83) to be a decoherence free subspace. The second condition, (4.87), is the requirement that a density operator belonging to \mathcal{S} be decoherence free, and the first condition, (4.86) is the condition that the unitary evolution under \mathcal{S} does not take a density operator originally in the operator space \mathcal{S} out of \mathcal{S} . (If this condition did not hold, the density operator may evolve to a density operator which *is* subject to decoherence.)

We now derive further conditions for a decoherence free subspace. Consider the Liouvillian operator of (4.81), and a subspace \mathbb{V} of the form (4.83). Further suppose that the elements of this subspace obey the relation

$$F_j |\phi_\alpha\rangle = \lambda_j |\phi_\alpha\rangle, \quad j = 1, \dots, M, \quad \alpha = 1, \dots, n, \quad (4.88)$$

where the F_j are the operators that appear in (4.81). That is, the basis states ϕ_α are degenerate eigenstates of all the operators F_j . ('Degenerate' because the eigenvalues do not depend on the index α .) Any density matrix defined on the space \mathbb{V} has the form (4.84). Substituting this expression into (4.81), and evaluating the matrix element, we obtain

$$\langle \phi_\epsilon | \mathcal{L} \left[\sum_{\alpha, \beta=1}^n \varrho_{\alpha, \beta} |\phi_\alpha\rangle \langle \phi_\beta| \right] | \phi_\eta \rangle = 0, \quad \forall \alpha, \beta, \quad (4.89)$$

from which we deduce that $\mathcal{L} |\phi_\alpha\rangle \langle \phi_\beta| = 0$.

Thus, if the elements of \mathbb{V} satisfy (4.88), the second condition for a decoherence free subspace is satisfied. It is important to note that this result holds *irrespective* of the values of the γ_{ij} of (4.81). One would have to test whether condition (4.86) was satisfied before one could conclude that \mathbb{V} was a decoherence free subspace.

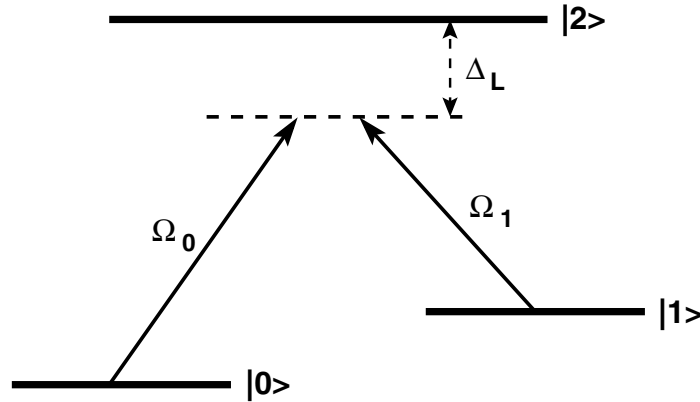


Fig. 4.15. The level diagram for the Lambda system driven by two laser fields of Rabi frequencies Ω_0 and Ω_1

We illustrate this result by considering the Lambda system of Fig. 4.15. The levels $|0\rangle$ and $|1\rangle$ are connected to level $|2\rangle$ by monochromatic fields of

frequencies ω_0 and ω_1 respectively, and Rabi frequencies Ω_0 and Ω_1 respectively. Each field is detuned by the same amount Δ_L from resonance, and it is assumed that the transition from $|0\rangle$ to $|1\rangle$ is forbidden.

The Hamiltonian H of the system is

$$H/\hbar = \sum_{j=0}^2 E_j A_{jj} + \frac{1}{2} (\Omega_0 e^{i\omega_0 t} A_{02} + \Omega_1 e^{i\omega_1 t} A_{12} + \text{H.c.}) , \quad (4.90)$$

where, as usual, $A_{ij} \equiv |i\rangle\langle j|$ and ‘H.c.’ means that the Hermitean conjugate of the preceding expression is to be added. We apply the unitary transform $U = \exp[-i \sum_{j=0}^2 (E_j - \Delta\delta_{j2}) A_{jj} t]$, when the transformed Hamiltonian $\hat{H} = U^\dagger H U - iU^\dagger \dot{U}$ becomes time independent

$$\hat{H}/\hbar = \Delta_L A_{22} + \frac{1}{2} (\Omega_0 A_{02} + \Omega_1 A_{12} + \text{H.c.}) . \quad (4.91)$$

Now consider the decoherence term, which is here due to spontaneous emission. We suppose that the dipole moments of the two transitions are perpendicular, so that the spontaneous decay is described by the following Liouvillian

$$\begin{aligned} \mathcal{L}\varrho = & \frac{1}{2} \gamma_{02} (2A_{02}\varrho A_{20} - A_{20}A_{02}\varrho - \varrho A_{20}A_{02}) \\ & + \frac{1}{2} \gamma_{12} (2A_{12}\varrho A_{21} - A_{21}A_{12}\varrho - \varrho A_{21}A_{12}) . \end{aligned} \quad (4.92)$$

We assume no spontaneous decay from the two lower levels. We may thus identify the ‘ F_j ’ operators of (4.81) for this Liouvillian as follows:

$$F_1 = A_{02} , \quad F_2 = A_{12} . \quad (4.93)$$

To search for a decoherence free subspace, we need to see if the eigenvalue equation

$$F_j |\phi_\alpha\rangle = \lambda_j |\phi_\alpha\rangle \quad (4.94)$$

has solutions where the λ_j are independent of α . From (4.94), we find

$$\begin{aligned} \langle \phi_\alpha | \lambda_2^* \lambda_1 | \phi_\alpha \rangle &= \langle \phi_\alpha | F_2^\dagger F_1 | \phi_\alpha \rangle \\ \text{i.e.} \quad \lambda_2^* \lambda_1 &= \langle \phi_\alpha | A_{21} A_{02} | \phi_\alpha \rangle = 0 . \end{aligned} \quad (4.95)$$

Thus either $\lambda_2 = 0$ or $\lambda_1 = 0$ (or both are zero). If $\lambda_1 = 0$, then (4.94) implies

$$A_{02} (|c_0|0\rangle + c_1|1\rangle + c_2|2\rangle) = 0 , \quad (4.96)$$

where we have expanded $|\phi_\alpha\rangle$ in terms of the atomic states. This equation implies $c_2 = 0$, and thus

$$|\phi\rangle = c_0|0\rangle + c_1|1\rangle . \quad (4.97)$$

where we drop the α subscript for convenience. It immediately follows that $A_{02}|\phi\rangle = 0$, and thus $\lambda_2 = \lambda_1 = 0$. The subspace that is free of spontaneous emission is the subspace spanned by the two lower levels

$$\mathbb{U} = \{|0\rangle, |1\rangle\} , \quad (4.98)$$

which is intuitively obvious as both these levels are assumed stable under spontaneous emission.

We must now see if the first condition for a decoherence free subspace, condition (4.86), can be satisfied. We require that the vector $\hat{H}|\phi\rangle$ should remain in the subspace \mathbb{U} , that is, it should not contain the state $|2\rangle$. We can write this condition as

$$A_{02}\hat{H}|\phi\rangle = 0 \quad \text{or} \quad (A_{02}\hat{H} - \hat{H}A_{02})|\phi\rangle = 0 , \quad (4.99)$$

since $A_{02}|\phi\rangle = 0$. We easily find that

$$(A_{02}\hat{H} - \hat{H}A_{02})/\hbar = \Delta_L A_{02} + \frac{1}{2}(\Omega_0 A_{00} + \Omega_1 A_{01} - \Omega_0 A_{22}) . \quad (4.100)$$

Applying this operator to the state $|\phi\rangle$, we obtain $|0\rangle(\Omega_0\langle 0|\phi\rangle + \Omega_1\langle 1|\phi\rangle) = 0$, giving us finally the condition $\Omega_0\langle 0|\phi\rangle + \Omega_1\langle 1|\phi\rangle = 0$. This determines the wave-function $|\phi\rangle$ as

$$|\phi\rangle = \frac{\Omega_1|0\rangle - \Omega_0|1\rangle}{\sqrt{\Omega_1^2 + \Omega_0^2}} . \quad (4.101)$$

It satisfies the relation $\hat{H}|\phi\rangle = 0$, showing that the particular combination in (4.101) undergoes destructive interference under evolution by the system Hamiltonian. The state $|\phi\rangle$ is completely decoupled from the dynamical evolution of the system.

The decoherence free subspace in this example is again one-dimensional, being simply the state $|\phi\rangle$. For quantum computing purposes, one-dimensional decoherence free subspaces are of little use: one requires multi-dimensional subspaces. However, the simple examples discussed above illustrate the underlying principles.

5 Coherence Effects in Multi-Level Systems

In the previous chapter, we looked at how atomic coherence effects could be produced by spontaneous emission, in the absence of external fields. A principal difference with this chapter is that here we examine how quantum interference and coherence can be induced by *applied fields*. We then proceed to show how these quantum properties can be exploited to control the nonlinear optical properties of multi-level atomic systems. One of the most striking phenomena that arises is electromagnetically induced transparency: a previously opaque optical medium can be rendered transparent to a probe field by applying an intense laser field of different frequency. This phenomenon, and related phenomena due to atomic coherence, have given rise to many important applications in nonlinear optics.

In order to present the basic phenomena in the simplest terms, we first limit ourselves to considering optically thin specimens, so that we do not need to consider propagation effects. We begin with a study of the Lambda, Vee and Ladder three-level systems, with particular emphasis on the Lambda system, and the phenomenon of coherent population trapping. The use of this effect in laser cooling and velocity selective coherent population trapping is described. Next, we discuss electromagnetically induced transparency and lasing without inversion.

After establishing the basic phenomena in this way, we introduce the wave equation, and discuss the features associated with spatial propagation of EM fields in optical media. We conclude with a discussion of some of the more important applications of EIT in nonlinear optics, such as the enhancement of nonlinear susceptibilities without increasing the absorption.

5.1 Three-Level Systems

There are three possible configurations for a three-level system illuminated by two monochromatic fields – the Lambda, Ladder and Vee configurations – as shown in Fig. 5.1. It is assumed that the direct transition $|1\rangle \leftrightarrow |2\rangle$ is forbidden in each case, and that the dipole moments of the two transitions are perpendicular, so that there are no cross-relaxation terms of the type discussed in Chap. 4. We have deviated from our customary labelling of the atomic levels for the Lambda and Ladder systems (but retained it for the

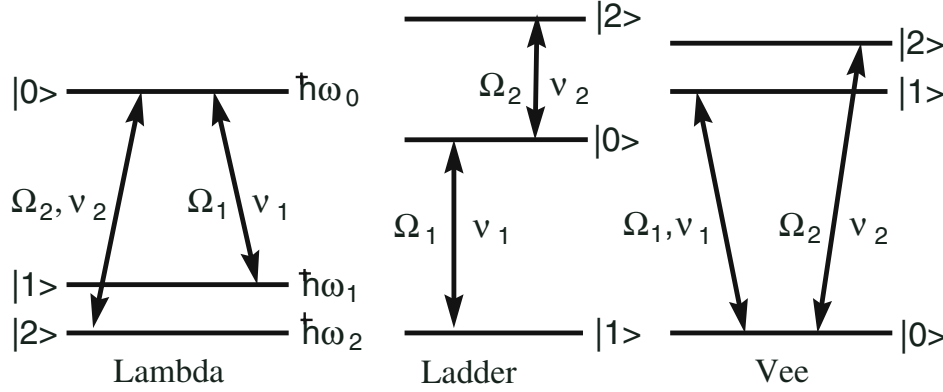


Fig. 5.1. Three-level systems in Lambda, Ladder and Vee configurations. The only allowed transitions are those shown in the figure, which in each case share the common level $|0\rangle$. The Rabi frequency for the transition $|0\rangle \leftrightarrow |k\rangle$ is denoted Ω_k and the corresponding laser frequency is denoted ν_k . Spontaneous emission also takes place on the allowed transitions, but this is not shown for clarity. The energy of the level $|k\rangle$ is $\hbar\omega_k$.

Vee) in order to make $|0\rangle$ the shared level in each case. The advantage of this notation is that, having found the solution for one configuration, it is easy to write down the solutions for the other two configurations. We shall, however, concentrate largely on the Lambda system in our discussions.

The basic physical effect underlying all the effects we describe in this chapter is called coherent population trapping (CPT). It differs in several respects from the population trapping described in Sect. 4.2, which was due to quantum interference induced by spontaneous emission in Vee systems with perpendicular dipole moments. Externally applied fields are essential for CPT: in fact, CPT may be described as the application of laser fields to an atomic system in such a way as to produce a coherent superposition of atomic states that does not absorb radiation from the EM field.

CPT was observed by Alzetta and co-workers at the University of Pisa in 1976 [98], using essentially the driven Lambda system of Fig. 5.1 in which the hyperfine levels of sodium played the role of levels $|1\rangle$ and $|2\rangle$. They demonstrated that when a two-photon resonance condition applied, the fluorescence from state $|0\rangle$, which is a measure of the population in that state, was greatly reduced. Effectively the population of $|0\rangle$ was reduced to zero. This can be understood in terms of quantum interference. There are two contributions to the probability amplitude for the population of state $|0\rangle$, one coming from state $|1\rangle$ and the other from state $|2\rangle$. When the experimental conditions are such that the probability amplitude from state $|1\rangle$ is equal in magnitude but opposite in sign to that from state $|2\rangle$, the quantum interference is completely destructive and the population of state $|0\rangle$ is zero. When this happens, we shall see that the state of the system is a coherent superposition of the levels $|1\rangle$ and $|2\rangle$.

5.1.1 The Basic Equations for Coherent Population Trapping

We first concentrate on the Lambda configuration. Because population is conserved in this system under spontaneous decay, the Wigner–Weisskopf approach cannot be employed here, and we must use the density matrix description. For the Lambda system the general master equation (2.49) reduces to

$$\frac{d\rho}{dt} = -\frac{i}{\hbar}[H_0 + V, \rho] + \mathcal{L}\rho, \quad (5.1)$$

where

$$H_0 = \hbar \sum_{k=1}^3 \omega_k A_{kk} \quad (5.2)$$

is the Hamiltonian of the atom,

$$V = \frac{1}{2}\hbar (\Omega_2 A_{20} e^{i\nu_2 t} + \Omega_1 A_{10} e^{i\nu_1 t} + \text{H.c.}) \quad (5.3)$$

is the interaction of the atom with the external laser fields, and

$$\begin{aligned} \mathcal{L}\rho = & \frac{1}{2}\zeta_{02} (2\rho_{00}A_{22} - \rho A_{00} - A_{00}\rho) \\ & + \frac{1}{2}\zeta_{01} (2\rho_{00}A_{11} - \rho A_{00} - A_{00}\rho) \end{aligned} \quad (5.4)$$

represents the damping of the atom by spontaneous emission.

Here, as usual, $A_{jk} = |j\rangle\langle k|$ and the energy of level $|j\rangle$ is $\hbar\omega_j$. Also, ν_j is the frequency of the driving laser on the $|0\rangle \leftrightarrow |j\rangle$ transition, and Ω_j is the corresponding Rabi frequency. The latter is in general assumed to be complex to allow for different phases between the two lasers. We have introduced the notation that ζ_{ij} is the spontaneous decay rate from $|i\rangle$ to $|j\rangle$, and hence $\gamma_i = \sum_j \zeta_{ij}$ is the total spontaneous decay rate of level $|i\rangle$.

The explicit time dependence in (5.3) can be removed by applying the unitary transformation $\rho = U\tilde{\rho}U^\dagger$, where

$$U = \exp\{it[(\omega_2 - \delta_2)A_{22} + (\omega_1 - \delta_1)A_{11} + \omega_0 A_{00}]\}, \quad (5.5)$$

with $\delta_j \equiv \nu_j - \omega_{0,j}$ the detuning of the relevant laser from the $|0\rangle$ to $|j\rangle$ transition and $\omega_{k,j} \equiv \omega_k - \omega_j$. Then the master equation for the transformed density operator $\tilde{\rho}$ takes the form

$$\dot{\tilde{\rho}} = -\frac{i}{\hbar} [\tilde{H}_0 + \tilde{V}, \tilde{\rho}] + \tilde{\mathcal{L}}\tilde{\rho}, \quad (5.6)$$

where

$$\begin{aligned} \tilde{H}_0 &= \hbar\delta_2 A_{22} + \hbar\delta_1 A_{11}, \\ \tilde{V} &= \frac{1}{2}\hbar (\Omega_2 A_{20} + \Omega_1 A_{10} + \text{H.c.}), \end{aligned} \quad (5.7)$$

and $\tilde{\mathcal{L}} = \mathcal{L}$.

5.1.2 The Solutions Under Two-Photon Resonance

The simplest case to consider is that in which the *two-photon resonance* condition holds in the transition $|1\rangle \leftrightarrow |2\rangle$ via the state $|0\rangle$. The condition may be written

$$\delta_1 = \delta_2 , \quad \text{or equivalently} \quad \omega_2 - \omega_1 = \nu_1 - \nu_2 . \quad (5.8)$$

In the remainder of this subsection, we assume this condition to be satisfied. Setting $\delta_1 = \delta_2 = \delta$ in (5.7), it is easily demonstrated by direct substitution that the pure state density matrix

$$\tilde{\rho}_{NC} = |\Psi_{NC}\rangle\langle\Psi_{NC}| , \quad (5.9)$$

where

$$|\Psi_{NC}\rangle = \frac{\Omega_2^*|1\rangle - \Omega_1^*|2\rangle}{\Omega_+} , \quad (5.10)$$

with

$$\Omega_+ = \sqrt{|\Omega_1|^2 + |\Omega_2|^2} , \quad (5.11)$$

satisfies (5.6) with $\dot{\tilde{\rho}} = 0$ – that is, $\tilde{\rho}_{NC}$ is a steady state solution of this equation.

The state (5.10) is called the “non-coupled state”, because one easily verifies that

$$\tilde{H}_0|\Psi_{NC}\rangle = \delta|\Psi_{NC}\rangle ; \quad \tilde{V}|\Psi_{NC}\rangle = 0 ; \quad \text{and also} \quad \tilde{\mathcal{L}}\tilde{\rho}_{NC} = 0 , \quad (5.12)$$

where the operators are defined in (5.7). Thus $|\Psi_{NC}\rangle$ is not coupled to any other state by either the applied electromagnetic fields or the vacuum electromagnetic field: it is stable with respect to the free evolution of the Hamiltonian and to spontaneous decay. If the system evolves into this state, it will remain in it indefinitely. Since transitions into this state are possible whereas transitions out of it are not, the system, starting from an arbitrary initial state, will eventually evolve into $|\Psi_{NC}\rangle$: population becomes “trapped” in the non-coupled state.

By contrast, the orthogonal state to $|\Psi_{NC}\rangle$, the “coupled” state

$$|\Psi_C\rangle = \frac{\Omega_1|1\rangle + \Omega_2|2\rangle}{\Omega_+} , \quad (5.13)$$

is strongly coupled via the applied and vacuum electromagnetic fields. One may use the set $\{|0\rangle, |\Psi_{NC}\rangle, |\Psi_C\rangle\}$ as an alternative basis, called the CPT basis, to describe the system in place of the basis $\{|0\rangle, |1\rangle, |2\rangle\}$, although we do not do so here. The states $\{|\Psi_{NC}\rangle, |\Psi_C\rangle\}$ have a similar structure to the

symmetric and antisymmetric states (4.14), but with the spontaneous decay rates replaced by the Rabi frequencies.

Let us suppose that the system has evolved into the state $|\Psi_{NC}\rangle$, where it remains. Using expressions (5.9) – (5.11), we obtain the steady-state density matrix elements under two-photon resonance as:

$$\begin{aligned} P_0(\infty) &= 0, & \tilde{\varrho}_{01}(\infty) &= 0, \\ P_1(\infty) &= |\Omega_2|^2/\Omega_+^2, & \tilde{\varrho}_{02}(\infty) &= 0, \\ P_2(\infty) &= |\Omega_1|^2/\Omega_+^2, & \tilde{\varrho}_{12}(\infty) &= -\Omega_1\Omega_2^*/\Omega_+^2, \end{aligned} \quad (5.14)$$

where $P_j(t) \equiv \langle j|\tilde{\varrho}(t)|j\rangle$ denotes the occupation probability of level $|j\rangle$.

The results (5.14) are at first sight surprising, as they show that the steady-state occupation probability of the excited level $|0\rangle$ is zero, even when it is strongly driven by two lasers from the lower levels $|1\rangle$ and $|2\rangle$, which themselves have an appreciable occupation probability. They can be understood as a consequence of the relations (5.12).

Notice that the results for the probabilities are independent of δ_1 (or δ_2) provided the two-photon resonance condition $\delta_1 = \delta_2$ is satisfied, and that they are also independent of the relative phase of the driving lasers. The steady-state coherence $\tilde{\varrho}_{12}(\infty)$ does however depend on the relative phase. Note also that the magnitude of the coherence $\tilde{\varrho}_{12}(\infty)$ is large. It is this feature – the induced two-photon coherence between two levels that are not coupled directly by the applied fields – that makes the three-level system such an interesting object of study.

Since the absorption coefficient for the transition $|0\rangle \leftrightarrow |j\rangle$, ($j = 1, 2$) is determined by $\tilde{\varrho}_{0j}(\infty)$, the fact that $\tilde{\varrho}_{0j}(\infty) = 0$ means that a monochromatic probe beam applied to the system would exhibit no absorption on this transition.

5.1.3 The General Equations of Motion for the Density Matrix

As in Sect. 4.3, it is convenient to work with the Laplace transform as defined in (4.45) and to make use of expression (4.46) for the Laplace transform of the differential coefficient

$$\tilde{\varrho}(z) \equiv \int_0^\infty dt \tilde{\varrho}(t) \exp(-zt), \quad (5.15)$$

and

$$\mathcal{L}(\dot{\tilde{\varrho}}) = z\tilde{\varrho}(z) - \tilde{\varrho}(0), \quad (5.16)$$

where $\tilde{\varrho}(0)$ is the value of $\tilde{\varrho}(t)$ at $t = 0$. As we are interested ultimately in the steady-state solutions, which do not depend upon the initial conditions, we choose a simple value for $\tilde{\varrho}(0)$, namely $\tilde{\varrho}(0) = |0\rangle\langle 0|$.

Before proceeding, we generalize the model to allow for an irreversible loss of population from the excited state $|0\rangle$ at the rate I , such as may be caused

by ionization. We can then examine the conditions for population trapping to occur in this situation [99].

The Laplace transforms of the equations of motion for the density matrix elements then become

$$(z + \gamma_0 + I)\tilde{\varrho}_{00} - 1 = \frac{i}{2} (\Omega_2\tilde{\varrho}_{02} + \Omega_1\tilde{\varrho}_{01} - \Omega_2^*\tilde{\varrho}_{20} - \Omega_1^*\tilde{\varrho}_{10}) , \quad (5.17a)$$

$$(z + \gamma_1)\tilde{\varrho}_{11} = \zeta_{01}\tilde{\varrho}_{00} - \frac{i}{2} (\Omega_1\tilde{\varrho}_{01} - \Omega_1^*\tilde{\varrho}_{10}) , \quad (5.17b)$$

$$z\tilde{\varrho}_{22} = \zeta_{02}\tilde{\varrho}_{00} + \zeta_{12}\tilde{\varrho}_{11} - \frac{i}{2} (\Omega_2\tilde{\varrho}_{02} - \Omega_2^*\tilde{\varrho}_{20}) , \quad (5.17c)$$

$$(z + \xi_{10})\tilde{\varrho}_{10} = \frac{i}{2} [\Omega_2\tilde{\varrho}_{12} - \Omega_1(\tilde{\varrho}_{00} - \tilde{\varrho}_{11})] , \quad (5.17d)$$

$$(z + \xi_{02})\tilde{\varrho}_{02} = -\frac{i}{2} [\Omega_1^*\tilde{\varrho}_{12} - \Omega_2^*(\tilde{\varrho}_{00} - \tilde{\varrho}_{22})] , \quad (5.17e)$$

$$(z + \xi_{12})\tilde{\varrho}_{12} = -\frac{i}{2} (\Omega_1\tilde{\varrho}_{02} - \Omega_2^*\tilde{\varrho}_{10}) , \quad (5.17f)$$

where we introduce the complex decay rates

$$\xi_{10} = \frac{1}{2} (\Gamma_{01} + I) + i\delta_1 , \quad (5.18a)$$

$$\xi_{02} = \frac{1}{2} (\Gamma_{02} + I) - i\delta_2 , \quad (5.18b)$$

$$\xi_{12} = \frac{1}{2} \Gamma_{12} + i\delta_1 - i\delta_2 , \quad (5.18c)$$

and $\tilde{\varrho}_{jk}(z) = \tilde{\varrho}_{kj}^*(z)$ ($j \neq k$). In (5.18), $\Gamma_{jk} = \gamma_j + \gamma_k$ is the sum of the spontaneous decay rates of levels $|j\rangle$ and $|k\rangle$, and $\gamma_0 = \zeta_{01} + \zeta_{02}$ is the total rate of spontaneous transitions out of level $|0\rangle$. Similarly, $\gamma_1 = \zeta_{12}$ is the total decay rate of level $|1\rangle$. For the Lambda system, we have assumed $|2\rangle$ is the ground state, so that we put $\gamma_2 = 0$. For brevity, we have suppressed the z -dependence of the $\tilde{\varrho}_{jk}$. Note that for the Lambda system, it is usually the case that $\zeta_{12} = \gamma_1$ is very small compared to the other decay rates. In fact, we shall show that for CPT to occur, it is necessary that $\gamma_1 = 0$.

In order to obtain an analytic solution to the set (5.17) of nine equations we first make a partial solution. We consider the subset of equations for the off-diagonal elements, and find the solution for the off-diagonal elements in terms of the diagonal elements. These solutions are then substituted into the remaining equations for the diagonal elements. After rearrangement, the resulting equations have the structure of a set of rate equations in Laplace space. Denoting the diagonal elements as $P_j(z) \equiv \tilde{\varrho}_{jj}(z)$, we have

$$zP_0 - 1 = -W_0P_0 + W_{10}P_1 + W_{20}P_2 , \quad (5.19a)$$

$$zP_1 = -W_1P_1 + W_{01}P_0 + W_{21}P_2 , \quad (5.19b)$$

$$zP_2 = -W_2P_2 + W_{02}P_0 + W_{12}P_1 , \quad (5.19c)$$

which have an obvious gain–loss interpretation in terms of the generalized transition rates from level $|j\rangle$ to level $|k\rangle$, W_{jk} , which like the P_j are functions of z . [See Fig. 5.2.] The W_j are the total transition rates *out of* level $|j\rangle$ – that is, $W_0 = W_{01} + W_{02} + I$, $W_1 = W_{10} + W_{12}$, and $W_2 = W_{21} + W_{20}$. In Laplace space, the left-hand side of the above equations represents the rate of change of the occupation probability of level $|j\rangle$, whilst the right-hand side is the difference between the rate of transitions *into* the level $|j\rangle$ and the rate of transitions *out of* it.¹

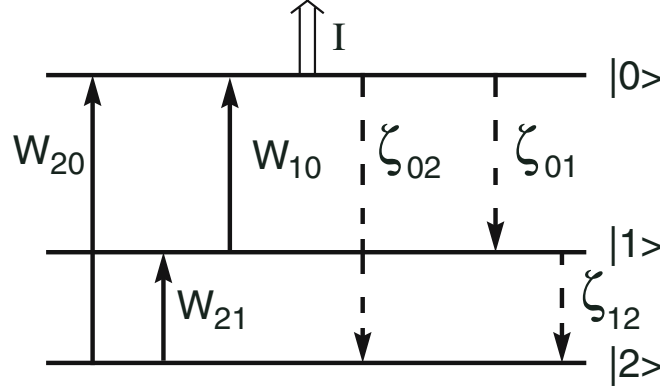


Fig. 5.2. The upward transition rates (*solid lines*) and the spontaneous decay rates (*dashed lines*) in the Lambda system. To each upward rate W_{jk} there corresponds a downward rate $W_{kj} = W_{jk} + \zeta_{kj}$, which we have not shown to avoid cluttering the diagram. The irreversible loss rate I from $|0\rangle$ is also shown

Explicitly, the upward rates are given by

$$W_{10} = W'_{10} - W_{21}; \quad W_{20} = W'_{20} - W_{21}, \quad (5.20a)$$

$$W'_{10} = 2\text{Re}[|\Omega_1|^2(\xi_{02}\xi_{12} + |\Omega_1|^2)/F], \quad (5.20b)$$

$$W'_{20} = 2\text{Re}[|\Omega_2|^2(\xi_{10}\xi_{12} + |\Omega_2|^2)/F], \quad (5.20c)$$

$$W_{21} = 2\text{Re}[|\Omega_2\Omega_1|^2/F], \quad (5.20d)$$

where

$$F = \xi_{10}\xi_{02}\xi_{12} + |\Omega_1|^2\xi_{10} + |\Omega_2|^2\xi_{02}. \quad (5.21)$$

Consider for example the expression for W_{10} . It may be understood in the following way [100]. The first term W'_{10} is the result of the *direct* process which takes the initial density matrix ϱ_{11} to the final density matrix ϱ_{00} under the atom-laser interaction via the process

¹ It is not coincidence that the density matrix equations for the Lambda system can be cast into the above form. It has been shown [100] that any time-independent density matrix equation with damping given by the Lindblad form can be rewritten as a set of rate equations in Laplace space.

$$\varrho_{11} \rightarrow \varrho_{01} \rightarrow \varrho_{00} , \quad (5.22)$$

and the Hermitean conjugate process ($\varrho_{11} \rightarrow \varrho_{10} \rightarrow \varrho_{00}$).

The second contribution, $-W_{21}$, is the contribution from the *indirect* (two-photon) process:

$$\varrho_{11} \rightarrow \varrho_{01} \rightarrow \varrho_{21} \rightarrow \varrho_{01} \rightarrow \varrho_{00} , \quad (5.23)$$

(plus conjugate process). The direct and indirect processes interfere to produce the net transition rate W_{10} .

The downward rates are obtained by adding the appropriate spontaneous emission rate to the upward rates:

$$W_{01} = \zeta_{01} + W_{10} , \quad (5.24a)$$

$$W_{02} = \zeta_{02} + W_{20} , \quad (5.24b)$$

$$W_{12} = \zeta_{12} + W_{21} . \quad (5.24c)$$

These expressions apply to the Lambda system.

For the Ladder and Vee systems, the upward and downward rates are different, as may be seen from Fig. 5.1. For the Ladder system for example, W_{10}, W_{02} and W_{12} are the upward transition rates, instead of W_{10}, W_{20} and W_{21} as in the case of the Lambda system. Our equations still apply, provided we make the interchanges

$$X_{02} \leftrightarrow X_{20} , \quad X_{21} \leftrightarrow X_{12} , \quad X = W, \zeta , \quad (\text{Ladder}) . \quad (5.25)$$

For example, for the Ladder system, we have the downward rates

$$W_{01} = \zeta_{01} + W_{10} , \quad (5.26a)$$

$$W_{20} = \zeta_{20} + W_{02} , \quad (5.26b)$$

$$W_{21} = \zeta_{21} + W_{12} , \quad (5.26c)$$

instead of (5.24). For the Vee system, the replacements are

$$X_{02} \leftrightarrow X_{20} , \quad X_{21} \leftrightarrow X_{12} , \quad X_{10} \leftrightarrow X_{01} , \quad X = W, \zeta , \quad (\text{Vee}) . \quad (5.27)$$

The solution to the set (5.19) is easily found:

$$P_0 = [(z + W_1)(z + W_2) - W_{12}W_{21}] / D , \quad (5.28a)$$

$$P_1 = [(z + W_2)W_{01} + W_{02}W_{21}] / D , \quad (5.28b)$$

$$P_2 = [(z + W_1)W_{02} + W_{01}W_{12}] / D , \quad (5.28c)$$

where

$$D = z [z^2 + z(W_0 + W_1 + W_2) + W_0W_1 + W_1W_2 + W_2W_0 - W_{01}W_{10} - W_{12}W_{21} - W_{20}W_{02}] + i(W_1W_2 - W_{12}W_{21}) . \quad (5.29)$$

The steady-state atomic occupation probabilities are obtained from the above solutions by making use of the Laplace identity

$$\lim_{t \rightarrow \infty} \tilde{\rho}_{jj}(t) = \lim_{z \rightarrow 0} z P_j(z) \equiv P_j(\infty) . \quad (5.30)$$

It will be observed that D must possess a factor of z in order to ensure that the steady-state atomic occupation probabilities are nonzero. The condition for this is clearly

$$W_1(0)W_2(0) - W_{12}(0)W_{21}(0) = 0 , \quad (5.31)$$

where we have indicated explicitly that z must be set to zero in the transition rates. Equation (5.31) is the condition for population trapping to occur in the system. For the Lambda system, it may be written

$$W'_{20}(0)W'_{10}(0) - W_{12}^2(0) = 0 . \quad (5.32)$$

That is, the condition for population trapping is that the indirect transition rate $W_{12}(0)$ be equal to the geometric mean of the direct transition rates $W'_{20}(0)$ and $W'_{10}(0)$.

From (5.20) and (5.24), it is straightforward to see that (5.32) is satisfied if

$$\delta_1 = \delta_2 \quad \text{and} \quad \zeta_{12} = 0 . \quad (5.33)$$

Thus, population trapping occurs in the Lambda system under conditions of two photon resonance, $\delta_1 = \delta_2$, provided there is no spontaneous decay between the two lower levels. It occurs if there is spontaneous emission between the excited level and the two lower levels, even in the presence of an irreversible loss from the excited state. We remark that is quite easy to generalize our treatment to deal with the case that the exciting lasers are not monochromatic, but have finite linewidths [99]. Then it can be shown that population trapping does *not* occur.

For the case of two-photon resonance in the Lambda system, we find on setting $\delta_1 = \delta_2$ and $\zeta_{12} = 0$ in (5.20):

$$W'_{10}(0) = |\Omega_1|^4 G , \quad (5.34a)$$

$$W'_{20}(0) = |\Omega_2|^4 G , \quad (5.34b)$$

$$W_{12}(0) = W_{21}(0) = |\Omega_1 \Omega_2|^2 G , \quad (5.34c)$$

where $G \equiv 2\text{Re}\{1/F(0)\}$. We find that the steady-state occupation probabilities for the lower two levels may be written in the form

$$P_1(\infty) = \Omega_2^2 [(I + \zeta_{01}) \Omega_2^2 + \zeta_{02} \Omega_1^2] / D_0 , \quad (5.35a)$$

$$P_2(\infty) = \Omega_1^2 [(I + \zeta_{01}) \Omega_2^2 + \zeta_{02} \Omega_1^2] / D_0 , \quad (5.35b)$$

$$P_0(\infty) = 0 , \quad (5.35c)$$

where

$$D_0 = (\Omega_1^2 + \Omega_2^2) [I (\Omega_1^2 + \Omega_2^2) + \zeta_{01}\Omega_2^2 + \zeta_{02}\Omega_1^2] . \quad (5.36)$$

In the case where the spontaneous decay rates ζ_{01} and ζ_{02} are much smaller than the ionization rate, these expressions reduce to

$$P_1(\infty) = \frac{\Omega_2^4}{(\Omega_1^2 + \Omega_2^2)^2} , \quad (5.37a)$$

$$P_2(\infty) = \frac{\Omega_1^2\Omega_2^2}{(\Omega_1^2 + \Omega_2^2)^2} , \quad (5.37b)$$

$$P_0(\infty) = 0 . \quad (5.37c)$$

It is clear that a fraction $\Omega_1^2/(\Omega_1^2 + \Omega_2^2)$ of the population is ionized. The steady-state of the system is

$$\tilde{\varrho}(\infty) = \frac{\Omega_2^2}{(\Omega_1^2 + \Omega_2^2)} |\Psi_{NC}\rangle\langle\Psi_{NC}| . \quad (5.38)$$

On the other hand, if we set $I = 0$ in (5.35), we find

$$P_1(\infty) = \frac{\Omega_2^2}{\Omega_1^2 + \Omega_2^2} , \quad (5.39a)$$

$$P_2(\infty) = \frac{\Omega_1^2}{\Omega_1^2 + \Omega_2^2} , \quad (5.39b)$$

$$P_0(\infty) = 0 , \quad (5.39c)$$

in agreement with (5.14). The steady-state of the system is now simply

$$\tilde{\varrho}(\infty) = |\Psi_{NC}\rangle\langle\Psi_{NC}| . \quad (5.40)$$

It is important to note that this result is independent of the decay rates ζ_{01} and ζ_{02} : the CPT steady-state does not depend upon these quantities in the absence of an irreversible loss from the excited state. In the next subsection we analyze the general case by numerical evaluations of (5.28).

5.1.4 Steady-State Solutions

When the two-photon resonance condition (5.8) is not satisfied, it is simplest to evaluate the expressions (5.37) numerically. First of all assuming $\delta_2 = 0$, we show the populations $P_j(\infty)$, $j = 0, 1, 2$, as a function of δ_1 for a range of parameter values in Fig. 5.3. In Frames (a) and (b) the decay rates are equal but the Rabi frequencies differ, in Frames (c) and (d) the decay rates are markedly different but the Rabi frequencies are equal. All quantities are measured in units of $\zeta_{01} \equiv \zeta$. It is clear that changing the relative values of the

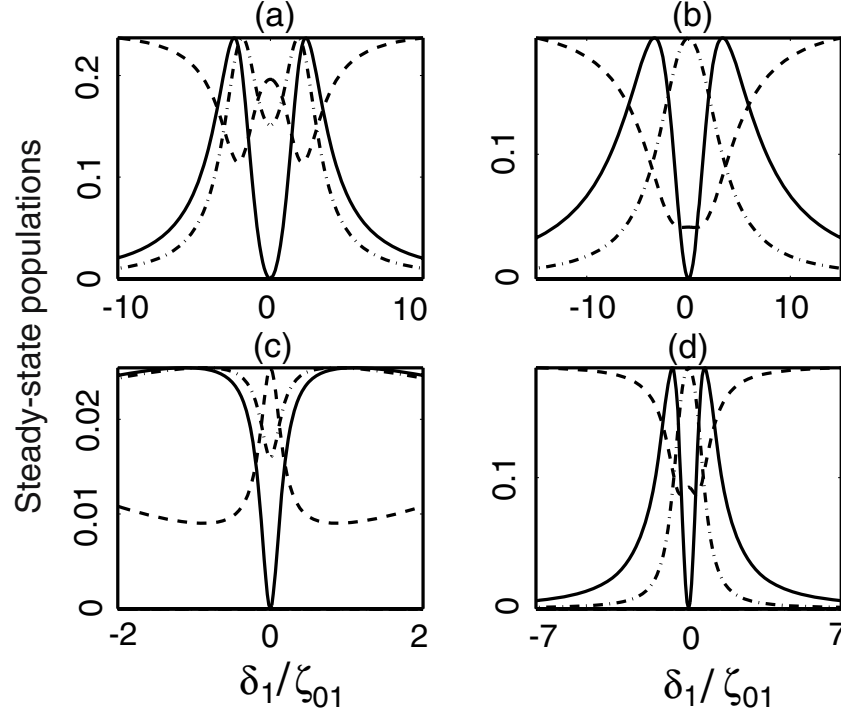


Fig. 5.3. The steady-state populations of state $|0\rangle$ (*solid line*), state $|1\rangle$ (*dashed line*) and state $|2\rangle$ (*dot-dashed line*) for $\delta_2 = 0$. In **(a)**, $\zeta_{01} = \zeta_{02} = \zeta$, $\Omega_1 = \zeta$, $\Omega_2 = 2\zeta$; in **(b)**, $\zeta_{01} = \zeta_{02} = \zeta$, $\Omega_1 = 2\zeta$, $\Omega_2 = \zeta$; in **(c)**, $\zeta_{01} = \zeta$, $\zeta_{02} = 5\zeta$, $\Omega_1 = \Omega_2 = 0.5\zeta$; in **(d)**, $\zeta_{01} = \zeta$, $\zeta_{02} = 0.2\zeta$, $\Omega_1 = \Omega_2 = 0.5\zeta$. All graphs in the same frame have been normalized to the maximum value of $P_0(\infty)$

Rabi frequencies and/or the decay rates produces qualitative changes in the graphs of $P_1(\infty)$ and $P_2(\infty)$. For $\delta_2 = 0$, the graphs are all symmetric about $\delta_1 = 0$. Of most interest is the plot for P_0 , which exhibits a zero when the two-photon resonance condition $\delta_1 = \delta_2 = 0$ is satisfied, as predicted analytically in subsection 5.1.2. As a function of δ_1 , it is always doubly peaked. The plots for P_1 and P_2 may have one, two or three turning points, and they may exhibit a maximum or a minimum at $\delta_1 = 0$. The plot for $P_0(\infty)$ in Frame (d) is similar to that which has been observed experimentally, as we discuss in the next subsection.

In Fig. 5.4, the parameter values are unchanged except for the value of δ_2 , which now is $\delta_2 = 5\zeta$. The probabilities are all now markedly asymmetric functions of δ_1 . For P_0 , the lineshape is dispersive around $\delta_1 = \delta_2$, and is reminiscent of the so-called Fano profiles, which arise when a discrete state is coupled to a continuum, as in the autoionizing resonances.² Both phenomena are due to quantum interference. Note also the very fine structures in Frames (c) and (d).

² U. Fano: Phys. Rev. **124**, 1866 (1961). Fano profiles and lineshapes are discussed in Chap. 6.

The switch between absorptive profile for P_0 for resonant excitation $\delta_2 = 0$ and dispersive profiles for off-resonant excitation $\delta_2 \neq 0$ is clearly seen in these two figures. Figure 5.5 shows $P_0(\infty)$ for some parameter values more

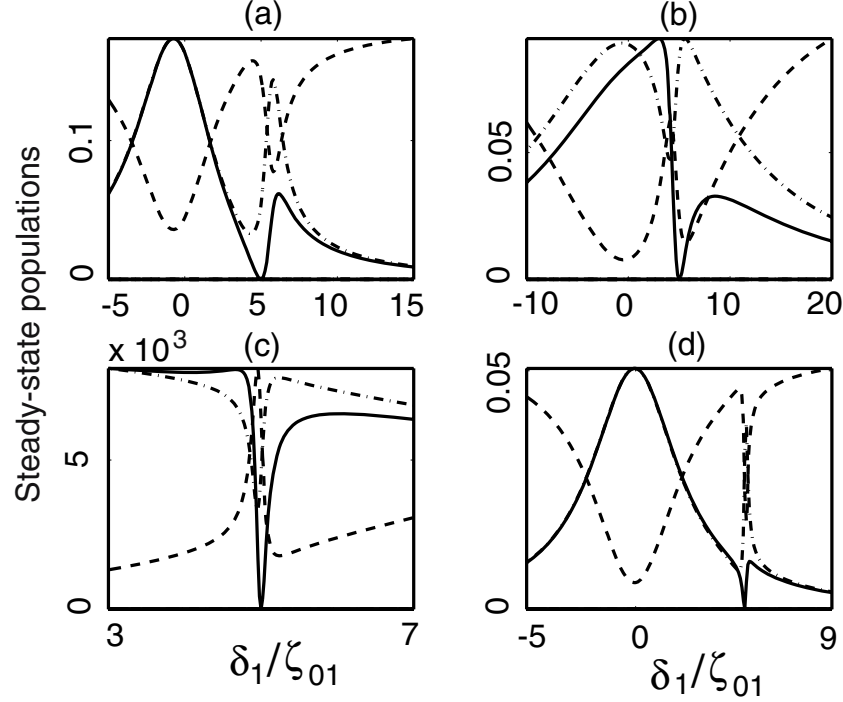


Fig. 5.4. The steady-state populations P_0 (solid line), P_1 (dashed line) and P_2 (dot-dashed line) for $\delta_2 = 5\zeta$. In (a), $\zeta_{01} = \zeta_{02} = \zeta$, $\Omega_1 = \zeta$, $\Omega_2 = 2\zeta$; in (b), $\zeta_{01} = \zeta_{02} = \zeta$, $\Omega_1 = 2\zeta$, $\Omega_2 = \zeta$; in (c), $\zeta_{01} = \zeta$, $\zeta_{02} = 5\zeta$, $\Omega_1 = \Omega_2 = 0.5\zeta$; in (d), $\zeta_{01} = \zeta$, $\zeta_{02} = 0.2\zeta$, $\Omega_1 = \Omega_2 = 0.5\zeta$. P_1 and P_2 are normalized to the maximum value of $P_0(\infty)$

likely to be used in experiments. Usually, an intense, ‘pump’ laser of fixed frequency and near saturating intensity is applied to one transition, whilst a weak ‘probe’ laser is scanned around the two-photon resonance condition on the other transition. In the first frame the pump laser is resonant whilst in the second it is off-resonant.

5.1.5 Observation of Coherent Population Trapping

A large number of investigators have observed CPT since the first experiment by Alzetta et al. in 1976 [98]. Here, we discuss only one or two, and refer the reader to the review by Arimondo [101] for a fuller account.

Among the earlier work, we may mention the contribution of Gray, Whitley and Stroud [102] in 1978 who used two independent single-mode dye lasers to perform accurate experiments on sodium atoms. The population of the upper level, as manifested by the fluorescence intensity, was measured

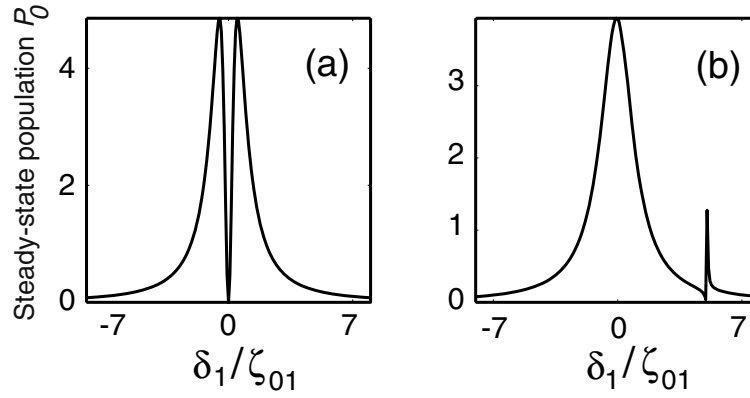


Fig. 5.5. The steady-state population $P_0(\infty)$ as a function of the detuning δ_1 for $\zeta_{01} = \zeta_{02} = \zeta$, $\Omega_1 = 0.05\zeta$, $\Omega_2 = 0.5\zeta$ and different δ_2 : (a) $\delta_2 = 0$, and (b) $\delta_2 = 5\zeta$

as function of the detuning of one laser, with the other fixed at resonance. The results are shown in Fig. 5.6. The first frame shows the theoretical predictions, which are to be compared with the experimental results, shown in Frame (b). It is seen that the agreement is very good. Frame (c) shows a range of experimental results for different values of the detuning of the fixed (pump) laser.

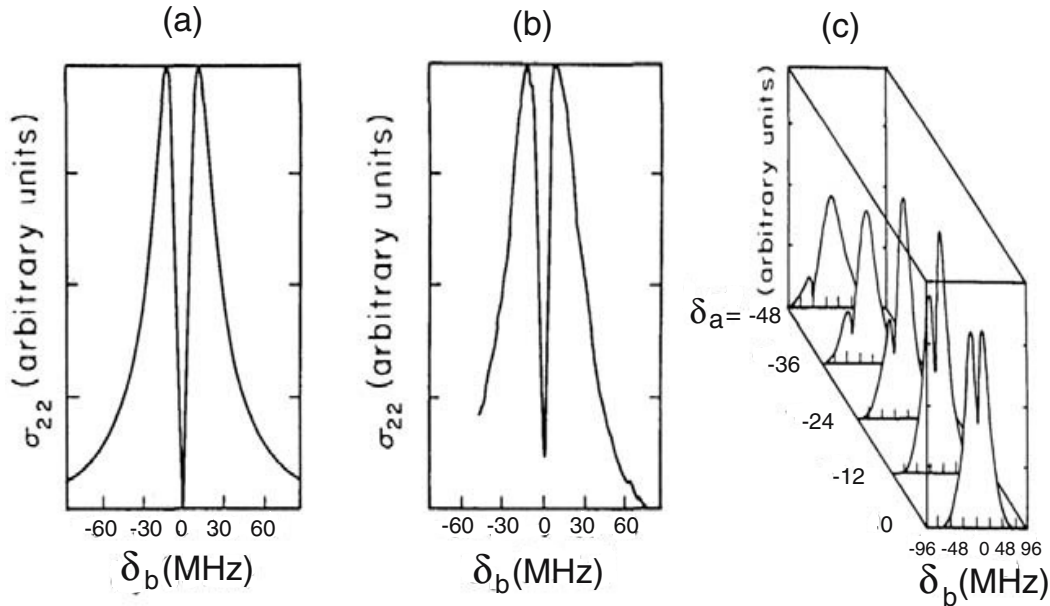


Fig. 5.6. (a) Theoretical predictions for the excited state population in the Lambda system with one laser fixed at resonance, as a function of the detuning δ_b of the other laser. (b) The corresponding experimentally observed excited state population. (c) A similar experimental plot but with the detuning of the fixed frequency laser taking the values $\delta_a = 0, -12, -24, -36$ and -48 MHz from exact resonance. From the paper by H.R. Gray, R.M. Whitley, C.R. Stroud Jr: Opt. Lett. **3**, 218 (1978)

The experiment of Kaviola et al. [103] was performed on a fast beam of metastable ^{40}Ca atoms comprising a Lambda system. The excited state lifetime ($\simeq 2\pi/\gamma_0$) was 10.7 ns, with 38% of the relaxation directed to level $|0\rangle$ and 53% to level $|1\rangle$. One transition ($|0\rangle \rightarrow |2\rangle$) was driven by a ‘pump’ field with fixed detuning, and the other ($|1\rangle \rightarrow |2\rangle$) by a weak, co-propagating ‘probe’ field, whose frequency was scanned over the two-photon resonance.

The density matrix equations (5.17) and the steady-state solutions (5.37) can be used to describe this system, but we must allow for the fact that the velocity of the Ca atoms is distributed over a (narrow) Maxwell distribution – that is, we must allow for the Doppler effect. This is accomplished by modifying the detunings δ_1 and δ_2 as follows

$$\delta_j \rightarrow \delta_j - v\omega_j/c, \quad j = 1, 2, \quad (5.41)$$

where v is the velocity of an atom and c is the velocity of light, which allows for the fact that the atoms ‘see’ Doppler-shifted frequencies. The excited state population was observed after an interaction time of 1.2 μs , but it was found that it was a good approximation to use the steady-state solution, $P_0(\infty)$. The solutions (5.37) must then be integrated over the Maxwell distribution of velocities. In fact, the velocities of the atoms in the beam were almost relativistic (the average velocity of the atoms was of the order $10^{-3}c$) and this also has to be allowed for. Some other generalizations were included in their theory.

Figure 5.7 shows their experimental results, together with their theoretical fit. (The correspondence between their notation as used in the figure and ours is $\Delta_{21} \rightarrow \delta_1, \alpha \rightarrow \Omega_1$ and $\beta \rightarrow \Omega_2$.) The only variable parameter was the overall amplitude of the theoretical fit, and this was adjusted to approximately fit the experimental amplitude. It can be seen that the agreement between theory and experiment is very good.

5.1.6 Velocity-Selective Coherent Population Trapping

Here, we discuss an application of CPT in laser cooling. The improvements in laser cooling developed over the last couple of decades have opened up exciting new areas for investigation in experimental physics, such as quantum gases and atom optics [104]. Some of these developments are discussed in the final chapter. It is well-known that the lowest temperature that can be achieved for two-level atoms by the conventional laser-Doppler cooling method is given by $\frac{1}{2}k_B T_D = \frac{1}{4}\hbar\gamma$, where γ is the lifetime of the excited state, which for Na atoms yields $T_D \simeq 240 \mu\text{K}$. This temperature is called the ‘Doppler limit’. The next limit is the recoil limit, given by $\frac{1}{2}k_B T_R = (\hbar k)^2/2m_a$, for an atom of mass m_a emitting a photon of momentum $\hbar k$. We are not concerned with giving a comprehensive account of laser cooling here, but we wish to describe one method to improve upon the latter limit which makes use of quantum interference. This is the so-called ‘velocity-selective coherent population’ trap-

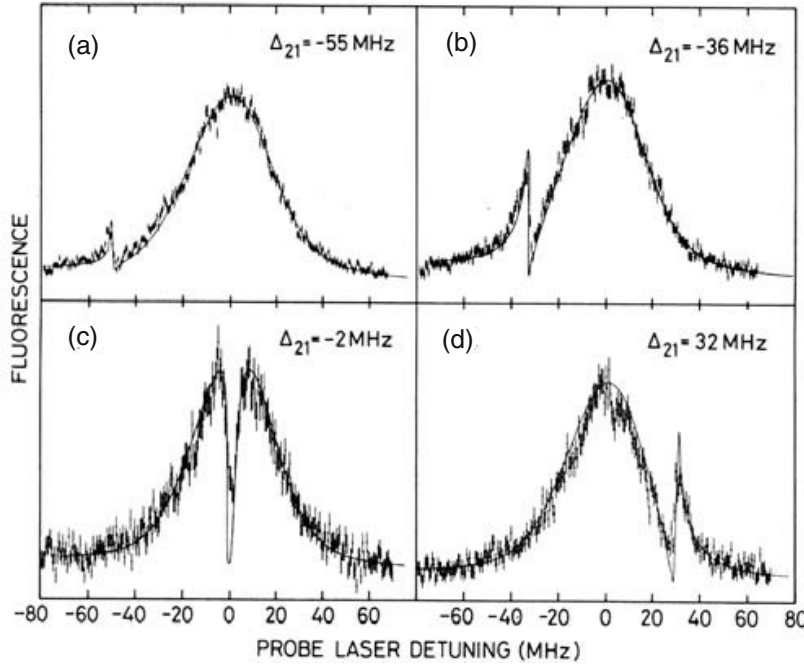


Fig. 5.7. Experimental spectra with the pump detunings $\Delta_{21} = -55, -36, -2$ and $+32$ MHz. The signal is the fluorescence from the excited level as a function of the probe laser detuning. In all cases, the Rabi frequency of the pump laser was $\alpha = 40/2\pi$ MHz and that of the probe laser $\beta = 5/2\pi$ MHz. The solid curves are the results of simulations based on the steady-state density-matrix calculations with experimental parameter values. Only the amplitude of the theoretical profile has been scaled to fit the experimental amplitude. From the paper by M. Kaivola, P. Thorsen, O. Poulsen: *Phys. Rev. A* **32**, 207 (1985). Copyright (1985) by the American Physical Society

ping (VSCPT) method, which permits the attainment of temperatures below the recoil limit.

The effect was demonstrated by Aspect et al. [105] in a subsonic beam of ^4He atoms in the triplet metastable state. The laser beams were directed perpendicular to the atomic beam, and cooling was observed in the direction of the laser beams. Thus, the cooling was one-dimensional. For this system, $T_D = 23 \mu\text{K}$ and $T_R = 4 \mu\text{K}$. Using VCSPT, they obtained a temperature of about $2 \mu\text{K}$. We outline the principles of this method below, with particular reference to this experiment.

We consider population trapping within the $J_g = 1 \rightarrow J_e = 1$ transitions of an atom. The degenerate magnetic sublevels have the quantum numbers $m = 0, \pm 1$. The atom is illuminated by counterpropagating lasers with circular polarizations σ^+ and σ^- with the same frequency ω_L , which induce the transitions shown in Fig. 5.8. We thus have effectively a three-level Lambda system with relevant states $|J_g = 1, m = -1\rangle$, $|J_g = 1, m = +1\rangle$ and $|J_e = 1, m = 0\rangle$, which we may denote in an abbreviated notation without ambiguity as $|-1\rangle$, $|+1\rangle$ for the ground states, and $|0\rangle$ for the excited state.

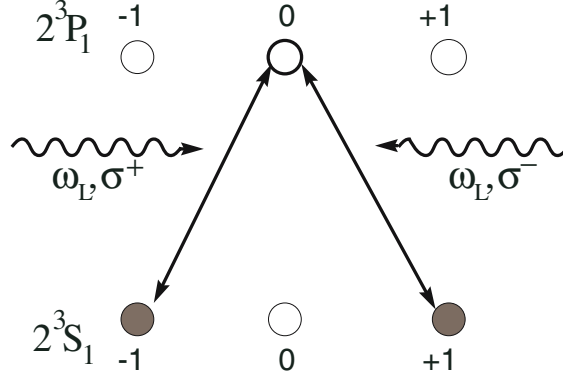


Fig. 5.8. Lambda system for VSCPT cooling in 1-D. Counterpropagating lasers with opposite circular polarizations but the same frequency excite transitions from the 2^3S_1 $m = \pm 1$ lower state sublevels to the 2^3P_1 $m = 0$ excited state sublevel

For simplicity, we consider the one-dimensional situation in which the atom is only free to move in the z -direction, which coincides with the direction of the counterpropagating lasers. Suppose the atom is moving with momentum p , and that the photons of the laser beams carry momentum $\pm \hbar k$. Since the atomic momentum changes by $\pm \hbar k$ when a photon at the laser frequency is emitted or absorbed, we have to include the momentum as a quantum number in the description of the atomic states.³ The relevant atomic basis then becomes

$$\{|0, p\rangle, | + 1, p + \hbar k\rangle, | - 1, p - \hbar k\rangle\} . \quad (5.42)$$

For each value of p , (5.42) defines a family of three states. The atom-laser interaction (5.7) is also modified to

$$\tilde{V} = \frac{1}{2} \Omega (| + 1, p + \hbar k\rangle \langle 0, p| + | - 1, p - \hbar k\rangle \langle 0, p| + \text{H.c.}) , \quad (5.43)$$

where, since this was the case in the experiments of [105], we assume the Rabi frequency is the same for both transitions: $\Omega_1 = \Omega_2 = \Omega$. We can also define noncoupled and coupled states analogously to (5.10) and (5.13). Explicitly, the coupled and non-coupled states in this case are

$$|\Psi_C(p)\rangle = \frac{1}{\sqrt{2}} (| + 1, p + \hbar k\rangle + | - 1, p - \hbar k\rangle) , \quad (5.44a)$$

$$|\Psi_{NC}(p)\rangle = \frac{1}{\sqrt{2}} (| + 1, p + \hbar k\rangle - | - 1, p - \hbar k\rangle) . \quad (5.44b)$$

The state $|\Psi_{NC}(p)\rangle$ is not coupled to the excited state $|0, p\rangle$ by the interaction (5.43), whereas $|\Psi_C(p)\rangle$ is, with Rabi frequency $\sqrt{2}\Omega$.

³ We provide only a cursory treatment of the effect of photon momentum on atomic motion here. A fuller account is given in Sect. 9.1.

First suppose the atom is at rest, and the lasers are exactly resonant with the atomic transitions. Then the two-photon resonance condition of Sect. 5.1.2 is satisfied, and, as we have seen in that section, the atom will reach a steady-state in which it occupies the non-coupled state $|\Psi_{NC}(0)\rangle$, given by (5.44b). Thus, coherent population trapping occurs, that is, the superposition state

$$|\Psi_{NC}(0)\rangle = \frac{1}{\sqrt{2}} (|+1, +\hbar k\rangle - |-1, -\hbar k\rangle) \quad (5.45)$$

is a stationary nonabsorbing state.

However, if the atom is moving with momentum $p \neq 0$, the two-photon resonance condition of Sect. 5.1.2 will no longer be satisfied. If some of the ground state population appears in the coupled state, this state can absorb a photon from one of the lasers beams, causing a transition to the excited state $|0, p\rangle$. A photon can be emitted from this state with a random component of momentum δp in the z -direction lying in the range $-\hbar k \leq \delta p \leq \hbar k$. The population will be transferred to the non-coupled state as well as the coupled state, with some probability. It can be shown that, the smaller the value of p , the longer the system spends in $\Psi_{NC}(p)$. The net effect of many such absorptions is a diffusion in momentum space leading to an accumulation of population in the non-coupled state (5.45) with zero atomic momentum – the only stable attracting state. Once atoms have evolved into the zero-velocity non-coupled state they remain trapped there. For a sufficiently long time of interaction of the atoms with the laser beam, the final atomic momentum distribution $\mathcal{P}(p)$ along Oz will feature two resolved peaks at $\pm\hbar k$ emerging above the initial distribution. This will be the signature of VSCPT cooling.

The experiment was performed with an atomic beam of excited He atoms in the 2^3S_1 state, with an intensity greater than 10^{12} atoms s^{-1} sr^{-1} and an average velocity of 1100 ms^{-1} . A schematic diagram of the experimental setup is shown in Fig. 5.9. A ring laser, with a linewidth less than 1 MHz and locked to the atomic transition, was employed. The laser beam was retroreflected to provide two counterpropagating plane waves with opposite circular polarizations and almost uniform intensity in the 40 -mm-diameter interaction region. The magnetic field was compensated to less than 1 mG in order to ensure that the magnetic sublevels were indeed degenerate.

The first frame of Fig. 5.10 shows the theoretical transverse momentum distribution profile at the end of the interaction region, for parameters close to the experimental situation, and compares it with the initial momentum distribution. The second frame of the figure shows the corresponding experimental results. The signature of VSCPT is apparent.

Velocity-selective optical pumping into a nonabsorbing state is a very efficient mechanism for accumulating atoms into a narrow velocity range. At present, temperatures in the nanokelvin range have been achieved. The method may be extended to samples of trapped ions or atoms. More details of both theory and experiment can be found in the review by Arimondo [101].

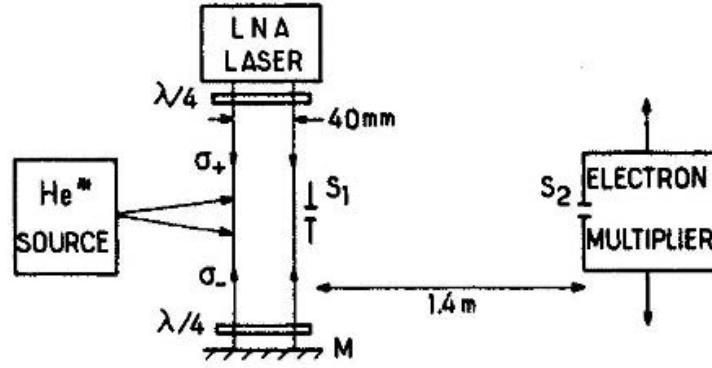


Fig. 5.9. Experimental setup of Aspect et al. [105]. The atomic source at 77 K produces a beam of metastable (2^3S_1) He atoms at average velocity of 1100 ms^{-1} , which interact with σ_+ and σ_- polarized counterpropagating waves at $1.08 \mu\text{m}$. The transverse velocity distribution at the end of the interaction region is analyzed with two slits S_1 and S_2 , $100 \mu\text{m}$ apart. From the paper by A. Aspect, E. Arimondo, R. Kaiser, N. Vansteenkiste, C. Cohen-Tannoudji: Phys. Rev. Lett. **61**, 826 (1988). Copyright (1988) by the American Physical Society

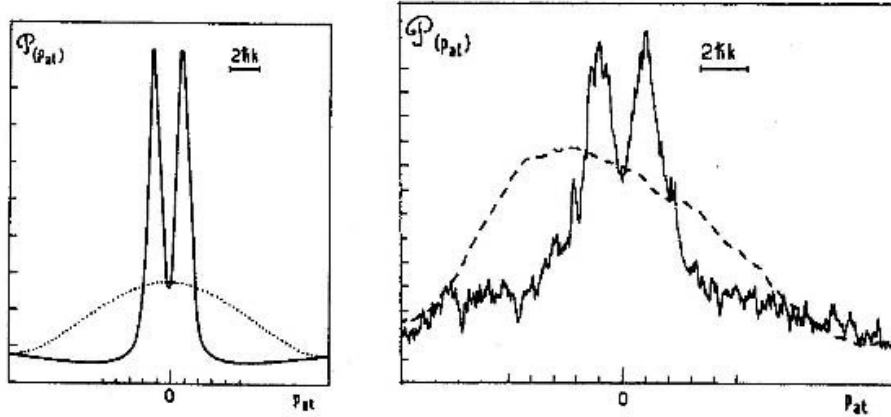


Fig. 5.10. First Frame: Calculated transverse atomic momentum distribution resulting from VSCPT cooling, for parameters close to the experimental situation. The initial distribution is represented by the dotted line. **Second Frame:** The experimentally measured transverse atomic momentum distribution at the end of the interaction region, with the laser on (*solid line*) and off (*dashed line*: this profile has been smoothed). The double peak at about $\pm \hbar k$ above the initial distribution is a clear signature of the VSCPT cooling effect. From the paper by A. Aspect, E. Arimondo, R. Kaiser, N. Vansteenkiste, C. Cohen-Tannoudji: Phys. Rev. Lett. **61**, 826 (1988). Copyright (1988) by the American Physical Society

5.2 Electromagnetically Induced Transparency in the Lambda System

Electromagnetically induced transparency (EIT) is a technique that allows a beam of electromagnetic radiation to propagate through a medium almost as

if the medium was not there. Under certain conditions, it may also be used to eliminate the self-focusing and defocusing of laser beams and to improve their transmission through inhomogeneous refracting gases and metal vapours. Another application is to create large populations of coherently driven, uniformly phased atoms – a new type of matter which has been called ‘phaseonium’ – that creates the potential for new optoelectronic devices [106]. The effect is related to other effects that were known earlier – ‘self-induced transparency’ and ‘Fano interferences’.

We first present an elementary review of the theory of the refractive index, establishing the results we need to describe EIT and its applications. A full account is presented when we consider propagation in an optically thick medium in Sect. 5.5. If the electric field and the polarization induced by it are expressed as

$$\begin{aligned} E(t) &= \text{Re} \sum_k E(\omega_k) e^{i\omega_k t} , \\ P(t) &= \text{Re} \sum_k P(\omega_k) e^{i\omega_k t} , \end{aligned} \quad (5.46)$$

then we may expand the *polarization* $P(\omega)$ at frequency ω , in terms of the *complex susceptibilities* $\chi_i(\omega)$ and the electric field $E(\omega)$ in the following way

$$P(\omega) = \epsilon_0 [\chi_1(\omega)E(\omega) + \chi_2(\omega)E(\omega)^2 + \chi_3(\omega)E(\omega)^3 + \dots] . \quad (5.47)$$

We concentrate on the linear susceptibility $P_1(\omega) = \epsilon_0 \chi_1(\omega)E(\omega)$. Dividing $\chi_1(\omega)$ into its real and imaginary parts, χ'_1 and χ''_1 , we have

$$P_1(\omega) = \epsilon_0 [\chi'_1(\omega) + i\chi''_1(\omega)] E(\omega) . \quad (5.48)$$

It is well-known that the linear susceptibility can be related to the refractive index n and absorption coefficient κ by the relation

$$(n + i\kappa)^2 = 1 + \chi , \quad (5.49)$$

which gives

$$\kappa = \frac{\chi''}{2n} , \quad n = \frac{1}{2} \left[1 + \chi' + \sqrt{(1 + \chi')^2 + (\chi'')^2} \right] , \quad (5.50)$$

so that, roughly speaking, the refractive index is largely determined by χ' and the absorption coefficient by χ'' . It is apparent that when χ' and χ'' are both zero, then $n = 1$ and $\kappa = 0$: the medium behaves like free space. More detailed analysis of the dispersive and absorptive properties of atomic media are presented in Sect. 5.5.

Here, we consider the especially simple case of an atom where only one transition, between the states $|0\rangle$ and $|1\rangle$ say, is important. The polarization is related to the dipole moment induced in the atom and the atomic density matrix through the expression

$$P_1 = \mathcal{N} \mu_{01} \rho_{10} , \quad (5.51)$$

where μ_{01} is the dipole matrix element for the transition, and we have assumed that if there is a density \mathcal{N} of two-level atoms, the polarization is just \mathcal{N} times the polarization for a single atom. For simplicity we have omitted to show the frequency dependence. From (5.48) and (5.51) we can determine the susceptibility.

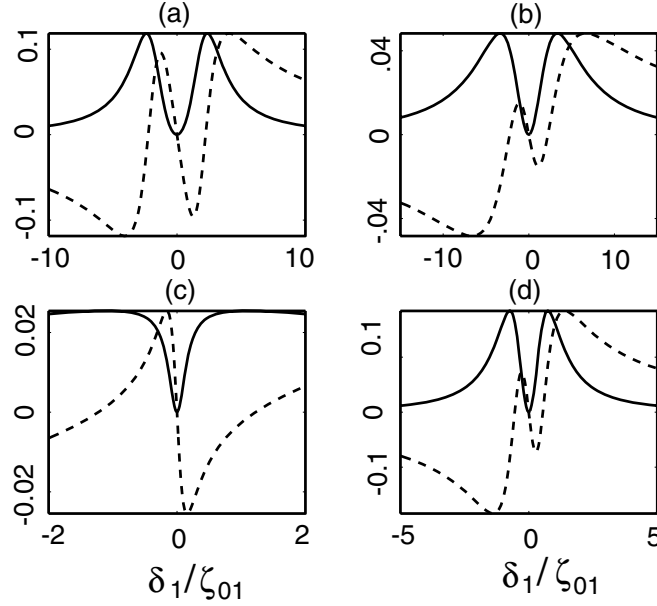


Fig. 5.11. The real (*dashed line*) and imaginary parts (*solid line*) of the coherence \tilde{q}_{10} as a function of δ_1 , for $\delta_2 = 0$. In (a), $\Omega_1 = 1$, $\Omega_2 = 2$, $\zeta_{01} = \zeta_{02} = 1$; in (b), $\Omega_1 = 2$, $\Omega_2 = 1$, $\zeta_{01} = \zeta_{02} = 1$; in (c), $\Omega_1 = \Omega_2 = 0.5$, $\zeta_{01} = 1$, $\zeta_{02} = 5$; in (d), $\Omega_1 = \Omega_2 = 0.5$, $\zeta_{01} = 1$, $\zeta_{02} = 0.2$

We now return to an analysis of the absorption properties of the Lambda system of Fig. 5.1, and show that it exhibits EIT. Note that, as long as it is metastable, the intermediate level $|1\rangle$ need not be close in energy to the ground state, $|2\rangle$. For radiation frequencies close to $\omega_0 - \omega_1$, it follows from (5.51) that the real and imaginary parts of \tilde{q}_{10} determine the refractive index and the absorption coefficient, respectively. For $\delta_2 = 0$ and $\Omega_2 \gg \Omega_1$, it is possible to show from (5.17) that

$$\tilde{q}_{10} \simeq \frac{\delta_1 \Omega_1 (P_0 - P_1)}{|\Omega_2|^2 - i\gamma_0 \delta_1 / 2 - \delta_1^2} , \quad (5.52)$$

and from (5.37) that $P_0 - P_1 \sim \delta_1$, so that

$$\begin{aligned} \chi_1'' &\sim \frac{\gamma_0 \delta_1^2 / 2}{(|\Omega_2|^2 - \delta_1^2)^2 + (\gamma_0 \delta_1 / 2)^2} , \\ \chi_1' &\sim \frac{|\Omega_2|^2 \delta_1}{(|\Omega_2|^2 - \delta_1^2)^2 + (\gamma_0 \delta_1 / 2)^2} . \end{aligned} \quad (5.53)$$

It is clear that the absorption is zero at zero detuning, in contrast with the situation for the two-level system, where the absorption is maximal for zero detuning. This is an important point, which we later exploit. If the intense coupling field is turned off, $\Omega_2 = 0$, the absorption is no longer zero. This is a signature of EIT. Thus, by applying an intense coupling laser, it is possible to induce atomic coherences which render the medium transparent.

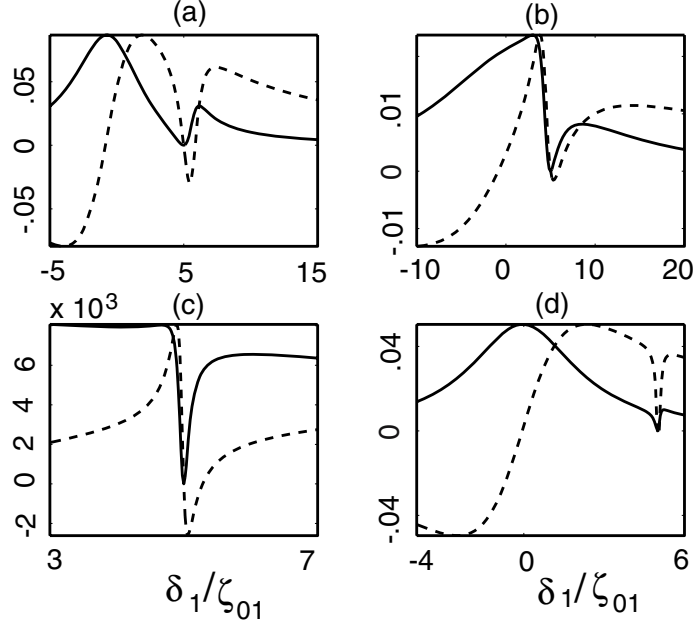


Fig. 5.12. The real (*dashed line*) and imaginary parts (*solid line*) of the coherence $\tilde{\rho}_{10}$ as a function of δ_1 , for $\delta_2 = 5$. In (a), $\Omega_1 = 1, \Omega_2 = 2, \zeta_{01} = \zeta_{02} = 1$; in (b), $\Omega_1 = 2, \Omega_2 = 1, \zeta_{01} = \zeta_{02} = 1$; in (c), $\Omega_1 = \Omega_2 = 0.5, \zeta_{01} = 1, \zeta_{02} = 5$; in (d), $\Omega_1 = \Omega_2 = 0.5, \zeta_{01} = 1, \zeta_{02} = 0.2$

In Fig. 5.11 we show the real and imaginary parts of $\tilde{\rho}_{10}$ for the case $\delta_2 = 0$, but we relax the condition $\Omega_2 \gg \Omega_1$ in these numerically generated plots. (We measure all quantities as multiples of ζ_{01} . All graphs in the same frame have been normalized to the maximum value of the imaginary part of $\tilde{\rho}_{10}$.) The imaginary part is a symmetric function of δ_1 , and the real part antisymmetric. Both parts are zero at two-photon resonance, $\delta_1 = 0$: in particular, there is no absorption at two-photon resonance. The real part may be singly or doubly dispersive. The slope may be very large near $\delta_1 = 0$, indicating that the group velocity of light propagating in this system may be much less than in free space. This is investigated in Chap. 7.

In Fig. 5.12 the parameters are the same as in Fig. 5.11, except that now $\delta_2 = 5$. The symmetry is lost, and both curves show dispersive-like features. As in the previous figure, both the real and imaginary parts are zero at two-photon resonance.

5.2.1 Realization of EIT

The basic configuration for observing electromagnetically induced transparency is the Lambda system, as shown in Fig. 5.13. The following notation is usually employed. The laser coupling levels $|1\rangle$ and $|0\rangle$ is intense (of saturating intensity) and is called the *coupling laser*, whilst the laser coupling levels $|2\rangle$ and $|0\rangle$ is called the *probe laser* – a name that wrongly suggests that it is always weak, as in experiments its intensity may be comparable to that of the coupling laser.

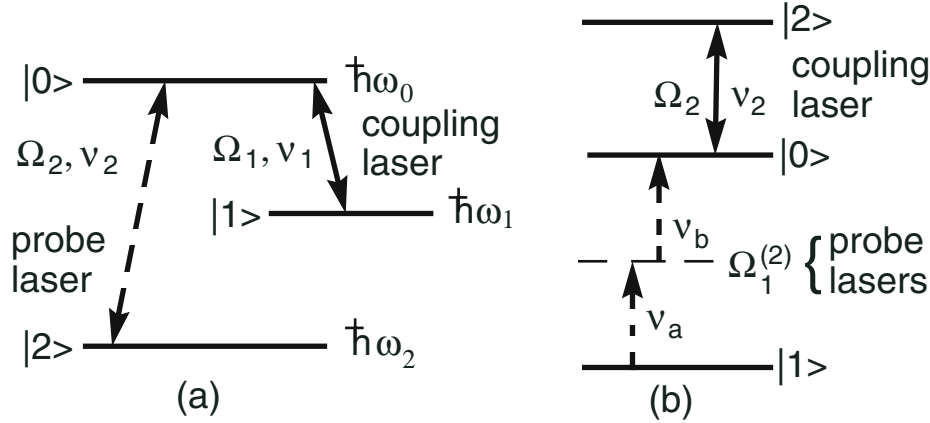


Fig. 5.13. (a) The basic ‘Lambda’ configuration for EIT. Usually, the laser at frequency ν_1 is called the coupling laser, and the laser at frequency ν_2 the probe laser. (b) The Ladder configuration of EIT. The transition $|1\rangle \rightarrow |0\rangle$ is effected by the absorption of *two* photons of frequencies ν_a and ν_b , with $\Omega_1^{(2)}$ being the corresponding two-photon Rabi frequency

It is also possible to observe EIT in the Ladder configuration, but it is necessary that the spontaneous decay rate of level $|0\rangle$ be much less than that of level $|2\rangle$. This can be achieved if the transition $|0\rangle \rightarrow |1\rangle$ is forbidden in the electric dipole approximation. The transition may then be affected by the absorption of *two* photons of frequencies ν_a and ν_b , with $\Omega_1^{(2)}$ being the corresponding two-photon Rabi frequency

$$\Omega_1^{(2)} = \sum_k \Omega_{0k} \Omega_{k1} \left(\frac{1}{\omega_k - \nu_a} + \frac{1}{\omega_k - \nu_b} \right), \quad (5.54)$$

where Ω_{mn} is the Rabi frequency for the transition $|m\rangle \rightarrow |n\rangle$ and the sum is over all intermediate atomic states $|k\rangle$.

The essential results for EIT have been obtained in the previous section. There it was pointed out that the imaginary and real parts of the coherence ϱ_{01} , which determine the absorption coefficient and refractive index respectively of a probe beam at the relevant frequency, are zero when the

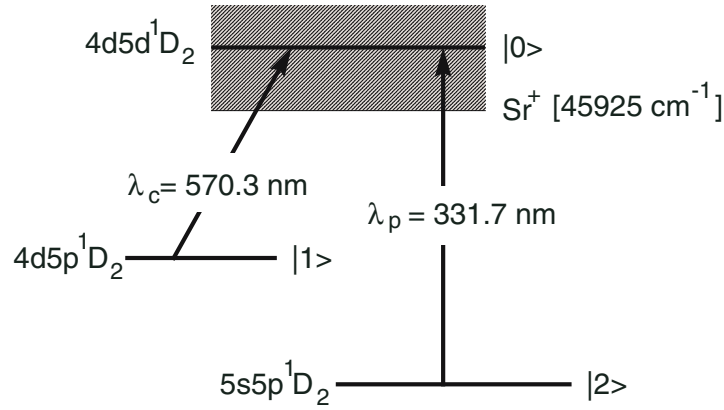


Fig. 5.14. Partial energy level diagram of strontium. The wavelength of the coupling laser λ_c is kept fixed, whilst the frequency of the probe laser λ_p is scanned

two-photon resonance condition is satisfied. Thus, under these conditions, the probe beam will propagate through the medium as though it was not present at all: in particular, it will be completely transparent.

A striking demonstration of EIT was presented in the early experiments of Boller, Imamoglu and Harris in 1991 at Stanford University [107], using normally opaque strontium vapour. A partial energy diagram is shown in Fig. 5.14. In order to have a broad absorption linewidth, the excited state $|0\rangle$ of the Lambda system was a level of strontium lying in the continuum. This level decays by autoionization, a process much faster than radiative decay.

The experimentally observed transmissions against probe laser detuning are shown in Fig. 5.15. The frames (a) and (b) show the situation when the population of the $5s5p^1P_1$ level is sufficiently low to allow some light at line centre to pass through without the coupling laser being applied. [Shown in Frame (a): minimum transmission is $\exp(-1.7 \pm 0.1)$]. When the coupling laser is applied, as shown in Frame (b), the transmission rises to near 100%. The dashed line is the theoretical curve, a Voigt profile convolved with the probe laser lineshape (linewidth 0.15 cm^{-1}).

The frames (c) and (d) of Fig. 5.15 show the situation when the $5s5p^1P_1$ level population is sufficiently high for the medium to be optically thick [minimum transmission is $\exp(-20 \pm 1)$]. When the coupling laser was appropriately applied, the ratio of transmitted to incident energy increased to 40% [transmission $\exp(-1.0 \pm 0.1)$].

5.3 Lasing Without Inversion

Lasing without inversion (LWI) and amplification without inversion are vast and important topics that depend upon atomic coherence for their existence. Space permits us only to outline the basic principles here. The topic has been

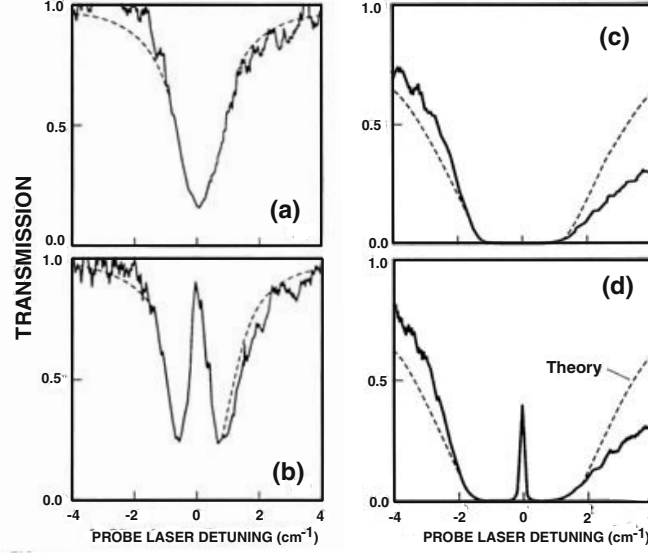


Fig. 5.15. The transmission versus probe laser tuning for (a) $\Omega_{23} = 0$ and (b) $\Omega_{23} = 1.3 \text{ cm}^{-1}$, with the coupling laser detuning $\delta_1 = -0.2 \text{ cm}^{-1}$. Minimum transmission is $\exp(-1.7)$. The right-hand frames show the transmission versus probe laser tuning for (c) $\Omega_{23} = 0$ and (d) $\Omega_{23} = 1.5 \text{ cm}^{-1}$, with $\delta_1 = -0.1 \text{ cm}^{-1}$. Minimum transmission is $\exp(-20)$. From the paper by K.J. Boller, A. Imamoglu, S.E. Harris: *Phys. Rev. Lett.* **66**, 2593 (1991). Copyright (1991) by the American Physical Society

reviewed by Arimondo [101] and by Mompert and Corbalan [108], the latter dealing exclusively with LWI, and summarizing the then state of the art.

A major motivation for the study of LWI is the possibilities it opens for developing lasers that operate at shorter wavelengths than presently possible. Conventional lasers require a population inversion in the lasing transition. This condition leads to the well-known fact that the pumping power required for laser action scales as at least the fourth power of the laser frequency, which is the origin of the difficulty in producing continuous wave x-ray lasers. By exploiting quantum interference, it is possible to break the symmetry between absorption and stimulated emission, and thus in principle to remove this stumbling block.

We first give a proof of principle demonstration that amplification without population inversion is possible. We consider the Lambda system discussed in Sect. 5.1 and shown in Fig. 5.16. There, we showed that the system may be described in terms of the so-called CPT (Coherent Population Trapping) basis

$$\left\{ |0\rangle, |\Psi_{NC}\rangle = \frac{\Omega_2^*|1\rangle - \Omega_1^*|2\rangle}{\Omega_+}, |\Psi_C\rangle = \frac{\Omega_1|1\rangle + \Omega_2|2\rangle}{\Omega_+} \right\}, \quad (5.55)$$

where $\Omega_+ = \sqrt{|\Omega_1|^2 + |\Omega_2|^2}$. We also showed that the system evolved into the steady-state $\tilde{\rho}_{NC} = |\Psi_{NC}\rangle\langle\Psi_{NC}|$, that is, the system ends up in the state $|\Psi_{NC}\rangle$, which is not coupled to the excited state $|0\rangle$ by the atom-laser

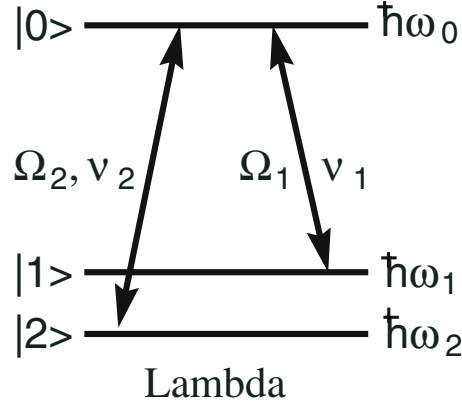


Fig. 5.16. The driven Lambda system. The Rabi frequency for the transition $|0\rangle \leftrightarrow |k\rangle$ of frequency ν_k is denoted Ω_k

interaction \tilde{V} of (5.7). *Thus the system absorbs no photons from the driving laser fields when it is in the state $|\Psi_{NC}\rangle$.*

Now suppose we instantaneously generate some population in the excited state, for example by broadband incoherent pumping, in such a way that the population is taken equally from the two ground states. Then the system will be described by the density matrix

$$\varrho' = \eta|0\rangle\langle 0| + (1 - \eta)|\Psi_{NC}\rangle\langle \Psi_{NC}|, \quad (5.56)$$

where η is small and positive. There will be no absorption from this system, for the reasons adduced above: $\langle 0|\tilde{V}|\Psi_{NC}\rangle = 0$. Because there *is* population in the excited state however, there will be stimulated emission. The rate of emission of a photon of frequency ν_k will be proportional to $|\langle 0|\tilde{V}|k\rangle|^2$, for $k = 1, 2$. We easily find that $\langle 0|\tilde{V}|1\rangle = \frac{1}{2}\Omega_1$ and $\langle 0|\tilde{V}|2\rangle = \frac{1}{2}\Omega_2$. Thus amplification of photons at the laser frequency is possible without their absorption, and there is no population inversion in the bare atomic basis.

It has been argued that, since the state $|\Psi_{NC}\rangle$ is effectively decoupled from the remaining states, the system should be considered as a two-level system, consisting of the states $|0\rangle$ and $|\Psi_C\rangle$, rather than a three-level system. In this two-level basis, we do have a population inversion initially, as the populations $\langle 0|\varrho|0\rangle = \eta$ and $\langle \Psi_C|\varrho|\Psi_C\rangle = 0$. This is an example of what is now termed “gain with hidden inversion”.

5.3.1 A Model for LWI

Whilst the above analysis suggests that LWI may be possible, we obviously need to consider a more realistic model in order to reach firmer conclusions. We discuss one such model in this section. A large number of schemes for achieving LWI have been put forward. We elect to describe a scheme due to Imamaoğlu, Field and Harris [109] here for several reasons: it is essentially a

Lambda system, it is similar to the model considered in Sect. 5.2.1 for realizing EIT, and all the processes involved, including pumping, can be described within this system.

The system, shown in Fig. 5.17, is essentially a Lambda system, but the intermediate level $|1\rangle$ is not necessarily close to the ground state $|2\rangle$, although we do consider it to be metastable. The transitions $|1\rangle \rightarrow |0\rangle$ and $|2\rangle \rightarrow |0\rangle$ are driven by coherent lasers of Rabi frequencies Ω_1 and Ω_2 respectively. For simplicity, we assume that both Rabi frequencies are real, and we also assume that these lasers are exactly resonant with their respective transitions: $\nu_1 = \omega_0 - \omega_1$ and $\nu_2 = \omega_0 - \omega_2$. In addition, these transitions are pumped incoherently at the rates R_{10} and R_{20} respectively. The laser at frequency ν_1 is the pump laser, and the laser at ν_2 the probe laser. We wish to see if amplification without population inversion is possible at the frequency ν_2 .

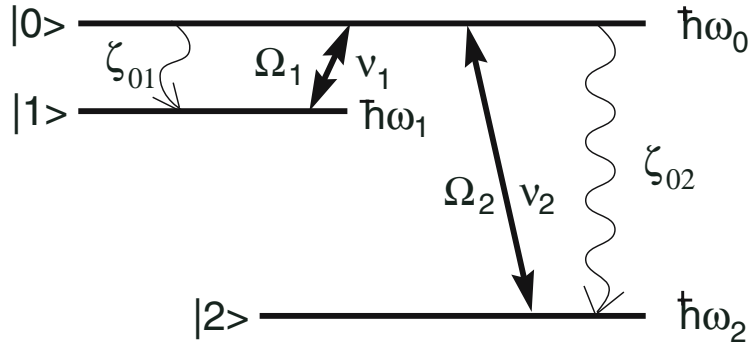


Fig. 5.17. The model system for LWI

The equations of motion for the density matrix are obtained by adapting equations (5.17) to include the incoherent pumping. On this occasion, we do not take Laplace transforms, but work directly in the time domain. We find the following equations of motion

$$\begin{aligned} \dot{\tilde{\rho}}_{00} = & -(\zeta_{01} + \zeta_{02}) \tilde{\rho}_{00} - \frac{1}{2}i\Omega_2 (\tilde{\rho}_{20} - \tilde{\rho}_{02}) - \frac{1}{2}i\Omega_1 (\tilde{\rho}_{10} - \tilde{\rho}_{01}) \\ & - R_{10} (\tilde{\rho}_{00} - \tilde{\rho}_{11}) - R_{20} (\tilde{\rho}_{00} - \tilde{\rho}_{22}) , \end{aligned} \quad (5.57a)$$

$$\dot{\tilde{\rho}}_{11} = \zeta_{01} \tilde{\rho}_{00} - \frac{1}{2}i\Omega_1 (\tilde{\rho}_{01} - \tilde{\rho}_{10}) + R_{10} (\tilde{\rho}_{00} - \tilde{\rho}_{11}) , \quad (5.57b)$$

$$\dot{\tilde{\rho}}_{22} = \zeta_{02} \tilde{\rho}_{00} - \frac{1}{2}i\Omega_2 (\tilde{\rho}_{02} - \tilde{\rho}_{20}) + R_{20} (\tilde{\rho}_{00} - \tilde{\rho}_{22}) , \quad (5.57c)$$

$$\dot{\tilde{\rho}}_{10} = -\frac{1}{2}\Gamma_{01} \tilde{\rho}_{10} + \frac{1}{2}i\Omega_2 \tilde{\rho}_{12} - \frac{1}{2}i\Omega_1 (\tilde{\rho}_{00} - \tilde{\rho}_{11}) , \quad (5.57d)$$

$$\dot{\tilde{\rho}}_{20} = -\frac{1}{2}\Gamma_{02} \tilde{\rho}_{20} + \frac{1}{2}i\Omega_1 \tilde{\rho}_{21} - \frac{1}{2}i\Omega_2 (\tilde{\rho}_{00} - \tilde{\rho}_{22}) , \quad (5.57e)$$

$$\dot{\tilde{\rho}}_{21} = -\frac{1}{2}\Gamma_{12} \tilde{\rho}_{21} + \frac{1}{2}i\Omega_1 \tilde{\rho}_{20} - \frac{1}{2}i\Omega_2 \tilde{\rho}_{01} , \quad (5.57f)$$

where

$$\Gamma_{12} = R_{10} + R_{20} , \quad (5.58a)$$

$$\Gamma_{02} = \zeta_{01} + \zeta_{02} + 2R_{20} + R_{10} , \quad (5.58b)$$

$$\Gamma_{01} = \zeta_{01} + \zeta_{02} + R_{20} + 2R_{10} . \quad (5.58c)$$

In (5.17), ζ_{jk} is the spontaneous decay rate from level $|j\rangle$ to level $|k\rangle$, and R_{k0} is the incoherent pump rate from $|0\rangle$ to $|k\rangle$.

From these equations, we wish to obtain expressions for the steady-state populations (so that we can judge if there is population inversion) and the condition for amplification at the probe field frequency ν_2 . The steady-state populations may be found straightforwardly, by setting the time derivatives in (5.57) to zero and solving the resulting homogeneous equations. It may thus be shown that

$$\frac{\varrho_{11} + \varrho_{00}}{\varrho_{22}} = \frac{R_{20}}{\zeta_{20} + R_{20}} \left[\frac{\Gamma_{01} (\zeta_{01} + 2R_{10}) + 2\Omega_1^2}{\Gamma_{01} R_{10} + \Omega_1^2} \right] . \quad (5.59)$$

The rate of change of the number of probe laser photons $\langle n_2 \rangle$ is given by [109]

$$\frac{d\langle n_2 \rangle}{dt} = -W_{\text{abs}} \varrho_{22} + W_{\text{em}} (\varrho_{11} + \varrho_{00}) , \quad (5.60)$$

where the stimulated absorption and emission rates are

$$W_{\text{abs}} = \frac{R_{20}^2 \Gamma_{12}}{(\Omega_1^2 + \Gamma_{12} \Gamma_{02})^2} , \quad (5.61)$$

$$W_{\text{em}} = \frac{\Omega_2^2 \Gamma_{01} [\Omega_1^2 (\zeta_{01} + \Gamma_{12}) + R_{10} \Gamma_{01}]}{(\Omega_1^2 + \Gamma_{12} \Gamma_{02})^3} . \quad (5.62)$$

The condition for no population inversion is $\varrho_{11} + \varrho_{22} > \varrho_{00}$, and the condition for net gain in the probe photons is $W_{\text{abs}} \varrho_{11} < W_{\text{em}} (\varrho_{11} + \varrho_{22})$. These conditions may be combined and written as

$$\frac{\zeta_{01}}{\Gamma_{12}} > \frac{\zeta_{02} (\Omega_1^2 + \Gamma_{12} R_{10})}{R_{20} \Omega_1^2} > \frac{\Omega_1^2 + (\Gamma_{01} + R_{10}) \zeta_{01}}{\Omega_1^2} . \quad (5.63)$$

The first inequality expresses the gain condition, while the second ensures no population inversion. These two inequalities are compatible, and may be satisfied in real atomic systems. Thus, steady-state lasing without population inversion is possible in a closed Lambda system.

5.3.2 Observation of LWI

Quite a number of groups have reported the observation of LWI. The experiments are reviewed in [101] and [108]. We discuss only one here, that by

Padmabandu et al. [110]. We choose this experiment because it corresponds quite closely to the theoretical model discussed in the last section. The experiment was performed within the sodium D_1 line of an atomic beam. Using a weak probe beam, they first demonstrated complete transparency, and then inversionless gain. After installing a laser cavity, they found that, when the probe was blocked, the laser started spontaneously from vacuum fluctuations. The sodium $3P_{1/2}$ and $3S_{1/2}$ levels are quite complicated due to hyperfine

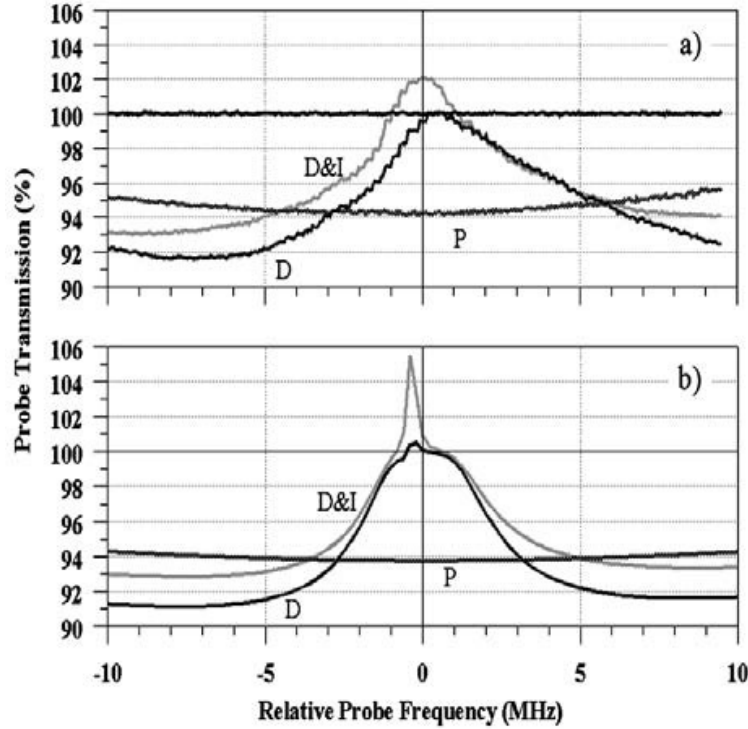


Fig. 5.18. Frequency dependence of the probe transmission in the neighbourhood of resonance: (a) experiment, (b) theory. The horizontal line at 100% is the transmission in the absence of the sodium beam, and provides normalization. Curve P is for the probe alone, curve D is for probe plus driving laser, and curve $D\&I$ is for the probe plus driving laser plus incoherent pump. From the paper by G.G. Padmabandu, G.R. Welch, I.V. Shubin, E.S. Fry, D.M. Nikonov, M.D. Lukin, M.O. Scully: *Phys. Rev. Lett.* **76**, 2053 (1996). Copyright (1996) by the American Physical Society

structure, but the lasing system may be considered to have essentially a Lambda-type structure as shown in Fig. 5.17. A strong driving field was applied to the $|1\rangle \rightarrow |0\rangle$ transition, and $|2\rangle \rightarrow |0\rangle$ was the lasing transition. An incoherent pump field was applied to generate population in the excited state $|0\rangle$.

Initially, a weak probe field was tuned through the $|2\rangle \rightarrow |0\rangle$ transition, to investigate EIT. The results for the probe absorption are shown in Fig. 5.18, where Frame (a) gives the experimental results and Frame (b) the theory,

based on a solution of the density matrix equations of the sodium D_1 system. Curve P is the transmission through the sodium atomic beam when only the probe laser is present – i.e. when the drive laser and the incoherent pumping are turned off. Curve D is the probe transmission when the probe field is present. It shows that at resonance, practically complete electromagnetically induced transparency occurs. Curve $D&I$ is the probe transmission when both the driving laser and the incoherent pump are applied. It shows clearly that gain occurs. Comparing Frames (a) and (b) we see that the agreement between theory and experiment is excellent. Up to 10% gain was obtained, when 16% absorption was observed in the absence of the driving laser.

After observing the probe gain, a ring cavity was installed to investigate cw laser oscillation. The results are shown in Fig. 5.19, which presents the output of the LWI oscillator as the resonant frequency of the laser cavity is scanned. Well-collimated outputs from the cavity were observed at approximately 600 MHz intervals of the cavity scan, with no observable output otherwise, as seen in the figure.

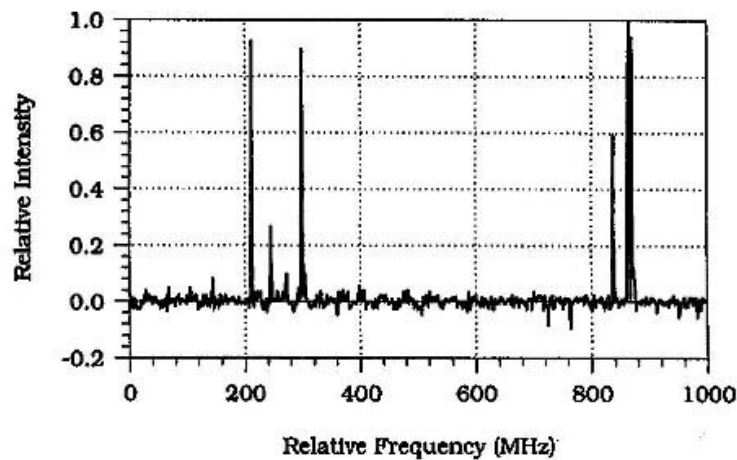


Fig. 5.19. Output of the LWI oscillator as the resonant frequency of the laser cavity is scanned. Observation parameters are peak gain of 5% corresponding to 9% linear absorption. From the paper by G.G. Padmabandu, G.R. Welch, I.V. Shubin, E.S. Fry, D.M. Nikonov, M.D. Lukin, M.O. Scully: *Phys. Rev. Lett.* **76**, 2053 (1996). Copyright (1996) by the American Physical Society

5.4 Spatial Propagation of EM Fields in Optical Media

We have already touched upon the fact that the refractive index and absorption coefficient can be modified by coherence effects. We delve into these matters more deeply in the following few sections.

We first review the theory of absorption and refraction in dense optical media. In traditional optically dense media, spatial propagation of a weak

field results in a very high absorption of the field within a short distance of the propagation. The absorption is accompanied by the uncontrolled process of spontaneous emission that leads to a significant dissipation of the propagating field. This dissipation is one of the sources of *decoherence* – the loss of information carried by the propagating field.

A weak EM field of amplitude $\mathbf{E}(\mathbf{r}, t)$ propagating in the \mathbf{r} direction in an optically dense medium experiences an exponential absorption described by

$$\frac{d}{dr}\mathbf{E}(\mathbf{r}, t) = -\frac{\alpha}{2}\mathbf{E}(\mathbf{r}, t) , \quad (5.64)$$

where $\mathbf{E}(\mathbf{r}, t)$ is the amplitude of the field at a distance r into the medium, and α is the absorption coefficient, assumed to be constant along the propagation distance. The absorption coefficient determines the rate with which the field is absorbed in the medium. For simplicity, we consider only isotropic media.

Equation (5.64) is a simple differential equation, and can be solved for an arbitrary initial value of $\mathbf{E}(0, t)$ of the field amplitude at the boundary $r = 0$ of the medium to give

$$\mathbf{E}(\mathbf{r}, t) = \mathbf{E}(0, t) \exp\left(-\frac{\alpha}{2}r\right) . \quad (5.65)$$

In experiments, we measure the intensity of the propagating field, which with (5.65) is given by

$$I(\mathbf{r}, t) = \langle \mathbf{E}^*(\mathbf{r}, t) \cdot \mathbf{E}(\mathbf{r}, t) \rangle = I(0, t) \exp(-\alpha r) . \quad (5.66)$$

Equation (5.66) is known as Beer's law, and is valid as long as α is not a function of the intensity. It shows that after propagation a distance r inside a dense medium, the intensity of the field is attenuated by $\exp(-\alpha r)$.

The numerical value of α depends on the structure of the dense medium. We have to relate α to the internal microscopic structure (atoms or molecules) of the medium and then we can interpret the absorptive properties in terms of the absorptive and emissive properties of individual atoms. Consider a propagating field in the form of a plane wave

$$\mathbf{E}(\mathbf{r}, t) = i\mathcal{E}(\mathbf{r}, t)e^{-i(\omega t - \mathbf{k} \cdot \mathbf{r})} + \text{c.c.} , \quad (5.67)$$

where the field amplitude $\mathcal{E}(\mathbf{r}, t)$ changes slowly with the optical wavelength, ω is the angular frequency of the field, and \mathbf{k} is the propagation vector.

The field induces in the medium a polarization of similar form

$$\mathbf{P}(\mathbf{r}, t) = i\mathcal{P}(\mathbf{r}, t)e^{-i(\omega t - \mathbf{k} \cdot \mathbf{r})} + \text{c.c.} , \quad (5.68)$$

with a complex and slowly varying amplitude $\mathcal{P}(\mathbf{r}, t)$ that typically is out of phase with $\mathcal{E}(\mathbf{r}, t)$, and oscillates at the same frequency ω as the electric field.

The propagating field and polarization satisfy the Helmholtz (wave) equation

$$\nabla^2 \mathbf{E}(\mathbf{r}, t) - \frac{1}{c^2} \frac{\partial^2 \mathbf{E}(\mathbf{r}, t)}{\partial t^2} = \mu_0 \frac{\partial^2 \mathbf{P}(\mathbf{r}, t)}{\partial t^2} . \quad (5.69)$$

In order to solve the wave equation, it is convenient to introduce Cartesian coordinates such that the propagation direction of the field is in the positive z direction, which is taken to be perpendicular to the input face of the medium

$$\begin{aligned} \mathbf{E}(\mathbf{r}, t) &= E(z, t) \bar{\mathbf{e}}_{xy} , \\ \mathbf{P}(\mathbf{r}, t) &= P(z, t) \bar{\mathbf{e}}_{xy} , \end{aligned} \quad (5.70)$$

where $\bar{\mathbf{e}}_{xy}$ is the unit polarization vector in the xy plane perpendicular to the direction of propagation.

Equation (5.69) then reduces to a one-dimensional Helmholtz equation

$$\frac{\partial^2 E(z, t)}{\partial z^2} - \frac{1}{c^2} \frac{\partial^2 E(z, t)}{\partial t^2} = \mu_0 \frac{\partial^2 P(z, t)}{\partial t^2} . \quad (5.71)$$

We simplify (5.71) by writing

$$\frac{\partial^2 E(z, t)}{\partial z^2} - \frac{1}{c^2} \frac{\partial^2 E(z, t)}{\partial t^2} = \left(\frac{\partial}{\partial z} + \frac{1}{c} \frac{\partial}{\partial t} \right) \left(\frac{\partial}{\partial z} - \frac{1}{c} \frac{\partial}{\partial t} \right) E(z, t) . \quad (5.72)$$

Further, we introduce the slowly varying amplitude, or adiabatic, approximation, which amounts to assuming that $E(z, t)$ varies slowly over distances comparable to an optical wavelength and over time scales comparable to an optical period. This approximation can be restated in a different form as

$$\begin{aligned} \frac{\partial^2 E(z, t)}{\partial z^2} &\ll k \frac{\partial E(z, t)}{\partial z} , \\ \frac{\partial^2 E(z, t)}{\partial t^2} &\ll \omega \frac{\partial E(z, t)}{\partial t} . \end{aligned} \quad (5.73)$$

Using the plane wave descriptions of the electric field and polarization, we note that

$$\left(\frac{\partial}{\partial z} - \frac{1}{c} \frac{\partial}{\partial t} \right) E(z, t) = 2ikE(z, t) , \quad (5.74)$$

and

$$\frac{\partial^2 P(z, t)}{\partial t^2} = -\omega^2 P(z, t) . \quad (5.75)$$

Hence, the Helmholtz equation (5.71) for the slowly varying amplitudes becomes

$$\left(\frac{\partial}{\partial z} + \frac{1}{c} \frac{\partial}{\partial t} \right) \mathcal{E}(z, t) = i \frac{k}{2\varepsilon_0} \mathcal{P}(z, t) , \quad (5.76)$$

or in terms of the real and imaginary parts of the polarization

$$\left(\frac{\partial}{\partial z} + \frac{1}{c} \frac{\partial}{\partial t} \right) \mathcal{E}(z, t) = -\frac{k}{2\varepsilon_0} \text{Im} [\mathcal{P}(z, t)] + i \frac{k}{2\varepsilon_0} \text{Re} [\mathcal{P}(z, t)] . \quad (5.77)$$

For a stationary field, $\mathcal{E}(z, t) = \mathcal{E}(z)$ and $\mathcal{P}(z, t) = \mathcal{P}(z)$. Then (5.77) reduces to a time-independent propagation equation

$$\frac{\partial}{\partial z} \mathcal{E}(z) = -\frac{k}{2\varepsilon_0} \text{Im} [\mathcal{P}(z)] + i \frac{k}{2\varepsilon_0} \text{Re} [\mathcal{P}(z)] . \quad (5.78)$$

The first-order differential equations (5.77) and (5.78) are the basic equations for the formal analysis of the propagation of an EM field inside an optical dense medium. The real part of the polarization contributes to the refractive index of the medium, whereas the imaginary part determines the absorption coefficient. Comparing (5.78) with (5.64), we see that the problem of finding the absorption coefficient α reduces to finding the polarization in terms of the propagating electric field.

5.5 Absorptive and Dispersive Properties of Optically Dense Media

The optical characteristics of a dense medium are determined by its dispersive and absorptive properties. The dispersion of radiation by a medium is certainly one of its most fundamental properties. This property of materials is governed by a linear susceptibility χ giving the response of the medium to a weak field. In order to study the dispersive and absorptive properties of the system its susceptibility has to be calculated in terms of the microscopic properties of materials, such as atomic dipole moments. For this purpose, a simplified physical model of the atom will be used, namely one in which the atom is composed of a finite number of discrete energy levels connected by nonzero transition dipole moments. Despite this simplicity, it will be possible to satisfactorily predict the macroscopic optical properties of materials.

Let us assume the medium is composed of identical and independent multi-level atoms, so that the macroscopic dipole moment per unit volume of the medium (polarization) is determined by the expectation value of the total dipole moment $\hat{\boldsymbol{\mu}}$ of a single atom at position \mathbf{r} at time t times the number density of the atoms \mathcal{N} as

$$\mathbf{P}(\mathbf{r}, t) = \mathcal{N} \langle \hat{\boldsymbol{\mu}}(\mathbf{r}, t) \rangle . \quad (5.79)$$

The form of the polarization is clearly displayed when we use the microscopic representation (2.5) for the total dipole moment and the density matrix approach, originally introduced by Bloembergen and Shen [111]. In this

representation, the polarization is related to the off-diagonal density matrix elements (coherences) of the individual atoms as

$$\mathbf{P}(\mathbf{r}, t) = \mathcal{N} \sum_{m=0}^M \sum_{n>m} [\boldsymbol{\mu}_{mn} \tilde{\varrho}_{nm}(t) e^{-i\omega_{nm}t} + \text{c.c.}] , \quad (5.80)$$

where $\boldsymbol{\mu}_{mn} = \boldsymbol{\mu}_{nm}^* = \langle m | \boldsymbol{\mu} | n \rangle$ is the dipole matrix element between two atomic levels $|m\rangle$ and $|n\rangle$, and

$$\tilde{\varrho}_{nm}(t) = \varrho_{nm}(t) \exp(i\omega_{nm}t) \quad (5.81)$$

is the slowly varying part of the atomic coherence. The time dependence of the density matrix elements is governed by the master equation (2.72), which allows us to study the macroscopic polarization in terms of the atomic parameters.

Suppose that in addition to possible driving fields, the system is probed by a weak tunable laser field of amplitude $\mathbf{E}_p(\mathbf{r})$ and frequency ω_p . In this case, the polarization is established by a combination of both driving and probe fields. If we are only interested in the response of the system to the probe field, we can express the polarization in the form [112]

$$\mathbf{P}(\mathbf{r}, t) = i\varepsilon_0 \chi(t) \mathbf{E}_p(\mathbf{r}) \exp(-i\omega_p t) , \quad (5.82)$$

where $\chi(t)$ is the linear susceptibility of the system. It measures the susceptibility of the system to polarization by an applied field.

By comparing (5.80) with (5.82), a relation between the linear susceptibility and the density matrix elements is obtained

$$\mathcal{N} \sum_{m=0}^M \sum_{n>m} \boldsymbol{\mu}_{mn} \tilde{\varrho}_{nm}(t) = i\varepsilon_0 \chi(t) \mathbf{E}_p(\mathbf{r}) \exp(-i\delta_p t) , \quad (5.83)$$

where $\delta_p = \omega_p - \omega_{nm}$ is the detuning of the probe field from the atomic transition frequency. In the derivation of (5.83), we have ignored the terms multiplied by $\exp(2i\omega_{mn}t)$ as they are rapidly oscillating in time and average to zero for many cycles of the oscillation. These terms arise from the contribution of the counter-rotating terms that for times $t \gg 1/\omega_{mn}$ are very small and can be neglected.

If the interaction of the system with the probe field is treated correctly to first order in the probe field amplitude, the density matrix elements $\tilde{\varrho}_{nm}$ can be written in an approximate Taylor series as

$$\tilde{\varrho}_{nm}(t) = \tilde{\varrho}_{nm}^{(0)}(t) + \tilde{\varrho}_{nm}^{(+1)}(t) \exp(i\delta_p t) + \tilde{\varrho}_{nm}^{(-1)}(t) \exp(-i\delta_p t) , \quad (5.84)$$

where $\tilde{\varrho}_{mn}^{(0)}(t)$ is the unperturbed solution for the density matrix element, and $\tilde{\varrho}_{mn}^{(\pm 1)}(t)$ is the first-order correction proportional to the Rabi frequency

of the probe field. The unperturbed density matrix elements are evaluated in the absence of the probe field and their values depend on the initial state of the system and the intensities and frequencies of the driving fields. In most situations we are interested only in the long time (steady-state) optical properties of a given system. In this case, the unperturbed solutions depend solely on the intensities and frequencies of the driving fields. In the simple situation of no driving field, all the unperturbed density matrix elements are zero, except $\tilde{\rho}_{00}^{(0)} = 1$.

By substituting (5.84) into (5.83) and equating coefficients of the exponentials $\exp(\pm i\delta_p t)$, we find that the susceptibility is determined by the part of the atomic coherence which oscillates with detuning $-\delta_p$:

$$\chi(t) = -i \frac{\mathcal{N}}{\varepsilon_0 \mathcal{E}_p} \sum_{m=0}^M \sum_{n>m} \mu_{mn} \tilde{\rho}_{nm}^{(-1)}(t) . \quad (5.85)$$

The dependence of the linear polarization on the density matrix elements is clearly displayed if the susceptibility is expressed in terms of the real (χ') and imaginary (χ'') parts as

$$\chi(t) = \chi'(t) + i\chi''(t) . \quad (5.86)$$

We see from (5.82) and (5.86) that the real part of the susceptibility determines the in-phase part of the polarization and the imaginary part determines the out-of-phase component. The former is associated with dispersion, the latter with absorption of the probe field.

Comparing (5.86) with (5.85), we find that the real and imaginary parts of the susceptibility are given by

$$\begin{aligned} \chi'(t) &= \frac{\mathcal{N}}{\varepsilon_0 \mathcal{E}_p} \sum_{m=0}^M \sum_{n>m} \mu_{mn} \text{Im} \left[\tilde{\rho}_{nm}^{(-1)}(t) \right] , \\ \chi''(t) &= -\frac{\mathcal{N}}{\varepsilon_0 \mathcal{E}_p} \sum_{m=0}^M \sum_{n>m} \mu_{mn} \text{Re} \left[\tilde{\rho}_{nm}^{(-1)}(t) \right] . \end{aligned} \quad (5.87)$$

Before exploring the physical properties of the real and imaginary parts of the susceptibility, it is instructive to analyze the relations between χ' and χ'' . The Fourier transforms of χ' and χ'' are related by the Kramers–Kröning relations

$$\begin{aligned} \chi'(\omega) &= \frac{1}{\pi} \mathcal{P} \int_{-\infty}^{\infty} d\omega' \frac{\chi''(\omega')}{\omega' - \omega} , \\ \chi''(\omega) &= -\frac{1}{\pi} \mathcal{P} \int_{-\infty}^{\infty} d\omega' \frac{\chi'(\omega')}{\omega' - \omega} , \end{aligned} \quad (5.88)$$

where \mathcal{P} is the principal value of the integral. With these forms, we note that a Lorentzian structure of one part of the susceptibility involves necessarily a

dispersion-like structure in the other part. For example, when the imaginary part of the susceptibility is represented by a Lorentzian $\chi'' = 1/(1 + \omega'^2)$, the real part of the susceptibility can be found straightforwardly by the residue theorem of complex analysis as

$$\begin{aligned}
 \chi'(\omega) &= \frac{1}{\pi} \mathcal{P} \int_{-\infty}^{\infty} d\omega' \frac{1}{(1 + \omega'^2)(\omega' - \omega)} \\
 &= \frac{1}{\pi} \mathcal{P} \int_{-\infty}^{\infty} d\omega' \frac{1}{(-i - \omega')(i - \omega')(\omega' - \omega)} \\
 &= \frac{1}{\pi} \left[2\pi i \frac{1}{(-i - \omega')(\omega' - \omega)} \Big|_{\omega' = i} - i\pi \frac{1}{(\omega' - i)(\omega' + i)} \Big|_{\omega' = \omega} \right] \\
 &= \frac{\omega}{1 + \omega^2} .
 \end{aligned} \tag{5.89}$$

The Lorentzian imaginary part is obtained from the dispersive structure in the same manner. In the following discussion of the absorptive and dispersive properties of atomic systems, we will observe continuous transitions between Lorentzian and dispersive structures by applying external driving fields. This is associated with the corresponding change of the polarization from being governed by population differences between the atomic levels to being governed by induced atomic coherences.

5.5.1 Absorptive and Dispersive Properties of Two-Level Atoms

Before continuing with the full development of the optical properties of a dense atomic medium, which requires the treatment of spatial propagation and therefore the cumulative effect of many multi-level atoms, it is important to understand the absorptive and dispersive properties of a simple system of independent two-level atoms driven by a strong, near resonant external field. Modelling of complex systems with analogous but elementary systems is a powerful and widely employed approach to gaining insight into physical problems. Many of the results predicted in elementary systems are analogous to phenomena that one would expect in complex systems. For this reason, a complete and detailed understanding of the dynamics displayed by elementary systems is important for modelling physical processes occurring in complex systems. We present the theory of the linear response of a driven two-level atom to a weak probe field, and display graphically the absorptive and dispersive responses as a function of frequency of the probe field.

Let us consider a two-level atom with excited level $|1\rangle$, ground level $|0\rangle$, and transition frequency ω_0 . The atom is driven by an arbitrarily intense coherent field at a frequency ω_L and resonant Rabi frequency Ω , and damped at the rate γ by spontaneous emission. In addition, the driven atom is monitored by a weak probe field at frequency ω_p and the Rabi frequency Ω_p . Both fields are tuned near the atomic resonance in the sense that the detunings are small compared to the atomic transition frequency. We express the optical

properties of the atom in terms of the linear susceptibility, which gives the response of the atom to the probe field as modified by the presence of the driving field.

Our mathematical analysis proceeds by calculating the response of the driven two-level atom to an external weak probe field. The total field applied to the atom is of the form

$$\mathbf{E}(\mathbf{r}, t) = \mathbf{E}_L(\mathbf{r}) \exp(-i\omega_L t) + \mathbf{E}_p(\mathbf{r}) \exp(-i\omega_p t) , \quad (5.90)$$

where $\mathbf{E}_L(\mathbf{r})$ and $\mathbf{E}_p(\mathbf{r})$ are the amplitudes of the driving field and weak probe field, respectively.

The dynamics of the driven and probed atom are governed by the master equation (2.75) which, for a two-level atom driven by two coherent fields, leads to three equations of motion for the density matrix elements

$$\begin{aligned} \dot{\varrho}_{10}(t) &= -\left(\frac{1}{2}\gamma + i\omega_0\right) \varrho_{10}(t) + \frac{1}{2}(\Omega e^{-i\omega_L t} + \Omega_p e^{-i\omega_p t}) [\varrho_{11}(t) - \varrho_{00}(t)] , \\ \dot{\varrho}_{01}(t) &= -\left(\frac{1}{2}\gamma - i\omega_0\right) \varrho_{01}(t) + \frac{1}{2}(\Omega e^{i\omega_L t} + \Omega_p e^{i\omega_p t}) [\varrho_{11}(t) - \varrho_{00}(t)] , \\ \dot{\varrho}_{11}(t) &= -\gamma \varrho_{11}(t) - \frac{1}{2}(\Omega e^{-i\omega_L t} + \Omega_p e^{-i\omega_p t}) \varrho_{01}(t) \\ &\quad - \frac{1}{2}(\Omega e^{i\omega_L t} + \Omega_p e^{i\omega_p t}) \varrho_{10}(t) , \end{aligned} \quad (5.91)$$

where the Rabi frequencies Ω and Ω_p have been chosen to be real and independent of the position \mathbf{r} . In addition, we have assumed that the population is conserved, i.e. $\varrho_{00}(t) + \varrho_{11}(t) = 1$. From these equations, we determine the susceptibility of the probe field by means of (5.85) that is valid for arbitrary values of the Rabi frequencies Ω and Ω_p .

Equations (5.91) are coupled first-order differential equations with time-dependent coefficients. In principle, the equations can be solved numerically by direct integration. This method, however, will not be used as it does not provide physical understanding of the atomic dynamics. Instead, we shall use other methods, which involve both analytical and numerical analysis. One of the standard techniques is to find a rotating frame in which the coefficients of the differential equations are independent of time. However, in the case considered here of two fields of different frequencies, it is not possible to find a frame in which the coefficients of the equations of motion (5.91) would be time independent. We can, however, simplify the time dependence appearing in (5.91) by choosing a frame rotating at the frequency ω_L . This allows us to express the time dependence in terms of a single parameter. Thus, we can introduce “rotated” density matrix elements

$$\begin{aligned} \tilde{\varrho}_{10}(t) &= \varrho_{10}(t) \exp(i\omega_L t) , \\ \tilde{\varrho}_{01}(t) &= \varrho_{01}(t) \exp(-i\omega_L t) , \\ \tilde{\varrho}_{11}(t) &= \varrho_{11}(t) , \end{aligned} \quad (5.92)$$

and find that the equations of motion (5.91) can then be transformed to

$$\begin{aligned}
\dot{\tilde{\varrho}}_{10}(t) &= -\left(\frac{1}{2}\gamma - i\Delta_L\right) \tilde{\varrho}_{10}(t) + \frac{1}{2}(\Omega + \Omega_p e^{-i\delta t}) [\tilde{\varrho}_{11}(t) - \tilde{\varrho}_{00}(t)] , \\
\dot{\tilde{\varrho}}_{01}(t) &= -\left(\frac{1}{2}\gamma + i\Delta_L\right) \tilde{\varrho}_{01}(t) + \frac{1}{2}(\Omega + \Omega_p e^{i\delta t}) [\tilde{\varrho}_{11}(t) - \tilde{\varrho}_{00}(t)] , \\
\dot{\tilde{\varrho}}_{11}(t) &= -\gamma \tilde{\varrho}_{11}(t) - \frac{1}{2}(\Omega + \Omega_p e^{-i\delta t}) \tilde{\varrho}_{01}(t) \\
&\quad - \frac{1}{2}(\Omega + \Omega_p e^{i\delta t}) \tilde{\varrho}_{10}(t) ,
\end{aligned} \tag{5.93}$$

where $\Delta_L = \omega_L - \omega_0$ is the detuning of the driving field from the atomic resonance, and $\delta = \omega_p - \omega_L$ is the detuning of the probe field from the driving frequency.

It is seen from (5.93) that the effect of the weak probe field on the time evolution of the density matrix elements is to induce small components oscillating at frequencies that differ by $\pm\delta$ from the frequencies of the unperturbed (i.e. $\Omega_p = 0$) components. Since the coefficients of the differential equations (5.93) are periodic in time with periodicity δ , we can study their dynamics by applying the Floquet method, in which the atomic dynamics are described in terms of Fourier harmonics of the density matrix elements. In this approach, we first make the Fourier decomposition

$$\tilde{\varrho}_{ij}(t) = \sum_{l=-\infty}^{\infty} \tilde{\varrho}_{ij}^{(l)}(t) e^{il\delta t} , \quad i, j = 0, 1 , \tag{5.94}$$

where $\tilde{\varrho}_{ij}^{(l)}(t)$ are slowly varying harmonic amplitudes. The Fourier decomposition (5.78) tells us that the atomic variables will respond at harmonics of the modulation frequency δ , and knowledge of $\tilde{\varrho}_{ij}^{(l)}(t)$ gives all the information about the system evolution and its optical properties.

Next, we substitute (5.94) into their respective equations of motion (5.93) and compare coefficients of the same power in $l\delta$. This leads to the following set of differential equations for the slowly varying amplitudes

$$\begin{aligned}
\dot{\tilde{\varrho}}_{10}^{(l)}(t) &= -\frac{1}{2}(\Omega\delta_{l,0} + \Omega_p\delta_{l+1,0}) - \left(\frac{1}{2}\gamma - i\Delta_L + il\delta\right) \tilde{\varrho}_{10}^{(l)}(t) \\
&\quad + \Omega\tilde{\varrho}_{11}^{(l)}(t) + \Omega_p\tilde{\varrho}_{11}^{(l+1)}(t) , \\
\dot{\tilde{\varrho}}_{01}^{(l)}(t) &= -\frac{1}{2}(\Omega\delta_{l,0} + \Omega_p\delta_{l-1,0}) - \left(\frac{1}{2}\gamma + i\Delta_L + il\delta\right) \tilde{\varrho}_{01}^{(l)}(t) \\
&\quad + \Omega\tilde{\varrho}_{11}^{(l)}(t) + \Omega_p\tilde{\varrho}_{11}^{(l-1)}(t) , \\
\dot{\tilde{\varrho}}_{11}^{(l)}(t) &= -(\gamma + il\delta) \tilde{\varrho}_{11}^{(l)}(t) - \frac{1}{2} \left[\Omega\tilde{\varrho}_{01}^{(l)}(t) + \Omega_p\tilde{\varrho}_{01}^{(l+1)}(t) \right] \\
&\quad - \frac{1}{2} \left[\Omega\tilde{\varrho}_{10}^{(l)}(t) + \Omega_p\tilde{\varrho}_{10}^{(l-1)}(t) \right] .
\end{aligned} \tag{5.95}$$

Thus, the Fourier decomposition transforms the system of three coupled equations with time-dependent coefficients into an infinite number of coupled equations with time independent coefficients. We can solve (5.95) by using the continued fraction technique, or we can write (5.95) in a matrix form and solve by matrix inversion. In both techniques, we have to use a truncated basis rather than the infinite basis of the harmonic amplitudes. The validity of the truncation is ensured by requiring that the solution does not change if the number of truncated harmonics is increased or decreased by one.

We solve the set of equations (5.95) for the steady-state ($t \rightarrow \infty$), which can be obtained directly by setting the left-hand side of (5.95) equal to zero. First, we find the steady-state values of the unperturbed density matrix elements in the presence of the driving field alone, which is obtained by putting $\Omega_p = 0$ and $l = 0$ in (5.95). In this limit, the steady-state solution of (5.95) is given by

$$\tilde{\varrho}_{10}^{(0)} = \frac{-2\Omega \left(\frac{1}{2}\gamma + i\Delta_L\right)}{\gamma^2 + 4\Delta_L^2 + 2\Omega^2}, \quad (5.96a)$$

$$\tilde{\varrho}_{01}^{(0)} = \frac{-2\Omega \left(\frac{1}{2}\gamma - i\Delta_L\right)}{\gamma^2 + 4\Delta_L^2 + 2\Omega^2}, \quad (5.96b)$$

$$\tilde{\varrho}_{11}^{(0)} = \frac{\Omega^2}{\gamma^2 + 4\Delta_L^2 + 2\Omega^2}, \quad (5.96c)$$

where $\tilde{\varrho}_{ij}^{(0)} \equiv \lim_{t \rightarrow \infty} \tilde{\varrho}_{ij}^{(0)}(t)$.

We now include the probe field, and solve (5.95) for the steady-state valid to first order in Ω_p . Eliminating $\tilde{\varrho}_{11}^{(0)}$ from (5.95) and retaining terms linear in Ω_p , the steady-state solutions for the coherences are found to satisfy the equations

$$\begin{aligned} \tilde{\varrho}_{10}^{(l)} &= -\frac{1}{2P_l R_l + \Omega^2} \left\{ R_l (\Omega \delta_{l,0} + \Omega_p \delta_{l+1,0}) + \Omega^2 \tilde{\varrho}_{01}^{(l)} \right. \\ &\quad \left. + \Omega \Omega_p \left[R_l \left(\tilde{\varrho}_{01}^{(l+1)} + \tilde{\varrho}_{10}^{(l+1)} \right) / R_{l+1} + \tilde{\varrho}_{01}^{(l+1)} + \tilde{\varrho}_{10}^{(l-1)} \right] \right\}, \\ \tilde{\varrho}_{01}^{(l)} &= -\frac{1}{2Q_l R_l + \Omega^2} \left\{ R_l (\Omega \delta_{l,0} + \Omega_p \delta_{l-1,0}) + \Omega^2 \tilde{\varrho}_{10}^{(l)} \right. \\ &\quad \left. + \Omega \Omega_p \left[R_l \left(\tilde{\varrho}_{10}^{(l-1)} + \tilde{\varrho}_{01}^{(l-1)} \right) / R_{l-1} + \tilde{\varrho}_{10}^{(l-1)} + \tilde{\varrho}_{01}^{(l+1)} \right] \right\}, \end{aligned} \quad (5.97)$$

where $P_l = \gamma/2 - i\Delta_L + il\delta$, $Q_l = \gamma/2 + i\Delta_L + il\delta$, and $R_l = \gamma + il\delta$.

The sensitivity of the atomic polarization to the population inversion and atomic coherences appears in these equations as a coupling between different harmonics. With the steady-state solutions (5.97) we find from (5.94) that the coherence $\tilde{\varrho}_{10}$ exhibits harmonic oscillations at an infinite number of frequencies of the form $n\omega_L \pm m\omega_p$, where n and m are integers. If the driving field is treated correctly to all orders in Ω while the probe field is treated only to first order in Ω_p , then $\tilde{\varrho}_{10}$ oscillates at three dominant frequencies: ω_L , ω_p ,

and $2\omega_L - \omega_p$. Then, we can express the coherence $\tilde{\varrho}_{10}$ in terms of the Fourier amplitudes as

$$\begin{aligned}\tilde{\varrho}_{10} = & \tilde{\varrho}_{10}(\omega_L) \exp(-i\omega_L t) + \tilde{\varrho}_{10}(\omega_p) \exp(-i\omega_p t) \\ & + \tilde{\varrho}_{10}(2\omega_L - \omega_p) \exp[-i(2\omega_L - \omega_p)t] .\end{aligned}\quad (5.98)$$

The amplitudes $\tilde{\varrho}_{10}(\omega_L)$ and $\tilde{\varrho}_{10}(\omega_p)$ are, respectively, the contributions linear in the Rabi frequencies Ω and Ω_p , whereas the amplitude $\tilde{\varrho}_{10}(2\omega_L - \omega_p)$ is a nonlinear (third-order) contribution proportional to $\Omega^2\Omega_p$.

The physical meaning of the three terms in $\tilde{\varrho}_{10}$ in (5.98) are as follows: the harmonics $\tilde{\varrho}_{10}(\omega_L)$ and $\tilde{\varrho}_{10}(\omega_p)$ give rise to absorption (or amplification) of the driving and probe fields, respectively, and the harmonic $\tilde{\varrho}_{10}(2\omega_L - \omega_p)$ is the so-called “mixing response”, because it gives rise to generation of a field with frequency $2\omega_L - \omega_p$. If such a field is already present, it may be amplified by the effect of this term.

According to (5.85), we only need the harmonic $\tilde{\varrho}_{10}^{(-1)}$ to find the susceptibility of the probe field. We find that to all orders in Ω and first order in Ω_p , the harmonic $\tilde{\varrho}_{10}^{(-1)}$ is given by

$$\begin{aligned}\tilde{\varrho}_{10}^{(-1)} = & -\frac{\Omega_p}{2D_{-1}} \left\{ (2Q_{-1}R_{-1} + \Omega^2) \left[1 + \frac{\Omega}{R_0} (\tilde{\varrho}_{01}^{(0)} + \tilde{\varrho}_{10}^{(0)}) \right] \right. \\ & \left. + 2\Omega Q_{-1}\tilde{\varrho}_{01}^{(0)} \right\} ,\end{aligned}\quad (5.99)$$

where $D_{-1} = 2P_{-1}Q_{-1}R_{-1} + \Omega^2(\gamma - 2i\delta)$, and $\tilde{\varrho}_{ij}^{(0)}$ are the zeroth-order solutions for $\tilde{\varrho}_{ij}$, given in (5.96).

With the solution (5.99), the linear susceptibility of the probe field is then given by

$$\begin{aligned}\chi = & i\frac{\mathcal{N}\mu^2}{\varepsilon_0\hbar D_{-1}\gamma} \left\{ (2Q_{-1}R_{-1} + \Omega^2) \left[\gamma + \Omega (\tilde{\varrho}_{01}^{(0)} + \tilde{\varrho}_{10}^{(0)}) \right] \right. \\ & \left. + 2\gamma\Omega Q_{-1}\tilde{\varrho}_{01}^{(0)} \right\} .\end{aligned}\quad (5.100)$$

The susceptibility (5.100) gives the atomic medium response to the probe field as modified by the presence of the driving field. The real (χ') and imaginary (χ'') parts of χ determine the dispersive and absorptive properties, respectively, of the probe field propagating in the atomic medium. The susceptibility (5.100) is a function of the detuning Δ_L , the Rabi frequency Ω , and the probe field detuning δ . To help gain insight into this rather complicated expression, we illustrate graphically the real χ' and imaginary χ'' parts of the susceptibility as a function of the probe field detuning δ , for a wide range of the parameters Δ_L and Ω .

In Fig. 5.20, the real and imaginary parts of χ are shown as a function of δ in the absence of the driving field ($\Omega = 0$). These graphs illustrate the Lorentzian-like and complementary dispersion-like features, as required by

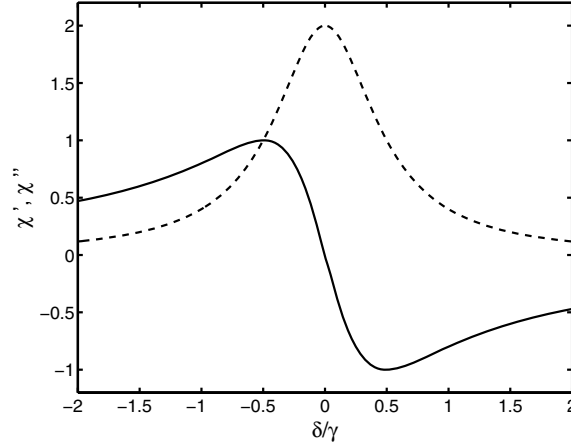


Fig. 5.20. The real χ' (*solid line*) and imaginary χ'' (*dashed line*) parts of the normalized linear susceptibility $\chi/(\mathcal{N}\mu^2/\varepsilon_0\hbar\gamma)$ as a function of the probe field detuning δ/γ in the absence of the driving field $\Omega = 0$

the Kramers–Kröning relations. At the atomic resonance, the absorption of the probe field is large and the dispersion vanishes. Outside the atomic resonance, the dispersion is large for those frequencies for which the absorption is large. Far from the atomic resonance both χ' and χ'' are very small.

It is instructive to calculate some typical values. Note that for $\delta = \pm\gamma$, we have $|\chi'| = |\chi''|$. We may take $\chi''(\delta = \gamma) \equiv \chi_t''$ as defining a typical value of χ'' and the maximum value of χ' . This illustrates the well-known fact that where the refractive index is enhanced in the neighborhood of an atomic resonance, the absorption is also large. We may write

$$\chi_t'' = \frac{3\mathcal{N}\lambda_p^3}{8\pi^2}, \quad (5.101)$$

where λ_p is the probe field wavelength. For a gas at one atmosphere, with $\mathcal{N} \sim 10^{22}$ atoms/m³, assuming a wavelength $\sim 10^{-6}$ m, we have $\chi_t'' \sim 40$. Since the rate of change of the electric field with distance z within the medium is given by

$$\frac{dE}{dz} = -\frac{\chi_t''}{\lambda_p} E, \quad (5.102)$$

we see that χ_t'' is the exponential loss rate per wavelength travelled. Thus, for the values we have chosen, practically all the radiation is absorbed within the distance of a single wavelength: the medium is opaque.

Figure 5.21 shows how the real and imaginary parts of the susceptibility are modified when a strong coherent field is simultaneously applied to the atom. The real part χ' exhibits Lorentzian like structures at frequencies $\omega_L \pm \Omega$ corresponding to the Rabi sidebands, whereas the imaginary part exhibits a dispersion-like form. Again, complementary behavior between absorptive

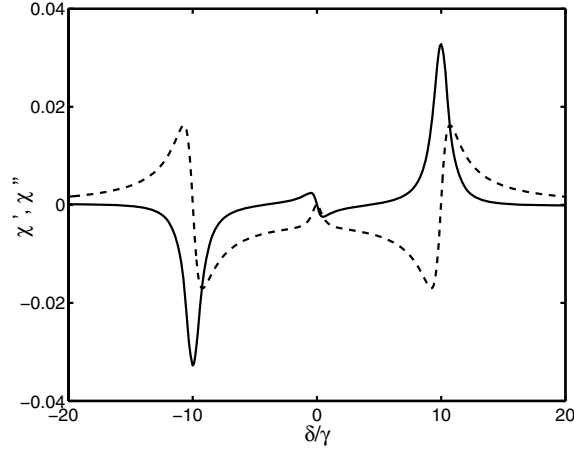


Fig. 5.21. The real χ' (*solid line*) and imaginary χ'' (*dashed line*) parts of the normalized linear susceptibility $\chi/(\mathcal{N}\mu^2/\varepsilon_0\hbar\gamma)$ as a function of δ/γ for $\Delta_L = 0$ and $\Omega = 10\gamma$

and dispersive structures is evident. The properties of the real part of the susceptibility were first studied by Mollow [113] and experimentally observed by Wu et al. [114]. The graphs show that there are three frequencies at which the absorption vanishes identically. These are $\omega_p = 0, \omega_L \pm \Omega$. For these frequencies the driven two-level atom displays EIT. In addition, at the Rabi sideband frequencies, the dispersion reaches a maximum value, whereas the absorption vanishes. Thus, the system can produce a large index of refraction accompanied by vanishing absorption [115, 116].

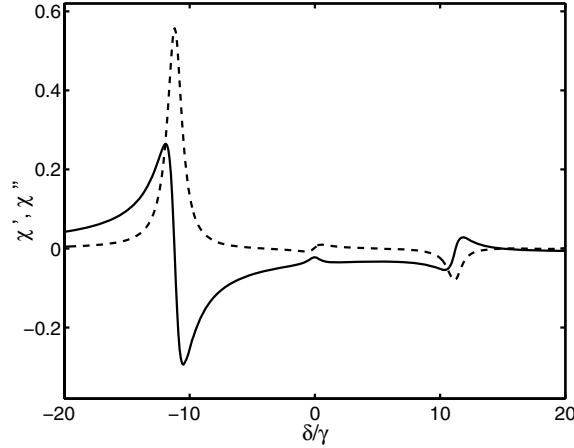


Fig. 5.22. The real χ' (*solid line*) and imaginary χ'' (*dashed line*) parts of the normalized linear susceptibility $\chi/(\mathcal{N}\mu^2/\varepsilon_0\hbar\gamma)$ as a function of δ/γ for $\Delta_L = 5\gamma$ and $\Omega = 10\gamma$

We also see from Fig. 5.21 that there are broad regions of the probe field frequency in which χ'' is negative, corresponding to probe field amplification. At these frequencies stimulated emission outweighs absorption, so that the probe field is amplified at the expense of the driving field. The amplification can be enhanced, but is limited to narrow ranges of the probe field frequencies, when the driving field is detuned from the atomic resonance. This is shown in Fig. 5.22, where we plot χ' and χ'' for an off-resonant driving field with $\Delta_L = 5\gamma$. Compared with Fig. 5.21, we note that at the Rabi sidebands, the imaginary part χ'' has a Lorentzian-like structure, whereas the imaginary part χ' exhibits a dispersion-like behavior. In contrast to the case of exact resonance ($\Delta_L = 0$), the dispersion is large in the frequency region where the absorption is large. The absorption rate consists of one absorption and one emission component at the Rabi sidebands, and a small dispersion-like component at the centre of the spectrum. The emission (gain) component indicates that in one Rabi sideband stimulated emission overweighs absorption, so that the probe field is amplified at the expense of the driving field.

5.5.2 Dressed-Atom Model of a Driven Two-Level Atom

The origin of the predicted multiple transparency windows and amplification can be well understood in terms of the dressed-atom model of the system, in which the spectral features are related to the energy eigenstates of the entangled atom-driving-field system and are viewed as arising from the transitions between them. An extended analysis of the dressed atom model can be found in the textbook of Cohen-Tannoudji, Dupont-Roc and Grynberg [117].

In the dressed-atom model, the driving laser field is considered to “dress” the atom with laser photons and to form along with it a single, entangled quantum system. This reflects the fact that photons are exchanged between the atom and driving field mode via absorption and stimulated emission process many times between successive spontaneous emissions by the atom into the vacuum modes. There are two equivalent treatments of the interaction: the semiclassical treatment, in which the Hamiltonian of the system, excluding the contribution of the probe field, is given by

$$H_s = H_{0s} + H_{Ls} , \quad (5.103)$$

where

$$H_{0s} = \hbar\Delta_L |1\rangle\langle 1| \quad (5.104)$$

is the Hamiltonian of the atom, and

$$H_{Ls} = -\frac{1}{2}i\hbar\Omega (S^+ - S^-) \quad (5.105)$$

is the interaction Hamiltonian between the atom and the driving field. In the semiclassical approach, the atom is treated quantum-mechanically, whereas the driving laser field is treated classically.

The eigenstates of H_s are the so called semiclassical dressed states, which are linear superpositions of the atomic states

$$\begin{aligned} |+\rangle &= \sin \theta |0\rangle + \cos \theta |1\rangle , \\ |-\rangle &= \cos \theta |0\rangle - \sin \theta |1\rangle , \end{aligned} \quad (5.106)$$

where $\tan 2\theta = \Omega/\Delta_L$.

If we use a fully quantum-mechanical description of the system, the Hamiltonian takes the form

$$H_q = H_{0q} + H_{Lq} , \quad (5.107)$$

where

$$H_{0q} = \hbar\omega_0 |1\rangle\langle 1| + \hbar\omega_L \hat{a}^\dagger \hat{a} \quad (5.108)$$

is the Hamiltonian of the uncoupled atom and the driving field, and

$$H_{Lq} = -i\hbar g (S^+ \hat{a} - \hat{a}^\dagger S^-) \quad (5.109)$$

is the atom-field interaction, g is the atom-field coupling constant, and \hat{a} (\hat{a}^\dagger) is the annihilation (creation) operator for the driving mode.

In the quantum treatment, the basis states are product (“undressed”) states $|i\rangle \otimes |n\rangle$, where $|i\rangle$ is an atomic state ($i = 0, 1$), and n is the number of photons in the driving mode. These states are the eigenstates of the uncoupled atom and field Hamiltonian (5.108), and the eigenstates (dressed states) of the total Hamiltonian \hat{H}_q are represented in the basis of these undressed states.

The undressed states, shown in Fig. 5.23(a), group into manifolds, which are labelled $\mathcal{E}(n)$. Neighboring manifolds are separated by frequency ω_L , while the states within each manifold are separated by Δ_L . The lowest manifold (the ground state) is a singlet $|0\rangle \otimes |0\rangle$. The energy manifolds with the number of photons $n \geq 0$ are composed of two nondegenerate states $|0\rangle \otimes |n\rangle$ and $|1\rangle \otimes |n-1\rangle$. The interaction H_{Lq} has non-vanishing matrix elements only between those undressed states between which the atom has a non-vanishing dipole moment and the number of photons in the field mode changes by one. Therefore, when we include the interaction H_{Lq} , the doublets recombine into new doublets with eigenstates

$$\begin{aligned} |+, n\rangle &= \sin \theta |0, n\rangle + \cos \theta |1, n-1\rangle , \\ |-, n\rangle &= \cos \theta |0, n\rangle - \sin \theta |1, n-1\rangle , \end{aligned} \quad (5.110)$$

corresponding to energies

$$E_{n,\pm} = \hbar n \omega_L \pm \frac{1}{2} \hbar \Omega' , \quad (5.111)$$

where $|i, m\rangle = |i\rangle \otimes |m\rangle$ ($i = 0, 1$; $m = n, n-1$), and

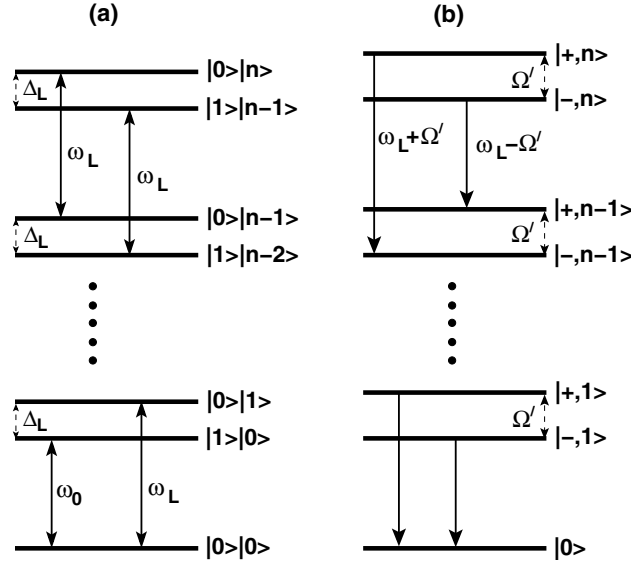


Fig. 5.23. (a) Energy levels of the undressed system, (b) Energy levels of the dressed-atom system

$$\Omega' = \sqrt{g^2 n + \Delta_L^2} \quad (5.112)$$

is the off-resonant Rabi frequency of the driving field. The Rabi frequency depends on the number of photons and varies with n . However, for a strong driving field $\langle n \rangle \gg 1$, and then we can approximate $n \approx \langle n \rangle$. In this limit, the Rabi frequency can be assumed constant independent of n .

The eigenstates $|\pm, n\rangle$ are the dressed states of the system. The states, shown in Fig. 5.23(b), form an infinite ladder of doublets. Two neighbouring doublets are separated by the energy $\hbar\omega$ of one laser photon, while the states within each doublet are separated by an energy $\hbar\Omega'$. An interesting property of the dressed states is that they are in the form of entangled atom-field states: the atom and field evolve as a single (entangled) system.

The absorption is represented in the dressed-atom model as transitions from one doublet to the doublet above. The system absorbs photons at three different frequencies, ω_L , $\omega_L + \Omega'$ and $\omega_L - \Omega'$, showing the effect of Rabi splitting. The amplitude of each absorption component is proportional to the population difference between the dressed states involved in the absorption. When the driving field frequency ω_L is equal to the atomic transition frequency ω_0 , the populations of the dressed states are equal, and therefore the absorption spectrum is composed of small dispersive features whose origin is in the small coherences between the dressed states. When $\omega_L \neq \omega_0$, the populations of the dressed states are different and therefore the probe tuned to one of the Rabi sidebands would experience absorption, and when tuned to the other, the probe would be amplified due to the population inversion between the dressed states. We see from Fig. 5.22 that apart from the amplification at one of the Rabi sidebands, the probe also exhibits an amplification

on one side of a small dispersion-like structure centered at ω_L . The amplification originates from the complicated multi-photon interference between absorption and emission processes and is not associated with any population inversion because the transition occurs between equally populated states both in the bare and in the dressed-atom basis.

5.5.3 Absorption and Dispersion with Multichromatic Driving Fields

The analysis of the absorptive and dispersive properties of a two-level atom can be extended to more complicated configurations of the driving fields, such as multichromatic or amplitude/phase modulated fields [118]. For example, a bichromatic field is formed by combining two coherent fields of different frequencies and different amplitudes, giving an effective time-dependent Rabi frequency

$$\begin{aligned}\Omega(t) &= \Omega_1 \exp(i\omega_{L1}t) + \Omega_2 \exp(i\omega_{L2}t) \\ &= \Omega [a_1 \exp(i\delta_B t) + a_2 \exp(-i\delta_B t)] \exp(i\omega_L t) ,\end{aligned}\quad (5.113)$$

where $a_i = \Omega_i/\Omega$, $\omega_L = (\omega_{L1} + \omega_{L2})/2$ is the average angular frequency of the driving fields, and $\delta_B = \omega_{L1} - \omega_L = \omega_L - \omega_{L2}$ is the beat frequency between the angular frequencies of the driving fields.

On the other hand, an amplitude or phase modulated field is formed by combining three coherent fields of different frequencies with a central (carrier) field of frequency ω_L and a pair of symmetrically detuned fields (modulators) of frequencies $\omega_L \pm \delta_m$. In this case, the effective Rabi frequency of the combined field is of the form

$$\begin{aligned}\Omega(t) &= \Omega_0 \exp(i\omega_L t) + \Omega_+ \exp(i\omega_{L+}t) + \Omega_- \exp(i\omega_{L-}t) \\ &= \Omega_0 \exp(i\omega_L t) \{1 + a_m e^{i\phi_m} [e^{i\delta_m t} + e^{-i\delta_m t}]\} ,\end{aligned}\quad (5.114)$$

where $a_m = \Omega_{\pm}/\Omega_0$ is the modulation amplitude, $\delta_m = \omega_{L+} - \omega_L = \omega_L - \omega_{L-}$, and ϕ_m the initial phase difference between the carrier and the sideband fields.

Depending on ϕ_m , the sideband fields can act as modulators of the amplitude or phase of Ω_0 . For $\phi_m = 0$ or π , the sidebands modulate the amplitude of Ω_0 as

$$\Omega(t) = \Omega_0 [1 \pm 2a_m \cos \delta_m t] \exp(i\omega_{L0}t) ,\quad (5.115)$$

where the sign “+” corresponds to $\phi_m = 0$, while “−” corresponds to $\phi_m = \pi$.

For $\phi_m = \pi/2$ or $\phi_m = 3\pi/2$, the sideband fields modulate the phase of Ω_0 as

$$\Omega(t) = \Omega_0 [1 \pm i2a_m \cos \delta_m t] \exp(i\omega_{L0}t) .\quad (5.116)$$

For $a_m \gg 1$, which is called a 100% amplitude or phase modulated field, the carrier component is effectively suppressed, so that the 100% modulated field corresponds to bichromatic driving with $a_1 = a_2$.

In the following, we illustrate results for absorption and dispersion with a bichromatic field and with an amplitude modulated field. We have obtained these graphs by the numerical integration of the set of equations of motion (5.91) with $\Delta_L = 0$ and $\Omega \rightarrow \Omega(t)$, i.e. the Rabi frequency Ω replaced by (5.114) for the bichromatic driving field and by (5.116) for the amplitude modulated field.

Figure 5.24 shows the absorption rate χ'' as a function of $\delta_p = (\omega_p - \omega_0)/\gamma$ for a strong bichromatic driving field. The absorption rate consists of a central component and a series of dispersion-like structures at the sideband frequencies and an absorption-like structure at the central frequency whose amplitude oscillates with the Rabi frequency of the driving fields. The absorption rate is symmetric about $\delta_p = 0$ and the central component displays amplitude oscillations with transparency windows (EIT) appearing at $\delta_B \approx \Omega/n$, where $n = 1, 2, 3, \dots$. The situation for the dispersive response is analogous when dispersion-like and absorption-like structures are interchanged. In contrast to the case of a monochromatic driving field, the positions of the sidebands are independent of the Rabi frequency of the driving field. The positions depend only on the detuning δ_B giving the possibility of producing multiple transparency windows at frequencies that are independent of the Rabi frequency of the driving field. However, the magnitudes of the spectral features depend strongly on both the Rabi frequency and the detuning δ_B .

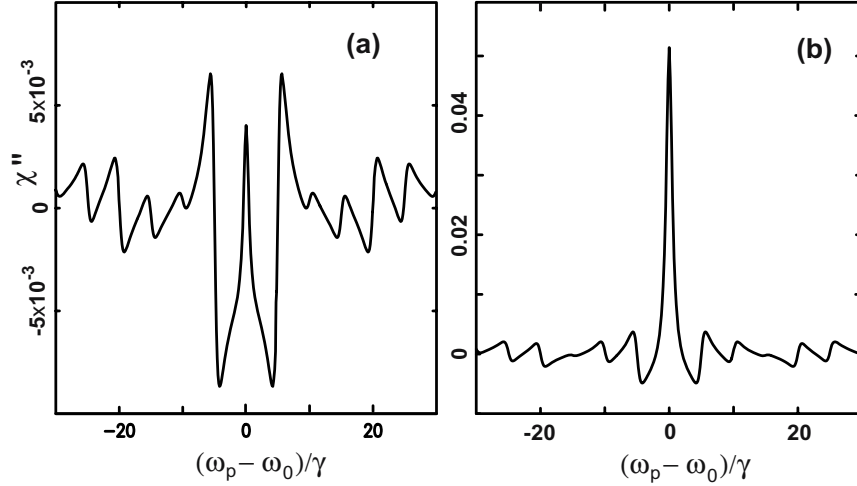


Fig. 5.24. The imaginary part χ'' of the normalized linear susceptibility $\chi/(\mathcal{N}\mu^2/\varepsilon_0\hbar\gamma)$ as a function of δ_p/γ for $\delta_B = 5\gamma$ and different Rabi frequencies: (a) $\Omega = 14\gamma$, (b) $\Omega = 15\gamma$

Figure 5.25 shows the absorption, χ' , and dispersion, χ'' , for a strong amplitude modulated field. The theoretical studies showed that the fluorescence and absorption spectra of the system are composed of a series of features located at frequencies [119, 120]

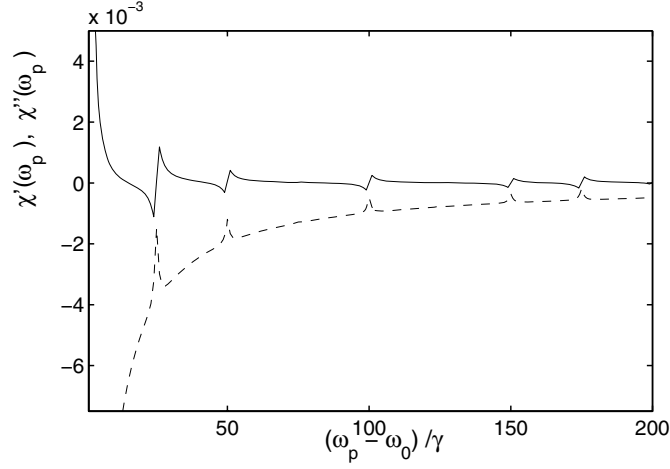


Fig. 5.25. The real χ' (*solid line*) and imaginary χ'' (*dashed line*) parts of the normalized linear susceptibility $\chi/(\mathcal{N}\mu^2/\varepsilon_0\hbar\gamma)$ as a function of δ_p for a strong amplitude modulated field with $\Omega_0 = 100\gamma$, $\Omega_{\pm} = 50\gamma$, and $\delta_m = 25\gamma$

$$\omega = \omega_0 \pm (\Omega_0 \pm m\delta) , \quad m = 0, 1, 2, \dots , \quad (5.117)$$

i.e. the system responds at the Rabi frequency of the central component and harmonics of the modulation frequency of the driving field. We see from Fig. 5.25 that the absorption vanishes at frequencies close to the harmonic resonances of the driving field. Moreover, at the harmonic resonances the dispersion is less negative and is almost equal to zero. Therefore, at the subharmonic resonances the system is almost transparent to the probe field. Consequently, multiple EIT can be observed in this system, with many transparency windows occurring near the subharmonic resonances. The positions of the transparency windows depend on the Rabi frequency Ω_0 .

The absorption and amplification properties at the central frequency $\omega_p = \omega_0$ can be controlled by the detuning δ such that below a harmonic resonance the probe is absorbed, whereas above the resonance the probe is amplified. This is shown in Fig. 5.25, where we plot χ' for ω_p close to the atomic resonance ω_0 , and different δ . By varying the detuning δ near one of the harmonic resonances the absorption at the central component of the spectrum can switch into amplification.

The amplification at the central component, seen in Fig. 5.26, is an example of amplification without any population inversion. We have calculated the stationary population inversion $\langle S^z \rangle = (\varrho_{11} - \varrho_{00})/2$, where ϱ_{11} and ϱ_{00} are the populations of the atomic upper and ground levels, respectively, and have found that for the same parameters as in Fig. 5.26, $\langle S^z \rangle = -1.2 \times 10^{-4} < 0$. Thus, there is no population inversion between the atomic bare states. In addition, there is no population inversion between dressed states of the system. This is easy to understand if one recalls that the net absorption at any frequency is proportional to the difference between the populations of the lower and upper states in the transitions. In the dressed-atom model the

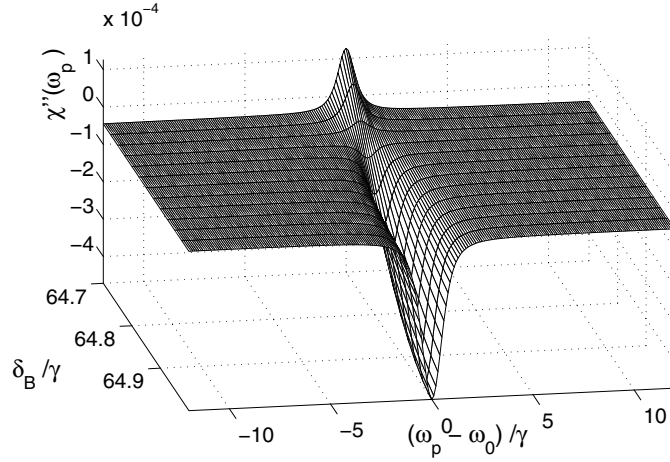


Fig. 5.26. The real χ' (*solid line*) and imaginary χ'' (*dashed line*) parts of the normalized linear susceptibility $\chi/(\mathcal{N}\mu^2/\varepsilon_0\hbar)$ as a function of δ_B for $\Delta_L = 5\gamma$ and $\Omega = 20\gamma$

transitions occur between dressed states of two neighbouring manifolds, say $|n, N\rangle$ and $|m, N+1\rangle$, where n and m label dressed states in each manifold. The frequency of the central component corresponds to transitions between dressed states with $n = m$, that are equally populated [117, 118]. Thus, the amplification seen in Fig. 5.26 is not due to a population inversion between the dressed states.

5.5.4 Collisional Dephasing and Coherent Population Oscillations

In the discussion of the absorptive and dispersive properties of a two-level atom, we have assumed that the damping rate of the atomic coherence (the transverse damping rate) is purely radiative, that is, it is equal to one half the damping rate of the population (the longitudinal damping rate). An interesting modification of the response of a driven atom to a probe field can be observed when the damping rate of the coherence γ_c is much larger than the damping rate of the population γ_p , i.e. $\gamma_c \gg \gamma_p$. This effect, known as rapid collisional dephasing, can arise e.g. from strong elastic collisions between atoms in a hot atomic vapour, or between phonons and atoms in a solid.

The inclusion of the collisional dephasing into the atomic dynamics causes the coherence to decay separately from the populations [121, 122]. The collisional dephasing modifies the equations of motion for the density matrix elements (5.93), such that the radiative damping rates of the coherence ($\gamma/2$) and the population (γ) are replaced by

$$\frac{1}{2}\gamma \longrightarrow \gamma_c \quad \text{and} \quad \gamma \longrightarrow \gamma_p. \quad (5.118)$$

Then, the equations of motion for the density matrix elements take the form

$$\begin{aligned}
\dot{\tilde{\varrho}}_{10}(t) &= -\gamma_c \tilde{\varrho}_{10}(t) + \frac{1}{2} (\Omega + \Omega_p e^{-i\delta t}) \tilde{\varrho}_z(t) , \\
\dot{\tilde{\varrho}}_{01}(t) &= -\gamma_c \tilde{\varrho}_{01}(t) + \frac{1}{2} (\Omega + \Omega_p e^{i\delta t}) \tilde{\varrho}_z(t) , \\
\dot{\tilde{\varrho}}_z(t) &= -\gamma_p - \gamma_p \tilde{\varrho}_z(t) - (\Omega + \Omega_p e^{-i\delta t}) \tilde{\varrho}_{01}(t) \\
&\quad - (\Omega + \Omega_p e^{i\delta t}) \tilde{\varrho}_{10}(t) ,
\end{aligned} \tag{5.119}$$

where $\tilde{\varrho}_z(t) = \tilde{\varrho}_{11}(t) - \tilde{\varrho}_{00}(t)$, and for simplicity, we have assumed that the driving field is on resonance with the atomic transition, i.e. $\Delta_L = 0$.

Following the approach of Boyd et al. [122], we solve (5.119) to first order in the Rabi frequency Ω_p of the probe field and to all orders in the Rabi frequency of the driving field. In this approximation, the long time coherence $\tilde{\varrho}_{10}(t)$ can be obtained from (5.119) by putting $\dot{\tilde{\varrho}}_{10}(t) = 0$, which gives

$$\tilde{\varrho}_{10}(t) \simeq \frac{1}{2\gamma_c} (\Omega + \Omega_p e^{-i\delta t}) \tilde{\varrho}_z(t) . \tag{5.120}$$

Substituting this result, together with the long time solution for $\tilde{\varrho}_{01}(t) = \tilde{\varrho}_{10}^*(t)$, into the equation of motion for $\tilde{\varrho}_z(t)$, we obtain

$$\dot{\tilde{\varrho}}_z(t) = -\gamma_p - \left[\gamma_p + \frac{1}{\gamma_c} (\Omega^2 + \Omega_p^2 + 2\Omega\Omega_p \cos \delta t) \right] \tilde{\varrho}_z(t) . \tag{5.121}$$

The long time solution of (5.121) can be written as

$$\tilde{\varrho}_z(t) = -\gamma_p \int_{-\infty}^t dt' e^{-u(t-t')} e^{-(\eta/\delta)(\sin \delta t - \sin \delta t')} , \tag{5.122}$$

where

$$\begin{aligned}
u &= \gamma_p + \frac{1}{\gamma_c} (\Omega^2 + \Omega_p^2) , \\
\eta &= \frac{2\Omega\Omega_p}{\gamma_c} .
\end{aligned} \tag{5.123}$$

Solving (5.122), we find that the long time population inversion is given by

$$\tilde{\varrho}_z(t) = \tilde{\varrho}_z^{(0)} + \tilde{\varrho}_z^{(\delta)} e^{i\delta t} + \tilde{\varrho}_z^{(-\delta)} e^{-i\delta t} , \tag{5.124}$$

where

$$\begin{aligned}
\tilde{\varrho}_z^{(0)} &= -\frac{\gamma_p}{u} , \\
\tilde{\varrho}_z^{(\delta)} &= \frac{\eta\gamma_p}{2u} \frac{u + i\delta}{\delta^2 + u^2} , \\
\tilde{\varrho}_z^{(-\delta)} &= \tilde{\varrho}_z^{(\delta)*} .
\end{aligned} \tag{5.125}$$

The solution (5.124) shows that the long time population inversion oscillates in time with frequencies $\pm\delta$. These oscillations are called coherent population

oscillations, and are significant when $\delta < u$, that is, when the detuning δ is less than the rate of population-inversion decay.

To see how the oscillations in the long time population inversion affect the response of the atom to the probe field, we substitute (5.124) into (5.120) and collect only those terms in $\tilde{\rho}_{10}(t)$ which oscillate at the probe frequency ω_p . This gives

$$\tilde{\rho}_{10}(t) = -\frac{\Omega_p}{2\gamma_c} \left[\frac{\gamma_p}{u} - \frac{\Omega^2 \gamma_p}{u \gamma_c} \frac{u - i\delta}{\delta^2 + u^2} \right]. \quad (5.126)$$

It is seen that the long time coherence oscillating at the probe frequency ω_p is composed of two terms: the part proportional to Ω_p is driven directly by the probe field, while the part proportional to Ω^2 results from the coherent population oscillations at the detuning δ .

Using the Floquet method, outlined in Sect. 5.5.1, we solve (5.119) for the steady state with $\Omega_p \ll \Omega, \gamma_p, \gamma_c$, and obtain

$$\chi(\omega_p) = i \frac{\mathcal{N} \mu^2}{\varepsilon_0 \hbar} \frac{u_z}{\mathcal{D}(\omega_p)} \left[(\gamma_p - i\delta)(\gamma_c - i\delta) + \frac{i\delta \Omega^2}{2\gamma_c} \right], \quad (5.127)$$

where

$$\mathcal{D}(\omega_p) = (\gamma_c - i\delta) [(\gamma_p - i\delta)(\gamma_c - i\delta) + \Omega^2], \quad (5.128)$$

and

$$u_z = \frac{\gamma_c \gamma_p}{\gamma_c \gamma_p + \Omega^2}. \quad (5.129)$$

The susceptibility (5.127) gives the atomic medium response to the probe field as modified by the presence of the collisional dephasing and the driving field. Figure 5.27 illustrates the effect of rapid collisional dephasing on the absorption and dispersion profiles for different Rabi frequencies of the driving field. For weak driving fields the absorption and dispersion profiles are qualitatively different from the case of pure radiative damping ($\gamma_c = \gamma_p/2 = \gamma/2$). The rapid collisional dephasing burns a narrow hole at the central frequency of the absorption spectrum, as seen in Fig. 5.27. The width of the hole is determined by the parameter Γ , which in units of γ_c is given by

$$\Gamma/\gamma_c = \frac{\gamma_p}{\gamma_c} \left(1 + \frac{\Omega^2}{\gamma_c \gamma_p} \right). \quad (5.130)$$

It shows that the hole in the absorption spectrum can be very narrow when $\gamma_c \gg \gamma_p$. It also shows the effects of power broadening, in that the width of the hole increases with Ω . In addition to hole burning in the absorption spectrum, the coherent population oscillations lead to a very steep positive dispersion in the frequency region of the narrow absorption dip, as seen in

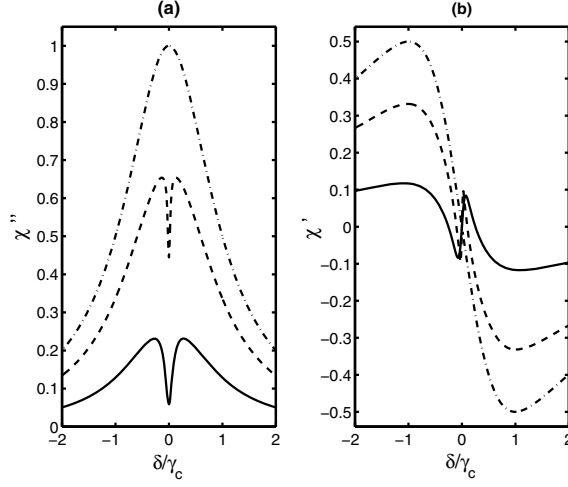


Fig. 5.27. (a) The imaginary χ'' and (b) real χ' parts of the normalized linear susceptibility $\chi/(\mathcal{N}\mu^2/\varepsilon_0\hbar\gamma_p)$ as a function of δ/γ_p for $\gamma_p = 0.02\gamma_c$ and different Ω : $\Omega = 0.25\gamma_c$ (solid line), $\Omega = 0.1\gamma_c$ (dashed line), $\Omega = 0$ (dashed-dotted line)

Fig. 5.27. As we see later, the hole burning can produce a very slow group velocity of the probe field.

The coherent population oscillations are also responsible for the hole burning and consequently the amplification at the central component of the absorption spectrum for the case of a bichromatic driving field, which we have seen in Fig. 5.25. In this case the two sideband components of the driving field enhance the population oscillations that can outweigh the first term in (5.127) giving a negative value for the imaginary part of χ , and consequently an amplification without population inversion.

5.6 Applications of EIT in Nonlinear Optics

The phenomenon of electromagnetically induced transparency and related coherence effects has proved very valuable in nonlinear optics, with many applications. We describe a few of these here: more can be found in the review by Arimondo [101]. One of the most important applications is the enhancement of nonlinear susceptibilities, discussed in the next subsection. The first experiment to demonstrate this was performed by Hakuta et al. [123]. They employed a dc electric coupling of the $2s$ and $2p$ states in atomic hydrogen to resonantly enhance the second-order susceptibility with reduced absorption at the second-harmonic wavelength, and with exact phase-matching at the centre of the Stark-split components. Electromagnetically induced transparency has been used to overcome a transmission as low as $\exp(-10^5)$, creating a situation in which the nonlinear polarization is as large as the linear polarization, with almost complete energy conversion occurring in a single wavelength. This work opens up the possibility of frequency converters and

optical parametric amplifiers with very large bandwidths. Applications to optical interferometry, including a magnetometer, have been suggested. The modification of the refractive properties of the medium is likewise very important. In particular, the breaking of the connection between high refractive index and high absorption leads to the creation of media with very unusual optical properties. This is discussed briefly at the end of this section. There are excellent reviews on these topics by Harris [124] and Marangos [125].

5.6.1 Enhancement of Nonlinear Susceptibilities

It is well-known that higher-order susceptibilities can be resonantly enhanced as the applied laser frequency approaches a resonance with an atomic transition to the ground state. However, in the conventional situation, the linear susceptibility is similarly enhanced: this means that as, for example, the third order susceptibility increases, so does the absorption, the medium rapidly becoming opaque. The resonant enhancement cannot be used to advantage. Using the techniques of quantum coherence and interference, we show in this subsection how it is possible to counter the opacity effects so as to obtain resonant enhancement of the nonlinear susceptibility without losing transparency.

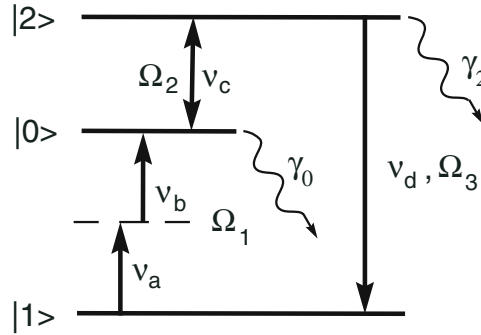


Fig. 5.28. Energy level diagram for the sum frequency generation at $\nu_d = \nu_a + \nu_b + \nu_c$. The Rabi frequency Ω_1 is the effective two-photon Rabi frequency. The level $|0\rangle$ is assumed to be metastable, so that the decay rates satisfy $\gamma_2 \gg \gamma_0$

The energy diagram for a suitable (ladder) system is shown in Fig. 5.28. We have assumed a labelling of levels consistent with Fig. 5.1. The level $|0\rangle$ is assumed to be metastable, with a small spontaneous decay rate γ_0 , so that it can only be accessed from the ground state $|1\rangle$ by the absorption of two photons of frequencies ν_a and ν_b say, with effective (two-photon) Rabi frequency Ω_1 . An intense coupling laser at frequency ν_c couples levels $|0\rangle$ and $|2\rangle$ in a one-photon transition with Rabi frequency Ω_2 . Sum-frequency generation can take place on the $|1\rangle \leftrightarrow |2\rangle$ transition at the frequency $\nu_d = \nu_a + \nu_b + \nu_c$, with Rabi frequency Ω_3 . The spontaneous decay rate from level $|3\rangle$ is $\gamma_3 \gg \gamma_0$.

Following Harris, Field and Imamoglu [126], we can write the wave function at time t as

$$|\psi(t)\rangle = b_1(t)|1\rangle + b_0(t)|0\rangle + b_2(t)|2\rangle . \quad (5.131)$$

If we treat the decays as occurring to levels outside this system, we can write down the equations for the time dependent coefficients $b_k(t)$ as

$$\dot{b}_1 = \frac{1}{2}i(\Omega_1 b_0 + \Omega_3 b_2) , \quad (5.132a)$$

$$\dot{b}_0 = -i(\delta_{10} - i\gamma_0)b_0 + \frac{1}{2}i(\Omega_1^* b_0 + \Omega_2 b_2) , \quad (5.132b)$$

$$\dot{b}_2 = -i(\delta_{12} - i\gamma_2)b_2 + \frac{1}{2}i(\Omega_1^* b_0 + \Omega_3^* b_1) , \quad (5.132c)$$

where

$$\begin{aligned} \delta_{10} &= \omega_1 - \omega_0 - \nu_a - \nu_b , \\ \delta_{12} &= \omega_2 - \omega_0 - \nu_c , \end{aligned} \quad (5.133)$$

and

$$\Omega_1 = \sum_k \Omega_{0k} \Omega_{k1} [(\omega_k - \nu_a)^{-1} + (\omega_k - \nu_b)^{-1}] , \quad (5.134)$$

with the sum over k taken over all other atomic levels with energy $\hbar\omega_k$.

Since the coupling between levels $|1\rangle$ and $|0\rangle$ is weak, the population in state $|1\rangle$ will remain close to unity if the initial condition is $b_1(0) = 1$. Hence we may substitute $b_1 = 1$ in the right-hand sides of the final two equations of (5.132), which are then easily solved to give the steady-state solution

$$\begin{aligned} b_2(\infty) &= \frac{\Omega_3/2}{\delta_{12} - i\gamma_2 - \frac{|\Omega_2|^2/4}{\delta_{10} - i\gamma_0}} \\ &+ \frac{\Omega_1}{\delta_{10} - i\gamma_0 - \frac{|\Omega_2|^2/4}{\delta_{12} - i\gamma_2}} \frac{\Omega_2}{\delta_{12} - i\gamma_2} . \end{aligned} \quad (5.135)$$

The first term on the right-hand side of (5.135) may be understood as arising from the direct, single-photon transition between levels $|0\rangle$ and $|2\rangle$: it gives rise to the linear susceptibility. The second term is the result of the step-wise, or two-photon process between the two levels, and it gives rise to the third order susceptibility. Using (5.80), and the fact that $\varrho_{21} = b_1^* b_2 \simeq b_2$, the steady-state susceptibility at frequency ω_d can be determined from the relation

$$P(\omega_d) = \mathcal{N} \text{Re} [\mu_{12} b_2(\infty)] , \quad (5.136)$$

where \mathcal{N} is the density of atoms. We find

$$\varepsilon_0 \chi_1 = \frac{\mathcal{N} |\mu_{12}|^2}{\delta_{12} - i\gamma_2 - \frac{|\Omega_2|^2/4}{\delta_{10} - i\gamma_0}} , \quad (5.137a)$$

$$\varepsilon_0 \chi_3 = \frac{\mathcal{N} \mu_{12} \mu_{20} \mu_{01}^{(2)}}{(\delta_{10} - i\gamma_0)(\delta_{12} - i\gamma_2) - |\Omega_2|^2/4} , \quad (5.137b)$$

where

$$\mu_{01}^{(2)} = \sum_k \mu_{0k} \mu_{k1} [(\omega_k - \nu_a)^{-1} + (\omega_k - \nu_b)^{-1}] , \quad (5.138)$$

and we have made use of the relations (5.80).

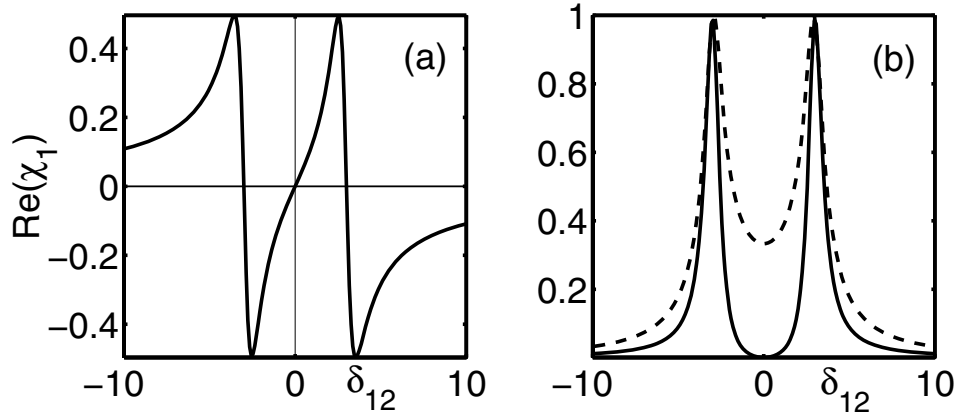


Fig. 5.29. (a) The real part of the linear susceptibility as a function of $\delta_{12} = \delta_{10}$, for $\Omega_2 = 6$ and $\gamma_0 = 0.01$, all quantities being measured in terms of $\gamma_2 = 1$. (b) The data for $\text{Im}(\chi_1)$ (solid line) and $|\chi_3|$ (dashed line). The units for the y -axes are arbitrary

In Fig. 5.29 we illustrate $\text{Re}(\chi_1)$, $\text{Im}(\chi_1)$ and $|\chi_3|$. We assume the coupling laser is resonant with the $|0\rangle \rightarrow |2\rangle$ transition: $\delta_{20} \equiv \omega_2 - \omega_0 - \nu_c = 0$, which implies $\delta_{10} = \delta_{12}$. We plot the susceptibilities as a function of the detuning $\delta_{12} = \delta_{10}$. In this figure, we take $\Omega_2 = 6$ and $\gamma_0 = 0.01$, all quantities being measured in terms of $\gamma_2 = 1$. In Frame (b), it is evident that the third order susceptibility is appreciable in the neighborhood of $\delta_{12} = 0$, when the absorption is close to zero.

We would expect all processes to be enhanced if the transition from $|1\rangle$ to $|0\rangle$ is resonant, so we first of all set $\delta_{10} = 0$:

$$\varepsilon_0 \chi_1 = \frac{\mathcal{N} |\mu_{12}|^2 \gamma_0}{\gamma_0 (\delta_{12} - i\gamma_2) - 4i|\Omega_2|^2} , \quad (5.139)$$

and

$$\varepsilon_0 \chi_3 = \frac{\mathcal{N} \mu_{12} \mu_{20} \mu_{01}^{(2)}}{-\gamma_0 (\mathrm{i} \delta_{12} + \gamma_2) + 4|\Omega_2|^2} . \quad (5.140)$$

We wish to choose the parameters so that the third order susceptibility χ_3 is as large as possible, whilst at the same time the absorption, as determined by $\mathrm{Im}(\chi_1)$, is as small as possible. More precisely, we wish to maximize the ratio

$$R \equiv \frac{|\chi_3|}{\mathrm{Im}(\chi_1)} . \quad (5.141)$$

It is apparent by inspection of (5.139) and (5.140), or (5.137), that $\chi_1 = 0$ when $\gamma_0 = 0$, whilst $\chi_3 \neq 0$: this represents the ideal situation. In practice, we seek to make γ_0 as small as possible – that is, the level $|0\rangle$ should be metastable, as we have anticipated. For $\gamma_0 \neq 0$, the susceptibilities depend upon the value of δ_{12} . We may obtain typical values for these quantities by evaluating them at $\delta_{12} = 0$. Assuming $\delta_{10} = 0$, we then easily find

$$R = \frac{|\mu_{20} \mu_{01}^{(2)}|}{|\mu_{21}|} \frac{2}{\gamma_0} . \quad (5.142)$$

Clearly, we increase the value of R by increasing the values of μ_{20} and $\mu_{01}^{(2)}$, and decreasing the values of γ_0 and μ_{21} .

For a more realistic modelling of the situation, we need to take into account such factors as Doppler broadening, collisions, and laser linewidths. If the wave-vector for the laser of frequency ν_j , ($j = a, b, c$) is \mathbf{k}_j , then we may model Doppler broadening for an atom moving with the velocity \mathbf{v} by making the substitutions

$$\delta_{21} \rightarrow \delta_{21} + \mathbf{k}_d \cdot \mathbf{v} , \quad \delta_{10} \rightarrow \delta_{10} + (\mathbf{k}_a + \mathbf{k}_b) \cdot \mathbf{v} , \quad (5.143)$$

where $\mathbf{k}_d = \mathbf{k}_a + \mathbf{k}_b + \mathbf{k}_c$, assuming that the sum frequency is emitted in a predominantly phase-matched direction. It is then necessary to integrate the resulting expressions over the Maxwell distribution of velocities.

We may allow for the effect of finite laser linewidths by assuming their broadening to be due to phase diffusion. Taking the linewidth of laser j to be given by L_j , ($j = a, b, c$), we may take this effect into account by the substitution

$$\gamma_0 \rightarrow \gamma_0 + L_c \quad (5.144)$$

in (5.139), and by the substitutions

$$\begin{aligned} \gamma_2 &\rightarrow \gamma_2 + L_a + L_b + L_c , \\ \gamma_0 &\rightarrow \gamma_0 + L_a + L_b \end{aligned}$$

in (5.140). The effect of collisions may be modelled by adding the collisional damping terms C_{01} and C_{12} to the decay rates γ_0 and γ_2 respectively. However, we do not consider the effect of collisions further here.

Figure 5.30 shows the effect of Doppler broadening, assuming a Doppler width $\sigma_D = 4$ for the solid line and $\sigma_D = 400$ for the dashed line. The important feature is the sharp transition from opacity to transparency that occurs when the Rabi frequency of the coupling laser increases through the value $\Omega_2 \simeq \sigma_D$. Frame (a) shows the results for monochromatic laser excitation whilst in Frame (b) phase diffusion linewidths equal to γ_2 have been assumed for each laser. It is apparent that nonzero laser linewidths make a significant difference to the maximum value of R attainable.

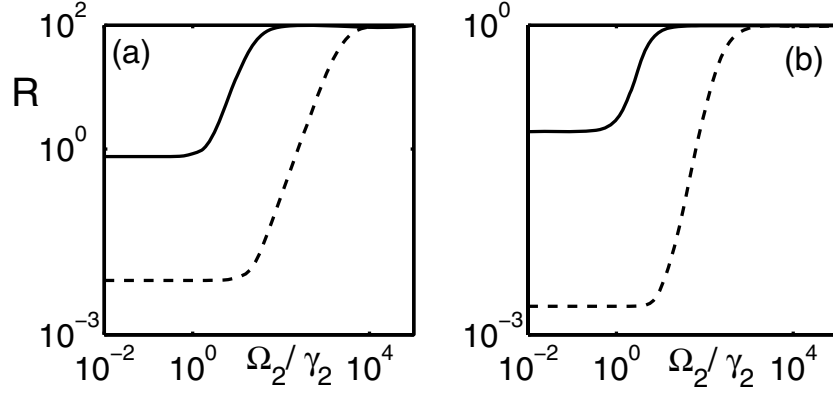


Fig. 5.30. (a) The effect of Doppler broadening, assuming a Doppler width $\sigma_D = 4$ for the solid line and $\sigma_D = 400$ for the dashed line, as a function of the Rabi frequency of the coupling laser. All quantities are measured as ratios of γ_2 , which is fixed at the value unity. (b) The same as Frame (a), except that we have included phase-diffusion laser linewidths $L_a = L_b = L_c = 1$

It is possible to obtain an analytic approximation for the maximum enhancement of R that can be achieved by employing a high intensity laser to couple levels $|0\rangle$ and $|2\rangle$. The greatest enhancement occurs when the coupling laser is strongly saturating [127]. Defining λ to be the ratio of the value of R in the limit $\Omega_2 \rightarrow \infty$ to its value when $\Omega_2 = 0$, we find

$$\lambda = \frac{(\gamma_2 + L_{ab}) [\kappa^2 + (\gamma_0 + L_{ab})]^2}{\gamma_2 (\gamma_0 + L_c) (\gamma_0 + L_{ab})}, \quad (5.145)$$

where $L_{ab} = L_a + L_b$ and the quantity $\kappa = (\mathbf{k}_a + \mathbf{k}_b) \cdot \bar{\mathbf{v}}$ with $\bar{\mathbf{v}}$ being the mean velocity of the atoms, is related to the Doppler width. This expression agrees very well with numerical results.

5.6.2 Observation of Enhancement of Nonlinear Susceptibilities

An observation of the enhancement of the third-order susceptibility in a system similar to that shown in Fig. 5.28 was made by Zhang et al. [128] in the system of atomic hydrogen. Corresponding to the ground state $|1\rangle$ of Fig. 5.28 was the $1s$ level of hydrogen, to the intermediate state $|0\rangle$ the metastable $2s$

level, and to state $|2\rangle$ corresponded the $3p$ level. The $1s$ and $2s$ levels were connected by the absorption of two photons of frequency 243 nm, and levels $2s$ and $3p$ by the coupling laser at 656 nm. Sum frequency radiation was generated in the $2p \rightarrow 1s$ transition, at the Lyman- β frequency.

A difference with the ideal situation of Fig. 5.28 was that the radiation at 243 nm could ionize the $2s$ level, and the radiation at 656 nm could ionize the $2p$ level. Thus to γ_2 and γ_0 must be added the terms γ_2^{ion} and γ_0^{ion} representing the irreversible ionization of these levels. A consequence is that, at the power levels used, the rate of ionization decay exceeds the spontaneous decay rate of state $|0\rangle$, so that it is no longer metastable, and perfect transparency cannot be achieved. However, the total decay rates satisfy $\gamma_2 \gg \gamma_0^{\text{total}}$, so that the absorption at the $3p-1s$ is significantly reduced. In fact, the photoionization was turned to advantage in the experiments, as it was taken as a measure of the transparency at the generated Lyman- β frequency.

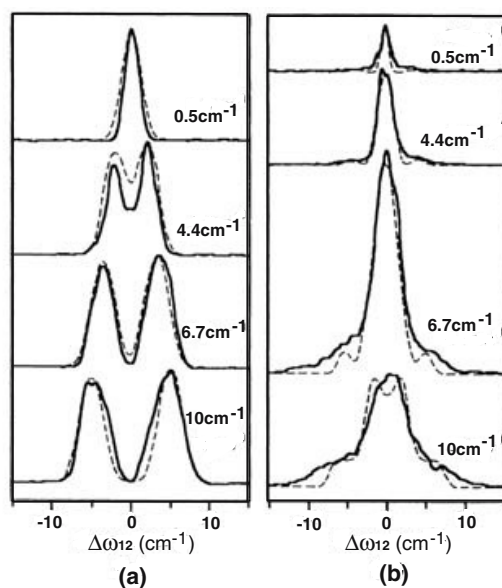


Fig. 5.31. Characteristics for photoionization **(a)** and sum-frequency generation **(b)** for different coupling Rabi frequencies, against frequency detuning. Solid and dashed lines correspond to observed and calculated signals respectively. The parameter $\mathcal{N}L$, the product of atom density and interaction length, is fixed at $7 \times 10^{14} \text{ cm}^{-2}$. From G.Z. Zhang, K. Hakuta, B.P. Stoicheff: Phys. Rev. Lett. **71**, 3099 (1993). Copyright (1993) by the American Physical Society

Figure 5.31 shows some of their results. It presents the characteristics for photoionization (representing transparency) and sum frequency generation as a function of the detuning δ_{01} for a range of different coupling laser Rabi frequencies. The experimental curves are compared with the corresponding theoretical ones, the latter being obtained by a solution of the propagation equations and an integration over the velocity distribution, assuming a Doppler width of 1.8 cm^{-1} .

At the lowest coupling intensity presented, $\Omega_2 = 0.5 \text{ cm}^{-1}$, we have $\Omega_2 < \sigma_D$, where σ_D is the Doppler width. Under these conditions, the photoionization signal is a single sharp peak, indicating that the medium is opaque at the $3p - 1s$ transition. For larger values of Ω_2 , the signal splits into two peaks, and when Ω_2 reaches 6.7 cm^{-1} , it exceeds the Doppler tails, and the value at line centre is only 5% of the peak value. If quantum interference was not involved, the value at line centre would be 20%. At the largest value of presented, $\Omega_2 = 10 \text{ cm}^{-1}$, the photoionization signal at line centre is almost zero, indicating almost perfect transparency.

By contrast, the sum frequency generation, presented in Fig. 5.31(b), shows that the signal at line centre increases rapidly as Ω_2 exceeds the Doppler width of 1.8 cm^{-1} . The signal takes a maximum value at $\Omega_2 = 6.7 \text{ cm}^{-1}$, when the conversion efficiency was estimated to be 1×10^{-4} . The decline in the sum frequency signal at $\Omega_2 = 10 \text{ cm}^{-1}$ is attributed to suppression of the nonlinear susceptibility due to the large Autler–Townes splitting.

5.6.3 Enhancement of Refractive Index

For some purposes, a transparent medium with high refractive index is needed. Examples of such possible applications are laser particle acceleration, optical microscopy, precision magnetometry, and atomic tests of the fundamental interactions. Several schemes making use of quantum interference and coherence have been suggested for realizing such a medium, but to date only small enhancements of the refractive index have been reported.

For example, Zibrov et al. [129] have reported a change in refractive index of about 0.1. They considered a three-level ladder system in ^{87}Rb , in which four-wave mixing took place. They employed a probe laser tuned to the $5S_{1/2}, F = 2 \rightarrow 5P_{3/2}, F' = 3$ transition, and a drive laser connecting the $5P_{3/2}, F' = 3$ and $5D_{5/2}, F'' = 2, 3, 4$ levels, both lasers being linearly polarized with orthogonal polarizations. They used a very dense atomic medium (up to $3 \times 10^{15} \text{ atoms cm}^{-3}$), and it is interesting to note that coherence processes are present at these densities, when such effects as radiation trapping and collision broadening have detrimental effects.

The laser beams were superimposed on the inner window surface of a glass cell containing a natural mixture of Rb at a temperature of about 150°C , corresponding to a Doppler width of 600 MHz. The probe and drive lasers were counterpropagating, giving a residual width of about 3 MHz for the two-photon transition. The Rb vapour was completely transparent for the driving field, but the probe field had an absorption length of $3 \times 10^{-4} \text{ cm}$ in the presence of the driving field.

A selective reflection technique was used to measure the refractive index of the coherently driven Rb vapor. The maximum measured resonant change in the refractive index was $\Delta n \simeq 0.1$. In addition, a four-wave-mixing process took place that could reach up to 90% efficiency.

6 Field Induced Quantum Interference

In this chapter we consider several distinct features of quantum interference and coherence that can arise in systems when external fields are applied.

First, we remind the reader that in Chap. 4, we studied quantum interference in systems with parallel dipole moments, with no external fields applied. Then, in Chap. 5, we studied coherence induced by external fields in systems with perpendicular dipole moments. In the first three sections of this chapter, we consider the modification of atomic properties due to quantum interference and coherence in systems in which external fields are applied, and the system may also have parallel dipole moments. The latter property is essential for the modifications of resonance fluorescence studied in Sect. 6.1, and superbunching studied in Sect. 6.3, but is not essential for the phase control discussed in Sect. 6.2. In these sections, we show for example, that quantum interference leads to extremely narrow lines in the resonance fluorescence spectrum, and that quantum interference phenomena in three-level systems can be controlled by varying the relative phase of the two driving lasers. In the phenomenon of superbunching, the existence of extremely large values in the second-order field correlation coefficient is discussed in Sect. 6.3.

As we have emphasized, many of the phenomena we have described in these pages depend upon finding atomic systems with parallel, or nearly parallel, transition dipole moments. It has frequently been remarked that it is extremely difficult to find such systems, and that has proved to be a severe handicap to the experimental investigation of these effects. In Sect. 6.4, we discuss ways of getting around this difficulty by examining different kinds of systems, usually systems with perpendicular dipole moments, which nevertheless emulate the properties of systems with parallel dipole moments. The hope is that experiments on these systems may prove much easier than experiments on systems with parallel dipole moments.

Finally, we remark that so far we have restricted our attention to atomic systems with discrete levels. In the final sections of this chapter, we examine systems in which structure is imposed in a *continuum* by means of interactions or external fields, in such a way that this structure has much of the character of a bound atomic state. Thus we discuss Fano profiles, laser-induced continuum structures, and finally, population trapping and spontaneous emission in

photonic bandgap materials. The similarities between these different systems, and the importance of quantum interference effects, is emphasized.

6.1 Resonance Fluorescence in Driven Vee Systems

We begin by studying quantum interference effects in a driven three-level Vee system, which is shown in Fig. 6.1.

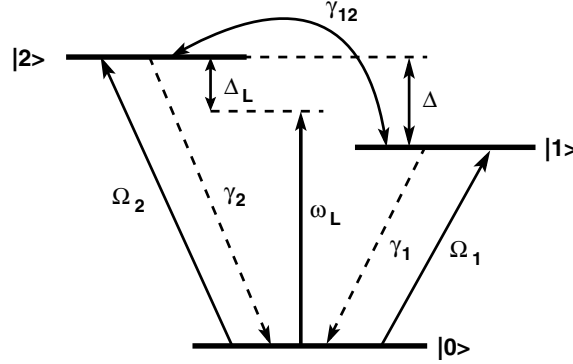


Fig. 6.1. Energy-level scheme of a three-level atom in the Vee configuration driven by a single laser field coupled to both atomic transitions

This system is best analyzed using the master equation approach for multi-level systems, described in Chap. 2. It is convenient to assume that the applied laser field can be treated classically. Then the semiclassical Hamiltonian for the system is

$$H' = \hbar\omega_1 A_{11} + \hbar\omega_2 A_{22} + \frac{\hbar}{2} (\Omega_1 A_{10} + \Omega_2 A_{20} + \text{H.c.}) , \quad (6.1)$$

where Ω_k ($k = 1, 2$) is the Rabi frequency of the k th transition, $A_{ij} = |i\rangle\langle j|$ as usual, Δ is the frequency separation of the two excited states, and Δ_L is the detuning of the applied laser from the $|0\rangle \leftrightarrow |2\rangle$ transition frequency. We make a transformation to the reference frame rotating at the frequency ω_L of the laser field by means of the unitary transform $U = \exp[-i\omega_L(A_{11} + A_{22})]$ to obtain the Hamiltonian

$$H/\hbar = (\Delta_L - \Delta) A_{11} + \Delta_L A_{22} + \frac{1}{2} (\Omega_1 A_{10} + \Omega_2 A_{20} + \text{H.c.}) . \quad (6.2)$$

In order to concentrate on the essential features of quantum interference, we have neglected the level shifts of (2.72), and assumed that no thermal photons are present, i.e. we put $\delta_i^\pm = N = 0$ in (2.72).

In the rotating frame, the master equation is of the form

$$\dot{\rho} = -i[H/\hbar, \rho] + \mathcal{L}\rho , \quad (6.3)$$

where the damping term, the term describing spontaneous decay, arising from the vacuum interaction, is

$$\begin{aligned}\mathcal{L}\varrho = & \frac{1}{2}\gamma_1 (2A_{01}\varrho A_{10} - A_{11}\varrho - \varrho A_{11}) \\ & + \frac{1}{2}\gamma_2 (2A_{02}\varrho A_{20} - A_{22}\varrho - \varrho A_{22}) \\ & + \frac{1}{2}\gamma_{12} (2A_{01}\varrho A_{20} - A_{21}\varrho - \varrho A_{21}) \\ & + \frac{1}{2}\gamma_{12} (2A_{02}\varrho A_{10} - A_{12}\varrho - \varrho A_{12}) .\end{aligned}\quad (6.4)$$

The expressions in (6.4) show explicitly the terms that arise from the cross-damping (quantum interference) between the transitions $|1\rangle \rightarrow |0\rangle$ and $|2\rangle \rightarrow |0\rangle$. They are proportional to the parameter β , the cosine of the angle between the two dipole moment vectors. If the dipole moments are parallel, $\beta = 1$, and then the cross-damping term is maximal with $\gamma_{12} = \sqrt{\gamma_1\gamma_2}$, while $\gamma_{12} = 0$ if, as is usually the case, the dipole moments are perpendicular ($\beta = 0$), and the quantum interference term vanishes.

For simplicity, we henceforth consider the case where $\gamma_1 = \gamma_2 = \gamma$ and we also assume $\Omega_2 = \Omega_1 = \Omega$. We gain considerable insight by studying this situation. The symmetric and antisymmetric superposition states of the excited levels then become simply:

$$|s\rangle = \frac{1}{\sqrt{2}} (|1\rangle + |2\rangle) , \quad (6.5a)$$

$$|a\rangle = \frac{1}{\sqrt{2}} (|1\rangle - |2\rangle) , \quad (6.5b)$$

and the decay term in (6.3) is diagonalized. In terms of the superposition states, the master equation (6.3) takes the form:

$$\begin{aligned}\dot{\varrho} = & -i[H/\hbar, \varrho] \\ & + \frac{1}{2}\gamma (1 + \beta) (2A_{0s}\varrho A_{s0} - A_{ss}\varrho - \varrho A_{ss}) \\ & + \frac{1}{2}\gamma (1 - \beta) (2A_{0a}\varrho A_{a0} - A_{aa}\varrho - \varrho A_{aa}) ,\end{aligned}\quad (6.6)$$

with

$$H/\hbar = \Delta_1 (A_{ss} + A_{aa}) - \frac{\Delta}{2} (A_{sa} + A_{as}) + \frac{\Omega}{\sqrt{2}} (A_{s0} + A_{0s}) , \quad (6.7)$$

and

$$\Delta_1 = \Delta_L - \frac{\Delta}{2} . \quad (6.8)$$

It is apparent that the laser field couples only to the symmetric state and both states decay independently to the ground state with different decay rates.

The separation between the two levels, Δ acts like a coupling field causing transitions between the two superposition states: if the original levels $|1\rangle$ and $|2\rangle$ are degenerate, this coupling vanishes.

If we now suppose that we have perfect quantum interference in the spontaneous emission – that is, the transition dipole moments are parallel so that $\beta = 1$ – it is clear that the antisymmetric level is perfectly stable. If we further assume that $\Delta_1 = 0$, which corresponds to the symmetric and antisymmetric states being degenerate, then it is easy to verify that a steady-state solution of (6.6) is

$$\varrho(t \rightarrow \infty) = |\Psi\rangle\langle\Psi| , \quad (6.9)$$

where

$$|\Psi\rangle = \frac{\Delta|0\rangle + \sqrt{2}\Omega|a\rangle}{\sqrt{\Delta^2 + 2\Omega^2}} . \quad (6.10)$$

In terms of the original atomic states,

$$|\Psi\rangle = \frac{\Delta|0\rangle + \Omega|1\rangle - \Omega|2\rangle}{\sqrt{\Delta^2 + 2\Omega^2}} \quad (6.11)$$

is the pure state into which the system evolves.

Thus, even though the level $|s\rangle$ is being driven by the applied field, the system eventually evolves into a pure state in which the population of $|s\rangle$ is zero, as illustrated in Fig. 6.2. This pure state, a superposition of the

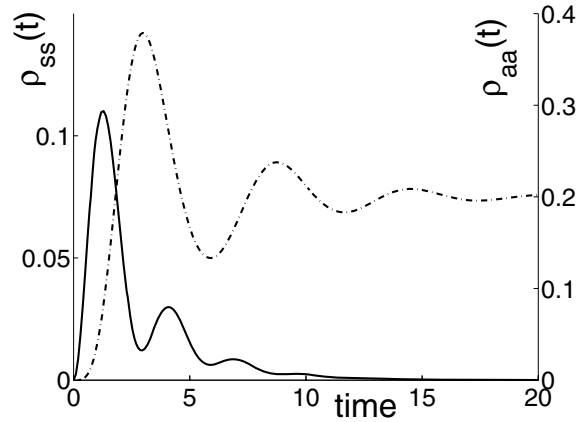


Fig. 6.2. The density matrix elements ϱ_{ss} (*solid line*), and ϱ_{aa} (*dot-dashed line*), plotted as functions of time for $\Omega = 0.25\gamma$, $\Delta = \gamma$ and $\beta = 1$

ground state $|0\rangle$ and the antisymmetric state $|a\rangle$, is perfectly ‘dark’ – that it, it emits no light whatsoever. (This is clear because both states in the superposition have zero spontaneous emission rates.) Thus, for this particular combination of parameter values, spontaneous emission has been eliminated

from the system. We stress that for this suppression to occur we require the driving field to be tuned to the midpoint of the two excited state energy levels:

$$\Delta_L = \frac{1}{2}\Delta . \quad (6.12)$$

This system also illustrates the phenomenon of population trapping. Suppose the system is initially in the ground state when the driving field is switched on. At first, population will be driven into the symmetric state as well as into the antisymmetric state, but the population that is transferred into the antisymmetric state remains there, resulting in the eventual complete depletion of the population in the symmetric state. Population becomes trapped in the antisymmetric state.

If we relax the condition that $\Omega_1 = \Omega_2$, but still assume that $\beta = 1$, we can show that the condition for complete quenching of spontaneous emission is now

$$\Delta_L = \frac{\Delta\Omega_2^2}{\Omega_1^2 + \Omega_2^2} . \quad (6.13)$$

For $\Omega_1 = \Omega_2$, this reduces to condition (6.12), $\Delta_L = \Delta/2$, or equivalently, $\Delta_1 = 0$.

Figure 6.3 shows the population in states $|s\rangle$ and $|a\rangle$ as a function of the detuning Δ_1 . In frame (a), where $\beta = 1$, the population $\varrho_{ss} = 0$ when $\Delta_1 = 0$. However, in frame (b), where the quantum interference is only slightly less than perfect, $\beta = 0.98$, it is evident that there is a significant population in level $|s\rangle$ even when $\Delta_1 = 0$. Thus the population trapping is very sensitive to the value of β .

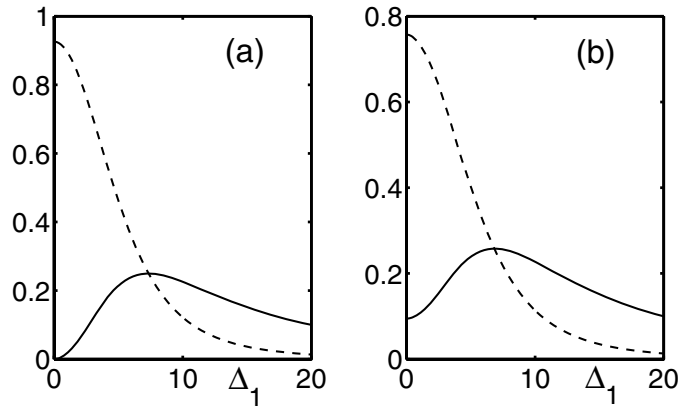


Fig. 6.3. The steady-state values of the density matrix elements ϱ_{ss} (solid line), and ϱ_{aa} (dashed line), plotted as functions of the detuning Δ_1 for $\Omega = 5\gamma$ and $\Delta = \gamma$. In (a), $\beta = 1$ and in (b), $\beta = 0.98$. (The values for negative Δ_1 may be obtained by noting that the graphs are symmetric about the y -axes)

The equations of motion of the reduced density matrix elements for the atomic variables take the form

$$\begin{aligned}
\dot{\varrho}_{10} &= - \left[\frac{1}{2}\gamma_1 + i(\Delta_L - \Delta) \right] \varrho_{10} - \frac{\gamma_{12}}{2}\varrho_{20} + \frac{1}{2}\Omega_2\varrho_{12} + \frac{1}{2}\Omega_1(\varrho_{11} - \varrho_{00}) , \\
\dot{\varrho}_{20} &= - \left(\frac{1}{2}\gamma_2 + i\Delta_L \right) \varrho_{20} - \frac{1}{2}\gamma_{12}\varrho_{10} + \frac{1}{2}\Omega_1\varrho_{12} + \frac{1}{2}\Omega_2(\varrho_{22} - \varrho_{00}) , \\
\dot{\varrho}_{21} &= - \left[\frac{1}{2}(\gamma_1 + \gamma_2) + i\Delta \right] \varrho_{21} - \frac{1}{2}\gamma_{12}(\varrho_{22} + \varrho_{11}) - \frac{1}{2}\Omega_1\varrho_{20} - \frac{1}{2}\Omega_2\varrho_{01} , \\
\dot{\varrho}_{11} &= -\gamma_1\varrho_{11} - \frac{1}{2}\gamma_{12}(\varrho_{12} + \varrho_{21}) - \frac{1}{2}\Omega_1(\varrho_{01} + \varrho_{10}) , \\
\dot{\varrho}_{22} &= -\gamma_2\varrho_{22} - \frac{1}{2}\gamma_{12}(\varrho_{12} + \varrho_{21}) - \frac{1}{2}\Omega_2(\varrho_{02} + \varrho_{20}) .
\end{aligned} \tag{6.14}$$

We can reduce the number of parameters by defining $\alpha = \mu_{10}/\mu_{20}$ as the ratio of the dipole moment magnitudes of the two allowed transition pathways. Assuming that the atomic levels shown in Fig. 6.1 are the only ones we need to consider, we have the relationships

$$\gamma_1 = \alpha^2\gamma_2 \equiv \alpha^2\gamma , \quad \text{and} \quad \Omega_1 = \alpha\Omega_2 \equiv \alpha\Omega . \tag{6.15}$$

The detuning that produces complete quenching of spontaneous emission when $\beta = 1$ is

$$\Delta_L = \Delta/(1 + \alpha^2) . \tag{6.16}$$

For $\alpha = 1$, this corresponds to the laser being tuned to the midpoint of the two atomic transitions.

The resonance fluorescence spectrum of a driven Vee atom is greatly modified by quantum interference between the two transition pathways from the excited doublet to the common ground level. It is well-known that the incoherent resonance fluorescence spectrum of a two-level atom driven by an intense, resonant laser has the Mollow [130] form: it has a symmetric three-peaked profile, with the central peak having the natural linewidth γ , and the two sidepeaks, which are displaced from the center-frequency by the Rabi frequency, are one third the height of the central peak with 1.5 times the linewidth.

For our Vee system, we may use (2.140) together with the quantum regression theorem to calculate the incoherent resonance fluorescence spectrum, following the approach outlined in Sect. 4.2.2. For the case of a degenerate excited doublet, the spectrum exhibits a Mollow-like triplet, but radiative interference broadens the spectral lines. More interesting quantum interference phenomena emerge when the excited doublet is nondegenerate. The fluorescent emission can be completely suppressed if the atomic dipole moments are parallel (maximum quantum interference) and the coherent field is tuned to

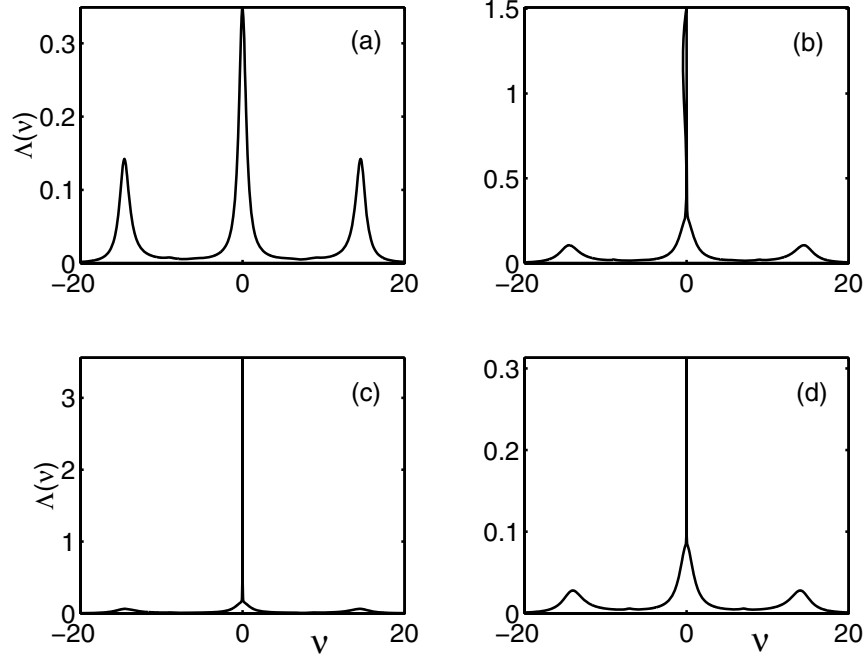


Fig. 6.4. The incoherent resonance fluorescence spectrum as a function of $\nu = (\omega - \omega_L)/\gamma$ for the excited doublet frequency separation $\Delta = \gamma$ and Rabi frequency $\Omega = 10\gamma$, with laser detunings $\Delta_L = 4\gamma$ in the frames (a) – (c) and $\Delta_L = 0.5\gamma$ in (d). The value of β is $\beta = 0$ in (a), $\beta = 0.99$ in (b), and $\beta = 0.999$ in (c) and (d)

the average atomic transition frequency. Otherwise, significant spectral narrowing at line centre takes place over a wide range of parameters, for parallel or nearly parallel dipole transition moments.

We have assumed monochromatic excitation. However, if the linewidth of the driving laser is taken into account the atom can never be trapped in a dressed state, so that no fluorescence quenching occurs. The spectral lines can still be significantly narrowed provided the laser linewidth does not greatly exceed the natural width.

These effects have a straightforward interpretation in the dressed state representation. The quantum interference between the two transition pathways can drive the atom into a dressed state that is decoupled from the fields, preventing any fluorescence, even though population inversion is achieved when the coherent field is tuned to the average frequency of the atomic transitions. The dressed state decays very slowly for small excited doublet splittings and nearly maximum quantum interference. It is the slow decay that gives rise to the striking narrow spectral profile at line centre. The width of the narrow spectral line is proportional to the square of the ratio of the level splitting to the effective Rabi frequency, and may thus be very narrow for small splittings.

We illustrate these features for the nondegenerate case, where the ultra-narrow lines may appear at line centre. In Fig. 6.4, we display the resonance fluorescence spectrum for $\Delta = \gamma$, $\Omega = 10\gamma$, with $\Delta_L = 4\gamma$ in the first three

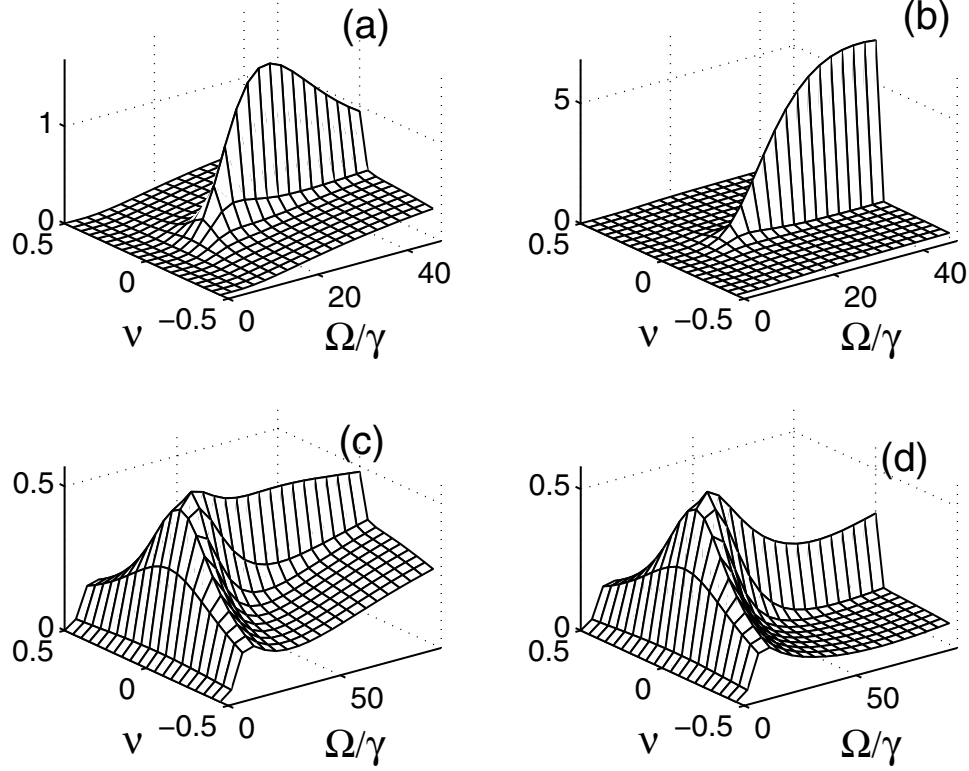


Fig. 6.5. The central part of the incoherent resonance fluorescence spectrum for excited doublet frequency separation $\Delta = 30\gamma$ as a function of $\nu = (\omega_p - \omega_L)/\gamma$ and Ω/γ , for laser detunings $\Delta_L = 5\gamma$ in (a) and (b), and $\Delta_L = 20\gamma$ in (c) and (d). We take $\beta = 0.99$ in frames (a) and (c), and $\beta = 0.999$ in frames (b) and (d). The full width of the ν range displayed represents one natural linewidth, γ .

frames and $\Delta_L = 0.5\gamma$ in the last frame, for different degrees of quantum interference. The smaller the ratio of the level splitting to the Rabi frequency, the more pronounced the narrow spectral profile. The final two frames demonstrate that the extent of line-narrowing depends strongly on the detuning.

The line-narrowing effect occurs over a wide range of parameter values. In Fig. 6.5, we show the central region of the spectrum as a function of Ω/γ for some different values of the splitting and detuning. Frames (c) and (d) show clearly how the broad, natural linewidth apparent for very small Ω evolves rapidly into a much narrower peak as Ω increases. Similar narrow spectral features were shown also in related Lambda and four-level systems [131, 132].

6.2 Phase Control of Quantum Interference

Spontaneous emission in a multi-level atom can be controlled not only by changing the mutual orientation of the dipole moments of two interfering transitions, but also by changing the phase difference of the driving lasers used for the excitation of the atom [132, 133, 134, 135].

Phase dependent effects in spontaneous emission have been predicted in atomic systems with non-orthogonal dipoles as well as for systems with orthogonal dipole moments. In the first case the phase dependent effects, which arise from quantum interference between two non-orthogonal dipole moments, can be observed with two driving fields [136, 137, 138, 139]. In the latter case the observation of phase dependent effects requires at least three driving fields [133, 140]. It is of particular interest to observe the phase dependent effects, as they represent interference effects which can be induced by driving fields even in the absence of the vacuum induced quantum interference.

6.2.1 Phase Control of Population Distribution

Our analysis of the phase control of spontaneous emission will concentrate on the example of a Vee type atom with nondegenerate transitions and non-orthogonal dipole moments driven by two laser fields. The lasers can have equal or different frequencies and each laser can couple to only one or both atomic transitions.

The interaction Hamiltonian of the atom with two laser fields can be written as

$$H_{\text{int}} = -\frac{1}{2}\hbar \left\{ \Omega_1 (A_{10} + \eta A_{20}) e^{-i(\nu_1 t + \phi_1)} + \Omega_2 (\eta A_{10} + A_{20}) e^{-i(\nu_2 t + \phi_2)} + \text{H.c.} \right\}, \quad (6.17)$$

where $\Omega_1 \exp(i\phi_1)$, $\Omega_2 \exp(i\phi_2)$ are the complex Rabi frequencies and ν_1 , ν_2 are the angular frequencies of the laser fields. The parameters η stands for two possible configurations of the coupling of the lasers to the atomic transitions. The case of $\eta = 0$ corresponds to each laser only coupled to one of the atomic transitions, whereas $\eta = 1$ corresponds to the case of each laser being coupled equally strongly to both transitions. Note that in this chapter, the Ω_i are real quantities, whereas in Chap. 5 they were complex, containing the phase implicitly.

The dynamics of the system are determined by the master equation with the interaction Hamiltonian (6.17). We make the following unitary transformation of the density operator of the system

$$\tilde{\rho} = e^{iH_{0L}t/\hbar} \rho e^{-iH_{0L}t/\hbar}, \quad (6.18)$$

with $H_{0L}/\hbar = \nu_1|1\rangle\langle 1| + \nu_2|2\rangle\langle 2|$, and find that the master equation of the system takes the following form

$$\begin{aligned}
\frac{d\tilde{\rho}}{dt} = & -\frac{i}{\hbar} \left[\tilde{H}_0 + \tilde{H}_{\text{int}}, \tilde{\rho} \right] \\
& -\frac{1}{2}\gamma_1 (A_{11}\tilde{\rho} + \tilde{\rho}A_{11} - 2A_{01}\tilde{\rho}A_{10}) \\
& -\frac{1}{2}\gamma_2 (A_{22}\tilde{\rho} + \tilde{\rho}A_{22} - 2A_{02}\tilde{\rho}A_{20}) \\
& -\frac{1}{2}\gamma_{12} (A_{21}\tilde{\rho} + \tilde{\rho}A_{21} - 2A_{01}\tilde{\rho}A_{20}) e^{-i[(\nu_1-\nu_2)t+\delta\phi]} \\
& -\frac{1}{2}\gamma_{12} (A_{12}\tilde{\rho} + \tilde{\rho}A_{12} - 2A_{02}\tilde{\rho}A_{10}) e^{i[(\nu_1-\nu_2)t+\delta\phi]}, \quad (6.19)
\end{aligned}$$

where

$$\tilde{H}_0 = \hbar (\Delta_1 |1\rangle\langle 1| + \Delta_2 |2\rangle\langle 2|), \quad (6.20a)$$

$$\begin{aligned}
\tilde{H}_{\text{int}} = & -\frac{1}{2}\hbar \left\{ \Omega_1 \left(A_{10} + \eta A_{20} e^{i[(\nu_1-\nu_2)t+\delta\phi]} \right) \right. \\
& \left. + \Omega_2 \left(\eta A_{10} e^{i[(\nu_1-\nu_2)t+\delta\phi]} + A_{20} \right) + \text{H.c.} \right\}, \quad (6.20b)
\end{aligned}$$

and $\Delta_1 = \omega_1 - \nu_1$, $\Delta_2 = \omega_2 - \nu_2$ are the detunings of the laser fields from the atomic transitions, and $\delta\phi = \phi_1 - \phi_2$.

In the transformed form the η and γ_{12} dependent terms are accompanied by a phase dependent terms $\exp(\pm i\delta\phi)$. These terms are also accompanied by the time dependent factors $\exp[i(\nu_1 - \nu_2)t]$, which oscillate with the difference of the laser frequencies. This shows that in any attempt to calculate phase dependent effects, it is important to assume that the lasers have equal frequencies. Otherwise, for unequal frequencies the time dependent terms rapidly oscillate in time and average out over a long period of the detection time. Furthermore, we note from (6.20) that in the case of $\eta = 1$ a phase dependence can be observed even in the absence of the vacuum induced quantum interference terms ($\gamma_{12} = 0$). Only for $\eta = 0$, i.e. when each laser only couples to one of the transitions, do the phase terms depend solely on the vacuum induced quantum interference. However, this condition can be achieved only for imperfect interference ($\beta \neq 1$) between the atomic transitions (the dipole moments of the transitions are not parallel). From an experimental point of view the condition that each laser should only couple to one of two almost parallel dipole moments may be difficult to achieve. In Chap. 7.2, we discuss a possible solution of this problem.

Figure 6.6 shows the steady-state population inversion between the upper state $|1\rangle$ and the ground state $|0\rangle$, computed from the master equation (6.19), for $\eta = 0$ and different values of the phase difference $\delta\phi$ and the interference parameter β . It is seen that in the presence of quantum interference the population can be inverted on the $|1\rangle \rightarrow |0\rangle$ transition and the inversion can be controlled by the phase difference between the driving laser fields [138].

Paspalakis and Knight [139] have considered a Vee type three-level system driven from an auxiliary level by two laser fields of the same frequencies. They

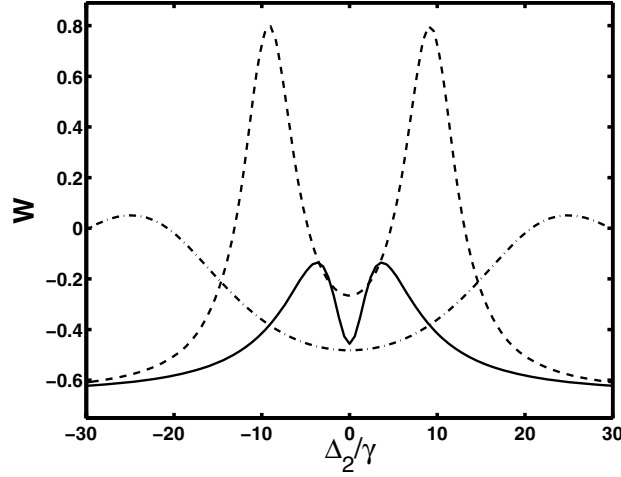


Fig. 6.6. The steady-state population inversion $W = \varrho_{22} - \varrho_{00}$ as a function of Δ_2 for two fields of the same angular frequencies, $\gamma_1 = 12\gamma$, $\gamma_2 = 0.02\gamma$, $\Omega_1 = 40\gamma$, $\Omega_2 = 2\gamma$ and different β and $\delta\phi$: $\beta = 0.95$, $\delta\phi = 0$ (*solid line*), $\beta = 0.95$, $\delta\phi = \pi$ (*dashed line*), $\beta = 0$, $\delta\phi = 0$ (*dashed-dotted line*)

have predicted linewidth narrowing and cancellation of the fluorescence that can be controlled via the phase difference between the two laser fields used for the excitation. Ghafoor et al. [133] have considered a four-level system in which quantum interference can be generated by three driving fields and have shown that the linewidths and intensities of the spectral lines can be controlled by the phases and amplitudes of the driving fields.

6.2.2 Phase Control of the Fluorescence Spectrum

Consider now the phase control of the fluorescence spectrum. The equations derived in Sect. 4.2 apply equally well if we consider the transitions $|1\rangle \rightarrow |3\rangle$ and $|1\rangle \rightarrow |2\rangle$ to be driven by two distinct lasers, rather than the one we assumed there, provided we consider that one laser couples only to the transition $|1\rangle \rightarrow |3\rangle$, with Rabi frequency Ω_3 and that the other laser couples only to the transition $|1\rangle \rightarrow |2\rangle$, with Rabi frequency Ω_2 . The advantage of this interpretation is that we may allow the relative phase ϕ of the two lasers to vary, so that we can investigate how the spectrum changes in response to variations in ϕ . We thus consider the system of Fig. 4.6, with this re-interpretation. We also take the frequencies of the two lasers to be the same, ω , so that we may concentrate on phase effects. Then the definition of the detunings (4.40) is unchanged, and the solution (4.48) still applies.

Figure 6.7 demonstrates the phase effects, for the three cases $\beta = 1, 0$ and $= -1$. Because the three values of β give spectra with very different heights, we have scaled the values of the $\beta = \pm 1$ spectra to the same peak value as the $\beta = 0$ value. The $\beta = 0$ spectra show the least change with ϕ , the spectra being three-peaked except for the $\phi = 0$ case, when the spectra

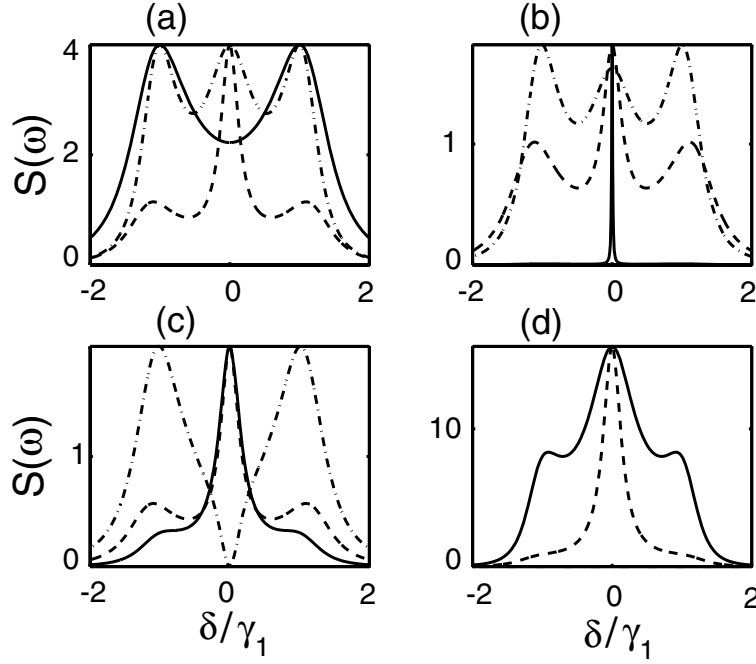


Fig. 6.7. The fluorescence spectrum for the four level system of Fig. 4.6 with $\gamma_3 = \gamma_2 = \gamma_1$, $\Omega_3 = \Omega_2 = \gamma_1$, $\Delta_1 = \gamma_1$ and $\Delta_2 = -\gamma_1$. The *solid line* is for $\beta = 1$, the *dashed line* is the corresponding spectrum in which $\beta = 0$, and the *dot-dashed line* is for $\beta = -1$. In Frames (a) – (d), the relative laser phase is $\phi = 0, 0.1\pi, 0.5\pi$ and π , respectively. In (a), the $\beta = 1$ spectrum has been scaled by a factor of 5, and in (b), (c) and (d) by 0.011, 0.25 and 4, respectively. The $\beta = -1$ spectra have been scaled by 0.56 and 3.25 in (b) and (c), respectively. In (d), the $\beta = -1$ spectrum has the value zero everywhere

possess pronounced shoulders. The $\beta = 1$ spectra change from a broad, two-peaked form when $\phi = 0$ to a very sharp, single peak when $\phi = 0.1\pi$, before broadening out as ϕ increases, eventually acquiring a three-peaked structure for $\phi = \pi$. The $\beta = -1$ spectra begin with three peaks of equal height for $\phi = 0$. For $\phi = 0.1\pi$, the structure is still three-peaked, but the central peak is now of slightly lower height than the sidepeaks. For $\phi = \pi/2$, we have a dark line at line centre. Alternatively, the spectrum may be considered two-peaked. Finally, for $\phi = \pi$, the $\beta = -1$ spectrum disappears completely: we have complete quenching of the spontaneous emission spectrum due to destructive quantum interference.

6.2.3 Experimental Evidence of Phase Control of Quantum Interference

Evidence for phase control of quantum interference effects has been provided in experiments by Windholz's group in Graz [141]. In these experiments a pair of laser beams, each composed of two different frequencies, was propagated through a sodium vapor cell, and the transmitted field intensity was

measured as a function of the relative phase between the laser beams. The energy levels of the sodium atoms in a double-Lambda configuration relevant to the experiments are shown in Fig. 6.8. Two hyperfine sublevels $F = 1$ and

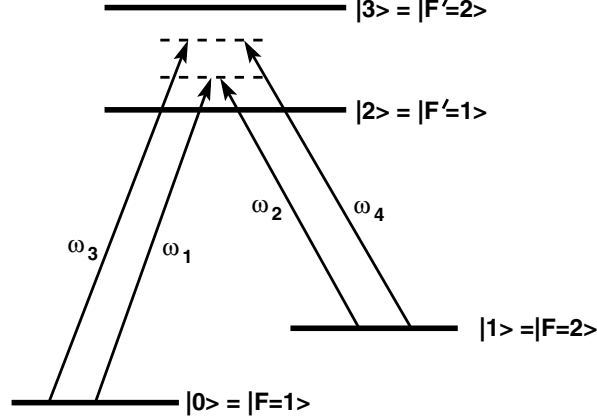


Fig. 6.8. Energy levels of a double Lambda system in sodium atoms and relevant laser frequencies used in the experiment of Korsunsky et al. [141]

$F = 2$ of the sodium ground state $3^2S_{1/2}$ served as lower states of the required double-Lambda system. The first excited sodium state $3^2P_{1/2}$ served as the common upper level of the system as the two corresponding hyperfine sublevels $F' = 1$ and $F' = 2$, separated by only 189 MHz, were spectroscopically unresolved within the Doppler broadening of approximately 1 GHz. The polarizations of the driving fields were adjusted such that the two pairs of frequencies produced from the outputs from the lasers were coupled to transitions of different polarizations. One of the pairs was coupled to the σ^+ transitions, whereas the other was coupled to the σ^- transitions.

The principal elements of their apparatus, shown in Fig. 6.9, consisted of a sodium cell, two CW dye lasers to excite the atoms, and photodetectors to register the intensity of the input and transmitted fields. Each Ar^+ -laser pumped CW dye laser provided linearly polarized light of linewidth 1 MHz, which was modulated by an electro-optical modulator (EOM-1, EOM-2) to create first-order sidebands with a frequency difference matched to the splitting of the atomic lower levels $|0\rangle$ and $|1\rangle$. The two EOMs were driven by two tunable rf generators (FG-1, FG-2), which were synchronized to produce a definite phase relation between the two frequency pairs (ω_1, ω_2) and (ω_3, ω_4) . The two laser beams were combined at a beam-splitter and passed through a Fabry–Perot interferometer that suppressed the carrier frequency of the laser fields. Next, the laser beams were directed onto the sodium cell and the transmitted field was detected by a photodetector PD1. The input field intensity was detected by a photodetector PD2. The phase difference between the two pairs of the frequencies produced by the EOMs was changed by a

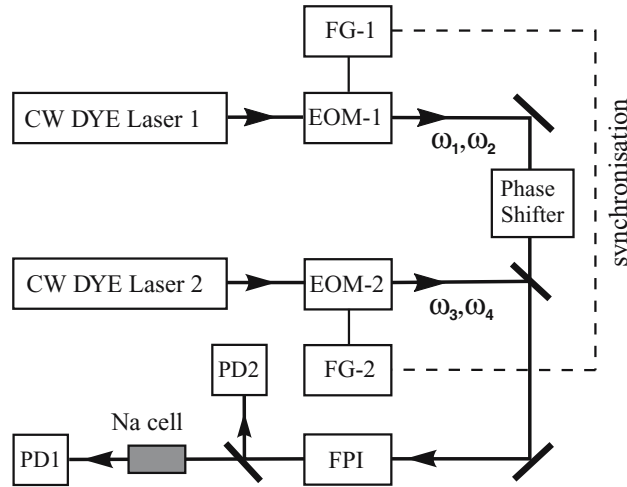


Fig. 6.9. Experimental setup to observe phase control of transmission through a sodium vapor cell. From E.A. Korsunsky, N. Leinfellner, A. Huss, S. Balushev, L. Windholz: Phys. Rev. A **59**, 2302 (1999). Copyright (1999) by the American Physical Society

phase shifter (PS), and the frequency difference $\delta_{12} = \omega_1 - \omega_2 \approx \omega_3 - \omega_4$ was swept through the frequency splitting of the lower energy levels $|0\rangle$ and $|1\rangle$.

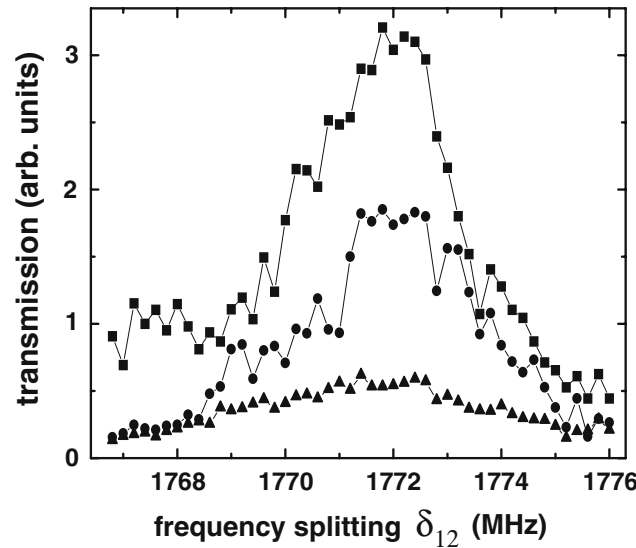


Fig. 6.10. Experimental results of Korsunsky et al. demonstrating the phase control of transmission through a sodium vapor cell. The graph shows the transmitted light intensity as a function of δ_{12} for different phases Φ : $\Phi = 0$ (*squares*), $\Phi = \pi/2$ (*circles*), $\Phi = \pi$ (*triangles*). From E.A. Korsunsky, N. Leinfellner, A. Huss, S. Balushev, L. Windholz: Phys. Rev. A **59**, 2302 (1999). Copyright (1999) by the American Physical Society

The experimental results are shown in Fig. 6.10. When the frequencies of the laser beams were out of phase ($\Phi = \pi$), the propagating fields were strongly absorbed inside the sodium cell. This is shown by the triangles curve in Fig. 6.10. However, when the frequencies were in phase ($\Phi = 0$), the transmission was large, in particular, at the frequency 1771.6 MHz corresponding to the two-photon resonance condition for perfect destructive interference in the Lambda system. This is shown in by the squares curve in Fig. 6.10. The experiment clearly demonstrated a phase-dependent quantum interference in the double Lambda system leading to phase controlled coherent population trapping and transparency.

6.3 Superbunching

We have seen in Chaps. 1 and 3 that quantum interference can produce interesting effects in the second-order correlation function. Here, we study photon correlations in a three-level Vee-type atom consisting of two excited levels coupled to a singlet ground level by electric dipole interactions. It is found that, under appropriate conditions, and with full quantum interference, the maximum value of the normalized, intensity–intensity correlation function can be made huge (values of the order of hundreds or thousands) whereas the corresponding maximum in the absence of quantum interference is ‘normal’ (values of the order of unity) [142]. We term these very large values of the second-order correlation function “superbunching”.

These effects arise in the system studied in Sect. 4.2. The energy-level scheme is shown in Fig. 6.1. The atom consists of two nondegenerate excited levels $|1\rangle$ and $|2\rangle$ separated from the ground level $|0\rangle$ by transition frequencies ω_1 and ω_2 , and connected by the electric dipole moments $\boldsymbol{\mu}_{10}$ and $\boldsymbol{\mu}_{20}$, respectively. Direct transitions between the excited levels are forbidden in the electric dipole approximation.

We may assume that our photo-detectors respond to the total field incident upon them. We shall refer to this situation as the “indistinguishable case”, since we assume that the detected photons arriving from different transitions are not differentiated against in any way. In this case, and choosing $w(\mathbf{R}) = 1$ in (2.137) and (2.138), we obtain the following expression for the correlation functions

$$G^{(1)}(t) = \sum_{i,j=1}^2 \gamma_{ij} \langle A_{i0}(t) A_{0j}(t) \rangle , \quad (6.21a)$$

$$\begin{aligned} G^{(2)}(t, \tau) = & \sum_{i,j,k,l=1}^2 \gamma_{il} \gamma_{jk} \langle A_{i0}(t) A_{j0}(t + \tau) \\ & \times A_{0k}(t + \tau) A_{0l}(t) \rangle , \end{aligned} \quad (6.21b)$$

where $\gamma_{ii} = \gamma_i$ is the spontaneous decay constant of the excited sublevel $|i\rangle$ ($i = 1, 2$) to the ground level $|0\rangle$, whereas $\gamma_{12} = \gamma_{21} = \beta\sqrt{\gamma_1\gamma_2}$ arises from the cross-damping (quantum interference) between the transitions $|1\rangle \rightarrow |0\rangle$ and $|2\rangle \rightarrow |0\rangle$. It is defined in (4.8). As discussed in Sect. 4.2, if the dipole moments are parallel, the cross-damping term is maximal with $\gamma_{12} = \sqrt{\gamma_1\gamma_2}$ ($\beta = 1$), whilst $\gamma_{12} = 0$ if the dipole moments are perpendicular ($\beta = 0$). The normalized correlation function $g^{(2)}(t, \tau)$ is defined analogously to the classical expression (1.34):

$$g^{(2)}(t, \tau) = \frac{G^{(2)}(t, \tau)}{G^{(1)}(t)G^{(1)}(t + \tau)} . \quad (6.22)$$

On the other hand, it is possible that, by means of filters or other devices, our detectors can be arranged in such a way that they detect photons from only one transition. We refer to this situation as the “distinguishable case”. If, for example, a detector only detects photons emitted on the $|1\rangle \rightarrow |0\rangle$ transition, then only the term with $i = j = k = l = 1$ should be included in the final term in (6.21) when calculating the correlation functions. Fortunately, this case and other special cases are covered by the expressions (6.21) if we set the appropriate γ_{ij} equal to zero or unity. For example, if $g_{ij}^{(2)}(t, \tau) \equiv G_{ij}^{(2)}(t, \tau) / [G_{ii}^{(1)}(t)G_{jj}^{(1)}(t + \tau)]$ relates to the probability of observing a photon emitted on the $|i\rangle \rightarrow |0\rangle$ transition at time t and a photon emitted on the $|j\rangle \rightarrow |0\rangle$ transition at time $t + \tau$, we have

$$g_{ij}^{(2)}(t, \tau) = \frac{\langle A_{i0}(t) A_{j0}(t + \tau) A_{0j}(t + \tau) A_{0i}(t) \rangle}{\langle A_{i0}(t) A_{0i}(t) \rangle \langle A_{j0}(t + \tau) A_{0j}(t + \tau) \rangle} . \quad (6.23)$$

Returning to the full expressions (6.21), we note that they take on a more transparent form if we employ the symmetric and antisymmetric superposition states (4.14) of Sect. 4.2, in terms of which the correlation functions (6.21) can be written as

$$\begin{aligned} G^{(1)}(t) &= (\gamma_1^2 + \gamma_2^2 + 2\beta\gamma_1\gamma_2) \langle A_{s0}(t) A_{0s}(t) \rangle \\ &\quad + 2(1 - \beta) \gamma_1\gamma_2 \langle A_{a0}(t) A_{0a}(t) \rangle \\ &\quad + (1 - \beta) \sqrt{\gamma_1\gamma_2} (\gamma_1 - \gamma_2) \langle A_{s0}(t) A_{0a}(t) \\ &\quad + A_{a0}(t) A_{0s}(t) \rangle \end{aligned} \quad (6.24a)$$

$$\begin{aligned} G^{(2)}(t, \tau) &= (\gamma_1^2 + \gamma_2^2 + 2\beta\gamma_1\gamma_2) \langle A_{s0}(t) U(t + \tau) A_{0s}(t) \rangle \\ &\quad + (1 - \beta) \sqrt{\gamma_1\gamma_2} \{ 2\sqrt{\gamma_1\gamma_2} \langle A_{a0}(t) U(t + \tau) A_{0a}(t) \rangle \\ &\quad + (\gamma_1 - \gamma_2) \langle A_{s0}(t) U(t + \tau) A_{0a}(t) \\ &\quad + A_{a0}(t) U(t + \tau) A_{0s}(t) \rangle \} , \end{aligned} \quad (6.24b)$$

where

$$\begin{aligned}
U(t + \tau) = & (\gamma_1^2 + \gamma_2^2 + 2\beta\gamma_1\gamma_2) A_{s0}(t + \tau) A_{0s}(t + \tau) \\
& + (1 - \beta) \sqrt{\gamma_1\gamma_2} \{ 2\sqrt{\gamma_1\gamma_2} A_{a0}(t + \tau) A_{0a}(t + \tau) \\
& + (\gamma_1 - \gamma_2) [A_{s0}(t + \tau) A_{0a}(t + \tau) \\
& + A_{a0}(t + \tau) A_{0s}(t + \tau)] \} .
\end{aligned} \tag{6.25}$$

In the expression for $G^{(2)}(t)$, the first term arises from processes in which the first transition is $|s\rangle \rightarrow |0\rangle$, the second from processes in which the first transition is $|a\rangle \rightarrow |0\rangle$, and the third term is due to the coupling between them. A similar interpretation applies to $G^{(1)}(t)$.

Although these terms look complicated, it is apparent that pronounced simplification arises when $\beta = 1$ and/or $\gamma_1 = \gamma_2$. For parallel dipole moments ($\beta = 1$) only the transition $|s\rangle \rightarrow |0\rangle$ contributes to the fluorescence intensity and the second-order correlation function, indicating that in this case the system reduces to a two-level system. However, correlations between the emitted photons can be significantly different from those one would expect for a two-level system.

We concentrate on the case of a strong driving field and consider the case where the fields emitted from the individual atomic transitions are measured separately (distinguishable photons) before considering the case where only the total emitted field is measured (indistinguishable photons).

6.3.1 Distinguishable Photons

If the photons emitted from the excited states to the ground state are distinguishable, e.g. by having significantly different polarizations or frequencies, then the second-order correlation functions in the steady-state may be written in the form [143]:

$$g_{ij}^{(2)}(\tau) = \lim_{t \rightarrow \infty} g_{ij}^{(2)}(t, \tau) = \frac{P_{0 \rightarrow j}(\tau)}{P_j}, \quad i, j = 1, 2, \tag{6.26}$$

where

$$P_{0 \rightarrow j}(\tau) = \frac{\langle A_{i0} A_{j0}(\tau) A_{0j}(\tau) A_{0i} \rangle}{\langle A_{i0} A_{0i} \rangle} \tag{6.27}$$

is the probability that at time $t + \tau$ the atom is in the upper state $|j\rangle$ of the transition $|j\rangle \rightarrow |0\rangle$ if it was in the lower state $|0\rangle$ of the $|i\rangle \rightarrow |0\rangle$ transition at time t , and $P_i = \langle A_{i0} A_{0i} \rangle$ is the steady-state population of the state $|i\rangle$. In particular, we consider the following correlation functions

$$g_{11}^{(2)}(\tau) = g_{21}^{(2)}(\tau) = \frac{P_{0 \rightarrow 1}(\tau)}{P_1}, \tag{6.28}$$

$$g_{22}^{(2)}(\tau) = g_{12}^{(2)}(\tau) = \frac{P_{0 \rightarrow 2}(\tau)}{P_2}. \tag{6.29}$$

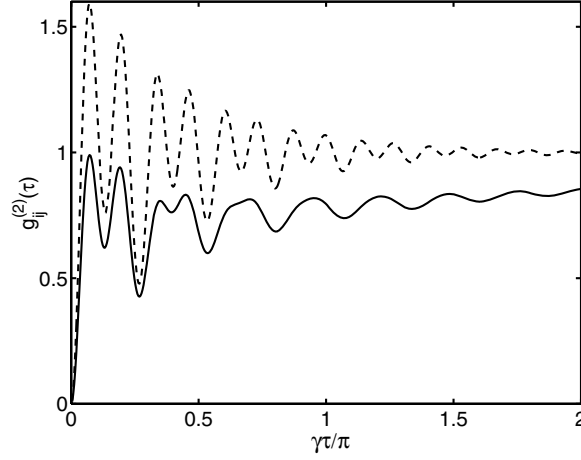


Fig. 6.11. Second-order intensity-intensity correlation functions for distinguishable photons, $g_{ij}^{(2)}(\tau)$, $i, j = 1, 2$, for $\gamma_1 = \gamma_2 = \gamma$, $\Delta = 5\gamma$, $\Delta_L = 5\gamma$, and $\Omega = 10\gamma$. The *solid line* is the plot for $\beta = 0.99$, and the *dashed line* for $\beta = 0.99$ (no quantum interference)

Figure 6.11 shows the correlation functions for distinguishable photons and $\Delta_L = \Delta/2$. In our numerical calculations, we assume the simple case $\gamma_1 = \gamma_2 = \gamma$ and $\Omega_1 = \Omega_2 = \Omega$: then all four second-order correlation functions are equal. For correlated dipole moments with $\beta = 0.99$, the values of $g_{11}^{(2)}(\tau)$ and $g_{22}^{(2)}(\tau)$ remain below unity for all times. This shows that for any τ the probability of emission of two photons from levels $|1\rangle$ or $|2\rangle$ is very small. We can interpret this as extended *simultaneous* periods of darkness in the fluorescence from the two atomic transitions: after detection of a photon at time $\tau = 0$, detection of another photon at time $\tau > 0$, emitted from levels $|1\rangle$ or $|2\rangle$, is very unlikely. We emphasize that the simultaneous periods of darkness appear only for correlated transitions with $\beta \neq 0$. This indicates that in the presence of quantum interference the atomic states $|1\rangle$ and $|2\rangle$ are not the preferred radiative states of the atom. It is also necessary that Δ be not too small, because for $\Delta = 0$, the behavior of the correlation functions resembles that of a two-level atom.

It is apparent that there are oscillations at more than one frequency present in Fig. 6.11. In fact, there are oscillations at the Rabi frequency 2Ω as well as at Ω .

6.3.2 Indistinguishable Photons

Now we consider the situation in which the detection scheme employed is such that the photons emitted from the two atomic transitions are not distinguished in any way – that is, the detectors register photons emitted from either transition with equal efficiency. Then the detector responds to the total field for which the correlation functions are given by (6.24). (However, note

that even for $\beta \approx 1$ we may in principle still distinguish between photons emitted from the $|s\rangle \rightarrow |0\rangle$ and $|a\rangle \rightarrow |0\rangle$ transitions as they may have different polarizations. It is easy to see from (4.14) that the dipole moments $\boldsymbol{\mu}_s$ and $\boldsymbol{\mu}_a$ of the respective $|s\rangle \rightarrow |0\rangle$ and $|a\rangle \rightarrow |0\rangle$ transitions are oriented in different directions unless $\boldsymbol{\mu}_1 = \boldsymbol{\mu}_2$, and then $\boldsymbol{\mu}_a = 0$.)

Therefore, we consider separately the following correlation functions

$$g_{ss}^{(2)}(\tau) = \frac{P_{0 \rightarrow s}(\tau)}{P_s}, \quad (6.30)$$

$$g_{aa}^{(2)}(\tau) = \frac{P_{0 \rightarrow a}(\tau)}{P_a}. \quad (6.31)$$

For $\beta \approx 1$, the correlation function $g_{ss}^{(2)}(\tau)$ corresponds essentially to that of the total fluorescence field as the contribution from the asymmetric state, which is proportional to $(1 - \beta)$, is negligible.

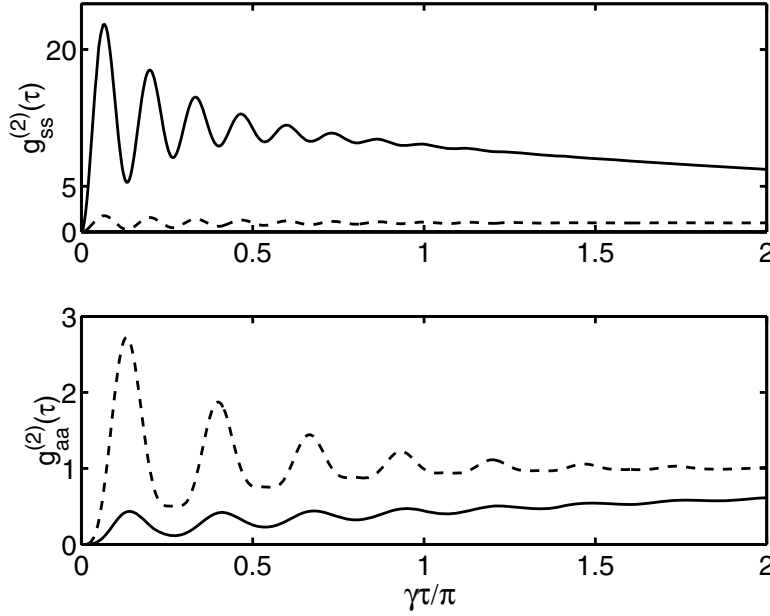


Fig. 6.12. Second-order correlation functions for the case of indistinguishable photons for $\Delta = 10\gamma$, $\Delta_L = \Delta/2$ and $\Omega = 5\gamma$. In the upper plot we present $g_{ss}^{(2)}(\tau)$ and in the lower $g_{aa}^{(2)}(\tau)$. The *solid line* is for $\beta = 0.99$ and the *dashed line* for $\beta = 0$. If we change β and Δ to $\beta = 1$ and $\Delta = 4\gamma$ for example, the graphs are almost identical

In Fig. 6.12, we plot the correlation functions (6.30) and (6.31) for indistinguishable photons and $\Delta_L = \Delta/2$. Again, the solid line is for $\beta = 0.99$ and the dashed line for $\beta = 0$. It is apparent from the graphs that with quantum interference ($\beta = 0.99$), there are very strong correlations of photons on the $|s\rangle \rightarrow |0\rangle$ transition, whereas the photons are strongly anticorrelated on the $|a\rangle \rightarrow |0\rangle$ transition. The correlation function $g_{ss}^{(2)}(\tau)$ oscillates with

the frequency $2\sqrt{2}\Omega$, which is the Rabi frequency in the symmetric basis, and attains the maximum value at time $\tau = (2\sqrt{2}\Omega)^{-1}\pi$. Moreover, the correlations decay at a very low rate and it takes a time in excess of $300\pi/\gamma_1$ before $g^{(2)}$ gets close to unity. The correlation function $g_{aa}^{(2)}(\tau)$ oscillates with frequency $\sqrt{2}\Omega$, and in the presence of quantum interference is less than unity for all times, whereas for $\beta = 0$, the values can exceed unity, with a maximum value of around 2.8.

We emphasize that very large values of $g_{ss}^{(2)}(\tau)$ are possible for $\beta \simeq 1$ (*superbunching*), whereas the maximum value of $g_{ss}^{(2)}(\tau)$ remains of the order of unity for $\beta = 0$. Thus in Fig. 6.12 it is seen that the maximum value is about 22.5 for $\beta \simeq 1$. In fact, we have chosen the parameters to ensure a particularly *small* maximum value for $g_{ss}^{(2)}(\tau)$ with $\beta = 0.99$ in order for the correlation function with $\beta = 0$ to be visible on the same set of axes. For example, if we reduce the value of Ω to γ_1 , leaving other parameters unchanged, then the maximum value of $g_{ss}^{(2)}(\tau)$ with $\beta = 0.99$ increases to almost 1500!

If we reduce the value of Δ , the difference between the $\beta = 0$ and $\beta = 0.99$ graphs for $g_{ss}^{(2)}(\tau)$ becomes less pronounced. Indeed for sufficiently small Δ the correlation functions for $\beta = 0$ and $\beta = 0.99$ oscillate in a similar fashion with $g_{ss}^{(2)}(\tau) < 2$ for all times τ .

6.3.3 Physical Interpretation

The effect of quantum interference ($\beta \simeq 1$) on the second-order correlation function is very sensitive to the splitting Δ of the excited levels. For degenerate excited levels ($\Delta = 0$) or small splittings ($\Delta \approx 0$) the photon emissions are similar to those of a two-level atom, independent of quantum interference. For large splittings and ($\beta \simeq 1$), the ‘distinguishable’ correlation functions $g_{ij}^{(2)}(\tau)$, $i, j = 1, 2$ and $g_{aa}^{(2)}(\tau)$ are smaller than unity for all times τ , while $g_{ss}^{(2)}(\tau)$ exhibits strong correlations ($g_{ss}^{(2)}(\tau) \gg 1$) for $\tau \approx (2\sqrt{2}\Omega)^{-1}\pi$ which decay at a very low rate.

We can explain these features by considering the master equation (6.14). For $\Delta = 0$ the equations of motion show that the states $|1\rangle$ and $|2\rangle$ are equally driven by the laser and the coherences ϱ_{10} and ϱ_{20} oscillate in phase with frequency Δ_L . The coherences are directly coupled by the cross-damping term γ_{12} . However, for a strong driving field ($\Omega \gg \gamma_i, \gamma_{12}$) the Rabi oscillations dominate over the spontaneous exchange of photons, resulting in independent oscillations of the atomic dipole moments.

The situation is different when $\Delta \neq 0$ and $\Delta_L = \Delta/2$. In this case the coherences oscillate with opposite phases indicating that there is an exchange of photons between the states $|1\rangle$ and $|2\rangle$ which prevents photons being emitted from the atomic levels. The coherences oscillate with $\pm\Delta/2$ which introduces the modulation of the Rabi oscillations, seen in Fig. 6.11. The exchange of

photons between the atomic levels is better seen in the basis of the symmetric and antisymmetric states (4.14). In terms of these states, setting $\gamma_1 = \gamma_2 = \gamma$ for simplicity, the equations of motion (6.14) for the populations take the form

$$\dot{\varrho}_{ss} = -\frac{1}{2}\gamma(1+\beta)\varrho_{ss} - \frac{1}{2}i\Delta(\varrho_{sa} - \varrho_{as}) - i\sqrt{2}\Omega(\varrho_{s0} - \varrho_{0s}) , \quad (6.32)$$

$$\dot{\varrho}_{aa} = -\frac{1}{2}\gamma(1-\beta)\varrho_{aa} + \frac{1}{2}i\Delta(\varrho_{sa} - \varrho_{as}) . \quad (6.33)$$

It is evident that the antisymmetric state is populated by the coupling to the

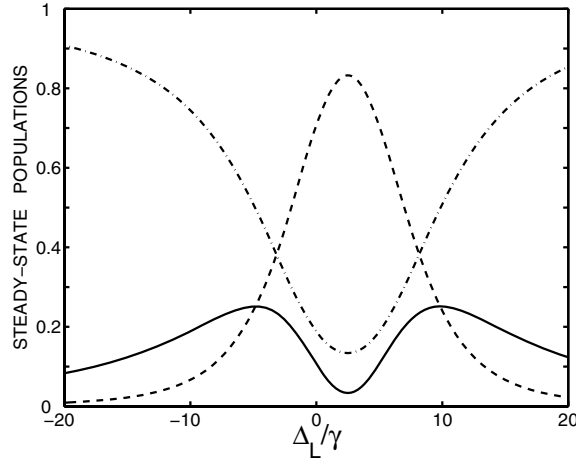


Fig. 6.13. The steady-state populations ϱ_{ss} (solid line), ϱ_{aa} (dashed line) and ϱ_{00} (dot-dashed line) as functions of Δ_L/γ for $\Omega = \Delta = 5\gamma$ and $\beta = 0.99$

symmetric state. Since the decay rate of the antisymmetric state, $\gamma(1-\beta)$, is very small for $\beta \approx 1$, the population stays in this state for a long time. If $\Delta = 0$ the state is decoupled from the symmetric state and $\varrho_{aa}(t)$ is zero if its initial value is zero. In this case the system reduces to a two-level atom. For the case $\Delta \neq 0$, the transfer of the population to a slowly decaying state leaves the symmetric state almost unpopulated even if the driving field is strong. This is shown in Fig. 6.13, where we plot the steady-state populations ϱ_{ss} , ϱ_{aa} and ϱ_{00} as a function of Δ_L . It is evident that the symmetric state is almost unpopulated for $\Delta_L = \Delta/2$. This indicates that in the presence of quantum interference, the driving field does not saturate the transition $|0\rangle \rightarrow |s\rangle$, even for very large Rabi frequencies. The lack of population in the state $|s\rangle$ increases the probability of returning the atom to this state from the ground state by the driving field. Consequently, $g_{ss}^{(2)}(\tau)$ attains a very large value at the time $\tau = (2\sqrt{2}\Omega)^{-1}\pi$ corresponding to half of the Rabi cycle between $|0\rangle$ and $|s\rangle$. However, $g_{aa}^{(2)}(\tau)$ attains a maximum at $\tau \approx (\sqrt{2}\Omega)^{-1}\pi$, i.e. at half the Rabi period. This results from the fact that the driving laser takes the population from $|0\rangle$ to $|s\rangle$ in a time equal to half of the Rabi period. Then the

population can be transferred to $|a\rangle$ in a time equal to that the population will stay in $|s\rangle$ i.e. in a time equal to half of the Rabi period. Therefore, the total time of transferring the population from $|0\rangle$ to $|a\rangle$ is equal to the Rabi period.

6.4 Implementation of Quantum Interference

As we have pointed out in Chap. 4, the direct observation of the quantum interference effects described in that chapter and the previous sections of this one requires the use of systems with parallel or nearly parallel transition dipole moments, which are very difficult to come by in nature. This has proved a serious obstacle in performing experiments. In this section, we consider alternative approaches that enable us to bypass this difficulty. The intention is find more easily accessible systems, such as those with perpendicular dipole moments, which simulate the properties of systems with parallel dipole moments, in the hope that experiments on such systems will prove much easier.

6.4.1 External Field Mixing

A mixing of atomic or molecular states can be implemented by applying external fields. Consider, for example, a Vee type atom with the upper states connected to the ground state by perpendicular dipole moments, $\boldsymbol{\mu}_{01} \perp \boldsymbol{\mu}_{02}$. When the two upper states are coupled by a resonant microwave field, the relevant states are linear superpositions of the bare states

$$\begin{aligned} |+\rangle &= \frac{1}{\sqrt{2}} (|1\rangle + |2\rangle) , \\ |-\rangle &= \frac{1}{\sqrt{2}} (|1\rangle - |2\rangle) . \end{aligned} \quad (6.34)$$

It is easy to find from (6.34) that the dipole matrix elements between the superposition states and the ground state $|0\rangle$ are

$$\begin{aligned} \boldsymbol{\mu}_{+0} &= \frac{1}{\sqrt{2}} (\boldsymbol{\mu}_{01} + \boldsymbol{\mu}_{02}) , \\ \boldsymbol{\mu}_{-0} &= \frac{1}{\sqrt{2}} (\boldsymbol{\mu}_{01} - \boldsymbol{\mu}_{02}) . \end{aligned} \quad (6.35)$$

When $|\boldsymbol{\mu}_{01}| \neq |\boldsymbol{\mu}_{02}|$, the dipole moments $\boldsymbol{\mu}_{+0}$ and $\boldsymbol{\mu}_{-0}$ are not perpendicular. However, the dipole moments cannot be made perfectly parallel or antiparallel. If $|\boldsymbol{\mu}_{02}| \ll |\boldsymbol{\mu}_{01}|$, the angle between the two dipoles $\boldsymbol{\mu}_{+0}$ and $\boldsymbol{\mu}_{-0}$ is approximately $\theta_{+-} = \arccos(1 - 2\mu_{02}^2/\mu_{01}^2)$.

An alternative method for creating a Vee-type system with parallel or antiparallel dipole moments is to apply a strong laser field to one of the

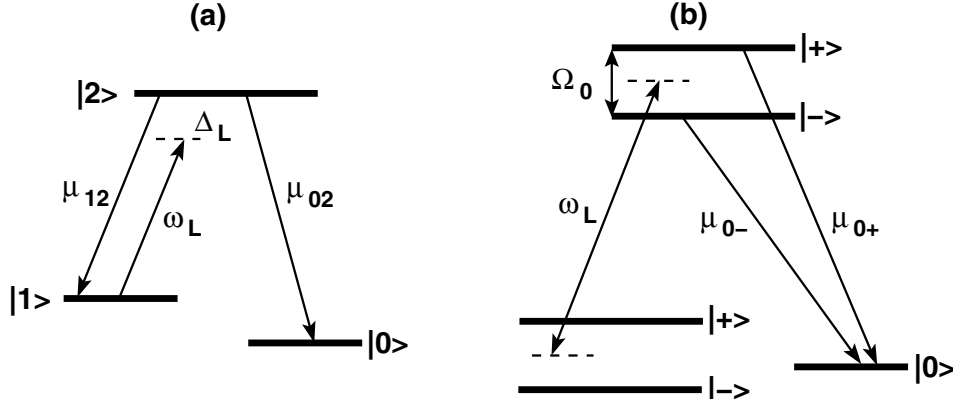


Fig. 6.14. Laser induced Vee type system with nondegenerate transitions. A laser field applied to the $|1\rangle \rightarrow |2\rangle$ transition of a Lambda system creates nondegenerate dressed states separated by the Rabi frequency Ω . The subsystem with the upper dressed states $|+\rangle$ and $|-\rangle$ and the ground state $|0\rangle$ form a Vee system with the dipole moments of the two transitions parallel

two transitions in a Lambda-type atom. Let the ground states be denoted $|0\rangle$ and $|1\rangle$, and the excited state $|2\rangle$. The scheme is shown in Fig. 6.14. When the dipole moments of the $|0\rangle \rightarrow |2\rangle$ and $|1\rangle \rightarrow |2\rangle$ transitions are perpendicular, a laser may be employed to couple exclusively to the $|1\rangle \rightarrow |2\rangle$ transition. It then produces dressed states

$$\begin{aligned} |+\rangle &= \sin \theta |1\rangle + \cos \theta |2\rangle, \\ |-\rangle &= \cos \theta |1\rangle - \sin \theta |2\rangle, \end{aligned} \quad (6.36)$$

with

$$\cos^2 \theta = \frac{1}{2} + \frac{\Delta_L}{2\Omega}, \quad (6.37)$$

where Δ_L is the detuning of the laser frequency from the atomic transition, $\Omega = \sqrt{\Omega_0^2 + \Delta_L^2}$ and Ω_0 is the on-resonance semi-Rabi frequency of the laser field.

From (6.36), we find that the dipole matrix elements between the dressed states and the ground state $|0\rangle$ are

$$\begin{aligned} \mu_{+0} &= \mu_{12} \sin \theta, \\ \mu_{-0} &= \mu_{12} \cos \theta. \end{aligned} \quad (6.38)$$

Thus, the subsystem with the upper dressed states $|a\rangle, |b\rangle$ and the ground state $|1\rangle$ behaves as a Vee type system with parallel dipole moments. This system has the advantage that the magnitudes of the transition dipole moments and the upper levels splitting can be controlled by the Rabi frequency and detuning of the driving laser field.

6.4.2 Two-Level Atom in a Polychromatic Field

Transitions with parallel or antiparallel dipole moments can be created not only in multi-level atoms, but also in a two-level atom driven by a polychromatic field. To show this, consider a two-level atom driven by a bichromatic field composed of a strong resonant laser field and a weaker laser field detuned from the atomic resonance by the Rabi frequency of the strong field. Treating the fields quantum-mechanically, the effect of the strong field alone is to produce dressed states

$$\begin{aligned} |+, n\rangle &= \frac{1}{\sqrt{2}} (|0, n\rangle + |1, n-1\rangle) , \\ |-, n\rangle &= \frac{1}{\sqrt{2}} (|0, n\rangle - |1, n-1\rangle) , \end{aligned} \quad (6.39)$$

with energies $E_{1,2} = \hbar (n\omega_0 \pm \frac{1}{2}\Omega)$, where n is the number of photons in the field mode, Ω is the Rabi frequency, and ω_0 is the atomic transition frequency.

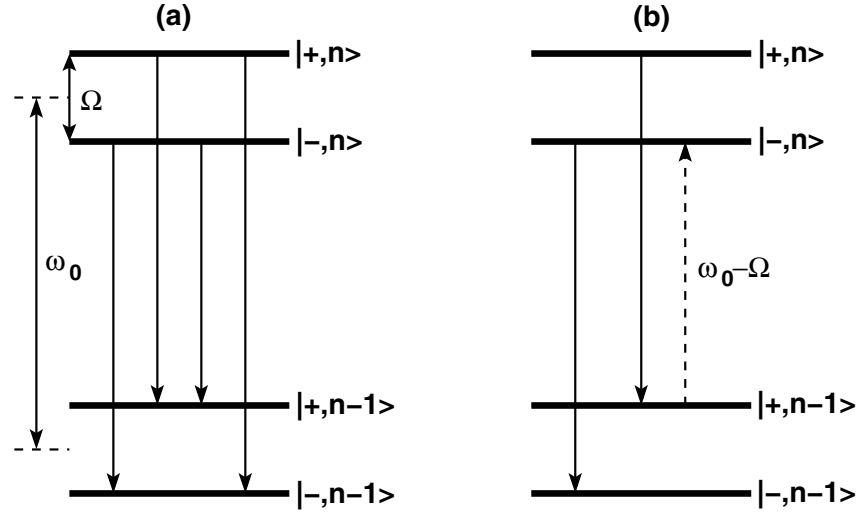


Fig. 6.15. (a) Two neighbouring manifolds of dressed states of a driven two-level atom. The arrows indicate nonzero dipole moments of magnitudes $\pm\mu_{10}$. (b) An additional coherent laser field is applied (dashed arrow) of frequency $\omega_0 - \Omega$ to couple the dipole moments of the two degenerate transitions at ω_0

The dressed states are shown in Fig. 6.15(a). We see that in the dressed atom basis the system is no longer a two-level system. It is a multi-level system with three different transition frequencies, ω_0 and $\omega_0 \pm \Omega$, and four nonvanishing dipole moments $\mu_{ij,n} = \langle n, i | \mu | j, n-1 \rangle$ connecting dressed states between neighbouring manifolds

$$\mu_{++ , n} = \mu_{+- , n} = -\mu_{-+ , n} = -\mu_{-- , n} = \frac{1}{2}\mu_{10} , \quad (6.40)$$

where μ_{10} is the dipole moment of the bare atom.

There are two transitions with antiparallel dipole moments, $\mu_{++,n}$ and $\mu_{--,n}$, that oscillate with the same frequency ω_0 . This makes the system an ideal candidate for quantum interference. However, they are not coupled (i.e. not correlated), preventing these dipole moments from being a source of quantum interference. This can be shown by calculating the correlation functions of the dipole moment operators of the dressed-atom transitions $\sigma_{ijn}^+ = |i, n\rangle \langle n-1, j|$, ($i, j = 1, 2$). The correlation functions $\langle \sigma_{iin}^+ \sigma_{jjn}^- \rangle$, ($i \neq j$), are equal to zero, showing that the dipole moments oscillate independently.

In order to correlate them, we introduce a second (weaker) laser field of frequency $\omega_0 - \Omega$ and Rabi frequency $\Omega_2 < \Omega$, which couples the degenerate transitions with dipole moments $\mu_{++,n-1}$ and $\mu_{--,n}$, as indicated in Fig. 6.15(b). Treating the second field perturbatively, at zeroth order the coupling results in new “doubly-dressed” states

$$|\bar{n}, p\pm\rangle = \frac{1}{\sqrt{2}} (|1, n-p-1, m+p+1\rangle \pm |0, n-p, m+p\rangle) , \quad (6.41)$$

where m is the number of photons in the weaker field mode, and $\bar{n} = n + m$ is the total number of photons.

On calculating the transition transition rates of spontaneous emission between the dressed states of two neighbouring manifolds, we find that the transition rates $\gamma_{\pm,\pm}$ between the doubly dressed states $|\bar{n}, p+\rangle \rightarrow |\bar{n}-1, p+\rangle$ and $|\bar{n}, p-\rangle \rightarrow |\bar{n}-1, p-\rangle$ are equal to zero. Thus, in the doubly driven atom the effective transition rates at ω_0 are zero due to quantum interference between the two degenerate dipole moments of opposite phases. A consequence of this cancellation is the disappearance of the central component in the fluorescence spectrum of the doubly driven two-level atom [144].

Figure 6.16 shows the fluorescence spectrum for resonant excitation of the bare two-level atom. The atomic transition frequency is ω_0 , γ is the spontaneous decay rate of the bare two-level atom, and the strong and weak lasers have frequencies ω_1 and ω_2 respectively. Supposing the strong laser to be resonant, $\omega_1 = \omega_0$, the detuning of the weak laser field from the Rabi sideband frequency induced by the strong field is defined by $\Delta_2 = \omega_1 + \Omega - \omega_2$.

In Fig. 6.16 we assume resonant excitation by the strong laser with different values of the weak laser detuning Δ_2 . For large Δ_2 , the spectrum exhibits the well-known Mollow triplet, as illustrated in Frame (a). For small but nonzero Δ_2 , the spectrum consists of a triplet at the centre frequency, with components at $\omega = \{\omega_1 \text{ and } \omega_1 \pm \Omega_2\}$, and doublets $\omega = \{\omega_2 \text{ and } \omega_2 + \Omega_2\}$; $\omega = \{2\omega_1 - \omega_2 \text{ and } 2\omega_1 - \omega_2 - \Omega_2\}$. See Fig. 6.16(b).

The situation is quite different when $\Delta_2 = 0$: then, the incoherent central peak at $\omega = \omega_1$ is suppressed, whilst additional peaks occur at $\omega = \omega_1 + \Omega - \Omega_2/2$ and $\omega = \omega_1 - \Omega + \Omega_2/2$, converting the outer doublets into triplets, as shown in Frame (c). These interesting features are due to quantum interference, and arise from the cancellation of the transition dipole moments between the dressed states of the system [144].

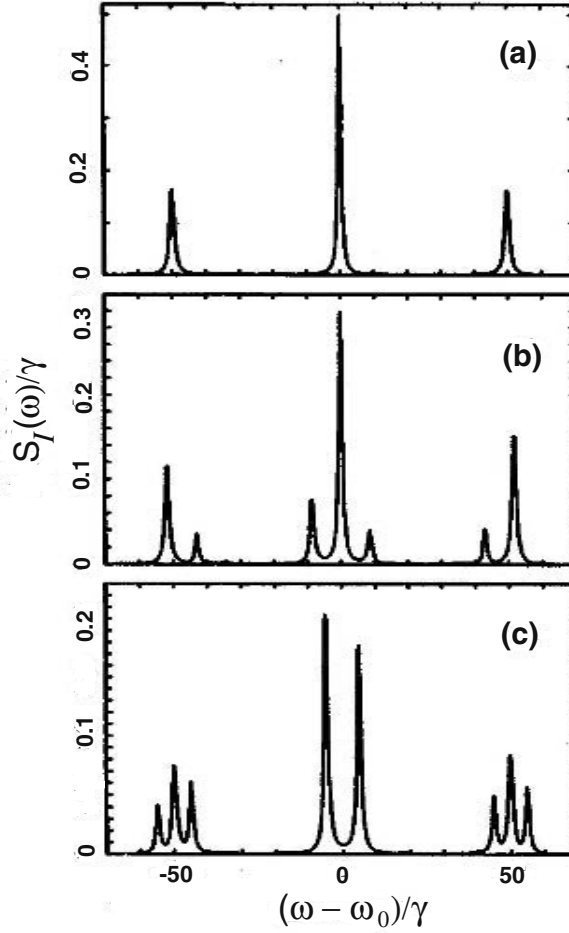


Fig. 6.16. The resonance fluorescence spectrum for resonant excitation by the strong laser, with detunings of the weak laser that are large in (a), small but nonzero in (b), and zero in (c)

6.4.3 dc Field Simulation of Quantum Interference

In this section, we study a system employing a dc field that permits the observation of the novel features predicted for three-level systems showing strong quantum interference, but without the need for parallel dipole moments [145]. To be more precise, consider the three-level Vee system discussed in Sect. 6.3, which we depict in Fig. 6.17(a). We shall show that the alternative three-level Vee type atom with *perpendicular* dipole moments coupling the nearly degenerate upper levels with the ground level, shown in Fig. 6.17(b), is capable of simulating this. In this alternative system, one of the dipole transitions is driven by a strong laser field, and a dc field couples the two upper levels.

The atom in Fig. 6.17(a) consists of two nondegenerate excited levels $|1\rangle$ and $|2\rangle$ separated from the ground level $|0\rangle$ by transition frequencies ω_1 and ω_2 , and connected by the electric dipole moments μ_1 and μ_2 , respectively. The dipole moments are assumed almost parallel. The excited sublevels decay to the level $|0\rangle$ by spontaneous emission, whereas direct spontaneous

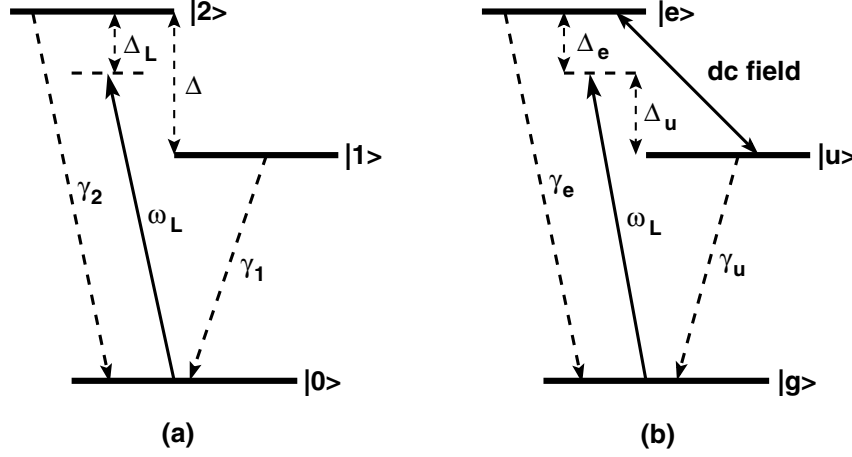


Fig. 6.17. (a) Energy-level scheme of a three-level atom in the Vee configuration driven by a single laser field coupled to both atomic transitions, with parallel transition dipole moments. (b) Energy-level scheme of the three-level atom with perpendicular transition dipole moments. The single laser couples only one of the atomic dipole transitions, whilst a dc field couples the two upper levels

transitions between the excited sublevels are dipole forbidden. For simplicity, we assume that $\gamma_1 = \gamma_2 = \gamma$, and $\Omega_1 = \Omega_2 = \Omega$.

Under these conditions, we have shown in Sect. 6.1 that the equations of motion (6.14) simplify considerably when we transform to the symmetric/antisymmetric basis states (6.5), $|s, a\rangle = 2^{-1/2}(|1\rangle \pm |2\rangle)$, which diagonalize the decay term of (6.4). We recall that in this new basis, the Hamiltonian becomes

$$H/\hbar = \Delta_1 (A_{ss} + A_{aa}) - \frac{\Delta}{2} (A_{sa} + A_{as}) + \frac{\sqrt{2}\Omega}{2} (A_{s0} + A_{0s}) , \quad (6.42)$$

and the damping term becomes

$$\mathcal{L}\varrho = \frac{1}{2} \sum_{k=s,a} \gamma (1 \pm \beta) (2A_{0k}\varrho A_{k0} - A_{kk}\varrho - \varrho A_{kk}) , \quad (6.43)$$

where $\Delta_1 = \Delta_L - \Delta/2$, the ‘plus’ sign refers to the ‘s’ decay rate and the minus sign to the ‘a’ decay rate. In these equations, $A_{ij} \equiv |i\rangle\langle j|$ is the usual transition operator.

It is apparent that the laser field couples only to the symmetric state and both states decay independently to the ground state with different decay rates. In fact, if the dipole moments are almost parallel, so that $\beta \simeq 1$, it is clear that the antisymmetric level is metastable: $\gamma_a \equiv \gamma(1 - \beta) \simeq 0$.

If we ignore the $\Delta_1 A_{aa}$ term in (6.42), we observe that the system described by (6.43) and (6.42) is equivalent to that of a three-level system in which the ground state $|0\rangle$ is connected to the excited state $|s\rangle$ by a laser field detuned from resonance with the state $|s\rangle$ by the amount Δ_1 , whilst $|s\rangle$ is also coupled to the other excited state, $|a\rangle$, for example, by a dc field. If

$\Delta_1 = 0$ ($\Delta_L = \Delta/2$) the system described by (6.43) is unitarily equivalent to the system exhibiting quantum interference shown in Fig. 6.17(a).

However, in order to realize such a system we would need to find a Vee system with degenerate excited levels, and one of these levels would have to be nearly metastable in order to realize near perfect quantum interference ($\beta \simeq 1$). Such systems may be difficult to find in practice. Hence, in the remainder of this section, we consider a generalization of this system in which we allow the two excited states to be nondegenerate, and their decay rates to the ground state to be arbitrary. For notational consistency, we also redefine the coupling constants to be equal to the corresponding Rabi frequencies, and we denote the ground state henceforth as $|g\rangle$, rather than $|0\rangle$, and the upper states as $|e\rangle$ and $|u\rangle$. Explicitly the system we consider is described, in the rotating frame, by the Hamiltonian

$$H/\hbar = \Delta_e A_{ee} + \Delta_u A_{uu} - \frac{1}{2}D(A_{eu} + A_{ue}) + \frac{1}{2}\Omega(A_{eg} + A_{ge}) , \quad (6.44)$$

and Liouvillian

$$\begin{aligned} \mathcal{L}\varrho = & \frac{1}{2}\gamma_e(2A_{ge}\varrho A_{eg} - A_{ee}\varrho - \varrho A_{ee}) \\ & + \frac{1}{2}\gamma_u(2A_{gu}\varrho A_{ug} - A_{uu}\varrho - \varrho A_{uu}) , \end{aligned} \quad (6.45)$$

where D is the Rabi frequency of the dc field directly coupling the upper states. This is the system denoted in Fig. 6.17(b).

Comparing (6.43) and (6.45), we may define

$$\tilde{\beta} = \cos^{-1} \theta = (\gamma_e - \gamma_u)/(\gamma_e + \gamma_u) \quad (6.46)$$

as a measure of quantum interference in this new system. We may expect that the level $|u\rangle$ has to be metastable ($\gamma_u \ll \gamma_e$; $\tilde{\beta} \simeq 1$) if we are to see maximal effects of quantum interference.

However, we wish to investigate how far the effects of quantum interference are duplicated by the system (6.44) and (6.45) when the detunings are unequal, so that there is no unitary equivalence with the system of Fig. 6.17(a), which we shall refer to as System 1, and when we relax the condition $\gamma_u \ll \gamma_e$. Below, we shall show that the system described by (6.44) and (6.45), to be referred to henceforth as System 2, behaves in a largely similar way to System 1. However, System 1 requires dipole moments that are almost parallel, whilst perpendicular moments are assumed for the System 2.

The Intensity–Intensity Correlation Function

We demonstrated in Sect. 6.3 that the Vee system with near maximal quantum interference can exhibit extraordinarily large values of the normalized intensity–intensity correlation function. Here, we show that System 2 of

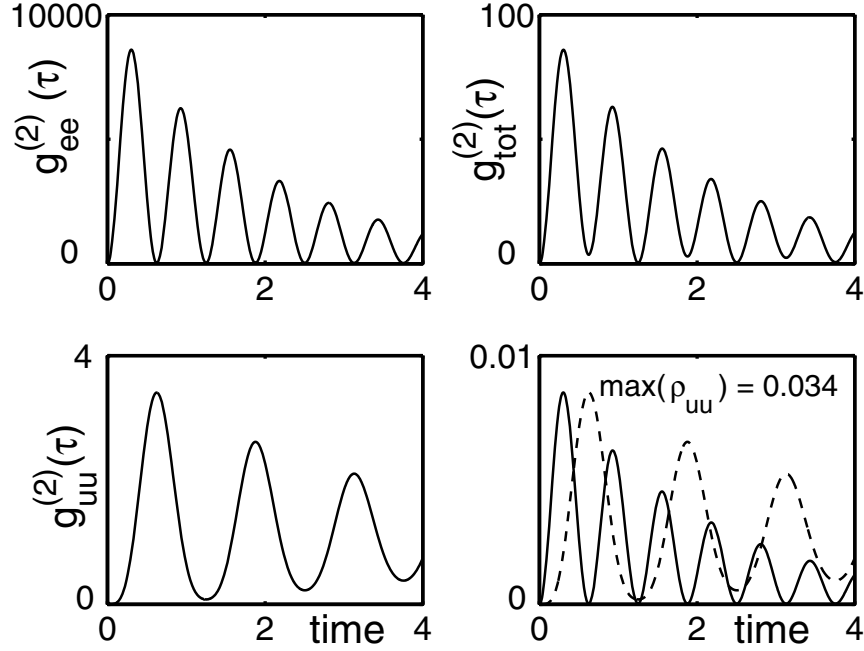


Fig. 6.18. Second-order intensity–intensity correlation functions and the density matrix elements for $D = 10$, $\Omega = 1$, $\Delta_e = \Delta_u = 0$, and $\gamma_u = 0.01$. The fourth frame shows ρ_{ee} as a solid line. The dotted line represents $\rho_{uu}(t) / \max(\rho_{uu}) \times \max(\rho_{ee})$. To enable absolute values of ρ_{uu} to be estimated, its maximum value is indicated in the fourth frame. In this and all subsequent figures, $\gamma_e = 1$

Fig. 6.17(b) exhibits a similar type of behavior for a wide range of parameter values. The intensity–intensity correlations functions may be calculated using the same methods as outlined in Sect. 6.3. We illustrate the general features of these correlation functions by considering a few examples. In the following figures, we measure quantities as ratios of γ_e (i.e. we take $\gamma_e = 1$), and throughout this section we take $D = 10$, $\Omega = 1$.

In Fig. 6.18 we take $\gamma_u = 0.01$, $\Delta_e = \Delta_u = 0$. In this case, System 2 is unitarily equivalent to System 1, with the dipole moments almost parallel (c.f. (6.46)). The most obvious feature of this plot is the extraordinarily large maximum value of $g_{ee}^{(2)}$. Note, that $g_{\text{tot}}^{(2)}$ also exhibits very strong photon correlations, as expected, whilst $g_{uu}^{(2)}$ as shown in the third frame, displays much weaker correlations.

The properties of this system may be partially understood by considering the special case $\Delta_u = \gamma_u = 0$. That is, we assume the laser is resonant with level $|u\rangle$, which is completely stable. It is then very easy to show that the steady-state solution is

$$\begin{aligned} \rho_{ee} &= \rho_{eu} = \rho_{eg} = 0 , \\ \rho_{uu} &= \frac{\Omega^2}{D^2 + \Omega^2} , \quad \rho_{ug} = \frac{\Omega D}{D^2 + \Omega^2} . \end{aligned} \quad (6.47)$$

Thus, the system eventually evolves into the pure state

$$|\Psi\rangle = \frac{D|g\rangle + \Omega|u\rangle}{\sqrt{D^2 + \Omega^2}}, \quad (6.48)$$

independently of the values of Δ_e and γ_e and of the initial state of the system. Although the laser is driving the transition $|g\rangle \rightarrow |e\rangle$, there is no population in the state $|e\rangle$ in the steady-state in spite of the ground state $|g\rangle$ being populated, and the system is ‘dark’ – i.e. no radiation at all is emitted. We have a coherent population trapping situation.

However, if we consider the evolution of the system from the initial density matrix

$$\varrho(\tau = 0) = |g\rangle\langle g|, \quad (6.49)$$

(so that $\varrho_{jj}(\tau) = P(g, 0 \rightarrow j, \tau)$, as appears in (6.28) and (6.29) there will, for short times, be population in the state $|e\rangle$, and fluorescence will occur. For $\gamma_u = 0$, one cannot define the steady-state intensity–intensity correlation function, as all the relevant quantities are zero. It would, however, be meaningful to define *transient* intensity–intensity correlation functions, but we do not consider these here [146].

If we now suppose γ_u to be small but nonzero, then there will be fluorescence even in the steady-state, but the mean number of photons emitted in unit time will be very small. If we concentrate on the photons emitted on the $|e\rangle \rightarrow |g\rangle$ transition for definiteness, then the steady-state value of ϱ_{ee} will be very small, whilst $P(g, 0 \rightarrow e, \tau)$ will be much larger for shorter times. Thus the short-time values of $g^{(2)}(\tau)$ will be very large. According to the expressions (6.47), we expect these values to become larger if the ratio Ω/ω increases, and this we find to be so in our numerical investigations.

Next, we investigate the effect of introducing finite detunings, and of relaxing the condition that γ_u be metastable. The system is then no longer unitarily equivalent to System 1. We take the detunings $\Delta_u = 0$, and $\Delta_e = 5$, and increase the value of γ_u to $\gamma_u = 1$. We still obtain quite large values for $g_{ee}^{(2)}$. This is rather surprising at first, as the fact that $|u\rangle$ can no longer be considered a metastable level may have been expected to reduce the maximum values of $g^{(2)}(\tau)$ to values of the order of unity. However, the steady state population of $|e\rangle$ is still much smaller than the steady state population of $|u\rangle$, but this is now due to the detuning of the $|e\rangle \rightarrow |g\rangle$ transition from resonance. Thus we can dispense with the requirements that $|u\rangle$ be metastable, and $|e\rangle$ and $|u\rangle$ be degenerate, and still obtain large values for $g_{ee}^{(2)}$. These features are illustrated in Fig. 6.19.

Resonance Fluorescence Spectra

Another interesting feature of System 1 is that it has been shown to exhibit very sharp peaks in the incoherent fluorescence spectrum under certain conditions. We show that this feature is also shared by System 2. We consider

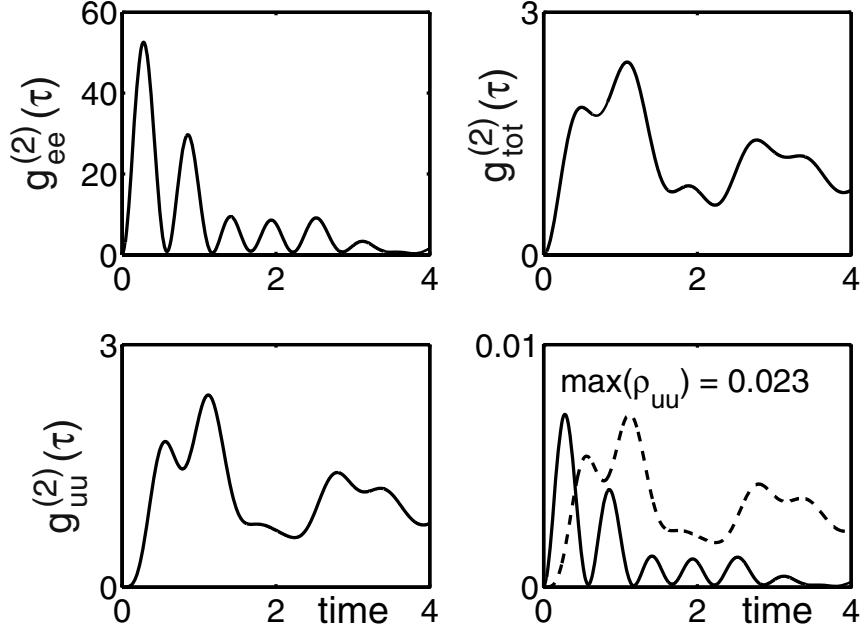


Fig. 6.19. Second-order intensity–intensity correlation functions as in Fig. 6.18, except that $\gamma_u = 1$, $D = 10$, $\Omega = 1$, $\gamma_u = 1$, $\Delta_e = 5$ and $\Delta_u = 0$

the degenerate case $\Delta_u = \Delta_e = 0$, taking $\gamma_u = 0.001$, in Fig. 6.20(a) which shows the existence of an ultra-narrow line at the center of the resonance fluorescence spectrum. The sharpness of the line is decreased by increasing the value of γ_u . (The spectrum is actually five-peaked, but the inner side-peaks are so small as to be barely noticeable in the figure.) We emphasize that the sharp line shown in Fig. 6.20(a) is due to incoherent scattering, as the coherent contribution has been excluded from our figures.

The ratio of the relative weight of the inner side-peaks to the outer side-peaks increases with the value of D/Ω , as we show in Fig. 6.20(b). In this case, the five-peaked nature of the spectrum is obvious, and the fluorescence spectrum does not exhibit the sharp line at the central frequency.

6.4.4 Pre-selected Cavity Polarization Method

Patnaik and Agarwal [147] have proposed a method of generating a nonzero cross-damping rate in a three-level atom with perpendicular dipole moments which interacts with a single-mode cavity of a pre-selected polarization. In this system the polarization index s of the cavity mode is fixed to only one of the two possible directions. This arrangement of the polarization can lead to a nonzero cross-damping term γ_{12} in the master equation of the system, even if the dipole moments of the atomic transitions are perpendicular. If the polarization of the cavity field is fixed, say $\bar{e}_s = \bar{e}_x$, the polarization direction along the x -quantization axis, then the cross-damping rate (4.10) becomes

$$\gamma_{12} = \sqrt{\gamma_1 \gamma_2} \cos \theta_1 \cos \theta_2, \quad (6.50)$$

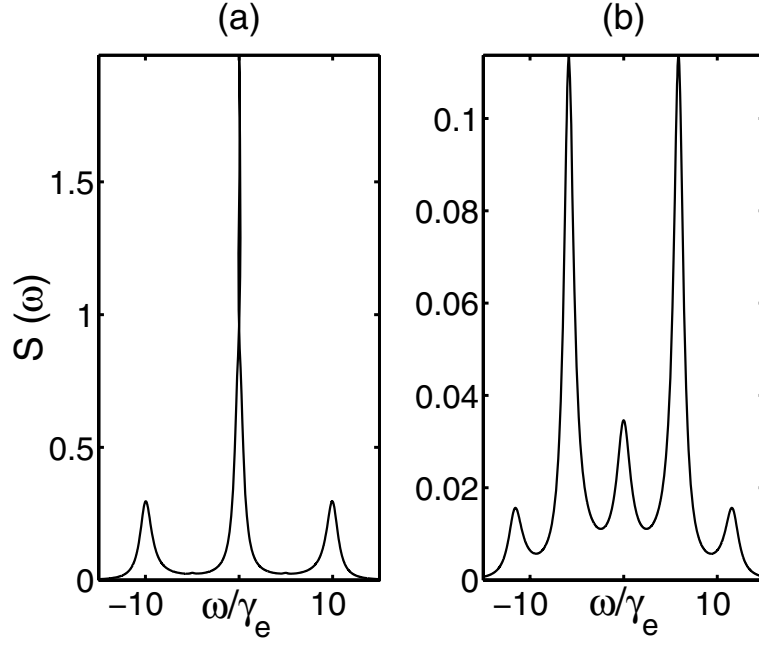


Fig. 6.20. The resonance fluorescence spectrum $S(\omega)$ for $\Delta_e = \Delta_u = 0$, and **(a)** $\Omega = 10$, $D = 0.5$, $\gamma_u = 0.001$; **(b)** $\Omega = 6$, $D = 6$, and $\gamma_u = 1$. All quantities are measured as ratios of γ_e

where θ_j is the angle between $\boldsymbol{\mu}_j$ and the preselected polarization vector, and usually $\theta_1 + \theta_2 = \pi/2$.

Zhou et al. [148] have shown that the idea of the pre-selected polarization can be applied to engineer systems with parallel or anti-parallel dipole moments. To illustrate how this scheme works, we consider a Vee-type atom with the ground state $|0\rangle$ coupled by a single mode cavity field to the excited states $|1\rangle$ and $|2\rangle$. The corresponding energies are $E_0 = 0$, $E_1 = \hbar\omega_1$ and $E_2 = \hbar\omega_2$. Spontaneous emission is ignored in this system, but the cavity mode, characterized by the annihilation and creation operators \hat{a} and \hat{a}^\dagger and the frequency ω_c , is damped at the rate κ . The important assumption is that only one pre-selected polarization of the cavity mode, say $\bar{\mathbf{e}}_s = \bar{\mathbf{e}}_1$, is supported by the cavity.

With direct transitions between the doublet states forbidden, the equation of motion for the total density matrix ϱ_T in the frame rotating with the average transition frequency $\omega_0 = (\omega_1 + \omega_2)/2$ is

$$\dot{\varrho}_T = -i[(H_A + H_{AC})/\hbar, \varrho_T] + \mathcal{L}\varrho_T, \quad (6.51)$$

where

$$\begin{aligned} H_A/\hbar &= \delta \hat{a}^\dagger \hat{a}, \\ H_{AC}/\hbar &= \frac{1}{2} \Delta (A_{22} - A_{11}) + i[(g_1 A_{01} + g_2 A_{02}) \hat{a}^\dagger - \text{H.c.}], \\ \mathcal{L} &= \kappa (2\hat{a} \varrho_T \hat{a}^\dagger - \hat{a}^\dagger \hat{a} \varrho_T - \varrho_T \hat{a}^\dagger \hat{a}), \end{aligned} \quad (6.52)$$

with $\delta = \omega_c - \omega_0$ and g_j is the atom-cavity coupling constant. Here, as usual, $\Delta = \omega_2 - \omega_1$, $A_{ij} = |i\rangle\langle j|$ are the atomic operators, and $\boldsymbol{\mu}_{ij}$ is the dipole moment of the transition $|i\rangle \rightarrow |j\rangle$.

We assume that the *bad cavity limit* applies

$$\kappa \gg g_j, \quad j = 1, 2. \quad (6.53)$$

That is, we assume that the atom-cavity coupling is weak, and that the cavity has a low Q -factor, so that cavity field decay dominates. The cavity response to the continuum modes is much faster than that produced by its interaction with the atom, so that the atom always experiences the cavity mode in the state induced by the vacuum reservoir. Under these conditions, one can adiabatically eliminate the cavity mode variables, giving rise to a master equation involving only the atomic variables. As the derivation is tedious, we present only the results here. Details of the method may be found in [65].

If ϱ denotes the reduced density operator for the atom only, $\varrho = \text{Tr}(\varrho_T)$, we find

$$\begin{aligned} \dot{\varrho} = & -i[H_A/\hbar, \varrho] + \sum_{j=1,2} F_j \left[|g_j|^2 (A_{0j} \varrho A_{j0} - A_{jj} \varrho - \varrho A_{jj}) \right. \\ & \left. + g_1 g_2^* (A_{02} \varrho A_{10} - A_{12} \varrho) + \text{H.c.} \right], \end{aligned} \quad (6.54)$$

where

$$F_1 = \left[\kappa + i \left(\delta + \frac{1}{2} \Delta \right) \right]^{-1} \quad \text{and} \quad F_2 = \left[\kappa + i \left(\delta - \frac{1}{2} \Delta \right) \right]^{-1}. \quad (6.55)$$

Equation (6.54) clearly describes the cavity-induced atomic decay into the cavity mode. The real and imaginary parts of $F_j |g_j|^2$ represent the cavity-induced decay rate and frequency shift of the atomic level $|j\rangle$. The cross-terms $F_j g_1 g_2^*$, however, represent cavity induced correlated transitions of the atom, i.e. processes of the type $|1\rangle \rightarrow |0\rangle \rightarrow |2\rangle$ or $|2\rangle \rightarrow |0\rangle \rightarrow |1\rangle$ which typify quantum interference effects.

Note that our assumption that the cavity support only one polarization mode is crucial to obtaining the quantum interference terms. If both polarization modes were supported, the factor $g_1 g_2^*$ appearing in the expression for the cross-terms would be replaced by expressions involving a sum over the polarization index s , of the form

$$\sum_{s=1,2} g_1(s) g_2^*(s) \propto \sum_{s=1,2} (\bar{\mathbf{e}}_s \cdot \boldsymbol{\mu}_{01}) (\bar{\mathbf{e}}_s \cdot \boldsymbol{\mu}_{02}^*) \propto \boldsymbol{\mu}_{01} \cdot \boldsymbol{\mu}_{02}^*. \quad (6.56)$$

Quantum interference would thus vanish if, as is usually the case, the dipole moments were perpendicular.

If we assume that

$$\kappa \gg \delta, \Delta, \quad (6.57)$$

and introduce the cavity-induced decay rates

$$\gamma_j^c = \frac{|g_j|^2}{\kappa}, \quad (6.58)$$

the damping term $\mathcal{L}\rho$ has the same form as (6.4) but with γ_j replaced by γ_j^c and γ_{12} replaced by $\sqrt{\gamma_1^c \gamma_2^c}$. The latter replacement indicates that the quantum interference in this cavity system is maximal.

Generally, the cavity-induced decay rates have the form

$$\gamma_j = \frac{\kappa |g_j|^2}{\kappa^2 + (\delta \pm \Delta)^2}. \quad (6.59)$$

The effects of quantum interference are most pronounced in the frequency region where $\Delta \leq 2\gamma_j$.

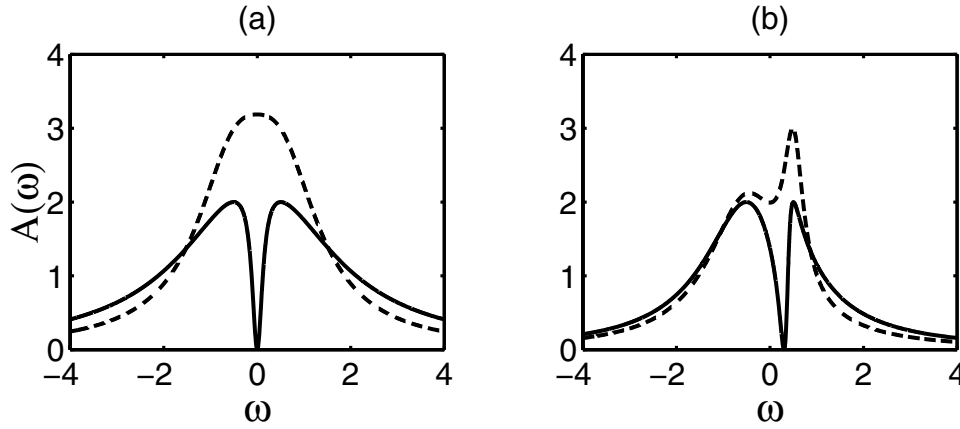


Fig. 6.21. The absorption spectra for $\kappa = 100$, $\delta = 0$, and $g_1 = g_2 = 10$ in (a), $g_1 = 10$, $g_2 = 5$ in (b), all quantities being measured in terms of Δ , ($\Delta = 1$). The *solid lines* represent the spectra with pre-selection of polarization (full quantum interference), and the *dashed lines* the spectra for no pre-selection (no quantum interference)

We give one example, the probe absorption spectrum, which is illustrated in Fig. 6.21 for the case $\kappa = 100$, $\Delta = 1$, $\delta = 0$, and $g_1 = g_2 = 10$ in frame (a), and $g_1 = 10$, $g_2 = 5$ in frame (b). The solid line is when pre-selection of polarization takes place, and the dotted for when it does not. (The cases of maximal and zero quantum interference respectively.)

6.4.5 Anisotropic Vacuum Approach

Agarwal [149] has proposed a totally different mechanism to produce correlations between two perpendicular dipole moments. In this method the interference between perpendicular dipole moments is induced by an anisotropic

vacuum field. Using second-order perturbation theory, it is shown that the transition probability from the ground state $|0\rangle$ of a four-level system to the final state $|f\rangle$ through two intermediate states $|i\rangle$ and $|j\rangle$ is given by

$$T_{gf} = \frac{1}{\hbar^2} \sum_{i,j} \Omega_i \Omega_j \frac{\boldsymbol{\mu}_{fj}^* \mathbf{C}(\omega_L - \omega_{f0}) \boldsymbol{\mu}_{fi}}{(\omega_{i0} - \omega_L)(\omega_{j0} - \omega_L)}, \quad (6.60)$$

where Ω_i is the Rabi frequency of the $|0\rangle \rightarrow |i\rangle$ transition, ω_L is the frequency of the driving laser, and $\mathbf{C}(\omega_L - \omega_{f0})$ is the Fourier transform of the tensor $\mathbf{C}(\tau)$, the anti-normally ordered correlation function of the vacuum field operators. The anisotropy of the vacuum enters through the tensor \mathbf{C} . With perpendicular dipole moments $\boldsymbol{\mu}_{fj}$ and $\boldsymbol{\mu}_{fi}$, the transition probability responsible for the quantum interference between the $|i\rangle \rightarrow |f\rangle$ and $|j\rangle \rightarrow |f\rangle$ transitions may be nonzero only if the tensor \mathbf{C} is anisotropic. For an isotropic vacuum the tensor \mathbf{C} is proportional to the unit tensor and then the transition probability vanishes if $\boldsymbol{\mu}_{fi}$ and $\boldsymbol{\mu}_{fj}$ are perpendicular.

Examples of systems which may exhibit an anisotropic vacuum are doped active centers on anisotropic glasses, atoms in a waveguide, atoms adsorbed on metallic or dielectric surfaces, and an atom between two conducting plates. Some results for the final case were presented in [149].

6.5 Fano Profiles

So far, we have only considered quantum interference in systems with discrete levels. Here we consider quantum interference in systems involving continua. The basic principles are the same as in the purely discrete systems we have considered heretofore, but the situation is complicated by the fact that we have to deal with the “dressing” of discrete states by the continuum.

We consider a discrete state $|b\rangle$ whose energy overlaps a band of continuum states. First of all, we neglect the interaction between them. A bare continuum state is denoted $|E\rangle$, with E being the bare energy. We have

$$H_0|b\rangle = E_b|b\rangle, \quad H_0|E\rangle = E|E\rangle, \quad (6.61)$$

where H_0 is the atomic Hamiltonian, neglecting the bound-continuum interaction. The adjective ‘bare’ has been added to emphasize that the interaction between states is neglected. The situation is depicted in Fig. 6.22. Usually, $|b\rangle$ is an autoionizing state.

Suppose now that there is an interaction V , such as the configuration interaction, connecting the discrete state to the continuum, so that we have the following matrix elements

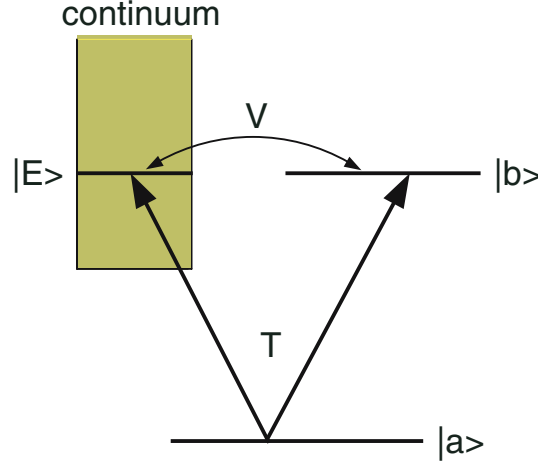


Fig. 6.22. The state $|b\rangle$ is embedded in the continuum by the interaction V . The resulting dressed state $|\Psi_\varepsilon\rangle$ is then probed by a weak laser connecting it to another bound state $|a\rangle$. In the bare picture, the probe interaction T couples $|a\rangle$ to both $|b\rangle$ and the continuum states $|E\rangle$

$$\langle b|H|b\rangle = E_b , \quad (6.62a)$$

$$\langle E'|H|b\rangle = V_{E',b} , \quad (6.62b)$$

$$\langle E'|H|E''\rangle = E'\delta(E'' - E') , \quad (6.62c)$$

where $H = H_0 + V$ is the full atomic Hamiltonian. We assume the eigenvectors of H to be of the form

$$|\Psi_\varepsilon\rangle = c_a(\varepsilon)|b\rangle + \int_0^\infty dE c_E(\varepsilon)|E\rangle , \quad (6.63)$$

where the real, continuous variable ε is the energy of the interacting system. Each energy value ε in the neighbourhood of E_b is an eigenvalue. The states $|\Psi_\varepsilon\rangle$ partake of the nature of the bound state and the continuum, and are often called dressed states, where the dressing is brought about by the discrete-continuum interaction. Substituting into the stationary Schrödinger equation

$$H|\Psi_\varepsilon\rangle = \varepsilon|\Psi_\varepsilon\rangle \quad (6.64)$$

and using the procedure of Fano [150], we find that the eigenvalues may be written in the form

$$|\Psi_\varepsilon\rangle = \frac{\sin \Delta}{\pi V_{\varepsilon,b}}|B\rangle - \cos \Delta|\varepsilon\rangle , \quad (6.65)$$

where

$$\tan \Delta = -\frac{\Gamma_b}{\varepsilon - \tilde{E}_b} , \quad (6.66a)$$

$$\tilde{E}_b = E_b + \mathcal{P} \int dE' \frac{V_{E',b}}{\varepsilon - E'} , \quad (6.66b)$$

$$|B\rangle = |b\rangle + \mathcal{P} \int dE' \frac{V_{E',b}}{\varepsilon - E'} |E'\rangle , \quad (6.66c)$$

$$\Gamma_b = \pi |V_{\varepsilon,b}|^2 . \quad (6.66d)$$

The quantity \tilde{E}_b is the energy of the state $|b\rangle$ shifted by its interaction with the continuum. The symbol \mathcal{P} indicates that the principal part is to be taken. Similarly, $|B\rangle$ is the state $|b\rangle$ modified by its interaction with the continuum.

We note that the coefficients in (6.65) may be expressed as

$$\frac{\sin \Delta}{\pi V_{\varepsilon,b}} = \frac{-V_{\varepsilon,b}^*}{\left[(\varepsilon - \tilde{E}_b)^2 + \Gamma_b^2\right]^{1/2}} , \quad (6.67a)$$

$$\cos \Delta = \frac{\varepsilon - \tilde{E}_b}{\left[(\varepsilon - \tilde{E}_b)^2 + \Gamma_b^2\right]^{1/2}} , \quad (6.67b)$$

which make explicit their strongly resonant nature as ε sweeps through the value \tilde{E}_b . The half-width of the resonance is $\Gamma_b = \pi |V_{\varepsilon,b}|^2$.

To summarize, the internal, atomic interaction V that connects the discrete atomic state $|b\rangle$ to the atomic continuum states gives rise to a shift in the energy of the discrete state and a dressing of it by the continuum. The original continuum states are also modified by V to produce the dressed state $|\Psi_\varepsilon\rangle$. The half-width of the structure in the continuum due to the embedding of the discrete state $|b\rangle$ is Γ_b .

Now we consider the effect of an additional, weak, applied field, described by an interaction Hamiltonian T , which connects another discrete state, $|a\rangle$, which has no energy overlap with the continuum, to the dressed state $|\Psi_\varepsilon\rangle$. This single route between $|a\rangle$ and the dressed continuum state $|\Psi_\varepsilon\rangle$ is equivalent to two interfering routes in the old, bare picture using the eigenstates of H_0 , as indicated by the arrows in Fig. 6.22. In effect, we have a kind of Vee system.

The relevant matrix element is

$$\langle \Psi_\varepsilon | T | a \rangle = \frac{\sin \Delta}{\pi V_{\varepsilon,b}^*} \langle B | T | a \rangle - \cos \Delta \langle \varepsilon | T | a \rangle . \quad (6.68)$$

There is a sharp variation in Δ as ε passes through the resonance at $\varepsilon = \tilde{E}_b$, which produces a sharp variation in $\langle \Psi_\varepsilon | T | a \rangle$. Since $\sin \Delta$ is an even function of $\varepsilon - \tilde{E}_b$ and $\cos \Delta$ an odd function, the two contributions on the right hand side of (6.68) interfere with opposite phase on the two sides of the transition.

It is apparent that the transition amplitude will vanish when $\varepsilon = \varepsilon_0$ is such that

$$\tan \Delta(\varepsilon_0) = \frac{\pi V_{\varepsilon_0,b}^* \langle \varepsilon_0 | T | a \rangle}{\langle B | T | a \rangle} \quad (6.69)$$

is satisfied. Introducing the Fano q factor by the relation

$$q = \frac{\langle B | T | a \rangle}{\pi V_{\varepsilon,b}^* \langle \varepsilon | T | a \rangle}, \quad (6.70)$$

we can express the ratio of the dressed and undressed transition probabilities as

$$R \equiv \frac{|\langle \Psi_\varepsilon | T | a \rangle|^2}{|\langle \varepsilon | T | a \rangle|^2} = \frac{(q + \eta)^2}{(1 + \eta^2)}, \quad (6.71)$$

where

$$\eta = \frac{\varepsilon - \tilde{E}_b}{\pi |V_{\varepsilon,b}|^2} \quad (6.72)$$

is a dimensionless energy variable.

The quantity R gives, when perturbation theory is valid, the enhancement in the probability of the transition induced by the weak probe field T due to the bound-continuum coupling V . We plot it as a function of η for the values $q = 0, 1, 2, 4$ and $q = 10, 20, 30$ in Fig. 6.23.

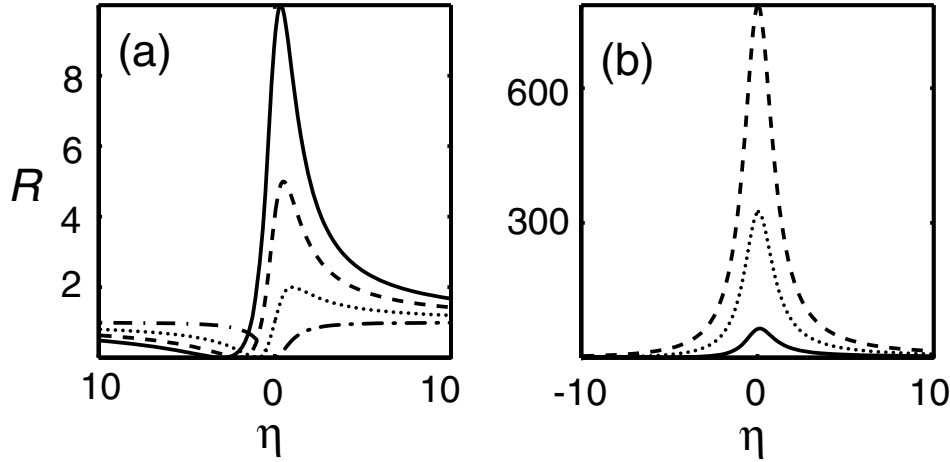


Fig. 6.23. (a): A plot of R against η for $q = 0$ (*dashed-dotted line*), $q = 1$ (*dotted line*), $q = 2$ (*dashed line*), and $q = 4$ (*solid line*). For negative values of q , the plot may be obtained by reflecting the above curves in the R axis. (b) The same but for $q = 10$ (*solid line*), $q = 20$ (*dotted line*), and $q = 30$ (*dashed line*)

When $q = 0$, the profile is symmetric, and flat except near $\eta = 0$. In general, the zero at $\eta = -q$ indicates complete quantum interference. For $q > 0$ there is destructive interference for negative η and constructive interference

for $\eta > 0$. (For $q < 0$, the interference is *constructive* for $\eta < 0$.) The magnitude of the peak increases rapidly with the value of q . The markedly asymmetric profile in Fig. 6.23 for $q \sim 1$ is referred to as the Fano profile, and similar profiles occur in a variety of situations involving continua. We note that as $q \rightarrow \infty$, the spectrum again becomes symmetric, as demonstrated in Fig. 6.23(b).

6.6 Laser-Induced Continuum Structure

In the previous section, we did not explicitly define the interaction V or T , and consequently, our analysis is quite general. In autoionization, the situation envisaged by Fano, V is the configuration interaction, caused by a residual electrostatic interaction between the electrons. The mixing of the bound state $|b\rangle$ and the continuum states $|E\rangle$ via V introduced a sharp structure into the continuum which enabled the interference phenomena discussed in the previous section.

In 1975, Armstrong, Beers and Feneuille [151] pointed out that structure could also be introduced into the continuum if the bound state $|b\rangle$ lay below the continuum threshold in energy, but was connected to a continuum state by a monochromatic laser of frequency ω_1 . Then V must be taken to be the atom-laser coupling Hamiltonian – usually the electric dipole interaction. The theory goes through in much the same way as in the last section, with the laser field treated quantum-mechanically and V interpreted as the atom-laser coupling. The situation is shown in Fig. 6.24. These laser-induced continuum resonances are directly analogous to autoionizing resonances and can be exploited in much the same way, but they have the advantage that they can be tuned in frequency, and their width varied, by altering the laser frequency or intensity. We first consider the situation where the probe field is weak so that perturbation theory may be applied.

6.6.1 Weak-Field Treatment

The treatment given here is fully analogous to that presented in the Sect. 6.5. For the moment, we ignore the lower bound atomic state $|a\rangle$ and the perturbation T , and consider just the single bound state $|b\rangle$ interacting with the continuum via the atom-laser interaction V . We treat the laser field quantum-mechanically, and we replace the bound state $|b\rangle$ of Fig. 6.22 by the composite atom-field state $|b'\rangle \equiv |b, n_1\rangle$ – the product of the bound state with the field state having n_1 photons in the laser mode of frequency ω_1 . The energy of this product state is $E_b + n_1 \hbar \omega_1$, and it is degenerate with the continuum state $|E'\rangle \equiv |E, n_1 - 1\rangle$, of energy $E' + (n_1 - 1) \hbar \omega_1$. The states $|b'\rangle$ and $|E'\rangle$ are analogous to the states $|b\rangle$ and $|E\rangle$ of Fig. 6.22. These two degenerate states may be mixed by the atom-field interaction V to form a state analogous to the state $|\Psi_\epsilon\rangle$ of (6.65). This situation is depicted in the figure in two

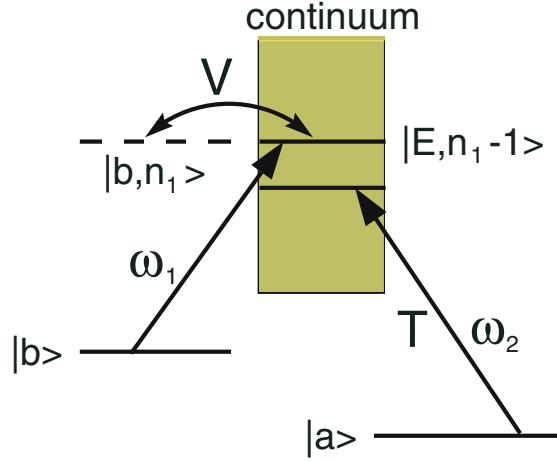


Fig. 6.24. Laser-induced continuum structure. The composite atom-field state $|b, n_1\rangle$ is embedded into the continuum by the atom-field interaction V . This structure is probed by a second laser connecting the atomic bound state $|a\rangle$ to the continuum via a second atom-field interaction T

ways. Firstly, as a transition from the atomic state $|b\rangle$ to the continuum state $|E\rangle$ by absorption of a single photon from the laser field, and secondly, as a mixing of the degenerate states $|b, n_1\rangle$ and $|E, n_1 - 1\rangle$ by the interaction V . (Henceforth, a prime on a ket vector denotes a composite atom-field state.)

We may use the results of the previous section to immediately write down the eigenfunctions of this system as

$$H'|\Psi'_\varepsilon\rangle = \varepsilon'|\Psi'_\varepsilon\rangle, \quad (6.73)$$

where $H' = H_A + V$, with H_A being the atomic Hamiltonian, V the atom-laser field interaction, and $\varepsilon' = \varepsilon + (n - 1)\hbar\omega_1$. With $|\varepsilon'\rangle \equiv |\varepsilon, n_1\rangle$, we have

$$|\Psi'_\varepsilon\rangle = \frac{\sin \Delta}{\pi V_{\varepsilon', b'}} |B'\rangle - \cos \Delta |\varepsilon'\rangle, \quad (6.74a)$$

$$\tan \Delta = -\frac{\pi |V_{\varepsilon', b'}|^2}{\varepsilon' - \tilde{E}'_b}, \quad (6.74b)$$

$$\tilde{E}'_b = E_{b'} + \mathcal{P} \int dE_1 \frac{V_{E'_1, b'}}{\varepsilon' - E'_1}, \quad (6.74c)$$

$$|B'\rangle = |b\rangle + \mathcal{P} \int dE_1 \frac{V_{E'_1, b'}}{\varepsilon' - E'_1} |E'_1\rangle. \quad (6.74d)$$

Now suppose that a second monochromatic laser of frequency ω_2 is applied to an atomic bound state $|a\rangle$ with the same parity as $|b\rangle$. To maintain consistency of notation with Sect. 6.5, we use T to denote the interaction between the atom and this second laser field. (See Fig. 6.24.) Consider the probability of a transition from the composite state $|a'\rangle \equiv |a, n_1 - 1, n_2\rangle$ to the dressed continuum of states $|\Psi'_\varepsilon\rangle$. In lowest order perturbation theory, this probability is proportional to the square of the following matrix element

$$\langle \Psi'_\varepsilon | T | a' \rangle = \frac{\sin \Delta}{\pi V_{\varepsilon', b'}^*} \langle B' | T | a' \rangle - \cos \Delta \langle \varepsilon' | T | a' \rangle . \quad (6.75)$$

We introduce the quantity q by analogy with (6.70) and use the assumed property $\langle b | T | a \rangle = 0$ to simplify the expression to

$$q \equiv \frac{\langle B' | T | a' \rangle}{\pi V_{b', \varepsilon'} T_{\varepsilon' a'}} = \frac{1}{\pi V_{b', \varepsilon'} T_{\varepsilon' a'}} \mathcal{P} \int dE_1 \frac{V_{b', E'_1} T_{E'_1, a'}}{\varepsilon' - E'_1} . \quad (6.76)$$

Written in this way, q is seen to be the ratio of the real and imaginary parts of the two-photon Rabi frequency which couples the state $|a\rangle$ to state $|b\rangle$ via the continuum

$$q = \text{Re}(\Omega_2) / \text{Im}(\Omega_2) , \quad (6.77)$$

where the two-photon Rabi frequency is defined by

$$\Omega_2 = \int dE_1 \frac{V_{b', E'_1} T_{E'_1, a'}}{\varepsilon' - E'_1 + i\alpha} , \quad \alpha = 0^+ . \quad (6.78)$$

In general, the integral over the continuum in (6.78) should be replaced by a sum over all discrete states and an integral over all continua.

There are two routes from the state $|a'\rangle$ to the dressed continuum states $|\Psi'_\varepsilon\rangle$ given by (6.75). The direct transition from $|a'\rangle$ to the bare continuum part of the wave function $|\Psi'_\varepsilon\rangle$ is represented by the final term, whilst the first term is the transition to the embedded state $|B'\rangle$, which proceeds indirectly via the bare continuum. The parameter q may also be viewed as the ratio of these matrix elements, multiplied by a factor to make it dimensionless.

6.6.2 Observation of Laser-Induced Structures

Laser-induced structures in photoionization were first observed by Heller et al. [152] in cesium. In the experiment, a circularly-polarized Nd:YAG laser was employed to embed the $8s^2S_{1/2}$ excited state into the continuum. A frequency-doubled tunable dye laser at $33,315 \text{ cm}^{-1}$ was employed as a probe laser to investigate the position of the laser-induced structure, using linearly polarized light, which may be regarded as an equal superposition of left (σ_-) and right (σ_+) circularly polarized light. The σ_+ component sees a structured continuum, whilst the σ_- component sees an unperturbed continuum, as Fig. 6.25 makes clear.

When the probe laser is tuned to the centre of the laser induced structure, the σ_+ light is strongly absorbed as a result of the q^2 enhancement predicted by the Fano formula (6.71), whereas the σ_- light shows no such enhancement. As a consequence, the plane of polarization of the probe beam will be rotated as the field propagates. If the probe laser is tuned to the zero in the Fano profile, the σ_+ light will not suffer any absorption. Thus, as the probe laser

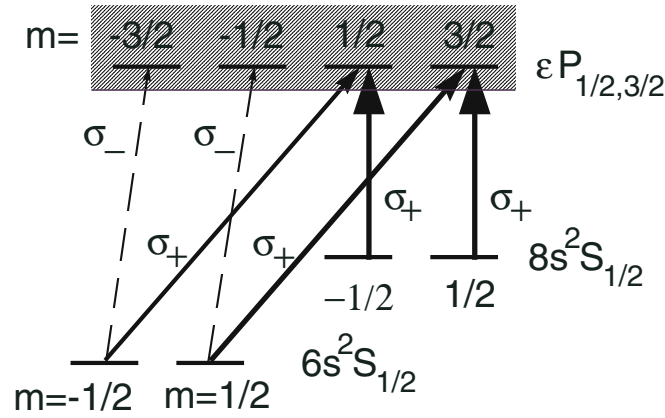


Fig. 6.25. An intense, circularly polarized dressing laser couples the magnetic sublevels of the $8s^2S_{1/2}$ bound state and the $\varepsilon P_{1/2,3/2}$ continuum in cesium. A weak, linearly polarized laser couples the magnetic sublevels of the $6s^2S_{1/2}$ and $8s^2S_{1/2}$ bound states. Treating the linearly polarized light as an equal superposition of left (σ_-) and right (σ_+) circularly polarized light, we see that the σ_+ probe field couples to the dressed continuum states and the σ_- probe field couples to the bare continuum states

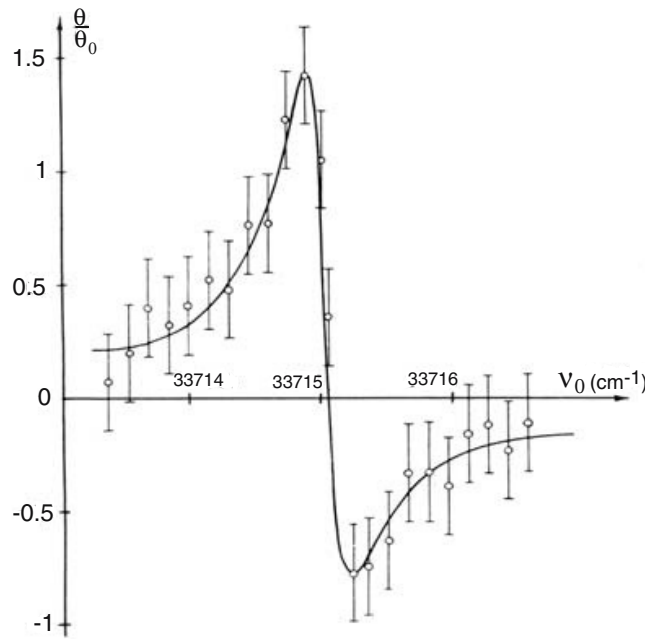


Fig. 6.26. The rotation of the polarization of the circularly polarized light used to probe the dressed continuum as a function of the probe detuning. From Y.I. Heller, V.I. Lukinykh, A.K. Popov, V.V. Slabko: Phys. Lett. **82A**, 4 (1981). Copyright (1981), with permission from Elsevier

is tuned through the zero, the polarization rotation angle will change sign, the rotation angle being zero at the Fano zero. The experimental results are shown in Fig. 6.26. Heller et al. [152] deduced a q value of about 6.8.

Laser-induced Fano resonances can be used to enhance the ultra-violet intensity in frequency up-conversion, just as autoionizing Fano resonances can. For example, such laser enhanced third harmonic generation has been observed in sodium vapour [153].

6.7 Nonperturbative Treatment of Laser-Induced Continuum Structure

In the previous section, we treated the interactions of the bound states $|b\rangle$ and $|a\rangle$ with the continuum in quite different ways. This is justified if the interaction V is strong and the interaction T is weak, but is inappropriate if the two interactions are of comparable magnitudes. In the latter situation, we can follow the approach of Fano [150] as applied the laser-induced structure situation by Coleman and Knight [154] and look for eigenstates of the full system of the form

$$H|\Phi_\varepsilon\rangle = \varepsilon|\Phi_\varepsilon\rangle, \quad (6.79)$$

with

$$|\Phi_\varepsilon\rangle = c_a|a\rangle + c_b|b\rangle + \int_0^\infty dE c_E|E\rangle, \quad (6.80)$$

in which both $|a\rangle$ and $|b\rangle$, and V and T , are treated on an equal footing. An arbitrary state $|\psi(t)\rangle$ of the system may then be expanded in terms of these eigenfunctions as

$$|\psi(t)\rangle = \int_0^\infty d\varepsilon A(\varepsilon)e^{-i\varepsilon t}|\Phi_\varepsilon\rangle, \quad (6.81)$$

where the expansion coefficients $A(\varepsilon)$ are determined from the initial conditions. Here, we shall assume the initial condition

$$|\psi(0)\rangle = |a\rangle. \quad (6.82)$$

The occupation probabilities for the bare states are then given by

$$P_k(t) = |\langle k|\psi(t)\rangle|^2, \quad k = a, b. \quad (6.83)$$

The usual ‘pole’ approximation is made in the calculation of induced shifts and decay rates, and non-Markovian threshold effects are ignored. It is convenient to introduce the notation \bar{E}_k to denote the the energy of the discrete level $|k\rangle$ with the dynamic Stark shift due to the laser coupling to the continuum included.

After some algebra, the following expressions are obtained for the occupation probabilities:

$$P_k(t) = |P_k(+)\mathrm{e}^{-\mathrm{i}\lambda_+t} - P_k(-)\mathrm{e}^{-\mathrm{i}\lambda_-t}|^2, \quad k = a, b, \quad (6.84)$$

where

$$P_a(\pm) = \frac{1}{2} [-\Delta_{b,a} + \mathrm{i}\pi (|V_{\varepsilon,b}|^2 - |T_{\varepsilon,a}|^2) \pm \Omega] / \Omega, \quad (6.85)$$

$$P_b(\pm) = \pi V_{a,\varepsilon} T_{\varepsilon,b} (q - \mathrm{i}) / \Omega. \quad (6.86)$$

Here, $\Delta_{b,a} = \bar{E}_b - \bar{E}_a$ is the detuning including the Stark shifts, Ω is the complex effective Rabi frequency

$$\Omega = \left\{ [\Delta_{b,a} - \mathrm{i}\pi (|V_{\varepsilon,b}|^2 - |T_{\varepsilon,a}|^2)]^2 + 4|V_{\varepsilon,b}T_{\varepsilon,a}|^2\pi^2(q - \mathrm{i})^2 \right\}^{\frac{1}{2}}, \quad (6.87)$$

and the eigenvalues λ_{\pm} are

$$\lambda_{\pm} = \frac{1}{2} [-\Delta_{b,a} - \mathrm{i}\pi (|V_{\varepsilon,b}|^2 + |T_{\varepsilon,a}|^2) \pm \Omega]. \quad (6.88)$$

The q factor employed here is the same as defined in (6.76).

In Fig. 6.27, we plot the populations of the initially occupied level $|a\rangle$ and the initially empty level $|b\rangle$ as functions of time, assuming the values $q = 5$, $T_{\varepsilon,a} = 5V_{\varepsilon,b}$ and $\Delta_{b,a} = 0$, and that the fields V and T maintain constant values after $t = 0$. We also plot the ionization rate $P_I(t) = 1 - P_a(t) - P_b(t)$. The figure shows that population is transferred periodically between the two ‘bound’ levels, with an overall decay in amplitude as population is lost by ionization. As population is transferred to $|b\rangle$ from $|a\rangle$, the ionization rate slows, because the ionization rate from $|a\rangle$ is 25 times greater than the ionization rate from $|b\rangle$. This is the origin of the obvious plateau in the ionization probability.

As in the conventional Lambda systems we have discussed elsewhere, population can be trapped in a coherent superposition state of levels $|a\rangle$ and $|b\rangle$, which is stable. Hence, $P_I(t \rightarrow \infty)$ need not be unity as may have been expected. The condition for population trapping is that at least one of the eigenvalues λ_{\pm} have zero imaginary part. (This corresponds to zero decay contributions to at least one of the exponentials in (6.86).) The condition may be shown to be

$$\Delta_{b,a} = \pi q (|V_{\varepsilon,b}|^2 - |T_{\varepsilon,a}|^2). \quad (6.89)$$

To see that this is so, we substitute (6.89) into (6.87) for Ω , when we find Ω becomes

$$\Omega = \pi(q - \mathrm{i})(|V_{\varepsilon,b}|^2 - |T_{\varepsilon,a}|^2). \quad (6.90)$$

Substituting this expression for Ω in (6.88) we see that the imaginary part of the eigenvalue λ_+ vanishes.

With the detuning satisfying (6.89), we find the following expressions for the steady-state populations

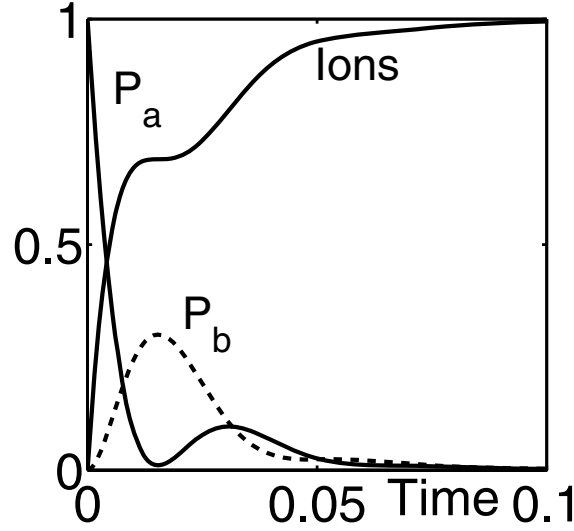


Fig. 6.27. The time-dependent populations of the initially populated level $|a\rangle$ and the initially empty level $|b\rangle$, calculated by treating both levels on an equal footing (i.e. non-perturbatively). The ionization probability is also shown. Here, $q = 5$, $T_{\varepsilon,a} = 5V_{\varepsilon,b}$ and $\Delta_{b,a} = 0$

$$P_a(t \rightarrow \infty) = \frac{q^2 |V_{\varepsilon,b}|^4 + |T_{\varepsilon,a}|^4}{(q^2 + 1)(|V_{\varepsilon,b}|^2 + |T_{\varepsilon,a}|^2)^2} , \quad (6.91a)$$

$$P_b(t \rightarrow \infty) = \frac{|V_{\varepsilon,b}|^2 |T_{\varepsilon,a}|^2}{(|V_{\varepsilon,b}|^2 + |T_{\varepsilon,a}|^2)^2} , \quad (6.91b)$$

$$P_I(t \rightarrow \infty) = \frac{q^2 |T_{\varepsilon,a}|^2 + |V_{\varepsilon,b}|^2}{(q^2 + 1)(|V_{\varepsilon,b}|^2 + |T_{\varepsilon,a}|^2)} . \quad (6.91c)$$

It is interesting to compare the above expressions with those for the corresponding Lambda system in which the set of continuum states is replaced by a single bound state, which we may label $|c\rangle$. The rest of the system is as shown in Fig. 6.24. Under two-photon resonance, population trapping occurs, and the steady-state populations of the two lower states are

$$P_a(t \rightarrow \infty) = \frac{|T_{c,a}|^4}{(|V_{c,b}|^2 + |T_{c,a}|^2)^2} , \quad (6.92a)$$

$$P_b(t \rightarrow \infty) = \frac{|V_{c,b}|^2 |T_{c,a}|^2}{(|V_{c,b}|^2 + |T_{c,a}|^2)^2} . \quad (6.92b)$$

Note that (6.91a) and (6.91b) reduce to (6.92) under the two opposite conditions $q \rightarrow 0$ and $q \rightarrow \infty$. Under these conditions, the Fano spectrum becomes symmetric. When q is very small, the time evolution of the bound state populations does not exhibit Rabi oscillations, whereas for q very large, the Rabi oscillations are extremely rapid.

The population trapping is illustrated in Fig. 6.28, where we assume the parameter values $q = 5$, $T_{\varepsilon,a} = V_{\varepsilon,b}$ and $\Delta_{b,a} = 0$. The population trapping

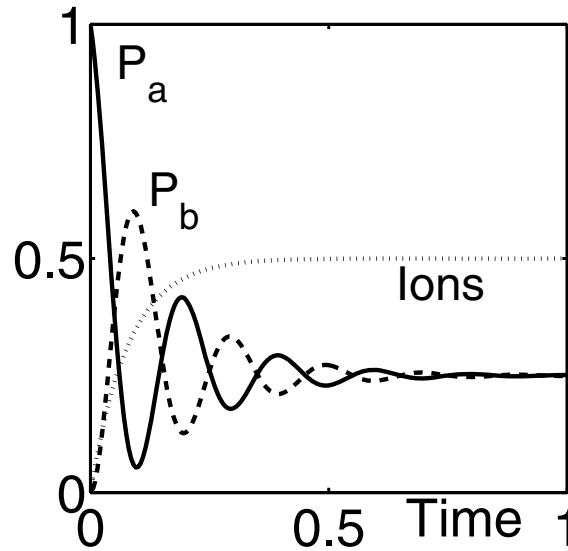


Fig. 6.28. The time-dependent populations of the initially populated level $|b\rangle$, the initially empty level $|a\rangle$, and the ionization probability, with $q = 5$, $T_{\varepsilon,a} = V_{\varepsilon,b}$ and $\Delta_{b,a} = 0$. Population trapping is demonstrated

in this two channel ionization system is clearly closely relation to the population trapping we have previously discussed in discrete Lambda systems. The reason for this is that the close coupling so structures the continuum that it behaves like a quasi bound state. The close similarity of (6.92) to the steady-state populations of the discrete Lambda model, (5.37), under two-photon resonance is obvious.

6.8 Quantum Interference in Photonic Bandgap Structures

There are very interesting quantum interference effects that can arise in spontaneous emission when atoms are imbedded in photonic bandgap structures [155, 156]. For example, for a two-level atom whose excited state lies in the band gap, it is found that the spontaneous emission does not exhibit a simple exponential decay, but also shows oscillations. A photon-atom bound state is produced, even when the atomic resonant frequency lies outside, but near, the gap. This bound state leads to trapping of the atomic population in the excited state. These features are due to the structured nature of the density of states available to the photon, in contrast with the essentially flat spectrum available for emission into free space.

It has been shown that in photonic bandgap structures, the propagation of light can be prohibited in all directions for some frequency range. The energy of the field can consequently be localized in a spatial region without propagating away. If we now consider an excited atom embedded in a photonic band-gap structure, it will create excitations in the forbidden band, which

will be localized field modes. The atom will interact with field modes in the propagating frequency bands as well as with those self-created ones in the forbidden band. It has been shown that for a two-level atom in this situation, population can be trapped in the upper level, even when the atomic transition frequency lies in the propagating band. The final state is a dressed state of the atom with a localized field mode of the forbidden band.

For a three-level atom, consisting of a ground state $|g\rangle$ and an excited state doublet $|e_1\rangle$ and $|e_2\rangle$, we may arrange for the transition $|g\rangle \rightarrow |e_1\rangle$ to lie near the band edge whilst the transition $|g\rangle \rightarrow |e_2\rangle$ lies well outside it. The spectrum of spontaneous emission on the latter transition displays a doublet, analogous to the Autler–Townes doublet observed in resonance fluorescence. In this case, however, there is no external field, and the splitting is due to the interaction between the atom and its own radiation field. The linewidth of one of the peaks can be much smaller than the natural linewidth of the transition $|g\rangle \rightarrow |e_2\rangle$. The spectral profile is reminiscent of the Fano profile, and exhibits a zero at the frequency corresponding to the difference between the gap edge and the atomic transition frequency. The spontaneous emission from this system also displays quasi-periodic oscillations in the populations of the two upper levels, which is due to quantum interference between the two transitions.

Here, we consider an idealized bandgap material in which the dispersion relation near the gap edge can be approximated by

$$\omega_k = \omega_c + M(k - k_0)^2, \quad (6.93)$$

where M and k_0 are constants. This is the so-called isotropic model. It gives rise to a density of states $\mathcal{D}(\omega)$ which is singular near the band-edge:

$$\mathcal{D}(\omega) = \frac{k^2}{\pi^2} \frac{dk}{d\omega} \propto (\omega_k - \omega_c)^{-\frac{1}{2}}. \quad (6.94)$$

A three-level atom, consisting of a ground state $|g\rangle$ and an excited state doublet $|+\rangle$ and $|-\rangle$, is embedded in this structure. The level structure is such that one excited state lies in the gap and the other outside it. The energies of the atomic states are $\hbar\omega_0$, $\hbar\omega_+$ and $\hbar\omega_-$ respectively, as shown in Fig. 6.29.

We study the spontaneous emission from this system when the atom is initially prepared in a superposition of the two upper levels. Analytic expressions can be obtained in the special case that the two upper levels $|+\rangle$ and $|-\rangle$ are displaced symmetrically either side of the band edge at ω_c by an amount Δ , and these two states are coupled by the vacuum interaction to the ground state with the same interaction strength v_k . We restrict our attention to this situation, and, after applying the rotating wave approximation at ω_c , consider the Hamiltonian

$$H/\hbar = \sum_k \left\{ \omega_{k,c} \hat{a}_k^\dagger \hat{a}_k + \left[i v_k \hat{a}_k^\dagger |g\rangle (\langle +| + \langle -|) + \text{H.c.} \right] \right\}, \quad (6.95)$$

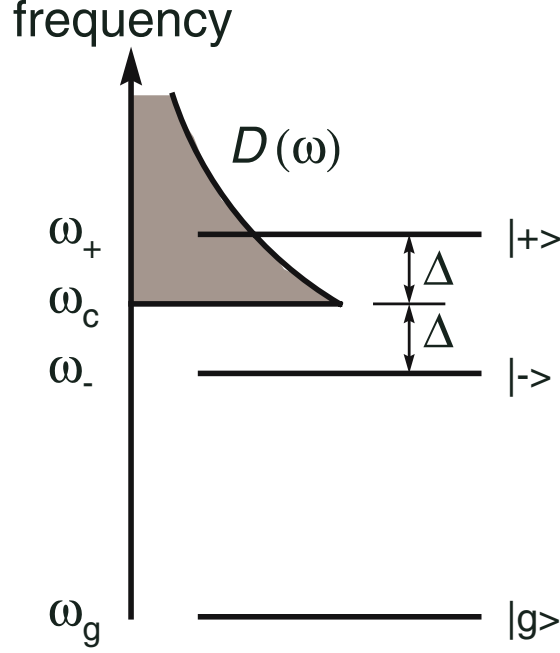


Fig. 6.29. A three-level atom embedded in an ideal photonic bandgap structure, whose density of states $\mathcal{D}(\omega)$ is shown shaded. We consider the case where the two upper levels $|+\rangle$ and $|-\rangle$ are displaced symmetrically either side of the band edge at ω_c by an amount Δ

where $\omega_{k,c} \equiv \omega_k - \omega_c$, and \hat{a}_k^\dagger is the creation operator for a photon in mode k . The first term is the Hamiltonian of the free, quantized vacuum field, and the second term describes the interaction of the atom with the vacuum modes. The state vector at an arbitrary time t is given by

$$|\psi(t)\rangle = \left[b_+(t)|+\rangle + b_-(t)|-\rangle + \sum_k b_k(t)|g\rangle \hat{a}_k^\dagger \right] |\{0\}\rangle, \quad (6.96)$$

where $|\{0\}\rangle$ is the state vector of the free vacuum. The first two terms in (6.96) denote the probability amplitudes for the atom to be found in the corresponding upper level with the field in its vacuum state, whilst the final term is the probability amplitude that the atom will be found in its ground state with one spontaneously emitted photon present in mode k .

The details of the method of the solution can be found in [155], but briefly the method is to substitute (6.96) into the Schrödinger equation, using (6.95), to obtain a set of coupled differential equations for the $b_j(t)$. These are converted to algebraic equations by using the Laplace transform

$$\tilde{b}(s) = \int_0^\infty dt b(t) e^{-st}, \quad (6.97)$$

and the system solved. The sum over wave-vectors is converted into an integral over k , making use of (6.93). This integral has to be evaluated exactly,

since the frequently employed ‘pole’, or Wigner–Weisskopf, approximation cannot be employed with such a rapidly varying photon density of states.

6.8.1 The Two-Level Atom

Before considering the three-level system, we discuss the properties of a two-level atom embedded in a photon bandgap structure [155]. To this end, we consider Fig. 6.29 and equations (6.95) and (6.96) but with the level $|-\rangle$ ignored. It is then straightforward to solve the Laplace transformed equations to obtain

$$\tilde{b}(s) = \left[s + \frac{\omega_+^2 \mu^2}{6\pi^2 \varepsilon_0 \hbar} \int \frac{k^2 dk}{\omega_k [s + i(\omega_k - \omega_+)]} \right]^{-1}, \quad (6.98)$$

where we have followed the usual procedure of replacing the sum over the field modes by an integral over the wave-vectors k .

For a slowly varying, broadband density of states, such as in free space, the pole approximation may be employed. This involves including only the contribution from the pole in the integrand of (6.98):

$$\lim_{s \rightarrow 0} \frac{1}{s + i(\omega_k - \omega_+)} = -i\mathcal{P} \frac{1}{\omega_k - \omega_+} + \pi\delta(\omega_k - \omega_+), \quad (6.99)$$

which yields

$$\tilde{b}(s) = [s + i\Lambda + \gamma/2]^{-1}, \quad (6.100)$$

where Λ and γ are the usual Lamb shift and spontaneous emission rate, respectively. The spontaneous decay is clearly purely exponential in this approximation.

For the rapidly varying density of states given by (6.93) the pole approximation cannot be applied, and an exact evaluation of the integral in (6.98) must be performed. The result is

$$\tilde{b}(s) = \frac{(s - i\Delta)^{1/2}}{s(s - i\Delta)^{1/2} - (i\beta)^{3/2}}, \quad (6.101)$$

where

$$\beta^{3/2} = \frac{\omega_+^{7/2} \mu^2}{6\pi \varepsilon_0 \hbar c^3}. \quad (6.102)$$

The inverse Laplace transform has the form [155]

$$b_+(t) = 2a_1x_1 \exp(\beta x_1^2 t + i\Delta t) + a_2(x_2 + y_2) \exp(\beta x_2^2 t + i\Delta t) - \sum_{j=1}^3 a_j y_j \left[1 - \operatorname{erf} \left(\sqrt{\beta x_j^2 t} \right) \right] \exp(\beta x_j^2 t + i\Delta t), \quad (6.103)$$

where the x_j are the roots of the polynomial $x(x^2 + i\Delta) - (i\beta)^{3/2} = 0$, $y_j = \sqrt{x_j^2}$, the a_j are the corresponding residues, and $\text{erf}(x)$ is the error function. For large βt , we note that the final term may be approximated as

$$\frac{\exp(i\Delta t)}{2\pi^{1/2}(\beta t)^{3/2}} \sum_{j=1}^3 \frac{a_j}{x_j^2} . \quad (6.104)$$

It can be inferred, providing $|\Delta|$ is not too large so that the energy level of $|+\rangle$ is not too far from the band edge, that β can be considered as a resonant energy splitting, analogous to the vacuum Rabi splitting of cavity quantum electrodynamics. The atomic level splits into dressed states caused by the interaction of the atom with its own radiation. They occur at frequencies $\omega_c - \theta\beta$ where $\theta \sim 1$. The terms giving rise to the splitting derive from the poles of (6.101). The branch point yields what has been called a ‘quasi-dressed’ state at the band-edge frequency ω_c . The quantum interference between the dressed and quasi-dressed states leads to oscillations in the spontaneous decay.

It can be shown that x_1^2 is pure imaginary. It therefore corresponds to a photon-atom dressed state with no decay. A photon emitted from this state will exhibit tunnelling on a length scale given by the localization length before being Bragg reflected back to the emitted atom. The presence of this stable dressed state means that population will be trapped in the excited state:

$$P_+(\infty) = \lim_{t \rightarrow \infty} |b_+(t)|^2 = 4|ax_1|^2 . \quad (6.105)$$

One level of the doublet is a localized state within the band gap, whereas the other is a resonance in the extended state continuum. The frequency of oscillations is determined by the magnitude of the atomic level splitting. These features are illustrated in Fig. 6.30(a), where $P_+(t) \equiv |b_+(t)|^2$ is shown for various values of Δ/β .

It is important to realize that the photon-atom bound state exists even when the atomic transition frequency ω_+ lies in the region where the density of states is nonzero – that is, outside the band gap. This feature is further illustrated in Fig. 6.30(b), where we plot the steady state population in the excited state, $P_+(\infty)$, as a function of Δ/β . It can be seen that the steady-state population is nonzero for detunings outside the band gap, although it tends to zero rapidly as the distance of the detuning from the band edge increases.

The nature of the dressed state can be examined by observing the spontaneous emission from this level to a third level, whose decay rate is γ_1 , which makes a Lambda configuration with the existing two levels. We suppose the transition frequency from $|+\rangle$ to this level, ω_+ , lies well outside the gap, so that the pole approximation may be employed to calculate the spontaneous emission on this transition. The expression for $\tilde{b}(s)$ is then modified to

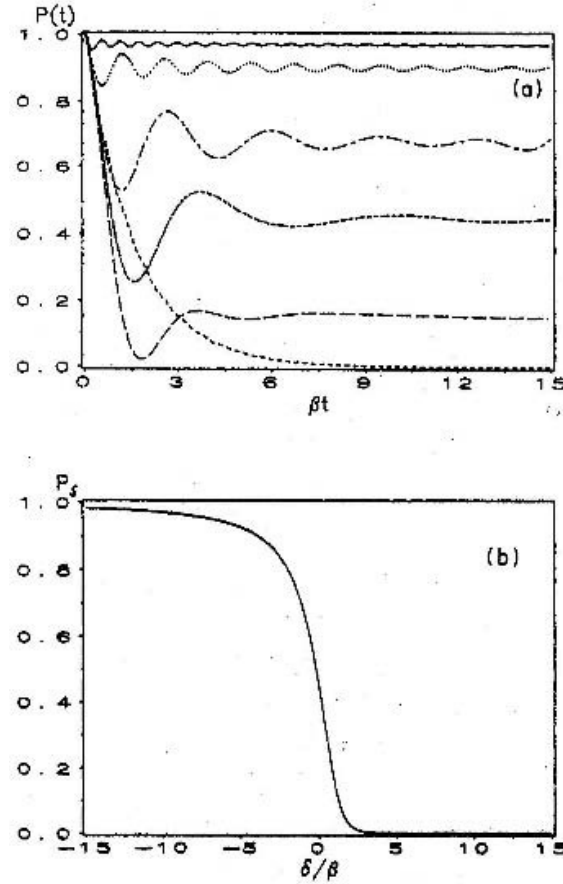


Fig. 6.30. (a) The atomic population in the excited state as a function of βt for the values of the detunings from the band edge of $\delta = -10\beta$ (solid line), $\delta = -4\beta$ (dotted line), $\delta = -\beta$ (long dash-short dash line), $\delta = 0$ (short dash line), $\delta = -4\beta$ (dotted line), $\delta = \beta$ (long dash line), and $\delta = 10\beta$ (short-dash line). (b) The steady-state excited state atomic population as a function of δ/β . From the paper of S. John, T. Quang: Phys. Rev. A **50**, 1764 (1994). Copyright (1994) by the American Physical Society

$$\tilde{b}(s) = \frac{(s - i\Delta)^{1/2}}{(s + \gamma_1/2)(s - i\Delta)^{1/2} - (i\beta)^{3/2}}. \quad (6.106)$$

The spectrum of spontaneous emission from $|+\rangle$ to this third level is given by

$$S(\nu) \sim |\tilde{b}(s = -i\nu)|^2, \quad (6.107)$$

where ν is the detuning from the transition frequency ω_+ . Examples of these spectra are shown in Fig. 6.31. For positive detunings Δ the curves exhibit markedly the effects of quantum interference, and are almost Fano-like, whereas for large positive detunings (the level $|+\rangle$ well away from the band edge) the spectrum is almost symmetric.

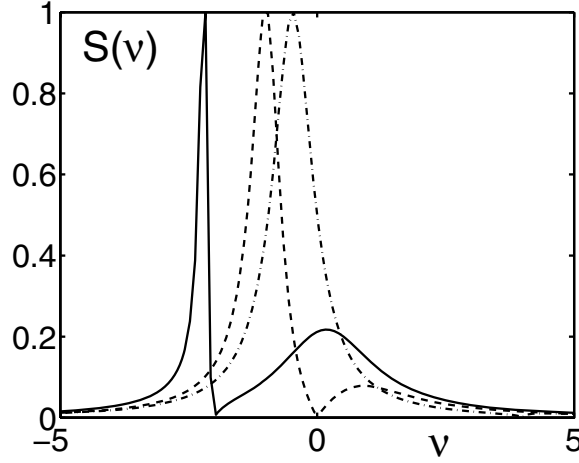


Fig. 6.31. The spontaneous emission spectrum from $|+\rangle$ to the third level, assuming $\beta = \gamma_1 = 1$, for $\Delta = 2$ (solid line), $\Delta = 0$ (dashed line), and $\Delta = -4$ (dot-dashed line)

6.8.2 The Three-Level Atom

Now we return to the study of the three level system shown in Fig. 6.29, in which both excited levels are close to the band gap, but equally displaced either side of the gap edge at ω_c . The Laplace-transformed equations for the upper-state amplitudes are easily solved to give:

$$b_{\pm}(s) = \frac{b_{\pm}(0)\sqrt{s}(s - i\Delta) \mp \delta b(0)(i\beta)^{3/2}}{\sqrt{s}(s^2 + \Delta^2) - 2s(i\beta)^{3/2}}, \quad (6.108)$$

where $\delta b(0) = b_+(0) - b_-(0)$, β is given by (6.102), and $\omega_0 = (\omega_+ + \omega_-)/2 - \omega_g$, with $\mu = \mu_{+g} = \mu_{-g}$ being the dipole moment of the transition $|g\rangle \rightarrow |\pm\rangle$.

The right-hand side of (6.108) contains four poles, $s_i = x_i^2$, $i = 1, 2, 3, 4$, corresponding to the roots of the equation

$$x^4 + \Delta^2 - 2x(i\beta)^{3/2} = 0. \quad (6.109)$$

These poles are located in the second, fourth, third and first quadrants of the complex plane, respectively.

Taking the inverse Laplace transform yields

$$b_{\pm}(t) = \sum_{i=1}^4 c_{\pm,i} \left[x_i + y_i \left(1 + \operatorname{erfc}(t\sqrt{x_i^2}) \right) \right] e^{x_i^2 t}, \quad (6.110)$$

where $\operatorname{erfc}(X) \equiv 1 - \operatorname{erf}(X)$ is the complementary error function, $c_{\pm,i}$ is the expansion coefficient corresponding to the pole x_i , and $y_i = x_i^2$. If x_i lies in the right half-plane, we have $y_i = x_i$, and if x_i is in the left half-plane, then $y_i = -x_i$, in order to keep the phase angle of x_i^2 within the range $-\pi$ to π .

The radiated electric field amplitude may be expressed as the sum of three terms:

$$E(r, t) \rightarrow I_1(t) + I_2(t) + I_3(t) \quad \text{as} \quad t \rightarrow \infty. \quad (6.111)$$

The first term, $I_1(t)$, describes a localized field. It arises from the x_4 term, and does not decay in time, although for large r its amplitude decays exponentially with distance as $\exp(-r/l_c)$, where $l_c = \sqrt{D}/|x_4|$. Its frequency, $(\omega_c - |x_4|^2)$ lies within the forbidden band, whilst its amplitude is proportional to $[1 - i\sqrt{\omega_c}/(kr|x_4|^2)]$, and tends to zero as Δ increases.

The second term, $I_2(t)$, stems from the x_2 pole, and describes an exponential pulse with phase velocity v_p and energy velocity v_e , where

$$v_p^{-1} = \left[1 + \text{Re} \left(\sqrt{ix_2^2/\omega_c} \right) \right] k_0/z_1, \quad (6.112)$$

$$v_e^{-1} = -\text{Im} \left(\sqrt{ix_2^2/\omega_c} \right) k_0/z_2, \quad (6.113)$$

with

$$\begin{aligned} z_1 &= \omega_c - \text{Im}(x_2^2), \\ z_2 &= -\text{Re}(x_2^2), \end{aligned} \quad (6.114)$$

and α is the frequency of the pulse that lies within the forbidden band. The energy velocity is much less than the speed of light in vacuum c and could be close to zero. The phase and amplitude propagation is proportional to $\exp[-i\alpha(t - r/v_p)] \exp[-z_2(t - r/v_e)]$.

The third part I_3 can only be evaluated approximately, for large βt . It contains only a phase propagating factor $\exp[-i(\omega_c t - k_0 r)]$. Unlike I_2 , it does not contain a factor such as $\exp[\eta(t - r/v)]$, which represents a wave travelling away from the origin. It represents a decaying field: at any fixed time, the amplitude of I_3 decreases exponentially with r , and at any fixed position, the amplitude decays with a factor $t^{-3/2}$.

The evolution of the atomic populations is influenced by the particular superposition state in which the atom is initially prepared, and by quantum interference between the two interaction channels. A study of the possible evolutions builds up a picture of how the energy is transferred between the atoms and the travelling wave and localized fields. Examples are shown in the following figures, which are taken from Zhu, Chen and Huang [156].

In Fig. 6.32, the population is initially in state $|+\rangle$. Quantum interference leads to the oscillating population transfer between levels $|+\rangle$ and $|-\rangle$ evident in the figure. The dominant decay follows a $(\gamma t)^{-1/2}$ law. The populations undergo many cycles before they settle down to their nonzero steady-state values – population trapping occurs. The large amplitude of the oscillations is due to the enhancement of quantum interference caused by the localized field. The energy in the decaying localized field, provided initially from the atom, is transferred back to the atom, and then becomes the energy of the travelling wave and the localized field. This accounts for the small value of V_g . For

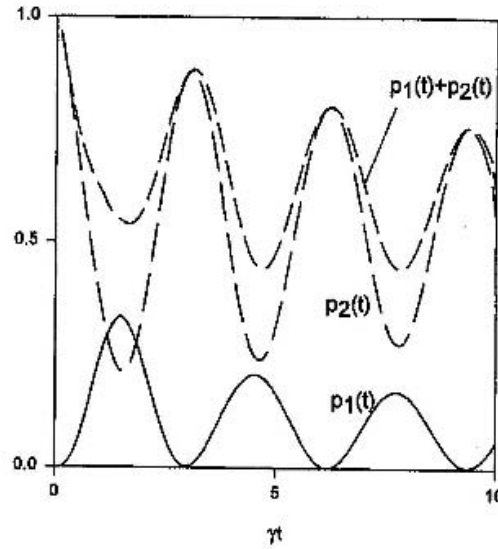


Fig. 6.32. Time evolution of the atomic populations for the atom in state $|+\rangle$ at $t = 0$, with $\Delta = \gamma$. The curves $p_1(t)$ and $p_2(t)$ are the populations of states $|+\rangle$ and $|-\rangle$, respectively. From the paper of S.-Y. Zhu, H. Chen, H. Huang: Phys. Rev. Lett. **79**, 205 (1997). Copyright (1997) by the American Physical Society

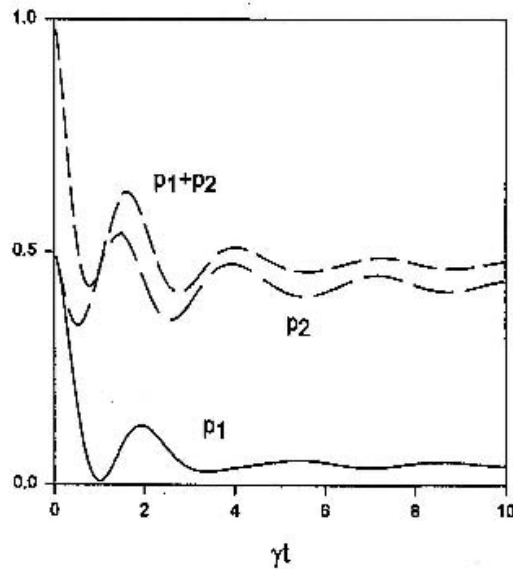


Fig. 6.33. The atomic populations for the initial state $2^{-1/2}(|+\rangle + |-\rangle)$ at $t = 0$, with $\Delta/\gamma = 1$. Notice the significantly different timescale for decay as compared with Fig. 6.32. From the paper of S.-Y. Zhu, H. Chen, H. Huang: Phys. Rev. Lett. **79**, 205 (1997). Copyright (1997) by the American Physical Society

the particular initial state illustrated in Fig. 6.33, it can be shown that the amplitude of the oscillations is a minimum, and that the population decays as $t^{-3/2}$ – the same law as for a two-level atom.

The proportion of population trapped in the upper levels depends upon the initial state. Population in the band gap level $|-\rangle$ may be transferred

to the transmitting band level $|+\rangle$, which can then emit the travelling wave. The final state contains an upper level part, and a lower level part with one photon in the localized mode.

Thus, in a photonic band gap material, the interference in the spontaneous emission of a three-level atom can be significantly enhanced, without the presence of the driving field that is essential in free space.

7 Slow and Fast Light and Storage of Photons

In Chap. 5 we have seen how coherent population trapping and electromagnetically induced transparency (EIT) can modify the absorptive properties of multi-level atoms. The basic manifestation of EIT is a significant reduction of light absorption in an atomic medium near a resonance transition frequency. Detailed analysis has shown that in the presence of a strong driving field an atomic system can establish frequencies at which the atomic absorption vanishes or may even be negative. This unusual effect results from the quantum coherence between two atomic transitions created by a strong driving field applied to one of the two transitions and a weak probe field applied to the other. The origin of these effects has been explained in terms of superposition states induced in a multi-level atom driven by two laser fields. One of these superpositions, referred to as the “coupled” or “bright” state, strongly interacts with the driving field, whereas the other superposition is completely decoupled from the interaction, and therefore is referred to as a “non-coupled” or “dark state”. The cancellation of the interaction results in zero absorption of the probe field, thereby allowing the field to propagate without attenuation. Another interesting property of EIT is that atoms prepared in a coherent superposition of their energy levels can produce a large, controllable index of refraction in frequency regions of vanishing absorption. A more important reason for interest in EIT is that the transparency is usually accompanied by a very fast variation of the refractive index with the frequency of the propagating light. The fast variation can result in a dramatic reduction of the group velocity of light, which can be viewed as temporary storage of light energy in the transparent medium. Carefully controlled, the slow group velocity of light might lead to a very efficient nonlinear interaction between laser fields of extremely low intensities, even down to the level of a single photon field. This property represents a significant difference from earlier single-photon interactions and has been suggested as a means to create quantum entanglement between single photons without an ultrahigh finesse cavity, and therefore is of great interest for quantum information processing. The field of applications of slow light is rich, and interesting proposals range from controllable optical delay lines and optical data storage to optical memories and fast optical switches.

In this chapter, we continue our study of the effect of EIT on the propagation of a weak probe field in an optically dense medium composed of a large number of multi-level atoms. First of all, we will be interested in the dispersive properties of a material system transparent to a propagating probe field. In particular, we will analyze the effect of EIT on spatial propagation and the possibility of slowing down the group velocity of the propagating probe field. We shall show that, associated with the transparency, is a very large variation (dispersion) of refractive index with probe frequency. When the dispersion is very steep and increases with increasing frequency (positive or normal dispersion), we can obtain a substantial reduction of the group velocity of the probe field. By reducing the group velocity in the presence of EIT, the probe field can travel slowly through the atomic medium without absorption and can even be brought to a full stop. In this process the probe field and, most importantly, its quantum state, can be completely transferred to the atomic system and stored in the form of quasi-particles called dark-state polaritons. The process can then be reversed, the stored quantum state can be transferred back to the field with perfect fidelity, and the light field regenerated. Another interesting property of an optically dense medium is that its dispersion can be prepared to be very steep and decreasing with increasing frequency (negative or anomalous dispersion). Negative-dispersion media have various odd properties. The group velocity for instance, can be greater than that of the velocity of light in vacuum. Moreover, under special conditions, the group velocity can even be negative. A negative group velocity corresponds to the case when the peak of a propagating field emerges from a medium before the same peak enters the medium.

7.1 Refractive Index and Group Velocity

In our discussion of the dispersion–absorption relation, we found it convenient to introduce the electric susceptibility of the medium. We have seen that the dispersive properties of an atomic system are determined by the real part of the susceptibility. We can relate the susceptibility to the measurable quantities such as refractive index and group velocity of the propagating field [157, 158].

A simple way to obtain the refractive index in terms of the susceptibility is to write the polarization in the direction z as

$$P(z, t) = \varepsilon_0 \chi(\omega_p) E(z, t) , \quad (7.1)$$

and next expand $\chi(\omega_p)$ around the center frequency ω_0 , which usually is equal to the transition frequency of the atoms composing the optical medium, or is equal to the frequency ω_L of an additional strong field driving the medium. Retaining terms up to those quadratic in $\Delta\omega = \omega_p - \omega_0$, we obtain the dispersive relation

$$\chi(\omega_p) = \chi_0 + \left. \frac{\partial \chi(\omega_p)}{\partial \omega_p} \right|_{\omega_p=\omega_0} \Delta\omega + \frac{1}{2} \left. \frac{\partial^2 \chi(\omega_p)}{\partial \omega_p^2} \right|_{\omega_p=\omega_0} \Delta\omega^2, \quad (7.2)$$

where $\chi_0 = \chi(\omega_0)$ is the susceptibility of the medium at the transition frequency. This dispersion relation can be used to obtain the propagation equation for the slowly-varying amplitude of the probe field.

Inserting the expansion of $\chi(\omega_p)$ into (7.1) and noting that

$$\begin{aligned} \Delta\omega \tilde{E}(z, t) &= i \frac{\partial \tilde{E}(z, t)}{\partial t}, \\ \Delta\omega^2 \tilde{E}(z, t) &= - \frac{\partial^2 \tilde{E}(z, t)}{\partial t^2}, \end{aligned} \quad (7.3)$$

where

$$\tilde{E}(z, t) = E(z, t) \exp(-i\omega_p t) \quad (7.4)$$

is the slowly varying amplitude of the field, we obtain

$$\begin{aligned} \tilde{P}(z, t) &= \varepsilon_0 \chi_0 \tilde{E}(z, t) + i\varepsilon_0 \left. \frac{\partial \chi(\omega_p)}{\partial \omega_p} \right|_{\omega_p=\omega_0} \frac{\partial \tilde{E}}{\partial t} \\ &\quad - \frac{1}{2} \varepsilon_0 \left. \frac{\partial^2 \chi(\omega_p)}{\partial \omega_p^2} \right|_{\omega_p=\omega_0} \frac{\partial^2 \tilde{E}}{\partial t^2}. \end{aligned} \quad (7.5)$$

In terms of this model, we can determine the group velocity of the propagating probe field and the group-velocity dispersion through the application of the propagation equation (5.74). On substituting (7.5) into (5.74), we obtain the following probe-field propagation equation

$$\frac{\partial \tilde{E}}{\partial z} + \left(\frac{\alpha}{2} - i\beta \right) \tilde{E} + \beta_1 \frac{\partial \tilde{E}}{\partial t} + \beta_2 \frac{\partial^2 \tilde{E}}{\partial t^2} = 0, \quad (7.6)$$

where $\alpha = (k/2)\text{Im}(\chi_0)$ is the absorption coefficient, and

$$\begin{aligned} \beta &= \frac{k}{2} \text{Re}(\chi_0), \\ \beta_1 &= \frac{1}{c} + \frac{k}{2} \left. \frac{\partial \chi(\omega_p)}{\partial \omega_p} \right|_{\omega_p=\omega_0}, \\ \beta_2 &= \frac{ik}{4} \left. \frac{\partial^2 \chi(\omega_p)}{\partial \omega_p^2} \right|_{\omega_p=\omega_0}. \end{aligned} \quad (7.7)$$

Let us examine the physical significance of the parameters β , β_1 , and β_2 . The parameters β_1 and β_2 have their origin in the frequency dependence of the propagation of the probe field. In particular, β_1 is related to the group velocity v_g by $\beta_1 = 1/v_g$, whereas β_2 is related to the frequency dependence of v_g as

$$\beta_2 = \frac{d}{d\omega_p} \left(\frac{1}{v_g} \right) . \quad (7.8)$$

For this reason, β_2 is called the group-velocity dispersion parameter. This parameter is responsible for the distortion of a pulse propagating through a dispersive medium. Since the transit time through a medium of length L is given by $T = L/v_g = L\beta_1$, the spread in transient times is given approximately by

$$\Delta T = L\Delta\beta_1 \simeq L\beta_2\Delta\omega , \quad (7.9)$$

where $\Delta\omega$ is a measure of the frequency bandwidth of the pulse. Thus, the propagating pulse broadens when $\beta_2 \neq 0$, and the shape of the pulse remains unchanged when $\beta_2 = 0$.

Using the plane-wave representation for the probe field, the propagation equation (7.6) leads to the dispersive relation

$$k = \frac{\omega_p}{c} \left[1 + \frac{1}{2}\text{Re}\chi_0 + \frac{\omega_p}{2}\text{Re} \left(\frac{\partial\chi(\omega_p)}{\partial\omega_p} \right)_{\omega_p=\omega_0} \right] - i \left[\frac{\alpha}{2} - \omega_p^2\text{Im}(\beta_2) \right] , \quad (7.10)$$

where the real part represents the refractive index and its dispersion, whereas the imaginary part represents the absorption rate and the group-velocity dispersion.

By writing $k = \omega_p/v_g$, we can analyze the group velocity normalized to the speed of light in vacuum as

$$\frac{c}{v_g} = n + \omega_p \frac{dn}{d\omega_p} , \quad (7.11)$$

where

$$n = 1 + \frac{1}{2}\text{Re}(\chi_0) \quad (7.12)$$

is the refractive index of the medium, and

$$\frac{dn}{d\omega_p} = \frac{1}{2}\text{Re} \left[\frac{\partial\chi(\omega_p)}{\partial\omega_p} \right]_{\omega_p=\omega_0} , \quad (7.13)$$

is the refractive-index dispersion. The medium dispersion can be positive (normal dispersion) or negative (anomalous dispersion). For normal dispersion the index of refraction increases with increasing frequency, whereas for anomalous dispersion the refractive index decreases with increasing frequency.

Equation (7.11) predicts the variation of group velocity with refractive index, and refractive-index dispersion. That is, the group velocity of a probe

field propagating in a medium can be significantly reduced when the refractive index is large and/or when the refractive-index dispersion is positive in the spectral region centered at $\omega_p = \omega_0$. In a driven atom, the refractive index usually remains nearly unity at the central frequency, $\text{Re}(\chi_0) = 0$. In this case, the group velocity can still be reduced. It happens when the refractive index dispersion is very steep and positive. It is also possible to have negative dispersion in the region of $\text{Im}(\chi_0) = \text{Re}(\chi_0) = 0$, which is characterized by a negative value of the second term on the right-hand side of (7.11). In Sect. 7.1.4, we present an example of an atomic system that can exhibit anomalous dispersion. According to (7.11), a strong negative (anomalous) dispersion leads to an increase in the group velocity that can even be greater than the speed of light in vacuum, c . In addition, a negative value of the second term in (7.11), larger than the first term n , gives a negative group velocity which implies that the probe field can travel backwards. In other words, a negative group velocity implies that the peak of the propagating probe pulse emerges from a material medium before the peak of the same pulse enters the medium. This counterintuitive situation has been observed experimentally, and some of the experiments will be discussed in Sect. 7.3. It should be mentioned here that in spite of the counterintuitive nature of propagation with a negative group velocity, there is no violation of the principle of causality. Propagation of a pulse with a negative group velocity is a result of interference within a wave-packet between spectral components of the pulse moving with the phase velocity $v_p = c/n$.

In the following sections, we present some examples of modified dispersive atomic media where the interesting effects of light guiding light and slow group velocities have been predicted and experimentally observed. We shall discuss the phenomenon of slow propagation in two schemes; a driven Lambda-type atom and a Vee-type atom with decay-induced coherences. In addition, we illustrate a scheme for phase control of group velocity that can produce superluminal velocities.

7.1.1 Light Guiding Light

Our examination of the dispersion–absorption relation in optical systems has thus far been confined to the simplest model of the atomic medium: two-level atoms. We now examine the dispersive and absorptive properties in three-level atoms. We first consider Vee-type atoms interacting with two external fields. One of the fields is a strong laser beam tuned to the $|0\rangle \rightarrow |2\rangle$ transition, and the other is a weak (probe) laser beam tuned to the $|0\rangle \rightarrow |1\rangle$ transition. The dipole moments of the atomic transitions are perpendicular to each other, and the transitions $|1\rangle \leftrightarrow |2\rangle$ are forbidden in the electric dipole approximation.

The master equation (2.72) for the Vee-type atom interacting with two laser fields leads to the following equations of motion for the density matrix elements

$$\begin{aligned}
\dot{\varrho}_{11} &= -\gamma_1 \varrho_{11} - \frac{1}{2} \Omega_p (\tilde{\varrho}_{10} + \tilde{\varrho}_{01}) , \\
\dot{\varrho}_{22} &= -\gamma_2 \varrho_{22} - \frac{1}{2} \Omega (\tilde{\varrho}_{02} + \tilde{\varrho}_{20}) , \\
\dot{\tilde{\varrho}}_{10} &= -\left(\frac{1}{2} \gamma_1 - i\delta_p\right) \tilde{\varrho}_{10} + \frac{1}{2} \Omega_p (\varrho_{11} - \varrho_{00}) + \frac{1}{2} \Omega \varrho_{12} , \\
\dot{\tilde{\varrho}}_{20} &= -\frac{1}{2} \gamma_2 \tilde{\varrho}_{20} + \frac{1}{2} \Omega_p \varrho_{12} + \frac{1}{2} \Omega (\varrho_{22} - \varrho_{00}) , \\
\dot{\varrho}_{12} &= -\left[\frac{1}{2} (\gamma_1 + \gamma_2) - i\delta_p\right] \varrho_{12} - \frac{1}{2} \Omega \tilde{\varrho}_{10} - \frac{1}{2} \Omega_p \tilde{\varrho}_{02} , \tag{7.14}
\end{aligned}$$

where γ_1 and γ_2 are the damping rates of the $|1\rangle \rightarrow |0\rangle$ and $|2\rangle \rightarrow |0\rangle$ transitions, respectively, Ω_p is the Rabi frequency of the probe field, $\delta_p = \omega_p - \omega_{10}$ is the detuning of the probe field from the $|1\rangle \leftrightarrow |0\rangle$ resonance, and

$$\tilde{\varrho}_{20}(t) = \varrho_{20}(t) \exp(i\omega_L t) , \quad \tilde{\varrho}_{10}(t) = \varrho_{10}(t) \exp(i\omega_p t) , \tag{7.15}$$

are the slowly varying parts of the off-diagonal density matrix elements. In the derivation of (7.14), we have assumed that the frequency of the driving field is on resonance with the $|0\rangle \rightarrow |2\rangle$ transition.

The equations of motion for the remaining off-diagonal density matrix elements ϱ_{21} , $\tilde{\varrho}_{02}$, and $\tilde{\varrho}_{01}$ are obtained from (7.14) by complex conjugation of the equations of motion for ϱ_{12} , $\tilde{\varrho}_{20}$, and $\tilde{\varrho}_{10}$, respectively.

We solve (7.14) in the steady-state, and find that to first order in Ω_p and equal damping rates $\gamma_1 = \gamma_2 = \gamma$, the stationary coherence $\tilde{\varrho}_{10}^{(-1)}$ is given by

$$\tilde{\varrho}_{10}^{(-1)} = -\Omega_p \frac{\gamma (2\gamma^2 + \Omega^2) - 2i\delta_p (\gamma^2 + \Omega^2)}{U(\omega_p)} , \tag{7.16}$$

where $U(\omega_p) = (\gamma^2 + 2\Omega^2) (2\gamma^2 + \Omega^2 - 4\delta_p^2 - 6i\gamma\delta_p)$.

Hence, the susceptibility of the atomic medium at the probe transition takes the form

$$\chi(\omega_p) = i \frac{2\mathcal{N}|\mu_{02}|^2}{\varepsilon_0 \hbar} \frac{\gamma (\gamma^2 + \Omega^2) - 2i\delta_p (\gamma^2 + \Omega^2)}{U(\omega_p)} . \tag{7.17}$$

We shall focus on the real part of the susceptibility, which determines the refractive index of the medium.

Figure 7.1 shows the refractive index as a function of the probe field frequency for different Rabi frequencies of the driving field. Depending on the frequency ω_p , the probe field can experience a refractive index greater or smaller than unity. In particular, a probe field tuned to the red of the resonance ($\omega_p < \omega_{10}$) will experience a refractive index greater than one, and vice versa, a probe tuned to the blue ($\omega_p > \omega_{10}$) will experience a refractive index smaller than one. In addition, the magnitude of $\chi(\omega_p)$ decreases with increasing Ω , causing a decrease in refractive index. Therefore, by creating a

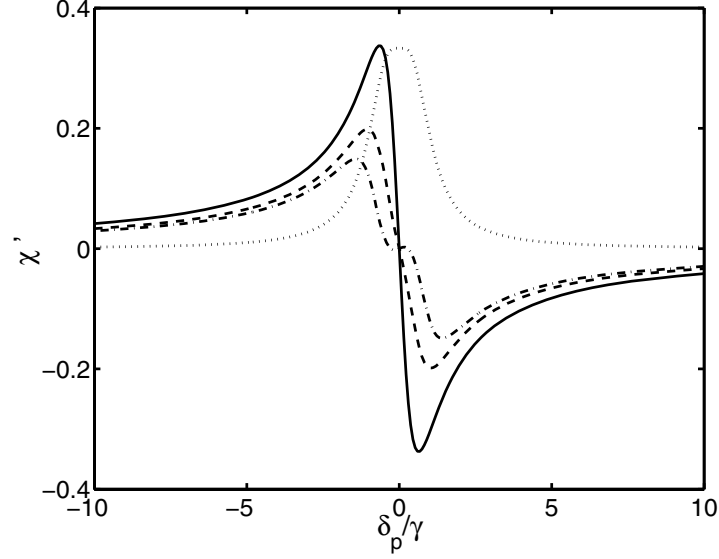


Fig. 7.1. The normalized real part of the susceptibility as a function of the probe field detuning δ_p for different Rabi frequencies of the driving field: $\Omega = 0.5\gamma$ (*solid line*), $\Omega = 1.0\gamma$ (*dashed line*), $\Omega = 1.5\gamma$ (*dashed-dotted line*). The dotted line shows the absorption rate for $\Omega = \gamma$

spatial transverse structure of the Rabi frequency of the driving field, e.g. a doughnut shaped structure such that Ω inside the doughnut is much smaller than along the ring, makes the refractive index dependent on the spatial coordinate of the propagating probe beam. The red detuned probe beam in the presence of the doughnut shaped driving field will see a local refractive index in the region of the doughnut ring smaller than in the central region, and therefore will tend to be refracted away from the strong field region.

Following this observation, Truscott et al. [159] experimentally demonstrated an optically written waveguide in an atomic vapor, showing that one of two fields applied to the vapor can be guided by the other. In the experiment, shown schematically in Fig. 7.2, they used rubidium vapor at temperature of 100°C placed inside a 10-cm-long cell. A weak Gaussian probe beam was tuned close to the rubidium D_2 line ($5^2S_{1/2} \rightarrow 5^2P_{3/2}$) of the wavelength 780 nm, while a strong doughnut shaped driving field was tuned to the rubidium D_1 line ($5^2S_{1/2} \rightarrow 5^2P_{1/2}$) of the wavelength 795 nm. The driving field was a Laguerre–Gaussian charge 3 doughnut beam, produced by illuminating a computer generated blazed phase hologram with a Ti-S laser. The Rabi frequency of such a beam is

$$\Omega = \frac{\Omega_0}{6\pi} \left(\frac{2r}{w^2(z)} \right)^3 \frac{1}{w^2(z)} \exp \left[-\frac{2r^2}{w^2(z)} \right], \quad (7.18)$$

where $w(z)$ is the beam width at a point z , r is the transverse radius of the beam, and Ω_0 is proportional to the power of the beam.

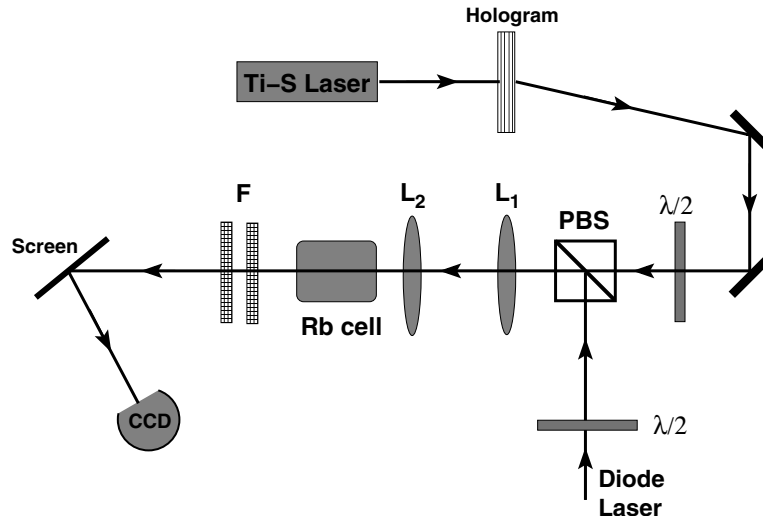


Fig. 7.2. Schematic diagram of the Truscott et al. [159] experiment to demonstrate the light guiding light effect in rubidium vapor

In the experiment, the driving and probe beams were combined using a polarization beamsplitter cube (PBS) and their intensities were adjusted using $\lambda/2$ plates. Two lenses L_1 and L_2 were used to bring both beams to a focus so that the probe beam was focused onto the entrance window of the cell, while the driving beam was focused into the center of the cell. The output field was sent into two 780 nm interference filters (F) to separate the probe beam from the driving beam. The image of the probe beam, observed on the screen, was recorded using a CCD camera.

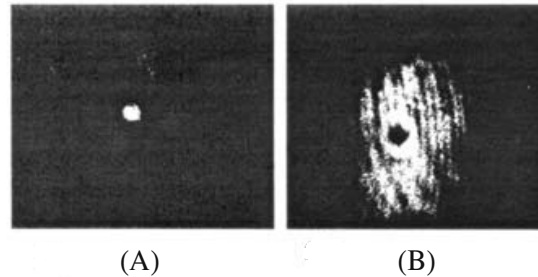


Fig. 7.3. Experimental results of Truscott et al. [159] showing the light guiding light effect in rubidium vapor. Frame (A) shows the image of the probe beam tuned to the red of the rubidium D_2 line, and frame (B) shows the image of the probe beam tuned to the blue of the rubidium line. From A.G. Truscott, M.E.J. Friese, N.R. Heckenberg, H. Rubinsztein-Dunlop: Phys. Rev. Lett. **82**, 1438 (1999). Copyright (1999) by the American Physical Society

The results of the experiment are shown in Fig. 7.3. Here, frame (A) shows an image of the probe beam tuned 2.5 GHz to the red of the rubidium D_2

resonance. The observed spot of the output probe beam is much smaller than the size of the input probe beam, which is clear evidence that the probe beam was guided into the dark center of the doughnut beam. Frame (B) shows an image of the probe beam tuned 3.8 GHz to the blue of the rubidium D₂ line. In this case, the probe beam was guided to the ring of the doughnut beam leaving a black spot at the center.

The experimental observation agrees perfectly with the above simple theoretical analysis involving a Vee-type energy-level system. A more extended explanation of the experimental results was provided by Kapoor and Agarwal [160]. A complete theoretical analysis of the experimental system involving all the rubidium D₁ and D₂ sublevels was presented by Andersen et al. [161].

7.1.2 Group Velocity Reduction in a Driven Lambda-Type Atom

We now turn our attention to the dispersive and absorptive properties of three-level atoms at resonant frequencies where both absorption and dispersion vanish due to the EIT. However, at these frequencies, the refractive-index dispersion can be nonzero, which leads to many interesting and unusual effects.

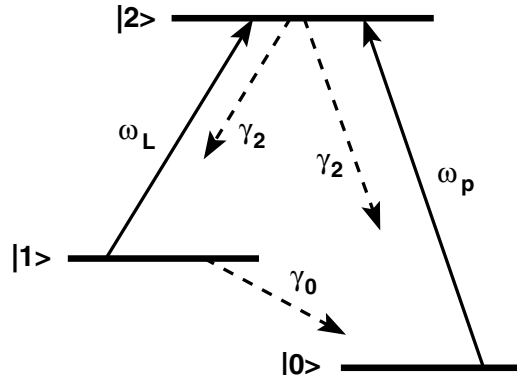


Fig. 7.4. Energy level diagram of a three-level Lambda system driven by a strong field of frequency ω_L and probed by a weak field of frequency ω_p . The lower state $|1\rangle$ is not metastable and decays with a rate γ_0

We first consider a Lambda-type atom where one of the two dipole allowed transitions is driven by a laser field of arbitrary intensity, whereas the other transition is probed by a weak tunable laser field. The dipole moments of the atomic transitions are taken to be perpendicular to each other, so there are no quantum interference effects due to spontaneous emission. In this system, quantum interference effects result from a quantum coherence between the atomic transitions induced by applying a strong driving field on one of the atomic transitions and a weak probe field coupled to the other transition.

Consider a scheme, proposed by Harris et al. [158] and shown in Fig. 7.4. A strong laser field of Rabi frequency Ω drives only the $|1\rangle \rightarrow |2\rangle$ transition, whereas a weak probe field is used to study the susceptibility associated with the $|0\rangle \rightarrow |2\rangle$ transition. The electric dipole moments of the atomic transitions are perpendicular to each other, and consequently each of the fields couples to only one of the atomic transitions. In contrast to the traditional EIT schemes, we will assume that the level $|1\rangle$ is not metastable and there is a small nonzero decay rate γ_0 from the lower state $|1\rangle$ to $|0\rangle$.

The master equation (2.72) for the Lambda-type atom driven by two coherent fields leads to the following equations of motion for the density matrix elements

$$\begin{aligned}
\dot{\varrho}_{22} &= -2\gamma_2\varrho_{22} - \frac{1}{2}\Omega(\tilde{\varrho}_{12} + \tilde{\varrho}_{21}) - \frac{1}{2}\Omega_p(\tilde{\varrho}_{02} + \tilde{\varrho}_{20}) , \\
\dot{\varrho}_{11} &= -\gamma_0\varrho_{11} + \gamma_2\varrho_{22} + \frac{1}{2}\Omega(\tilde{\varrho}_{12} + \tilde{\varrho}_{21}) , \\
\dot{\varrho}_{00} &= \gamma_0\varrho_{11} + \gamma_2\varrho_{22} + \frac{1}{2}\Omega_p(\tilde{\varrho}_{02} + \tilde{\varrho}_{20}) , \\
\dot{\tilde{\varrho}}_{21} &= -\frac{1}{2}(\gamma_0 + \gamma_2)\tilde{\varrho}_{21} + \frac{1}{2}\Omega(\varrho_{22} - \varrho_{11}) - \frac{1}{2}\Omega_p\tilde{\varrho}_{01} , \\
\dot{\tilde{\varrho}}_{20} &= -(\gamma_2 - i\delta_p)\tilde{\varrho}_{20} + \frac{1}{2}\Omega_p(\varrho_{22} - \varrho_{00}) - \frac{1}{2}\Omega\tilde{\varrho}_{10} , \\
\dot{\tilde{\varrho}}_{10} &= -\left(\frac{1}{2}\gamma_0 - i\delta_p\right)\tilde{\varrho}_{10} + \frac{1}{2}\Omega\tilde{\varrho}_{20} + \frac{1}{2}\Omega_p\tilde{\varrho}_{21} ,
\end{aligned} \tag{7.19}$$

where γ_2 is the damping rate of the $|2\rangle \rightarrow |0\rangle$ and $|2\rangle \rightarrow |1\rangle$ transitions, Ω_p is the Rabi frequency of the probe field, $\delta_p = \omega_p - \omega_{20}$ is the detuning of the probe field from the $|2\rangle \leftrightarrow |0\rangle$ resonance, and

$$\begin{aligned}
\tilde{\varrho}_{21}(t) &= \varrho_{21}(t) \exp(-i\omega_L t) , \\
\tilde{\varrho}_{20}(t) &= \varrho_{20}(t) \exp(-i\omega_p t) , \\
\tilde{\varrho}_{10}(t) &= \varrho_{10}(t) \exp(i(\omega_L - \omega_p)t) ,
\end{aligned} \tag{7.20}$$

are the slowly varying parts of the off-diagonal density matrix elements. In the derivation of (7.19), we have assumed that the frequency of the driving field is on resonance with the $|2\rangle \rightarrow |1\rangle$ transition.

Equations (7.19) represent the general interaction of a three-level Lambda-type atom with two laser fields. We look at the case of the steady state solutions of the equations of motion (7.19) when the probe field is much weaker than the driving field ($\Omega_p \ll \Omega$). We follow exactly the same technique we outlined in Sect. 5.5, and solve (7.19) in the steady state by decomposing the density matrix elements into the Fourier harmonics oscillating with frequencies $\pm l\delta_p$. According to (5.85), we only need the harmonic $\tilde{\varrho}_{20}^{(-1)}$ to find the susceptibility of the probe field.

We now focus on the steady-state coherence $\tilde{\varrho}_{20}^{(-1)}$ and find, after long but straightforward algebra, that to all orders in Ω and first order in Ω_p , the

stationary coherence is given by

$$\tilde{\rho}_{20}^{(-1)} = \frac{-\frac{1}{2}\Omega_p \left(\frac{1}{2}\gamma_0 - i\delta_p\right)}{D(\delta_p)}, \quad (7.21)$$

where $D(\delta_p) = \left(\frac{1}{2}\gamma_0 - i\delta_p\right)(\gamma_2 - i\delta_p) + \frac{1}{4}\Omega^2$.

Hence, the susceptibility of the atomic medium at the probe transition reads

$$\chi(\omega_p) = i \frac{\mathcal{N}|\mu_{02}|^2}{\varepsilon_0 \hbar} \frac{\left(\frac{1}{2}\gamma_0 - i\delta_p\right)}{D(\delta_p)}. \quad (7.22)$$

By taking the real and imaginary parts of $\chi(\omega_p)$ and the first and second derivatives of $\chi(\omega_p)$ over δ_p , we find the absorption rate of the medium, refractive index, refractive-index dispersion and group-velocity dispersion. These parameters are easily found from (7.22), and are given by

$$\begin{aligned} \chi' &= -\frac{\mathcal{N}|\mu_{02}|^2}{\varepsilon_0 \hbar} \frac{\left(\frac{1}{4}\gamma_0^2 + \delta_p^2 - \frac{1}{4}\Omega^2\right) \delta_p}{|D(\delta_p)|^2}, \\ \chi'' &= \frac{\mathcal{N}|\mu_{02}|^2}{\varepsilon_0 \hbar} \frac{\frac{1}{4}\gamma_0(\gamma_0\gamma_2 + \frac{1}{2}\Omega^2) + \gamma_2\delta_p^2}{|D(\delta_p)|^2}, \\ \frac{\partial\chi}{\partial\omega_p} &= \frac{\partial\chi}{\partial\delta_p} = \frac{\mathcal{N}|\mu_{02}|^2}{\varepsilon_0 \hbar} \frac{-\Upsilon^2 + \frac{1}{4}\Omega^2}{D^2(\delta_p)}, \\ \frac{\partial^2\chi}{\partial\omega_p^2} &= \frac{\mathcal{N}|\mu_{02}|^2}{\varepsilon_0 \hbar} \frac{2i[(\Upsilon + G)D(\delta_p) - \Upsilon G^2]}{D^3(\delta_p)}, \end{aligned} \quad (7.23)$$

where $\Upsilon = \left(\frac{1}{2}\gamma_0 - i\delta_p\right)$ and $G = (\gamma_0 + \gamma_2)/2 - 2i\delta_p$.

Equation (7.23) contains all the information about the dispersive and absorptive properties of the driven atom. At the atomic resonance, $\delta_p = 0$, and then the transmission depends only on the decay rate γ_0 . In the limit of $\gamma_0 = 0$, which is characteristic of the traditional EIT schemes, and at $\delta_p = 0$, both χ' and χ'' vanish indicating perfect transparency of the atomic medium: the probe field can propagate without absorption and refraction. Thus, at resonance, the refractive index is unity and the refractive-index dispersion term dominates in (7.11) leading to the possibility of observing a reduced group velocity of the propagating probe field. Another important property of the transparent medium is that on resonance the dispersion of the group velocity is zero, i.e. $\text{Re}(\partial^2\chi/\partial\delta_p^2) = 0$. This means that the probe field, if propagating as a pulse, will maintain its shape during the propagation. We may summarize as follows: in the limit of a large Rabi frequency of the driving field, a probe pulse can experience small loss, unity refractive index, slow group velocity, and zero group-velocity dispersion.

The predictions of this model are shown in Figs. 7.5, where we plot the real and imaginary parts of the susceptibility as a function of the probe field

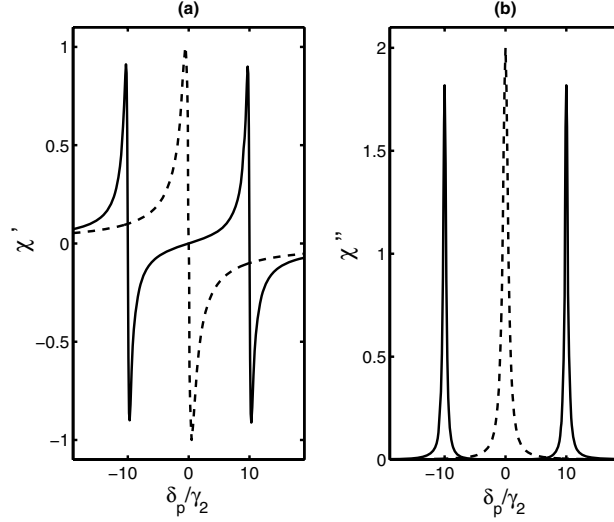


Fig. 7.5. (a) The real χ' and (b) the imaginary χ'' parts of the normalized linear susceptibility $\chi/(\mathcal{N}\mu_{20}^2/\varepsilon_0\hbar\gamma_2)$ as a function of δ_p for $\gamma_0 = 0.1\gamma_2$ and different Ω : $\Omega = 10\gamma_2$ (solid line), $\Omega = 0$ (dashed line)

detuning for two values of Ω . For $\Omega = 0$ the dispersion changes rapidly near $\delta_p = 0$, but in this frequency region the absorption is large. The properties of χ' and χ'' are dramatically different for $\Omega \neq 0$. In this case, the absorption vanishes at resonance, $\omega_p = \omega_{20}$. In addition, the dispersion χ' also vanishes at resonance indicating that at the central frequency, the system exhibits perfect transparency. In other words, at the central frequency, the probe field propagates without absorption and refraction and the refractive index remains nearly unity. However, near the central frequency the refractive-index dispersion is very steep and positive. This can lead to a reduction of the group velocity of the probe field.

Figure 7.6 shows the refractive-index dispersion $\text{Re}(\partial\chi/\partial\delta_p)$ as a function of the dimensionless detuning δ_p/γ_2 . We see that, depending on the frequency of the propagating probe field, the dispersion can be positive or negative, indicating that the group velocity can be smaller or larger than the speed of light in vacuum. For a positive dispersion, the group velocity of the probe field at frequency $\omega_p = \omega_{20}$ is given by

$$v_g = \frac{c}{1 + 2\omega_{20}|\mu_{20}|^2\mathcal{N}/(\varepsilon_0\hbar\Omega^2)} . \quad (7.24)$$

The group velocity depends on the Rabi frequency of the driving field and the atomic density. We see from (7.24) that one can make v_g smaller by decreasing the Rabi frequency or increasing the atomic density. In practice, the Rabi frequency should be sufficiently large to obtain a narrow transparency window and therefore a reduction of the group velocity is usually obtained by increasing the atomic density. There is an optimal Rabi frequency at which the group velocity reduction is maximal. It is seen from (7.23) that the

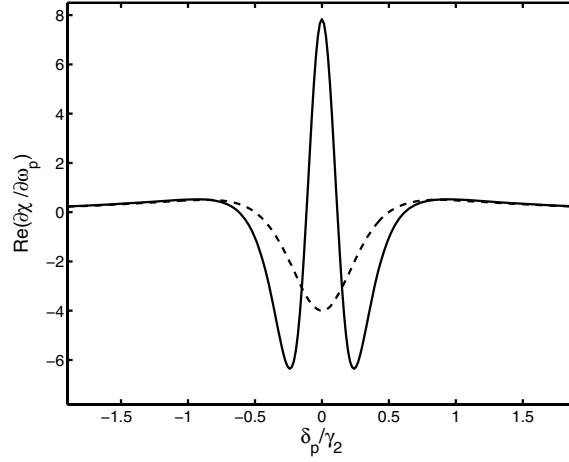


Fig. 7.6. The normalized refractive-index dispersion $\text{Re}(\partial\chi/\partial\delta_p)/(\mathcal{N}\mu_{20}^2/\varepsilon_0\hbar\gamma_2)$ as a function of δ_p for $\gamma_0 = 0.1\gamma_2$ and different Ω : $\Omega = 0.5\gamma_2$ (solid line), $\Omega = 0$ (dashed line)

derivative $\partial\chi/\partial\delta_p$ is maximal at $\delta_p = 0$ when $\Omega^2 = \gamma_0(2\gamma_0 + \gamma_2)$. Thus, group velocity reduction is limited by the relaxation rate of the lower state $|1\rangle$, and a reduction of γ_0 would allow very low group velocities to be reached.

Finally, we should point out that a number of other schemes for the generation of slow light have been investigated. These include four-level and even multi-level systems, some of which are modifications of the traditional scheme for slow group velocities.

7.1.3 Group Velocity Reduction in a System with Decay-Induced Coherences

For the example discussed in the previous section, the coherence between the atomic transitions was induced by the driving field. It is also possible to obtain slow light in a three-level system with the coherence induced by spontaneous emission. In this case, spontaneous emission in one of the atomic transitions can drive the other transition leading to quantum interference between the amplitudes of the atomic transitions. This interference creates a coherence between the atomic transitions, which is associated with the indistinguishability of photons arising from both transitions. We now investigate the effect of the spontaneously induced coherence on the group velocity in a three-level scheme proposed by Bortman-Arbiv et al. [162]. In this scheme, a three-level Vee-type atom with parallel transition dipole moments is probed by a weak tunable laser (pulse) field. The susceptibility of the system is calculated in the absence of driving fields: the only external field applied to the system is the probe field coupled to both atomic transitions. The absorption of the probe field in this system has been analyzed in Chap. 4, where we showed that the absorption spectrum exhibits ultranarrow transparency windows. We now examine the dispersive properties of the atom and show

that the transparency experienced by the probe field is accompanied by a steep linear and positive dispersion. As shown in Sect. 7.1, this property is the major factor in reducing the group velocity of the propagating field.

The master equation (2.74) for the Vee-type atom interacting with a single coherent (probe) field coupled to both atomic transitions leads to the following equations of motion for the density matrix elements

$$\begin{aligned}
\dot{\varrho}_{11} &= -\gamma_1 \varrho_{11} - \frac{1}{2} \gamma_{12} (\varrho_{12} + \varrho_{21}) - \frac{1}{2} \Omega_{p1} (\tilde{\varrho}_{01} + \tilde{\varrho}_{10}) , \\
\dot{\varrho}_{22} &= -\gamma_2 \varrho_{22} - \frac{1}{2} \gamma_{12} (\varrho_{12} + \varrho_{21}) - \frac{1}{2} \Omega_{p2} (\tilde{\varrho}_{02} + \tilde{\varrho}_{20}) , \\
\dot{\varrho}_{21} &= - \left[\frac{1}{2} (\gamma_1 + \gamma_2) + i\Delta \right] \varrho_{21} - \frac{1}{2} \gamma_{12} (\varrho_{22} + \varrho_{11}) - \frac{1}{2} \Omega_{p2} \tilde{\varrho}_{01} - \frac{1}{2} \Omega_{p1} \tilde{\varrho}_{20} , \\
\dot{\tilde{\varrho}}_{10} &= - \left[\frac{1}{2} \gamma_1 - i \left(\delta_p + \frac{1}{2} \Delta \right) \right] \tilde{\varrho}_{10} + \frac{1}{2} \Omega_{p1} (\varrho_{11} - \varrho_{00}) \\
&\quad + \frac{1}{2} \Omega_{p2} \varrho_{12} - \frac{1}{2} \gamma_{12} \varrho_{20} , \\
\dot{\tilde{\varrho}}_{20} &= - \left[\frac{1}{2} \gamma_2 - i \left(\delta_p - \frac{1}{2} \Delta \right) \right] \tilde{\varrho}_{20} + \frac{1}{2} \Omega_{p2} (\varrho_{22} - \varrho_{00}) \\
&\quad + \frac{1}{2} \Omega_{p1} \tilde{\varrho}_{12} - \frac{1}{2} \gamma_{12} \varrho_{10} ,
\end{aligned} \tag{7.25}$$

where γ_{12} is the cross-damping rate, defined in (2.45), Ω_{p1} and Ω_{p2} are the Rabi frequencies of the probed $|1\rangle - |0\rangle$ and $|2\rangle - |0\rangle$ transitions, respectively. The parameter $\delta_p = \omega_p - \omega_0$ is the detuning of the probe field frequency ω_p from the average frequency ω_0 of the two atomic dipole transitions, $\Delta = \omega_2 - \omega_1$ is the frequency splitting of the upper levels, and

$$\begin{aligned}
\tilde{\varrho}_{10} &= \varrho_{10} \exp(i\omega_p t) , & \tilde{\varrho}_{20} &= \varrho_{20} \exp(i\omega_p t) , \\
\tilde{\varrho}_{01} &= \varrho_{01} \exp(-i\omega_p t) , & \tilde{\varrho}_{02} &= \varrho_{02} \exp(-i\omega_p t) ,
\end{aligned} \tag{7.26}$$

are the slowly varying components of the atomic coherences.

As before, we solve the above equations in the steady-state and weak-field limits. For simplicity, we assume equal dipole moments of the atomic transitions, $\mu_{10} = \mu_{20} = \mu$. Then, $\gamma_1 = \gamma_2 = \gamma$, and $\Omega_{p1} = \Omega_{p2} = \Omega_p$. Since the probe field couples to both atomic transitions, the system responds at both atomic transition frequencies and then the susceptibility (5.85) is given by

$$\chi = -i \frac{\mathcal{N}}{\varepsilon_0 \mathcal{E}_p} \left(\mu_{01} \tilde{\varrho}_{10}^{(-1)} + \mu_{02} \tilde{\varrho}_{20}^{(-1)} \right) = -i \frac{\mathcal{N} \mu}{\varepsilon_0 \mathcal{E}_p} \left(\tilde{\varrho}_{10}^{(-1)} + \tilde{\varrho}_{20}^{(-1)} \right) , \tag{7.27}$$

where $\tilde{\varrho}_{01}^{(-1)}$ and $\tilde{\varrho}_{01}^{(-1)}$ are the steady-state values of the atomic coherences.

In the weak-field limit, the steady-state values for the atomic coherences can be readily found from (7.27), and then to lowest order in Ω_p , the linear susceptibility takes the form

$$\chi = \frac{\mathcal{N}|\mu|^2}{\varepsilon_0 \hbar} \frac{i(\gamma - \gamma_{12} - 2i\delta_p)}{D(\delta_p)}, \quad (7.28)$$

from which we find the first derivative over ω_p as

$$\frac{\partial \chi}{\partial \omega_p} = \frac{\mathcal{N}|\mu|^2}{\varepsilon_0 \hbar} \frac{-\gamma_a \left(\frac{1}{2}\gamma_a - 2i\delta_p \right) + 2\delta_p^2 + \frac{1}{2}\Delta^2}{D^2(\delta_p)}, \quad (7.29)$$

where

$$D(\delta_p) = \left[\frac{1}{2}\gamma - i \left(\delta_p + \frac{1}{2}\Delta \right) \right] \left[\frac{1}{2}\gamma - i \left(\delta_p - \frac{1}{2}\Delta \right) \right] - \frac{1}{4}\gamma_{12}^2, \quad (7.30)$$

and $\gamma_a = \gamma - \gamma_{12}$.

The solution (7.28) has been obtained assuming that the system is probed by a continuous laser field whose Rabi frequency is constant and independent of time. This solution can also be applied to a pulsed probe field whose Rabi frequency depends on time, subject the pulse being sufficiently long that the system reaches the steady-state before the pulse has died out. When such a pulse propagates in the medium, under the condition of steep and positive dispersion, its group velocity is significantly reduced.

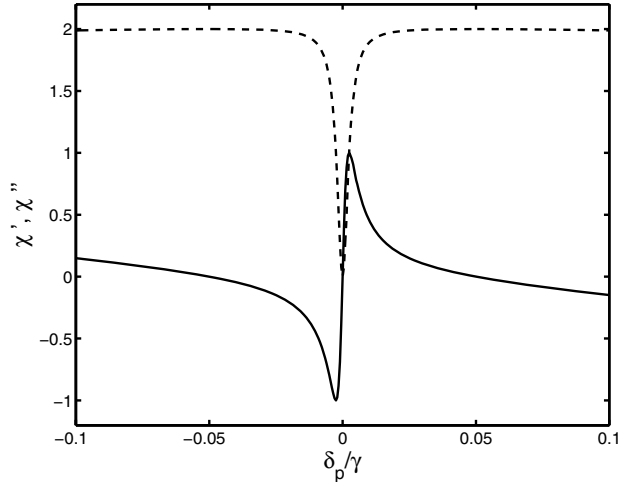


Fig. 7.7. The real χ' (solid line) and imaginary χ'' (dashed line) parts of the normalized linear susceptibility $\chi/(\mathcal{N}|\mu|^2/\varepsilon_0 \hbar \gamma)$ as a function of δ_p/γ for $\gamma_{12} = \gamma$ and $\Delta = 0.1\gamma$

We first analyze the absorptive and dispersive properties of the system. These are determined by the real and imaginary parts of χ , and are illustrated in Fig. 7.7 as a function of the dimensionless detuning δ_p/γ for $\Delta = 0.5\gamma$. Clearly, the system exhibits transparency ($\text{Im}(\chi) = 0$), and the dispersion is very steep and positive. In addition, $\text{Re}(\chi) = 0$ at $\delta_p = 0$ indicating that the refractive index is equal to unity at resonance. Thus, the probe field propagates in the medium without changing its amplitude and direction.

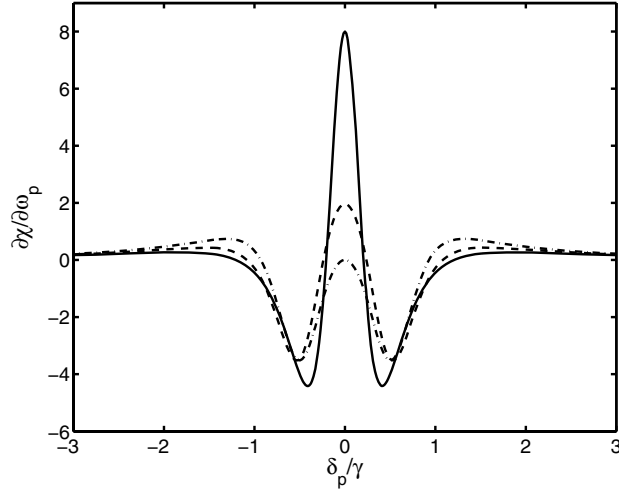


Fig. 7.8. The real part of the normalized refractive-index dispersion $(\partial\chi/\partial\omega_p)/(\mathcal{N}|\mu|^2/\varepsilon_0\hbar\gamma^2)$ as a function of δ_p/γ for $\Delta = \gamma$ and different γ_{12} : $\gamma_{12} = \gamma$ (solid line), $\gamma_{12} = 0.5\gamma$ (dashed line), $\gamma_{12} = 0$ (dashed-dotted line)

Figure 7.8 shows the corresponding behavior of the refractive-index dispersion $\text{Re}(\partial\chi/\partial\delta_p)$ which corresponds to the slope of the dispersion. The magnitude of the dispersion is large and positive near the resonance ω_0 , indicating that the group velocity can be significantly reduced at this frequency. It is interesting to note that the slope of the dispersion, and thus also the

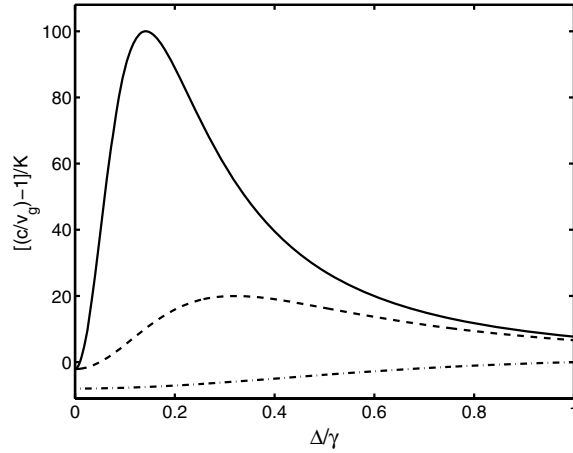


Fig. 7.9. The normalized group velocity parameter relative to the speed of light in vacuum $(c/v_g - 1)/K$, where $K = \omega_p\mathcal{N}|\mu|^2/(2\varepsilon_0\hbar\gamma^2)$ as a function of Δ for $\delta_p = 0$ and different γ_{12} : $\gamma_{12} = 0.99\gamma$ (solid line), $\gamma_{12} = 0.95\gamma$ (dashed line), $\gamma_{12} = 0$ (dashed-dotted line)

group velocity reduction, are very sensitive to the splitting Δ . The group velocity decreases as the splitting Δ increases. This is shown in Fig. 7.9, where we plot $(c/v_g - 1)$ as a function of Δ/γ for $\delta_p = 0$. This property can

be contrasted with the traditional EIT property where the Rabi frequency of the driving field, rather than Δ determines the group velocity reduction. This unusual dependence of the group velocity reduction on the splitting Δ can be easily understood by referring to the probe absorption spectrum discussed in Chap. 6. The width of the hole bored in the absorption spectrum is proportional to Δ^2 . Hence, the width of the dispersion is also proportional to Δ^2 . Thus, the slope of the dispersion decreases with increasing Δ leading to larger group velocities for larger Δ .

7.1.4 Phase Control of Group Velocity

As demonstrated in Chap. 4, spontaneous emission from a multi-level atom can be controlled not only by changing the mutual orientation of the atomic transition dipole moments, but also by changing the relative initial phases of driving laser fields applied for the excitation of the atom. Phase dependent effects in spontaneous emission have been predicted in atomic systems with nonorthogonal as well as with orthogonal transition dipole moments. In the first case the phase dependent effects, which arise from a spontaneously induced coherence between atomic transitions, can be observed with one or with two driving fields coupled simultaneously to all of the atomic transitions or to only some selected transitions. In the latter case the observation of phase dependent effects requires at least three driving fields. It is of particular interest to observe phase dependent effects, as they represent interference effects which can be induced by driving fields even in the absence of the vacuum induced quantum interference.

In this section, we shall take a closer look at the phase control of spontaneous emission as this effect can give rise to a wide range of behavior of the dispersion, ranging from absorptive to dispersive profiles with positive or negative slopes, leading to subluminal or superluminal group velocities. Our examination of the phase control of the group velocity through a variation of the initial relative phase of the driving fields follows the treatment of Bortman-Arbiv et al. [162] and concentrates on the example of a Vee-type atom with nondegenerate transition frequencies and non-orthogonal transition dipole moments. The atomic dipole transitions are driven by two lasers of equal angular frequencies but different polarizations and phases such that each laser couples to only one of the two dipole allowed atomic transitions. The laser fields are treated as weak perturbing fields such that saturation effects and ac Stark shifts (Rabi splittings) are neglected.

The external field interacting with the atom is of the form

$$\begin{aligned} \mathbf{E}(\mathbf{r}, t) &= \mathbf{E}_1(\mathbf{r}) \exp[-i(\omega_L t + \phi_1)] + \mathbf{E}_2(\mathbf{r}) \exp[-i(\omega_L t + \phi_2)] \\ &= \left[\mathbf{E}_1(\mathbf{r}) + \mathbf{E}_2(\mathbf{r}) e^{-i\delta\Phi} \right] \exp[-i(\omega_L t + \phi_1)] , \end{aligned} \quad (7.31)$$

where $\delta\Phi = \phi_2 - \phi_1$ is the relative (time independent) phase between the two components of the driving field.

The relevant equations of motion for the density matrix elements are derived from the master equation (2.74). Introducing slowly varying parts of the density matrix elements

$$\begin{aligned}\tilde{\varrho}_{10} &= \varrho_{10} \exp [i (\omega_p t + \phi_1)] , \\ \tilde{\varrho}_{20} &= \varrho_{20} \exp [i (\omega_p t + \phi_2)] , \\ \tilde{\varrho}_{21} &= \varrho_{21} \exp (i\delta\Phi) ,\end{aligned}\tag{7.32}$$

we find from the master equation the following equations of motion

$$\begin{aligned}\dot{\varrho}_{11} &= -\gamma_1 \varrho_{11} - \frac{1}{2} \gamma_{12} \left(\tilde{\varrho}_{12} e^{i\delta\Phi} + \tilde{\varrho}_{21} e^{-i\delta\Phi} \right) - \frac{1}{2} \Omega_1 (\tilde{\varrho}_{01} + \tilde{\varrho}_{10}) , \\ \dot{\varrho}_{22} &= -\gamma_2 \varrho_{22} - \frac{1}{2} \gamma_{12} \left(\tilde{\varrho}_{12} e^{i\delta\Phi} + \tilde{\varrho}_{21} e^{-i\delta\Phi} \right) - \frac{1}{2} \Omega_2 (\tilde{\varrho}_{02} + \tilde{\varrho}_{20}) , \\ \dot{\varrho}_{21} &= - \left[\frac{1}{2} (\gamma_1 + \gamma_2) + i\Delta \right] \tilde{\varrho}_{21} - \frac{1}{2} \gamma_{12} e^{i\delta\Phi} (\varrho_{22} + \varrho_{11}) \\ &\quad - \frac{1}{2} \Omega_2 \tilde{\varrho}_{01} - \frac{1}{2} \Omega_1 \tilde{\varrho}_{20} , \\ \dot{\varrho}_{10} &= - \left[\frac{1}{2} \gamma_1 - i \left(\delta_p + \frac{1}{2} \Delta \right) \right] \tilde{\varrho}_{10} + \frac{1}{2} \Omega_1 (\varrho_{11} - \varrho_{00}) \\ &\quad + \frac{1}{2} \Omega_{p2} \tilde{\varrho}_{12} - \frac{1}{2} \gamma_{12} \tilde{\varrho}_{20} e^{-i\delta\Phi} , \\ \dot{\varrho}_{20} &= - \left[\frac{1}{2} \gamma_2 - i \left(\delta_p - \frac{1}{2} \Delta \right) \right] \tilde{\varrho}_{20} + \frac{1}{2} \Omega_2 (\varrho_{22} - \varrho_{00}) \\ &\quad + \frac{1}{2} \Omega_1 \tilde{\varrho}_{21} - \frac{1}{2} \gamma_{12} \tilde{\varrho}_{10} e^{i\delta\Phi} ,\end{aligned}\tag{7.33}$$

where $\delta_p = \omega_p - \omega_0$, $\Delta = \omega_2 - \omega_1$, and Ω_1 (Ω_2) is the Rabi frequency of the $|1\rangle \rightarrow |0\rangle$ ($|2\rangle \rightarrow |0\rangle$) transition.

Note that the cross-damping terms are accompanied by the phase-dependent terms, $\exp(\pm i\delta\Phi)$. In other words, phase control of the atomic dynamics is only possible in the presence of the vacuum induced coherence, $\gamma_{12} \neq 0$. This dependence represents a striking departure from the traditional studies of absorption and dispersion, and will lead of course to some interesting phenomena.

Following the Floquet method outlined in Sect. 5.5, we analyze the absorptive and dispersive properties of the system at the transition frequencies ω_1 and ω_2 . These are determined by the coherences $\tilde{\varrho}_{10}$ and $\tilde{\varrho}_{20}$, which we find by solving the equations of motion (7.33) in the steady-state and the weak-field limits. After some algebra, we find

$$\tilde{\varrho}_{10} = -\Omega_1 \frac{[\gamma_2 - 2i(\delta_p - \frac{1}{2}\Delta)] - \tilde{\Omega} \gamma_{12} \exp(i\delta\Phi)}{[\gamma_1 - 2i(\delta_p + \frac{1}{2}\Delta)] [\gamma_2 - 2i(\delta_p - \frac{1}{2}\Delta)] - \gamma_{12}^2} ,\tag{7.34}$$

and

$$\tilde{\varrho}_{20} = -\Omega_1 \frac{\tilde{\Omega} [\gamma_1 - 2i(\delta_p + \frac{1}{2}\Delta)] - \gamma_{12} \exp(-i\delta\Phi)}{[\gamma_1 - 2i(\delta_p + \frac{1}{2}\Delta)] [\gamma_2 - 2i(\delta_p - \frac{1}{2}\Delta)] - \gamma_{12}^2}, \quad (7.35)$$

where $\tilde{\Omega} = \Omega_2/\Omega_1$.

We first find from (7.34) the condition for the phase difference which gives zero absorption and dispersion at $\delta_p = 0$ that is, $\text{Im}(\chi_{10}) = 0$ and $\text{Re}(\chi_{10}) = 0$, where

$$\chi_{10} = \frac{-i\mathcal{N}\mu_{10}}{\varepsilon_0\mathcal{E}_1} \tilde{\varrho}_{10}^{(-1)}. \quad (7.36)$$

Under this condition, a weak probe field can propagate nearly unchanged. The dispersion $\text{Re}(\chi_{10})$ is zero when the phase difference obeys the relation

$$\delta\Phi = \arcsin \left[\left(\frac{2\tilde{\Omega}\Delta}{\gamma_{12}} \right) \frac{\gamma_2}{\gamma_1 + \gamma_2} \right]. \quad (7.37)$$

In the case of $\gamma_1 = \gamma_2$ and $\Omega_{p1} = \Omega_{p2}$, it simplifies to

$$\delta\Phi = \arcsin \left(\frac{\Delta}{\gamma_{12}} \right), \quad (7.38)$$

which shows that the phase difference required for an undisturbed propagation of a probe field is determined solely by the internal parameters of the specific system. Thus, by an appropriate choice of the phases of the probe fields, we can efficiently control the behavior of absorption and dispersion and thus the propagation of the probe field.

Figure 7.10 shows the real and imaginary parts of the susceptibility χ that determine the dispersive and absorptive properties of the system. The behavior of the susceptibility is seen to be qualitatively different from the traditional EIT schemes. At the central frequency, the slope of the dispersion can switch from a positive to a negative value as the phase difference changes. This can result in a change of the group velocity of the propagating probe field from subluminal to superluminal.

With a different choice of the phases, one can create much steeper positive dispersions, and consequently smaller group velocities, accompanied by an amplification of the probe field. This feature is shown in Fig. 7.11, where we plot χ' and χ'' for two different values of $\delta\Phi$. The gain features are observed at $\delta_p = 0$ and the slope of the positive dispersion increases with increasing amplification.

The results clearly demonstrate the crucial role of phase control in determining probe propagation. They also demonstrate that subluminal propagation without changing the shape of the probe field is only possible if the phase difference between the two probe fields satisfies certain conditions imposed by the internal properties of the atomic system. In addition, the superluminal propagation is accompanied by a large absorption.

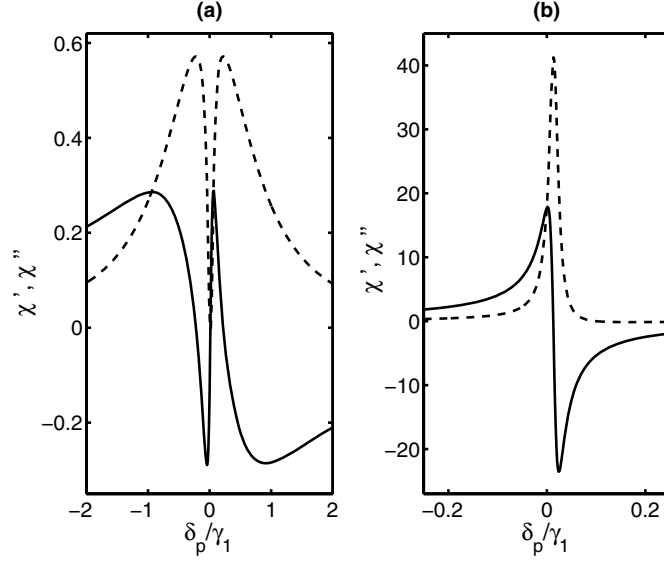


Fig. 7.10. The real χ' (*solid line*) and imaginary χ'' (*dashed line*) parts of the normalized linear susceptibility $\chi/(\mathcal{N}\mu^2/\varepsilon_0\hbar\gamma_1)$ as a function of δ_p/γ_1 for $\gamma_2 = 0.75\gamma_1$, $\tilde{\Omega} = \gamma_1$, and (a) $\gamma_{12} = 0.89\sqrt{\gamma_1\gamma_2}$ and $\delta\Phi$ satisfying the condition (7.37), (b) $\gamma_{12} = \sqrt{\gamma_1\gamma_2}$ and $\delta\Phi = \pi$

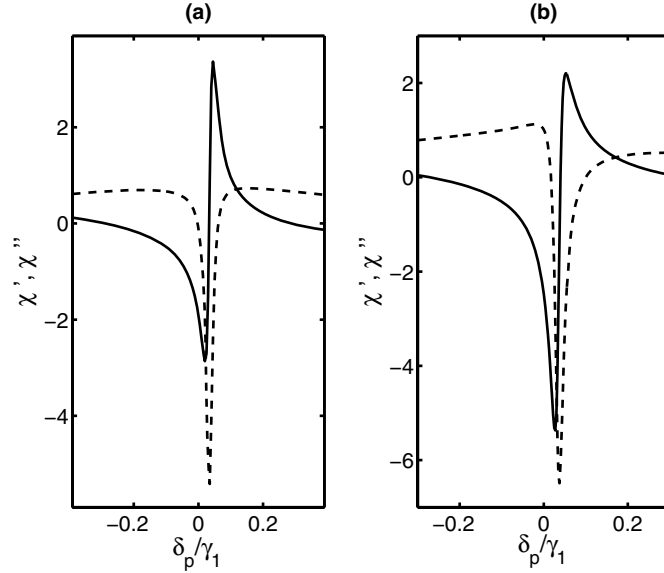


Fig. 7.11. The real χ' (*solid line*) and imaginary χ'' (*dashed line*) parts of the normalized linear susceptibility $\chi/(\mathcal{N}\mu^2/\varepsilon_0\hbar\gamma_1)$ as a function of δ_p/γ_1 for $\gamma_2 = 0.75\gamma_1$, $\gamma_{12} = \sqrt{\gamma_1\gamma_2}$, $\tilde{\Omega} = \gamma_1$, and (a) $\delta\Phi$ satisfying the condition (7.37), (b) $\delta\Phi = 0$

One of the most interesting aspects of phase control of the group velocity is that the effects can be associated with the indistinguishability of spontaneously emitted photons from different transitions. According to (7.34), the effects become maximal if the transition dipole moments are parallel and

the transition frequencies are almost equal, i.e. photons arising from both transitions are essentially indistinguishable. If our system is further prepared in a superposition of the upper levels $|1\rangle$ and $|2\rangle$, e.g. by a dc field, the phase-dependent effects are observed even if $\gamma_{12} = 0$, as pointed out by Bortman-Arbiv et al. [162].

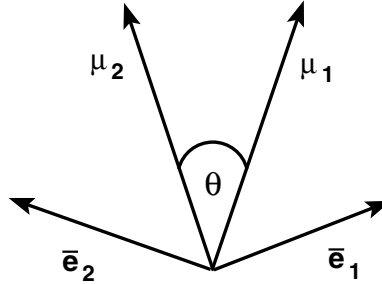


Fig. 7.12. The arrangement for the polarization of two laser fields each coupled to only one of the nonorthogonal atomic dipole moments. The angle θ between the dipole moments is smaller than $\pi/2$. The unit polarization vector \bar{e}_1 of the field \mathbf{E}_1 is perpendicular to μ_2 , and the unit polarization vector \bar{e}_2 of the field \mathbf{E}_2 is perpendicular to μ_1 .

We conclude this section by emphasizing that the phase control of the group velocity predicted here can be observed experimentally only in atomic systems with nonorthogonal transition dipole moments, and the phase-dependent effects are maximal if the dipole moments are parallel. However, the transition dipole moments cannot be chosen to be parallel in order to ensure that each of the probe fields couples *exclusively* to one of the atomic transitions. This requirement might be difficult to achieve in traditional experimental situations as it is difficult to find atomic or molecular systems with transition dipole moments oriented at an angle $0 < \theta < \pi/2$. However, there is, at least theoretically, a scheme to overcome this difficulty involving different linear polarizations of the driving fields relative to the orientations of the transition dipole moments. The scheme is shown in Fig. 7.12. According to this scheme, we select the polarization vectors \bar{e}_1 and \bar{e}_2 of the laser fields \mathbf{E}_1 and \mathbf{E}_2 such that $\mu_1 \cdot \mathbf{E}_2 = \mu_2 \cdot \mathbf{E}_1 = 0$. Since μ_1 is not parallel to μ_2 , we find that $\mu_1 \cdot \mathbf{E}_1 \neq 0$ and $\mu_2 \cdot \mathbf{E}_2 \neq 0$, giving the required selective coupling of each field to only one of the non-orthogonal atomic dipole moments.

7.2 Experimental Observations of Slow Propagation of Light

As we have shown in Sect. 7.1, a practical requirement for the production of slow light is the achievement of a very steep normal dispersion in the presence of EIT. Early experimental observations of slow propagation of light in

EIT systems showed group velocities as slow as $v_g = c/165$ in a Pb vapour cell [163], and measurements of steep dispersion in a cesium vapour cell [164] indicated the possibility of observing group velocities as low as $v_g = c/3000$. These initial experiments demonstrated that it is possible to achieve slow light propagating with almost zero absorption through an optically dense medium. Shortly after these observations, extremely slow group velocities of a few meters per second were observed experimentally with weak laser pulses propagating in hot and ultracold atomic gases. It has also been possible to observe slow group velocities in a ruby crystal at room temperature and in cold crystals doped by rare-earth ions. These experimental studies demonstrated group velocity reductions in EIT media and variations of the group velocity with the intensity of the driving field (width of a transparency window) and the temperature of the atomic gases. In addition, the experiments with atomic gases showed a range of unusual nonlinear optical effects, such as giant Kerr nonlinearities and nonlinear field generation.

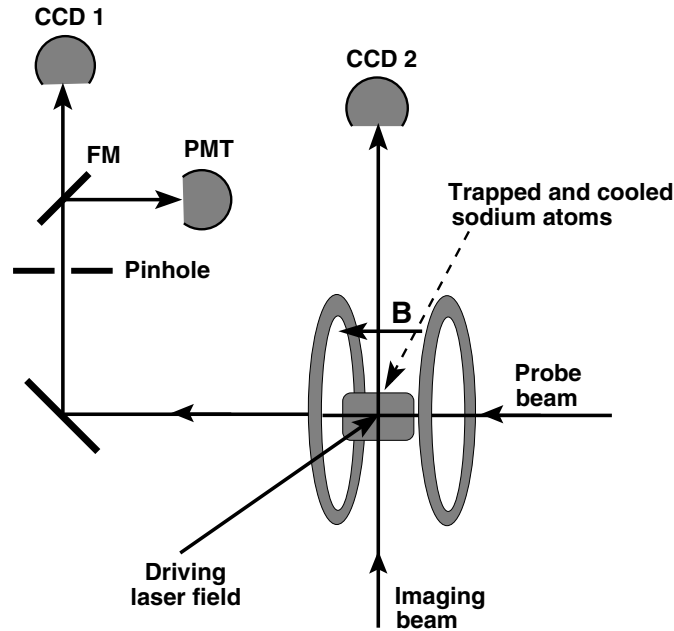


Fig. 7.13. Schematic diagram of the experimental setup of Hau et al. [165] to observe slow propagation of light through a cloud of cold sodium atoms

Propagation of a weak laser pulse through an optically dense EIT sample of cold atoms was investigated by Hau et al. [165] who observed group velocities reduced to $v_g = 17 \text{ ms}^{-1}$. The experimental arrangement, shown schematically in Fig. 7.13, consisted of a magneto-optical trap and an evaporative cooling system. In the experiment, the sodium atoms were first trapped and cooled using laser light in a magneto-optical trap. In few seconds they collected a cloud of 10^{10} atoms at a temperature of 1 mK and a density of $6 \times 10^{11} \text{ cm}^{-3}$. After being further cooled to 50 μK and optically pumped into

a suitable magnetic sublevel, the atoms were then loaded into a pure magnetic trap, providing an essentially harmonic confining potential with axial and transverse oscillation frequencies of 21 and 69 Hz, respectively. At this point, the technique of evaporative cooling was employed to achieve a further reduction in the temperature of the cloud. Briefly, this cooling technique is based on the preferential removal of atoms with an energy higher than the average energy. Subsequential rethermalisation of the cloud by elastic collisions produced an equilibrium state at a lower temperature. This technique enabled the attainment of a temperature of 450 nK, close to the critical temperature $T_c \approx 435$ nK for a Bose–Einstein condensate of the atomic sample. The next step was to pass a short probe light pulse through a cloud of trapped and cold sodium atoms driven by another long laser pulse. The relevant energy levels of the sodium atoms are shown in Fig. 7.14. Two hyperfine sublevels

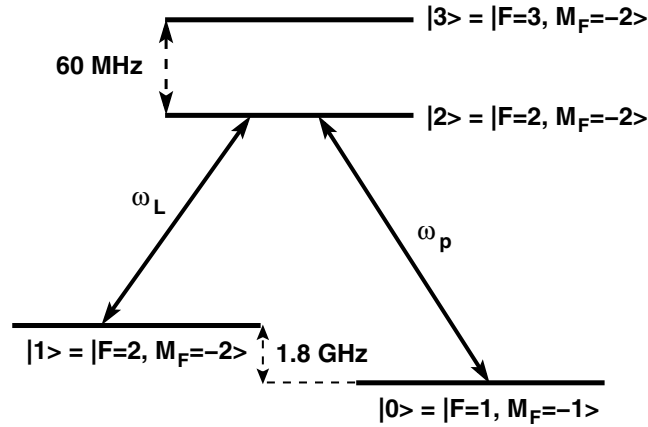


Fig. 7.14. Energy level diagram for sodium atoms with the driven and probed transitions relevant in the experiment of Hau et al.

$F = 1$ and $F = 2$ of the sodium ground state $3^2S_{1/2}$, separated by 1.8 GHz, served as lower states of the required Lambda system. The common upper level of the system was the hyperfine state $3^2P_{1/2}$. In terms of the energy levels, a long linearly-polarized laser pulse, the driving field, was applied to the $|1\rangle \rightarrow |2\rangle$ transition. The hyperfine state $|3\rangle$ of the atoms is separated from $|2\rangle$ by 60 MHz, and therefore was weakly coupled to the state $|2\rangle$ through the driving field. The coupling led to a small shift of the $|2\rangle \rightarrow |1\rangle$ transition. A weak probe laser field (left circularly polarized) was applied to the $|0\rangle \rightarrow |2\rangle$ transition to form a traditional EIT system. Both driving and probe fields were derived from the same dye laser. Due to the very low temperature of the sample, the Doppler broadenings of the atomic transitions were less than the natural linewidths, and hence were not important. This allowed the observation of a very narrow transparency window, with a width much smaller than the linewidth of the $|2\rangle \rightarrow |0\rangle$ transition. Consequently, the dispersion was

much steeper at the probe resonance than one could obtain with hot atomic samples.

In the absence of the probe pulse, the initial population distributed among $|0\rangle$ and $|1\rangle$ was quickly transferred by the driving field and spontaneous emission from the state $|2\rangle$ to the ground state $|0\rangle$. The probe pulse was launched 4 μs after the driving field was turned on. In the presence of both fields, the atoms adiabatically evolved to the bright and dark superpositions of the lower states $|0\rangle$ and $|1\rangle$. At the end of the probe pulse, the atoms adiabatically returned to the original ground state $|0\rangle$. During the pulse propagation through the atomic cloud, a pinhole was used to select only the part of the probe beam that had passed through the central 15 μm of the cloud where the atom density was the greatest. The size of the atomic cloud in the direction of propagation of the probe field and in the transverse directions was measured using charge-coupled-device (CCD) cameras. Figure 7.15 shows the

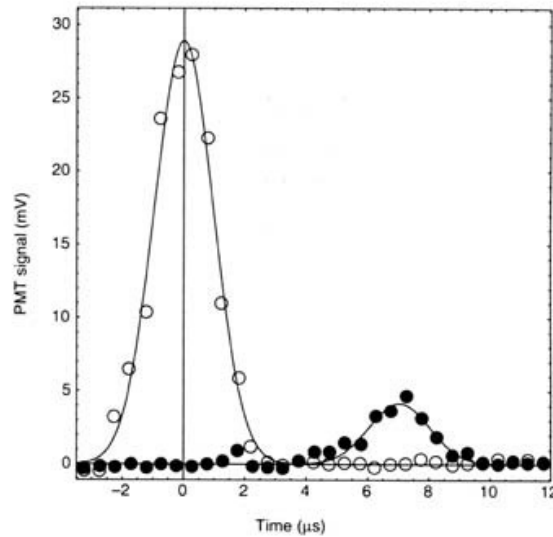


Fig. 7.15. Experimentally observed pulse delay after passing through a cold sample of atoms. The front pulse (open circles) is a reference pulse with no atoms in the sample. The other pulse (black circles) is the delayed pulse after passing through a dense cloud of cold atoms. From L.V. Hau, S.E. Harris, Z. Dutton, C.H. Behroozi: *Nature* **397**, 594 (1999), with permission

experimental results. The front pulse is the reference pulse when it was transmitted through the system but devoid of atoms. By contrast, when the system contained a 229- μm -long atom cloud cooled to temperature of 450 nK, the transmitted pulse was delayed by 7.05 μs . The resulting group velocity of the pulse was 32.5 ms^{-1} . When the atoms were cooled to a lower temperature of 50 nK, which resulted in higher densities of the atoms, the measured group velocity was much lower, reduced to 17 ms^{-1} . The observed decreasing of the group velocity with the increasing atom density was clearly in agreement with

the theoretical prediction, given by (5.117). Thus, EIT induced in the system enhanced the slow propagation of the laser pulse, which would normally be totally absorbed by the atoms.

A further demonstration of group velocity reduction in optically dense media, this time with hot atomic beams, was reported by Kash et al. [166]. In their experiment the very large group delay of a weak pulse was observed in a cell of hot (360 K) isotopically pure ^{87}Rb atoms. In this system, the lower states $|0\rangle$ and $|1\rangle$ of the required Lambda system were the hyperfine states $5^2\text{S}_{1/2}(F=2)$ and $5^2\text{P}_{1/2}(F=2)$, separated by 6.8 GHz, and the common upper state $|2\rangle$ was the state ($F=2$) of the closely spaced hyperfine structure $5^2\text{P}_{1/2}(F=1,2)$. The driving field was tuned to the $|1\rangle \rightarrow |2\rangle$ transition, and a copropagating probe laser pulse was tuned to the $|0\rangle \rightarrow |2\rangle$ transition. Both fields were phase locked and the probe laser power was 5% of the driving laser power. The probe field was amplitude modulated by approximately 50% at a frequency that was varied in the range of 0.1 – 10 kHz. The group velocity delay in passing through the cell was measured by observing the time retardation of the amplitude modulated field upon passing through the cell. The time delay was independent of the modulation frequency up to the linewidth of the EIT window, which allowed them to perform the experiment with many different pulses of the probe field.

The main idea of the experiment with hot atoms was that a narrow EIT window can be obtained in a broadened absorption profile by suppressing the line-broadening mechanisms arising from the motion of the atoms. The dominant broadening mechanism in a hot gas is the Doppler effect, which can be eliminated by making the driving field copropagate with the probe field. To illustrate why this is the case, consider the susceptibility of an atom moving with a velocity \mathbf{v} . The motion changes the frequencies of the driving and probe fields “seen” by the atom. The frequencies of the fields are Doppler-shifted and became $\omega_L - \mathbf{k}_d \cdot \mathbf{v}$ and $\omega_p - \mathbf{k}_p \cdot \mathbf{v}$, where \mathbf{k}_d and \mathbf{k}_p are the propagation vectors of the driving and probe fields, respectively. Assuming that the atomic velocities obey the Maxwell–Boltzmann distribution, we may find the susceptibility of a EIT Lambda-type system by averaging the susceptibility (5.115) of the motionless atoms over the thermal velocity distribution, and obtain

$$\chi(\omega_p) = i \frac{\mathcal{N}|\mu_{02}|^2}{\varepsilon_0 \hbar} \left\langle \frac{\left\{ \frac{1}{2} \gamma_1 - i [\delta_p - \Delta + (\mathbf{k}_d - \mathbf{k}_p) \cdot \mathbf{v}] \right\}}{D_v(\delta_p)} \right\rangle_v, \quad (7.39)$$

where

$$D_v(\delta_p) = \left\{ \frac{1}{2} \gamma_1 - i [\delta_p - \Delta + (\mathbf{k}_d - \mathbf{k}_p) \cdot \mathbf{v}] \right\} \times [\gamma_2 - i (\delta_p + \mathbf{k}_p \cdot \mathbf{v})] + \frac{1}{4} \Omega^2, \quad (7.40)$$

and $\langle \dots \rangle_v$ denotes an average over the velocity distribution.

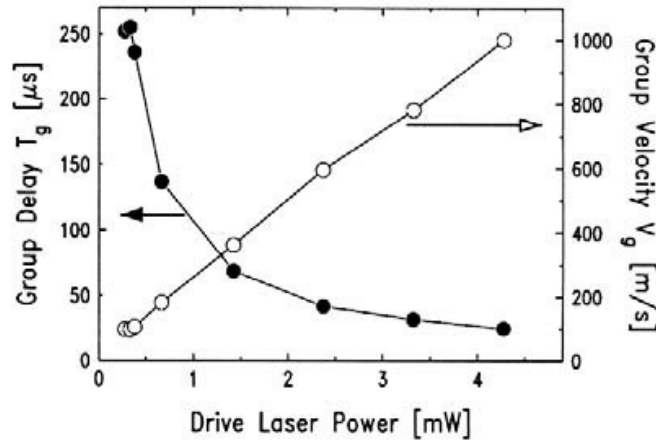


Fig. 7.16. Experimental results of Kash et al. [166] demonstrating the dependence of the group velocity on strength of the driving field. From M.M. Kash, V.A. Sautenkov, A.S. Zibrov, L. Hollberg, G.R. Welch, M.D. Lukin, Y. Rostovsev, E.S. Fry, M.O. Scully: *Phys. Rev. Lett.* **82**, 5229 (1999). Copyright (1999) by the American Physical Society

By comparison with the result (7.22) obtained with motionless atoms, we see that the position of the resonance (EIT window) is now spread over the distribution of \mathbf{v} , which leads to a broadening of the resonance. However, the term in the numerator of (7.39), primarily responsible for the width of the EIT resonance, depends on the difference of the two propagation vectors. Thus, for copropagating and nearly equal frequency driving and probe fields, the velocity dependent term essentially vanishes.

Figure 7.16 shows the measured group delay and average group velocity as a function of the power of the driving field. From the measured group delays, it was determined that the group velocity of the probe pulses was reduced to values of order 90 ms^{-1} for the driving laser power of 4.3 mW. The observed reduced group velocity was the best achievable in this system in view of the finite decay rate γ_1 of the lower state $|1\rangle$. It was concluded that a reduction of γ_1 would allow one to reach much lower group velocities of the order of 10 ms^{-1} in this system. This could be achieved, for example, by increasing the driving field diameter.

Using a similar technique, Budker et al. [167] have succeeded in the observation of ultraslow group velocities as low as $v_g = 8 \text{ ms}^{-1}$. This extremely slow group velocity was observed in resonant light propagation through a rubidium vapor contained in a cell with an antirelaxation wall coating. This experiment also demonstrated the relation between group velocity reduction and nonlinear magneto-optic rotation. Their apparatus, shown schematically in Fig. 7.17, consisted of a vapour cell contained in a multilayer magnetic shield and a glass Faraday rotator coil, causing a rotation of the polarization of the light before the cell. The cell and the Faraday rotator were positioned between crossed polarizer and analyzer. The cell was 10 cm in diameter and

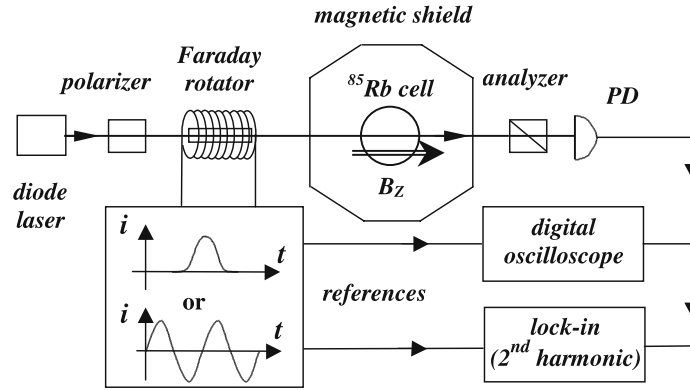


Fig. 7.17. Diagram of the principal elements of the apparatus used by Budker et al. [167] to observe the slow group velocities of probe pulses propagating through a rubidium vapor. From D. Budker, D.F. Kimball, S.M. Rochester, V.V. Yashchuk: Phys. Rev. Lett. **83**, 1767 (1999). Copyright (1999) by the American Physical Society

contained ^{85}Rb atoms. The experiment was performed on the D1 line of the rubidium atoms, and similar observations were also made on the D2 line. In this atomic system, two groups of transitions from the two ground hyperfine sublevels $F_g = 2$ and $F_g = 3$ to unresolved hyperfine levels ($F_e = 1, 2, 3, 4$) of the excited state form a degenerate three-level Lambda system. A selected magnetic sublevel of the excited state decays with different polarizations to the ground levels. Therefore, driving and probe fields of different polarizations each couple exclusively to one of the atomic transitions. A diode laser was used to produce a cw driving field at 795 nm (D1 transition) or 780 nm (D2 transition). In the experiment, the probe was of the same central frequency as the driving field and was produced from the driving field by slightly rotating the input polarization with the Faraday rotator. In this way, it was possible to produce a weak probe pulse of a time-dependent intensity $I_p(t) \propto i^2(t)$, where $i(t)$ is the time dependent current applied to the Faraday rotator. The driving field was considered constant and unchanged after passing the Faraday rotator. The polarization of the probe field was adjusted to be perpendicular to the polarization of the driving field so as to obtain the selective coupling of each field to only one of the atomic transitions.

Figure 7.18 shows the experimental results for the transmission, nonlinear optical rotation and phase shift of the probe pulse obtained by varying the magnetic field amplitude. The observed negative phase shifts corresponded to negative group velocities. From the measured phase shift, it was determined that the group delay of the pulse was 13 ms corresponding to the group velocity of the pulse $v_g \approx 8 \text{ ms}^{-1}$. In the absence of the magnetic field, the maximum phase delay of the pulse was observed, and no delay was observed when a strong magnetic field was applied or the laser fields were detuned from the atomic resonances. This observation is in perfect agreement with

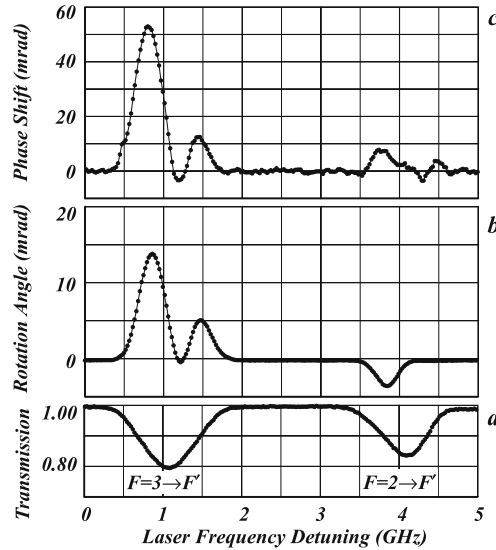


Fig. 7.18. Observation by Budker et al. [167] of (a) the transmission, (b) nonlinear optical rotation and (c) phase shift of the probe pulse propagating through a rubidium vapor. From D. Budker, D.F. Kimball, S.M. Rochester, V.V. Yashchuk: *Phys. Rev. Lett.* **83**, 1767 (1999). Copyright (2001) by the American Physical Society

the theoretical prediction. In the absence of the magnetic field and with the laser fields tuned to the atomic resonances, the fields satisfy the two-photon resonance condition for EIT and a steep dispersion. When the magnetic field is applied to the system, it splits the lower degenerate atomic levels leaving the laser fields off-resonant with the atomic transitions. This destroys the two-photon resonance required for EIT and also the dark state, as we discussed in Chap. 5.

In the preceding experiments, extremely slow group velocities were observed in atomic gases. A different example of optical systems and techniques to produce reduced group velocities are the experiments of Turukhin et al. [168] and Bigelow et al. [169], which measured ultraslow group velocities of light in optically dense crystals. In the experiment of Turukhin et al. [168], slow light with a velocity 45 ms^{-1} was observed in a solid material, Pr doped Y_2SiO_5 (Pr:YSO), maintained at a cryogenic temperature of 5 K. The apparatus involved a Pr:YSO crystal of thickness 3 mm in the light propagation direction and cooled to 5 K. Acousto-optic frequency shifters were used to generate three different coherent laser beams from the output of a single dye laser. The laser beams were focused to a diameter of $\sim 100 \text{ }\mu\text{m}$ in the crystal and intersected at angles in the range of $10 - 20 \text{ mrad}$. All beams were linearly polarized along the crystal axis to obtain maximum absorption. Figure 7.19 shows the relevant energy levels of the Pr:YSO crystal. The driving field of frequency ω_L and intensity 470 W/cm^2 was coupled to the $^3\text{H}_4(\pm 1/2) \rightarrow ^1\text{D}_2(\pm 3/2)$ transition, while the probe field of frequency $\omega_p \neq \omega_L$ and intensity 1.1 W/cm^2 was coupled to

the ${}^3\text{H}_4(\pm 3/2) \rightarrow {}^1\text{D}_2(\pm 3/2)$ transition to form a nondegenerate three-level Lambda system. The driving and probe fields produce coherence between the lower states ${}^3\text{H}_4(\pm 1/2 \leftrightarrow \pm 3/2)$. In addition, a pump field of frequency ω_A was applied to refill the spectral hole burned by the driving and probe fields so as to provide a high optical density for EIT. To measure the group velocity, the probe field was chopped and its phase delay was measured using a lock-in amplifier. Group delays greater than 65 μs were measured, which corresponded to group velocities of $\sim 45 \text{ ms}^{-1}$.

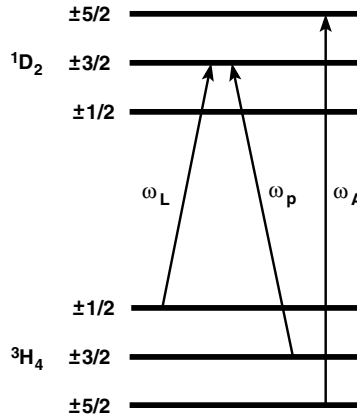


Fig. 7.19. Energy levels of the Pr:YSO crystal and laser frequencies used in the slow light experiment of Turukhin et al. [168]

With the use of a spectral hole burning technique, Bigelow et al. [169] were able to demonstrate that the hole burned in the absorption spectrum of a probe field, due to population oscillations, discussed in Sect. 5.5.3, can be extremely narrow, resulting in a rapid frequency variation of refractive index, and consequently, a reduction of the group velocity to values as low as 57.5 ms^{-1} . This experiment looked at the propagation of a probe field in a medium of two-level atoms, and therefore differs significantly from the experiments based on EIT in three-level Lambda-type atoms. In the experiment, they used a 7.25 cm long ruby crystal kept at room temperature and illuminated by long laser pulses. For the pulse sources, they used a single-line argon-ion laser operating at 514.5 nm. The laser beam was sent through a variable attenuator and an electro-optic modulator which produced long pulses of light with almost no background intensity. A glass slide was used to separate a small part of the laser pulses for reference. The remaining light was focused with a 40 cm focal lens to a beam waist of $84 \mu\text{m}$ to excite the ruby crystal. The beam then passed through the crystal into a detector, and the detected signal was stored along with the reference beam signal on a digital oscilloscope. The reference and transmitted signals were compared on a computer and the relative delay was measured. The largest delay observed in the experiment was 1.26 ms with an input power of 0.25 W, which corresponded to the group

velocity $v_g = 57.5 \text{ ms}^{-1}$. The experimental team has also observed that with this technique it is not necessary to apply separate driving and probe fields to the ruby crystal in order to observe reduced group velocities. Additional measurements showed that a single intense pulse of light is able to provide the saturation required to modify the group velocity. These pulses can be considered as producing their own driving field and were thus self-delayed.

7.3 Experimental Observation of Negative Group Velocities

In slow light propagation, the experimental techniques have made use of EIT to produce optically transparent medium with refractive index close to unity and with positive refractive-index dispersion strong enough to reduce the group velocity of the propagating field. As we have discussed in Sect. 7.1, group velocities may be faster than the speed of light in vacuum, and can even be negative. A practical requirement for the production of fast light is the attainment of a very large anomalous dispersion in the absence of absorption and group-velocity dispersion. According to (7.11), the group velocity of a propagating pulse can be negative when $n/\omega_p < dn/d\omega_p < 0$.

One of the first experimental observations of fast light was made by Basov et al. [170], who investigated the propagation of a pulse through a laser amplifier for the case in which the intensity of the pulse was high enough to induce a nonlinear optical response. They found that nonlinear optical saturation of the amplifier gave rise to superluminal light. Subsequent experiments conducted by Chu and Wong [171] in early 1980's observed negative group velocities of laser pulses, propagating with $v_g = -c/23$ in a GaP:N crystal as the laser frequency was tuned through the absorption resonance arising from the bound A-exciton line.

In more recent experiments, Akulshin et al. [172, 173] have proposed an interesting technique based on the phenomenon of electromagnetically induced absorption (EIA) to render the material medium highly transparent while still retaining the strong *negative* dispersion required for the creation of superluminal light and even negative group velocities. Using this technique, they were able to observe negative group velocities of propagating probe pulses through atomic vapours. In their earlier experiment, they measured a steep anomalous dispersion in a degenerate two-level rubidium atoms. Though they did not directly measure the delay of the probe pulses propagating through the atomic medium, they indirectly determined negative group velocities reduced to $v_g = -c/23000$. However, the propagation was accompanied by an absorption.

In a subsequent experiment [174] they directly measured the advance and delay of pulses propagating through an atomic cell and observed both slow and fast group velocities, but still in the presence of absorption. In the experiment, the absorption was enhanced, but the value of the absorption was

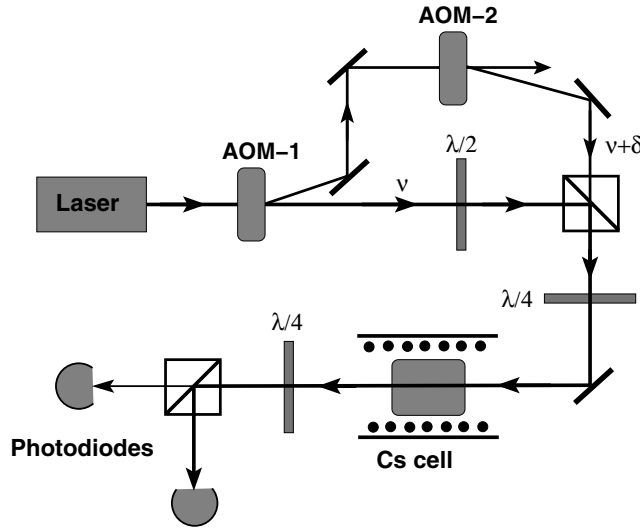


Fig. 7.20. Experimental setup of Akulshin et al. [174] to measure negative group velocities in Cs vapor

not very critical for negative v_g . The width of the EIA resonance was much more important for high dispersion. The experimental scheme is illustrated in Fig. 7.20. In the experiment, a 2-cm-long Cs cell was excited by two fields of the same frequency but opposite circular polarizations to ensure that each of the fields coupled to different atomic transitions. The fields were obtained from an extended-cavity diode laser whose output was sent through acousto-optic modulators to produce the mutually coherent driving and probe beams. The two beams were then carefully combined into a copropagating bichromatic beam and their polarizations were set with polarizers and quarter wave plates. The bichromatic beam was sent through the Cs cell to produce a coherence between ground-state sublevels belonging to the same hyperfine level of the Cs atoms. After passing through the cell, the beams were separated by a Glan–Thomson prism and detected with fast photodiodes.

The induced coherence between the Zeeman sublevels affected the shape of the probe pulse during the propagation through the cell. Figure 7.21 shows the experimentally observed distortion of the probe pulse. In the region of EIT, the observed transmitted intensity was increasing with time due to pumping of the atoms into a dark state. In the EIA region, the situation was reversed: at the beginning of the pulse the transmitted intensity was higher and decreased with time due to pumping the atoms into a bright state. Figure 7.22 gives experimental results for negative pulse delays in the Cs vapour with steep anomalous dispersion as a function of the duration of the pulses. Note the visible advance of the propagating pulse relative to the reference pulse and the increase of the advance with the density of the Cs vapor. For an atomic density of $1.5 \times 10^{11} \text{ cm}^{-3}$, the observed advance was $\Delta T = 0.1 \pm 0.01 \text{ } \mu\text{s}$, and a larger advance of $\Delta T = 0.34 \pm 0.01 \text{ } \mu\text{s}$ was observed with the atomic density $7 \times 10^{11} \text{ cm}^{-3}$. The advanced propagations

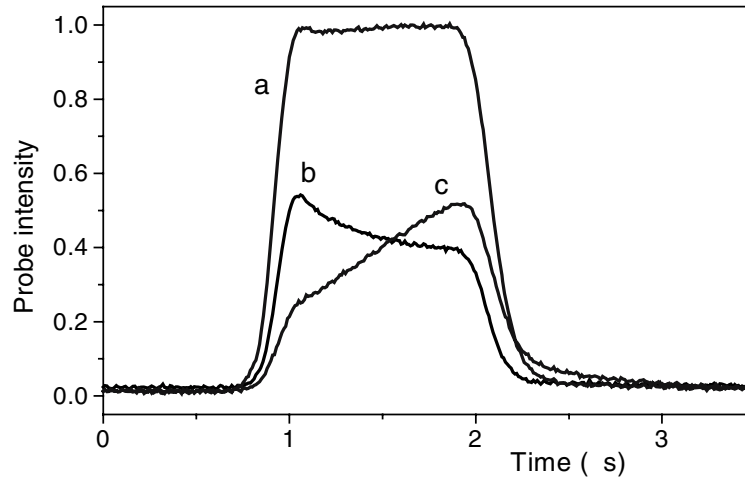


Fig. 7.21. Shapes of probe pulses propagating in Cs vapour. The trace *a* is an off-resonance reference pulse propagating with $v_g \approx c$. Trace *b* is the shape of the probe pulse propagating in the EIA frequency region of the atomic vapour, and trace *c* is the shape of the probe pulse propagating in the EIT frequency region. From A.M. Akulshin, A. Cimmino, A.I. Sidorov, P. Hannaford, G.I. Opat: Phys. Rev. A **67**, 011801 (2003). Copyright (2003) by the American Physical Society

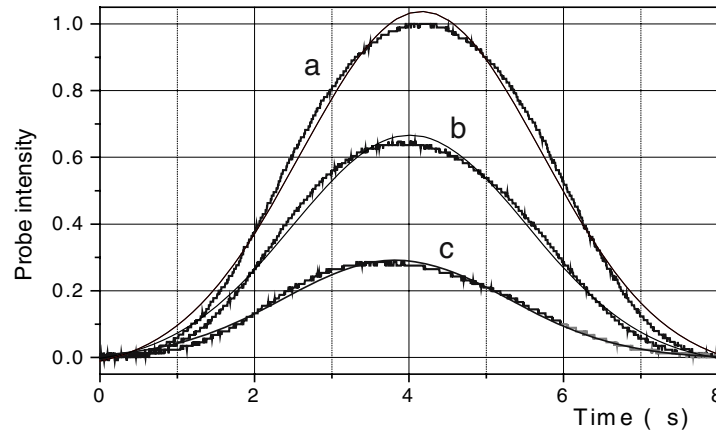


Fig. 7.22. Negative pulse delays observed by Akulshin et al. [174] in Cs vapour with steep anomalous dispersion. The trace *a* is a reference pulse. Traces *b* and *c* are advanced probe pulses propagating at different atomic densities, $1.5 \times 10^{11} \text{ cm}^{-3}$ and $7 \times 10^{11} \text{ cm}^{-3}$, respectively. From A.M. Akulshin, A. Cimmino, A.I. Sidorov, P. Hannaford, G.I. Opat: Phys. Rev. A **67**, 011801 (2003). Copyright (2003) by the American Physical Society

corresponded to negative group velocities of $v_g = -c/1500$ and $v_g = -c/5100$, respectively.

Another compelling experimental observation of a negative group velocity was reported by Wang et al. [175] who observed a negative group velocity in the spectral region between two closely spaced Raman gain lines in Cs vapor. The advantage of using Raman gain lines is that a suitably tuned probe

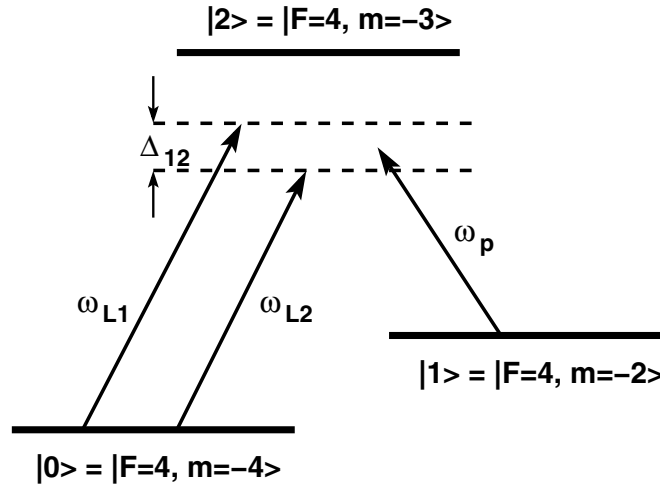


Fig. 7.23. Cesium energy levels and laser fields used in the superluminal light experiment of Wang et al. [175]

pulse can propagate without absorption. The atomic system employed in the experiment was a cell of cesium (Cs) atoms kept at a temperature of 30°C . The atomic cell was placed in a weak (1.0 G) uniform magnetic field which split the hyperfine $6S_{1/2}$ magnetic sublevels into nondegenerate levels to produce the required nondegenerate Lambda-type atomic system. The relevant atomic levels are shown in Fig. 7.23. The atoms were first optically pumped by two laser fields into the hyperfine magnetic sublevel $|F = 4, m = -4\rangle$, which served as the ground state $|0\rangle$ of the system. Next, two laser fields of slightly different frequencies were propagated through the atomic medium to drive the atomic $|0\rangle \rightarrow |2\rangle$ transition. The frequencies of the driving fields differed by 2.7 MHz and both fields were significantly detuned from the atomic transition frequency ω_{20} , as shown in Fig. 7.23. A tunable probe field was applied to the $|1\rangle \rightarrow |2\rangle$ transition to produce Raman transitions causing the atoms to absorb a photon from the driving fields and emit a photon into the probe field. This process results in the atoms making a transition from $|0\rangle$ to $|1\rangle$. Obviously, there are two frequencies at which the probe field is amplified. These frequencies correspond to two-photon resonances of the probe field with the two frequencies of the driving fields. The most important for the experiment was that between the gain lines the system was transparent for the probe field and produced a steep and anomalous dispersion. Before entering the atomic cell, the probe field was divided at a beam-splitter into two parts: one directed into a detector as a reference pulse, and the other directed into the atomic cell and detected after passing the cell. The probe field was tuned midway between the gain features to make use of the maximum anomalous dispersion.

Experimental results are shown in Fig. 7.24. The solid line shows the time evolution of the probe pulse in the absence of the driving fields, and the dashed line shows the time evolution in the presence of the driving fields. We

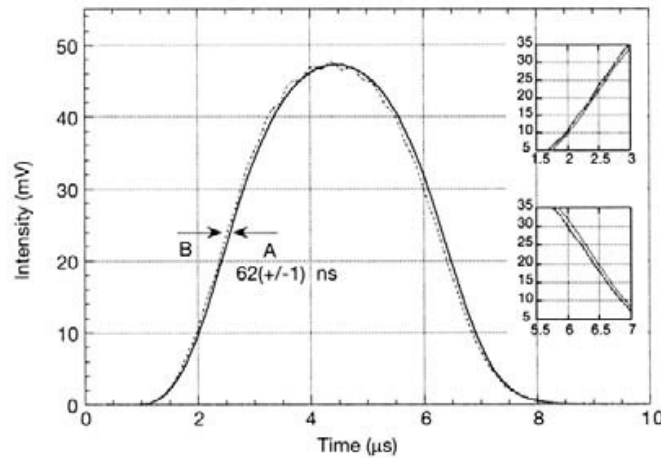


Fig. 7.24. Superluminal propagation without absorption and pulse distortion observed by Wang et al. [175]. The solid line represents the pulse propagating in vacuum, the dashed line is the transmitted pulse through the anomalous medium. The inserts are enlargements of the leading and falling edges of the pulse. From L.J. Wang, A. Kuzmich, A. Dogariu: *Nature* **406**, 277 (2000), with permission

see that in the presence of the driving fields the probe pulse is advanced by 62 ns, corresponding to $v_g = -c/310$. It was observed that the shape of the pulse did not change much during the propagation, as it had been believed that severe pulse reshaping necessarily accompanies superluminal propagation. The ratio of the pulse advancement to pulse width in this experiment was of the order of 1.5%. Thus, the experiment also demonstrated that superluminal light propagation can occur under conditions such that the input laser pulse undergoes negligible reshaping.

7.4 Bright- and Dark-State Polaritons

Since the first experimental observations of Hau et al. [165], the techniques for the production of extremely slow light have improved and it became possible to bring light pulses to a full stop and store them in a material systems for long time intervals. Experimental success with the production of slow light has spurred on theoretical interpretations of this unusual effect and investigations into so-called dark and bright polaritons – a coherent mixture of field and atomic variables.

In order to understand the process of preparation of a dark polariton and storage of light in atomic media, we consider the propagation of a weak probe pulse in an EIT medium [176]. For simplicity, we limit our analysis to propagation in one dimension and assume that the pulse propagates in the positive z direction. In traditional EIT systems, a strong driving field of Rabi frequency Ω couples to one of the two dipole transitions in a Lambda-type

atom, say $|1\rangle \rightarrow |2\rangle$, and a probe pulse with the field amplitude $\mathbf{E}(z, t)$ couples to the other dipole transition, $|0\rangle \rightarrow |2\rangle$. The probe field can be described classically or quantum-mechanically as a time- and spatially-dependent electric field

$$\mathbf{E}(z, t) = i\bar{\mathbf{e}}\mathcal{E}(z, t)e^{-i(\omega_p t - kz)} + \text{c.c.} , \quad (7.41)$$

where $\mathcal{E}(z, t)$ is the amplitude (pulse envelope) of the probe field and $\bar{\mathbf{e}}$ is the polarization vector which is perpendicular to the propagation direction.

In the adiabatic approximation, the propagation of the probe pulse through an atomic medium is governed by the Helmholtz equation (5.76), which with the help of (5.80) can be written in the form

$$\left(\frac{\partial}{\partial t} + c \frac{\partial}{\partial z} \right) \tilde{\mathcal{E}}(z, t) = \frac{1}{2} igM \tilde{\varrho}_{20}(z, t) , \quad (7.42)$$

where M is the number of atoms, and

$$\begin{aligned} \tilde{\mathcal{E}}(z, t) &= \left(\frac{\hbar\omega_p}{2\varepsilon_0\mathcal{V}} \right)^{-\frac{1}{2}} \mathcal{E}(z, t) , \\ g &= \frac{2(\boldsymbol{\mu}_{20} \cdot \bar{\mathbf{e}})}{\hbar} \sqrt{\frac{\hbar\omega_p}{2\varepsilon_0\mathcal{V}}} . \end{aligned} \quad (7.43)$$

are the dimensionless probe field amplitude and the vacuum Rabi frequency in the interaction volume \mathcal{V} , respectively. The position and time dependent function $\tilde{\varrho}_{20}(z, t)$ is the slowly varying density matrix element (coherence) of the continuous ensemble of atoms at position z , defined as

$$\tilde{\varrho}_{20}(z, t) = \frac{1}{L} \int dz \tilde{\varrho}_{20}(t) , \quad (7.44)$$

where L is the length of the interaction volume in the propagation direction of the probe field.

The time evolution of the atomic system is governed by the master equation, which for the EIT Lambda-type system leads to the following set of equations of motion

$$\begin{aligned} \dot{\varrho}_{22} &= -(\gamma_0 + \gamma_2)\varrho_{22} - \frac{1}{2}\Omega(\tilde{\varrho}_{12} + \tilde{\varrho}_{21}) - \frac{1}{2}\Omega_p(\tilde{\varrho}_{02} + \tilde{\varrho}_{20}) , \\ \dot{\varrho}_{11} &= \gamma_2\varrho_{22} + \frac{1}{2}\Omega(\tilde{\varrho}_{12} + \tilde{\varrho}_{21}) , \\ \dot{\varrho}_{00} &= \gamma_0\varrho_{22} + \frac{1}{2}\Omega_p(\tilde{\varrho}_{02} + \tilde{\varrho}_{20}) , \\ \dot{\tilde{\varrho}}_{21} &= -\frac{1}{2}(\gamma_0 + \gamma_2)\tilde{\varrho}_{21} + \frac{1}{2}\Omega(\varrho_{22} - \varrho_{11}) - \frac{1}{2}\Omega_p\tilde{\varrho}_{01} , \\ \dot{\tilde{\varrho}}_{20} &= -\frac{1}{2}(\gamma_0 + \gamma_2)\tilde{\varrho}_{20} + \frac{1}{2}\Omega_p(\varrho_{22} - \varrho_{00}) - \frac{1}{2}\Omega\tilde{\varrho}_{10} , \\ \dot{\tilde{\varrho}}_{10} &= \frac{1}{2}\Omega\tilde{\varrho}_{20} + \frac{1}{2}\Omega_p\tilde{\varrho}_{12} , \end{aligned} \quad (7.45)$$

where the parameter γ_0 is the damping rate of the $|2\rangle \rightarrow |0\rangle$ transition, γ_2 is the damping rate of the $|2\rangle \rightarrow |1\rangle$ transition, Ω is the Rabi frequency of the driving field coupled exclusively to the $|0\rangle \rightarrow |1\rangle$ transition, Ω_p is the Rabi frequency of the probe field coupled exclusively to the $|0\rangle \rightarrow |2\rangle$ transition, and

$$\begin{aligned}\tilde{\varrho}_{21}(t) &= \varrho_{21}(t) \exp(-i\omega_L t) , \\ \tilde{\varrho}_{20}(t) &= \varrho_{20}(t) \exp(-i\omega_p t) , \\ \tilde{\varrho}_{10}(t) &= \varrho_{10}(t) \exp(i(\omega_L - \omega_p)t) ,\end{aligned}\tag{7.46}$$

are the slowly varying parts of the off-diagonal density matrix elements. In the derivation of (7.45), we have assumed that the driving and probe fields propagate in the same z direction, and the lower states $|0\rangle$ and $|1\rangle$ are metastable so that we have ignored the damping rates of these states due to e.g. collisions or any other dephasing process.

As in traditional EIT systems, we assume that the probe field is much weaker than the driving field, and solve the propagation equation (7.42) to all orders in Ω and first order in the probe field amplitude $\tilde{\mathcal{E}}(z, t)$. In this case, we can treat the equations of motion (7.45) perturbatively and solve them to the first order in $\tilde{\mathcal{E}}(z, t)$. In zeroth order, which corresponds to the absence of the probe field, $\varrho_{00}(z, t) = 1$ and all the remaining density matrix elements are zero. This results from the presence of the driving field and spontaneous emission which transfer any population present in the state $|1\rangle$ into the state $|0\rangle$ via the upper state $|2\rangle$. To first order in $\tilde{\mathcal{E}}(z, t)$, we find

$$\tilde{\varrho}_{20} = \frac{2}{\Omega} \frac{\partial}{\partial t} \tilde{\varrho}_{10} .\tag{7.47}$$

With this solution, the wave equation (7.42) can be expressed in terms of the lower states coherence $\tilde{\varrho}_{10}$ as

$$\left(\frac{\partial}{\partial t} + c \frac{\partial}{\partial z} \right) \tilde{\mathcal{E}}(z, t) = \frac{gM}{\Omega} \frac{\partial}{\partial t} \tilde{\varrho}_{10} ,\tag{7.48}$$

and

$$\tilde{\varrho}_{10} = -\frac{\Omega_p}{\Omega} - \frac{2}{\Omega} \left(\frac{\partial}{\partial t} + \gamma \right) \left(\frac{2}{\Omega} \frac{\partial}{\partial t} \tilde{\varrho}_{10} \right) ,\tag{7.49}$$

where $\gamma = (\gamma_0 + \gamma_2)/2$.

We now introduce two dimensionless field operators corresponding to quasi-particles, called dark- and bright-state *polaritons*

$$\Psi = \tilde{\mathcal{E}}(z, t) \cos \theta(t) - \sqrt{M} \tilde{\varrho}_{10}(z, t) \sin \theta(t) ,\tag{7.50}$$

$$\Phi = \tilde{\mathcal{E}}(z, t) \sin \theta(t) + \sqrt{M} \tilde{\varrho}_{10}(z, t) \cos \theta(t) ,\tag{7.51}$$

with

$$\begin{aligned}\cos \theta(t) &= \frac{\Omega(t)}{\sqrt{\Omega^2(t) + g^2 M}} , \\ \sin \theta(t) &= \frac{g\sqrt{M}}{\sqrt{\Omega^2(t) + g^2 M}} .\end{aligned}\quad (7.52)$$

Using a plane wave representation of the new field operators

$$\hat{\Psi}(z, t) = \sum_k \hat{\Psi} e^{ikz} , \quad \hat{\Phi}(z, t) = \sum_k \hat{\Phi} e^{ikz} , \quad (7.53)$$

we find that the operators obey the following commutation relations

$$\begin{aligned}[\hat{\Psi}_k, \hat{\Psi}_{k'}^\dagger] &= [\cos^2 \theta + (\tilde{\varrho}_{00} - \tilde{\varrho}_{11}) \sin^2 \theta] \delta_{kk'} , \\ [\hat{\Phi}_k, \hat{\Phi}_{k'}^\dagger] &= [\sin^2 \theta + (\tilde{\varrho}_{00} - \tilde{\varrho}_{11}) \cos^2 \theta] \delta_{kk'} , \\ [\hat{\Psi}_k, \hat{\Phi}_{k'}^\dagger] &= [1 - (\tilde{\varrho}_{00} - \tilde{\varrho}_{11})] \sin \theta \cos \theta \delta_{kk'} .\end{aligned}\quad (7.54)$$

In the limit of a weak probe field, $\tilde{\varrho}_{00} \approx 1$, $\tilde{\varrho}_{11} \approx 0$, and then the commutation relations (7.54) reduce to the familiar bosonic commutation relations

$$\begin{aligned}[\hat{\Psi}_k, \hat{\Psi}_{k'}^\dagger] &= [\hat{\Phi}_k, \hat{\Phi}_{k'}^\dagger] = \delta_{kk'} , \\ [\hat{\Psi}_k, \hat{\Phi}_{k'}^\dagger] &= 0 .\end{aligned}\quad (7.55)$$

Thus, we can associate the new field operators with quasi-particles – polaritons.

In terms of Ψ and Φ , the equations of motion (7.48) and (7.49) take the forms

$$\left[\frac{\partial}{\partial t} + c \cos^2 \theta(t) \frac{\partial}{\partial z} \right] \Psi = -\dot{\theta} \Phi - c \sin \theta \cos \theta \frac{\partial}{\partial z} \Phi , \quad (7.56)$$

and

$$\Phi = \frac{4 \sin \theta}{g^2 M} \left(\frac{\partial}{\partial t} + \gamma \right) \left(\tan \theta \frac{\partial}{\partial t} \right) (\Psi \sin \theta - \Phi \cos \theta) , \quad (7.57)$$

where $\theta \equiv \theta(t)$.

Our objective is to obtain a propagation equation for the dark polariton (7.56). The solution of this equation is somewhat involved, and requires several simplifying approximations. In particular, we make the adiabatic approximation, which amounts to assuming that probe amplitude $\tilde{\mathcal{E}}(z, t)$ varies slowly over distance comparable to an optical wavelength and over time scale comparable to an optical period. This approximation can be restated in a different form that the time derivatives appearing on the right-hand side of (7.57) are zero, and then we have $\Phi \approx 0$.

Consequently, the dark polariton Ψ obeys the following equation of motion

$$\left[\frac{\partial}{\partial t} + v_g(t) \frac{\partial}{\partial z} \right] \Psi = 0 , \quad (7.58)$$

where

$$v_g(t) = c \cos^2 \theta(t) \quad (7.59)$$

is the group velocity of the laser pulse.

The solution of (7.58) is of the form

$$\Psi(z, t) = \Psi \left(z - \int_0^t d\tau v_g(\tau), 0 \right) \quad (7.60)$$

and describes slow propagation with an invariant spatial pulse shape.

For $\theta(t) \rightarrow 0$, i.e. for a strong driving field $\Omega^2(t) \gg g^2 M$, the dark polariton has purely photonic character, $\Psi = \tilde{\mathcal{E}}(z, t)$, and according to (7.59) the propagation velocity is equal to the speed of light in vacuum. In the opposite limit of a weak driving field $\Omega^2(t) \ll g^2 M$ ($\theta \rightarrow \pi/2$), the polariton becomes purely atomic, $\Psi = -\sqrt{M} \tilde{\varrho}_{10}(z, t)$, and its propagation velocity approaches zero.

7.4.1 Collective Atomic Trapping States

The above analysis of the adiabatic transfer and storage of light in an atomic medium showed that in the limit of a weak driving field, $\Omega^2 \ll g^2 M$, the dark polariton reduces to the atomic spin variable. Thus, the following mapping of the field amplitude into an atomic coherence can be realized

$$\tilde{\mathcal{E}}(z) \Leftrightarrow \tilde{\varrho}_{10}(z) . \quad (7.61)$$

This is the essence of the transfer technique from quantum states of photon wave-packets propagating with the speed of light to stationary atomic superposition states. An obvious question arises whether we could predict the stationary state of the atomic system in which the quantum state of the probe photons is stored.

Consider a system of M three-level atoms in the traditional Lambda configuration. As before, the transition $|0\rangle \rightarrow |2\rangle$ of each of the atoms is coupled to a probe (quantized) field, whereas the transition $|1\rangle \rightarrow |2\rangle$ is driven by a classical coherent field of the Rabi frequency $\Omega(t)$. The system is described by the interaction Hamiltonian

$$H = \hbar g \sum_{i=1}^M \left(\hat{a} A_{20}^{(i)} + \text{H.c.} \right) + \frac{1}{2} \hbar \Omega(t) \sum_{i=1}^M \left(A_{21}^{(i)} + \text{H.c.} \right) , \quad (7.62)$$

where $A_{mn}^{(i)} = |m\rangle_{ii}\langle n|$ are the dipole operators of the i th atom, and g is the coupling constant of the atoms to the quantized probe field. For simplicity, we assume that both g and $\Omega(t)$ are the same for all atoms. This is equivalent to the small sample model approximation, or the Dicke model, discussed in Chap. 2, that the time required for the fields to cross the system is small in comparison to the time Δt required for appreciable changes in the atomic levels, i.e. $L \ll v_g \Delta t$, where L is the length of the atomic medium.

If initially all atoms were in their ground states described by the state vector $|0\rangle = |0_1, 0_2, \dots, 0_M\rangle$, the only states coupled by the interaction (7.62) are the collective symmetric states

$$\begin{aligned}
 |0\rangle &= |0_1, 0_2, \dots, 0_M\rangle, \\
 |1\rangle &= \frac{1}{\sqrt{M}} \sum_{i=1}^M |0_1, \dots, 1_i, \dots, 0_M\rangle, \\
 |2\rangle &= \frac{1}{\sqrt{M}} \sum_{i=1}^M |0_1, \dots, 2_i, \dots, 0_M\rangle, \\
 |11\rangle &= \frac{1}{\sqrt{2M(M-1)}} \sum_{i \neq j=1}^M |0_1, \dots, 1_i, \dots, 1_j, \dots, 0_M\rangle, \\
 |21\rangle &= \frac{1}{\sqrt{2M(M-1)}} \sum_{i \neq j=1}^M |0_1, \dots, 2_i, \dots, 1_j, \dots, 0_M\rangle, \\
 |22\rangle &= \frac{1}{\sqrt{2M(M-1)}} \sum_{i \neq j=1}^M |0_1, \dots, 2_i, \dots, 2_j, \dots, 0_M\rangle, \\
 &\text{etc.} \quad ,
 \end{aligned} \tag{7.63}$$

where $|m_i, n_j, \dots, k_l\rangle \equiv |m\rangle_i \otimes |n\rangle_j \otimes \dots \otimes |k\rangle_l$.

The interaction (7.62) has a family of dark states, i.e. states satisfying the eigenvalue equation

$$H|D, n\rangle \equiv 0, \tag{7.64}$$

where n is the number of photons in the quantized field,

$$|D, n\rangle = \sum_{k=0}^n \sqrt{\frac{n!}{k!(n-k)!}} (-\sin \theta)^k \cos^{n-k} \theta |1^k, n-k\rangle, \tag{7.65}$$

are the dark states of the system, with

$$\tan \theta = \frac{g\sqrt{M}}{\Omega(t)}, \tag{7.66}$$

and $|1^k, n-k\rangle = |11\dots\rangle \otimes |n-k\rangle$.

For $\theta = 0$, the dark state $|D, n\rangle$ reduces to the product state $|0\rangle \otimes |n\rangle$, and for all $n \leq M$ by changing θ from zero to $\pi/2$, the state changes to $|1^n\rangle \otimes |0\rangle$. Thus, if the initial state of the quantized probe field was a mixed state described by a density operator ϱ_p , the interaction generates an atomic collective state as

$$\begin{aligned} \varrho_p \otimes |0\rangle\langle 0| &= \sum_{n,m} \varrho_{nm} |n\rangle\langle m| \otimes |0\rangle\langle 0| \\ &\longrightarrow |0\rangle\langle 0| \otimes \sum_{n,m} \varrho_{nm} |1^n\rangle\langle 1^m|. \end{aligned} \quad (7.67)$$

The collective dark state model provides a very elegant picture of the transfer of a quantum state of the field to collective atomic states. An adiabatic rotation of the angle θ leads to a complete and reversible transfer of the photon state to the collective atomic states. The most important property of the dark states (7.65) is that they do not contain the excited states of the atoms, and therefore are immune to spontaneous emission. In addition, the subspace composed of the dark states is completely decoupled from the remaining states, and thus forms a decoherence free subspace.

7.4.2 Experimental Realization of Light Storage in Atomic Media

Evidence for the trapping and storage of weak pulses has been observed experimentally in ultracold and hot atomic vapours. In these experiments, probe pulses propagating in a EIT medium were brought to a complete stop and released after some storage time interval. The idea of these experiments was to show that the probe pulse propagating through an atomic medium exists, under the EIT conditions, as a dark polariton that can be completely converted into a spin wave when the driving field is turned off, and reappears again when the driving field is turned back on.

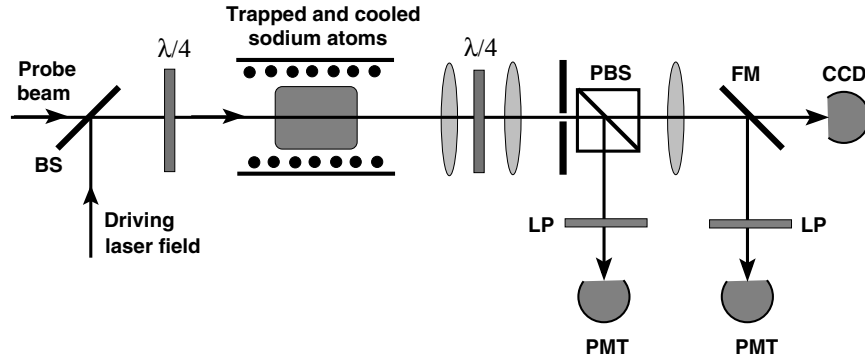


Fig. 7.25. Experimental setup of Liu et al. [177] to observe the stopping of short light pulses in cold sodium atoms

The experiment of Liu et al. [177], shown schematically in Fig. 7.25, involved a sample of sodium atoms magnetically trapped in a single state and cooled to a temperature of $0.9 \mu\text{K}$, which was just above the critical temperature for the Bose–Einstein condensation of the sample. The experiment was performed on the fine structure transitions $3\text{S} \rightarrow 3\text{P}$ of the sodium atoms. The relevant energy levels of the system are shown in Fig. 7.26. The driving field was resonant with the $|1\rangle \rightarrow |3\rangle$ transition, and the probe pulse was tuned to the $|0\rangle \rightarrow |3\rangle$ transition. The laser beams were combined with the help of a beamsplitter, circularly polarized with a quarter-wave plate ($\lambda/4$), and then injected into the atomic sample. After leaving the sample, the laser beams passed a second quarter-wave plate to restore their original linear polarizations and next were separated with a polarizing beam-splitting cube. The atom cloud was imaged onto an external image plane with a pinhole positioned at the center of the cloud image. The pinhole and the flipper mirror selected only those portions of the driving and probe beams that passed through the central region of the cloud. The atom cloud was then imaged onto a CCD camera.

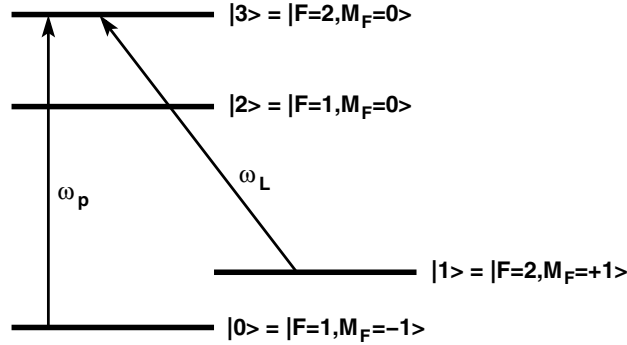


Fig. 7.26. Sodium energy levels and frequencies of the driving and probe lasers used in the stopped-light experiment of Liu et al. [177]

The experimental results illustrating the observed trapping and storage of a short laser pulse are shown in Fig. 7.27. The upper figure shows three traces. The dashed line represents the time evolution of the continuous driving field, referred to as the coupling field in the figure. The sharp peak centered at $t = 0$ (dotted line) is a reference pulse obtained from the transmission of a probe pulse in the absence of atoms. The pulse propagated essentially with the speed of light in vacuum. The smaller delayed peak is the transmitted pulse propagated through the medium of cold atoms and tuned to the atomic transition. The observed delay time of $11.8 \mu\text{s}$ corresponded to a pulse group velocity of 28 ms^{-1} . Crucial for the experiment was the spatial compression of the probe pulse as it entered the atomic medium. It was necessary that the entire pulse be contained within the atomic medium. The compression process was performed at time $t = 6.3 \mu\text{s}$, indicated by the arrow in the Fig. 7.27(a).

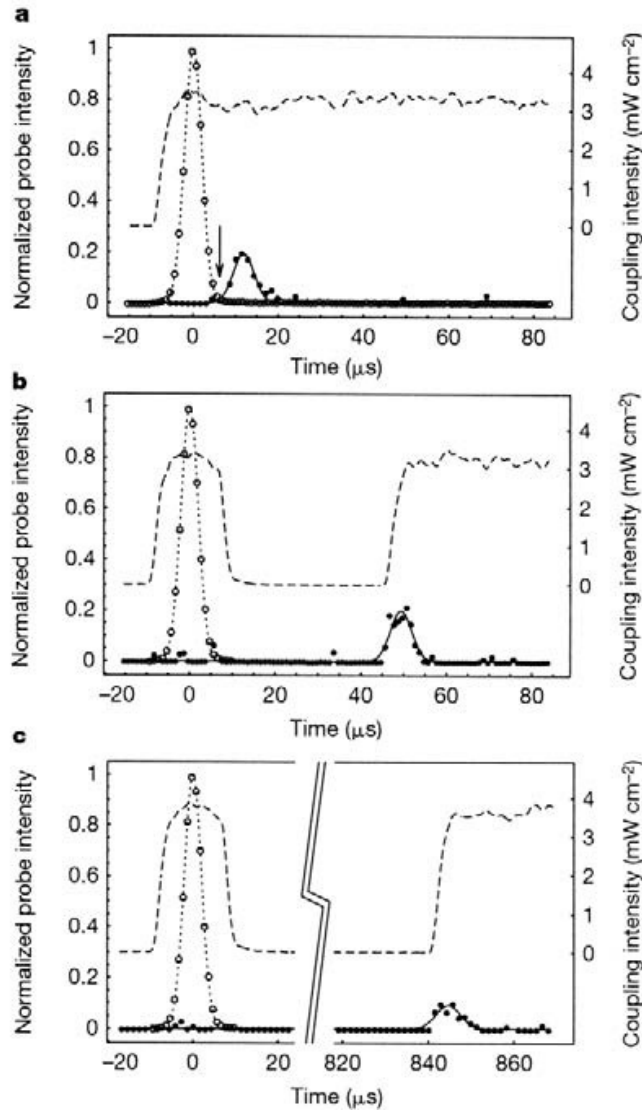


Fig. 7.27. Experimental results of Liu et al. demonstrating the pulse storage in a sodium vapour. From C. Liu, Z. Dutton, C.H. Behroozi, L.V. Hau: *Nature* **409**, 490 (2001), with permission

To demonstrate storage of the probe pulse inside the medium, the driving field was turned off at about $t = 10 \mu\text{s}$ and left off until $t = 44.3 \mu\text{s}$, at which it was turned back on. During the time interval in which the driving field was turned off, no transmission of the pulse was observed, indicating a storage of the pulse in the atomic medium. The probe pulse was regenerated when the driving field was turned back on at $t = 44.3 \mu\text{s}$. The regenerated pulse had the same shape as the propagating pulse in the EIT situation, see Fig. 7.27(a), indicating that no dissipation of the pulse energy took place during the storage process.

In a closely related experiment, Phillips et al. [178] have demonstrated very similar results through the use of hot rubidium atoms. The experiment,

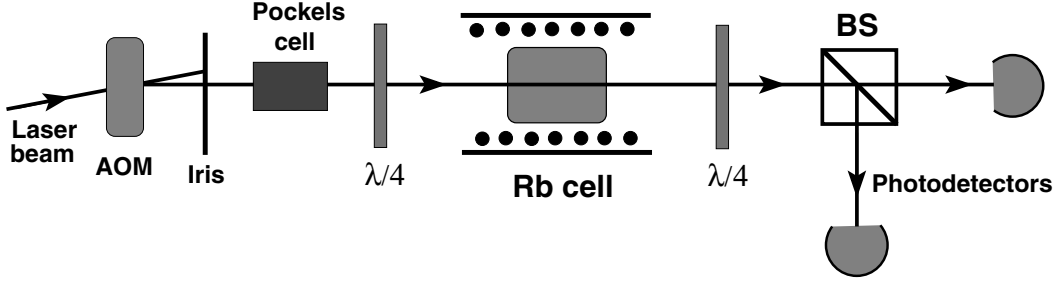


Fig. 7.28. Experimental setup of Phillips et al. [178] to observe stopping of light pulses in hot rubidium atoms

shown schematically in Fig. 7.28, involved degenerate Zeeman hyperfine sublevels of the ground state of hot ^{87}Rb atoms and used polarization control techniques to manipulate coupling of applied fields to these sublevels. The driving field of σ_+ circular polarization was derived from an extended cavity diode laser by carefully controlling the light polarization. A fast Pockels cell was used to create a weak probe pulse of left circularly polarized light. The probe pulse had a temporal length of about $10 - 30 \mu\text{s}$. The input powers of the driving and probe fields were 1 mW and $100 \mu\text{W}$, respectively. The fields were propagated collinearly and focused onto a 4-cm-long cell containing ^{87}Rb atoms kept at temperatures of about $70 - 90^\circ\text{C}$, which corresponded to atomic densities of about $10^{11} - 10^{12} \text{ cm}^{-3}$.

The transmission of the probe pulse was monitored using a quarter-wave plate and polarizing beam splitter. In order to minimize collision-induced transitions, which would destroy the long lifetime of the atomic Zeeman coherences, the Rb cell was magnetically shielded and filled with about 5 Torr of He buffer gas. To achieve trapping and storage of the pulse inside the cell, an acousto-optic modulator was used to turn off the driving field smoothly over about $3 \mu\text{s}$, while most of the probe field was contained inside the cell. After some time interval, the driving field was turned back on, thereby releasing the stored probe pulse. The driving field was tuned to the transition $|5^2\text{S}_{1/2}, F = 2, M_F = 0\rangle \rightarrow |5^2\text{P}_{1/2}, F = 1\rangle$, between the Zeeman hyperfine sublevel $5^2\text{S}_{1/2}, F = 2, M_F = 0$ and the first excited state $5^2\text{P}_{1/2}, F = 1$, whereas the probe pulse was tuned to the $|5^2\text{S}_{1/2}, F = 2, M_F = 2\rangle \rightarrow |5^2\text{P}_{1/2}, F = 1\rangle$ transition involving the same upper state $5^2\text{P}_{1/2}, F = 1$. The Zeeman sublevels and the common excited state served as the lower levels $|0\rangle, |1\rangle$ and the upper level $|2\rangle$, respectively, of the required Lambda-type system.

Some of the experimental results for different storage times of the probe pulse are shown in Fig. 7.29. The solid line shows the transmitted probe pulse, the dashed line represents the driving field, and the dotted line represents the input probe pulse. During the time interval in which the driving field was turned off, the probe pulse did not propagate indicating that the pulse was stored in the medium. The probe pulse was observed again after the driving

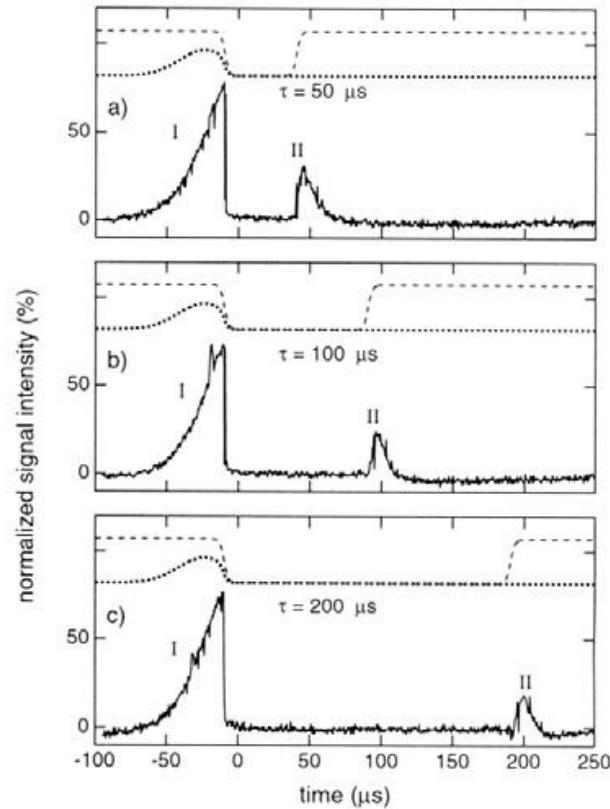


Fig. 7.29. Experimental results of Phillips et al. [178] showing storage of a laser pulse in an atomic medium. From D.F. Phillips, A. Fleischhauer, A. Mair, R.L. Walsworth, M.D. Lukin: *Phys. Rev. Lett.* **86**, 783 (2001). Copyright (2001) by the American Physical Society

field was turned back on. It was also observed that the amplitude of the released pulse decreased with an increasing storage time interval. This effect was related to a long but nonzero lifetime of the Zeeman atomic coherence.

To summarize our study of the adiabatic transfer and photon storage phenomena, we briefly explain the meaning of storage of light in an atomic medium. One could think about the storage of a light pulse as a temporary stopping of the pulse within the medium. In fact, the concept of dark polaritons showed us that the propagating pulse is coherently transformed into an atomic spin state (a so-called spin wave) when the driving field is turned off during the propagation, and later turned back into an optical field when the driving field is again turned on. In addition, the transformation of the pulse into the spin state is not accompanied by a transfer of energy and momentum from the probe pulse to the atomic ensemble. In the EIT process, an absorption from the probe pulse is followed by a stimulated emission into the driving field, and therefore the energy and momentum are actually deposited in the driving field.

8 Quantum Interference in Phase Space

So far, we have considered the effects of quantum interference on the *atomic* properties of systems. Here we wish to study the influence of quantum interference on the *electromagnetic fields* themselves. As we shall see, this requires completely different approaches and methods. These methods have become known as phase-space methods. The use of semiclassical methods in phase space provides us with some physical insight into the properties of EM fields.

We need to introduce a statistical description of the fields in the phase space framework. The density matrix ϱ is the conventional way of introducing probabilistic concepts into quantum mechanics. Whilst it is computationally useful, it is not an easy object to visualize, as its matrix elements are in general complex. The so-called *quasi-probability distributions*, to be defined in Sect. 8.2, however are real valued functions and may be represented by conventional 3D graphs. They also enable quantum-mechanical averages to be calculated in ways analogous to the averages in phase space of classical theory. The first few sections of this chapter are devoted to an introduction to these quantities, with the detailing of their relevant elementary properties. In fact, the quasi-probability function on which we concentrate is the Wigner distribution function, and we show how a knowledge of this quantity for a given field enables us to discuss the photon number distribution of that field. We then present the Wigner functions for some important fields. In later sections we calculate the photon number distribution for particular fields, concentrating on those fields that exhibit pronounced nonclassical properties. Finally, we discuss the Area of Overlap method, which provides physical insight into the appearance of nonclassical features in such properties as the photon number distribution.

8.1 Phase Space in Classical and Quantum Mechanics

In classical mechanics, the state of a system is specified by the values of the M (generalized) coordinates q_j and momenta p_j at some particular time. These quantities evolve uniquely according to the laws of motion. The quantity $(q_1, q_2, \dots, q_M; p_1, p_2, \dots, p_M) \equiv (\mathbf{q}, \mathbf{p})$ may be visualized as a point in a $2M$ -dimensional space, called *phase space*, which moves along a uniquely defined trajectory.

Classical statistical mechanics deals with the situation where the initial values of the coordinates and momenta are not known with certainty, but can only be specified by a probability distribution $P_{\text{cl}}(\mathbf{q}, \mathbf{p})$ for these quantities. Instead of a single initial point as in the deterministic case, we now have a whole ‘cloud’ of initial points, each of which evolves as time progresses. We can imagine the cloud changing its position and shape with time. The expectation value of any function of the coordinates and momenta may be evaluated as an integral over the whole of phase space:

$$\langle f(\mathbf{q}', \mathbf{p}') \rangle_{\text{cl}} = \int d\mathbf{q}' d\mathbf{p}' f(\mathbf{q}', \mathbf{p}') P_{\text{cl}}(\mathbf{q}', \mathbf{p}') , \quad (8.1)$$

where $d\mathbf{v} = dv_1 dv_2, \dots dv_N$, $\mathbf{v} = \mathbf{q}, \mathbf{p}$. From the joint probability, conditional probabilities can be obtained for the coordinates by integrating over the momenta, and for the momenta by integrating over the coordinates:

$$P_{\text{cl}}(\mathbf{q}') = \int d\mathbf{p}' P_{\text{cl}}(\mathbf{q}', \mathbf{p}') , \quad (8.2)$$

$$P_{\text{cl}}(\mathbf{p}') = \int d\mathbf{q}' P_{\text{cl}}(\mathbf{q}', \mathbf{p}') . \quad (8.3)$$

When quantum mechanics was being developed, it was natural for the pioneers to try to incorporate quantum-mechanical uncertainties in a phase space environment in a manner analogous to that used in introducing uncertainties into classical mechanics. However, it is clear that such an analogy cannot be complete, because in quantum mechanics the p_j and q_j are represented by non-commuting operators, which means that their values cannot be measured *simultaneously* to arbitrary accuracy. Thus there is no quantum-mechanical joint probability giving the probability density for the coordinates to have the particular value \mathbf{q}' whilst, *at the same time*, the momenta have the particular value \mathbf{p}' . Nevertheless, useful phase-space quantities have been developed, called *quasi-probability distributions*, which we employ in this chapter to describe quantum interference effects in single mode electromagnetic fields.

We base our discussion here on the harmonic oscillator, which also provides a description of a single mode of the electromagnetic field. It is described in the second-quantized formulation by the Bose annihilation and creation operators \hat{a} and \hat{a}^\dagger . If we have a prescription for calculating the averages of an arbitrary product of these operators, then we can evaluate any function of them that can be expanded in a power series. Actually, we need only a prescription for averages of a particular type of ordering of the factors of the product, for example the normally ordered products $\langle (\hat{a}^\dagger)^m \hat{a}^n \rangle$, in which all the creation operators are placed to the left of the annihilation operators, since any differently ordered product can be manipulated into a sum of products of this type by means of the commutation relation $[\hat{a}, \hat{a}^\dagger] = 1$. In the next section, we describe how such averages may be evaluated.

The annihilation and creation operators are related to the position and momentum operators of a one-dimensional harmonic oscillator of mass m and

frequency ω by the relations

$$\hat{q} = \sqrt{\frac{\hbar}{2m\omega}}(\hat{a} + \hat{a}^\dagger) , \quad (8.4a)$$

$$\hat{p} = -i\sqrt{\frac{m\hbar\omega}{2}}(\hat{a} - \hat{a}^\dagger) . \quad (8.4b)$$

Whilst it is possible to develop the phase-space theory in terms of the operators \hat{q} and \hat{p} , it is more convenient for the electromagnetic field to base our description on the operators \hat{a} and \hat{a}^\dagger .

8.2 The Quasi-probability Distributions

The density matrix ρ is the conventional way of introducing probabilistic quantities into quantum mechanics. Whilst it is computationally useful, it is not usually an easy object to visualize, as its matrix elements are in general complex. The so-called *quasi-probability distributions*, to be defined in Sect. 8.2, however are real valued functions and may be represented by conventional 3D graphs. They also enable quantum-mechanical averages to be calculated in ways analogous to the averages in phase space of classical theory. We shall see that a knowledge of some of these distributions enables us to infer easily whether a given field is nonclassical – something that cannot usually be achieved from by inspection of the form of the density matrix.

The quasi-probabilities are introduced through the *characteristic functions*. We define three of these, which are functions of the complex variable ξ , to deal with the three common kinds of operator ordering

$$C^{(n)}(\xi) = \text{Tr}[\rho \exp(\xi \hat{a}^\dagger) \exp(-\xi^* \hat{a})] , \quad (8.5a)$$

$$C^{(a)}(\xi) = \text{Tr}[\rho \exp(-\xi^* \hat{a}) \exp(\xi \hat{a}^\dagger)] , \quad (8.5b)$$

$$C^{(s)}(\xi) = \text{Tr}[\rho \exp(\xi \hat{a}^\dagger - \xi^* \hat{a})] . \quad (8.5c)$$

Normally ordered, antinormally ordered, and symmetrically ordered averages may then be computed using the appropriate characteristic functions in a manner analogous to that employed with classical characteristic functions

$$\langle (\hat{a}^\dagger)^m \hat{a}^n \rangle = \frac{\partial^{(m+n)}}{\partial \xi^m \partial (-\xi^*)^n} C^{(n)}(\xi) \Big|_{\xi=0} , \quad (8.6a)$$

$$\langle \hat{a}^n (\hat{a}^\dagger)^m \rangle = \frac{\partial^{(m+n)}}{\partial \xi^m \partial (-\xi^*)^n} C^{(a)}(\xi) \Big|_{\xi=0} , \quad (8.6b)$$

$$\langle \mathcal{S}_0 [(\hat{a}^\dagger)^m \hat{a}^n] \rangle = \frac{\partial^{(m+n)}}{\partial \xi^m \partial (-\xi^*)^n} C^{(s)}(\xi) \Big|_{\xi=0} , \quad (8.6c)$$

where $\mathcal{S}_0 [\dots]$ indicates that the symmetrical ordering of the product in the brackets is to be taken. The symmetrically ordered product of a product of

annihilation and creation operators is defined to be the average of all possible orderings. For example, $\mathcal{S}_0 [\hat{a}^2 \hat{a}^\dagger] = (\hat{a} \hat{a} \hat{a}^\dagger + \hat{a} \hat{a}^\dagger \hat{a} + \hat{a}^\dagger \hat{a} \hat{a}) / 3$.

These three definitions may be combined into one by making use of the Baker–Hausdorff–Campbell formula. If two operators \hat{A} and \hat{B} have a commutator which is a c-number, this formula states that

$$e^{\hat{A}+\hat{B}} = e^{\hat{A}} e^{\hat{B}} e^{-[\hat{A}, \hat{B}]/2} . \quad (8.7)$$

In particular, we have

$$\hat{D}(\xi) \equiv e^{\xi \hat{a}^\dagger - \xi^* \hat{a}} = e^{\xi \hat{a}^\dagger} e^{-\xi^* \hat{a}} e^{-|\xi|^2/2} , \quad (8.8)$$

from which follows the relationships

$$C^{(s)}(\xi) = C^{(n)}(\xi) e^{-|\xi|^2/2} = C^{(a)}(\xi) e^{|\xi|^2/2} . \quad (8.9)$$

The unitary operator $\hat{D}(\xi)$ is an important quantity in quantum optics, and is known as the *displacement operator*. It is the generator of a number of important states. For example, acting on $|0\rangle$, the vacuum state of the electromagnetic field, it produces the *coherent state* $|\xi\rangle$, and acting on the Fock state $|n\rangle$ it produces the *displaced number state* $|\xi, n\rangle$. The displacement operators form a complete set of operators, in the sense that an arbitrary bounded operator \hat{F} may be expanded in terms of them. These properties are summarized below.

$$\hat{D}^\dagger(\xi) = \hat{D}(-\xi) = [\hat{D}(\xi)]^{-1} , \quad (8.10a)$$

$$|\xi\rangle \equiv \hat{D}(\xi)|0\rangle , \quad (8.10b)$$

$$|\xi, n\rangle \equiv \hat{D}(\xi)|n\rangle , \quad (8.10c)$$

$$\hat{F} = \int \frac{d^2\xi}{\pi} f(\xi) \hat{D}(-\xi) , \quad (8.10d)$$

where

$$f(\xi) = \text{Tr}[\hat{F} \hat{D}(\xi)] . \quad (8.11)$$

To combine the three definitions (8.5), we introduce the parameter $p = 0, \pm 1$. We define the characteristic function $C_p(\xi)$ and present the inverse relation for the density matrix ϱ below

$$C_p(\xi) \equiv \text{Tr}[\varrho \exp(\xi \hat{a}^\dagger - \xi^* \hat{a} + p|\xi|^2/2)] , \quad (8.12a)$$

$$\varrho = \int \frac{d^2\xi}{\pi} C_p(\xi) \exp(-\xi \hat{a}^\dagger + \xi^* \hat{a} - p|\xi|^2/2) , \quad (8.12b)$$

where $p = 0, \pm 1$. Then we have

$$C^{(n)}(\xi) = C_1(\xi) ; \quad C^{(a)}(\xi) = C_{-1}(\xi) ; \quad C^{(s)}(\xi) = C_0(\xi) . \quad (8.13)$$

The relation (8.12a) represents a mapping from the operator ϱ , which is a function of the two operators \hat{a} and \hat{a}^\dagger , to the scalar function C_p , which is a function of the complex variable ξ .

Using the notation $\mathcal{S}_p[\cdots]$ to denote the normally ordered form of its argument if $p = 1$, the anti-normally ordered form if $p = -1$, and the symmetrically-ordered form if $p = 0$, we may write the three equations of (8.6) as one:

$$\langle \mathcal{S}_p [(\hat{a}^\dagger)^m \hat{a}^n] \rangle = \frac{\partial^{(m+n)}}{\partial \xi^m \partial (-\xi^*)^n} C_p(\xi) \Big|_{\xi=0} . \quad (8.14)$$

However, the relation (8.14) does not always provide a convenient, practical route for calculating the average of functions of the \hat{a} and \hat{a}^\dagger . More convenient quantities for this and other purposes are the quasi-probabilities, which we are now in a position to introduce.

Following the classic papers of Cahill and Glauber [179, 180], we define the three quasi-probability functions corresponding to the characteristic functions (8.12) by the relation

$$W_p(\alpha) \equiv \int \frac{d^2\xi}{\pi} C_p(\xi) \exp(\alpha\xi^* - \alpha^*\xi) , \quad (p = 0, \pm 1) . \quad (8.15)$$

The inverse relation is

$$C_p(\xi) = \int \frac{d^2\alpha}{\pi} W_p(\alpha) \exp(\alpha^*\xi - \alpha\xi^*) . \quad (8.16)$$

We note that (8.15) and (8.16) define essentially the two-dimensional Fourier transform and its inverse.

From (8.15 and (8.16) we prove a useful relation between functions corresponding to two different density matrices – that is, to two different systems. We use the notation $C_{p,k}(\xi)$ and $W_{p,k}(\xi)$ to denote the characteristic function and quasi-probability corresponding to the density matrix ϱ_k . Substituting from (8.16) into the integral over the product of the two characteristic functions

$$\begin{aligned} \int d^2\xi C_{p,1}(\xi) C_{p,2}(\xi) &= \int d^2\alpha \int d^2\beta W_{p,1}(\alpha) W_{p,2}(\beta) \\ &\quad \times \int \frac{d^2\xi}{\pi^2} \exp[(\alpha^* + \beta^*)\xi - (\alpha + \beta)\xi^*] , \end{aligned} \quad (8.17)$$

and using the two-dimensional delta function

$$\delta^{(2)}(\alpha) \equiv \delta(x) \delta(y) = \frac{1}{\pi^2} \int d^2\xi \exp(\alpha\xi^* - \alpha^*\xi) , \quad (8.18)$$

where $x = \text{Re}(\alpha)$, $y = \text{Im}(\alpha)$, we find

$$\int d^2\xi C_{p,1}(\xi)C_{p,2}(\xi) = \int d^2\xi W_{p,1}(\xi)W_{p,2}(-\xi) . \quad (8.19)$$

By a similar argument, we can show that the following relation is satisfied

$$\int d^2\xi C_{p,1}(\xi)C_{p,2}(-\xi) = \int d^2\xi W_{p,1}(\xi)W_{p,2}(\xi) . \quad (8.20)$$

It may be shown that the symmetrized averages of (8.6) may also be evaluated as integrals of the appropriate quasi-probability functions:

$$\langle \mathcal{S}_p [(\hat{a}^\dagger)^m \hat{a}^n] \rangle = \int \frac{d^2\xi}{\pi} (\xi^*)^m \xi^n W_p(\xi) , \quad (8.21)$$

where the integral is carried out over the entire complex ξ plane. This expression demonstrates why the W_p functions are called quasi-probabilities: the right-hand-side is formally identical to that for the classical average of a function with respect to a probability distribution $W_p(\xi)$. However, the function $W_p(\xi)$ in the quantum case we are considering here is not necessarily positive everywhere, and so cannot be generally identified with a probability distribution. This is one reason why it is termed a *quasi*-probability distribution.

These functions are of great importance in quantum optics and have been given special names, as indicated in the Table 8.1, where we employ the more-or-less standard notation.

Table 8.1. Quasi-probability distribution functions

| p | Name | Notation |
|----------|---------------------------------|---|
| 1 | Glauber–Sudarshan P -function | $W_1(\xi) \equiv P(\xi)$ |
| 0 | Wigner function | $W_0(\xi) \equiv W(\xi)$ |
| -1 | Husimi Q -function | $W_{-1}(\xi) \equiv Q(\xi) = \langle \xi \varrho \xi \rangle$ |

In the following pages we cite a number of results without proof. Whilst all three quasi-probabilities are much used in quantum optics, we shall deal almost exclusively with the Wigner function, $W_0(\xi)$ here. It satisfies the relations

$$\int \frac{d^2\xi}{\pi} W_0(\xi) = 1 , \quad (8.22a)$$

$$-2 \leq W_0(\xi) \leq 2 , \quad (8.22b)$$

for all density operators.

We note that a different normalization is often used in the literature:

$$\int d^2\xi W(\xi) = 1 . \quad (8.23)$$

We use the symbol $W = W_0/\pi$ to denote the Wigner function with this normalization. The normalization we have chosen leads to expressions which are symmetric between the characteristic functions and the quasi-probability functions. The use of W_0 assumes a phase-space ‘volume’ of $d^2\xi/\pi$ whereas the use of W assumes a phase-space ‘volume’ of $d^2\xi$.

It can be shown that [63]

$$W_0(\alpha) = 2e^{-2|\alpha|^2} \int \frac{d^2\xi}{\pi} \langle -\xi | \varrho | \xi \rangle e^{-2(\xi\alpha^* - \xi^*\alpha)} . \quad (8.24)$$

This expression provides a direct way of calculating the Wigner function from the density operator.

To conclude this section we remark that the Wigner function is more frequently defined as

$$W(p, q) = \frac{1}{\pi\hbar} \int_{-\infty}^{\infty} dy e^{-2yp/\hbar} \langle q - y | \varrho | q + y \rangle , \quad (8.25)$$

where p and q are defined in (8.4). It can be shown [63] that this definition is equivalent to (8.15).

In this chapter, we have presented only a scant outline of the quasi-probability functions and their properties. The interested reader is referred to the text by Schleich [181] and the papers by Cahill and Glauber [179, 180].

8.3 Wigner Functions for Some Common Fields

In this section we present analytic expressions that we illustrate with plots for some common states of the single-mode electromagnetic field. Our main purpose in this is just to give the reader some feeling for the nature of the Wigner functions for these common fields. The importance of Gaussian function in these expressions will become apparent. Also, for a couple of these classes of fields – the Fock states and the squeezed states – we shall report the experimental measurements of their Wigner functions, and these can be compared with our theoretical plots.

8.3.1 Fock States

First we calculate the symmetric characteristic function when the field is in a Fock state $|n\rangle$ with exactly n photons in the field. The density matrix is then $\varrho = |n\rangle\langle n|$. From the last of equations (8.5), we see that the symmetric characteristic function is

$$C_{0,n}(\xi) = \langle n | \exp(\xi\hat{a}^\dagger - \xi^*\hat{a}) | n \rangle = D_{n,n}(\xi) , \quad (8.26)$$

where the notation $C_{0,n}(\xi)$ indicates the characteristic function for a state of the single-mode field with exactly n photons in it.

We need to evaluate the final factor of (8.26). Cahill and Glauber [179] obtain the more general result

$$\begin{aligned}\langle n|D(\xi)|m\rangle &\equiv D_{n,m}(\xi) \\ &= \left(\frac{m!}{n!}\right)^{1/2} \xi^{n-m} e^{-|\xi|^2/2} L_m^{(n-m)}(|\xi|^2),\end{aligned}\quad (8.27)$$

from which we deduce

$$C_{0,n}(\xi) = L_n(|\xi|^2) \exp(-|\xi|^2/2), \quad (8.28)$$

where $L_n(x)$ is the Laguerre polynomial of degree n . They also show [180] that the Wigner function for a Fock state with n photons is given explicitly by

$$W_{0,n}(\xi) = 2(-1)^n D_{n,n}(2\xi) = 2(-1)^n e^{-2|\xi|^2} L_n(4|\xi|^2), \quad (8.29)$$

from which expression follows the result

$$W_{0,n}(0) = 2(-1)^n, \quad (8.30)$$

demonstrating explicitly that the Wigner function can take negative values. Negative values of the Wigner function are taken as an indication that the quantum state of the field it describes has no classical analogue – that is, the field is *nonclassical*. Equation (8.30) shows that Fock states – at least those for odd n – are highly nonclassical.

Since $L_0(|\xi|^2) = 1$, the Wigner function for the electromagnetic vacuum is

$$W_{0,0}(\xi) = 2 \exp(-2|\xi|^2). \quad (8.31)$$

The $W_{0,n}(\xi)$ are functions of $|\xi|^2$ only – that is, they have cylindrical symmetry. This indicates that with Fock states, the photon number is precisely defined but the phase is undetermined: the Wigner function is independent of the phase of ξ .

The Wigner functions describing the first few Fock states ($n = 0, 1, 2, 3$) are shown in Fig. 8.1. The property that the Wigner functions for Fock states with $n \geq 1$ take negative values is clear in the graphs, and enables one to infer immediately that the corresponding states are nonclassical.

We have stated before that the continuous, real-valued Wigner function possesses the advantage of clear visualization over the discrete, complex-valued density matrix. The Fock states however provide an exception to this rule, for the density matrix in this case is given, in the Fock state basis, by the expression $\varrho_{n,m} = \delta_{n,m}$, which could not be simpler! However, this expression does not convey obvious information about the non-classicality of the state.

8.3.2 Coherent States

If the field is in a pure coherent state, $\varrho = |\alpha\rangle\langle\alpha|$ and then the Wigner function is

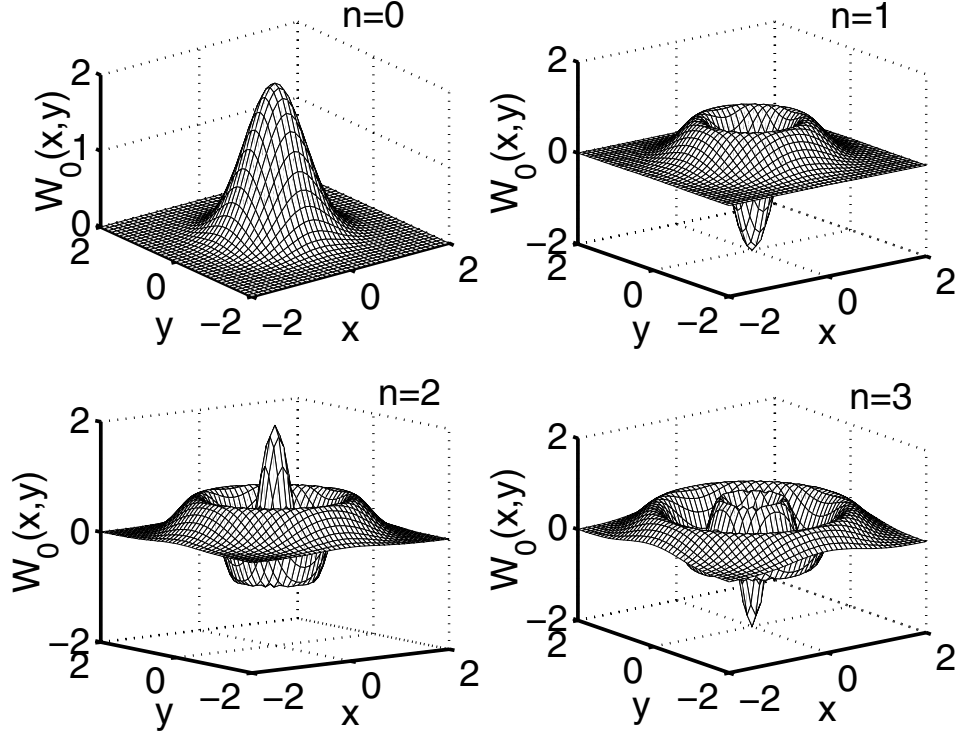


Fig. 8.1. Wigner functions for the $n = 0, 1, 2$, and 3 Fock states as a function of $x \equiv \text{Re}(\xi)$ and $y \equiv \text{Im}(\xi)$

$$W_{0,\alpha}(\xi) = 2 \exp(-2|\xi - \alpha|^2) . \quad (8.32)$$

This differs from the Wigner function of the vacuum field (8.31) only in that it is centred on $\xi = \alpha$ instead of on $\xi = 0$. Therefore, we do not present a separate plot for this function.

8.3.3 Chaotic Field

For the single-mode chaotic field with mean number of photons \bar{n} ,

$$\varrho = \frac{1}{\bar{n} + 1} \sum_{n=0}^{\infty} \frac{\bar{n}}{\bar{n} + 1} |n\rangle \langle n| , \quad (8.33)$$

and the Wigner function is again a Gaussian

$$W_0(\xi) = \frac{2}{2\bar{n} + 1} \exp\left(-\frac{2|\xi|^2}{2\bar{n} + 1}\right) , \quad (8.34)$$

whose width $\sqrt{\bar{n} + 1/2}$ increases as \bar{n} increases.

8.3.4 Squeezed Coherent States

All the Wigner functions considered so far have been cylindrically symmetric. Next we consider the case of a squeezed state, which does not have this

characteristic, but does retain the Gaussian property. A single-mode squeezed state $|\alpha, \varepsilon\rangle$ is defined as

$$|\alpha, \varepsilon\rangle = \hat{D}(\alpha)\hat{S}(\varepsilon)|0\rangle, \quad (8.35)$$

where

$$\hat{S}(\varepsilon) = \exp \left[\frac{1}{2} \varepsilon^* \hat{a}^2 - \frac{1}{2} \varepsilon (\hat{a}^\dagger)^2 \right], \quad (8.36)$$

is the squeeze operator, with $\varepsilon = r \exp(2i\psi)$, r being the squeeze factor and $\hat{D}(\alpha)$ the displacement operator. We take $\psi = 0$ for simplicity. Writing $\xi = x + iy$, $\alpha = x_0 + iy_0$, the Wigner function for $\psi = 0$ is

$$W_{0,\text{sq}}(\xi) = 2 \exp \left[-2(x - x_0)^2 e^{-2r} - 2(y - y_0)^2 e^{2r} \right]. \quad (8.37)$$

The Wigner function for a squeezed state with $r = 1$, and $\alpha = 0$ is shown in Fig. 8.2. The choice $r = 1$ corresponds to the fluctuations in the y -direction being squeezed, and those in the x -direction increased. The contours of this Wigner function are ellipses, as is apparent from (8.37), with semi-major ellipse $\exp(r)$ and semi-minor ellipse $\exp(-r)$. The Wigner function for $\alpha \neq 0$ would be similar, except that it would be centred on $\xi = \alpha$ rather than on $\xi = 0$.

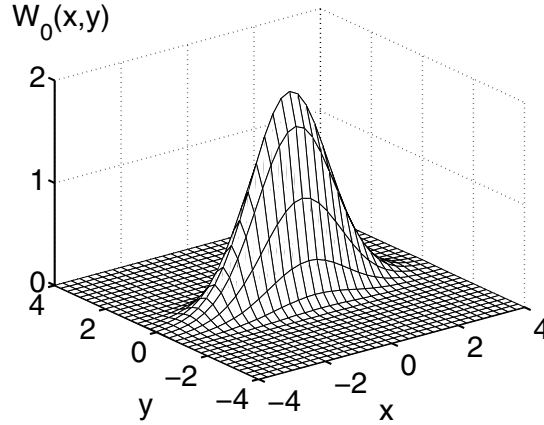


Fig. 8.2. The Wigner function for the squeezed state $|\alpha, \varepsilon\rangle$ with $\alpha = \psi = 0$ and $r = 1$

8.4 Expansion in Fock States

In this section, we obtain a general expression for the Wigner function, which we decompose into a classical, ‘mixture’ part and a term that we identify with the quantum interference contributions.

The Fock states, $|n\rangle$, ($n = 0, 1, 2, 3, \dots$) form a complete set, and so we may expand an arbitrary density operator ϱ in terms of these states as

$$\varrho = \sum_{m,n=0}^{\infty} \varrho_{m,n} |m\rangle\langle n| . \quad (8.38)$$

We write (8.12a) as $C_0(\xi) = \text{Tr}[\varrho D(\xi)]$ and substitute for ϱ from (8.38) to obtain the expression

$$C_0(\xi) = \sum_{m,n=0}^{\infty} \text{Tr}[\varrho_{m,n} D_{n,m}(\xi)] . \quad (8.39)$$

We may now substitute for $C_0(\xi)$ in the definition (8.15) of the Wigner function, when we find

$$\begin{aligned} W_0(\alpha) &= \int \frac{d^2\xi}{\pi} \sum_{m,n=0}^{\infty} \varrho_{m,n} D_{n,m}(\xi) \exp(\alpha\xi^* - \alpha^*\xi) \\ &= \sum_{m,n=0}^{\infty} \varrho_{m,n} T_{n,m}(\alpha) , \end{aligned} \quad (8.40)$$

where

$$\hat{T}(\alpha) \equiv \int \frac{d^2\xi}{\pi} \exp(\alpha\xi^* - \alpha^*\xi) \hat{D}(\xi) \quad (8.41)$$

is an operator introduced by Cahill and Glauber [179]. They showed that

$$T_{n,m}(\alpha) \equiv \langle n | \hat{T}(\alpha) | m \rangle = 2(-1)^m D_{n,m}(2\alpha) , \quad (8.42)$$

which, in conjunction with (8.40), gives us

$$W_0(\alpha) = 2 \sum_{m,n=0}^{\infty} (-1)^m \varrho_{m,n} D_{n,m}(2\alpha) . \quad (8.43)$$

Using (8.27), we may rewrite this expression explicitly in terms of Laguerre polynomials:

$$\begin{aligned} W_0(\alpha) &= 2 \sum_{m,n=0}^{\infty} (-1)^m \varrho_{m,n} \left(\frac{m!}{n!} \right)^{1/2} (2\alpha)^{n-m} \\ &\quad \times e^{-2|\alpha|^2} L_m^{(n-m)}(4|\alpha|^2) . \end{aligned} \quad (8.44)$$

We have seen that quantum interference is associated with the persistence of coherences – that is, off-diagonal density matrix elements. It is therefore convenient to separate (8.44) into the sum of two terms, the first of which,

the ‘mixture’ part, represents the contribution of a corresponding system in which the density matrix (8.38) is replaced by the diagonal form

$$\varrho \rightarrow \varrho^{\text{mix}} = \sum_{n=0}^{\infty} \varrho_{n,n} |n\rangle \langle n| , \quad (8.45)$$

and the second of which is the sum of off-diagonal terms, which we take to represent quantum interference effects. This procedure leads to

$$W_0(\alpha) = W_0^m(\alpha) + W_0^q(\alpha) , \quad (8.46)$$

where

$$\begin{aligned} W_0^m(\alpha) &= 2e^{-2|\alpha|^2} \sum_{n=0}^{\infty} (-1)^n \varrho_{n,n} L_n(4|\alpha|^2) , \\ W_0^q(\alpha) &= 4e^{-2|\alpha|^2} \sum_{m>n=0}^{\infty} (-1)^m \left(\frac{m!}{n!} \right)^{1/2} (2|\alpha|)^{n-m} |\varrho_{m,n}| \\ &\quad \times L_m^{(n-m)}(4|\alpha|^2) \cos [\theta_{n,m} + \phi(m-n)] , \end{aligned} \quad (8.47)$$

with $L_n(x) \equiv L_n^{(0)}(x)$, and the sum in the final line is over values of m and n with $m > n$. We have written $\alpha = |\alpha| \exp(i\phi)$, $\varrho_{m,n} = |\varrho_{m,n}| \exp(i\theta_{m,n})$ and made use of the hermiticity of ϱ and D . The summand in (8.47) is the complex conjugate of the corresponding term with m and n interchanged. Written in this fashion, expression (8.47) makes clear that W_0^q depends on the phases of the density matrix and the complex variable α .

The term $W_0^m(\alpha)$ is the Wigner function which describes an initially coherent quantum system in which all the off-diagonal elements have decayed away (by decoherence), resulting in a ‘mixed’ density matrix.

8.5 Superpositions of Fock States

In this section, we consider states which are superpositions of two Fock states. Such states were of interest some years ago because they exhibit nonclassical properties such as photon antibunching and quadrature squeezing. They provide one of the simplest illustrations of the ideas of quantum interference in phase space, as well as a simple illustration of the use of (8.46).

We study states of the type

$$|\Psi_n\rangle = A_0|0\rangle + A_n|n\rangle , \quad |A_0|^2 + |A_n|^2 = 1 , \quad (8.48)$$

where we shall consider only the cases $n = 1$ and $n = 2$. We always include the vacuum state, because its low noise properties (as compared with higher-order Fock states) are needed in order to make fluctuations below the vacuum level possible.

A number of schemes have been suggested for preparing superpositions of Fock states. The state $|\Psi_1\rangle = A_0|0\rangle + A_1|1\rangle$ for example may be produced in a Jaynes–Cummings system with the cavity field prepared initially in the vacuum state and the two-level atom prepared in a coherent superposition of its upper and lower states. Alternatively, one can employ a linear directional coupler with the vacuum state in one input port and the one-photon state in the other port.

If we take the *quadrature operators* \hat{X}_1 and \hat{X}_2 to be the real and imaginary parts of the annihilation operator, we have

$$\hat{X}_1 = \frac{\hat{a} + \hat{a}^\dagger}{2}, \quad \hat{X}_2 = \frac{\hat{a} - \hat{a}^\dagger}{2i}. \quad (8.49)$$

These operators satisfy the Heisenberg uncertainty relation

$$\langle(\Delta\hat{X}_1)^2\rangle\langle(\Delta\hat{X}_2)^2\rangle \geq \frac{1}{16} \equiv C^2, \quad (8.50)$$

where $\langle(\Delta\hat{X})^2\rangle \equiv \langle\hat{X}^2\rangle - \langle\hat{X}\rangle^2$ denotes the variance of the operator \hat{X} . If the fluctuations in one quadrature, say \hat{X}_1 , are reduced below the vacuum level C :

$$\langle(\Delta\hat{X}_1)^2\rangle < C, \quad (8.51)$$

then they are said to be *squeezed*. The fluctuations in the quadrature \hat{X}_2 must be correspondingly enhanced, so that (8.50) is satisfied. Squeezed fields, as defined above, are nonclassical fields – they have no classical analogue [182].

If, in addition to (8.51) being satisfied, the equality in (8.50) holds, i.e.

$$\langle(\Delta\hat{X}_1)^2\rangle\langle(\Delta\hat{X}_2)^2\rangle = C^2, \quad (8.52)$$

the squeezing is said to be ‘ideal’.

It is straightforward to obtain the expressions

$$\text{Var}(\hat{X}_1) = \frac{1}{4} + \frac{1}{2} \left[\langle\hat{a}^\dagger\hat{a}\rangle + \text{Re}\langle\hat{a}^2\rangle - 2(\text{Re}\langle\hat{a}\rangle)^2 \right], \quad (8.53a)$$

$$\text{Var}(\hat{X}_2) = \frac{1}{4} + \frac{1}{2} \left[\langle\hat{a}^\dagger\hat{a}\rangle - \text{Re}\langle\hat{a}^2\rangle + 2(\text{Im}\langle\hat{a}\rangle)^2 \right]. \quad (8.53b)$$

For the case $n = 1$, the variance in \hat{X}_1 is found to be

$$\langle(\Delta\hat{X}_1)^2\rangle = \frac{1}{4} + |A_1|^2 \left[\frac{1}{2} - (1 - |A_1|^2 \cos^2 \zeta) \right], \quad (8.54)$$

where $A_n = |A_n| \exp(i\zeta)$, and the variance in \hat{X}_2 is given by the same expression except for $\cos \zeta$ being replaced by $\sin \zeta$. The minimum in $\langle(\Delta\hat{X}_1)^2\rangle$ occurs when $|A_1| = 1/2$ and $\zeta = 0$.

For the case $n = 2$, the variances in $\hat{X}_{1,2}$ are

$$\langle (\Delta \hat{X}_{1,2})^2 \rangle = \frac{1}{4} + |A_2|^2 \pm \frac{\sqrt{2}}{2} |A_2| \sqrt{1 - |A_2|^2} \cos \zeta, \quad (8.55)$$

the ‘plus’ sign referring to \hat{X}_1 and the ‘minus’ sign to \hat{X}_2 . The minimum in $\langle (\Delta \hat{X}_1)^2 \rangle$ occurs when $|A_2|^2 = 1/2 - \sqrt{1/6}$ and $\zeta = 0$.

The Wigner functions of squeezed states possess contours that do not exhibit cylindrical symmetry, unlike the other examples of Wigner functions we have considered to date. They depend upon the phase ϕ of the phase-space variable $\alpha = |\alpha| \exp(i\phi)$ – hence squeezing is said to be a phase-dependent nonclassical property. Typically, the contours are roughly elliptical, with the minor axis of the ellipse corresponding to reduced (i.e. squeezed) fluctuations compared to the vacuum level, and the major axis to enhanced fluctuations.

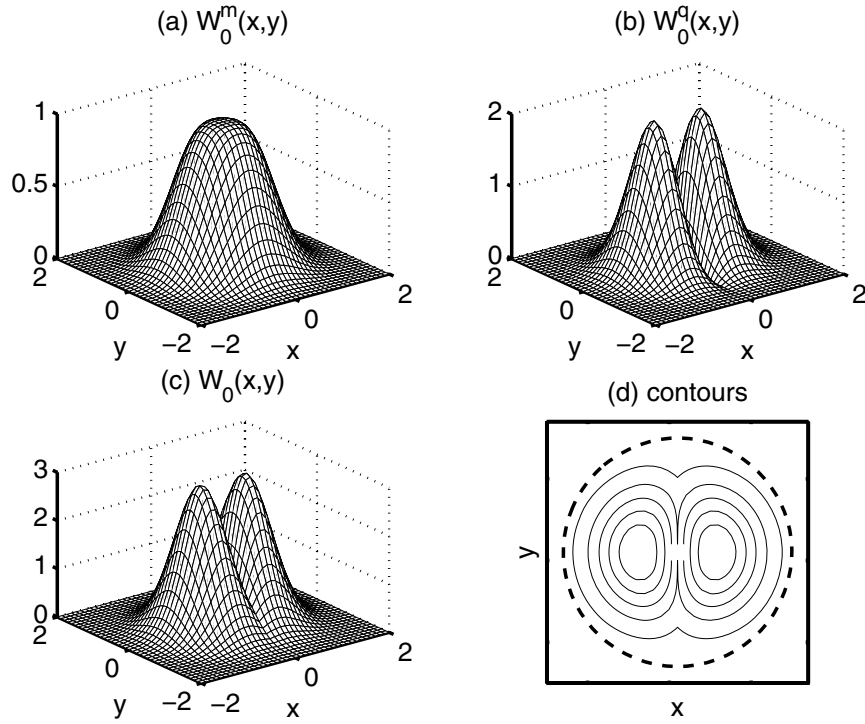


Fig. 8.3. The Wigner function for the state $|\Psi_1\rangle$ as a function of $x \equiv \text{Re}(\xi)$ and $y \equiv \text{Im}(\xi)$. Frames (a) and (b) present $W_0^m(\xi)$ and $W_0^q(\xi)$, whilst Frame (c) gives their sum, $W_0(\xi)$. A_0 and A_1 are assumed real, with $A_1 = 1/2$. Frame (d) presents the base contours for $W_0(\xi)$ (solid line), together with one circular contour from $W_0^m(\xi)$ (at height 0.1 – dashed line) for comparison. The elliptically symmetric contours for $W_0(\xi)$ indicate phase-sensitive noise properties. In this case, there is modest squeezing

The Wigner function for the superposition state (8.48) is easily evaluated from (8.46). It is displayed in Fig. 8.3 as a function of $x \equiv \text{Re}(\xi)$ and $y \equiv \text{Im}(\xi)$ for the case $n = 1$ – the state $|\Psi_1\rangle$ is a linear superposition of the vacuum and $n = 1$ states. In the figure, we take $A_1 = 1/2$ and $A_0 = \sqrt{3}/2$. Thus A_0 and A_1 are assumed real. These values are the ones that give rise

to maximum squeezing, although the maximum squeezing possible for this state is quite modest: the minimum value of $\langle(\Delta\hat{X}_1)^2\rangle$ is $\langle(\Delta\hat{X}_1)^2\rangle_{\min} = 3/16$, as compared with the vacuum level, $\langle(\Delta\hat{X}_1)^2\rangle_{\text{vac}} = 1/4$. Frames (a) and (b) present the cylindrically symmetric mixed part $W_0^m(\xi)$ and the phase-dependent quantum interference part $W_0^q(\xi)$, respectively, whilst Frame (c) gives the sum, the total Wigner function $W_0(\xi)$. In Frame (d), the contours of $W_0(\xi)$ are presented. It is seen that the contours change from circular in the case of the mixed part $W_0^m(\xi)$ to elliptically symmetric for $W_0(\xi)$, indicating that the fluctuations have become phase-dependent in the latter. It is apparent that the fluctuations in the y -direction are reduced compared to those in the x -direction. The state $|\Psi_1\rangle$ also exhibits photon antibunching.

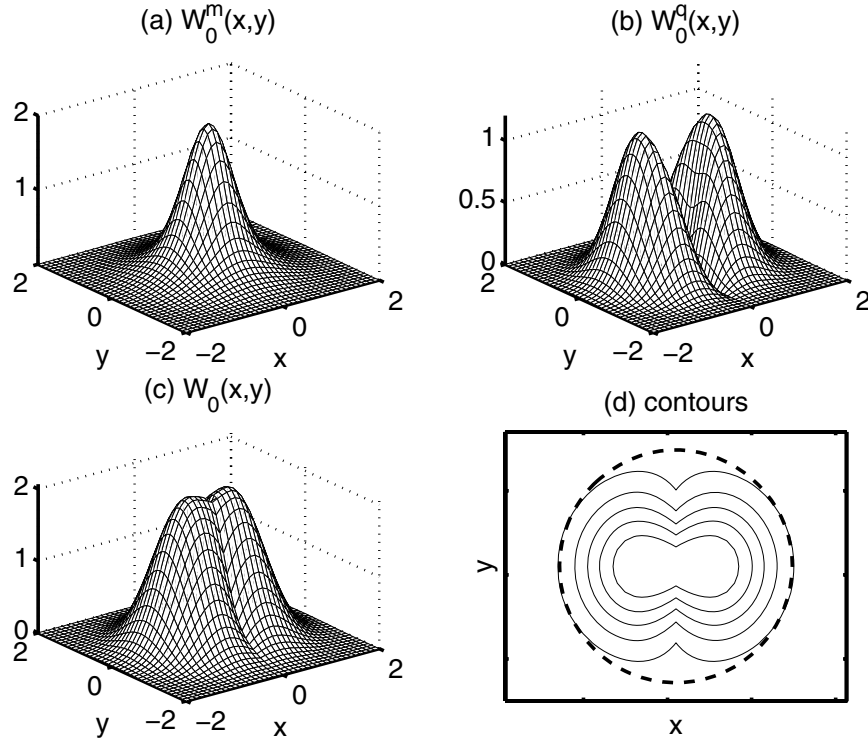


Fig. 8.4. The Wigner function for the state $|\Psi_2\rangle$ as a function of $x \equiv \text{Re}(\xi)$ and $y \equiv \text{Im}(\xi)$. Frames (a) and (b) present $W_0^m(\xi)$ and $W_0^q(\xi)$, whilst Frame (c) gives their sum, $W_0(\xi)$. In these three frames, $A_2 = (1/2 - \sqrt{1/6})^{1/2}$, and A_0 is also real. Frame (d) presents the base contours for $W_0(\xi)$ (*solid line*), together with one circular contour from $W_0^m(\xi)$ (at height 0.1 – *dashed line*) for comparison

We now repeat the calculation for the case of $|\Psi_2\rangle$ – the superposition of the $n = 0$ and $n = 2$ Fock states. In this case, the value of A_2 for maximum squeezing is $A_2 = (1/2 - \sqrt{1/6})^{1/2}$, and A_0 and A_2 are assumed real. Somewhat better squeezing is possible for this system, $\langle(\Delta\hat{X}_1)^2\rangle_{\min} = 0.138$, as compared with $\langle(\Delta\hat{X}_1)^2\rangle_{\min} = 0.1875$ for the one-photon superposition state. The Wigner functions and contours for $|\Psi_2\rangle$ are shown in Fig. 8.4.

It is straightforward to show that for the n -photon superposition state

$$\langle \hat{a}^k \rangle = \int \frac{d^2\xi}{\pi} \xi^k W_0(\xi) = \sqrt{n!} A_0^* A_n \delta_{k,n} . \quad (8.56)$$

This demonstrates that superpositions of Fock states may possess nonzero values of $\langle \hat{a}^k \rangle$, $k \neq 0$, in contrast with pure Fock states. This is a necessary condition for the occurrence of phase-sensitive nonclassical features such as quadrature squeezing. In particular, the state $|\Psi_1\rangle$ exhibits a nonzero mean value of the electric field.

8.6 Experimental Considerations

Here we briefly consider how some of the states we have discussed in the previous sections can be investigated experimentally. In particular, we will illustrate experimental reconstruction of Wigner functions and production of single-photon states.

8.6.1 Reconstruction of Wigner Functions

It is possible to experimentally reconstruct the Wigner functions of field states, using recently developed methods of quantum state reconstruction. There is not sufficient space to discuss these methods here. Instead, we refer the reader to the text by Leonhardt [183], for example.

We mention the experiments of Breitenbach et al. [184], in which the Wigner functions for the coherent state and quadrature squeezed states were reconstructed from measurements of the quantum statistics of their electric fields. Figure 8.5 illustrates these. Using the technique of optical homodyne tomography, they were also able to measure the photon statistics and the absolute values of the density matrix elements of these states.

The Wigner function of the single-photon Fock state has also been reconstructed [185]. In these experiments, also by the Konstanz group and making use of homodyne tomography, single photon states were produced by the process of parametric down conversion. Using tight filtering, the state produced by this system approached a single-photon state in a reasonably well-defined optical mode. However, various unavoidable experimental effects resulted in the admixture of the vacuum into the measured state. The results are shown in Fig. 8.6. It can be seen from the diagonal density matrix element plot that about 45% of the vacuum state is mixed into the one-photon state. However, the reconstructed Wigner function still shows nonclassical features – it becomes negative in the neighbourhood of the origin. (Although its minimum value is much less than the minimum value of $-2/\pi$ for the pure one-photon Fock state.)

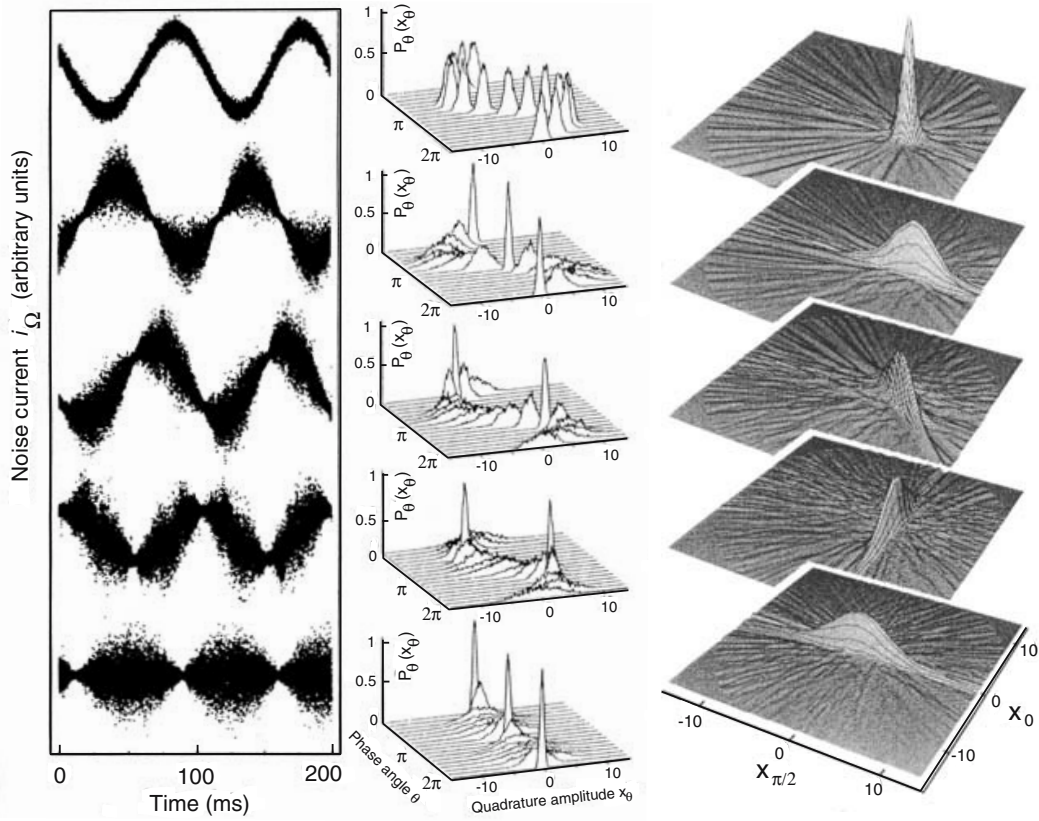


Fig. 8.5. The left-hand side shows the noise current and the centre shows the quadrature distributions. The right-hand side shows the reconstructed Wigner functions of generated quantum states. From the top, these are: coherent state, phase-squeezed state, state squeezed in the $\phi = 48^\circ$ quadrature, amplitude squeezed state, and vacuum state. The noise traces as a function of time show the electric fields' oscillations in a 4π interval for the upper four states, whereas for the squeezed vacuum a 3π interval is shown. The quadrature distributions can be interpreted as the time evolution of the wave packets (position probability densities) during one oscillation period. For the reconstruction of the quantum states, a π interval suffices. From the paper by G. Breitenbach, S. Schiller, J. Mlynek: *Nature* **387**, 471 (1997). Copyright (1997) by Nature, with permission

8.6.2 Production of Single-Photon States

As we have seen, pure Fock states are highly nonclassical, and it is of great interest for fundamental physics to have convenient means of producing them. In particular, much attention has recently been devoted to the problem of producing single-photon Fock states, on demand. This is because these states are needed for such applications as quantum cryptography, quantum information processing, and quantum computation. It is important for these applications that the single-photon state is pure – that is, there should be negligible admixture of states $|n\rangle$ with $n \neq 1$.

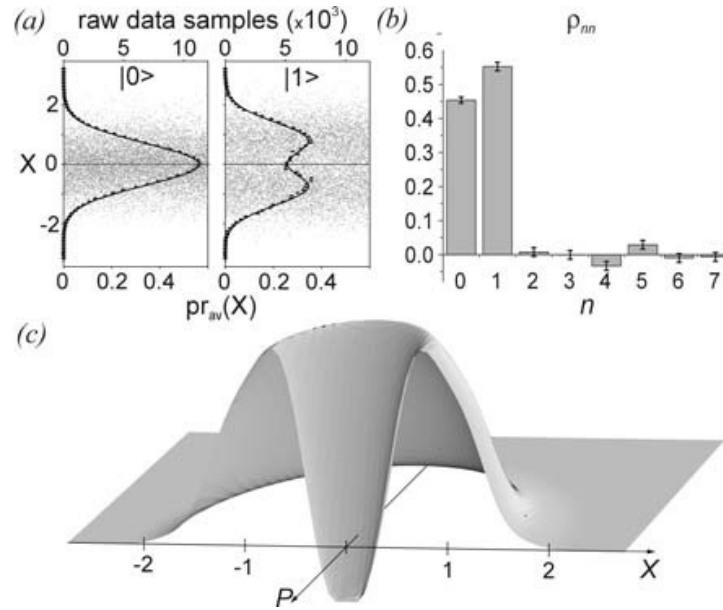


Fig. 8.6. Experimental results of Lvovsky et al. [185]: (a) raw quantum noise data for the vacuum (left) and Fock states (right) along with their histograms corresponding to their phase-randomized marginal distributions; (b) diagonal density matrix elements of the state measured; (c) reconstructed Wigner function, which is negative near the origin. The measured efficiency is 55%. From A.I. Lvovsky, H. Hansen, T. Aichele, O. Benson, J. Mlynek, S. Schiller: Phys. Rev. Lett. **87**, 050402 (2001). Copyright (2001) by the American Physical Society

One way of producing single photons is by the excitation of a single atom or molecule, which then decays by spontaneous emission, emitting a single photon. The first demonstration of the production of $|n = 1\rangle$ states by De Martini et al. in 1996 [186] employed this approach. In their experiments, a single Oxazine 720 molecule in a microcavity trap was excited with a mode-locked laser at a rate of 100 MHz. It was demonstrated that single-photon states were generated over a single field mode with a markedly sub-Poissonian distribution.

Since this time, single-photons sources have been demonstrated in a range of systems, including molecules, mesoscopic quantum wells, colour centres, trapped ions and semi-conductor quantum dots. References to these works can be found in the paper by Santori et al. [187]. Research in this field continues to be very active.

8.7 Photon Number Distribution

The photon number distribution, P_n , is an important property of the single-mode field. It is given by the diagonal elements of ϱ in the Fock state basis.

$$P_n \equiv \varrho_{n,n} . \quad (8.57)$$

For the field in a pure state expanded in terms of the Fock states,

$$|\Phi\rangle = \sum_{n=0}^{\infty} c_n |n\rangle , \quad (8.58)$$

and then P_n is easily determined by

$$P_n = |c_n|^2 , \quad n = 0, 1, \dots, \infty . \quad (8.59)$$

Thus for the states studied in the last section, $|\Psi_n\rangle = A_0|0\rangle + A_n|n\rangle$, the photon number distribution is very simple:

$$P_k = \begin{cases} |A_0|^2 , & k = 0 \\ |A_n|^2 , & k = n \\ 0 , & \text{any other } k . \end{cases} \quad (8.60)$$

For the coherent state

$$|\alpha\rangle = e^{-|\alpha|^2/2} \sum_{n=0}^{\infty} \frac{\alpha^n}{(n!)^{1/2}} |n\rangle , \quad (8.61)$$

the photon number distribution is a Poisson distribution

$$P_n = |\langle n|\alpha\rangle|^2 = \frac{|\alpha|^2}{n!} e^{-|\alpha|^2} . \quad (8.62)$$

To conclude, we wish to derive a general expression for the photon number distribution in terms of the Wigner function for the system under consideration. Substituting (8.12b), the inverse Fourier transform which relates the density matrix to the symmetric characteristic function, in the expression $P_n = \langle n|\varrho|n\rangle$, we obtain

$$P_n = \int \frac{d^2\xi}{\pi} C_0(\xi) \langle n|\exp(-\xi\hat{a}^\dagger + \xi^*\hat{a})|n\rangle . \quad (8.63)$$

Using (8.26) we find

$$P_n = \int \frac{d^2\xi}{\pi} C_0(\xi) C_{0,n}(-\xi) , \quad (8.64)$$

or using (8.20), this may be written as

$$P_n = \int \frac{d^2\xi}{\pi} W_0(\xi) W_{0,n}(\xi) , \quad (8.65)$$

where $W_{0,n}(\xi)$ is the Wigner function for a Fock state with n photons.

It is apparent from (8.65) that the photon number distribution of an arbitrary field is given by the overlap of the Wigner function for that field with the Wigner functions of the Fock states.

8.8 Superpositions of Coherent States

In this section, we show how quantum interference between the component states in a superposition of coherent states may result in nonclassical effects. Quantum interference will be associated with nonzero values of the coherences – the off-diagonal elements of the density matrix in the coherent state basis. We calculate the Wigner functions for some examples of these states, and examine such properties as the photon statistics and squeezing for nonclassical features.

8.8.1 Superposition of N Coherent States

We first consider the general case of a state $|\Psi_N\rangle$ which is a superposition of N coherent states $|\alpha_j\rangle$ before specializing in later sections to the case $N = 2$. The state is

$$|\Psi_N\rangle = Z^{1/2} \sum_{j=1}^N e^{i\theta_j} |\alpha_j\rangle, \quad (8.66)$$

where $Z^{1/2}$ is a normalization factor, given by

$$Z = \left\{ N + 2 \sum_{k>j}^N e^{-\frac{1}{2}|\alpha_j - \alpha_k|^2} \cos[\theta_j - \theta_k - \text{Im}(\alpha_j^* \alpha_k)] \right\}^{-1}. \quad (8.67)$$

The values of the phases θ_j determine whether the quantum interference between the coherent states is constructive or destructive.

The corresponding density matrix is

$$\varrho = Z \sum_{j=1}^N |\alpha_j\rangle\langle\alpha_j| + Z \sum_{j,k=1}^{N'} |\alpha_j\rangle\langle\alpha_k| e^{i(\theta_j - \theta_k)}, \quad (8.68)$$

where the prime on the sum means that terms with $j = k$ are excluded. The corresponding Wigner function is therefore

$$W_{0,\alpha_1,\dots,\alpha_N}(\beta) = Z \sum_{j=1}^N W_{0,\alpha_j}(\beta) + Z \sum_{j,k=1}^{N'} W_{0,jk}(\beta), \quad (8.69)$$

where

$$W_{0,\alpha_j}(\beta) = 2 \exp(-2|\beta - \alpha_j|^2) \quad (8.70)$$

is the Wigner function of the coherent state $|\alpha_j\rangle$, and $W_{0,jk}(\beta)$ is the Wigner function describing the quantum interference between the states $\exp(i\theta_j)|\alpha_j\rangle$ and $\exp(i\theta_k)|\alpha_k\rangle$. It is given by the expression

$$W_{0,jk}(\beta) = 2 \exp \left\{ -\frac{1}{2} |\alpha_j - \alpha_k|^2 - 2 \operatorname{Re} [(\alpha_j - \beta)^* (\alpha_k - \beta)] \right\} \quad (8.71)$$

$$\times \cos \Phi_{j,k} ,$$

where

$$\Phi_{j,k} = \theta_j - \theta_k - \operatorname{Im} (\alpha_j^* \alpha_k) + 2 \operatorname{Im} [(\alpha_j - \beta)^* (\alpha_k - \beta)] . \quad (8.72)$$

With the aid of a little algebra, (8.71) and (8.72) may be rewritten as

$$W_{0,jk}(\beta) = 2 \exp [-2 |\beta - (\alpha_j + \alpha_k)/2|] \cos \Phi_{j,k} , \quad (8.73a)$$

$$\Phi_{j,k} = \theta_j - \theta_k + \operatorname{Im} (\alpha_j^* \alpha_k) + 2 \operatorname{Im} [\beta^* (\alpha_j - \alpha_k)] . \quad (8.73b)$$

Using (8.64), the photon number distribution may be evaluated and similarly written as the sum of two terms:

$$P_{n,\alpha_1,\dots,\alpha_N} = Z \sum_{j=1}^N P_{n,\alpha_j} + Z \sum_{j,k=1}^{N'} P_{n,jk} , \quad (8.74)$$

where

$$P_{n,\alpha_j} = \frac{|\alpha_j|^{2n}}{n!} \exp (|\alpha_j|^2) , \quad (8.75)$$

and

$$P_{n,jk} = \frac{(\alpha_j \alpha_j^*)^n}{n!} \exp \left[\frac{1}{2} (|\alpha_j|^2 + |\alpha_k|^2) \right]$$

$$\times \cos (\theta_j - \theta_k - n \theta_{jk}) , \quad (8.76)$$

with θ_{jk} given by

$$\tan \theta_{jk} = \frac{\operatorname{Im} (\alpha_j^* \alpha_k)}{\operatorname{Re} (\alpha_j^* \alpha_k)} , \quad (8.77)$$

where P_{n,α_j} is just the photon number distribution of the coherent state $|\alpha_j\rangle$, and $P_{n,jk}$ is the contribution due to quantum interference between the two coherent states $\exp(i\theta_j)|\alpha_j\rangle$ and $\exp(i\theta_k)|\alpha_k\rangle$.

8.8.2 Two Coherent State Superpositions

Here we study superpositions of the form

$$|\Psi_2\rangle = Z^{1/2} (|\alpha\rangle + e^{i\theta} |-\alpha\rangle) , \quad (8.78)$$

where

$$Z = \left[2 \left(1 + e^{-2\alpha^2} \cos \theta \right) \right]^{-1} , \quad (8.79)$$

and α is real. The state $|\Psi_2\rangle$ is an eigenstate of the square of the annihilation operator

$$\hat{a}^2 |\Psi_2\rangle = \alpha^2 |\Psi_2\rangle . \quad (8.80)$$

States of this form, with particular values of θ , have been much studied. Table 8.2 lists these, with their common notations.

Table 8.2. State names for various θ values

| θ | State name |
|----------|-----------------------------|
| 0 | Even coherent state |
| π | Odd coherent state |
| $\pi/2$ | Yurke–Stoler coherent state |

These states have been termed ‘Schrödinger cat states’. Schrödinger’s cat was a cat kept in a box in a quantum mechanical state that was a linear combination of the states ‘cat dead’ and ‘cat alive’. Only when a measurement was made did the cat definitely belong to just one or the other of these states. Until this measurement was made, the cat was neither alive nor dead. The state (8.79) is in some ways analogous to the Schrödinger cat state, with $|\alpha\rangle$ say corresponding to the cat being alive, and the state $|\alpha\rangle$ to the cat being dead. The important difference is that the states $|\pm\alpha\rangle$ are no way near as complicated as the wave-function of a cat! However, we remind the reader that the coherent states are the best approximation to a classical state, with well-defined amplitude and phase, that one can obtain in quantum mechanics. For large amplitudes, these may be considered in a sense macroscopic states.

The contribution to the Wigner function from the diagonal terms in (8.68) is

$$W_{0,d} = 2 \left[\exp(-2|\beta - \alpha|^2) + \exp(-2|\beta + \alpha|^2) \right] , \quad (8.81)$$

whilst the quantum interference contribution, which arises from the off-diagonal terms, may be written

$$W_{0,od} = 2 \exp(-2|\beta|^2) \cos[\theta - 4\alpha \operatorname{Im}(\beta)] . \quad (8.82)$$

The Wigner function corresponding to the diagonal terms of ϱ is shown in Fig. 8.7(a). It is essentially the Wigner function which would be obtained if the system was described by a statistical mixture of states

$$\varrho^{\text{mix}} = \sum_{j=1}^N |\alpha_j\rangle \langle \alpha_j| . \quad (8.83)$$

This is the density matrix which one would expect to obtain if strong decohering processes were operating. These would have the effect of eventually making the off-diagonal (quantum interference) terms of (8.68) zero.

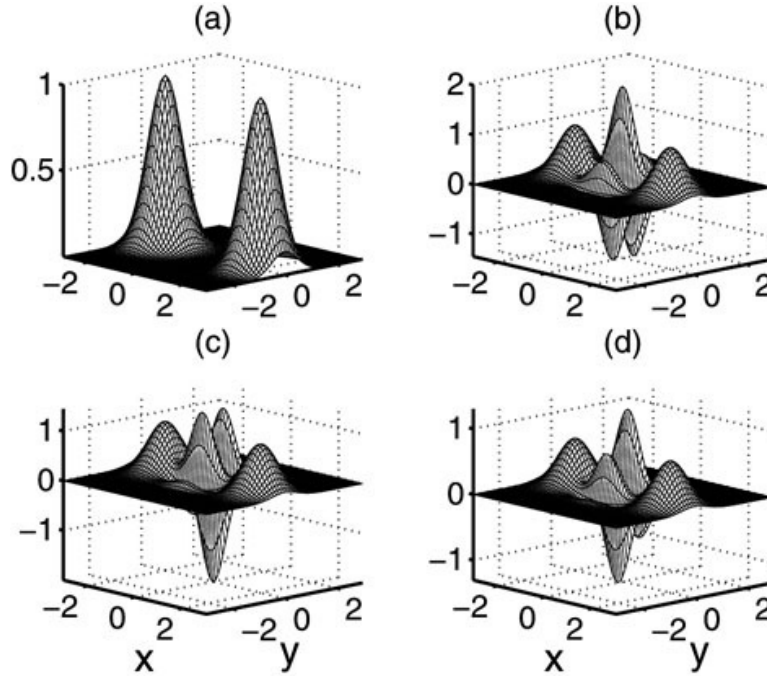


Fig. 8.7. The Wigner function of (b) the even coherent state, (c) the odd coherent state and (d) the Yurke-Stoler coherent state, against $x \equiv \text{Re}\beta$ and $y \equiv \text{Im}\beta$, for $\alpha = 2$. Frame (a) presents the Wigner function of the mixed density matrix (8.83) for comparison

Figure 8.7 presents the Wigner function of the even, odd and Yurke–Stoler coherent states, respectively, for the case $\alpha = 2$. It is evident that the off-diagonal terms of (8.68) strongly modify the diagonal terms, which are shown in Frame (a). The nonclassical nature of the states corresponding to Frames (b) – (d) is apparent from the areas of phase space where the Wigner functions become strongly negative. These states may therefore be expected to show nonclassical physical properties, some of which we now describe.

First we consider the photon number distribution. From (8.76), this may be written as

$$P_n^{(\eta)} = \frac{\alpha^{2n}}{n!} \frac{1 + \eta(-1)^n}{e^{\alpha^2} + \eta e^{-\alpha^2}}, \quad (8.84)$$

where $\eta \equiv \cos \theta = +1, -1$, or 0 depending on whether we are treating an even, odd or Yurke–Stoler coherent state, respectively. It is immediately clear that the photon number distribution is zero for odd values of n for an even coherent state, and zero for even values of n for an odd coherent state. The nonzero values of P_n possess a Poissonian envelope. The zeros in the photon

number distribution for $\eta = \pm 1$ are very striking manifestations of quantum interference. The photon number distribution of the Yurke–Stoler coherent state is simply a Poisson distribution.

To give an explicit example, the photon number distribution of the even coherent state is

$$P_n^{(1)} = \frac{\alpha^{2n}}{n!} \frac{1}{\cosh(\alpha^2)} \Delta_n, \quad (8.85)$$

where $\Delta_n = 1$ if n is even, and $\Delta_n = 0$ if n is odd. This distribution is illustrated in Fig. 8.8 for $\alpha = 4$.

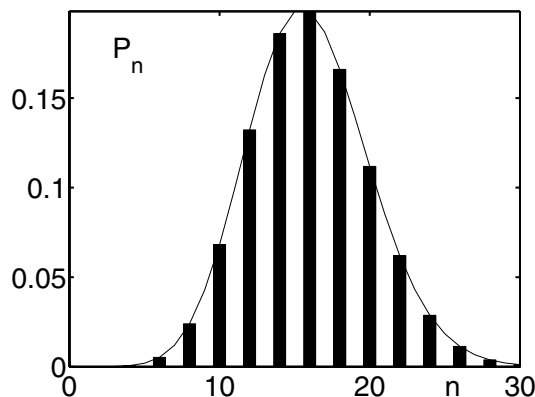


Fig. 8.8. The photon number distribution of the even coherent state, with $\alpha = 4$. The zeros at odd values of n are due to quantum interference. The solid line is the corresponding Poisson envelope

Another nonclassical feature is sub-Poissonian statistics. We recall that a coherent state, the quantum field that most closely approximates a classical field, possesses Poissonian statistics. A Poisson distribution $P_n, n = 0, 1, 2, \dots$ possesses the property that its variance $\langle n^2 \rangle - \langle n \rangle^2$ is equal to the mean $\langle n \rangle$: $\langle n^2 \rangle - \langle n \rangle^2 = \langle n \rangle$. If the variance of a quantum field is such that $\langle n^2 \rangle - \langle n \rangle^2 < \langle n \rangle$, the field has no classical description, at least in terms of the P -function, defined in Sect. 8.2. Deviations from Poissonian behavior are frequently measured in terms of the Mandel Q parameter, defined by

$$Q \equiv \frac{\langle n^2 \rangle - \langle n \rangle^2 - \langle n \rangle}{\langle n \rangle}. \quad (8.86)$$

If a field is such that $Q = 0$, the field is called *Poissonian*, if $Q > 0$, the field is called *super-Poissonian*, and if $Q < 0$, the field is called *sub-Poissonian*. The latter is the case of most interest, because it describes a field with no classical analogue – that is, a nonclassical field.

From (8.84) we find, for the field described by the state (8.79)

$$\langle n \rangle = \alpha^2 (\tanh \alpha^2)^\eta, \quad (8.87a)$$

$$\langle n^2 \rangle = \langle n \rangle + \alpha^4, \quad (8.87b)$$

from which we deduce that

$$Q_\eta = \frac{2\alpha^2\eta}{\sinh(2\alpha^2)} . \quad (8.88)$$

Thus the even coherent state (with $\eta = 1$) possesses super-Poissonian statistics, the odd coherent state (with $\eta = -1$) possesses sub-Poissonian statistics, and the Yurke–Stoler coherent state (with $\eta = 0$) is Poissonian.

Finally, we briefly discuss squeezing in these cat states. Using (8.5), we find

$$\text{Var}(\hat{X}_1) = \frac{1}{4} + \frac{\alpha^2}{1 + \eta e^{-2\alpha^2}} , \quad (8.89a)$$

$$\text{Var}(\hat{X}_2) = \frac{1}{4} - \alpha^2 e^{-2\alpha^2} \frac{(\eta + e^{-2\alpha^2})}{(1 + \eta e^{-2\alpha^2})^2} . \quad (8.89b)$$

Quadrature squeezing occurs if either variance satisfies $\text{Var}(\hat{X}_i) < 1/4$. It is clear that there is no squeezing in \hat{X}_1 whatever the value of η . However, squeezing occurs for $\alpha > 0$ in \hat{X}_2 if $\eta = 1$ or $\eta = 0$. No squeezing occurs in the odd coherent state ($\eta = -1$) in either quadrature.

It is worth remarking that the concept of higher order squeezing has been introduced by Hong and Mandel [188]. It defines a nonclassical effect when the variance of the N th power of a quadrature operator ($\text{Var}(\hat{X}_i^N)$, $N > 1$) is smaller than its value in a coherent state of the field. This is termed $2N$ th order squeezing. It has been demonstrated that fourth order squeezing can occur for the \hat{X}_2 quadrature, for certain values of α , for all three cat states, $\eta = \pm 1, 0$.

8.9 Photon Number Distribution of Displaced Number States

As another example of a field that shows quantum interference effects in its photon number distribution, we consider the displaced Fock states, defined in (8.10c) as $|\xi, k\rangle = D(\xi)|k\rangle$. It can be shown that their photon number distribution is given by

$$P_n^k(r) = \frac{e^{-r} r^{n-k}}{n!k!} \left| \sum_{m=0}^k \frac{n!k!r^k(-r)^m}{m!(n-m)!(k-m)!} \right|^2 , \quad r = |\xi|^2 . \quad (8.90)$$

In particular, for $k = 1$ and 2 , we have

$$P_n^1(r) = \frac{e^{-r} r^n}{n!r} (r - n)^2 , \quad (8.91a)$$

$$P_n^2(r) = \frac{e^{-r} r^n}{2n!r^2} [n^2 - n(r+1) + r^2]^2 . \quad (8.91b)$$

These are shown in Fig. 8.9 for $r = 20$. For this value of r , the distribution $P_n^1(r)$ has an exact zero at $n = 20$ and $P_n^2(r)$ has exact zeros at $n = 16$ and $n = 25$ (total destructive interference).

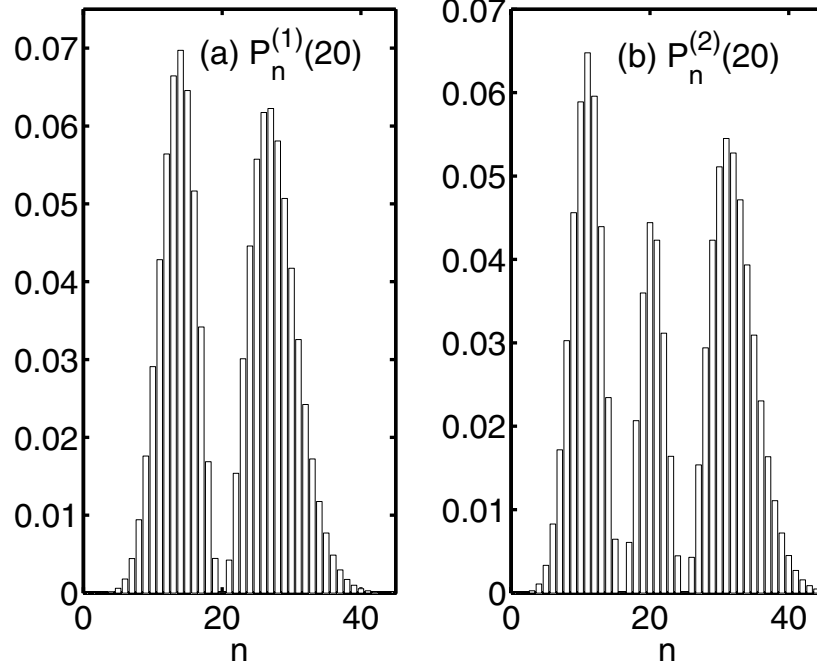


Fig. 8.9. The displaced number states $P_n^k(r)$ for $r = |\varepsilon|^2 = 20$ for (a) $k = 1$ and (b) $k = 2$

8.10 Photon Number Distribution of a Highly Squeezed State

A state with an interesting photon number distribution is the squeezed state, (8.35). For small degrees of squeezing, the photon number distribution does not show any particularly exciting features, but for large degrees of squeezing, it exhibits interesting oscillations in the tail, and can show zeros. Such oscillations and cancellations are typical of interference effects, and we shall show below how they can be attributed to quantum interference. An example is presented in Fig. 8.10, where we take $\alpha = 5$ and $r = 1.5$, with phase $\psi = 0$. This corresponds to a state (8.37) highly squeezed in the y -direction.

We substitute into (8.64), using (8.37) and (8.29) with α assumed real. We also write $\varepsilon = \exp(2r)$ and $\xi = x + iy$. Then we have

$$P_n = \int \frac{d^2\xi}{\pi} f(x, y) , \quad (8.92)$$

where

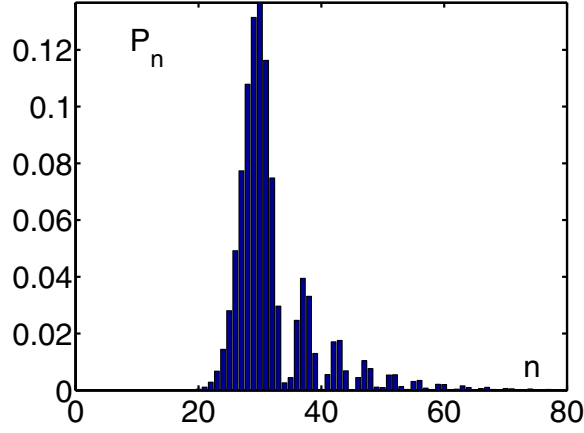


Fig. 8.10. The photon number distribution of the squeezed state (8.35) with $\alpha = 5$ and $r = 1.5$ ($\varepsilon = \exp(2r) \simeq 20$), and phase $\psi = 0$

$$\begin{aligned}
 f(x, y) &= W_0(\xi)W_{0,n}(\xi) \\
 &= 4(-1)^n \exp(-2|\xi|^2)L_n(4|\xi|^2) \\
 &\quad \times \exp(-2\varepsilon y^2) \exp[-2(x - \alpha)^2/\varepsilon] , \quad (8.93)
 \end{aligned}$$

treating $d^2\xi$ as $dx dy$.

To gain insight, we plot the two factors of the integrand, and the integrand itself, in Fig. 8.11. The state is highly squeezed in the y direction: $\varepsilon \simeq 20$. The Wigner function for this state is illustrated in Frame (a). Its contours are ellipses, severely elongated in the x -direction. In Frame (b) we plot the Wigner function for the Fock state with $n = 30$: $W_{0,30}(\xi)$. [Note that in general, $W_{0,n}(\xi)$ has n zeros.] This function is cylindrically symmetric about the z -axis, but we show only a segment of it. Note that the x - and y -ranges vary between different Frames of the figure. The significant feature of the $W_{0,30}$ plot is that it consists of a series of maxima and minima oscillating between positive and negative values until the final zero is reached, after which the function is wholly positive, reaching a maximum value and thereafter decaying monotonically to zero. [This is easier to see in Frame (a) of Fig. 8.12, where we present the radial variation of $W_{0,30}(\xi)$ in a two-dimensional plot.] We shall refer to the region of phase space from the final zero of $W_{0,30}(\xi)$ to the value of $|\xi|$ where $W_{0,30}(\xi)$ first ceases to be significant as the outer ring of the Fock Wigner function.

The significant contributions to the integral (8.92) come from the areas of overlap of the two Wigner functions shown in Frames (a) and (b). We consider this to consist of two parts. The first part derives from the overlap of $W_{0,sq}$ with the outer ring of $W_{0,n}$ – this contribution is always positive. The area of phase space that contributes the most to the integral comes from two diamond shaped regions where a suitable elliptic contour of $W_{0,sq}$ overlaps with the outer ring of $W_{0,n}$. The other part derives from the overlap of $W_{0,sq}$ with the inner, oscillating regions of $W_{0,n}$. The overlap takes on positive and negative values as we move through this region of phase space.

The overlap (i.e. product) of the two functions in Frames (a) and (b), is the integrand $f(x, y)$, which is shown in Frame (c), where it is apparent that it is symmetric about the plane $y = 0$. As described in the previous paragraph, the integrand is positive in the outer ring, whilst the region between consists of peaks and troughs which oscillate in sign. Frame (d) shows half the section of Frame (c), that is, the section sliced through the $y = 0$ plane, in order to display the central deep trough (which is largely obscured in the elevation chosen for Frame (c).) Again, these features are easier to visualize in Fig. 8.12, where we present the section of $f(x, y)$ through the $x = 4$ plane. In this figure, the contribution from the outer ring is small, but this is not necessarily always the case: the relative contribution of the two parts of the integrand depends upon the value of n .

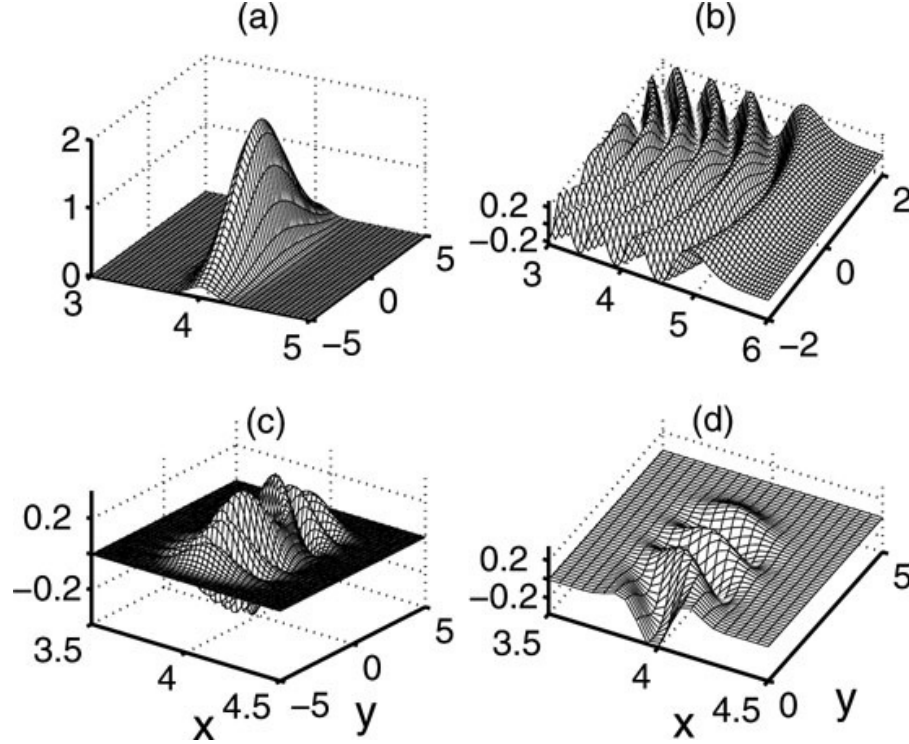


Fig. 8.11. Three-dimensional plots of the Wigner functions for (a) the squeezed state (8.35), with $x_0 = 4$ and $\varepsilon = \exp(2r) \simeq 20$, and (b) the Fock state with thirty photons. Frame (c) presents the product, or overlap, $f(x, y)$ of these two quantities. It is the integrand in (8.92) for P_n . For the outer two peaks, the integrand is positive, whilst it oscillates between positive and negative values in the inner region. Frame (d) shows half the region presented in (c), sectioned through the $y = 0$ plane, in order to emphasize the deep central trough, not evident in (c)

Following this analysis, we perform the integrals by splitting the range over y into the three ranges $-\infty < y < y_{-m}$, $y_{-m} < y < y_m$, and $y_m < y < \infty$, where $y_{\pm m}(x)$ denotes the two extreme zeros of $f(x, y)$. Making use of the symmetry of the integrand, we have

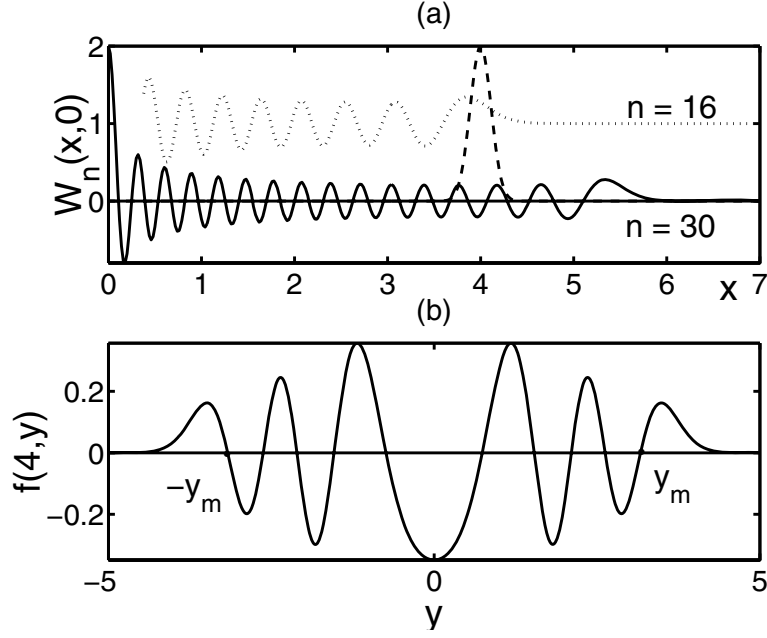


Fig. 8.12. Two dimensional sections from Fig. 8.11. In (a), the radial variation of the Fock state Wigner function, $W_{0,n}(x, 0)$, $n = 30$, is shown [c.f. Fig. 8.11(b)] as the *solid line*, and $W_{0,16}(x, 0)$, shifted upwards by one unit, is shown *dotted*. The $y = 0$ section of the Wigner function for the squeezed state is shown *dashed*. For $n \simeq 30$, the overlap of $W_{0,sq}$ with the outer ring is very small, and the bulk of the contribution comes from the inner region. This contribution varies rapidly with n , and so P_n is small and shows rapid oscillations. As the value of n is reduced, the overlap of $W_{0,sq}$ with the outer ring increases, and the maximum values of P_n increase. For $n \simeq 16$, as we see in Frame (a), almost all the contribution comes from the (positive) outer ring, and P_n becomes large. Eventually though, as n decreases further, the overlap of $W_{0,sq}$ with the outer region decreases, and for sufficiently small n , tends to zero. Then $P_n \simeq 0$. Thus the main features of Fig. 8.10 may be understood. In (b), the $x = 4$ section of the integrand $f(x, y)$ from Fig. 8.11(c) is presented (for $n = 30$). The extreme zeros of this function are denoted y_m and $-y_m$, and divide the integrand into outer regions where it has the same sign (positive for n even and negative for n odd) and an inner region where its value oscillates in sign

$$P_n = 2 \int_{-\infty}^{\infty} dx \int_{y_m(x)}^{\infty} dy f(x, y) + \int_{-\infty}^{\infty} dx \int_{y_{-m}(x)}^{y_m(x)} dy f(x, y) . \quad (8.94)$$

These integrals can be evaluated, at least approximately. See Schleich et al. [189] for details. They show that the first integral yields the result

$$\left(\frac{\varepsilon}{4\pi} \right)^{1/2} \frac{e^{-\varepsilon(n + \frac{1}{2} - \alpha^2)}}{(n + \frac{1}{2} - \alpha^2)^{1/2}} \equiv 2A_n , \quad (8.95)$$

whilst the second gives

$$2A_n \cos(2\phi_n) , \quad (8.96)$$

where

$$\begin{aligned}\phi_n &= \int_{x_0}^{x_n} dx \sqrt{x_n^2 - x^2} - \pi/4 , \\ x_n &= \sqrt{n + 1/2} .\end{aligned}\tag{8.97}$$

The first integral is the contribution from the outer ring of the Fock state Wigner function, and the second is the contribution from the inner regions. We take ϕ_n to be zero if $x_n < x_0$.

Combining these expressions gives the final result

$$P_n \simeq 4A_n \cos^2 \phi_n .\tag{8.98}$$

This equation, which is of central importance, shows obvious interference effects, through the presence of the factor $\cos^2 \phi_n$.

8.11 Quantum Interference in Phase Space

In this section we give a general presentation of interference effects in quantum-mechanical phase space. A full treatment requires extensive discussion of semiclassical methods, which we do not have space to deal with here. Hence we present the main results, usually without proof. First we recall the Wentzel–Kramers–Brillouin method of obtaining solutions to the Schrödinger equation, as it plays a central role in the next topic, the Area of Overlap method. We then use this approach to obtain an approximate expression for the photon number distribution, whose accuracy we test by applying it to the calculation of the photon number distribution for coherent and squeezed states, whose exact photon number distributions are known.

8.11.1 The WKB Method

The Wentzel–Kramers–Brillouin (WKB) method outlined here provides a convenient way of obtaining approximate solutions to the one-dimensional Schrödinger equation for a particle of mass m under the influence of a potential $V(x)$. We consider potentials where the corresponding classical problem gives rise to closed orbits in phase space. The WKB solutions to the quantum problem are excellent approximations in regions away from the classical turning-points of the potential, in the case of a potential $V(x)$ that does not vary too rapidly.

We seek eigensolutions $u_k(x)$ of the one-dimensional Schrödinger equation

$$\frac{d^2 u_k(x)}{dx^2} + \frac{2m}{\hbar^2} [E_k - V(x)] u_k(x) = 0 ,\tag{8.99}$$

where E_k is the corresponding energy eigenvalue. Setting

$$p_k(x) = \{2m [E_k - V(x)]\}^{1/2} ,\tag{8.100}$$

the Schrödinger equation becomes

$$\frac{d^2 u_k(x)}{dx^2} + \frac{p_k^2(x)}{\hbar^2} u_k(x) = 0 . \quad (8.101)$$

This system has the classical phase-space trajectory

$$p_{\text{class}}(x) = \{2m[E - V(x)]\}^{1/2} , \quad (8.102)$$

a possible example of which is shown below in Fig. 8.13.

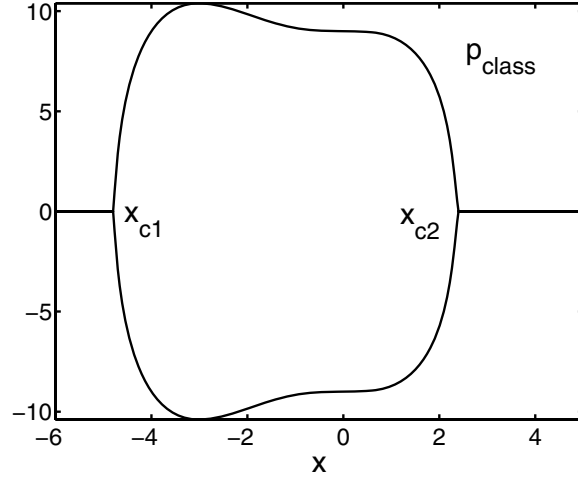


Fig. 8.13. The classical trajectory and classical turning points, x_{c1} and x_{c2} of the one-dimensional Schrödinger equation for a particle of mass m under the influence of a potential $V(x)$

The WKB solution is

$$u_k^{\text{WKB}}(x) = N_k \frac{\cos[S_k(x) - \pi/4]}{\sqrt{p_k(x)}} , \quad (8.103)$$

where the normalization factor is

$$N_k = \left[\frac{1}{2} \int_{x_{c1}}^{x_{c2}} \frac{dx}{p_k(x)} \right]^{-1/2} , \quad (8.104)$$

and the phase-like contribution is

$$S_k(x) = \frac{1}{\hbar} \int_x^{x_{c2}} dx p_k(x) . \quad (8.105)$$

The value of the energy eigenvalue E_k is given by the Bohr–Sommerfeld quantization condition

$$J_k \equiv \oint dx p_k(x) = 2\pi\hbar \left(k + \frac{1}{2} \right) , \quad (8.106)$$

where J_k is the *action*. We have that $J_{k+1} - J_k = 2\pi\hbar$, so that we may visualize the state $u_k(x)$ as occupying an area $2\pi\hbar$ in phase space, with the Bohr–Sommerfeld trajectory in the middle, see Fig. 8.14. We shall refer to this area as the Bohr–Sommerfeld band.

These concepts are most useful in discussing quantum interference in phase space.

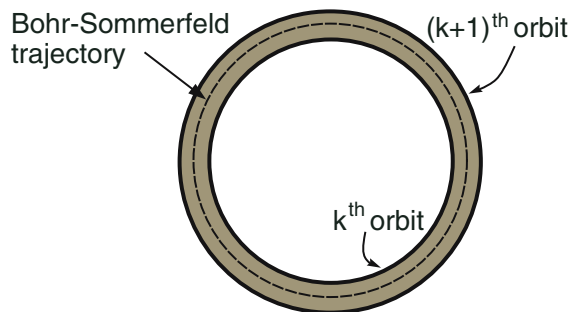


Fig. 8.14. The Bohr–Sommerfeld band (shown shaded) corresponding to the energy eigenstate $u_k(x)$. It occupies the area of phase space between the classical orbits corresponding to energy eigenvalues given by $J_k = 2\pi\hbar k$ and $J_{k+1} = 2\pi\hbar(k+1)$. The Bohr–Sommerfeld trajectory (8.106) lies in the centre of the band

8.12 Area of Overlap Formalism

The Area of Overlap method describes a general way of picturing quantum interference effects in phase space, in the semiclassical limit. In quantum mechanics, it is the probabilities amplitudes which are additive, not the probabilities themselves as in classical mechanics. The Area of Overlap method identifies areas of phase space as contributors to the magnitude of the probability amplitudes, and other areas as contributing to the phase.

We frequently need to calculate the inner product of two wave-functions. For example, if a field is described by a pure state $|\psi\rangle$, the photon counting distribution is given by

$$P_n = |\langle\psi|n\rangle|^2, \quad (8.107)$$

where $|n\rangle$ denotes the Fock state. In the coordinate representation, the inner product is given by

$$\langle\psi|n\rangle = \int dx \psi(x) \phi_n(x), \quad (8.108)$$

where

$$\phi_n(x) = \langle x|n \rangle = \left(\pi^{1/2} 2^n n! \right)^{-1/2} H_n(x) \exp(-x^2/2) \quad (8.109)$$

is the Fock state wave-function in the coordinate representation, $H_n(x)$ being a Hermite polynomial. The value of the inner product is determined by the extent to which the two wave functions overlap.

In general, the magnitude of an inner product $M_{j,k} \equiv \langle u_j(x)|v_k(x) \rangle$ of two wave-functions $u_j(x)$ and $v_k(x)$ is determined by the degree to which the two wave-functions ‘overlap’. For large quantum numbers, the overlap may be visualized as the overlap of the corresponding Bohr–Sommerfeld orbits in phase space. In general, the centres of the orbits do not coincide. A possible example is shown in Fig. 8.15.

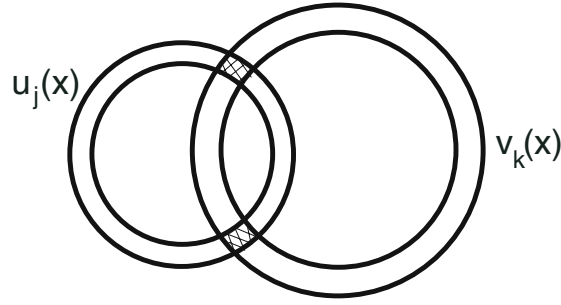


Fig. 8.15. The overlap of the Bohr–Sommerfeld bands in phase space for the states $u_j(x)$ and $v_k(x)$. The overlap is shown shaded

For simplicity, we restrict ourselves in this section to the case where the Bohr–Sommerfeld orbits overlap in just two distinct regions, as shown in Fig. 8.15. After some labour, it can be shown that in the limit of large quantum numbers j and k [181]

$$M_{j,k} \simeq A_{j,k}^{1/2} \exp(i\varphi_{j,k}) + A_{j,k}^{1/2} \exp(-i\varphi_{j,k}) , \quad (8.110)$$

where $A_{j,k}$ is the area of overlap of the Bohr–Sommerfeld bands of the two states, and the phase is the area enclosed between the two Bohr–Sommerfeld trajectories, as shown in Fig. 8.16. The transition probability is

$$W_{j,k} = |M_{j,k}|^2 = 4A_{j,k} \cos^2 \varphi_{j,k} , \quad (8.111)$$

an expression of the same form as the Wigner overlap integral (8.98). Equations (8.110) and (8.111) are the formulae we shall use as the basis of our discussions of quantum interference in phase space.

Our principal interest is in calculating the photon number distribution according to (8.107), so we take one of our functions, say $v_k(x)$ to be the Fock state wave-function. The appropriate potential is that for a harmonic oscillator of frequency ω

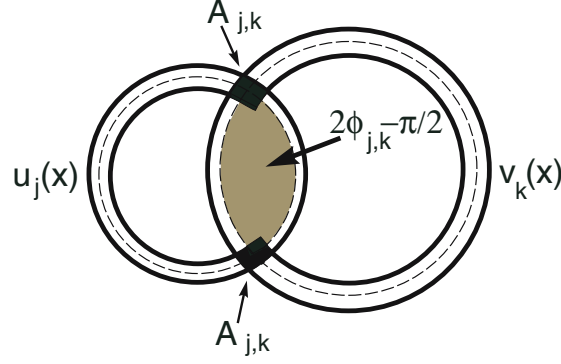


Fig. 8.16. The amplitude $A_{j,k}$ is the area of overlap between the two Bohr–Sommerfeld bands, the diamond shape shown as the black area, and the phase, $\varphi_{j,k}$, is the area between the two Bohr–Sommerfeld trajectories, shown shaded

$$V(x) = \frac{1}{2}m\omega^2 x^2 . \quad (8.112)$$

This gives rise to the classical phase space trajectories

$$E_k = \frac{p^2}{2m} + \frac{1}{2}m\omega^2 x^2 = \hbar\omega \left(k + \frac{1}{2} \right) , \quad (8.113)$$

which are ellipses.

We introduce the dimensionless phase space variables X and P , by the relations

$$X = x\sqrt{\frac{m\omega}{2\hbar}} , \quad P = \frac{p}{\sqrt{2\hbar m\omega}} . \quad (8.114)$$

Corresponding to the operator relations (8.4), we have the simpler expressions

$$\hat{X} = \frac{\hat{a} + \hat{a}^\dagger}{2} , \quad \hat{P} = \frac{\hat{a} - \hat{a}^\dagger}{2i} . \quad (8.115)$$

The operators \hat{X} and \hat{P} are identical to the quadrature operators \hat{X}_1 and \hat{X}_2 , defined in (8.49).¹ In terms of these new variables, the trajectory (8.113) becomes a circle of radius $\sqrt{k + 1/2}$:

$$P^2 + X^2 = k + 1/2 . \quad (8.116)$$

Hence, the Fock states $v_k(x)$ are represented in the phase space $\{X, P\}$ by a Bohr–Sommerfeld *trajectory* of radius $\sqrt{k + 1/2}$, with the Bohr–Sommerfeld *band* occupying an area of π between the circles of radius \sqrt{k} and $\sqrt{k + 1}$.

¹ As before, we use the ‘hat’ symbol to indicate an operator when there is the possibility of confusion with a scalar with similar notation.

8.12.1 Photon Number Distribution of Coherent States

We demonstrate the area of overlap method by obtaining an approximate expression for the photon number distribution of a coherent state $|\alpha\rangle = \hat{D}(\alpha)|0\rangle$, which we consider as a displaced vacuum state. For simplicity, we take α to be real here. From (8.115), this corresponds to a displacement

$$X_0 = \alpha, \quad P_0 = 0. \quad (8.117)$$

According to the final paragraph of the last subsection, the ground state of the harmonic oscillator, $k = 0$, is represented in the phase space $\{X, P\}$ by a Bohr–Sommerfeld band of radius $1/\sqrt{2}$. In this case, the ‘band’ is a circular disc, centred on the origin. The coherent state $|\alpha\rangle$, which corresponds to the vacuum state with its centre shifted by X_0 , is therefore represented by the Bohr–Sommerfeld band defined by

$$(X - X_0)^2 + P^2 = \frac{1}{2}. \quad (8.118)$$

To calculate P_n , we need the area of overlap between the Bohr–Sommerfeld bands of the coherent state and the n th Fock state. These are shown in Fig. 8.17. This is not a typical example, because the area of overlap in this

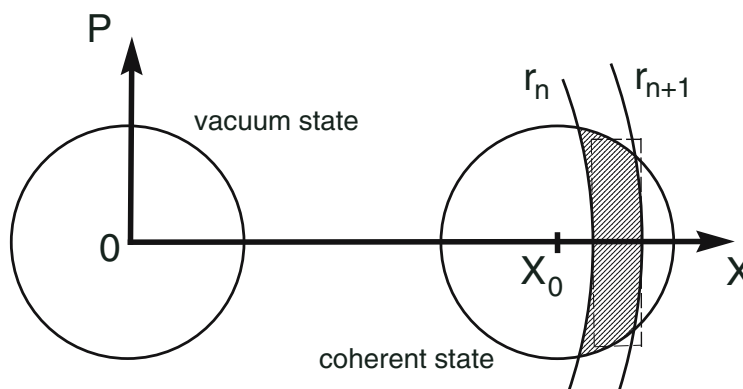


Fig. 8.17. The Bohr–Sommerfeld bands for the coherent state and the n th Fock state. The former is a circle of radius $1/\sqrt{2}$ centred on $(X_0, 0)$, and the latter is the annulus between the circles of radii $r_n = \sqrt{n}$ and $r_{n+1} = \sqrt{n+1}$. The area of overlap of the coherent and Fock bands, $A_{n,\alpha}$, is shown shaded, and the rectangle that approximates it is indicated by narrow, dashed lines

case is just a single area, not two as depicted in Fig. 8.15. The phase φ is thus zero.

The Bohr–Sommerfeld bands which pass near the centre of the coherent state circle have n values which satisfy

$$\sqrt{n+1}/2 \simeq X_0 = \alpha. \quad (8.119)$$

Bearing in mind that the radius of the coherent state circle is $1/\sqrt{2}$, only bands satisfying

$$X_0 - 1/\sqrt{2} < \sqrt{n+1/2} < X_0 + 1/\sqrt{2} , \quad (8.120)$$

have an area of overlap. For values of n outside this range, the area of overlap method predicts that the photon number distribution is zero: $P_n = 0$, and there is no quantum interference.

We can approximate the area $A_{n,\alpha}$ by a rectangle, and calculate its width by elementary geometry. We assume $\alpha \gg 1$. The rectangle corresponding to the n th Bohr–Sommerfeld band is centred at $X_n = \sqrt{n+1/2}$. The breadth of the rectangle is

$$B_n = \sqrt{n+1} - \sqrt{n} \simeq \frac{1}{2\sqrt{n}} \simeq \frac{1}{2X_0} , \quad (8.121)$$

the last step being valid near the centre of the distribution. Its height is twice the value of $P(X)$ at $X = X_n$:

$$H_n = 2 [1/2 - (X_n - X_0)^2]^{1/2} . \quad (8.122)$$

This gives, essentially, the photon number distribution of the coherent state according to the area of overlap method, as there is no phase φ to consider here. We therefore find

$$P_n \simeq A_{n,\alpha} \simeq \frac{[1/2 - (X_n - X_0)^2]^{1/2}}{X_0} , \quad (8.123)$$

Using $X_n = \sqrt{n+1/2}$ and $X_0 = \alpha$, this may be written as

$$P_n = A_{n,\alpha} \simeq \frac{1}{2\alpha^2} \left[2\alpha^2 - \left(n + \frac{1}{2} - \alpha^2 \right) \right]^{1/2} . \quad (8.124)$$

The photon number distribution of the coherent state is well-known to be given exactly by a Poisson distribution:

$$P_n^{\text{coh}} = \frac{\alpha^{2n}}{n!} e^{-\alpha^2} \quad (8.125a)$$

$$\simeq \frac{1}{\alpha\sqrt{\pi}} \exp \left[- \left(\frac{n + \frac{1}{2} - \alpha^2}{\alpha\sqrt{2}} \right)^2 \right] , \quad (8.125b)$$

where the second line is the well-known Gaussian limit of a Poisson distribution. We have therefore to compare (8.124) and (8.125b).

The distribution P_n^{coh} has its maximum value at $n = \alpha^2 - 1/2$, as does $A_{n,\alpha}$, but the half-widths are somewhat different. Furthermore, $A_{n,\alpha}$ is zero for values of n outside the range (8.120), whereas P_n^{coh} is not. Clearly, the

area of overlap method in this form provides a rough approximation to the true distribution, but the qualitative agreement is not very good.

There is, however, an improved version we can employ. In fact, it is a better approximation to take the area of overlap to be given by

$$\mathcal{A}_{j,k} = \iint_{D_j} \frac{dX dP}{\pi} W_{0,k}(X, P) , \quad (8.126)$$

where D_j is the domain covered by the Bohr–Sommerfeld band of the j th Fock state and $W_{0,k}$ is the Wigner function of the field whose photon number distribution is being calculated. We shall call this approach the ‘WW-overlap’ method (‘WW’ for ‘Wigner-weighted’), calling $\mathcal{A}_{j,k}$ the ‘WW-overlap’.

In the present case

$$W_{0,\text{coh}}(X, P) = 2 \exp \left[-2(X - X_0)^2 - 2P^2 \right] . \quad (8.127)$$

In the limit $m \gg 1$, when the breadth of the n th band is very small, we have

$$\begin{aligned} \mathcal{A}_{n,\alpha} &\simeq \frac{2B_n}{\pi} \exp \left[-2(X_n - X_0)^2 \right] \int_{-\infty}^{\infty} dP e^{-2P^2} \\ &\simeq \frac{1}{\alpha\sqrt{\pi}} \exp \left[- \left(\frac{n + \frac{1}{2} - \alpha^2}{\alpha\sqrt{2}} \right)^2 \right] , \end{aligned} \quad (8.128)$$

where we have used (8.119), in agreement with (8.125). It is clear that the WW-overlap, (8.126), is much superior to the unweighted area of overlap.

8.12.2 Photon Number Distribution of Squeezed State

Next we consider the particular squeezed state (8.35) whose Wigner function is

$$W_{0,\text{sq}}(X, P) = 2 \exp \left[-2\varepsilon(X - X_0)^2 - \frac{2P^2}{\varepsilon} \right] , \quad (8.129)$$

where $\varepsilon = \exp(2r)$ is assumed large, so that there is pronounced squeezing. For the moment, we restrict our attention to the case where the squeezing ellipse is parallel to one of the principal axes. The situation is depicted in Fig. 8.18, which shows the Bohr–Sommerfeld bands of the n th Fock state and a contour of the Wigner function of the squeezed state. It is clear that when $X_0 \simeq \sqrt{n+1/2}$, the overlap area, shown black in Frame (a) of the figure, is particularly large.

The WW-overlap is given by

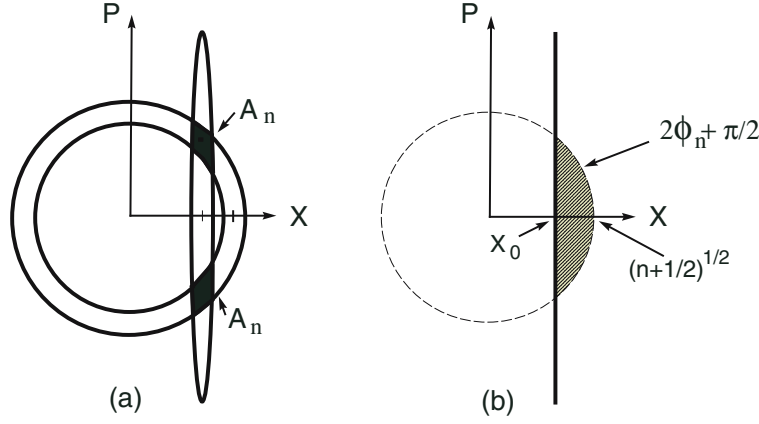


Fig. 8.18. The areas of overlap, shown black, between the Bohr-Sommerfeld bands of the n th Fock state and the Wigner function of the squeezed state (8.129) in (a). Only one contour of the Wigner function is depicted. The corresponding Bohr-Sommerfeld trajectories are shown in (b). The overlap phase φ is shown as the shaded area

$$\begin{aligned} \mathcal{A}_{n,\text{sq}} &= \frac{2}{\pi} \int_{-\infty}^{\infty} dX \exp \left[-2\varepsilon (X - X_0)^2 \right] \\ &\quad \times \int_{\sqrt{n-X^2}}^{\sqrt{n+1-X^2}} dP \exp (-2P^2/\varepsilon) \\ &\simeq \frac{2}{\sqrt{\varepsilon\pi}} \int_{\sqrt{n-X_0^2}}^{\sqrt{n+1-X_0^2}} dP \exp (-2P^2/\varepsilon) , \end{aligned} \quad (8.130)$$

where we have approximated the X -integration by the delta function $\sqrt{\pi/\varepsilon}\delta(X - X_0)$. The P -integration may be performed by replacing P by its mean value when the integrand becomes constant. The result, using $X_0 = \alpha$, is

$$\mathcal{A}_{n,\text{sq}} = \frac{1}{\sqrt{\pi\varepsilon}} \frac{\exp \left[-2 \left(n + \frac{1}{2} - \alpha^2 \right) / \varepsilon \right]}{\sqrt{\left(n + \frac{1}{2} - \alpha^2 \right)}} . \quad (8.131)$$

The phase φ_n is given by the shaded area shown in Fig. 8.18(b).

$$\begin{aligned} \varphi_n &= \frac{1}{2} \text{shaded area} - \pi/4 \\ &= \left(n + \frac{1}{2} \right) \tan^{-1} \left[\frac{1}{\alpha} \sqrt{n + \frac{1}{2} - \alpha^2} \right] \\ &\quad - \alpha \sqrt{n + \frac{1}{2} - \alpha^2} - \frac{\pi}{4} . \end{aligned} \quad (8.132)$$

The photon number distribution is given by

$$P_n^{\text{sq}} = 4\mathcal{A}_{n,\text{sq}} \cos^2 \varphi_n . \quad (8.133)$$

The exact expression for the photon number distribution of a squeezed state is

$$P_{n,\text{sq}} = \frac{1}{n!\mu} \left(\frac{\nu}{2\mu} \right)^n \exp \left[-|\beta|^2 - \text{Re} \left(\frac{\nu\beta^2}{\mu} \right) \right] \left| H_n \left(\frac{\beta}{\sqrt{2\mu\nu}} \right) \right|^2 , \quad (8.134)$$

where

$$\nu = \sinh(re^{i\psi}) , \quad \mu = \cosh r , \quad \text{and} \quad \beta = \mu\alpha + \nu\alpha^* . \quad (8.135)$$

Expression (8.133), with $\mathcal{A}_{n,\text{sq}}$ given by (8.130) and φ_n given by (8.132), agrees with the asymptotic value of the exact photon number distribution (8.134), in the limit $n \gg \alpha^2$. Because our approach is valid only in the limit of large quantum numbers, we take both $\mathcal{A}_{n,\text{sq}}$ and φ_n to be zero when $n < \alpha^2$.

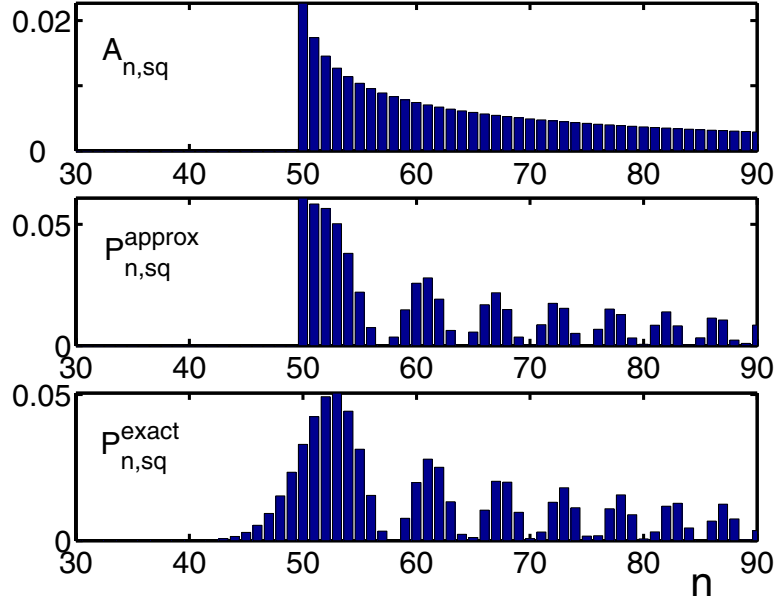


Fig. 8.19. The WS-overlap for the squeezed state. $\mathcal{A}_{n,\text{sq}}$ is presented in (a), the approximate photon number distribution obtained from (8.133) is shown in (b), and the exact photon number distribution from (8.134) in (c). The parameters are $\alpha = 7$, $r = 2.65$ and $\psi = 0$

In Fig. 8.19, we compare the exact expression for the squeezed state photon number distribution, in Frame (c), with the approximate expression (8.133), in Frame (b). We also present the plot for $\mathcal{A}_{n,\text{sq}}$ in Frame (a). We take $\alpha = 7$ and $r = 2.65$. For this value of r the ratio of the major to minor semi-axes of the squeezing ellipse is $(\exp(2r))^2 = 200^2$.

It can be seen that the agreement between the exact and approximate expressions for the photon number distribution is qualitatively good for values of n somewhat larger than α^2 . It is also apparent that the influence of

the phase φ_n is essential for producing the modulations in the tail of the distribution, which are characteristic interference features.

We conclude this chapter with some suggestions for further reading. An excellent account of the Wigner function and other phase space quasi-probabilities can be found in the classical paper of Cahill and Glauber [179, 180]. A review of quantum interference effects in phase space is provided by Bužek and Knight [190]. A comprehensive account of all aspects of quantum optics in phase space, including quasi-probabilities and quantum interference effects, is to be found in the recent text by Schleich [181].

9 Quantum Interference in Atom Optics

Atom optics is simply too vast for us to follow all the recent developments, much less to survey only these effects involving phase coherence and interference phenomena in atomic motion and Bose–Einstein condensation (BEC), the major topic of the present book. Early BEC studies were mainly concerned with the very cold nature of BEC and did not reveal properties that directly reflected its coherent nature such as the phase of a condensate [191]. Understanding the coherent nature is essential for characterizing condensates as sources of coherent matter waves, and the formulation of the relative phase between two condensates has been a central issue of many theoretical and experimental studies. It is well established that a condensate behaves like a “giant matter wave” that exhibits long-range coherent properties because its atoms occupy the same quantum state, with uniform spatial phase.

We have chosen to focus attention on quantum interference effects in atomic systems where atom motion is significant. We emphasize phenomena in which phase and coherence between condensates are important, and we discuss different theories of the condensate phase. Throughout the book we have paid most attention to the interaction of atoms with laser fields and assumed that the atoms were stationary during the interaction. Since every photon carries momentum, the atomic momentum can be changed in the process of absorption and emission of photons. Therefore, the dynamical behavior of atoms can be varied by the interaction with a radiation field. For a weak driving field, the influence of this field on the atomic motion can be neglected. However, the intensities of laser fields are generally very strong, and then the motion of the atoms can be considerably changed by the laser field. Here, we discuss this aspect, especially the effect of a driving field on the motion of atoms and the atomic momentum distribution. (We touched on this effect when we discussed the use of VSCPT methods in laser cooling in Sect. 5.1.6.) In particular, we consider the diffraction of atoms on by standing-wave laser field. We show that the standing wave forms an optical potential that creates a diffraction grating of the passing atoms.

9.1 Interference and Diffraction of Cold Atoms

Consider a beam of two-level atoms, each with ground state $|0\rangle$ and excited state $|1\rangle$, moving in the xy -plane and passing through a plane standing-wave laser field, as shown schematically in Fig. 9.1. The standing wave can be treated as a thin phase modulator that creates an optical potential to produce a diffraction grating for the moving atoms. Suppose that the laser field propagates in the horizontal x direction, and the momentum of the atoms, before entering the laser field, is $\mathbf{P}_0 = P_x \hat{\mathbf{i}} + P_y \hat{\mathbf{j}}$.

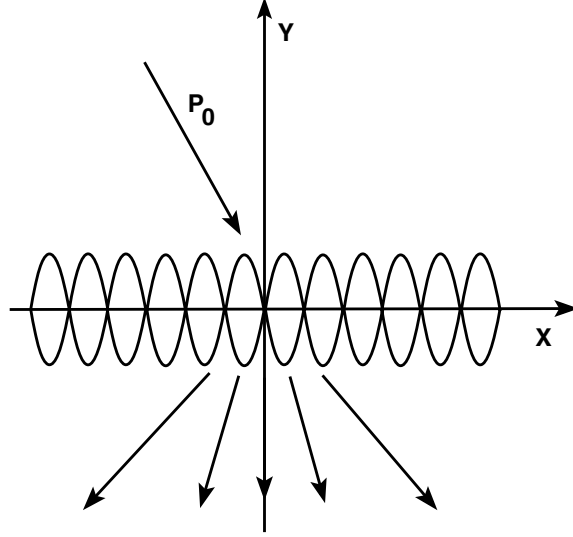


Fig. 9.1. Diffraction of moving atoms on a standing-wave propagating in the horizontal x direction

The standing-wave laser field is equivalent to a superposition of two running-wave fields of the same amplitude, but opposite propagation vectors

$$\begin{aligned} \mathbf{E}(x, t) &= 2\mathbf{E}_0 \cos(kx) \cos(\omega_L t) \\ &= [\mathbf{E}_0 \cos(\omega_L t - kx) + \mathbf{E}_0 \cos(\omega_L t + kx)] , \end{aligned} \quad (9.1)$$

where ω_L is the angular frequency of the laser field, and $k = 2\pi/\lambda$ is the wave number.

The Hamiltonian of the system of moving atoms interacting with a standing-wave laser field can be written in the standard form

$$H = H_A + H_F + H_{\text{int}} , \quad (9.2)$$

where

$$H_A = \hbar\omega_0 S^z + \frac{\mathbf{P}^2}{2m} \quad (9.3)$$

is the Hamiltonian of the atoms that includes the kinetic energy $\mathbf{P}^2/2m$, and $S^z = (|1\rangle\langle 1| - |0\rangle\langle 0|)/2$ is the atomic energy operator.

The Hamiltonian

$$H_F = \sum_{i=1}^2 \hbar\omega_L \hat{a}_i^\dagger \hat{a}_i \quad (9.4)$$

determines the energy of the laser field that is composed of two fields of the same frequency ω_L and wave-vectors \mathbf{k}_i satisfying the relation

$$\mathbf{k}_1 = -\mathbf{k}_2 = \mathbf{k} . \quad (9.5)$$

The interaction Hamiltonian of the moving atoms with the standing-wave laser field can be written as

$$H_{\text{int}} = \frac{1}{2} \hbar g \sum_{i=1}^2 \left[S^+ \hat{a}_i e^{i\mathbf{k}_i x} - S^- \hat{a}_i^\dagger e^{-i\mathbf{k}_i x} \right] , \quad (9.6)$$

where x is the coordinate of the atom along the direction of propagation of the laser field.

Using the Hamiltonian (9.2), we find from the Schrödinger equation the state vector of the system, which allows us to analyze the time evolution of the atomic momentum due to the interaction with the laser field.

Assume that initially the atoms were in their ground states, and had a momentum \mathbf{P}_0 . Moreover, assume that there were n_i photons in the i th field. Hence, the initial state of the system can be written as

$$|\Phi_0\rangle = |n_1\rangle |n_2\rangle |0, \mathbf{P}_0\rangle . \quad (9.7)$$

Moving atoms enter the field, and then they can absorb photons from either of the two running-wave laser fields. When an atom absorbs a photon from the field “1”, the state vector changes to

$$|\Phi_1\rangle = |n_1 - 1\rangle |n_2\rangle |1, \mathbf{P}_0 + \hbar\mathbf{k}\rangle . \quad (9.8)$$

When the atom absorbs a photon from the field “2”, the state vector changes to

$$|\Phi_2\rangle = |n_1\rangle |n_2 - 1\rangle |1, \mathbf{P}_0 - \hbar\mathbf{k}\rangle . \quad (9.9)$$

This provides us with a simple picture of the effect of the atom-field interaction on the atomic motion. Momentum transfer from the laser field affects the motion of the atom in the x direction only. Each time the atom absorbs energy from the field component propagating in the $+x$ -direction, the atomic momentum is increased by $\hbar k$. Similarly, if the atom absorbs energy from the field component propagating in the $-x$ -direction, the atomic momentum is decreased by $\hbar k$.

Suppose that the interaction of the atom with the laser fields is strong and the transit time through the field is short so that we can ignore spontaneous emission from the upper atomic level, leaving only the possibility of stimulated emission into either of the two laser fields.

If the system is in the state $|\Phi_1\rangle$, the atom can be stimulated to emit a photon of wave vector \mathbf{k}_1 or \mathbf{k}_2 . If the wave vector of the emitted photon is \mathbf{k}_1 , the system returns to the initial state $|\Phi_0\rangle$. If the wave vector of the emitted photon is \mathbf{k}_2 , the state vector changes to

$$|\Phi_3\rangle = |n_1 - 1\rangle |n_2 + 1\rangle |0, \mathbf{P}_0 + 2\hbar\mathbf{k}\rangle . \quad (9.10)$$

Similarly, if the system was in the state $|\Phi_2\rangle$ and the atom emits a photon of momentum $\hbar\mathbf{k}_1$, the state vector changes to

$$|\Phi_4\rangle = |n_1 + 1\rangle |n_2 - 1\rangle |0, \mathbf{P}_0 - 2\hbar\mathbf{k}\rangle . \quad (9.11)$$

Since the interaction of the atom with the laser fields is strong, there is a large number of absorption and emission processes during the passage time through the field, which leads to the final state

$$|\Phi_n\rangle = \left|n_1 - \frac{n}{2}\right\rangle \left|n_2 + \frac{n}{2}\right\rangle |0, \mathbf{P}_0 + n\hbar\mathbf{k}\rangle , \quad (9.12)$$

when n is an even number, and

$$|\Phi_n\rangle = \left|n_1 - \frac{n+1}{2}\right\rangle \left|n_2 + \frac{n-1}{2}\right\rangle |1, \mathbf{P}_0 + n\hbar\mathbf{k}\rangle , \quad (9.13)$$

when n is an odd number.

Equations (9.12) and (9.13) show that the atomic beam with the initial momentum \mathbf{P}_0 is split by the standing wave into multiple components with momenta $n\hbar\mathbf{k}$.

We will treat the states $|\Phi_n\rangle$ as complete basis states of the noninteracting system, and find the state vector of the atom-field interacting system as a linear superposition

$$|\Phi(t)\rangle = \int d\mathbf{P} \sum_n C_n(\mathbf{P}, t) |\Phi_n\rangle . \quad (9.14)$$

The coefficients $C_n(\mathbf{P}, t)$ (probability amplitudes) are found by solving the Schrödinger equation for the state vector $|\Phi(t)\rangle$. With the Hamiltonian (9.2), the Schrödinger equation leads to the following set of coupled differential equations for the probability amplitudes

$$\begin{aligned} i\hbar \frac{d}{dt} C_n = & \left\{ (n_1 + n_2) \hbar\omega_L + \frac{1}{2m} (\mathbf{P}_0 + n\hbar\mathbf{k})^2 - \frac{1}{2} \hbar\omega_0 \right\} C_n \\ & + \frac{\hbar}{2} ig \left(\sqrt{n_1 - \frac{n}{2}} C_{n-1} - \sqrt{n_2 + \frac{n}{2}} C_{n+1} \right) , \end{aligned} \quad (9.15)$$

when n is an even number, and

$$\begin{aligned} i\hbar \frac{d}{dt} C_n = & \left\{ (n_1 + n_2 - 1) \hbar \omega_L + \frac{1}{2m} (\mathbf{P}_0 + n\hbar \mathbf{k})^2 + \frac{1}{2} \hbar \omega_0 \right\} C_n \\ & + \frac{\hbar}{2} ig \left(\sqrt{n_1 - \frac{n-1}{2}} C_{n-1} - \sqrt{n_2 + \frac{n-1}{2}} C_{n+1} \right), \end{aligned} \quad (9.16)$$

when n is an odd number.

We simplify the differential equations by introducing the notation

$$E_N = \left(n_1 + n_2 - \frac{1}{2} \right) \hbar \omega_L + \frac{1}{2m} (P_x^2 + P_y^2), \quad (9.17)$$

and transformation

$$\tilde{C}_n = C_n \exp(iE_N t). \quad (9.18)$$

With these simplifications, the differential equations (9.15) and (9.16) reduce to (n even)

$$\begin{aligned} i \frac{d}{dt} \tilde{C}_n = & \frac{1}{2} \Delta_L \tilde{C}_n + \left(\frac{n^2 \hbar}{2m} k^2 + \frac{n \mathbf{P}_0 \cdot \mathbf{k}}{m} \right) \tilde{C}_n \\ & + \frac{1}{2} ig \left(\sqrt{n_1 - \frac{n}{2}} \tilde{C}_{n-1} - \sqrt{n_2 + \frac{n}{2}} \tilde{C}_{n+1} \right), \end{aligned} \quad (9.19)$$

and (n odd)

$$\begin{aligned} i \frac{d}{dt} \tilde{C}_n = & -\frac{1}{2} \Delta_L \tilde{C}_n + \left\{ \frac{\hbar n^2}{2m} k^2 + \frac{n \mathbf{P}_0 \cdot \mathbf{k}}{m} \right\} \tilde{C}_n \\ & + \frac{1}{2} ig \left(\sqrt{n_1 - \frac{n-1}{2}} \tilde{C}_{n-1} - \sqrt{n_2 + \frac{n-1}{2}} \tilde{C}_{n+1} \right), \end{aligned} \quad (9.20)$$

where $\Delta_L = \omega_L - \omega_0$.

For a strong driving field, the number of photons in the laser fields satisfy $n_1, n_2 \gg 1$, and then we can make the following approximations

$$\begin{aligned} \sqrt{n_i - \frac{n}{2}} & \approx \sqrt{n_i} \approx \sqrt{\langle n_L \rangle}, \\ \sqrt{n_i \pm \frac{n-1}{2}} & \approx \sqrt{n_i} \approx \sqrt{\langle n_L \rangle}, \end{aligned} \quad (9.21)$$

where $\langle n_L \rangle$ is the average number of photons in the laser fields. Hence, the differential equations for \tilde{C}_n simplify to

$$\begin{aligned} i \frac{d}{dt} \tilde{C}_n = & \frac{1}{2} \Delta_L \tilde{C}_n + \left[\hbar \frac{n^2 k^2}{2m} + \frac{n P_x k}{m} \right] \tilde{C}_n \\ & + \frac{1}{2} i \Omega (\tilde{C}_{n-1} - \tilde{C}_{n+1}), \quad n \text{ even}, \end{aligned} \quad (9.22)$$

and

$$\begin{aligned} i \frac{d}{dt} \tilde{C}_n = & -\frac{1}{2} \Delta_L \tilde{C}_n + \left[\hbar \frac{n^2 k^2}{2m} + \frac{n P_x k}{m} \right] \tilde{C}_n \\ & + \frac{1}{2} i \Omega \left(\tilde{C}_{n-1} - \tilde{C}_{n+1} \right) , \quad n \text{ odd} , \end{aligned} \quad (9.23)$$

where $\Omega = g\sqrt{\langle n_L \rangle}$ is the Rabi frequency of the laser field.

We introduce two parameters

$$\hbar b = \frac{\hbar^2 k^2}{2m} , \quad q = \frac{P_x}{\hbar k} . \quad (9.24)$$

The parameter $\hbar b$ corresponds to the recoil kinetic energy of the atom after absorption or emission of a photon, and q is the ratio of the initial momentum of the atom in the x direction to the momentum of photons.

With the parameters (9.24), the differential equations for \tilde{C}_n take the form

$$\begin{aligned} \frac{d}{dt} \tilde{C}_n = & -i \left[\frac{1}{2} \Delta_L + b(n^2 + 2nq) \right] \tilde{C}_n \\ & + \frac{1}{2} \Omega \left(\tilde{C}_{n-1} - \tilde{C}_{n+1} \right) , \quad n \text{ even} , \end{aligned} \quad (9.25)$$

and

$$\begin{aligned} \frac{d}{dt} \tilde{C}_n = & -i \left[-\frac{1}{2} \Delta_L + b(n^2 + 2nq) \right] \tilde{C}_n \\ & + \frac{1}{2} \Omega \left(\tilde{C}_{n-1} - \tilde{C}_{n+1} \right) , \quad n \text{ odd} . \end{aligned} \quad (9.26)$$

Equations (9.25) and (9.26) form two sets of an infinite number of coupled differential equations, which can be solved, for example, by the continued fraction technique. However, in the special case of $\Delta_L = 0$, we can find the coefficients \tilde{C}_n by comparing (9.25) and (9.26) with recurrence relations for special functions.

We now illustrate solutions of the above differential equations for \tilde{C}_n , from which we find the time evolution of the atomic momentum under the interaction of the atom with a standing-wave laser field.

Consider two special cases:

$$\begin{aligned} 1. \quad & P_x = 0 , \quad \Delta_L = 0 , \\ 2. \quad & P_x \neq 0 , \quad \Delta_L = 0 . \end{aligned} \quad (9.27)$$

In the first case, $q = 0$, and assuming that the Rabi frequency is much larger than the recoil energy, the Raman–Nath approximation, we obtain

$$\frac{d}{dt} \tilde{C}_n = \frac{1}{2} \Omega \left(\tilde{C}_{n-1} - \tilde{C}_{n+1} \right) . \quad (9.28)$$

Introducing a parameter $s = \Omega t$, we find that the coefficients \tilde{C}_n satisfy the recurrence relation

$$2 \frac{d}{ds} \tilde{C}_n(s) = \tilde{C}_{n-1}(s) - \tilde{C}_{n+1}(s) . \quad (9.29)$$

Comparing this with the recurrence relation for the Bessel function $J_n(x)$:

$$2 \frac{d}{dx} J_n(x) = J_{n-1}(x) - J_{n+1}(x) , \quad (9.30)$$

we see that the coefficients \tilde{C}_n are defined by

$$\tilde{C}_n(t) = J_n(\Omega t) , \quad (9.31)$$

where J_n is the n th order Bessel function.

Hence, the atomic momentum $n\hbar k$ in the x direction is

$$P_n(t) = \left| \tilde{C}_n(t) \right|^2 = J_n^2(\Omega t) . \quad (9.32)$$

Figure 9.2 shows the horizontal spatial distribution of the diffracted atoms after interacting with the standing-wave field. For the initial time $t = 0$, the distribution $P_n = 0$. As t increases, the distribution $P_n(t)$ increases indicating that the probability of finding atoms with momentum $n\hbar k$ increases. This means that an atomic beam with initial zero momentum in the x direction is split by the standing wave into multiple components with momenta $n\hbar k$ and populations $P_n(t)$.

Consider now the second case, in which the moving atoms have nonzero initial momentum component in the x direction. Since $P_x \neq 0$, the term $2nbq$ is different from zero. Again, we use the Raman–Nath approximation in which we ignore the recoil energy, and obtain

$$\frac{d}{dt} \tilde{C}_n = -2inbq \tilde{C}_n + \frac{1}{2} \Omega \left(\tilde{C}_{n-1} - \tilde{C}_{n+1} \right) . \quad (9.33)$$

It is convenient to make a further transformation

$$\bar{C}_n = \tilde{C}_n e^{inbqt} . \quad (9.34)$$

Then

$$\begin{aligned} \frac{d}{dt} \bar{C}_n &= -inbq \bar{C}_n + \frac{1}{2} \Omega \left(\bar{C}_{n-1} e^{ibqt} - \bar{C}_{n+1} e^{-ibqt} \right) \\ &= -inbq \bar{C}_n + \frac{1}{2} \Omega \cos(bqt) \left(\bar{C}_{n-1} - \bar{C}_{n+1} \right) \\ &\quad + \frac{i}{2} \Omega \sin(bqt) \left(\bar{C}_{n-1} + \bar{C}_{n+1} \right) . \end{aligned} \quad (9.35)$$

Introducing the parameter

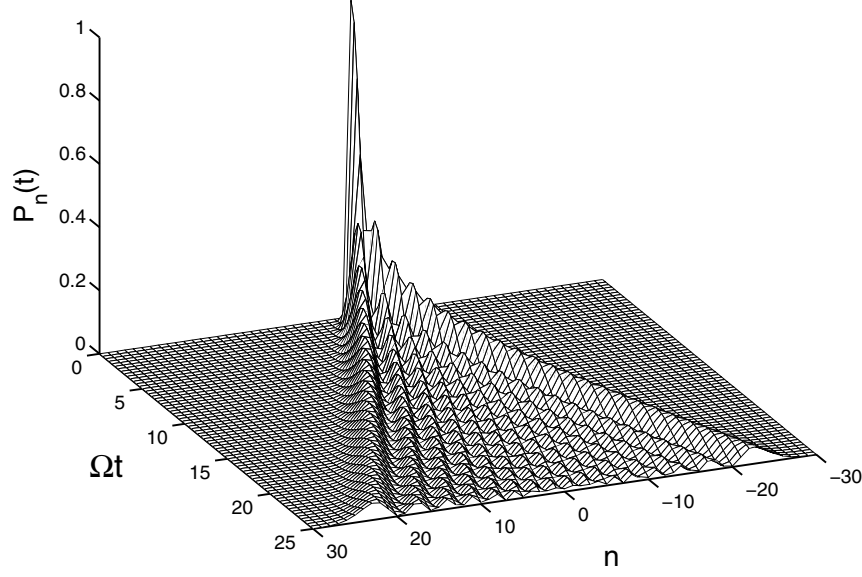


Fig. 9.2. The atomic momentum distribution function for $P_x = 0$ and different values of Ωt

$$z = \frac{\Omega}{bq} \sin(bqt) , \quad (9.36)$$

we transform (9.35) into

$$\begin{aligned} 2 \frac{d}{dz} \bar{C}_n = & -i \frac{bq}{\Omega \cos(bqt)} [2n\bar{C}_n - z(\bar{C}_{n-1} + \bar{C}_{n+1})] \\ & + (\bar{C}_{n-1} - \bar{C}_{n+1}) . \end{aligned} \quad (9.37)$$

To evaluate (9.37), we make use of two recurrence relations for the Bessel functions

$$\begin{aligned} 2nJ_n(x) &= x[J_{n-1}(x) + J_{n+1}(x)] , \\ 2 \frac{d}{dx} J_n(x) &= J_{n-1}(x) - J_{n+1}(x) , \end{aligned} \quad (9.38)$$

and find the result

$$\bar{C}_n(t) = J_n \left(\frac{\Omega}{bq} \sin bqt \right) . \quad (9.39)$$

Hence, the atomic momentum distribution function is

$$P_n(t) = |\bar{C}_n(t)|^2 = J_n^2 \left(\frac{\Omega}{bq} \sin bqt \right) . \quad (9.40)$$

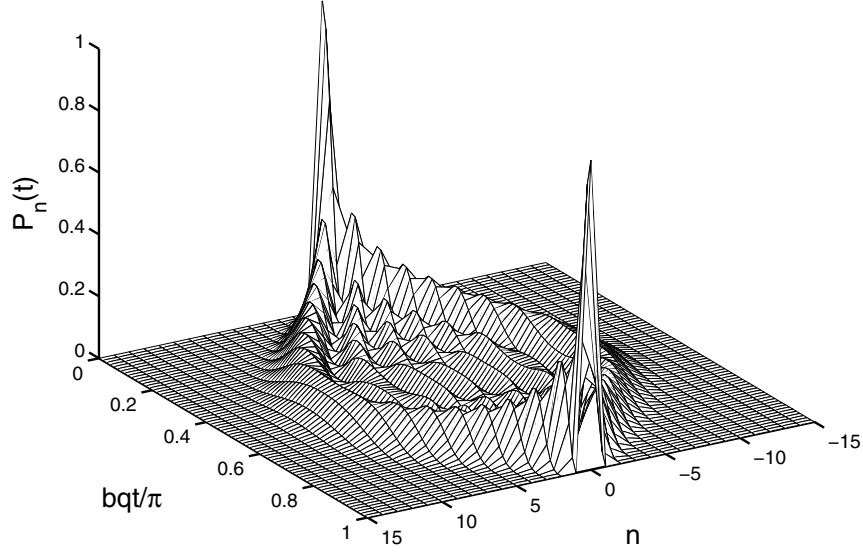


Fig. 9.3. The atomic momentum distribution function for $P_x \neq 0$, $\Omega/bq = 10$, and different values of bqt

The atomic distribution oscillates in time with the frequency bq . In Fig. 9.3 we show the distribution for different values of bqt . As t increases from the initial value $t = 0$, the width of the distribution increases to its maximum value at $bqt = \pi/2$, and then the width decreases and reduces to zero for $bqt = \pi$. The maximum amplitude of the atomic distribution during each period of oscillation is equal to $\pm\Omega/(bq)$.

Thus, the diffraction of atoms with an initial momentum $P_x \neq 0$ is fundamentally different from that of $P_x = 0$. Instead of a continuous spreading of the atoms, the atomic distribution oscillates in time, periodically focusing and defocusing. This periodicity is observed in momentum space as an oscillation of the populations between the different momentum components.

In the derivation of (9.32) and (9.40), we have ignored spontaneous emission from the atoms. It might be difficult to achieve this in actual experimental situations, in particular when the detuning $\Delta_L = 0$. Alternatively, one can assume laser detunings large compared with the spontaneous rate and the Rabi frequency, $\Delta_L \gg \gamma, \Omega$. In this case, spontaneous emission can be neglected, as the atoms mostly reside in their ground states, with the upper atomic level adiabatically eliminated. To illustrate this, consider again the equations of motion (9.25) and (9.26), which in the Raman–Nath regime and with $P_x = 0$, reduce to

$$\frac{d}{dt}\tilde{C}_{2n} = -\frac{i}{2}\Delta_L\tilde{C}_{2n} + \frac{1}{2}\Omega\left(\tilde{C}_{2n-1} - \tilde{C}_{2n+1}\right), \quad (9.41)$$

and

$$\frac{d}{dt}\tilde{C}_{2n-1} = \frac{i}{2}\Delta_L\tilde{C}_{2n-1} + \frac{1}{2}\Omega\left(\tilde{C}_{2n-2} - \tilde{C}_{2n}\right). \quad (9.42)$$

According to (9.13), the equation of motion (9.42) for odd n corresponds to the time evolution of the probability amplitude of the excitation of the atomic upper state $|1\rangle$. When $\Delta_L \gg \Omega$, we can adiabatically eliminate \tilde{C}_{2n-1} assuming that the amplitude does not change in time. Then, we put $d\tilde{C}_{2n-1}/dt = 0$ in (9.42), and obtain

$$\tilde{C}_{2n-1} = \frac{i\Omega}{\Delta} \left(\tilde{C}_{2n-2} - \tilde{C}_{2n} \right). \quad (9.43)$$

Substituting (9.43) into (9.41) and solving for \tilde{C}_{2n} , we find the probability amplitudes of the ground state

$$\tilde{C}_{2n} = \left[1 + 2 \left(\frac{\Omega}{\Delta} \right)^2 \right]^{-\frac{1}{2}} \exp \left[-i \left(\frac{1}{2}\Delta_L + \frac{\Omega^2}{\Delta_L} \right) t \right] J_n \left(\frac{\Omega^2 t}{\Delta_L} \right), \quad (9.44)$$

and then the probability distribution function is given by

$$P_{2n} = \left[1 + 2 \left(\frac{\Omega}{\Delta} \right)^2 \right]^{-1} J_n^2 \left(\frac{\Omega^2 t}{\Delta_L} \right). \quad (9.45)$$

The above result holds for large detunings, but is in a form similar to (9.32), obtained for $\Delta_L = 0$. However, the result (9.45) is realistic experimentally as for $\Delta_L \gg \gamma$ spontaneous emission is negligible and can be ignored. The momentum distribution function (9.45) is an even function of n corresponding to the absorption of a photon from the $+\mathbf{k}$ component of the standing wave, followed by emission of a photon into the $-\mathbf{k}$ component. In this process, the atoms transfer photons from one component of the standing wave to the other, remaining in their ground states, but their momentum changes by $2n\hbar\mathbf{k}$.

9.2 Interference of Two Bose–Einstein Condensates

An important problem in atom optics is the study of the coherence properties of cold atomic samples forming Bose–Einstein condensates and the formulation of a theoretical model of the condensate phase. One can ask the question whether the phase of a condensate is a formal construct, not relevant to any real measurement, or whether it is experimentally observable. In analogy with optical systems, the phase of an unknown condensate can be measured using a homodyne or heterodyne detection scheme where the condensate is superimposed with another condensate of well-defined phase. An alternative scheme is to compare the condensate phase to itself at a different time, thereby examining the condensate phase dynamics, or one could

compare the phases of two separate condensates. In the latest approach, two separate condensates would be allowed to drop and, by virtue of their horizontal expansion, overlap as they reach an atomic detector. Cirac et al. [192] showed by analytical arguments that a system consisting of two condensates evolves into a state with a fixed relative phase if one detects the emitted bosonic atoms while observing their spatial interference pattern. The relative phase could also be established as a result of the measurement of the number of atoms in each of the condensates. Javanainen and Yoo [193] showed that an interference pattern between two condensates, and hence a relative phase, could be established via a measurement process. As atomic detections are performed, an uncertainty in the number of atoms in each condensate is build up, since we do not know from which condensate the detected atom is removed. This result can be regarded as a constructive example of spontaneous symmetry breaking. Each particular measurement produces a certain relative phase between the condensates [194].

9.2.1 Relative Phase Between Two Condensates

To explore the problem of the establishment of a relative phase between two interfering condensates via atomic detections, we follow the work of Javanainen and Yoo [193], and consider two condensates made to overlap at the surface of an atomic detector. Assume that prior to the detection each condensate contained $M/2$ (noninteracting) atoms of momenta k_1 and k_2 , respectively, and the detection at some point x is represented by a field operator which is a superposition of the atomic operators of the two condensates

$$\hat{\Psi}(x) = \frac{1}{\sqrt{2}} \left[\hat{a}_1 + \hat{a}_2 e^{i\phi(x)} \right] , \quad (9.46)$$

where $\phi(x) = (k_2 - k_1)x$ and \hat{a}_1 and \hat{a}_2 are the atom annihilation operators for the first and second condensate, respectively. For simplicity, we consider the situation where the condensates move in opposite directions, so $\mathbf{k}_2 = -\mathbf{k}_1$.

We look at the buildup of the relative phase between condensates initially in the Fock state

$$|\phi(0)\rangle = |M/2, M/2\rangle . \quad (9.47)$$

Since we start from a Fock state, no phase is initially present in the system. We now adopt a destructive measurement of atomic position, assuming that each atom can be absorbed (removed) upon detection. This allows us to apply the theory of absorptive photodetection from which we find the joint counting rate R^m of m atomic detections at positions $\{x_1, \dots, x_m\}$ and times $\{t_1, \dots, t_m\}$ as

$$\begin{aligned} R^m(x_1, t_1; \dots; x_m, t_m) = & \sigma^m \langle \Psi^\dagger(x_1, t_1) \dots \Psi^\dagger(x_m, t_m) \\ & \times \Psi(x_m, t_m) \dots \Psi(x_1, t_1) \rangle , \end{aligned} \quad (9.48)$$

where σ^m is a constant that incorporates the sensitivity of the detectors. Moreover, $R^m = 0$ if $m > M$, i.e. no more than M detections can occur.

Further assuming that all atoms are in fact detected, the joint probability density for detecting m atoms at positions $\{x_1, \dots, x_m\}$ follows as

$$p^m(x_1 \dots x_m) = \frac{(M-m)!}{M!} \langle \Psi^\dagger(x_1) \dots \Psi^\dagger(x_m) \Psi(x_m) \dots \Psi(x_1) \rangle . \quad (9.49)$$

The conditional probability density, which gives the probability of detecting an atom at the position x_m , given $m-1$ previous detections at positions $\{x_1, \dots, x_{m-1}\}$, is defined as

$$p(x_m | x_1, \dots, x_{m-1}) = \frac{p^m(x_1, \dots, x_m)}{p^{m-1}(x_1, \dots, x_{m-1})} . \quad (9.50)$$

The conditional probability density offers a straightforward means of directly simulating a sequence of atom detections. This follows from the fact that, by virtue of the form for $p^m(x_1, \dots, x_m)$, the conditional probabilities can all be expressed in the simple form

$$p(x_m | x_1, \dots, x_{m-1}) = 1 + \beta \cos(2\pi x_m + \phi) , \quad (9.51)$$

where β and ϕ are parameters that depend on $\{x_1, \dots, x_{m-1}\}$. This is a manifestation of the correlations between atomic positions embodied in the probabilities p^m .

The origin of the form (9.51) can be seen from the action of each measurement on the previous result

$$\langle \phi_m | \hat{\Psi}^\dagger(x) \hat{\Psi}(x) | \phi_m \rangle = (M-m) + 2A \cos[\theta - \phi(x)] , \quad (9.52)$$

where $A \exp(-i\theta) = \langle \phi_m | \hat{a}_1^\dagger \hat{a}_2 | \phi_m \rangle$.

We can now simulate an experiment. We begin with the distribution $p^1(x_1) = 1$, i.e. we choose the first random number x_1 , the position of the first atom detector, from a uniform distribution in the interval $[0, 1]$. After the first measurement, the state vector of the system is

$$\begin{aligned} |\phi_1\rangle &= \hat{\Psi}(x_1) |\psi_0\rangle \\ &= \sqrt{\frac{M}{2}} \left[|(M/2) - 1, M/2\rangle + |M/2, (M/2) - 1\rangle e^{i\phi(x)} \right] , \end{aligned} \quad (9.53)$$

which is an entangled state containing phase information resulting from the fact that we do not know from which condensate the detected atom came.

The corresponding conditional probability density for the second detection can be derived as

$$\begin{aligned} p(x | x_1) &= \frac{p^2(x_1, x)}{p^1(x_1)} = \frac{1}{M-1} \frac{\langle \hat{\Psi}^\dagger(x_1) \hat{\Psi}^\dagger(x) \hat{\Psi}(x) \hat{\Psi}(x_1) \rangle}{\langle \hat{\Psi}^\dagger(x_1) \hat{\Psi}(x_1) \rangle} \\ &= \frac{1}{2} \left\{ 1 + \frac{M}{2(M-1)} \cos[\phi(x) - \phi(x_1)] \right\} . \end{aligned} \quad (9.54)$$

Thus, the phase of the interference pattern depends on the first measurement x_1 , and for a large M , the maximum visibility of the interference fringes approaches $1/2$. The second position x_2 is chosen from the distribution (9.54), and again we find simple analytical formulae for the parameters β and ϕ . However, the expressions for β and ϕ become more complicated with increasing m , and in practice numerical methods are employed to simulate the conditional probability.

The result (9.54) suggests that the condensate behaves as if it had a phase as soon as there is a large occupation number of an individual quantum state. No interactions between the atoms were included to maintain the phase throughout the condensate. The appearance of the relative phase between two condensates has a simple interpretation in terms of the welcher-weg problem: the phase results from the lack of information as to which condensate provided the detected atom.

9.2.2 Relative Phase in Josephson Junctions

Another interesting manifestation of phase coherence between two trapped atomic Bose–Einstein condensates is the appearance of behaviour analogous to that observed in Josephson junctions, the well-known effect in superconductors.

The simplest and physically most relevant system to model this effect is that of a double-well trapping potential, with a barrier between the two condensates. In the context of BEC in an atomic vapour, it is possible to conceive of experimental configurations in which a condensate is trapped in just such a potential. For example, in the experiment of Andrews et al. on interference between two initially separated condensates, which we will discuss in more detail in Sect. 9.5, a double-well trapping potential was formed using an off-resonance laser beam to perturb the trap. A simple scheme of a symmetric double-well potential is shown in Fig. 9.4.

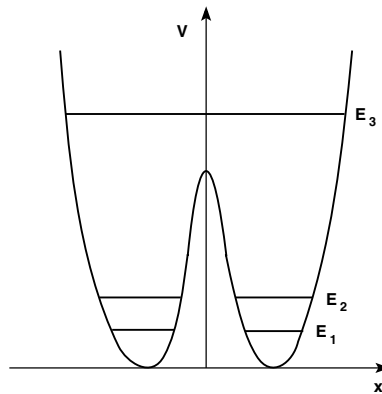


Fig. 9.4. Schematic diagram of double-well potential with only two energy levels, E_1 and E_2 , inside the wells

We assume that the two lowest energy levels of the system are closely spaced and well separated from the higher energy levels, which are well above the barrier potential. In this approximation, we can use a simple two state model of the condensates. Let $\Psi_0(\mathbf{r} \pm \mathbf{r}_0)$ be the ground state wave function of a single potential well with energy E_0 located at $\mathbf{r} \pm \mathbf{r}_0$. If we treat the barrier potential as a perturber we find, using perturbation theory, that the wave function of the double-well potential system can be approximated by the linear superpositions

$$\begin{aligned}\Psi_1(\mathbf{r}) &= \frac{1}{\sqrt{2}} [\Psi_0(\mathbf{r} - \mathbf{r}_0) - \Psi_0(\mathbf{r} + \mathbf{r}_0)] , \\ \Psi_2(\mathbf{r}) &= \frac{1}{\sqrt{2}} [\Psi_0(\mathbf{r} - \mathbf{r}_0) + \Psi_0(\mathbf{r} + \mathbf{r}_0)] ,\end{aligned}\quad (9.55)$$

with energies $E_1 \simeq E_0 - V$ and $E_2 \simeq E_0 + V$, where

$$V = \int d^3\mathbf{r} \Psi_0(\mathbf{r} + \mathbf{r}_0) H(\mathbf{r}) \Psi_0(\mathbf{r} - \mathbf{r}_0) , \quad (9.56)$$

and $H(\mathbf{r})$ is the single-particle Hamiltonian.

Using the two-state approximation, we introduce atom field operators

$$\begin{aligned}\hat{c}_1 &= \int d^3\mathbf{r} \Psi_0^*(\mathbf{r} - \mathbf{r}_0) \hat{\Psi}(\mathbf{r}, 0) , \\ \hat{c}_2 &= \int d^3\mathbf{r} \Psi_0^*(\mathbf{r} + \mathbf{r}_0) \hat{\Psi}(\mathbf{r}, 0) ,\end{aligned}\quad (9.57)$$

such that $[\hat{c}_i, \hat{c}_j^\dagger] = \delta_{ij}$.

Then, the multi-atom Hamiltonian can be written in terms of the operators \hat{c}_1 and \hat{c}_2 as

$$\begin{aligned}H &= E_0 (\hat{c}_1^\dagger \hat{c}_1 + \hat{c}_2^\dagger \hat{c}_2) + \frac{1}{2} \hbar \nu (\hat{c}_1^\dagger \hat{c}_2 + \hat{c}_2^\dagger \hat{c}_1) \\ &\quad + \hbar \kappa (\hat{c}_1^{\dagger 2} \hat{c}_1^2 + \hat{c}_2^{\dagger 2} \hat{c}_2^2) ,\end{aligned}\quad (9.58)$$

where $\nu = 2V/\hbar$ is the coupling constant (tunnelling frequency) between the condensates, and

$$\kappa = \frac{U_0}{2\hbar} \int d^3\mathbf{r} |\Psi(\mathbf{r}_0)|^4 \quad (9.59)$$

is the atom–atom coupling constant.

The two-state approximation requires that the multi-atom interactions only slightly modify the ground state properties of the individual potential wells. In practice, this corresponds to systems with a small number of atoms. Nevertheless, the dynamics of the condensates can still be strongly modified by the atom-atom interactions, represented by the last term in (9.58).

The Heisenberg equations of motion for the operators \hat{c}_1 and \hat{c}_2 take the form

$$\begin{aligned}\frac{d\hat{c}_1}{dt} &= -i\frac{E_0}{\hbar}\hat{c}_1 - \frac{1}{2}i\nu\hat{c}_2 - 2i\kappa\hat{c}_1^\dagger\hat{c}_1^2, \\ \frac{d\hat{c}_2}{dt} &= -i\frac{E_0}{\hbar}\hat{c}_2 - \frac{1}{2}i\nu\hat{c}_1 - 2i\kappa\hat{c}_2^\dagger\hat{c}_2^2,\end{aligned}\quad (9.60)$$

Equations (9.60) are nonlinear first-order differential equations, which we solve for the expectation values $\langle\hat{c}_1\rangle$ and $\langle\hat{c}_2\rangle$ in the semiclassical mean-field approximation. In this approximation, we factorize all products of the operators in these equations, and obtain

$$\begin{aligned}\frac{d\tilde{b}_1}{dt} &= -\frac{1}{2}i\nu\tilde{b}_2 - 2i\kappa M|\tilde{b}_1|^2\tilde{b}_1, \\ \frac{d\tilde{b}_2}{dt} &= -\frac{1}{2}i\nu\tilde{b}_1 - 2i\kappa M|\tilde{b}_2|^2\tilde{b}_2,\end{aligned}\quad (9.61)$$

where

$$\tilde{b}_i = b_i \exp\left(-i\frac{E_0 t}{\hbar}\right) \quad (9.62)$$

are the slowly varying parts of the atomic operators, and

$$b_i = \langle\hat{c}_i\rangle/\sqrt{M}. \quad (9.63)$$

The semiclassical equations (9.61) can be solved exactly. Consider the example that initially all atoms were localized in well “1”. i.e. $M_1(0) = M|b_1(0)|^2 = M$, and $M_2(0) = 0$. With this initial condition, one finds a solution of (9.46) of the form

$$M_1(t) = \frac{1}{2}M \left[1 + \text{cn}(\nu t|M^2/M_c^2)\right], \quad (9.64)$$

where $\text{cn}(x|y)$ is the Jacobi elliptic function, and M_c is the critical number of atoms, given by

$$M_c = \frac{\nu}{\kappa}. \quad (9.65)$$

For $M \ll M_c$, we can approximate the Jacobi elliptic function by the cosine function, and then the number of atoms (9.64) exhibits periodic oscillations with frequency ν , precisely like those in Josephson junctions. As the number of atoms increases, the oscillation period increases until, at $M = M_c$ it becomes infinite. For $M > M_c$, the oscillations are inhibited as the interaction energy now exceeds the energy level splitting and one finds a self-trapping effect in which a population imbalance is maintained between the two potential wells.

Unfortunately, the solution (9.64) does not provide any information about the phases of the two condensates. This is due to the randomness of the atom–atom interactions that average the phase to zero. However, we can still establish a relative phase between the condensates using this two-state system, by neglecting the atom–atom interactions. In this case, we put $\kappa = 0$ in (9.60), when we find the number of atoms in well “1” to be

$$M_1(t) = \langle \hat{c}_1^\dagger(t) \hat{c}_1(t) \rangle = \frac{1}{2} M [1 + \alpha \cos(\nu t) + \beta \sin(\phi) \sin(\nu t)] , \quad (9.66)$$

where $M = \langle \hat{c}_1^\dagger \hat{c}_1 + \hat{c}_2^\dagger \hat{c}_2 \rangle$ is the total number of atoms, $\alpha = \langle \hat{c}_1^\dagger \hat{c}_1 - \hat{c}_2^\dagger \hat{c}_2 \rangle$, and

$$\beta = \frac{2\langle \hat{c}_1^\dagger \hat{c}_2 \rangle}{M} e^{-i\phi} . \quad (9.67)$$

If the condensates are initially in number states with equal populations, then $\alpha = \beta \exp(i\phi) = 0$ and population oscillations do not occur. However, by virtue of spontaneous symmetry breaking induced by measurements of the number of atoms in one of the wells, it is possible for a relative phase between the condensates to be established ($\beta \exp(i\phi) \neq 0$) and then population oscillations can be observed.

9.3 Interference Between Colliding Condensates

The approach to the condensate phase, presented above, can be modified to include the effect of collisions between the atoms [195]. In this method, we calculate the times of the atom detections stochastically, with the evolution of the system in between these times determined by an effective Hamiltonian of the form

$$H_{\text{eff}} = \hbar\kappa \left[\left(\hat{a}_1^\dagger \hat{a}_1 \right)^2 + \left(\hat{a}_2^\dagger \hat{a}_2 \right)^2 \right] - \frac{1}{2} i\hbar\sigma \left(\hat{a}_1^\dagger \hat{a}_1 + \hat{a}_2^\dagger \hat{a}_2 \right) , \quad (9.68)$$

where σ and κ are the detection and collision rates, respectively. The Hamiltonian (9.68) includes only collisions between atoms from the same condensate, collisions between atoms from different condensates are ignored. At the time of an atom detection, the position at which the atom is detected is chosen using the conditional probability method outlined in Sect. 9.2. Following this method, we find that after m atom detections at positions $\{x_1, \dots, x_m\}$ and times $\{t_1, \dots, t_m\}$ the state vector of the system will be of the form

$$|\phi_m\rangle = \hat{\Psi}(x_m) e^{-iH_{\text{eff}}(t_m - t_{m-1})/\hbar} \dots \hat{\Psi}(x_1) e^{-iH_{\text{eff}}t_1/\hbar} |\phi_0\rangle . \quad (9.69)$$

To see how the collisions affect the interference fringes, we inspect the expectation value

$$\langle \phi_m | \hat{\mathcal{U}}(t) \hat{\Psi}^\dagger(x) \hat{\Psi}(x) \hat{\mathcal{U}}(t) | \phi_m \rangle , \quad (9.70)$$

where the evolution operator is given by

$$\hat{\mathcal{U}} = \exp \left\{ -i\kappa \left[\left(\hat{a}_1^\dagger \hat{a}_1 \right)^2 + \left(\hat{a}_2^\dagger \hat{a}_2 \right)^2 \right] t \right\} , \quad (9.71)$$

and the state vector after m detections is

$$|\phi_m\rangle = \sum_{k=0}^m c_k |M/2 - m + k, M/2 - k\rangle , \quad (9.72)$$

with $\sum |c_k|^2 = 1$.

Hence, we find that the expectation value (9.70) can be written as

$$\begin{aligned} \langle \phi_m | \hat{\mathcal{U}}(t) \hat{\Psi}^\dagger(x) \hat{\Psi}(x) \hat{\mathcal{U}}(t) | \phi_m \rangle &= M - m \\ &+ \sum_{k=1}^m \mathcal{A}(k) \cos [\phi(x) + 2\kappa t (2k - m - 1) + \Theta_k] , \end{aligned} \quad (9.73)$$

where the phase Θ_k is defined by

$$A e^{i\Theta_k} = c_k^* c_{k-1} , \quad (9.74)$$

and

$$\mathcal{A}(k) = 2A \sqrt{(M/2 - k + 1)(M/2 - m + k)} . \quad (9.75)$$

According to (9.50), the conditional probabilities are determined by the correlation function (9.73). A nonzero collision rate ($\kappa \neq 0$) introduces a time-dependent phase modulation of the interference terms (cosine terms). This leads to a dephasing of these functions in time and hence to a loss of coherence, and consequently interference fringes. Note that the time dependence of the cosine term is similar to that found for two nonidentical atoms.

9.4 Collapses and Revivals of an Atomic Interference Pattern

In trapped condensates one can predict another interesting quantum interference phenomenon, the collapses and revivals of the interference pattern of two colliding condensates. This effect is reminiscent of the collapses and revivals that occur in the optical Jaynes–Cummings model of a two-level atom interacting with a quantized EM field.

To illustrate this phenomenon in cold atoms, suppose that the atoms are released from two condensates with momenta k_1 and k_2 , respectively. The intensity of atoms at a detector is given by

$$\begin{aligned} I(x, t) &= I_0 \left\langle \left[\hat{a}_1^\dagger(t) e^{ik_1 x} + \hat{a}_2^\dagger(t) e^{ik_2 x} \right] \left[\hat{a}_1(t) e^{-ik_1 x} + \hat{a}_2(t) e^{-ik_2 x} \right] \right\rangle \\ &= I_0 \left\{ \langle \hat{a}_1^\dagger \hat{a}_1 \rangle + \langle \hat{a}_2^\dagger \hat{a}_2 \rangle + \left[\langle \hat{a}_1^\dagger \hat{a}_2 \rangle e^{-i\phi(x)} + \text{H.c.} \right] \right\} , \end{aligned} \quad (9.76)$$

where $\phi(x) = (k_2 - k_1)x$, \hat{a}_i (\hat{a}_i^\dagger) is the atom annihilation (creation) operator for the i th condensate, and the average is taken over the state of the system at time t .

If the only interactions in the system are collisions between atoms in each condensate, the state vector of the system will be of the form

$$|\varphi(t)\rangle = e^{-iHt/\hbar}|\varphi(0)\rangle, \quad (9.77)$$

where $|\varphi_0\rangle$ is the initial state of the system, and H is the interaction (collision) Hamiltonian

$$H = \hbar\kappa \left[\left(\hat{a}_1^\dagger \hat{a}_1 \right)^2 + \left(\hat{a}_2^\dagger \hat{a}_2 \right)^2 \right]. \quad (9.78)$$

If initially each condensate was in a coherent state of amplitude $|\alpha|$, with a relative phase ϕ between the two condensates, i.e.

$$|\varphi(t=0)\rangle = |\alpha\rangle|\alpha e^{-i\phi}\rangle, \quad (9.79)$$

then we obtain for the intensity

$$I(x, t) = 2I_0|\alpha|^2 \left\{ 1 + e^{2|\alpha|^2[\cos(2\kappa t)-1]} \cos[\phi(x) - \phi] \right\}. \quad (9.80)$$

From this expression, it is clear that the visibility of the interference pattern undergoes collapses and revivals. The collapses are described by the exponential term and appear whenever t is no longer a multiple of π/k . The revivals occur at times $t = n\pi/k$, where n is integer, i.e. the period of revivals is π/k .

Alternatively, we may consider two Bose–Einstein condensates which are initially in number states $|M/2\rangle$, with the relative phase between the condensates being established via an atomic detection. The state vector of the system, after m atoms have been detected, is given by

$$|\phi_m\rangle = \sum_{k=0}^m c_k |M/2 - m + k, M/2 - k\rangle. \quad (9.81)$$

With the state (9.81), the intensity can be approximated as

$$I(x, t) = I_0 \left\{ M - m + \sum_{k=1}^m \mathcal{A}(k) \cos[2(2k - m - 1)\kappa t] \cos[\phi(x) - \phi] \right\}. \quad (9.82)$$

Again, the intensity exhibits collapses and revivals, but now with a period of $\pi/(2\kappa)$.

This phenomenon has a simple interpretation. The collapses and revivals of the interference pattern originate from a dephasing of an oscillation due to quantum fluctuations in the number of atoms in the condensates. Since there

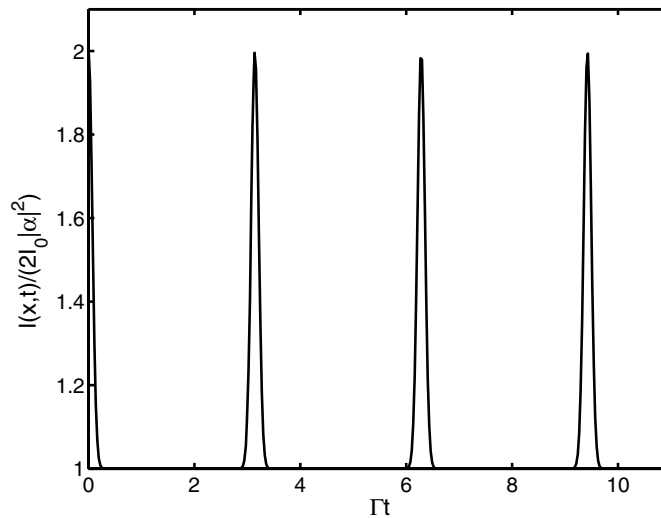


Fig. 9.5. Collapses and revivals in the time evolution of the intensity of two interfering condensates prepared initially in coherent states with equal amplitudes $|\alpha| = 5$

is no dissipation of energy in this process, the oscillations can eventually reappear (revival) after a certain time interval. Figure 9.5 shows the time evolution of the intensity (9.82) for $M = m = 1000$ and $\kappa = \Gamma$, where Γ is the detection rate. Clearly, the intensity exhibits periodic collapses and revivals with a period $\pi/(2\kappa)$.

9.5 Interference Experiments in Coherent Atom Optics

The phase of a condensate, or more generally an arbitrary wave field, is the argument of a complex number and is not an observable. Only the relative phase between two condensates can be measured. Here, we discuss some experiments involving atomic condensates where interference fringes were observed between two separated atomic condensates brought together to overlap at an atomic detector, which provides compelling evidence for coherence in such systems. The essential result of the experiment was that, even through no phase information was initially present, an interference pattern was found between the two overlapping condensates.

9.5.1 Experimental Evidence of Relative Phase Between Two Condensates

The first experimental observation of interference between weakly interacting Bose–Einstein condensates was made by Andrews et al. [196]. In the experiment, they observed high-contrast matter-wave interference fringes in the superposition of two initially separated condensates that were released from

the magnetic trap to expand and overlap at a detector. The two condensates were composed of sodium atoms optically cooled and trapped in a double-well potential. The atoms were further cooled by radio-frequency induced evaporation. The double-well potential was created by focusing an argon ion laser field into the center of the magnetic trap. The laser field generated a repulsive optical dipole force that cut a cigar-shaped atomic cloud into two spatially separated parts. The frequency of the laser field was far from the sodium resonance to avoid heating from spontaneous emission. The double condensate was directly observed by nondestructive phase-contrast imaging.

After switching-off the trapping potential and argon ion laser, the two independent condensates expanded freely, due to the repulsive atom–atom interactions, into the region between the wells where they eventually overlapped. A clean interference pattern of the two condensates was observed by absorption imaging. Figure 9.6 shows the observed interference pattern after 40 ms time-of-flight of the condensates and two different powers of the argon ion laser. The observed pattern was composed of straight interference fringes characteristic of two point-like sources. It was also observed that the fringe period become smaller for larger powers of the argon ion laser, since larger power increased the initial separation between the condensates.

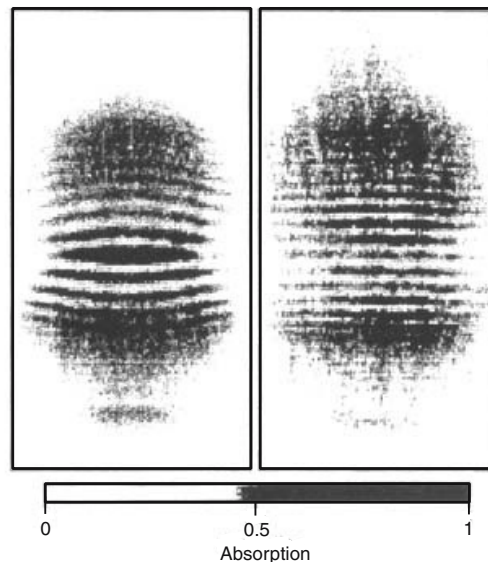


Fig. 9.6. Interference pattern of two expanding Bose–Einstein condensates observed by Andrews et al. The left graph shows the interference pattern for an argon ion laser power of 3 mW, and the right graph is for 5 mW. From M.R. Andrews, C.G. Townsend, H.-J. Miesner, D.S. Durfee, D.M. Kurn, W. Ketterle: *Science* **275**, 637 (1997). Copyright (1997) AAAS

We can understand the interference between the condensates by imagining the initial condensates as two point-like pulsed sources placed at distance d on the z axis. When the interference takes place in the region of space where

the density of the gas is small enough, then the condensate wave function is a linear superposition of two de Broglie waves. The fringe period is then equal to the de Broglie wavelength λ associated with the relative motion of atoms with mass m

$$\lambda = \frac{ht}{md}, \quad (9.83)$$

where h is the Planck's constant and t is the flight time of the condensates from switching-off the trap to the observation. Using the spacing between the two initial condensates as an estimate of the distance d , one gets a fringe period in excellent agreement with the experimental observation. With the experimental values of $t = 40$ ms and $d = 40$ μ s, we find $\lambda = 20$ μ m, which corresponds to the fringe period observed in the experiment.

To support the prediction that the fringe pattern was caused by two condensates, the observed pattern was compared with the pattern from a single condensate. It was observed that a single expanded condensate did not exhibit interference.

The observation of high-contrast interference fringes was clear evidence for spatial coherence extending over the whole sample, and confirmed that a trapped condensate has a uniform spatial phase and a released condensate develops a nonuniform phase profile.

9.5.2 Atomic Interferometers

Interferences between matter waves have been demonstrated with electrons, neutrons and neutral atoms, and have been extensively used for fundamental tests of quantum-mechanical predictions. The construction of an interferometer for atoms is rendered difficult by the fact that atoms carry no charge as electrons do, and cannot penetrate through condensate matter like neutrons. However, laser cooling of atoms enables us to increase the de Broglie wavelength of an atomic matter wave, thereby allowing us to observe interference effects with atoms travelling along well separated paths. The diffraction of atoms by a standing wave, discussed in Sect. 9.1, is an example of interference effects with neutral atoms.

We shall illustrate here two different interference experiments involving two different atomic interferometers. The first experiment is based on a Young's double slit arrangement, and the second one involves a Mach-Zehnder type arrangement.

Young's Double Slit Experiment with Atoms

In Chap. 1, we learnt that the simplest interference experiments are of the Young's double slit type where, in analogy to light, atoms can travel along two spatially well separated paths from a source to a detector. Carnal and

Mlynek [197] demonstrated that atoms emerging from the same source and split by two slits, produce an interference pattern at the atomic detector. The source of the atoms in their experiment was a thermal beam of metastable helium atoms. The velocity of the atoms was adjusted by setting the temperature of the source to $T = 295$ K, corresponding to a mean de Broglie wavelength of $\lambda_B = 0.56$ Å, or to $T = 83$ K, corresponding to $\lambda_B = 1.03$ Å. The atoms travelled through a slit with a width of $2\text{ }\mu\text{m}$ imprinted in a thin gold foil. Next, the atoms passed through two $1\text{-}\mu\text{m}$ -wide slits separated by $8\text{ }\mu\text{m}$, and the interference pattern was monitored by a detection system consisting of a secondary electron multiplier. The interference pattern of the detected atoms is shown in Fig. 9.7. With the atomic velocity corresponding

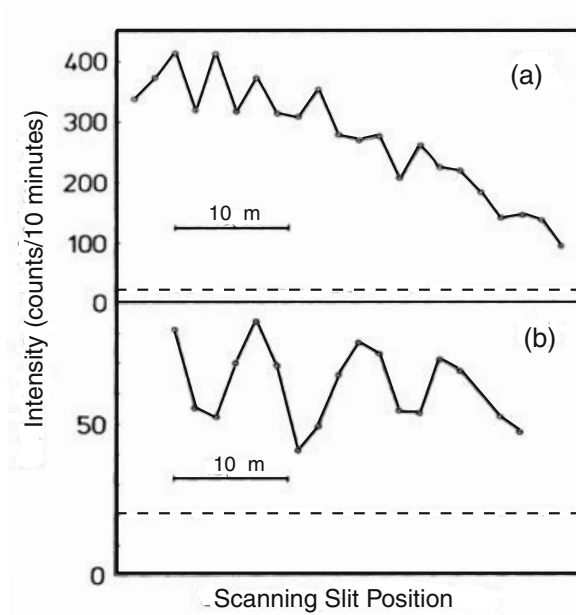


Fig. 9.7. Interference pattern observed in the Carnal and Mlynek [197] experiment with two different atomic wavelengths **(a)** $\lambda_B = 0.56$ Å and **(b)** $\lambda_B = 1.03$ Å. The dashed line represents the detector background with the atomic beam blocked in front of the entrance slit. From O. Carnal, J. Mlynek: Phys. Rev. Lett. **66**, 2689 (1991). Copyright (1991) by the American Physical Society

to the de Broglie wavelength of $\lambda_B = 0.56$ Å, the average distance between the observed interference fringes was $dx = 4.5 \pm 0.6\text{ }\mu\text{m}$. [See Fig. 9.7(a).] In order to improve the visibility of the interference pattern, the source of the atoms was cooled to the temperature $T = 83$ K, giving an average atomic velocity corresponding to the de Broglie wavelength of $\lambda_B = 1.03$ Å. In this case, the distance between the fringes increased, as seen from Fig. 9.7(b), giving a visibility of the interference pattern greater than 60%.

Atomic interferometers of the Young's double slit type with cold atoms provided a tool for many interesting experiments in atom optics. Since both paths are spatially well separated, it is possible to introduce a relative phase shift between the two paths by applying an external potential to the atoms. This allows the testing of certain quantum mechanical phenomena such as loss of interference when which-way information is available, the Aharonov–Casier effect, and Berry's phase.

Mach–Zehnder Interferometer with a Bose–Einstein Condensate

A trapped Bose–Einstein condensate could be an unique source for matter-wave interferometry because the condensate atoms occupy a single quantum state with uniform spatial phase. The uniform spatial phase profile of a condensate can be probed with matter-wave Bragg interferometry. The Bragg interferometer is an analog of the optical Mach–Zehnder interferometer, in which an atomic wavepacket is first split by an atomic beamsplitter, then the two components are redirected towards each other by atomic mirrors. Finally, the converging components are made to interfere by another atomic beamsplitter. In this interferometer, the condensate passes through an optical beam, consisting of a pair of monochromatic laser fields of different frequencies that cause optically off-resonant, spontaneous emission free, Raman excitations during the passage of the condensate. The optical beams play the role of beamsplitters and mirrors in the interferometer.

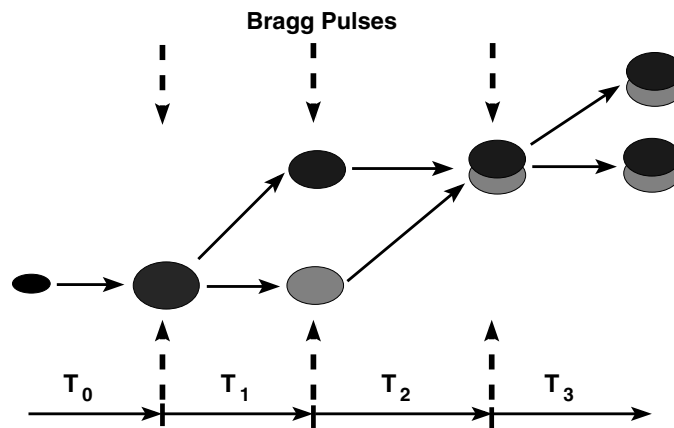


Fig. 9.8. Schematic diagram of the matter-wave interferometer of Simsarian et al. [198]. An expanding atomic condensate is split at T_0 into two condensates that are redirected at T_1 to overlap at T_2 , and the resulting interference pattern is detected at T_3

From the dependence of the fringe spacing on the overlap, one can extract the phase profile of the wave packets. A schematic diagram of the matter-wave Bragg interferometer of Simsarian et al. [198] is shown in Fig. 9.8. The

experiment was performed with a trapped condensate of 1.8×10^6 sodium atoms. Next, the condensate was released, so that the atoms expanded freely in space.¹ After an expansion time T_0 , the spatial phase profile of the condensate was probed in the interferometer. The interferometer was composed of three optically induced Bragg-diffraction pulses applied successively in time. Each pulse was composed of two counterpropagating laser beams of different frequencies detuned from the atomic resonance to avoid spontaneous emission. The first pulse, applied at time T_0 , coherently split the BEC into two condensates, with about the same number of atoms. The condensates differed only in their momenta, $p_1 = 0$ and $p_2 = 2\hbar k$. After a time T_1 the two condensates were completely separated, and a second Bragg pulse was applied to change the momenta of the condensates in order to bring them to overlap again. Then, a third pulse was applied of $T_3 = 6 \mu\text{s}$ duration to split the overlapping condensates into two momentum states. The interference of the overlapping condensates in each of the two momentum states allowed the determination of the local phase difference between them. By changing the time T_2 of the second pulse, the separation $\delta x = x_A - x_B$ of the two condensates was varied, and the phase profile of the condensates was measured as a function of δx .

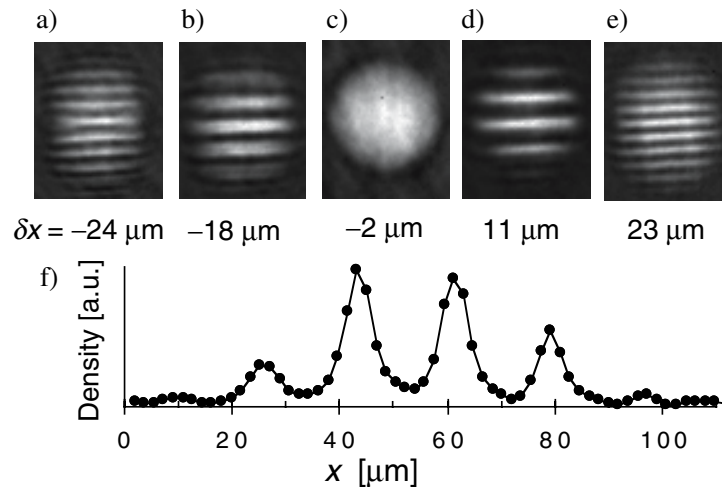


Fig. 9.9. Experimentally observed interference pattern after an expansion time $T_0 = 4$ ms. Graphs (a)-(e) show one of the two output ports of the interferometer for different δx (different T_2). Graph (f) shows the density along the x direction for $\delta x = 11 \mu\text{m}$. From J.E. Simsarian, J. Denschlag, M. Edwards, C.W. Clark, L. Deng, E.W. Hagley, K. Helmerson, S.L. Rolston, W.D. Phillips: Phys. Rev. Lett. **85**, 2040 (2000). Copyright (2000) by the American Physical Society

¹ It would be more correct to call the released condensate a cold coherent atomic wave packet expanding in free space, but in accordance with existing terminology, we also call it a condensate.

Figure 9.9 shows the experimentally observed interference fringes for different δx , corresponding to different T_2 , after an expansion time $T_0 = 4$ ms. Evenly spaced and straight fringes were observed with the fringe spacing decreasing with increasing $|\delta x - x_0|$. No fringes were observed for $\delta x = x_0 \neq 0$.

9.5.3 Collapses and Revivals of a Bose–Einstein Condensate

The phenomenon of collapses and revivals is well-known in quantum optics, and they have been observed in atomic Rydberg wave-packets [199, 200], molecular vibrations [201], and ions interacting with an EM field [202, 203].

A periodic series of collapses and revivals of the matter-wave field of a Bose–Einstein condensate was observed by Greiner et al. [204], who considered the dynamical evolution of a multiple matter-wave interference pattern. In the experiment, they created a quasi-pure Bose–Einstein condensate containing about 2×10^5 ^{87}Rb atoms in the $|F = 2, m_F = 2\rangle$ state and trapped in a harmonic magnetic potential with isotropic trapping frequencies of $\omega = 2\pi \times 24$ Hz. The trapped atoms were transferred into the optical lattice potential by slowly increasing the intensity of the lattice laser beam, so that a lattice potential depth $V_a \approx 11E_r$ was reached, where E_r is the recoil energy. The value $V_a = 11E_r$ was so chosen that the atoms were still in the condensate regime with a large probability of tunnelling between neighbouring potential wells. Then, the potential depth was rapidly increased to a value of about $35E_r$ within a time of $50 \mu\text{s}$. At this potential, the tunnelling was negligible so that the separate wells could be considered as completely independent from each other. The atoms were kept in these separated wells for different times t . After these hold times, the confining potential was suddenly turned off and the resulting multiple matter-wave interference pattern was observed after a time-of-flight period of 16 ms. The observed interference pattern for different hold times between $t = 0$ and up to $t = 550 \mu\text{s}$ is shown in Fig. 9.10. Evidently, the observed interference pattern exhibits

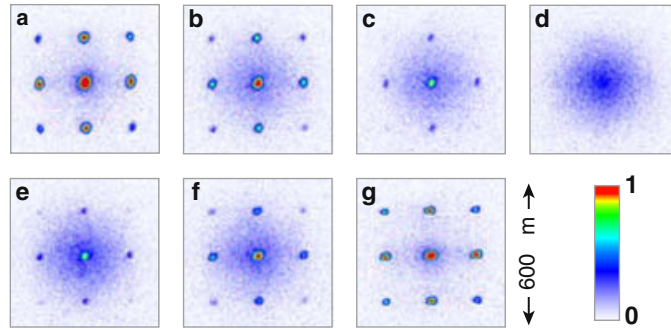


Fig. 9.10. Collapses and revivals of a macroscopic matter-wave observed by Greiner et al. [204] in a Bose–Einstein condensate of rubidium atoms. From M. Greiner, O. Mandel, T.W. Hänsch, I. Bloch: *Nature* **419**, 51 (2002), with permission

collapses and revivals. At the hold time $t = 0$, a distinct interference pattern is visible, showing that initially the system was in a macroscopic matter-wave state with well defined phase difference between different wells. After a hold time of 250 μs , the interference pattern is lost indicating a collapse of the macroscopic matter-wave field. However, after a hold time of 550 μs , the interference pattern was restored again, indicating a revival of the macroscopic matter-wave field.

Note that in this interference experiment, the number of atoms in each well remained constant during the evolution time. Therefore, this system can be regarded as completely different from the other systems discussed above, where the number of atoms in the condensates changed during the dynamical evolution. This property is very promising for further potential applications of this system in quantum information processing and quantum computation with neutral atoms.

9.6 Higher Order Coherence in a BEC

The experiment of Andrews et al. [196] confirmed that condensates can possess first-order coherence. Bose–Einstein condensates can also possess higher order coherences, a property that strengthens the analogy between condensates and optical photons. An obvious question is what physical properties of condensates can arise from the higher order coherences, and how to measure these coherences.

Ketterle and Miesner [205] have shown that the mean-field energy $\langle U \rangle$ of a condensate provides a direct measure of the normalized second-order correlation function. To illustrate this approach, we use second quantization and express the potential energy operator \hat{U} in terms of the field operators $\hat{\Psi}(\mathbf{r})$ as

$$\hat{U} = \frac{1}{2} \int d^3\mathbf{r}_1 d^3\mathbf{r}_2 \hat{\Psi}^\dagger(\mathbf{r}_1) \hat{\Psi}^\dagger(\mathbf{r}_2) U(|\mathbf{r}_1 - \mathbf{r}_2|) \hat{\Psi}(\mathbf{r}_2) \hat{\Psi}(\mathbf{r}_1) , \quad (9.84)$$

from which we find the expectation value for the interaction energy to be

$$\begin{aligned} \langle \hat{U} \rangle &= \frac{1}{2} \int d^3\mathbf{r}_1 d^3\mathbf{r}_2 U(|\mathbf{r}_1 - \mathbf{r}_2|) \\ &\quad \times \langle \hat{\Psi}^\dagger(\mathbf{r}_1) \hat{\Psi}(\mathbf{r}_1) \rangle \langle \hat{\Psi}^\dagger(\mathbf{r}_2) \hat{\Psi}(\mathbf{r}_2) \rangle g^{(2)}(\mathbf{r}_1, \mathbf{r}_2) , \end{aligned} \quad (9.85)$$

where

$$g^{(2)}(\mathbf{r}_1, \mathbf{r}_2) = \frac{\langle \hat{\Psi}^\dagger(\mathbf{r}_1) \hat{\Psi}^\dagger(\mathbf{r}_2) \hat{\Psi}(\mathbf{r}_2) \hat{\Psi}(\mathbf{r}_1) \rangle}{\langle \hat{\Psi}^\dagger(\mathbf{r}_1) \hat{\Psi}(\mathbf{r}_1) \rangle \langle \hat{\Psi}^\dagger(\mathbf{r}_2) \hat{\Psi}(\mathbf{r}_2) \rangle} . \quad (9.86)$$

For a short-range potential, we can use the pseudopotential

$$U(|\mathbf{r}_1 - \mathbf{r}_2|) = \frac{4\pi\hbar^2 a}{m} \delta(|\mathbf{r}_1 - \mathbf{r}_2|) , \quad (9.87)$$

and obtain

$$\langle U \rangle = \left(\frac{2\pi\hbar^2 a}{m} \right) g^{(2)}(\mathbf{r}, \mathbf{r}) \int d^3\mathbf{r}' \langle \Psi^\dagger(\mathbf{r}') \Psi(\mathbf{r}') \rangle^2, \quad (9.88)$$

where a is the s -wave scattering length, m is the atomic mass, and we have assumed that $g^{(2)}(\mathbf{r}, \mathbf{r}')$ depends only on $\mathbf{r}_1 - \mathbf{r}_2 = \mathbf{r}'$.

The mean energy of the condensate thus strongly depends on the type of fluctuations that exist in the density. In direct analogy with the correlation function of a coherent laser field, we expect $g^{(2)}(\mathbf{r}, \mathbf{r}) = 1$ for a pure condensate as it is represented by a coherent matter wave. For a noncondensed (thermal) cloud of atoms, we expect the atom-bunching effect $g^{(2)}(\mathbf{r}, \mathbf{r}) = 2$, which indicates large density fluctuations of the atomic cloud. Thus, the atom-bunching effect is expected to vanish in a condensate, precisely as photon bunching does in any ideal laser beam. This means that an experimental observation of $g^{(2)}(\mathbf{r}, \mathbf{r})$ values equal or close to one would be strong evidence for the suppression of local density fluctuations and the formation of a Bose–Einstein condensate.

We employ the experimental data on observed Bose–Einstein condensates to calculate values of $g^{(2)}(\mathbf{r}, \mathbf{r})$. With the sodium condensate of Mews et al. [206], the experimentally determined scattering length was $a = (52 \pm 5)a_0$, implying $g^{(2)}(\mathbf{r}, \mathbf{r}) = 1.25 \pm 0.58$. In a different experiment, Castin and Dum [207] analyzed similar time-of-flight data and extracted $a = (42 \pm 15)a_0$, implying $g^{(2)}(\mathbf{r}, \mathbf{r}) = 0.81 \pm 0.29$. Thus, the values of $g^{(2)}(\mathbf{r}, \mathbf{r})$ predicted from the experimentally observed condensates are consistent with the predictions of $g^{(2)}(\mathbf{r}, \mathbf{r}) = 1$ for a pure condensate.

Apart from the second-order correlation function, it is possible to determine higher order correlation functions, which also could be useful for determining the onset of an atomic Bose–Einstein condensate. For example, Kagan et al. [208] have pointed out that the atom loss rate due to three-body recombination is directly related to the probability of finding three atoms close to each other and therefore can be used as a measure of the third-order correlation function

$$g^{(3)}(\mathbf{r}_1, \mathbf{r}_2, \mathbf{r}_3) = \frac{\langle \Psi^\dagger(\mathbf{r}_1) \Psi^\dagger(\mathbf{r}_2) \Psi^\dagger(\mathbf{r}_3) \Psi(\mathbf{r}_3) \Psi(\mathbf{r}_2) \Psi(\mathbf{r}_1) \rangle}{\langle \Psi^\dagger(\mathbf{r}_1) \Psi(\mathbf{r}_1) \rangle \langle \Psi^\dagger(\mathbf{r}_2) \Psi(\mathbf{r}_2) \rangle \langle \Psi^\dagger(\mathbf{r}_3) \Psi(\mathbf{r}_3) \rangle}. \quad (9.89)$$

They have shown that three-body recombination in a condensate would be a factor of $3! = 6$ less rapid than in a thermal cloud at the same mean density.

The ratio of the non-condensate to the condensate rate constants for this loss process was found by Burt et al. [209]. They compared the trap loss due to the three-body recombination of a Rb condensate to that of a thermal cloud, and obtained 7.4 ± 2.0 for the $g^{(3)}(\mathbf{r}, \mathbf{r}, \mathbf{r})$ values, which is in good agreement with the predicted value of 6. The experiment was a clear demonstration of the third-order coherence of a Bose–Einstein condensate and proved that relative to the thermal atoms, the density fluctuations are suppressed for condensate atoms as in a laser field.

References

1. M. Born, E. Wolf: *Principles of Optics* (Pergamon, New York, 1964)
2. R.L. Pfleegor, L. Mandel: Phys. Rev. **159**, 1084 (1967)
3. E. Schrödinger: Naturwissenschaften **23**, 807 (1935)
4. C. Jönsson: Z. Phys. **161**, 454 (1961); A. Zeilinger, R. Gähler, C.G. Shull, W. Treimer, W. Mampe: Rev. Mod. Phys. **60**, 1067 (1988); O. Carnal, J. Mlynek: Phys. Rev. Lett. **66**, 2689 (1991)
5. R.J. Glauber in *Quantum Optics and Electronics*, ed by C. de Witt et al. (Gordon and Breach, 1965) p. 65
6. L.C. Ryff: Phys. Rev. A **52**, 2591 (1995); B.-G. Englert: Phys. Rev. Lett. **77**, 2154 (1996)
7. N. Bohr: *Atomic Theory and the Description of Nature* (Cambridge University Press, Cambridge, 1961)
8. R.P. Feynman, R.B. Leighton, M. Sands: *The Feynman Lectures on Physics*, vol 3 (Addison-Wesley Publishing Co., Reading 1965)
9. L.J. Wang, X.Y. Zou, L. Mandel: Phys. Rev. A **44**, 4614 (1991)
10. U. Eichmann, J.C. Bergquist, J.J. Bollinger, J.M. Gilligan, W.M. Itano, D.J. Wineland: Phys. Rev. Lett. **70**, 2359 (1993)
11. W.M. Itano, J.C. Bergquist, J.J. Bollinger, D.J. Wineland, U. Eichmann, M.G. Raizen: Phys. Rev. A **57**, 4176 (1998)
12. R. Hanbury-Brown, R.Q. Twiss: Nature **177**, 27 (1956)
13. R. Loudon: *Quantum Theory of Light*, 2nd edn (Oxford University Press, Oxford 1983)
14. H.J. Kimble, M. Dagenais, L. Mandel: Phys. Rev. Lett. **39**, 691 (1977); H.J. Kimble, M. Dagenais, L. Mandel: Phys. Rev. A **18**, 201 (1978)
15. J.D. Cresser, J. Hager, G. Leuchs, M.S. Rateike, H. Walther: In: *Dissipative Systems in Quantum Optics*, ed by R. Bonifacio (Springer, Berlin Heidelberg New York, 1982) pp 307–331
16. F. Diedrich, H. Walther: Phys. Rev. Lett. **58**, 203 (1987)
17. G.T. Foster, S.L. Mielke, L.A. Orozco: Phys. Rev. A **61**, 053821 (2000)
18. Th. Richter: Ann. Phys. (Leipzig) **36**, 266 (1979); L. Mandel: Phys. Rev. A **28**, 1929 (1983); R. Gosh, C.K. Hong, Z.Y. Ou, L. Mandel: Phys. Rev. A **34**, 3962 (1986); Z. Ficek, R. Tanaś, S. Kielich: J. Mod. Opt. **35**, 81 (1988)
19. H. Paul: Rev. Mod. Phys. **58**, 209 (1986)
20. Y. Ou, L. Mandel: Phys. Rev. Lett. **62**, 2941 (1989)
21. C.K. Hong, Z.Y. Ou, L. Mandel: Phys. Rev. Lett. **59**, 2044 (1987)
22. M.O. Scully, K. Drühl: Phys. Rev. A **25**, 2208 (1982)
23. A. Einstein, B. Podolsky, N. Rosen: Phys. Rev. **47**, 777 (1935)
24. M. Born, D.J. Hooten: Z. Phys. **142**, 201 (1955)

25. P.S. Epstein: Am. J. Phys. **13**, 127 (1945)
26. A. Elitzur, L. Vaidman: Foundation of Physics **23**, 987 (1993)
27. P.G. Kwiat, H. Weinfurter, T. Herzog, A. Zeillinger, M.A. Kasevich: Phys. Rev. Lett. **74**, 4763 (1995)
28. A.N. Boto, P. Kok, D.S. Abrams, S.L. Braunstein, C.P. Williams, J.P. Dowling: Phys. Rev. Lett. **85**, 2733 (2000)
29. E.M. Nagasako, S.J. Bentley, R.W. Boyd, G.S. Agarwal: Phys. Rev. A **64**, 043802 (2001)
30. M. D'Angelo, M.V. Chekhova, Y. Shih: Phys. Rev. Lett. **87**, 013602 (2001)
31. M.W. Mitchell, J.S. Lundeen, A.M. Steinberg: Nature **429**, 161 (2004)
32. P. Walther, J.-W. Pan, M. Aspelmeyer, R. Ursin, S. Gasparoni, A. Zeilinger: Nature **429**, 158 (2004)
33. Th. Richter: Phys. Rev. A **42**, 1817 (1990)
34. Z. Ficek, S. Swain: J. Mod. Opt. **49**, 3 (2002)
35. W.H. Louisell: *Statistical Properties of Radiation* (Wiley, New York, 1973)
36. R.H. Lehmberg: Phys. Rev. A **2**, 883 (1970)
37. G.S. Agarwal: In *Quantum Statistical Theories of Spontaneous Emission and their Relation to other Approaches*, ed by G. Höhler, Springer Tracts in Modern Physics, vol 70 (Springer, Berlin Heidelberg New York, 1974)
38. M. Lewenstein, T.W. Mossberg: Phys. Rev. A **37**, 2048 (1988); G. Kurizki, A.G. Kofman, V. Yudson: Phys. Rev. A **53**, R35 (1996); Z. Ficek, B.J. Dalton, M.R.B. Wahiddin: J. Mod. Opt. **44**, 1005 (1997)
39. G.M. Nikolopoulos, P. Lambropoulos: J. Mod. Opt. **49**, 61 (2002); H.T. Dung, L. Knöll, D.G. Welsch: Phys. Rev. A **66**, 063810 (2002)
40. H.S. Freedhoff: J. Phys. B: At. Mol. Opt. Phys. **22**, 435 (1989)
41. L. Allen, J.H. Eberly: *Resonance Fluorescence and Two-Level Atoms* (Wiley, New York, 1975)
42. L. Mandel, E. Wolf: *Optical Coherence and Quantum Optics* (Cambridge, New York, 1995)
43. J.R. Ackerhalt, P.L. Knight, J.H. Eberly: Phys. Rev. Lett. **30**, 456 (1973); P.W. Milonni: Phys. Rep. **25**, 1 (1976)
44. H.A. Bethe: Phys. Rev. **72**, 339 (1947)
45. F. DeMartini, M. Marrocco, P. Mataloni, L. Crescentini, R. Loudon: Phys. Rev. A **43**, 2480 (1991)
46. P. W. Milonni, P. L. Knight: Opt. Commun. **9**, 119 (1973)
47. D. Kleppner: Phys. Rev. Lett. **47**, 233 (1981)
48. C.W. Gardiner, P. Zoller: *Quantum Noise* (Springer, Berlin Heidelberg New York, 2000) pp 147–148
49. R.H. Dicke: Phys. Rev. **93**, 99 (1954)
50. Z. Ficek, R. Tanaś: Phys. Rep. **372**, 369 (2002)
51. M. Lax: Phys. Rev. **172**, 350 (1968); S. Swain: J. Phys. A **14**, 2577 (1981)
52. U. Akram, Z. Ficek, S. Swain: Phys. Rev. A **62**, 013413 (2000)
53. K.H. Drexhage: In *Progress in Optics XII*, ed by E. Wolf (Noth-Holland, Amsterdam, 1974) pp 165–192
54. H. Morawitz: Phys. Rev. **187**, 1792 (1969)
55. R.G. DeVoe, R.G. Brewer: Phys. Rev. Lett. **76**, 2049 (1996)
56. C. Hettich, C. Schmitt, J. Zitzmann, S. Kühn, I. Gerhardt, V. Sandoghdar: Science **298**, 385 (2002)

57. J.R.R. Leit, C.B. de Araujo: Chem. Phys. Lett. **73**, 71 (1980); Z. Ficek, R. Tanaś, S. Kielich: Optica Acta **30**, 713 (1983); G.V. Varada, G.S. Agarwal: Phys. Rev. A **45**, 6721 (1992); Z. Ficek, R. Tanaś: Quantum Opt. **6**, 95 (1994)
58. Th. Richter: Optics Commun. **80**, 285 (1991); C. Skornia, J. von Zanthier, G.S. Agarwal, E. Werner, H. Walther: Phys. Rev. A **64**, 063801 (2001)
59. P. Kochan, H.J. Carmichael, P.R. Morrow, M.G. Raizen: Phys. Rev. Lett. **75**, 45 (1995)
60. J. Eschner, Ch. Raab, F. Schmidt-Kaler, R. Blatt: Nature **413**, 495 (2001)
61. U. Dörner, P. Zoller: Phys. Rev. A **66**, 023816 (2002)
62. A. Beige, J. Pachos, H. Walther: Phys. Rev. A **66**, 063801 (2002)
63. M.O. Scully and M.S. Zubairy: *Quantum Optics* (Cambridge, New York, 1997)
64. G. Breit: Rev. Mod. Phys. **5**, 91 (1933)
65. P. Zhou, S. Swain: J. Opt. Soc. Am. B **15**, 2593 (1998)
66. G.C. Hegerfeldt, M.B. Plenio: Phys. Rev. A **47**, 2186 (1993)
67. Z. Ficek, R. Tanaś, S. Kielich: Optica Acta **33**, 1149 (1986)
68. B. Coffey, R. Friedberg: Phys. Rev. A **17**, 1033 (1978)
69. Th. Richter: Ann. Phys. **38**, 106 (1981)
70. H. Blank, M. Blank, K. Blum, A. Faridani: Phys. Lett. **105A**, 39 (1984)
71. E. De Angelis, F. De Martini, P. Mataloni: J. Opt. B: Quantum Semiclass. Opt. **2**, 149 (2000)
72. T. Hellmuth, H. Walther, A. Zajonc, W. Schleich: Phys. Rev. A **35**, 2532 (1987)
73. A. Zajonc: Phys. Lett. **96A**, 61 (1983)
74. Z. Ficek, R. Tanaś, S. Kielich: J. Mod. Opt. **35**, 81 (1988)
75. G.S. Agarwal, J. von Zanthier, C. Skornia, H. Walther: Phys. Rev. A **65**, 053826 (2002)
76. L. Mandel: Phys. Rev. **134**, A10 (1964)
77. G.M. Meyer, G. Yeoman: Phys. Rev. Lett. **79**, 2650 (1997)
78. H.T. Dung, K. Ujihara: Phys. Rev. Lett. **84**, 254 (2000)
79. T. Rudolph, Z. Ficek: Phys. Rev. A **58**, 748 (1998)
80. H. Kühn: J. Chem. Phys. **53**, 101 (1970)
81. P. Stehle: Phys. Rev. A **2**, 102 (1970)
82. E.M. Purcell: Phys. Rev. **69**, 681 (1946)
83. P. Goy, J.M. Raimond, M. Gross, S. Haroche: Phys. Rev. Lett. **50**, 1903 (1983)
84. R.J. Hulet, E.S. Hilfner, D. Kleppner: Phys. Rev. Lett. **55**, 2137 (1985)
85. W. Jhe, A. Anderson, E.A. Hinds, D. Meschede, L. Moi, S. Haroche: Phys. Rev. Lett. **58**, 666 (1987)
86. D.J. Heinzen, J.J. Childs, J.E. Thomas, M.S. Feld: Phys. Rev. Lett. **58**, 1320 (1987)
87. L.D. Landau: Z. Phys. **45**, 430 (1927) [English translation in *Collected Papers of L. D. Landau*, ed by D. Ter Haar (Gordon and Breach, New York, 1967) pp 8–18.]
88. P. Zhou and S. Swain: Phys. Rev. Lett. **78**, 832 (1997)
89. S-Y. Zhu, R.C.F. Chan, C.P. Lee: Phys. Rev. A **53**, 710 (1995)
90. S-Y. Zhu, M.O. Scully: Phys. Rev. Lett. **76**, 388 (1996)
91. H.R. Xia, C.Y. Ye, S.-Y. Zhu: Phys. Rev. Lett. **77**, 1032 (1996)
92. J. Wang, H.M. Wiseman, Z. Ficek: Phys. Rev. A **61**, 063811 (2000)
93. G.S. Agarwal: Phys. Rev. A **55**, 2457 (1997)
94. P.R. Berman: Phys. Rev. A **58**, 4886 (1998)

95. L. Li, X. Wang, J. Jang, G. Lazarov, J. Oi, A.M. Lyyra: Phys. Rev. Lett. **84**, 4016 (2000)
96. D.A. Lidar, K.B. Whaley: In *Irreversible Quantum Dynamics*, ed by F. Benatti and R. Floreanini, Springer Lecture Notes in Physics, vol. 622 (Springer, Berlin Heidelberg New York, 2003) pp 83–120
97. P.G. Kwiat, A.J. Berglund, J.B. Altepeter, A.G. White: Science **290**, 498 (2000)
98. G. Alzetta, A. Gozzini, L. Moi, G. Orriols: Nuovo Cimento B **36**, 5 (1976)
99. S. Swain: J. Phys. B: At. Mol. Phys. **15**, 3405 (1982)
100. S. Swain: Adv. At. Mol. Phys. **22**, 387 (1986)
101. E. Arimondo: In *Progress in Optics*, ed by E. Wolf (Elsevier, Amsterdam, 1996) pp 257–354
102. H.R. Gray, R.M. Whitley, C.R. Stroud Jr: Opt. Lett. **3**, 218 (1978)
103. M. Kaivola, P. Thorsen, O. Poulsen: Phys. Rev. A **32**, 207 (1985)
104. D. Leibfried, R. Blatt, C. Monroe, D. Wineland: Rev. Mod. Phys. **75**, 281 (2003)
105. A. Aspect, E. Arimondo, R. Kaiser, N. Vansteenkiste, C. Cohen-Tannoudji: Phys. Rev. Lett. **61**, 826 (1988)
106. M.O. Scully: Phys. Rep. **219**, 191 (1992)
107. K.J. Boller, A. Imamoglu, S.E. Harris: Phys. Rev. Lett. **66**, 2593 (1991)
108. J. Mompart, R. Corbalán: J. Opt. B: Quantum Semiclass. Opt. **2**, R7 (2000)
109. A. Imamoglu, J.E. Field, S.E. Harris: Phys. Rev. Lett. **66**, 1154 (1991)
110. G.G. Padmabandu, G.R. Welch, I.V. Shubin, E.S. Fry, D.M. Nikonov, M.D. Lukin, M.O. Scully: Phys. Rev. Lett. **76**, 2053 (1996)
111. N. Bloembergen, Y.R. Shen: Phys. Rev. **133**, 37 (1964)
112. R. Kubo: J. Phys. Soc. Jap. **12**, 570 (1957)
113. B.R. Mollow: Phys. Rev. A **5**, 1522, 2217 (1972)
114. F.Y. Wu, S. Ezekiel, M. Ducloy, B.R. Mollow: Phys. Rev. Lett. **38**, 1077 (1977)
115. M.O. Scully: Phys. Rev. Lett. **67**, 1855 (1991); M. Fleischhauer, C.H. Keitel, M.O. Scully, C. Su, B.T. Ulrich, S.-Y. Zhu: Phys. Rev. A **46**, 1468 (1992)
116. A.D. Wilson-Gordon, H. Friedmann: Optics Commun. **94**, 238 (1992); H. Freedhoff, T. Quang: Phys. Rev. A **48**, 3216 (1993); C. Szymanowski, C.H. Keitel: J. Phys. B **27**, 5795 (1994); C. Szymanowski, C.H. Keitel, B.J. Dalton, P.L. Knight: J. Mod. Opt. **42**, 985 (1995); R.S. Bennink, R.W. Boyd, C.R. Stroud, Jr., V. Wong: Phys. Rev. A **63**, 033804 (2001)
117. C. Cohen-Tannoudji, J. Dupont-Roc, G. Grynberg: *Atom-Photon Interactions* (Wiley, New York, 1992)
118. Z. Ficek, H.S. Freedhoff: In *Progress in Optics*, Vol. XXXX, ed by E. Wolf (North-Holland, Amsterdam, 2000) pp 389–441
119. Z. Ficek, J. Seke, A.V. Soldatov, G. Adam, N.N. Bogolubov, Jr.: Optics Commun. **217**, 299 (2003)
120. M. Kalin, I. Gromov, A. Schweiger: Phys. Rev. A **69**, 033809 (2004)
121. M. Sargent III: Phys. Rep. **43**, 233 (1978)
122. R.W. Boyd, M.G. Raymer, P. Narum, D.J. Harter: Phys. Rev. A **24**, 411 (1981)
123. K. Hakuta, L. Marmet, B. Stoicheff: Phys. Rev. Lett. **66**, 596 (1991)
124. S.E. Harris: Physics Today, July 1997, 36
125. J.P. Marangos: J. Mod. Opt. **45**, 471 (1998)
126. S.E. Harris, J.E. Field, A. Imamoglu: Phys. Rev. Lett. **64**, 1107 (1990)

127. P.A. Lakshmi, S. Swain: J. Mod. Opt. **38**, 2031 (1991)
128. G.Z. Zhang, K. Hakuta, B.P. Stoicheff: Phys. Rev. Lett. **71**, 3099 (1993)
129. A.S. Zibrov, A.B. Matsko, L. Hollberg, V.L. Velichansky: J. Mod. Optics **49**, 359 (2002)
130. B.R. Mollow: Phys. Rev. **188**, 1969 (1969)
131. J. Evers, D. Bullock, C.H. Keitel: Optics Commun. **209**, 173 (2002)
132. E. Paspalakis and P. L. Knight: Phys. Rev. Lett. **81**, 293 (1998)
133. F. Ghafoor, S.-Y. Zhu, M.S. Zubairy: Phys. Rev. A **62**, 013811 (2000)
134. S.-Y. Gao, F.-L. Li, S.-Y. Zhu: Phys. Rev. A **66**, 043806 (2002)
135. M. Macovei, J. Evers, C.H. Keitel: Phys. Rev. Lett. **91**, 233601 (2003)
136. M.A.G. Martinez, P.R. Herczfeld, C. Samuel, L.M. Narducci, C.H. Keitel: Phys. Rev. A **55**, 4483 (1997)
137. S. Menon, G.S. Agarwal: Phys. Rev. A **57**, 4014 (1998)
138. S.-Q. Gong, E. Paspalakis, P.L. Knight: J. Mod. Opt. **45**, 2433 (1998)
139. E. Paspalakis, S.-Q. Gong, P.L. Knight: Optics Commun. **152**, 293 (1998)
140. Z. Ficek, J. Seke, A. Soldatov, G. Adam: Optics Commun. **182**, 143 (2000)
141. E.A. Korsunsky, N. Leinfellner, A. Huss, S. Balushev, L. Windholz: Phys. Rev. A **59**, 2302 (1999); A.F. Huss, E.A. Korsunsky, L. Windholz: J. Mod. Opt. **49**, 141 (2002)
142. S. Swain, P. Zhou, Z. Ficek: Phys. Rev. A **61**, 43410 (2000)
143. H. Huang, S.-Y. Zhu, M.S. Zubairy, M.O. Scully: Phys. Rev. A **53**, 1834 (1996)
144. Z. Ficek, H.S. Freedhoff: Phys. Rev. A **53**, 4275 (1996)
145. Z. Ficek, S. Swain: Phys. Rev. A **69**, 023401 (2004)
146. M. Jakob, Y. Abranyos, J. A. Bergou: J. Opt. B: Quantum Semiclass. Opt. **3**, 130 (2001)
147. A.K. Patnaik, G.S. Agarwal: Phys. Rev. A **59**, 3015 (1999)
148. P. Zhou, S. Swain, L. You: Phys. Rev. A **63**, 033818 (2001)
149. G.S. Agarwal: Phys. Rev. Lett. **84**, 5500 (2000)
150. U. Fano: Phys. Rev. **124**, 1866 (1961).
151. L. Armstrong Jr., B.L. Beers, S. Feneuille: Phys. Rev. A **12**, 2447 (1975)
152. Y.I. Heller, V.I. Lukinykh, A.K. Popov, V.V. Slabko: Phys. Lett. **82A**, 4 (1981)
153. L.I. Pavlov, S.S. Dimov, D.I. Metchkov, G.M. Mileva, K.V. Stemanov, G.B. Altshuller: Phys. Lett. **89A**, 441 (1982)
154. P.E. Coleman, P.L. Knight: J. Phys. B: At. Mol. Phys. **15**, L235 (1982)
155. S. John, T. Quang: Phys. Rev. A **50**, 1764 (1994)
156. S.-Y. Zhu, H. Chen, H. Huang: Phys. Rev. Lett. **79**, 205 (1997)
157. S.E. Harris: Phys. Rev. Lett. **62**, 1033 (1989)
158. S.E. Harris, J.E. Field, A. Kasapi: Phys. Rev. A **46**, R29 (1992)
159. A.G. Truscott, M.E.J. Friese, N.R. Heckenberg, H. Rubinsztein-Dunlop: Phys. Rev. Lett. **82**, 1438 (1999)
160. R. Kapoor, G.S. Agarwal: Phys. Rev. A **61**, 053818 (2000)
161. J.A. Andersen, M.E.J. Friese, A.G. Truscott, Z. Ficek, P.D. Drummond, N.R. Heckenberg, H. Rubinsztein-Dunlop: Phys. Rev. A **63**, 023820 (2001)
162. D. Bortman-Arbiv, A.D. Wilson-Gordon, H. Friedmann: Phys. Rev. A **63**, 043818 (2001)
163. A. Kasapi, M. Jain, G.Y. Yin, S.E. Harris: Phys. Rev. Lett. **74**, 2447 (1995)
164. O. Schmidt, R. Wynands, Z. Hussein, D. Meschede: Phys. Rev. A **53**, R27 (1996)

165. L.V. Hau, S.E. Harris, Z. Dutton, C.H. Behroozi: *Nature* **397**, 594 (1999)
166. M.M. Kash, V.A. Sautenkov, A.S. Zibrov, L. Hollberg, G.R. Welch, M.D. Lukin, Y. Rostovsev, E.S. Fry, M.O. Scully: *Phys. Rev. Lett.* **82**, 5229 (1999)
167. D. Budker, D.F. Kimball, S.M. Rochester, V.V. Yashchuk: *Phys. Rev. Lett.* **83**, 1767 (1999)
168. A.V. Turukhin, V.S. Sudarshanam, M.S. Shahriar, J.A. Musser, B.S. Ham, P.R. Hemmer: *Phys. Rev. Lett.* **88**, 023602 (2002)
169. M.S. Bigelow, N.N. Lepeshkin, R.W. Boyd: *Phys. Rev. Lett.* **90**, 113903 (2003)
170. N.G. Basov, R.V. Ambartsumyn, V.S. Zuev, P.G. Kryukov, V.S. Letokhov: *Sov. Phys. Dokl.* **10**, 1039 (1966) [*Sov. Phys. JETP* **23**, 16 (1966)]
171. S. Chu, S. Wong: *Phys. Rev. Lett.* **48**, 738 (1982)
172. A.M. Akulshin, S. Barrerio, A. Lezama: *Phys. Rev. A* **57**, 2996 (1998)
173. A.M. Akulshin, S. Barrerio, A. Lezama: *Phys. Rev. Lett.* **83**, 4277 (1999)
174. A.M. Akulshin, A. Ciminno, A.I. Sidorov, P. Hannaford, G.I. Opat: *Phys. Rev. A* **67**, 011801 (2003)
175. L.J. Wang, A. Kuzmich, A. Dogariu: *Nature* **406**, 277 (2000)
176. M. Fleischhauer, M.D. Lukin: *Phys. Rev. Lett.* **84**, 5094 (2000)
177. C. Liu, Z. Dutton, C.H. Behroozi, L.V. Hau: *Nature* **409**, 490 (2001)
178. D.F. Phillips, A. Fleischhauer, A. Mair, R.L. Walsworth, M.D. Lukin: *Phys. Rev. Lett.* **86**, 783 (2001)
179. K.E. Cahill, R.J. Glauber: *Phys. Rev.* **177**, 1857 (1969)
180. K.E. Cahill, R.J. Glauber: *Phys. Rev.* **177**, 1882 (1969)
181. W.P. Schleich: *Quantum Optics in Phase Space* (Wiley, New York, 2001)
182. See e.g. *Quantum Squeezing*, ed by P.D. Drummond, Z. Ficek (Springer, Berlin Heidelberg New York, 2004)
183. U. Leonhardt: *Measuring the Quantum State of Light* (Cambridge University Press, Cambridge, 1997)
184. G. Breitenbach, S. Schiller, J. Mlynek: *Nature* **387**, 471 (1997)
185. A.I. Lvovsky, H. Hansen, T. Aichele, O. Benson, J. Mlynek, S. Schiller: *Phys. Rev. Lett.* **87**, 050402 (2001)
186. F. De Martini, G. Di Giuseppe, M. Marrocco: *Phys. Rev. Lett.* **76**, 900 (1996)
187. C. Santori, D. Fattal, J. Vučković, G.S. Solomon, Y. Yamamoto: *Nature* **409**, 594 (2002)
188. C.K. Hong, L. Mandel: *Phys. Rev. Lett.* **54**, 323 (1985)
189. W. Schleich, D.F. Walls, J.A. Wheeler: *Phys. Rev. A* **38**, 117 (1988)
190. V. Bužek, P.L. Knight: In *Progress in Optics*, vol. XXXIV, ed by E. Wolf (Elsevier Science, Amsterdam, 1995) p. 1
191. A.S. Parkins, D.F. Walls: *Phys. Rep.* **303**, 1 (1998)
192. J.I. Cirac, C.W. Gardiner, M. Naraschewski, P. Zoller: *Phys. Rev. A* **56**, R3714 (1996)
193. J. Javanainen, S.M. Yoo: *Phys. Rev. Lett.* **76**, 161 (1996)
194. Y. Castin, J. Dalibard: *Phys. Rev. A* **55**, 4330 (1997)
195. E.M. Wright, T. Wong, M.J. Collett, S.M. Tan, D.F. Walls: *Phys. Rev. A* **56**, 591 (1997)
196. M.R. Andrews, C.G. Townsend, H.-J. Miesner, D.S. Durfee, D.M. Kurn, W. Ketterle: *Science* **275**, 637 (1997)
197. O. Carnal, J. Mlynek: *Phys. Rev. Lett.* **66**, 2689 (1991)
198. J.E. Simsarian, J. Denschlag, M. Edwards, C.W. Clark, L. Deng, E.W. Hagley, K. Helmerson, S.L. Rolston, W.D. Phillips: *Phys. Rev. Lett.* **85**, 2040 (2000)

- 199. D.R. Meacher, P.E. Meyler, I.G. Hughes, P. Ewart: *J. Phys. B* **24**, L63 (1991)
- 200. J.A. Yeazell, C.R. Stroud, Jr.: *Phys. Rev. A* **43**, 5153 (1991)
- 201. M.J.J. Vrakking, D.M. Villeneuve, A. Stolow: *Phys. Rev. A* **54**, R37 (1996)
- 202. M. Brune, F. Schmidt-Kaler, A. Maali, J. Dreyer, E. Hagley, J.M. Raimond, S. Haroche: *Phys. Rev. Lett.* **76**, 1800 (1996)
- 203. D.E. Meekhof, C. Monroe, B.E. King, W.M. Itano, D.J. Wineland: *Phys. Rev. Lett.* **76**, 1796 (1996)
- 204. M. Greiner, O. Mandel, T.W. Hänsch, I. Bloch: *Nature* **419**, 51 (2002)
- 205. W. Ketterle, H.-J. Miesner: *Phys. Rev. A* **56**, 3291 (1997)
- 206. M.O. Mewes, M.R. Andrews, N.J. van Druten, D.M. Kurn, D.S. Durfee, W. Ketterle: *Phys. Rev. Lett.* **77**, 416 (1996)
- 207. Y. Castin, R. Dum: *Phys. Rev. Lett.* **77**, 5315 (1996)
- 208. Y. Kagan, B.V. Svistunov, G.V. Shlyapnikov: *Zh. Eksp. Teor. Fiz.* **42**, 169 (1985) [*JETP Lett.* **42**, 209 (1985)]
- 209. E.A. Burt, R.W. Ghrist, C.J. Myatt, M.J. Holland, E.A. Cornell, C.E. Wieman: *Phys. Rev. Lett.* **79**, 337 (1997)

Index

- absorption, 212
- absorption coefficient, 197, 200, 208, 295
- absorption spectrum, 82, 83, 151, 152, 155, 270, 309
- adiabatic approximation, 209, 329
- Aharonov–Casier effect, 399
- Airy function, 61
- amplification without population inversion, 202, 204, 225
- amplitude modulated field, 223
- anisotropic vacuum approach, 270
- anomalous dispersion, 294, 296, 297, 322, 325
- antinormal ordering, 339
- antisymmetric state, 90, 95, 96, 99, 102, 103, 111, 122, 123, 134, 137, 148, 240, 241
- Area of Overlap method, 366, 368
- areas of overlap, 363
- Autler–Townes spectrum, 83, 84
- autoionization, 275
- autoionizing resonances, 189, 275
- autoionizing state, 271

- bad cavity limit, 269
- Baker–Hausdorff–Campbell formula, 340
- beam splitter, 19, 26
- Beer’s law, 208
- Bell states, 171, 172
- Berry’s phase, 399
- Bessel function, 383
- bichromatic field, 223
- Bohr–Sommerfeld band, 368
- Bohr–Sommerfeld orbits, 369
- Bohr–Sommerfeld quantization condition, 367
- Bohr–Sommerfeld trajectory, 368
- Born approximation, 52
- Bose commutation rules, 20
- Bose–Einstein condensate, 315, 399, 401, 403
- Bose–Einstein condensation, 377
- Bragg interferometer, 399

- cancellation of spontaneous emission, 149
- cavity Q factor, 143
- chaotic field, 345
- characteristic functions, 339, 341, 343
- classical interference, 2, 41
- classical interferometric lithography, 38
- classical phase-space trajectory, 367
- coherence, 5, 122, 227
- coherent population oscillations, 226, 228, 229
- coherent population trapping, 148, 180, 181, 190, 195, 266
- coherent state, 64, 340, 344, 352, 355–358, 360, 361, 371, 372, 394
- collective operators, 95, 98
- collective states, 98, 100, 101
- collisional dephasing, 226, 228
- complementarity, 8, 10, 130, 134
- complementary error function, 288
- configuration interaction, 275
- constructive interference, 7
- continued fraction technique, 216
- continuum states, 275
- coupled state, 182
- CPT, 180
- CPT basis, 202
- cross-damping, 239
- cross-damping rate, 80, 88, 147, 267, 306

- cross-damping term, 57, 66, 88, 252
- dark and bright polaritons, 326
- dark line, 160
- dark state, 123, 148, 150, 332
- dc field, 262–264
- dc field simulation, 262
- de Broglie wavelength, 397, 398
- decay-induced coherence, 57
- decoherence, 139, 171, 208, 348
- decoherence free subspaces, 169, 177, 332
- degree of coherence, 5, 7
- degree of quantum interference, 152
- density matrix equations, 204
- density of states, 140
- density operator, 21, 47, 48, 50, 52, 54, 55, 65, 91, 181, 245, 332, 343
- destructive interference, 7
- Dicke model, 74, 96
- diffraction grating, 378
- dipole correlation functions, 80
- dipole matrix element, 49
- dipole–dipole interaction, 71, 72, 93, 94, 96, 103, 104, 109, 110
- Dirac delta function, 20, 53
- dispersion, 212
- dispersion–absorption relation, 294, 297
- displaced number state, 340
- displacement operator, 340
- distinguishable photons, 253
- Doppler broadening, 233, 234
- Doppler limit, 192
- Doppler width, 234, 236
- dressed states, 222, 225, 226
- dressed-atom model, 220, 222, 225
- Einstein A coefficient, 57
- electromagnetically induced transparency, 196, 200, 229
- enhanced spontaneous emission, 144
- enhancement of nonlinear susceptibilities, 230
- enhancements of the refractive index, 236
- entangled atom-field states, 222
- entangled states, 91–94, 96–98, 101, 103, 104, 111, 137
- entanglement, 91, 92, 98, 104
- EPR paradox, 32
- even coherent state, 358, 360, 361
- external field mixing, 258
- Fabry–Perot cavity, 60, 62
- Fano interferences, 197
- Fano profiles, 189, 237, 271
- Fano spectrum, 281
- fidelity, 171
- first-order coherence, 4, 5, 133
- first-order correlation function, 6, 16, 28, 79, 110–113
- first-order correlations, 17
- Floquet method, 215, 228, 310
- fluorescence spectrum, 82, 83
- Fock state, 340, 343, 344, 352, 354, 355, 363, 368, 369, 371, 373, 387
- Fock state wave-function, 369
- free space photon density of states, 142
- gain with hidden inversion, 203
- gain without population inversion, 155
- Gaussian distribution, 28
- generalized coordinates, 337
- Glauber–Sudarshan P -function, 342
- golden rule, 140, 142
- group velocity, 294–297, 303–309, 311, 313, 314, 316–319, 321, 322, 324, 330
- group-velocity dispersion, 295, 296, 303
- Hanbury-Brown and Twiss interferometer, 17
- harmonic decomposition, 75
- Heisenberg uncertainty relation, 32, 349
- Helmholtz equation, 209, 327
- Hermite polynomial, 369
- Hermitean conjugate process, 186
- Hermitian operator, 20
- hidden variables, 31
- higher order squeezing, 361
- hole burning, 229
- HOM dip, 26, 28
- homodyne tomography, 352
- Hong–Ou–Mandel interferometer, 25
- Husimi Q -function, 342
- identical atoms, 98, 100, 111

- imperfect quantum interference, 154
- implementation of quantum interference, 258
- index of refraction, 219
- indistinguishability, 23
- indistinguishable photons, 254
- inhibition of spontaneous emission, 143
- inhibition of spontaneous emission rate, 142
- intensity quenching, 122
- intensity–intensity correlation function, 264
- interaction picture, 65, 157
- interaction-free measurements, 32
- interference fringes, 1, 2, 7, 8, 17, 34, 40, 107, 113, 114, 135, 389, 392, 393, 396–398
- interference pattern, 1, 6, 7, 9, 11, 14–17, 41, 44, 111–113, 133, 393, 394, 396, 398, 401
- interference pattern with a dark center, 135–137
- interference-induced hole, 155
- interferometric interaction-free measurements, 32
- inversionless gain, 206
- iteration method, 51

- Jaynes–Cummings system, 349
- Josephson junctions, 389, 391

- Kramers–Kröning relations, 212, 218

- ladder configuration, 200
- ladder system, 179, 186, 230, 236
- Laguerre polynomial, 344
- Lamb shift, 59, 285
- lambda system, 179
- Lamor precession frequency, 132
- Laplace transform, 151, 158, 159, 183
- laser cooling, 192
- laser-induced continuum structure, 275, 279
- lasing without inversion, 201
- light guiding light, 297
- Lindblad form, 66, 174
- line narrowing, 160
- linear susceptibility, 197, 211, 231
- Liouville operator, 98
- Liouville–von Neumann equation, 50
- Liouvillean, 147, 176

- Mach–Zehnder interferometer, 19, 20, 33, 34, 36, 397, 399
- Mandel Q parameter, 360
- Markov approximation, 55
- master equation, 47, 51, 62, 65, 67, 84–88, 91, 95, 96, 98–100, 102, 111, 117, 120, 124, 126, 135, 136, 147, 164, 181, 238, 245, 306
- maximal quantum interference, 123, 152, 153, 155
- maximally entangled states, 92, 98, 101, 171
- modified spontaneous emission, 139
- Mollow triplet, 242, 261
- multichromatic driving fields, 223

- narrow spectral line, 154
- negative dispersion, 322
- negative-result measurements, 33
- non-coupled state, 182, 194, 195
- non-Markovian threshold effects, 279
- nonclassical correlations, 23
- nonidentical atoms, 98, 100, 104, 126, 128, 134
- normal ordering, 21, 339
- normalized first-order correlation function, 6
- normalized second-order correlation function, 15, 17, 18

- odd coherent state, 358, 361
- off-diagonal spontaneous decay, 147
- one-photon absorption rate, 39
- one-photon interference, 11
- operator ordering, 339
- optical homodyne tomography, 352
- optical interference, 1

- parametric down conversion, 23
- Paul trap, 107, 115
- perfect interference pattern, 12, 22, 23
- perfect transparency, 155
- perfectly correlated fields, 7
- phase control of quantum interference, 244
- phase control of spontaneous emission, 245

- phase control of the fluorescence spectrum, 247
- phase modulated field, 223
- phase space, 337
- phaseonium, 197
- photoelectrons, 18
- photon antibunching, 19, 84, 348
- photon anticorrelation, 19
- photon bunching, 18, 84
- photon number distribution, 354
- photon number distribution of squeezed state, 373
- photonic bandgap, 145
- photonic bandgap material, 139, 145
- photonic bandgap structures, 282
- photonic crystal, 145
- Pockels cell, 130, 335
- Poisson distribution, 355, 360, 372
- polaritons, 328
- polarization, 208, 210
- pole approximation, 279
- population inversion, 225
- population inversion without lasing, 153
- population trapping, 148, 153, 193, 241, 280, 281, 289
- pre-selected cavity polarization, 267
- principle of causality, 297
- principle of complementarity, 12, 13
- probe amplification, 156
- probing quantum interference, 150
- Q-function, 342
- quadrature operators, 349
- quadrature squeezing, 348, 361
- quantum beats, 85, 115–131, 134
- quantum computing, 30
- quantum correlation function, 23
- quantum cryptography, 30
- quantum eraser, 29
- quantum erasure, 28, 30, 85
- quantum fluctuations, 23, 394
- quantum interference, 1, 20, 21, 26, 42, 47, 48, 57, 66, 74, 82, 85, 86, 88, 107, 110, 115, 117–119, 122, 123, 126, 130, 134, 135, 139, 146–148, 151–156, 160, 162, 169, 180, 189, 192, 202, 236–246, 248, 251, 254–256, 261, 264, 269–271, 282, 283, 287, 289, 301, 305, 309, 337, 338, 346–348, 351, 356–358, 360–362, 368, 369, 372, 376, 377
- quantum interferometric lithography, 38
- quantum metrology, 42
- quantum nonlocality, 30
- quantum regression theorem, 82, 134, 151, 152
- quantum teleportation, 91
- quasi-probabilities, 341
- quasi-probability distributions, 338, 339
- quasi-probability functions, 342
- qubit, 30, 93
- Rabi frequency, 64, 72, 89, 96, 103, 112, 114, 123, 181, 194, 200, 211, 213, 222–225, 227, 230, 234, 238, 242–244, 247, 254, 256, 259–261, 264, 271, 280, 298, 299, 302–304, 307, 309, 310, 326, 328, 330, 382
- Rabi oscillations, 281
- Rabi sidebands, 218, 220, 222
- Raman–Nath approximation, 382, 383
- Rayleigh diffraction limit, 38
- recoil limit, 192
- reconstruction of Wigner functions, 352
- reduced density operator, 47, 51, 52, 62, 63, 68, 269
- refractive index, 83, 197, 200, 294, 296–299, 303, 307, 321, 322
- refractive-index dispersion, 303
- resonance fluorescence, 18
- resonance fluorescence spectrum, 242, 266
- rotating-wave approximation, 54
- Schrödinger cat states, 358
- Schrödinger equation, 157, 272, 284, 366, 367, 379, 380
- Schrödinger picture, 65, 72, 147
- second-order coherence, 15
- second-order correlation function, 15, 16, 22, 25, 30, 80, 111, 133, 134, 403
- self-delayed pulses, 322
- self-induced transparency, 197
- semiclassical dressed states, 221
- single photon diffraction limit, 40, 42

- single-mode squeezed state, 346
- single-photon states, 353
- slowly varying amplitude, 208, 209, 215
- sodium dimers, 162
- spatial coherence, 1
- spatial correlations, 25
- spatial nonclassical interference, 21
- spatial propagation of EM fields, 207
- spectral control of spontaneous emission, 156
- spontaneous decay, 127, 146, 147, 176, 181, 182, 184, 187, 230, 235
- spontaneous decay rate, 86, 143, 164
- spontaneous decay time, 106
- spontaneous emission rate, 57, 107, 109, 144
- spontaneous symmetry breaking, 387
- spontaneously induced coherences, 99
- squeeze operator, 346
- squeezed coherent state, 345
- squeezed fields, 349
- squeezing, 350
- Stark shift, 59, 279
- Stern–Gerlach apparatus, 31
- sub-Poissonian field, 360
- sub-Poissonian statistics, 360
- subradiant, 141
- super-Poissonian field, 360
- superbunching, 251, 264
- superluminal light, 322, 326
- superoperator, 164
- superposition of coherent states, 356
- superposition operators, 86, 101, 102
- superposition states, 85–91, 123, 148, 239, 252
- superpositions of N coherent states, 356
- superpositions of Fock states, 348
- superpositions of two coherent states, 357
- superradiant, 141
- superradiant effect, 127, 128
- susceptibility, 210
- symmetric and antisymmetric states, 150
- symmetric characteristic function, 343
- symmetric characteristic functions, 355
- symmetric ordering, 339
- symmetric state, 95, 96, 102, 111, 122, 123, 137, 148, 241
- temporal coherence, 1
- temporal correlations, 25
- terylene molecules, 109
- tests for decoherence free subspace, 173
- thermal field, 55
- third-order correlation function, 43–45
- three-photon classical interference, 43
- three-photon interference, 42
- time-to-digital converter, 108
- transmissivity, 11–13
- trapped ions, 13, 107
- trapping potential, 389, 396
- tunnelling, 401
- tunnelling frequency, 390
- two-dimensional Fourier transform, 341
- two-photon absorption rate, 40
- two-photon classical state, 40
- two-photon coherence, 183
- two-photon correlations, 25
- two-photon excitation, 109, 164
- two-photon interference, 23, 25, 27, 42
- two-photon quantum interference, 23
- two-photon Rabi frequency, 163, 230, 277
- two-photon resonance, 281, 282
- two-photon transition, 166
- uncertainty principle, 11, 23
- uncorrelated fields, 7
- unitary transformation, 86, 181
- vacuum induced coherences, 147
- vacuum interaction, 139, 147, 158
- vacuum Rabi frequency, 327
- Vee system, 146, 179, 186
- velocity-selective coherent population trapping, 192
- visibility, 7–9, 17, 22, 23, 30, 44–46, 114, 135–137, 389, 394, 398
- welcher weg experiment, 10
- welcher weg problem, 7, 10, 389
- Wentzel–Kramers–Brillouin method, 366
- which-way information, 29
- Wigner function, 342–348, 350–352, 355, 356, 358, 363, 366, 373, 376

- | | |
|--|---|
| Wigner–Weisskopf approximation, 158, 285 | Young’s double slit interferometer, 2, 13, 397, 399 |
| Wigner-weighted overlap method, 373 | Yurke–Stoler coherent state, 358, 360, 361 |
| WW-overlap method, 373 | Zeeman sublevels, 129, 132 |

